The Pennsylvania State University
The Graduate School
Department of Electrical Engineering

MULTISTATIC LIDAR PROFILE MEASUREMENTS OF LOWER TROPOSPHERIC AEROSOL AND PARTICULATE MATTER

A Thesis in
Electrical Engineering

by
Edward J. Novitsky

Submitted in Partial Fulfillment
of the Requirements
for the Degree of

Doctor of Philosophy

May 2002

We approve the thesis of Edward J. Novitsky.

Date of Signature

C. Russell Philbrick
Professor of Electrical Engineering
Thesis Advisor & Chair of Committee

Stewart K. Kurtz
Professor of Electrical Engineering

Dennis Lamb
Professor of Meteorology

Victor Pasko
Associate Professor of Electrical Engineering

Sven G. Bilen
Assistant Professor of Engineering Design
and Electrical Engineering

W. Kenneth Jenkins
Head of the Department of Electrical Engineering

ABSTRACT

There is growing interest in the continuous monitoring of the vertical transport and distribution of aerosols and particulates. Laser remote sensing offers a practical tool to accomplish this task. A U.S. Environmental Protection Agency-sponsored field study was conducted in the city of Philadelphia in the summer of 2001 as part of the North-East Oxidant and Particulate Study. This study brought together a consortium of researchers to measure and investigate pollutants and particulate matter in an urban environment. Our own investigation focused on the vertical atmosphere from 10 meters to 100 meters in altitude. Measurements of the parallel and perpendicular polarization components of the laser were taken and then divided to form a polarization ratio. Using the polarization ratio as opposed to analyzing a particular polarization component significantly reduces instrument errors and alleviates the need for range and volume corrections while still retaining the characteristics produced from scattering. In order to obtain aerosol distribution parameters, the polarization ratio measurements were fitted with an atmospheric model that combined Mie theory and a trimodal lognormal aerosol distribution. The aerosol distribution model used particles in the range from I nanometer to 35 micrometers. While the monitoring of vertical aerosol profiles was shown to be possible, accurate inversion of the aerosol parameters still poses significant challenges.

A theoretical investigation of the polarization ratio determined that the total observed scattering angle range should be at least 10 degrees for an atmosphere that contains ultrafine, fine and coarse aerosol modes (i.e., trimodal aerosol number density population). However, for distributions that are more monodispersed or for atmospheric distributions that contain a significant number of large particles (such as in the case of radiation fog), fewer observed scattering angles are needed. Additionally, the polarization ratio was found to be insensitive to the imaginary part of the refractive index but very sensitive to changes in the real part of the refractive index. Subsequently, the scattering model could not model the imaginary part of the index of refraction.

Experimental results of the nighttime atmosphere revealed the presence of aerosol variations over altitude. Further, a time sequence of several data sets showed rapid changes in the aerosol profile over time and in space. The overall observed nighttime atmospheric variability is in contrast to the daytime where convective forcing yields a much more uniformly distributed atmosphere. Modeling of the aerosol profile suggested the aerosol variations might depend on several factors, not necessarily only total number density. To specify the exact nature of the altitude dependence, direct measurement of the aerosols at the observed altitudes is needed. However, some data that was taken indicated a uniformly mixed atmosphere and thus allowed the retrieval of aerosol parameters. Fits of the model to this data used real refractive indices of refraction from 1.33 to 1.45 and clearly demonstrated the influence the refractive index has on the accuracy of the retrieved parameters.

TABLE OF CONTENTS

LIST OF FIGURES

LIST OF TABLES

ACKNOWLEDGEMENTS

The work presented in this thesis was supported in part by the United State Environmental Protection Agency, grant # R826373. However, not a word could have been written without the guidance, patience and understanding of C. Russell Philbrick. At the end of my days, if I find myself to be half the man he is, I will consider my life a success. I am forever in his debt.

1

Chapter 1: Introduction

Sometimes a scream is better than a thesis.

In 1996, Tim Stevens, pursuing his PhD at The Pennsylvania State University, conducted an experiment using light scattering techniques and a novel polarization ratio method to investigate coastal marine aerosols (Stevens, 1996). Stevens' experiment was instrumental in demonstrating that his approach could indeed be used to obtain particle size density information of the open atmosphere. Given that the atmosphere is a complicated and complex environment, Stevens' results, although admittedly limited, were nonetheless remarkable. The purpose of this work is to further expand the application of Stevens' approach while at the same time attempting to answer several critical questions that arose during the course of his study. However, while Stevens investigated a horizontal atmospheric path, our intention here is to examine a vertical atmospheric path (aka, a profile). This change in observed path posed several problems with which Stevens did not need to contend.

The interested reader who needs to conduct research in the area of light scattering by atmospheric particles is strongly encouraged to read and understand Stevens' thesis first as we make extensive use of it here. One will find Stevens' thesis, as we did, to be very well written and contains an exceptional amount of useful information and results. It is also our aspiration to make this study as useful to the reader and so we will try to be as inclusive as possible with the presented material. Thus, it is our desire that this study be able to stand on its own but not by itself.

1.1 INTRODUCTION

The goal of this work is to use light scattering techniques to investigate the vertical profile[‡] of atmospheric particulates and pollutants, sometimes collectively referred to as aerosols. As one would imagine, the atmosphere is a very large and dynamic place as it not only changes on a daily basis but also differs greatly based on geographic location. Because the atmosphere is so dynamic, researchers have understandably shied away from tackling it head-on but rather have decided to attack it via a "divide and conquer" strategy. Direct measurement of particulates and subsequent chemical analysis is the current approach used in the investigation of atmospheric particles. The light scattering used in this work, however, infers characteristics about atmospheric constituents and is not currently able to perform more precise measurements due to uncertainties with both the mathematical model and experimental limitations. Despite the uncertainties with using light scattering, the approach can do one thing that most other

[‡] The words "vertical profile" are redundant so from here on we will simply use "profile."

instruments cannot. Using light scattering as a remote sensing technique allows measurements to be taken continuously with no interruption and can also access regions of the atmosphere where it is not possible or practical to sustain measurements. In this work, we will use remote sensing by a lidar unit to investigate and help us understand the atmospheric profile of aerosols. Historically, it has been difficult to obtain such measurements with balloons and aircraft due to flight and manpower limitations.

The motivation of this study is to gauge the aerosol/particulate/pollutant profile and content under the nighttime planetary boundary layer (PBL) of the earth's atmosphere in an urban environment. The bulk of the work presented here was performed in the city of Philadelphia but some additional study was completed in State College, PA. As an overview, we used three CCD cameras to image a vertically-directed laser beam under nighttime conditions. Building on what Stevens accomplished, we wished to be able to infer the aerosol and particle composition present both in terms of the number size density and, if possible, by its chemical composition (via the index of refraction). The intent of this chapter is to be a simple and brief introduction to the work being presented (in essence an executive summary). As one will discover, the chapters that follow contain considerably more in-depth discussion.

1.2 BISTATIC METHODOLOGY

Stevens used a single linear diode array, mounted on the focal plane of a 35mm single lens reflex (SLR) camera, to image a 140-meter horizontal atmospheric path (Figure 1.1). By recording the parallel

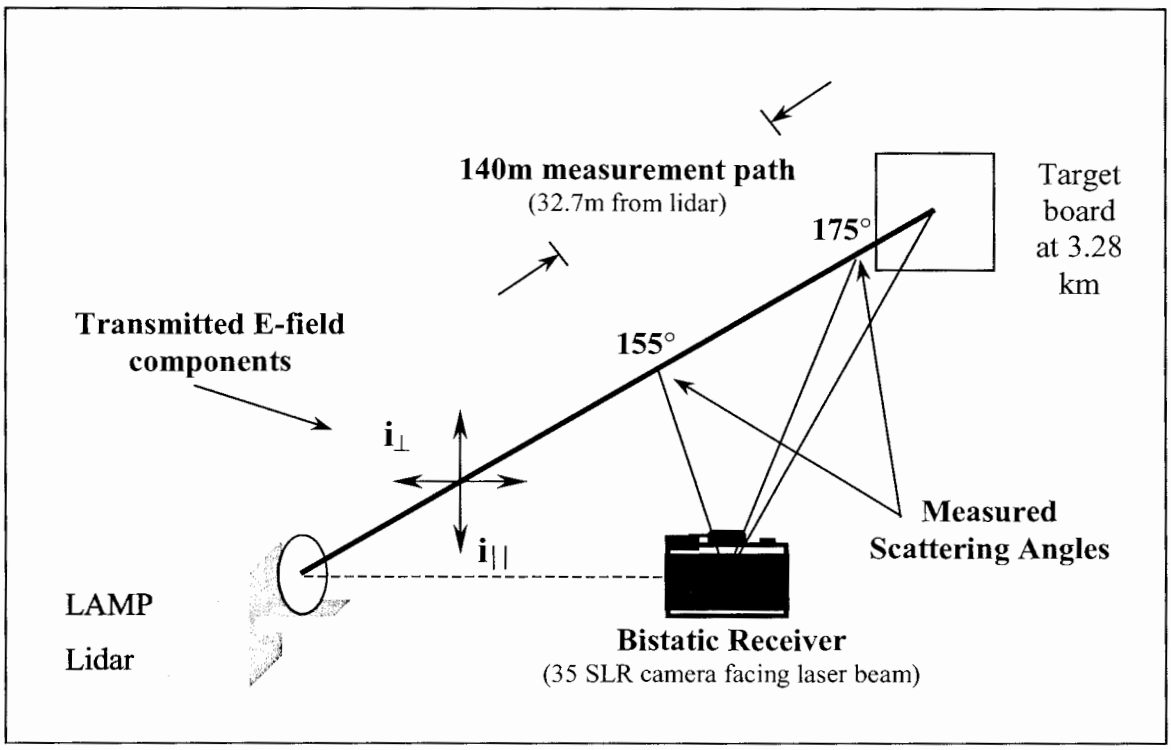

Figure 1-1: Bistatic arrangement used by Stevens.

and perpendicular polarizations of the laser beam and then ratioing the two measurements, Stevens was able to avoid many instrument-related errors that would corrupt the analysis of his data. Further, this polarization ratio approach also avoided having to make range and volume corrections to each pixel (See Chapter 5 for more information). Since the receiver (camera) is separate from the transmitter (lidar), this arrangement is termed bistatic (Figure 1.2). In our study, we will employ several independent imaging devices, which we term a multistatic configuration. Further, Stevens was operating in a warm and humid coastal marine environment, which allowed him to assume a fixed index of refraction thereby assuming (and rightly so) a particular chemical makeup of the aerosols present. On one notable night, Stevens observed the formation of radiation fog (a nearly monodispersed aerosol) and was able to successfully and quite astonishingly obtain an exceptionally close fit of the data to his model (Figure 1.3). However, this particular night's data was the exception rather than the rule as Stevens found difficulties in fitting the into model to the data (Figure 1.4). The results of Figure 1.3 are remarkable and further fuelled our research

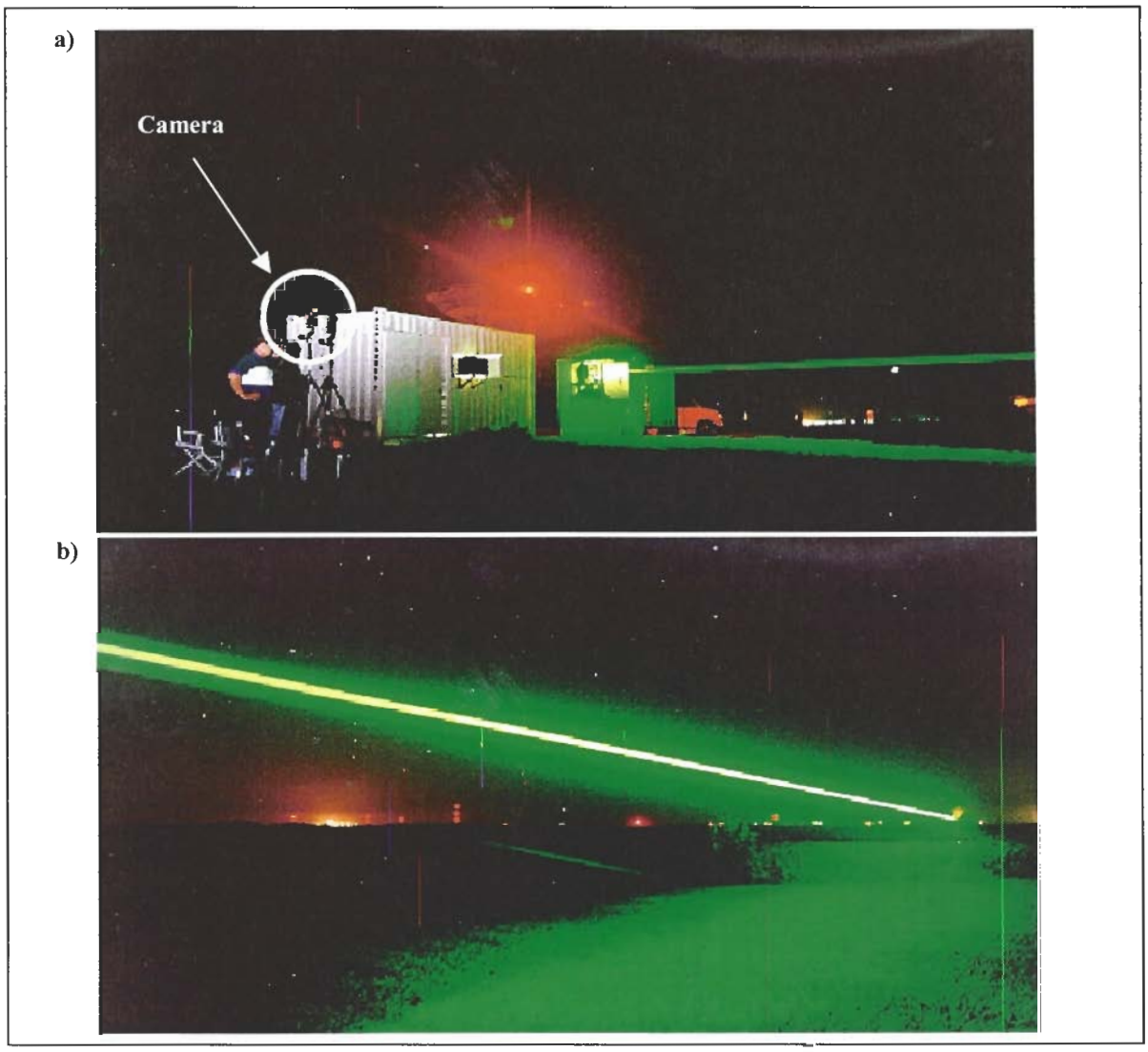

Figure 1-2: a) On-site operation of Stevens' bistatic receiver. b) Beam seen by receiver.

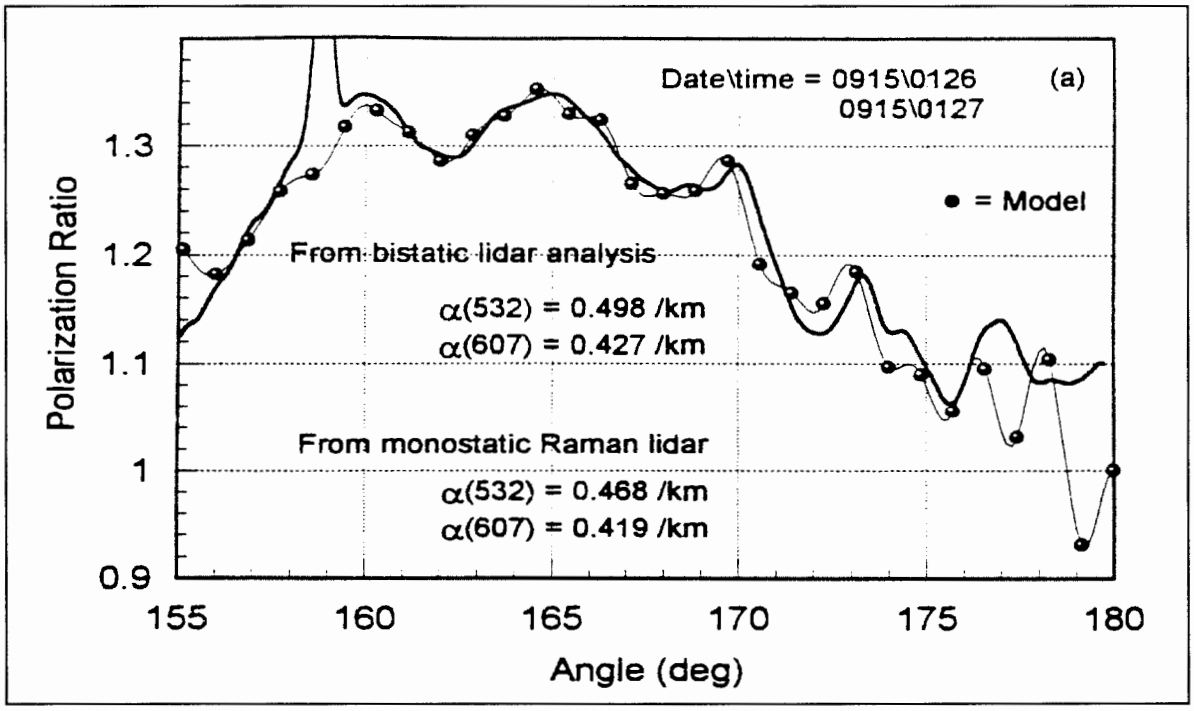

Figure 1-3: Very close fit of model to the observed data found by Stevens (Stevens, 1996, fig. 5-18).

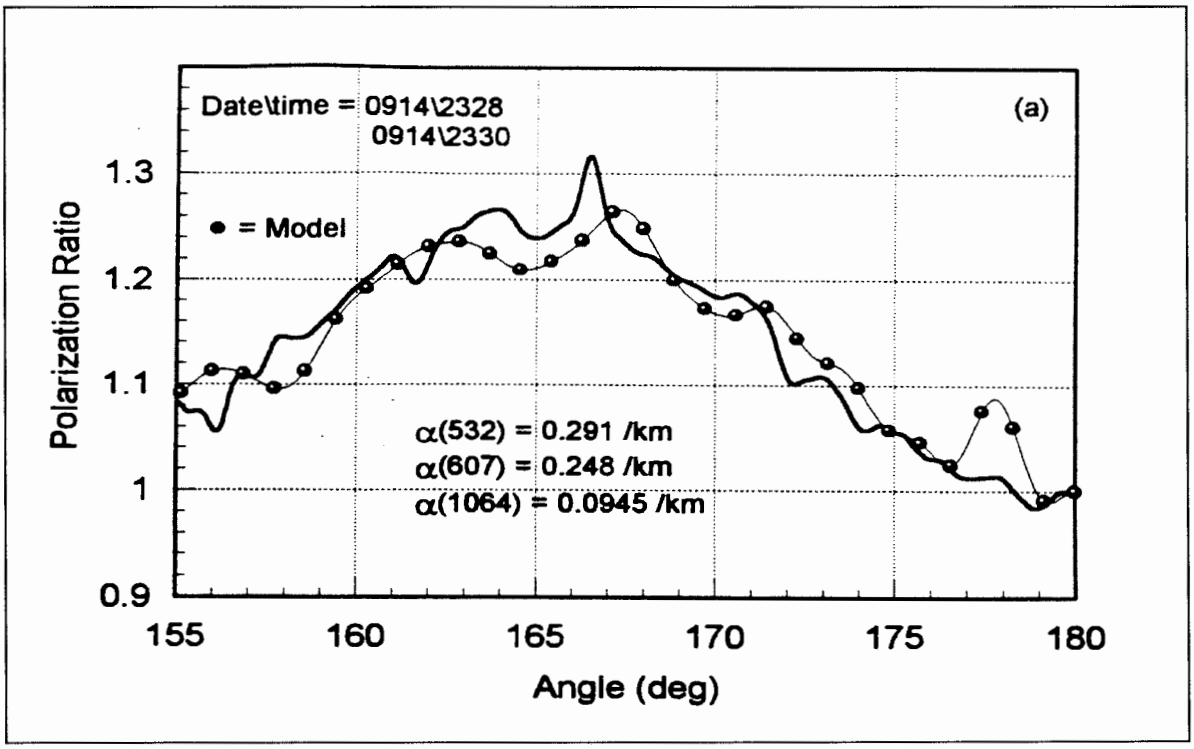

Figure 1-4: Typical results obtained by Stevens showed noticeable differences between the model and the observed data (Stevens, 1996, fig. 5-14).

the present study.

Overall, Stevens was able to obtain reasonable agreement between the data and the model. However, there were still several major questions that arose which had to be left for future studies. For example, Stevens did not have direct measurements of the actual particle size distributions with which to compare to the distributions he obtained through inversion. In other words, although Stevens obtained a mathematical solution, how close was this to the actual physical distribution actually present? Stevens certainly made plausible arguments based on supporting information but the most crucial piece of information that was needed to validate his results was that the physical mechanism he was observing (condensation) does yield large particles that are very narrowly distributed.

Additionally, in his atmospheric model, there are 10 parameters that can be varied in order to get the model to match the data of which he kept the index of refraction fixed at 1.38. Immediately, the question arises as to the impact a variable index of refraction will have during the inversion process. Since no one atmospheric study can possibly answer all questions, these and other questions were left unanswered.

1.3 GOALS & HYPOTHESIS OF THIS THESIS

The primary goal of this thesis is to determine how well the method used by Stevens could be used and adapted to investigate the aerosol profile of the lower troposphere. Specifically, there are several issues we wish to address.

The first major objective of this work was to determine what exactly was needed in terms of theory and equipment in order to adequately investigate the vertical aerosol composition and distribution. For example, how well could the approach employed by Stevens describe the vertical aerosol distribution? Independent and different approaches have not investigated aerosol profiles to the spatial resolution we are using in this thesis so additional, supportive information is difficult to find. As a preview, the results of this study were able to show not only the presence of a strong altitude dependence of the aerosols but also the presence of aerosol layers that could vary in size and composition.

The second major objective was to allow the index of refraction to change during the inversion process. In several of Stevens' inversions, there were instances that his model did not fit the data. Stevens suggested that it might be possible to get better fits if the index of refraction was allowed to change but he did not pursue this due to limitations in the available computing power. Our goal was to take a closer look at the effect the index of refraction has on the polarization ratio method and, if possible, infer the chemical composition of the aerosols present. The results of our investigation with the index of refraction are given in Chapters 3 and 5. From our investigation, we believe that the index of the refraction was not the source of the discrepancy between Stevens' data and model but rather that the atmospheric path was non-uniform.

The last major objective was to provide answers to questions that arose from Stevens' results. We do not simply want to re-visit his approach but rather to examine it critically and, by extending the analytical approach, provide more in-depth reasoning behind his and our work. We certainly have our work cut out for us.

2

Chapter 2: The Mathematics of the Lognormal Distribution

The truth is out there.

The lognormal distribution is a key element behind many mathematical models describing the aerosol size density distribution in the atmosphere. Although several other mathematical models have been and continue to be used in describing aerosol distributions, the lognormal function has been found to be valid over a wider range of particle sizes and under more atmospheric conditions than other distributions. However, the mathematical language employed by atmospheric scientists to describe lognormal distributions is different than the language used by mathematicians. In our research, we did not find a single source that was able to show both the mathematics of the lognormal distribution as well as the application of the distribution to atmospheric particles (Crow and Shimizu, 1988, provided a limited description). Here, we intend to show both the mathematical description and physical application of the lognormal function in atmospheric particle science. Those who are already familiar with lognormal distributions as they are used in the aerosol and particle scientific literature can easily skip this chapter but Section 2.4 would still be useful for understanding the function that will be used throughout this thesis. This is the first time that both an intensive mathematical derivation and a particle derivation of the lognormal function exist side by side in order to compare and contrast the statistics used by both. The reader is forewarned that this chapter is not an easy read. Although it might seem so, it was not our intention to confuse the reader with a barrage of equations but rather to give a complete and thorough description of the lognormal distribution.

Although this chapter is predominantly interested in a theoretical analysis of the lognormal distribution, at the end of this chapter we will tackle the lognormal distribution from an experimentalist's point of view and show why the definitions used in aerosol literature have evolved into different meanings than those used by statisticians. One last thing…we use the word distribution to refer to a collection of items, *i.e.*, the ordinate has some units. However, we use the word density to refer to the mathematical function that describes the statistics of the distribution. In the literature, these words are often used interchangeably and can cause confusion.

Our focus of using the lognormal function is to describe atmospheric aerosol size distributions. Thus, this chapter describes the lognormal function as it is used by the scientific research community. However, the true mathematical definitions and derivations of the lognormal function are included in Appendix A. While we do not directly make use of the results in Appendix A in this thesis, the information presented there is still beneficial to understanding the history of the lognormal function. The interested reader is directed to Appendix A before reading this chapter.

2.1 THE STANDARD PROBABILITY DENSITY FUNCTION

Most contemporary statistical texts simply state the normal distribution function and do not indicate its origins. We would like to step back and at least mention that the normal function is derived from the Bernoullian law (See Herdan, p. 74). The lognormal function can then be derived from the normal function (the mathematician's approach) but interestingly, the normal function can also be derived from the lognormal function (the physicist's approach).

2.1.1 Statistics of the Standard Normal Density Function

Consider the continuous probability density function (pdf)

$$f_Z(z) = \frac{1}{\sqrt{2\pi}} e^{-z^2/2} \tag{2-1}$$

which is called a standard normal pdf. Here, the upper case letter Z represents the random variable while the lower case z represents the value of the random variable. There are several properties that all continuous pdfs must obey (Papoulis, pp. 69-73):

1. $f_Z(z) \neq P(Z = z)$ if Z is a continuous random variable (Larsen and Marx, p. 185). The term, $P(Z = z)$, is the probability that the random variable Z takes on the value z.
2. $f_Z(z) \geq 0, \quad \forall z$.
3. $f_Z(z) = \frac{dF_Z}{dz}; \qquad F_Z(z) = \int_{-\infty}^{z} f_Z(z)dz$

   where $F_Z(z)$ is called the cumulative distribution function (cdf).
4. $\int_{-\infty}^{\infty} f_Z(z)dz = 1$. It can be shown that the standard normal pdf of Eqn. 2-1 satisfies this property by evaluating through the use of polar coordinates (Larsen and Marx, p. 320).
5. $P(z_1 \leq Z \leq z_2) = \int_{z_1}^{z_2} f_Z(z)dz$.

Although there are others, the primary statistics of pdfs are the expected value (mean) and variance. These two statistics give an indication of a pdf's average value and its dispersion (spread) around the mean respectively. As most are already familiar with normal density functions, determining the expected value and variance is trivial but is presented here for completeness.

2.1.1.1 Expected Value of the Standard Normal Density Function

The expected value (a.k.a. 1st moment) of a random variable is defined by

$$\mathbf{E}\{z\} = \int_{-\infty}^{\infty} z f_Z(z) dz \,. \tag{2-2}$$

By substituting Eqn. 2-1 into the above equation, the expected value of a standard normal density function is evaluated to be

$$\begin{aligned} \mathbf{E}\{z\} &= \frac{1}{\sqrt{2\pi}} \int_{-\infty}^{\infty} z e^{-z^2/2} dz \\ &= -\frac{1}{\sqrt{2\pi}} e^{-z^2/2} \Big|_{-\infty}^{\infty} \\ &= 0 \\ &\equiv \mu_Z \,, \end{aligned} \tag{2-3}$$

where μ_Z is used to represent the expected value of the random variable Z. It should be noted that the units of the expected value are the same as the random variable (Larsen and Marx, p.264).

2.1.1.2 Variance of the Standard Normal Density Function

The variance (a.k.a. 1st central moment about the mean) of a random variable is defined by

$$\begin{aligned} \mathbf{Var}\{z\} = \mathbf{E}\left\{(z-\mu_Z)^2\right\} &= \int_{-\infty}^{\infty} (z-\mu_Z)^2 f_Z(z) dz \\ &\equiv \sigma_Z^2 \,, \end{aligned} \tag{2-4}$$

where σ_Z^2 represents the variance and σ_Z represents the standard deviation of the random variable Z (as with the expected value above, the standard deviation, σ_Z, has the same units as the random variable). The variance is a measure of the concentration of the random variable near its mean (Papoulis, p. 108), *i.e.*, σ_Z^2 is the mean of the random variable $(z - \mu_Z^2)$. By expanding Eqn. 2-4, the variance can be written as

$$\sigma_Z^2 = \mathbf{E}\left\{z^2\right\} - \mathbf{E}^2\{z\}, \tag{2-5}$$

which requires the solution of the 2nd moment

$$\begin{aligned} \mathbf{E}\left\{z^2\right\} &= \int_{-\infty}^{\infty} z^2 f_Z(z) dz \\ &= \frac{1}{\sqrt{2\pi}} \int_{-\infty}^{\infty} z^2 e^{-z^2/2} dz. \end{aligned} \tag{2-6}$$

By using integration by parts with $u = z, dv = ze^{-z^2/2}dz$, the integral is found to yield a value of 1. Since the expected value of the standard normal density function was found to be zero, substituting into Eqn. 2-5 yields

$$\boldsymbol{\sigma}_Z^2 = 1 .$$

2.2 THE GAUSSIAN/NORMAL PROBABILITY DENSITY FUNCTION

The Gaussian or Normal pdf is frequently encountered and its statistics are well known. The derivation presented here results from procedures and rules using the standard pdf from section 2.1 as the starting point. It is these same rules that will be used in the next section to derive the lognormal pdf.

The standard normal random variable Z is related to the Gaussian random variable Y through the transformation (Larsen and Marx, p. 321)

$$Z = \frac{Y - \boldsymbol{\mu}}{\boldsymbol{\sigma}} = g(Y) . \tag{2-7}$$

Here, the random variable Z has been related to the random variable Y through scaling and shifting. Such a transformation would be necessary in converting Fahrenheit to Celsius. We next see what effect the above transformation has on the statistics of the random variable Y.

Rather than returning to elementary principles to determine the statistics of the Gaussian pdf, we can use several theorems to relate $f_Z(z)$ to $f_Y(y)$. Since the transformation, $g(Y)$, meets the criteria for being a random variable (Papoulis, p. 87), then fundamental theorems (Papoulis, eqns. 5-4, 5-5, p. 93) can be used to find the pdf of the new variable:

$$f_Y(y) = \frac{f_Z(z_1)}{|g'(z_1)|} + \cdots + \frac{f_Z(z_n)}{|g'(z_n)|}, \tag{2-8}$$

where z_i ($i = 1 \ldots n$) are the roots of $g(z)$ and $g'(z)$ is the derivative. Rearranging the transformation of Eqn. 2-7, we have

$$Y = \boldsymbol{\sigma} Z + \boldsymbol{\mu} = g(Z) . \tag{2-9}$$

There is only 1 root of $g(Z)$ which is given by Eqn. 2-7. Thus, evaluating Eqn. 2-8 yields,

$$f_Y(y) = \frac{f_Z\left(\frac{Y-\mu}{\sigma}\right)}{\left|g'\left(\frac{Y-\mu}{\sigma}\right)\right|}$$
$$= \frac{1}{\sigma} f_Z\left(\frac{Y-\mu}{\sigma}\right)$$
$$= \frac{1}{\sigma\sqrt{2\pi}} \exp\left(-\frac{1}{2\sigma^2}(y-\mu)^2\right), \tag{2-10}$$

which is the pdf for a Gaussian random variable.

2.2.1 Statistics of the Gaussian Random Variable

Direct integration using Eqns. 2-2, 2-4 and 2-6 (with the appropriate substitutions for the random variable *Y*) is, of course, plausible but, using properties and theorems of expected variables are much more desirable. This will be our approach in the next several subsections.

2.2.1.1 Expected Value of the Gaussian Probability Density Function

Using Eqn. 2-9, the relationship between the expected values of the random variables *Y* and *Z* is found to be

$$\mathbf{E}\{y\} = \mathbf{E}\{\sigma z + \mu\}$$
$$= \sigma \mathbf{E}\{z\} + \mu$$

(Larsen & Marx, p. 243, Theorem 5.3.1). Since the expected value of the standard normal random variable was found to be zero, the expected value of the Gaussian random variable is

$$\mathbf{E}\{y\} = \mu \tag{2-11}$$
$$\equiv \mu_Y.$$

2.2.1.2 Variance of the Gaussian Probability Density Function

Using the definition of variance, Eqn. 2-4, the relation between the variance of the random variables *Y* and *Z* yields

$$\mathbf{Var}\{y\} = \mathbf{E}\left\{(y-\mu_Y)^2\right\} \tag{2-12a}$$
$$= \mathbf{E}\left\{(\sigma z + \mu - \mu_Y)^2\right\}$$
$$= \mathbf{E}\left\{(\sigma z)^2\right\}$$
$$= \sigma^2 \mathbf{E}\left\{z^2\right\}$$
$$= \sigma^2$$
$$\equiv \sigma_Y^2. \tag{2-12b}$$

From the explicit definition of variance (Eqn. 2-11a), the variance is a measure of the concentration, or spread, of a random variable about its mean (Papoulis, p. 108; Larsen and Marx, pp. 263-264) and so the standard deviation provides a measure of a random variable's dispersity. The variance is actually the 2nd central moment† of a random variable (Papoulis, p. 109, eqn. 5-39). However, the moments about additional points (such as the mode or median) can also be obtained by replacing μ_y with the desired point. Such moments are termed generalized moments (Papoulis, p. 109, eqn. 5-41).

2.2.1.3 Illustration of the Gaussian Probability Density Function

A graphical example of the Gaussian pdf with $\mu = 0.5$ and $\sigma = 0.3$ is shown in Figure 2-1. A unique aspect of the Gaussian pdf is that the area under the curve up to each standard deviation point from the mean (*i.e.*, area under $\mu \pm \sigma$) is constant for any combination of the parameters μ and σ. Specifically,

$$\int_{-\infty}^{\mu-\sigma} f_Y(y)dy = 0.1593 \tag{2-13a}$$

$$\int_{-\infty}^{\mu+\sigma} f_Y(y)dy = 0.8419 \tag{2-13b}$$

$$\int_{\mu-\sigma}^{\mu+\sigma} f_Y(y)dy = 0.6826. \tag{2-13c}$$

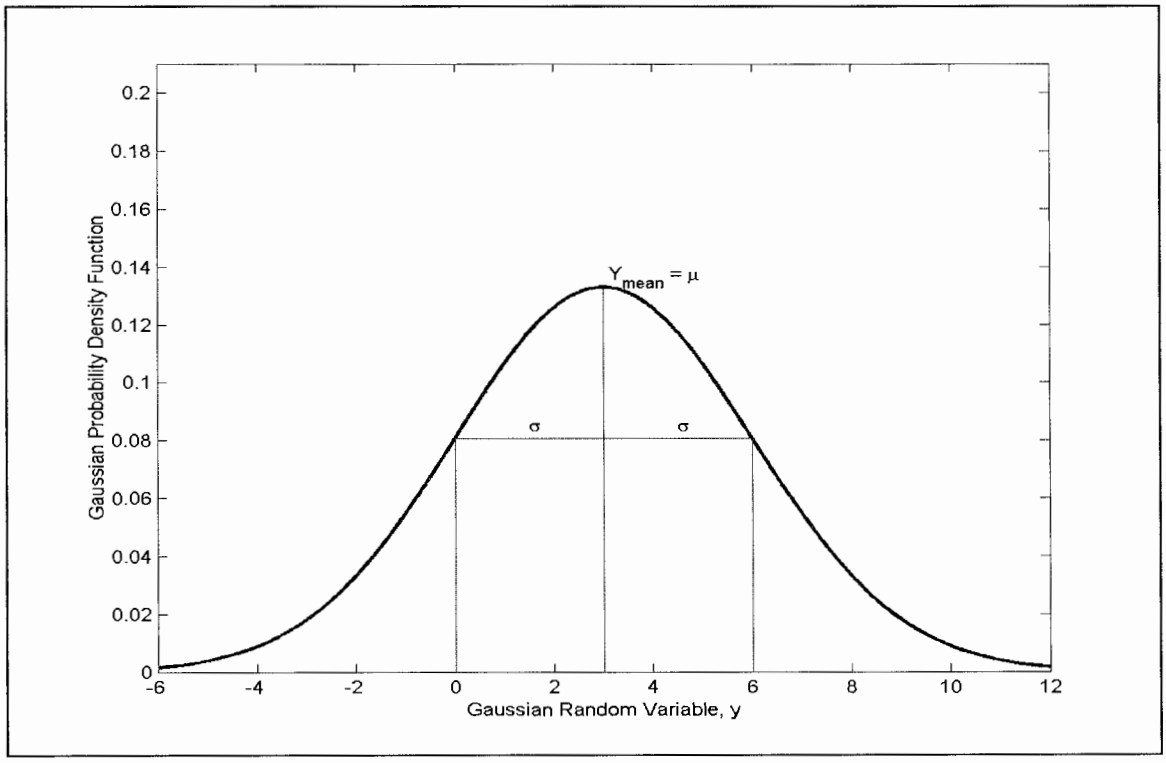

Figure 2-1: Illustration of the Gaussian probability density function with $\mu = 3$ and $\sigma = 3$.

† Central moments are always around the mean.

The question is, why is this true? This isn't true for every pdf (as we'll see for the lognormal pdf) so why is this true for the Gaussian pdf? A proof has not been found but a possibility lies in the fact that the 2nd derivative of the Gaussian pdf reveals that the inflection points occur at the same points as does the first derivative, *i.e.*, always at $\mu \pm \sigma$ (which represents points within one standard deviation of the mean). We will explore the use of derivatives in obtaining the characteristics of the various distributions in future sections.

2.2.2 Notation of the Gaussian and Lognormal Probability Density Functions

The notation used to describe the Gaussian pdf is typically given as $N(\mu, \sigma^2)$ or sometimes as $N(\mu, \sigma)$. For lognormal pdfs, the notation is $\Lambda(\mu, \sigma^2)$. From the statistics of the Gaussian pdf, we know that μ and σ^2 are the mean and variance. However, as we will see, the mean and variance for a lognormal pdf are quite different. Some confusion may arise by this notation because of the double meanings μ and σ have for the Gaussian pdf. Rather than thinking of μ and σ^2 to be the mean and variance of the Gaussian pdf, confusion may be eliminated if they are simply thought of as characterization parameters, *i.e.*, they describe the shape of the Gaussian pdf. It just so happens, that in the case of the Gaussian function, these parameters also double as the mean and variance.

2.3 THE LOGNORMAL PROBABILITY DENSITY FUNCTION

The transformation that relates the Gaussian random variable, Y, to the lognormal random variable, X, is (Papoulis, p. 97)

$$X = e^Y = g(Y), \tag{2-14}$$

which has the root, $y_1 = \ln x$. Using Eqn. 2-8, the lognormal pdf is given by

$$f_X(x) = \frac{f_Y(Y_1)}{|g'(Y_1)|} = \frac{f_Y(Y_1)}{|e^{Y_1}|},$$

and substituting for the root, y_1, yields

$$f_X(x) = \begin{cases} \dfrac{1}{\sqrt{2\pi}\cdot\sigma x}\exp\left(-\dfrac{1}{2\sigma^2}(\ln(x)-\mu)^2\right), & x > 0 \\ 0, & x < 0 \\ \text{undefined}, & x = 0 \text{ (singularity)}. \end{cases} \tag{2-15}$$

Equation 2-15 is the formal mathematical definition of the lognormal probability density function. This is a probability density function, not a distribution function.

The derivation of the statistics of the lognormal function is shown in Appendix A. Here, we simply summarize the (true) mathematical statistics. The mean, variance, median, and mode of the lognormal function are, respectively,

$$\begin{aligned} \mathbf{E}\{x\} &= e^{\mu+\sigma^2/2} \\ &\equiv \mu_{LN}, \end{aligned} \tag{2-16}$$

$$\begin{aligned} \mathbf{Var}\{x\} &= \left(e^{2\mu+2\sigma^2}\right) - \left(e^{2\mu+\sigma^2}\right) \\ &= \left(e^{2\mu+\sigma^2}\right)\left(e^{\sigma^2}-1\right) \\ &\equiv \sigma_{LN}^2, \end{aligned} \tag{2-17}$$

$$\mathbf{x}_{median} = e^{\mu}, \tag{2-18}$$

$$\mathbf{x}_{mode} = e^{\mu-\sigma^2}. \tag{2-19}$$

We note that for a lognormal random variable, the mode, median and mean occur at different points with

$$\mathbf{x}_{mode} \le \mathbf{x}_{median} \le \mathbf{x}_{mean}.$$

The geometric mean of a random variable X (not necessarily lognormally distributed) is defined as

$$\left(\prod_{i=1}^{n} x_i\right)^{1/n}$$

Much of the confusion between mathematical and physical definitions of the statistics of the lognormal distribution arises from the misusing the word "geometric". The word "geometric" should only be applied when evaluating the above expression and not attached to Equations 2-16 through 2-19. As we will show later in this chapter and in Appendix A, in the special case where a random variable is lognormally distributed, then the evaluation of its geometric mean will be its median point.

2.3.1.1 Illustration of the Lognormal Probability Density Function

A graphical example of the lognormal pdf with $\mu = 0.5$ and $\sigma = 0.3$ is shown in Figure 2-2a. Note that as discussed in section 2.2.1.2, the standard deviation is a measure of a random variable's spread with respect to the mean and is shown in Figure 2.2b (the mode and median points have been removed for clarity). Using the appropriate expressions from the previous sections, the (true) statistics for this example are:

$$\text{Mean, } \boldsymbol{\mu}_{LN} = \mathbf{x}_{mean} = 1.725,$$

$$\text{Median, } \mathbf{x}_{median} = 1.649,$$

$$\text{Mode, } \mathbf{x}_{mode} = 1.507,$$

$$\text{Variance, } \boldsymbol{\sigma}^2_{LN} = 0.28,$$

$$\text{Standard Deviation, } \boldsymbol{\sigma}_{stdev} = \sqrt{\boldsymbol{\sigma}^2_{LN}} = 0.529.$$

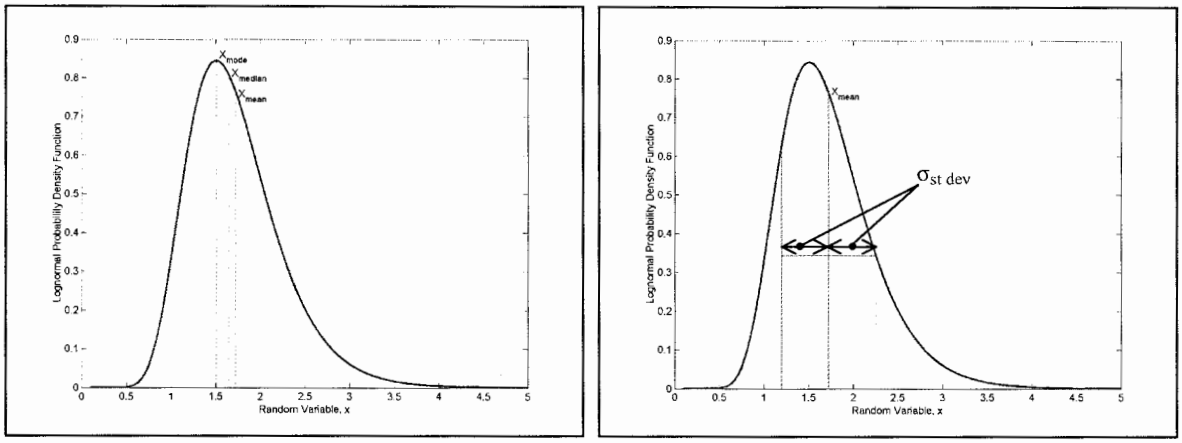

(a) **(b)**

Figure 2-2: Graphical display of lognormal probability density function with $\mu = 0.5$ and $\sigma = 0.3$.

We saw from the normal distribution (Eqns. 2-13a,b,c) that the area contained by each standard deviation point is always the same at 15.93% and 84.19%. This is not the case with lognormal distributions. Different sets of μ and σ will yield different statistics and areas. For the above example, the area included by the left first deviation point and the area included by the second deviation point is

$$A_{stdev1} = \int_0^{\mathbf{x}_{stdev1}} f_X(x)dx = \int_0^{\mathbf{x}_{mean} - \boldsymbol{\sigma}_{stdev}} f_X(x)dx = 0.1420,$$

$$A_{stdev2} = \int_0^{\mathbf{x}_{stdev2}} f_X(x)dx = \int_0^{\mathbf{x}_{mean} + \boldsymbol{\sigma}_{stdev}} f_X(x)dx = 0.8512,$$

$$A_{stdev2} - A_{stdev1} = \int_{\mathbf{x}_{stdev1}}^{\mathbf{x}_{stdev2}} f_X(x)dx = 0.7092.$$

This begs the question, are there statistical points for which the area under the curve for any two-parameter lognormal function remains constant similar to what we found with the Gaussian pdf? The answer is yes, but to see this, we need to make a slight change in our display of the lognormal function.

Because of its asymmetric shape, the lognormal function is often described as a skew distribution. Often, as we will see when we address lognormal functions from an empirical point of view, the random variable can vary over a large range of values, typically covering several orders of magnitude. A Cartesian coordiante system display would not be practical. The compression we use is to plot the lognormal function with a semilog horizontal axis. When the abscissa is changed to a semilog scale, something interesting happens: the lognormal shows the shape of its namesake, that of a normal function (Figure 2-3). In fact, this is exactly how Aitchison & Brown define a lognormal function. It is this display which has lead to greatest impact on the development of the statistics used by atmospheric scientists and small particle physicists and also causes the greatest amount of confusion in developing and interpreting these statistics. It should be explicitly stated that the random variable has not changed, only the way it is displayed has changed. Specifically, a cartesian coordinate system is characterized by having identical units of the abscissa and ordinate. In plotting on a semilog axis, we are actually changing the random variable. This transformation of the random variable will be discussed at length in section 2.4.

The constant areas, independent of any arbitrary μ and σ (similar to what we've found with the Gaussian normal distribution) are given by

$$\int_0^{e^{\mu-\sigma}} f_X(x)dx = 0.1593, \tag{2-20a}$$

$$\int_0^{e^{\mu+\sigma}} f_X(x)dx = 0.8419, \tag{2-20b}$$

$$\int_{e^{\mu-\sigma}}^{e^{\mu+\sigma}} f_X(x)dx = 0.6826. \tag{2-20c}$$

The curious reader may wonder where these expressions have come from and why they are true. A careful comparison between these expressions and the expressions given by Eqns. 2-13 show some interesting similarities that are not accidental because of the transformation of Eqn. 2-14. We will come back to this later, but for now, these expressions are true and should be accepted as fact.

Using the semilog scale can accentuate characteristics of the lognormal function that would otherwise be obscured using a Cartesian system. From Figure 2-3, we easily recognize the lognormal distribution is symmetric on a semilog (logarithmic) scale about its modal point. This can be demonstrated by considering logarithmic distances from the modal point. For the given example, we found the modal point to be at 1.507. If we add 13.563 to the modal point, we arrive at the point 15.07. The linear distance is 13.563 but the logarithmic distance is $\log_{10}(15.07/1.507) = 1$ (one decade). Similarly, if we move to the left of the mode point by a linear distance of 1.3563, we arrive at the point 0.1507 which corresponds to the

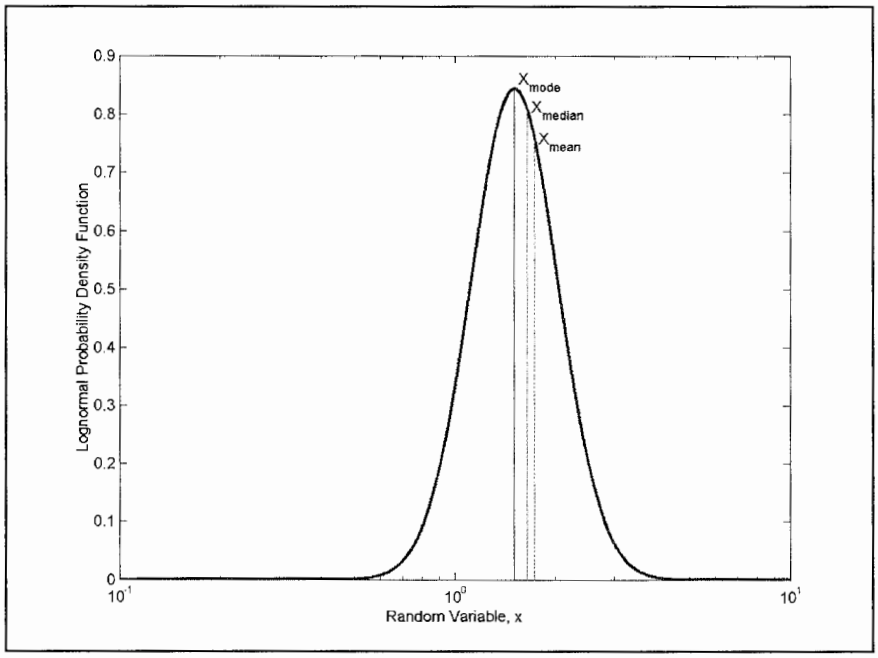

Figure 2-3: Plot of the lognormal function using a semilog scale. The curve has the familiar shape of a Gaussian function.

logarithmic distance $\log_{10}(1.507/0.1507) = 1$. To show symmetry, consider two points, x_1 and x_2 ($x_2 > x_1$), which are the same logarithmic distance from the modal point:

$$\log\left(\frac{x_2}{\mathbf{x}_{\text{mode}}}\right) = \log\left(\frac{\mathbf{x}_{\text{mode}}}{x_1}\right) \tag{2-21}$$

and, converting to natural log,

$$\ln\left(\frac{x_2}{\mathbf{x}_{\text{mode}}}\right) = \ln\left(\frac{\mathbf{x}_{\text{mode}}}{x_1}\right). \tag{2-22}$$

Now, let $x_1 = b \cdot \mathbf{x}_{\text{mode}}$ and $x_2 = b^{-1} \cdot \mathbf{x}_{\text{mode}}$ ($b \in \Re e$). Substituting these into Eqn. 2-21 or 2-22 indicates that these points are the same logarithmic distance apart. Therefore, logarithmic symmetry is shown by

$$f_X\left(b \cdot \mathbf{x}_{\text{mode}}\right) = f_X\left(b^{-1} \cdot \mathbf{x}_{\text{mode}}\right)$$

$$\frac{1}{\sqrt{2\pi}\cdot\boldsymbol{\sigma}\cdot b\cdot\mathbf{x}_{\text{mode}}}\exp\left(-\frac{1}{2\boldsymbol{\sigma}^2}\left(\ln\left(b\cdot\mathbf{x}_{\text{mode}}\right)-\boldsymbol{\mu}\right)^2\right) = \frac{1}{\sqrt{2\pi}\cdot\boldsymbol{\sigma}\cdot b^{-1}\cdot\mathbf{x}_{\text{mode}}}\exp\left(-\frac{1}{2\boldsymbol{\sigma}^2}\left(\ln\left(b\cdot\mathbf{x}_{\text{mode}}\right)-\boldsymbol{\mu}\right)^2\right).$$

Substituting for $\mathbf{x}_{\text{mode}}$ and simplifying,

$$\frac{1}{b}\exp\left(-\frac{1}{2\boldsymbol{\sigma}^2}\left(\ln(b)-\boldsymbol{\sigma}^2\right)^2\right) = b\exp\left(-\frac{1}{2\boldsymbol{\sigma}^2}\left(\ln\left(b^{-1}\right)-\boldsymbol{\sigma}^2\right)^2\right).$$

Taking the natural log of both sides and then reducing, yields,

$$-\frac{1}{2\sigma^2}\left(\ln(b)-\sigma^2\right)^2 = \ln\left(b^2\right)-\frac{1}{2\sigma^2}\left(\ln(b)+\sigma^2\right)^2$$

$$\ln^2(b)-2\sigma^2\ln(b)+\sigma^4 = -2\sigma^2\ln(b^2)+\ln^2(b)+2\ln(b)\sigma^2+\sigma^4$$

$$\begin{aligned} 2\ln(b) &= \ln\left(b^2\right) \\ &= \ln(b\cdot b) \\ &= \ln(b)+\ln(b) \\ &= 2\ln(b), \end{aligned}$$

which indicates that a lognormal function is logarithmically symmetric about its geometric mode point. This is an important point because the Gaussian function is symmetric around its mean, median and mode.

2.3.1.2 Illustration of the Base 10 Lognormal Probability Density Function

Appendix A shows the derivation of the lognormal function using base 10. The resulting pdf is[†]

$$f_X(x) = \frac{1}{\sqrt{2\pi}\cdot\sigma\, x\ln(10)}\exp\left(-\frac{1}{2\sigma^2}\left(\log_{10}(x)-\mu\right)^2\right). \tag{2-23}$$

Using the same μ and σ from section 2.3.1.1, the base 10 lognormal pdf has the following statistics:

Mean, $\mu_{10} = \mathbf{x}_{\text{mean}_{10}} = 4.014$,

Median, $\mathbf{x}_{\text{median}_{10}} = 3.162$,

Mode, $\mathbf{x}_{\text{mode}_{10}} = 1.962$,

Variance, $\sigma_{10}^2 = 9.855$,

Standard Deviation, $\sigma_{\text{stdev}_{10}} = \sqrt{\sigma_{10}^2} = 3.139$.

This example shows that for the same μ and σ, lognormal pdfs of different bases have different statistics. However, the parameters for base 10 that will yield identical statistics to the exponential base lognormal function (Figure 2-4) are μ = 0.2175 and σ = 0.130288 (see Appendix A).

From this example, we immediately see that describing lognormal functions of different bases in terms of their parameters μ and σ is not ideal since they would be different depending on the pdf used and would

---

[†] Throughout this thesis, log is always base 10 and ln is always the natural log.

hence cause unnecessary conversion and possibly confusion. In describing a distribution of particle sizes, it makes sense that only one set of parameters should be reported and that those parameters should be identical no matter what distribution function is used. This is exactly what is used in atmospheric science and small particle physics. However, the parameters used were not obtained from the standpoint of being identical for any base a distribution. In fact, the way these new parameters were found were almost by accident and were actually found from incorrect assumptions.

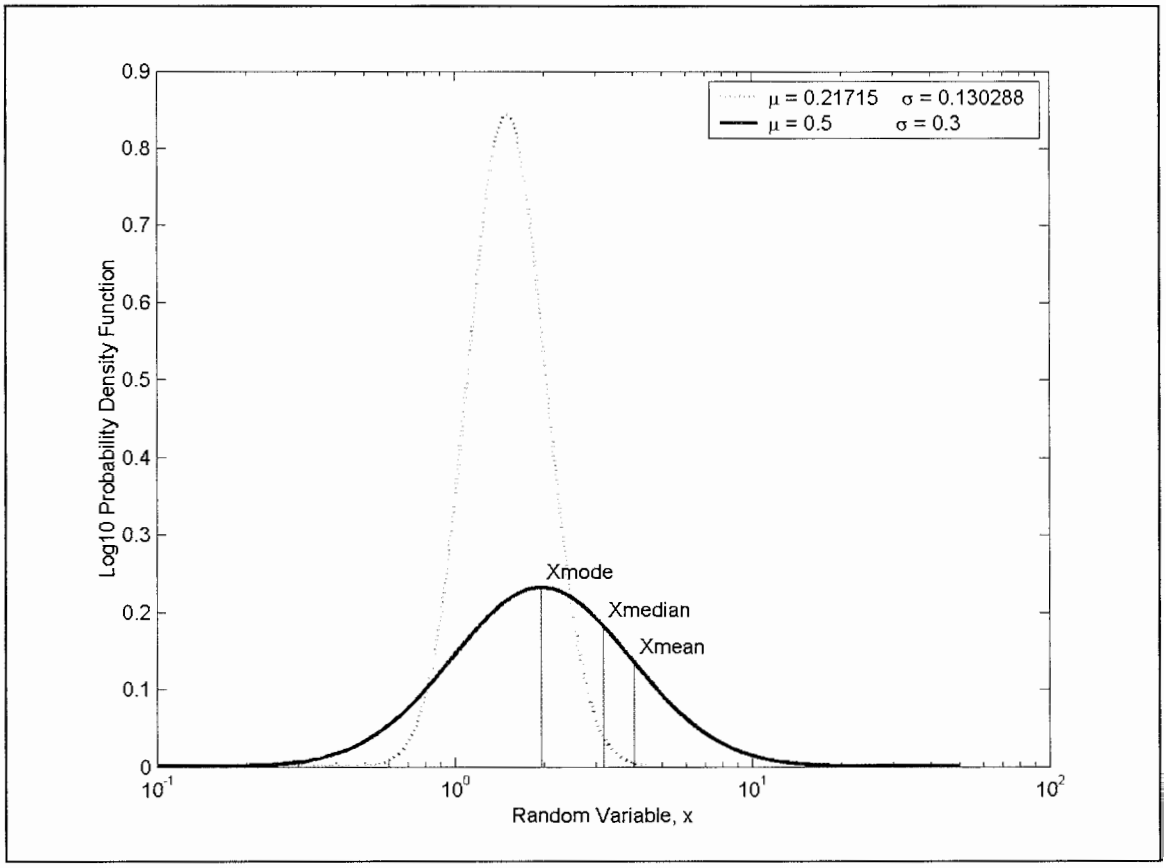

Figure 2-4: Lognormal pdf for different values of μ and σ.

2.3.1.3 Which Base Should be Used? The Chicken or the Egg?

The egg came first. Geneticists have known that a change in the genetic code is changed during embryonic development as the offspring may be physically different than the parent. It may seem that because the **ln** and **log** forms of the lognormal pdf report different statistics for identical μ and σ that one may be incorrect, or at the very least, that one base might be "more correct" than the other. Stevens (Stevens, p. 76) seems to have gotten caught in this statistical trap. In one sentence he states, "*For example, Eq. 4-12‡, is often incorrectly written with base 10 logarithms instead of natural logarithms to*

‡ The expression Stevens is referring is closest to Eqn. 2-13. As written, Stevens' expression is incorrect as it is missing an integral symbol.

describe atmospheric aerosol distributions." Two sentences later, he writes, "*However, many groups continue to use the base 10 logarithm...which causes confusion when trying to compare results from one experiment to another.*" How can research groups continue to use an incorrect expression for the lognormal function? Are their results wrong? No. Either expression (**log** or **ln**) can be used because the statistics that all of these groups use are shared. For now, one only has to be consistent in the use of either Eqn. 2-15 or Eqn. 2-23.

What Stevens may have meant is that one expression may be "more correct" than another rather than implying that one expression is wrong and one is right. The natural log, **ln**, didn't get its name for nothing. It is termed 'natural' because it is a naturally occurring function[‡‡] and is not a consequence of mathematical derivation. Basic texts covering natural response functions may be consulted for more perspective. All other logarithms, such as $\log_{10}$, are derived from the natural logarithm. The $\log_{10}$ function has found widespread use because it is easier to work with powers of 10 than powers of e. Kerker (Kerker, p. 353, Eqn. 7.5.5) shows many of the expressions using $\log_{10}$ (unfortunately, some of his expressions are inconsistent). With the true mathematical properties of the lognormal probability density function defined, we are now ready to set forth the statistics as used by atmospheric scientists and small particle physicists.

2.4 THE USE OF THE LOGNORMAL FUNCTION IN ATMOSPHERIC SCIENCE AND SMALL PARTICLE PHYSICS

It was a necessary evil to first establish the strict mathematical formulas of the lognormal function. The sections prior to this one stemmed from a few seemingly benign pages from Crow and Shimizu, 1988, pp. 331 – 346. In these pages, it was stated that the statistics used in small particle physics and aerosol science were not the correct mathematical statistics but he did not answer the questions, Why were they different? Are the expressions somehow incorrect? How do you relate the true statistics to those used in small particle physics? Crow did examine about 200 references in a variety of journals from 1970 – 1985 which made reference to the lognormal distribution. In the references regarding aerosols and small particles, Crow continually found the use of the geometric mean and geometric standard deviation to describe the statistics of particle size distributions. However, the (particle) geometric mean and (particle) geometric standard deviation have been defined as

$$\mathbf{r}_g = e^{\boldsymbol{\mu}}, \tag{2-24}$$

$$\boldsymbol{\sigma}_g = e^{\boldsymbol{\sigma}}, \tag{2-25}$$

which do not match the corresponding mathematical expressions of Eqns. 2-16 and (square root of) 2-17. Crow simply used these expressions to show that they were not the (true) mathematical expressions but he never identified how these terms were derived (it was never Crow's intention to do so). Reading these pages opened up many questions regarding the development and use of the lognormal function in particle

[‡‡] Actually, the exponential function, e, is the naturally occurring function to which the ln is related.

physics and atmospheric science. It was difficult to answer many of these questions as no one particular source had all of the answers. Even more, the sources used spanned over 80 years, by a variety of authors, under different backgrounds, and many contained user-defined mathematical language that hindered understanding.

Although, it is readily apparent that the (particle) geometric mean is actually the median of Eqn. 2-18, the origin of the (particle) geometric standard deviation is not so readily identified. This section aims at establishing how these definitions came into use and how they were derived. The first prudent course of action is to establish some sort of historical perspective.

2.4.1 A Brief History on the Development of the Lognormal Probability Density Function

Aitchison and Brown (Aitchison and Brown, pp. 1-6) provide a brief historical review of the use and development of the lognormal function in a variety of disciplines including sedimentary petrology, economics, hydrology, biological assays and small particle physics. Although the history of the lognormal function dates back roughly 120 years, its early history has been sporadic as its properties were slowly established and physical applications were found.

The first mathematical treatment of the lognormal function was in 1879 by Galton and McAllister where the statistical parameters of geometric mean and variance were set forth. In 1903, Kapteyn made significant contributions to the theory of lognormal functions by expanding its statistical properties, most notably with respect to its higher moments. Interestingly, Kapteyn made an analog machine that generated a lognormal distribution (Aitchison and Brown, p. 22). In 1917, Wicksell added a third parameter, τ, to the lognormal function. He used this three-parameter function to describe the first age of marriage. In the 1920s and 1930s, work on the lognormal distribution centered on establishing the physical mechanisms that were responsible for the lognormal distributions seen in small particle physics, distribution of incomes and other areas. Such work lead to The Theory of Proportionate Effect (Aitchison and Brown). Work continued in the 1940s and 1950s on establishing estimation procedures for fitting the theory with physical distributions.

In the 1920s, small particle physicists were finding success in using the lognormal function to fit to distributions of small particles. It was at this time that these physicists began an independent line of the use and development of the lognormal parameters. One of the first papers that began to establish the divergence (in terminology) was from Hatch and Choate in 1929.

Hatch and Choate used the technique of sieving through metal cloth screens of graduated mesh size in order to measure relatively large particle sizes (0.01 – 1.0 mm). Plotting the number of particles contained in these unequal mesh sizes showed that the distribution of particles had the shape of a normal function. The unequal grade scales are more mathematically recognized as the semilog plot of Figure 2-3. If Hatch and Choate had simply stopped at plotting the data in this manner, the mathematical and small particle statistical equations would have been identical. However, in these pre-computer days, manipulation,

analysis and display of data were formidable and thus, easier to use, more convenient ways had to be put forth. What evolved was the use of equal-width scales.

Analyzing the sieve mesh data was difficult because of the graduated grade scales used in the measuring process. It would be simpler for mathematical analysis if these graduated scales could be converted to equal-width class intervals. As Krumbein (Krumbein, 1936, p.37) writes,

> *It has long been common practice to plot the classes equal in width both to simplify the diagram and to give equal significance to each grade. The increased symmetry of the resulting frequency curve is ample justification of the procedure. Actually, of course, the logarithms of the diameters are being plotted when the classes are drawn equal in width, which means that for the independent variable* diameter *is being substituted the independent variable* log diameter.

It is the change of random variables, from **x** of Eqn. 2-15, to a new random variable, **log(x)** or **ln(x)**[†], that is the cause of the difference between the mathematical statistics and the small particle statistics equations. By changing to the random variable, **log(x)** or **ln(x)**, easier graphical methods using probability paper could be employed because, now, this new random variable leads to the well-understood Gaussian probability density function. The lognormal function of Eqn. 2-15 is only given the name, lognormal, not because we have derived it through the transformation of Eqn. 2-14, but because the distribution <u>of</u> the variate's logarithm obeys the (Gaussian) normal law of probability (Aitchison and Brown, p.1). Although Hatch and Choate, and Krumbein have stated and recognized this explicitly, formal treatments of the lognormal function for small particle physics have chosen to use the implications and so this fact seems to have been hidden through the years. This is probably why periodically, journal papers report 'new uses' of the lognormal function (E.X. Berry, 1967; Whitby, 1972) and their applications to particle/aerosols when in fact these new properties have already been used and reported.

Hatch & Choate (1933) also made the important discovery that related distributions by particle count to distributions by weight and were the first to establish the use of logarithmic moments that were originally put forth by Kapteyn (1903 – See p. 89, Ref. 15 of Herdan). This was an important realization that obviated the need for direct visual inspection of each sieve through a microscope in favor of simply weighing the sieves themselves and then converting back to particle count distributions (under a few assumptions). Krumbein (1936) formalized the logarithmic moments into the method of moments and gave expressions for particle size, surface area and volume (weight) distributions. Once again, these higher moment distributions of the lognormal function are not related to the true mathematical expressions but result from measuring techniques (we will discuss this more in section 2.5). Krumbein also gave expressions from a measurement point of view by suggesting that a base 2 transformation, *i.e.*, $\log_2$, should be used since the sieves sizes used were ½ the size of the previous sieve, and 2x the size of the next sieve. This transformation did not catch on.

[†] We will show later that, if done properly, it makes no difference to the statistics if the base 10 or natural log is used.

2.4.2 Definitions of (Particle) Lognormal Statistical Parameters from Empirical Measurements

The previous section indicated that the difference between the mathematical definitions and the definitions used by small particle physics for describing the statistics of the lognormal function have arisen because of the random variable being used: Mathematics/statistics use the random variable **x** where small particle physicists use the random variable **log(x)** or **ln(x)**. We now show the derivation of the statistics used by small particle physicists (Eqns. 2-24 & 2-25).

In our mathematical derivation of the lognormal's statistics, we used **x** to denote the random variable but attached no significance or units to it. The measurement of small particles started with the measurement of the particle's diameter, **D**, which should be used in place of **x**. However, when we get to light scattering, the important parameter is the particle's radius, **r**, and to be consistent, this will be the random variable to be used (It is a trivial matter to convert between radius and diameter). For convenience, Table 2-1 lists the pdf and corresponding statistics from section 2.3, with the random variable, **r**, being the particle radius.

2.4.2.1 Lognormal Distribution of Particle Number

The principal parameter of aerosol distributions is the radius where we assume, in conjunction with Mie Theory, that the particles are spherical. Although there is a great deal of evidence that aerosols are non-spherical (see references given in Chapter 4), Mie Theory has performed adequately by approximating the aerosols as spheres. In typical particle sampling measurements, it is the number density of particles, $\#/m^3$ or $\#/cm^3$, that is being collected. Particle sampling instruments place particles into standard sieve mesh sizes (which we will call bins or classes). It is important to remember that sampling instruments do

Table 2-1: The lognormal pdf function and statistics using radius, r, as the random variable.

Statistics	Probability Density Function	
	Base e, $\Lambda(\mu, \sigma^2)$	Base* 10, $\Lambda_{10}(\mu, \sigma^2)$
Functional Form	$\frac{1}{\sqrt{2\pi}\cdot\sigma r}\exp\left(-\frac{1}{2\sigma^2}(\ln(r)-\mu)^2\right)$	$\frac{1}{\sqrt{2\pi}\cdot\sigma r\ln(10)}\exp\left(-\frac{1}{2\sigma^2}(\log(x)-\mu)^2\right)$
Expected Value (Mean)	$e^{\mu+\sigma^2/2}$	$\mu_{10}\equiv 10^{\mu+\sigma^2\ln(10)/2}$
Variance	$\left(e^{2\mu+\sigma^2}\right)\left(e^{\sigma^2}-1\right)$	$\sigma_{10}^2\equiv\left(10^{2\mu+\sigma^2\ln(10)}\right)\left(10^{\sigma^2\ln(10)}-1\right)$
Median	e^{μ}	10^{μ}
Mode	$e^{\mu-\sigma^2}$	$10^{\mu-\sigma^2\ln(10)}$

* $\ln(10) = 2.303$

not measure the exact size of each particle since it is impossible both physically and mathematically. Why? Suppose a particle's radius is large enough to be measured with a ruler and was found to be 3 mm. The best the ruler can measure is within 0.5 mm. If we continue to use better instrumentation, such as microscopes and electron microscopes, we might find the radius is actually 3.2353 mm. But what is the actual size? (Keep moving ½ the way to a wall, you will never get there). Obviously there is a limit to any measuring device. Compounding the measurement problem is that most particles are not spherical. So, instead, an equivalent spherical radius or diameter is reported. Thus there is always some error in measurement. So, we make the bins small enough to get accurate readings. The question remains is "How small is small enough for the bin size?" Obviously we want the bin size small to not significantly affect the statistical properties of the distribution. But if a bin size (aka class interval) is too small then chance variations during measurement may dominate (Hald, p. 47, pp. 51-53).

In particle sampling measurements, the number of collected particles, Δn_i, in a class interval (bin), Δr_i, is plotted to obtain a graph similar to the one shown in Figure 2-5a. For convenience, the bins are shown to be equal in width. Typically, however, the bin sizes used in measurements are unequal (Whitby, 1972. p. 184) out of necessity of the measurement and accuracy of those measurements. To compensate for the unequal bin sizes, each Δn is divided by the respective bin size, Δr resulting in Figure 2-5b. Smith and Jordan (Smith and Jordan, p. 554), formally explain the reason. This issue is more pertinent to sampling measurements than the model we will develop in Chapter 4, but the bin sizes will still have some significance in our model.

The total particle density (#/cm^3), N_T is given by

$$N_T = \sum_{i=1}^{m} \Delta n_i \ . \tag{2-26}$$

In order to obtain the statistics of a particle size distribution, a histogram must be obtained. The definition of a histogram is a plot from which the pdf, and hence the statistics, of a random variable can be obtained. Therefore, since the pdf has unit area, the histogram must also have unit area. Dividing each class interval's ordinate of Figure 2-5b by N_T accomplishes this, resulting in the histogram of Figure 2-5c. The area of the ith rectangle in Figure 2-5c is the bin height multiplied by the bin width, given by

$$\left\{\frac{1}{N_T}\frac{\Delta n_i}{\Delta r_i}\right\}\cdot\{\Delta r_i\}.$$

As the number of bins is increased and the binsize is reduced (keeping the endpoints of the entire size range r_a and r_b fixed), the histogram becomes a continuous pdf (Herdan, p. 9)

$$\Delta r \xrightarrow{\lim} 0 \; \frac{1}{N_T} \sum_{i=1}^{m} \frac{\Delta n_i}{\Delta r_i} \cdot \Delta r_i = \int_{r_a}^{r_b} f_R(r) dr \; . \tag{2-27}$$

Removing the integral of Eqn. 2-27, we generalize to (Davies, 1974, eqn. 5, p. 285)

$$\frac{1}{N_T}\frac{dN}{dr} \equiv f_R(r) = \frac{1}{\sqrt{2\pi}\cdot\sigma r} \exp\left(-\frac{1}{2\sigma^2}(\ln(r)-\mu)^2 \right) \tag{2-28}$$

and, repositioning N_T, we can write

$$\frac{dN}{dr} = \frac{N_T}{\sqrt{2\pi}\cdot\sigma r} \exp\left(-\frac{1}{2\sigma^2}(\ln(r)-\mu)^2 \right). \tag{2-29}$$

Although the term, dN/dr, represents the rate of change of particles over a change in radius, it is more proper and intuitive to indicate that this term is the number of particles per volume (particle density), dN, contained in the interval, dr. To keep the units of the terms separate, dN is generally the number of particles per cubic centimeter (#/cm^3) and dr (for aerosols & small particles) is usually in μm. Therefore, the units of dN/dr are #/cm^3 per μm. Equation 2-29 represents neither the particle size distribution (the units are incorrect) nor the statistical expression of a lognormal pdf because it does not integrate to unity over **r**. However, Eqn. 2-29 represents the best possible compromise between the original particle size distribution and the statistical expression. The reason for this will be explained when we illustrate an actual data example (Smith and Jordan, p. 353). In any case, once the parameters, μ and σ, which yield the best-fit to the empirical data, are obtained, any mathematical expression can be used. The only requirement is that all subsequent mathematical expressions be derived from the original data set rather than a redefinition.

If we integrate Eqn. 2-29 over the entire size range, we have[†]

$$\int_{-\infty}^{\infty} \frac{dN}{dr} \cdot dr = \int_{-\infty}^{\infty} dN$$
$$= N_T \; ,$$

which is the total number of particles per cubic centimeter as expected. In light scattering models, we want to find the number of particles at a specific radius, *i.e.*,

$$N(r, r+dr) = \frac{N_T}{\sqrt{2\pi}\cdot\sigma} \int_r^{r+dr} \frac{1}{r} \exp\left(-\frac{1}{2\sigma^2}(\ln(r)-\mu)^2 \right) dr \tag{2-30}$$

[†] For a lognormal distribution the integral limits should be (0, ∞) since the random variable, **r**, cannot be negative. However, keeping the limits (∞, ∞) does not change the expressions.

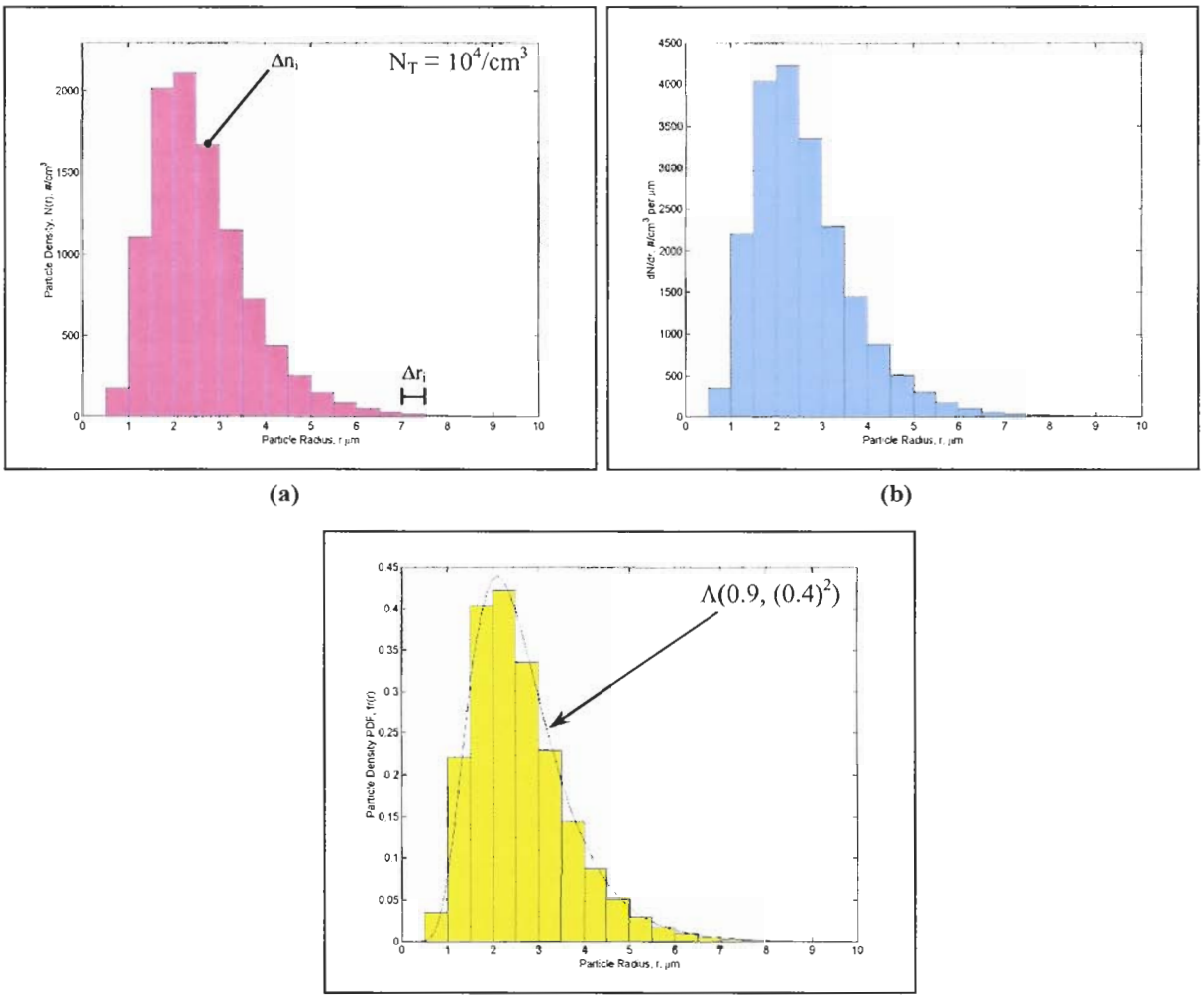

Figure 2-5: Evolution of sampled particle size density distribution data from the physics to the statistics. (a) Example of a particle distribution by count (frequency). This plot is the true particle number density distribution (described by Eqn. 2-30) as the ordinate of each bin is Δn_i. (b) The particle density distribution described by Eqn. 2-29. The ordinate of each bin is now of the form dN/dr. c) Histogram of the particle density distribution produced by normalizing dN/dr by N_T (Eqn. 2-28). The solid line is the lognormal pdf with μ =0.9 and σ =0.4 which best fits the data.

for which no closed-form expression has been found. Continuous random variable probability density functions, such as $f_R(r)$, do not represent the probability of a specific radius occurring since the probability of any one value occurring is zero. Only the probability for a range of values r_1 and r_2 given by

$$P\{r_1 \le r \le r_2\} = \int_{-\infty}^{\infty} f_R(r)dr \tag{2-31}$$

exists, is finite and can be calculated. So the number distribution, *N(r, r + dr)*, can only be calculated for a size range and not, *N(r)*, for a specific size. Stevens (Stevens, p.75, eqn. 4-12 and p. 78, Figure 4.3) confused his expressions by missing an integral for his eqn 4-12 and by mixing the total particle number

with his term, n_i, the number of particles at the modal radius. To use his n_i, Stevens must introduce a fourth parameter, the bin size, dr. This extra term only adds more difficulty and should be dropped in favor of the total particle density, N_T.

For display purposes, Figure 2-5 does not readily give a feel for the statistics of the distribution itself. These skewed distributions were difficult to analyze, especially with just pencil and paper. Methods were devised to enhance the visual display of the data and to develop a simple way of mathematically describing the statistics. The trick was to realize that the logarithm of the radius random variable was normally distributed and its statistics were readily available, widely used and easier to identify and display.

2.4.2.2 Derivation of the (Particle) Geometric Mean and (Particle) Geometric Standard Deviation

The results of this section are really rather beautiful as they will show that, although lognormal functions are of a wide variety and have different statistics for different bases and forms, there is an underlying expression that can be considered as the universal translator between all of the lognormal functions.

By moving the r from the term in front of the exponential of Eqn. 2-28, we have

$$r\frac{dN}{dr} = \frac{N_T}{\sqrt{2\pi}\cdot\boldsymbol{\sigma}}\exp\left(-\frac{1}{2\boldsymbol{\sigma}^2}(\ln(r)-\boldsymbol{\mu})^2\right) = \frac{dN}{dr/r}. \tag{2-32}$$

Since,

$$d\ln(r) = \frac{1}{r}dr, \tag{2-33}$$

Eqn. 2-32 can be written as

$$\frac{dN}{d\ln r} = \frac{N_T}{\sqrt{2\pi}\cdot\boldsymbol{\sigma}}\exp\left(-\frac{1}{2\boldsymbol{\sigma}^2}(\ln(r)-\boldsymbol{\mu})\right). \tag{2-34}$$

This result now uses the random variable, $\mathbf{lnr}$, rather than $\mathbf{r}$. The corresponding probability density function from Eqn. 2-34 is

$$f_R(\ln r) = \frac{1}{\sqrt{2\pi}\boldsymbol{\sigma}}\exp\left(-\frac{1}{2\boldsymbol{\sigma}^2}(\ln(r)-\boldsymbol{\mu})^2\right), \tag{2-35}$$

where the probability of occurrence is given by

$$P\{\ln r \le R \le \ln r + d\ln r\} = \int_{\ln r}^{\ln r + d\ln r} f_R(\ln r) d\ln r .$$

Using the parameters of Figure 2-2, the effect of using **lnr** as the random variable (via Eqn. 2-35) is shown in Figure 2-6. Comparing Figure 2-6 and Figure 2-2 we see that by moving from the random variable **r** to the random variable **lnr**, the curve loses its skewness and becomes symmetric. The resulting symmetry from using **lnr** as the random variable has been exploited in establishing the statistics of particle distributions. Figure 2-7 shows how the particle distributions of Figure 2-5 lose their skewness and become symmetric (via Eqn. 2-34). It is Eqns. 2-34 and 2-35 that are most often used for particle number distributions rather than Eqn. 2-28. As we will see, the reason is that Eqns. 2-34 and 2-35 are actually Guassian distributions in disguise, which is readily seen by comparing Eqn. 2-35 and Eqn. 2-10.

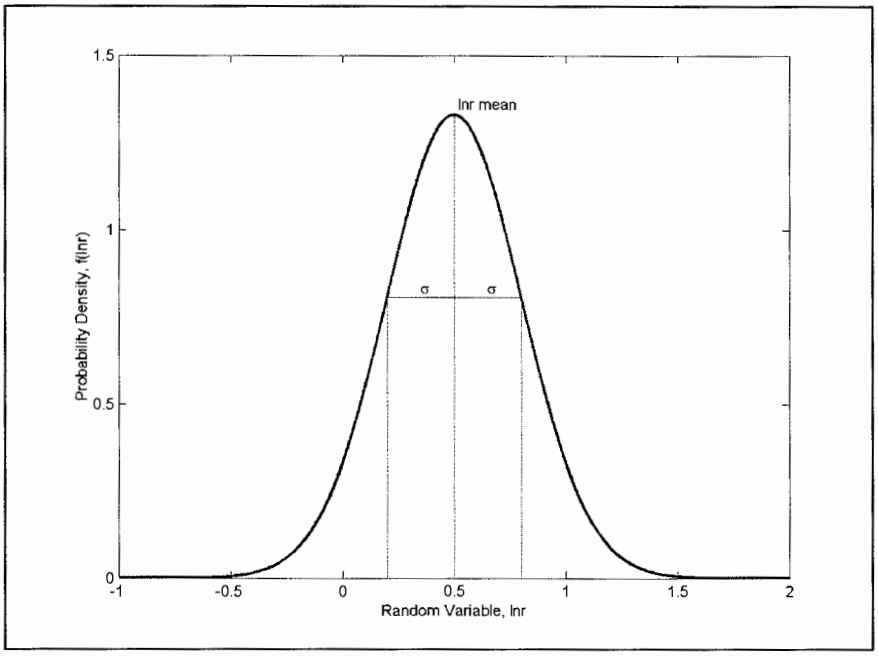

Figure 2-6: Distribution of the random variable lnr shown to be symmetric about its mean. Parameters used are the same as in Figure 2-2 ($\mu = 0.5$, $\sigma = 0.3$).

2.4.2.2.1 Statistics of the Random Variable lnr

The expected value of the pdf of Eqn. 2-35 is expressed as

$$\mathbf{E}\{\ln r\} = \int_{-\infty}^{\infty} (\ln r) f_R(\ln r) d\ln r . \qquad (2\text{-}36)$$

Making the change of variables, $y = \ln r$ and therefore $dy = d\ln r$ [†], the expected value can be re-written as

$$\begin{aligned}\mathbf{E}\{\ln r\} &= \int_{-\infty}^{\infty} y f_R(y)dy \\ &= \int_{-\infty}^{\infty} y \frac{1}{\sqrt{2\pi}\,\boldsymbol{\sigma}} \exp\left(\frac{1}{2\boldsymbol{\sigma}^2}(y-\boldsymbol{\mu})^2\right)dy ,\end{aligned} \tag{2-37}$$

which is the exact expression for the expected value of a Gaussian random variable (Eqn. 2-11), *i.e.*,

$$\mathbf{E}\{\ln r\} = \boldsymbol{\mu} . \tag{2-38}$$

When we first introduced lognormal functions, no additional significance was attached to the parameters μ and σ. From Eqn. 2-38, we see that these parameters are the (arithmetic) mean and (arithmetic) standard deviation of the Gaussian random variable, **lnr**. Since the random variable, **lnr**, is unitless, so are its moments (mean and standard deviation).

Since $f_R(\ln r)$ is a Guassin pdf, then from the results of section 2.2, Eqn. 2-38 also indicates that μ represents the median and mode points as well. From section 2.3, we found that the mean, mode and median points change for a given μ and σ. However, this is not so for a Guassian pdf: The mean, mode and median points are always coincident irrespective of the given set of parameters. The important point is that the median point (the 50% point) is dependent on only one parameter, μ. Since the median of the Gaussian random variable, **lnr**, occurs at μ, then, by the transformation of Eqn. 2-14, the median of the lognormal random variable, **r**, always occurs at

$$\begin{aligned}\mathbf{r}_{\text{median}} &= e^{\boldsymbol{\mu}} \\ &\equiv \mathbf{r}_g ,\end{aligned} \tag{2-39}$$

where $\mathbf{r}_g$ is used in the literature as the (particle) geometric mean of a particle distribution. From Eqn. 2-16, this is not the mean of the lognormal random variable but rather, by Eqn. 2-18, is the median. The nomenclature described in Eqn. 2-39 as the geometric mean of a particle distribution dates back to Hatch and Choate and was readily adopted by Herdan, Kerker, and others. Thus, $\mathbf{r}_g$ is not the mean, but median of a lognormal random variable and is also properly referred to as the geometric mean. But, we have not yet reached the good part. That's waiting for us with the (particle) geometric standard deviation.

From the above discussion, Eqn. 2-35 describes a Gaussian pdf with random variable **lnr**. From section 2.2, a Gaussian random variable always has its 16%, $\mathbf{y}_{16}$, and 84%, $\mathbf{y}_{84}$, points occur at $\mu \pm \sigma$ respectively. Therefore, using the transformation of Eqn. 2-14, these same points for a lognormal random variable occur at

---

[†] Notice that $d\ln r$ is not evaluated as dr/r since the random variable is **lnr**, not **r**. In essence, the reverse transformation of Eqn. 2-14 was used.

$$\mathbf{r}_{16} = e^{\boldsymbol{\mu}-\boldsymbol{\sigma}}$$
$$\mathbf{r}_{84} = e^{\boldsymbol{\mu}+\boldsymbol{\sigma}}. \tag{2-40}$$

The standard deviation for a Guassian random variable is defined as the concentration around the mean. We found from section 2.2 that standard deviation for a Gaussian random variable is given as

$$\begin{aligned}\boldsymbol{\sigma}_y &= \boldsymbol{\mu}_y - \mathbf{y}_{16} \\ &= \boldsymbol{\mu} - \mathbf{y}_{16} \\ &= \mathbf{y}_{50} - \mathbf{y}_{16} \\ &= \mathbf{y}_{84} - \mathbf{y}_{50} \\ &= \boldsymbol{\sigma}.\end{aligned} \tag{2-41}$$

Therefore, using the ideas of standard deviation for Gaussian random variables and the transformation of Eqn. 2-14, the (particle) geometric standard deviation, σ_g is defined as (See also Aitchison and Brown, eqn. 4.5, p. 32)

$$\begin{aligned}\boldsymbol{\sigma}_g &= e^{y_{50}-y_{16}} \\ &= \frac{e^{y_{50}}}{e^{y_{16}}} = \frac{\mathbf{r}_{\text{median}}}{\mathbf{r}_{16}} \\ &= \frac{e^{y_{84}}}{e^{y_{50}}} = \frac{\mathbf{r}_{84}}{\mathbf{r}_{\text{median}}} \\ &= e^{\boldsymbol{\sigma}}.\end{aligned} \tag{2-42}$$

Since σ_g is a ratio, it, as is σ, is unitless. The significance of σ is that it represents the logarithmic distance ($\boldsymbol{\sigma} = \ln(\boldsymbol{\sigma}_g)$) from the median to the 16% and 84% points of the lognormal random variable **r**. Using the variance expressions from Eqns. 2-4 and 2-12a, for the Gaussian random variable, **lnr**, the formalized expression for the (particle) geometric standard deviation can be derived as

$$\begin{aligned}\mathbf{Var}\{\ln r\} = \mathbf{E}\left\{(\ln r - \boldsymbol{\mu})^2\right\} = \boldsymbol{\sigma}^2 &= \int_{-\infty}^{\infty} (\ln r - \boldsymbol{\mu})^2 f_R(\ln r) d\ln r \\ \therefore \ln^2(\boldsymbol{\sigma}_g) &= \int_{-\infty}^{\infty} (\ln r - \ln \mathbf{r}_g)^2 f_R(\ln r) d\ln r \\ &= \int_{-\infty}^{\infty} \left(\ln\left(r / \mathbf{r}_g\right)\right)^2 f_R(\ln r) d\ln r \\ &= \int_{-\infty}^{\infty} \left(\ln\left(r / \mathbf{r}_{\text{median}}\right) - \ln\left(\mathbf{r}_{\text{median}} / \mathbf{r}_{\text{median}}\right)\right)^2 f_R(\ln r) d\ln r.\end{aligned} \tag{2-43}$$

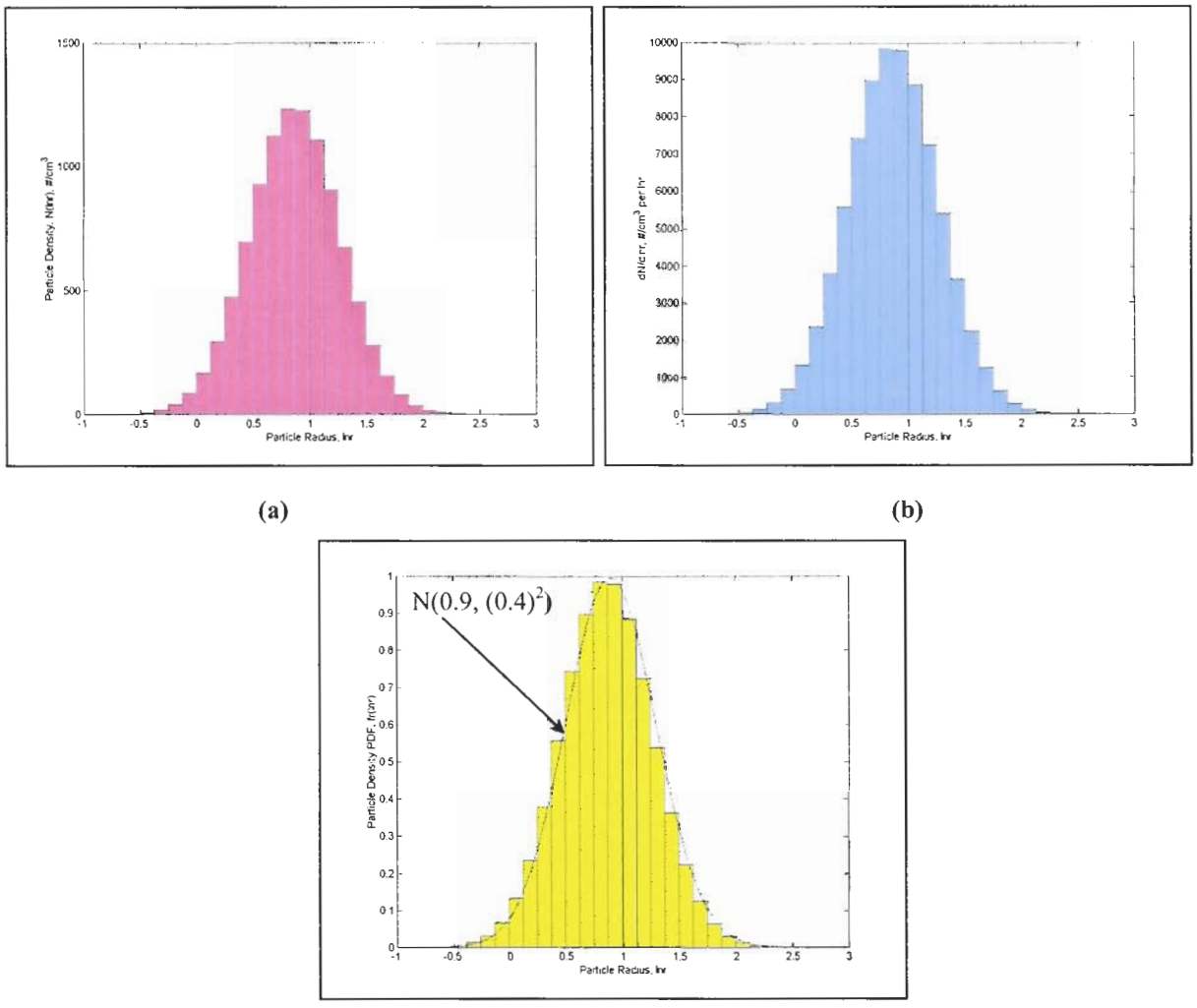

(a) (b)

(c)

Figure 2-7: Particle distributions as a function of the random variable lnr. (a) Transformed particle density distribution of Figure 2-5a (see Appendix A). (b) Particle density distribution normalized to the logarithmic bin size. The ordinate is dN/dlnr. (c) Histogram of the particle density distribution obtained by normalizing dN/dlnr by N_T . The solid line is the normal pdf using the Gaussian random variable lnr which best fits the distribution.

Equation 2-43 is written in a form that accentuates the meaning of σ_g: The (particle) geometric standard deviation, σ_g, represents the deviation of the ratios of distances about the median. Ratios are used because in the transformation to the Gaussian random variable, **lnr**, the logarithm of the ratio is the same logarithmic distance on either side of the mean of **lnr**. Therefore, σ_g belongs to the random variable **r** while σ belongs to the random variable **lnr**. Now, since,

$$f_R(\ln r)d\ln r = f_R(r)dr \tag{2-44}$$

Eqn. 2-43 can be written as (Kerker, eqn. 7.57, p.353)

$$\ln^2(\sigma_g) = \int_{-\infty}^{\infty} (\ln r - \ln(r_{median}))^2 f_R(r)\, dr \,. \tag{2-45}$$

Further, by using the definition of σ_g as the ratio about the median,

$$\sigma_g^2 = \int_{-\infty}^{\infty} \left(\frac{r_{median}}{r} \right)^2 f_R(r) dr \quad , \forall r < r_{median} + \int \left(\frac{r}{r_{median}} \right)^2 f_R(r) dr \quad , \forall r > r_{median} \,. \tag{2-46}$$

The reason for splitting Eqn. 2-46 into two integrals is because the ratio must be the same on either side of the r_{median} point and therefore the logarithmic distance will be identical. For example, suppose the median was determined to be at a value of 4. From Eqn. 2-46, at a value of 2, the ratio would be 4/2 = 2. At a value of 8, the ratio would be 8/4 = 2 (as opposed to 4/8 = 0.5 which would give erroneous results).

2.4.2.3 Particle Distribution Expressions in Terms of r_g and σ_g Using the Base *e* Lognormal Function

Using the expressions for the (particle) geometric mean, r_g, and (particle) geometric standard deviation, σ_g (Eqns. 2-39 & 2-42), we can rewrite the lognormal pdf of Eqns. 2-28 as

$$f_R(r) = \frac{1}{\sqrt{2\pi} \cdot \ln(\sigma_g) r} \exp\left(- \frac{1}{2 \ln^2(\sigma_g)} (\ln(r) - \ln(r_g))^2 \right)$$

$$= \frac{1}{\sqrt{2\pi}\, \ln(\sigma_g) r} \exp\left(- \frac{1}{2 \ln^2(\sigma_g)} \left(\ln\left(r / r_g \right) \right)^2 \right) \tag{2-47a}$$

$$= \frac{1}{\sqrt{2\pi}\, \ln(\sigma_g) r} \exp\left(- \frac{1}{2 \ln^2(\sigma_g)} \left(\ln\left(r / r_{median} \right) \right)^2 \right) \tag{2-47b}$$

$$= \frac{1}{N_T} \frac{dN}{dr} .$$

A review of the recent literature indicates that many researchers are avoiding confusion between using terminology of mean and geometric mean and are instead simply referring to r_g as the median. To further this, the parameter r_g will no longer be used for the remainder of this document in favor of r_{median}.

The particle distribution expression of Eqn. 2-34 can also be rewritten in terms of r_{median} and σ_g as

$$\frac{dN}{d \ln r} = \frac{N_T}{\sqrt{2\pi} \cdot \ln(\sigma_g)} \exp\left(- \frac{1}{2 \ln^2(\sigma_g)} \left(\ln\left(r / r_g \right) \right)^2 \right) \tag{2-48a}$$

$$= \frac{N_T}{\sqrt{2\pi} \cdot \ln(\sigma_g)} \exp\left(- \frac{1}{2 \ln^2(\sigma_g)} \left(\ln\left(r / r_{median} \right) \right)^2 \right) . \tag{2-48b}$$

From Eqn. 2-48, the number of particles within a logarithmic bin size can be obtained by

$$N(\ln r, \ln r + d\ln r) = \frac{1}{\sqrt{2\pi}\cdot\sigma}\int_{\ln r}^{\ln r + d\ln r} \exp\left(-\frac{1}{2\ln^2(\sigma_g)}\left(\ln\left(r/r_{median}\right)\right)^2\right) d\ln r\,. \tag{2-49}$$

2.4.2.4 Particle Distribution Expressions Using r_g and σ_g for the Base 10 Lognormal Function

Compared to the exponential base, the decimal base is far easier to manipulate. We can use the conversion of

$$\log_a(x) = \frac{\ln(x)}{\ln(a)} \tag{2-50}$$

with a = 10 together with Eqn. 2-47b, to obtain the lognormal pdf for base 10 in terms of r_{median} and σ_g as

$$f_R(r) = \frac{1}{\sqrt{2\pi}\cdot\log(\sigma_g)\ln(10)\,r}\exp\left(-\frac{1}{2\log^2(\sigma_g)}\left(\log\left(r/r_{median}\right)\right)^2\right). \tag{2-51}$$

To turn this pdf into a particle distribution, we simply attach units of particle density to the function by multiplying by the total number of particles, N_T. Therefore,

$$\frac{dN}{dr} = \frac{N_T}{\sqrt{2\pi}\cdot\log(\sigma_g)\ln(10)\,r}\exp\left(-\frac{1}{2\log^2(\sigma_g)}\left(\log\left(r/r_{median}\right)\right)^2\right), \tag{2-52}$$

which is equivalent to Eqn. 2-47b. This expression can also be written using the base parameters of μ_{10} and σ_{10} as[†]

$$\frac{dN}{dr} = \frac{N_T}{\sqrt{2\pi}\cdot\sigma_{10}\ln(10)\,r}\exp\left(-\frac{1}{2\sigma_{10}^2}(\log(r)-\mu_{10})^2\right), \tag{2-53}$$

where (see Appendix A),

[†] The subscript 10 is used to signify that these parameters are different from the μ and σ from using base e.

$$\boldsymbol{\mu}_{10} = \frac{\ln(e)}{\ln(10)}\boldsymbol{\mu} = \log\left(\mathbf{r}_{\text{median}}\right) \tag{2-54a}$$

$$\boldsymbol{\sigma}_{10} = \frac{\ln(e)}{\ln(10)}\boldsymbol{\sigma} = \log\left(\boldsymbol{\sigma}_g\right). \tag{2-54b}$$

Similar to Eqn. 2-30, the particle density (#/cm^3) within a size range of r to $r+dr$, using the base 10 lognormal function, is written as

$$N(r, r+dr) = \frac{N_T}{\sqrt{2\pi}\cdot\boldsymbol{\sigma}_{10}\ln(10)}\int_{\mathbf{r}}^{\mathbf{r+dr}}\frac{1}{r}\exp\left(-\frac{1}{2\boldsymbol{\sigma}_{10}^2}\left(\log(r)-\boldsymbol{\mu}_{10}\right)^2\right)dr \tag{2-55a}$$

$$= \frac{N_T}{\sqrt{2\pi}\,\log\left(\boldsymbol{\sigma}_g\right)\ln(10)}\int_{\mathbf{r}}^{r+dr}\frac{1}{r}\exp\left(-\frac{1}{2\log^2\left(\boldsymbol{\sigma}_g\right)}\left(\log\left(r/\mathbf{r}_{\text{median}}\right)\right)^2\right)dr. \tag{2-55b}$$

Using the data from the base e lognormal function of Figure 2-5, plots of Eqns. 2-55b, 2-53 and 2-51 are shown in Figure 2-8. We see immediately that the plots are identical and therefore will have identical statistics; only the underlying parameters μ, σ and μ_{10}, σ_{10} are different.

2.4.2.4.1 Statistics of the Random Variable $\log_{10}(\mathbf{r})$

By moving the $\ln(10)r$ term from the denominator to the left hand side of Eqn. 2-53,

$$\frac{dN}{dr}\ln(10)r = \frac{N_T}{\sqrt{2\pi}\boldsymbol{\sigma}_{10}}\exp\left(-\frac{1}{2\boldsymbol{\sigma}_{10}^2}\left(\log(r)-\boldsymbol{\mu}_{10}\right)^2\right), \tag{2-56}$$

and, using

$$d\log(r) = \frac{dr}{r\ln(10)} = \frac{d\ln r}{\ln(10)}, \tag{2-57}$$

we can express Eqn. 2-56 in terms of the random variable **logr** as

$$\frac{dN}{d\log r} = \frac{N_T}{\sqrt{2\pi}\cdot\boldsymbol{\sigma}_{10}}\exp\left(-\frac{1}{2\sigma_{10}^2}\left(\log(r)-\boldsymbol{\mu}_{10}\right)^2\right) \tag{2-58a}$$

$$= \frac{N_T}{\sqrt{2\pi}\cdot\log\left(\boldsymbol{\sigma}_g\right)}\exp\left(-\frac{1}{2\log^2\left(\boldsymbol{\sigma}_g\right)}\left(\log\left(r/\mathbf{r}_{\text{median}}\right)\right)^2\right) \tag{2-58b}$$

and the particle density within a logarithmic size range is

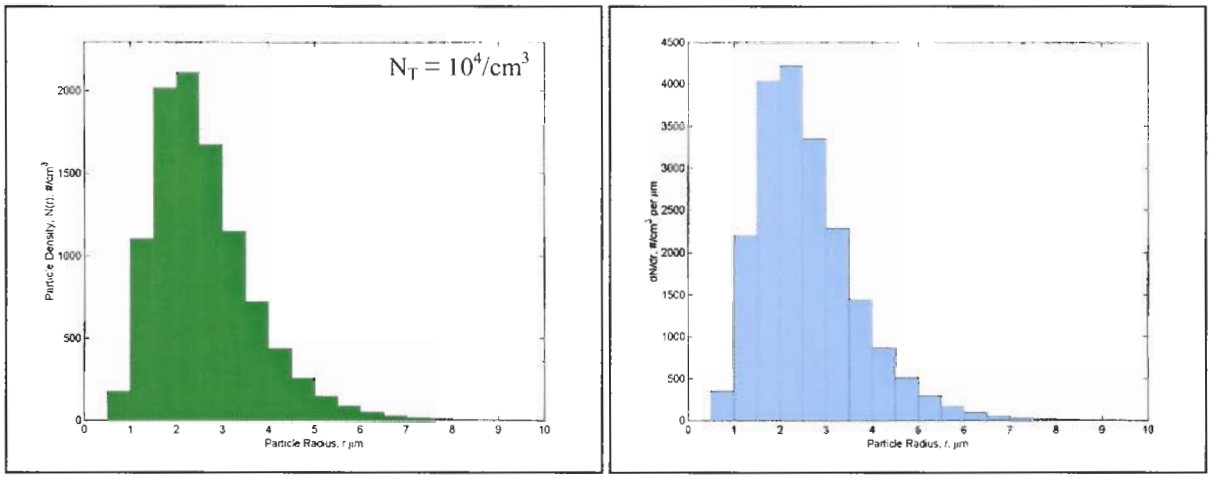

(a) **(b)**

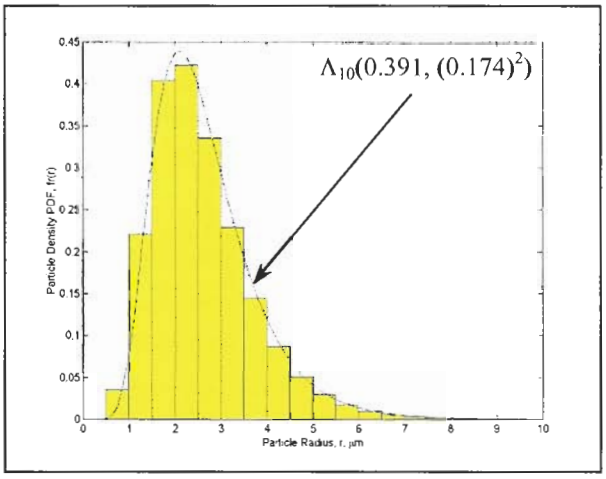

(c)

Figure 2-8: Evolution of particle size density distributions using a Base 10 lognormal function. These plots match those of Figure 2-5 indicating identical statistics. (a) Particle density as a function of radius (Eqn. 2-55b). (b) Plot of Eqn. 2-53. Here, the ordinate of each bin has been normalized to the bin width to yield dN/dr. (c) Histogram of the particle density distribution produced by normalizing dN/dr by N_T (Eqn. 2-51). The solid line is the base 10 lognormal pdf[†] with μ_{10} =0.391 and σ_{10} =0.174 that best fits the data.

[†] The subscript 10 on the term Λ_{10} indicates that $\log_{10}$ is used for the lognormal function and the parameters given are specific to that base (i.e., μ_{10} and σ_{10}). The symbol Λ without a subscript indicates that base e lognormal function is being used (default).

$$N\{\log r, \log r + d\log r\} = \frac{N_T}{\sqrt{2\pi}\cdot\boldsymbol{\sigma}_{10}}\int_{\mathbf{logr}}^{\log r + d\log r}\exp\left(-\frac{1}{2\boldsymbol{\sigma}_{10}^2}(\log(r)-\boldsymbol{\mu}_{10})^2\right)d\log r \tag{2-59a}$$

$$= \frac{N_T}{\sqrt{2\pi}\cdot\log(\boldsymbol{\sigma}_g)}\int_{\log r}^{\log r + d\log r}\exp\left(-\frac{1}{2\log^2(\boldsymbol{\sigma}_g)}\left(\log\left(\frac{r}{\mathbf{r}_{\text{median}}}\right)\right)^2\right)d\log r\,. \tag{2-59b}$$

Comparing Eqns. 2-48b and 2-58b we have the relation between expressions using the random variable **lnr** and expressions using the random variable **logr** as (Davies, eqn. 5, p. 295, 1974)

$$\frac{dN}{d\ln r} = \frac{1}{2.303}\frac{dN}{d\log r}. \tag{2-60}$$

Normalizing Eqn. 2-58 by N_T, yields the pdf

$$f_R(\log r) = \frac{1}{\sqrt{2\pi}\cdot\boldsymbol{\sigma}_{10}}\exp\left(-\frac{1}{2\boldsymbol{\sigma}_{10}^2}(\log(r)-\boldsymbol{\mu}_{10})^2\right). \tag{2-61}$$

Upon comparing Eqn. 2-61 and Eqn. 2-35, we see immediately we see that we have a Gaussian pdf with random variable **logr**. The expected value of the Gaussian random variable **logr** is given by

$$\mathbf{E}\{\log r\} = \int_{-\infty}^{\infty}\log r\cdot f_R(\log r)d\log r\,. \tag{2-62}$$

Making a change of variables,

$$y = \log r$$
$$\therefore dy = d\log r$$

and substituting, yields

$$\begin{aligned}\mathbf{E}\{\log r\} &= \int_{-\infty}^{\infty} y f_R(y)dy \\ &= \frac{1}{\sqrt{2\pi}\cdot\boldsymbol{\sigma}_{10}}\int_{-\infty}^{\infty}\frac{1}{y}\exp\left(-\frac{1}{2\boldsymbol{\sigma}_{10}^2}(y-\boldsymbol{\mu}_{10})^2\right)dy \\ &= \boldsymbol{\mu}_{10} \\ &= \log(\mathbf{r}_g) \\ &= \log(\mathbf{r}_{\text{median}})\,.\end{aligned} \tag{2-63}$$

The variance of the random variable **logr** is given by

$$\begin{aligned}\mathbf{Var}\{\log r\} &= \mathbf{E}\left\{(\log r - \boldsymbol{\mu}_{10})^2\right\} \\ &= \mathbf{E}\left\{\log^2 r\right\} - \boldsymbol{\mu}_{10}^2 \\ &= \boldsymbol{\sigma}_{10}^2 \ , \end{aligned} \tag{2-64}$$

where we have made use of the fact that **logr** is a Gaussian random variable so the results of section 2.2 were used. Thus, the standard deviation is σ_{10}, which, by Eqn. 2-54b, is $\log(\sigma_g)$.

As shown in Figure 2-9, by transforming to the random variable **logr**, the graphs of Figure 2-8 once again show the characteristic shape of a Gaussian curve. However, we also see that the position and shape of these curves are not identical to the curves of Figure 2-7. We have already seen that the position and shape of the curves for base *e* and base 10 lognormal functions of random variable **r** were identical (Figure 2-5 and Figure 2-8) so why are Figures 2-7 and 2-9 not identical? Although it is probably obvious, it is worth repeating that the difference has to do with the random variable being used. In Figure 2-7, it is **lnr** while in Figure 2-9, it is **logr** and so the positions and shapes of the curves will be off by the ln(10) = 2.303 scale factor (See Equations 2.54a and 2.54b). Having such visual discrepancy would be irritating but can be taken care of by other means.

Plotting distribution curves versus radius leads to a skewed shape, which is not very conducive to obtaining or displaying the statistics of the distribution. However, transforming to **lnr** or **logr** yields the characteristic shape of a Gaussian curve whose statistics are readily obtained and easily displayed. Unfortunately, the abscissa being **lnr** or **logr** would give different positions and shapes of the curves. So, one more trick is applied – transform the abscissa back to the random variable **r** while keeping the ordinate as an unchanged Gaussian curve of either **lnr** or **logr**. This transformation is easily accomplished using a semilog graph and is justified because not only is it 1:1, but also our fundamental parameters of $\mathbf{r}_{median}$ and σ_g are the same for base *e* or base 10 lognormal functions and therefore the shape and position given by these parameters is invariant over the base of the lognormal function. Figure 2-10 shows plots of the particle number density distribution and the normalized density distribution, *dN/dlogr*.

The plots of Figure 2-10 both use **logr** as the random variable, *i.e.*, the expressions of Eqn. 2-58 are used. Here, the ordinate values have been reattached to a new abscissa, r. Although the random variable is still **logr**, having r as the abscissa allows us to display both $\mathbf{r}_{median}$ ($\mathbf{r}_g$) and σ_g. Now, since $\mathbf{r}_{median}$ and σ_g are the same for the random variable **lnr** and **logr**, the corresponding functions will not only have identical statistics but using a semilog scale allows the same geometrical picture to be displayed. However, it is worth mentioning that, by Eqn. 2-60, plots of dN/dlnr will differ by a scale factor from plots of dN/dlogr because of the random variable being used in each case. This scale factor, (ln(10) = 2.303), does not change the statistics of the underlying functions because Eqns. 2-35 and 2-61 will yield identical statistics (in terms of $\mathbf{r}_{median}$ and σ_g) since we have used the relations of Eqns. 2-54a and 2-54b.

The reason for using N(logr) rather than N(r) in Figure 2-10a is to indicate that the expressions used in its determination (Eqns. 2-58) use **logr** as the random variable, rather than **r**. The red circles are calculated data points and although the points have been connected by a solid line, the curve of particle number density distribution should not be thought of as being continuous but rather discrete. This is a consequence

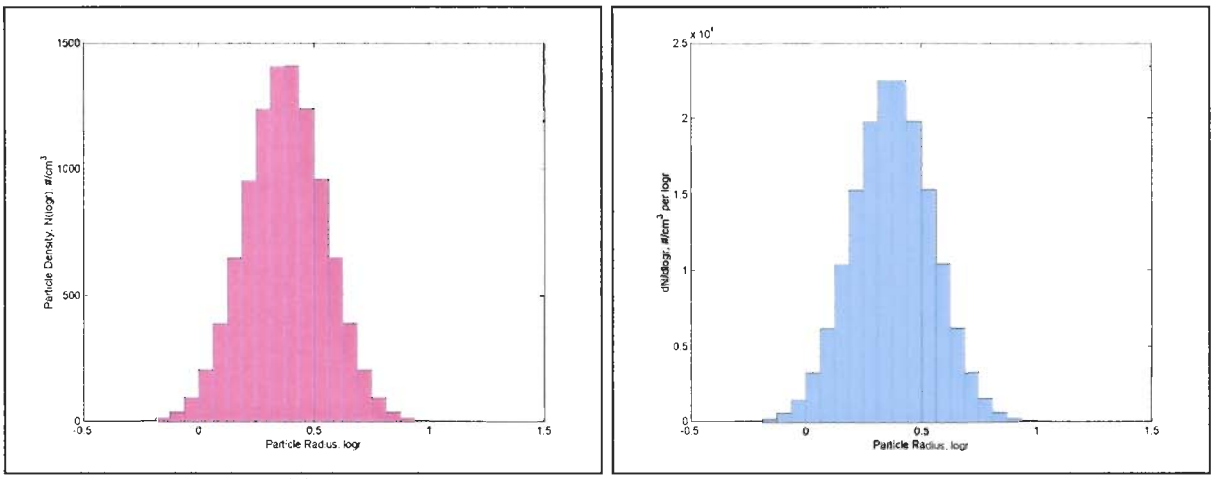

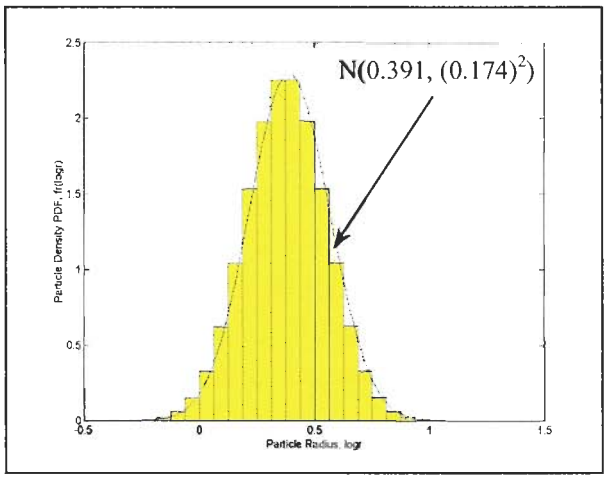

Figure 2-9: Particle distributions as a function of the random variable log*r*. (a) Transformed particle density distribution of Figure 2-8a. (See Eqn. 2-59a) (b) Particle density distribution normalized to the logarithmic bin size. The ordinate is dN/dlogr and is given by Eqn. 2-58a. (c) Histogram of the particle density distribution obtained by normalizing dN/dlogr by N_T (Eqn. 2-61). The solid line is the normal pdf using the Gaussian random variable logr which best fits the distribution.

of the underlying statistics that indicate that the probability of a particle of specific radius occuring is zero. Number density plots such as N(r), N(lnr) or N(logr) are actually thought of as cumulative plots (Monin, eqn. 7.1, p.62; Hobbs (by Jaenicke) eqn. 4, p.13).

As will be discussed more thoroughly in Chapter 4, atmospheric aerosols have most often been encountered as a trimodal lognormal distribution given by

$$y(r) = \frac{dN}{d\log r} = \sum_{i=1}^{3} \frac{N_{T_i}}{\sqrt{2\pi}\cdot\log(\sigma_{g_i})} \exp\left(-\frac{1}{2\log^2(\sigma_{g_i})}\left(\log\left(r/r_{\text{median}_i}\right)\right)^2\right), \qquad (2\text{-}65)$$

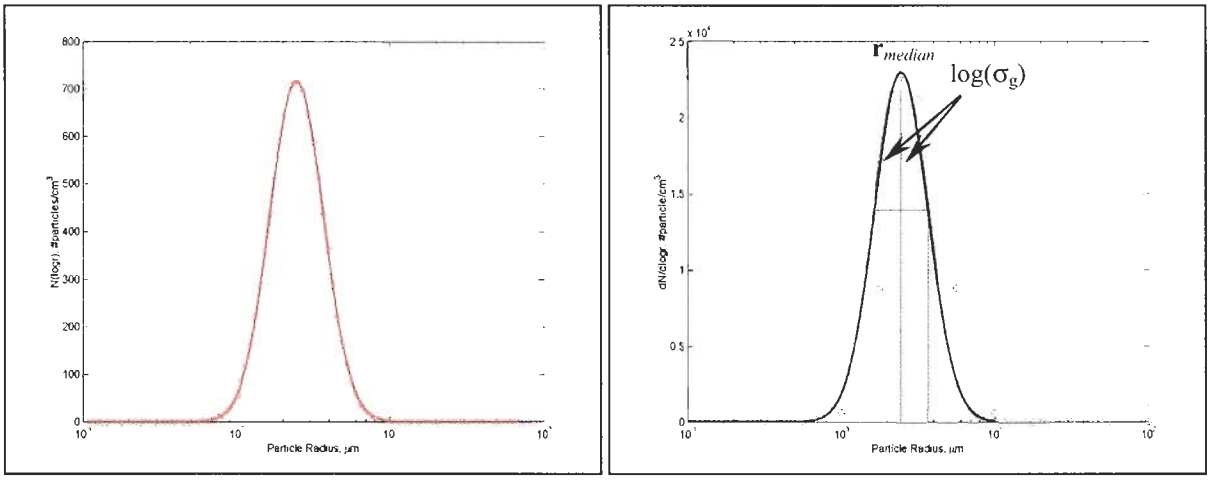

(a) (b)

Figure 2-10: Distribution plots of Figure 2-9a,b using a semilog axis. (a) Particle density distribution, N(logr) vs logr (shown on semilog scale). (b) Theoretical plot of dN/dlogr using Eqn. 2-58. The red, green and blue circles illustrate the effect of bin size (red represents the binsize is equal to the integration width, dlogr, green represents binsizes that are 4x the integration width, and blue represents 8x the width). As the bin sizes are increased the true statistics of the distribution become more obscured. Also one can only show r_{median} and σ_g on N(r), N(logr) plots when the integration width and the binsize are equal. (It is more correct to show r_{median} and σ_g on plots of dN/dlogr than on plots of N(logr) or N(r)).

where the subscript *i* indicates the mode. Using the parameters from Stevens, Eqn. 2-65 is shown in Figures 2-11a and b. Figure 2-12 integrates Figure 2-11b with respect to **logr** and shows the particle number density distribution over radius. Plots like Figure 2-12 will be used in the scattering model.

Although our scattering model will be mostly concerned with finding data like Figure 2-12, other distributions, based on particle size, can also yield information more pertinent to specific applications and uses. These additional distributions, termed "higher moments" of the lognormal function, are discussed next in section 2.5.

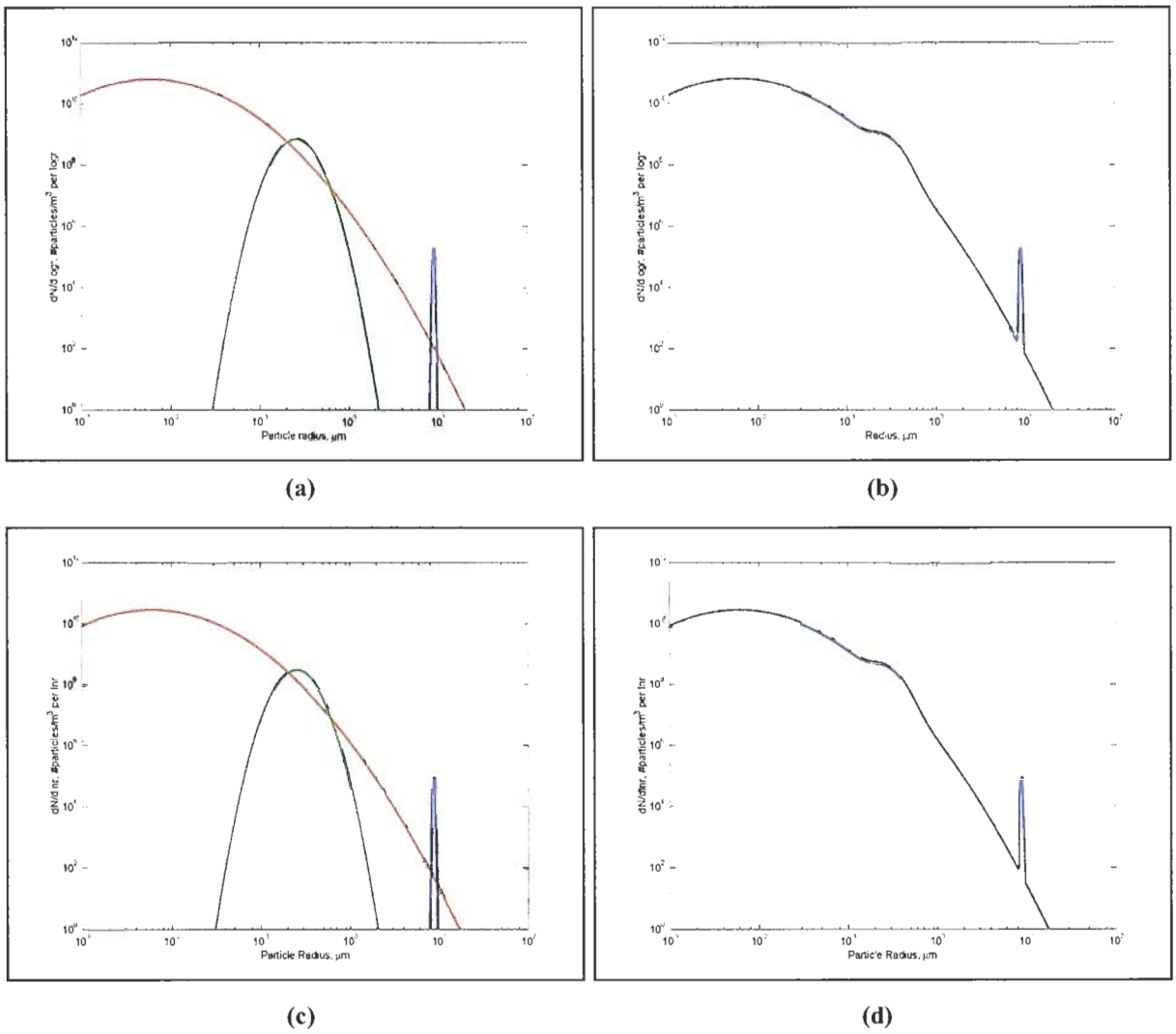

Figure 2-11: Example of a trimodal aerosol distribution of partice sizes. (a) Individual modes. (b) Summation of modes. (c) Individual modes adapted from Stevens' eqn. 4.12. (d) Summation of Stevens' modes. As expected, plots a), b) differ from c), d) by the scale factor ln(10).

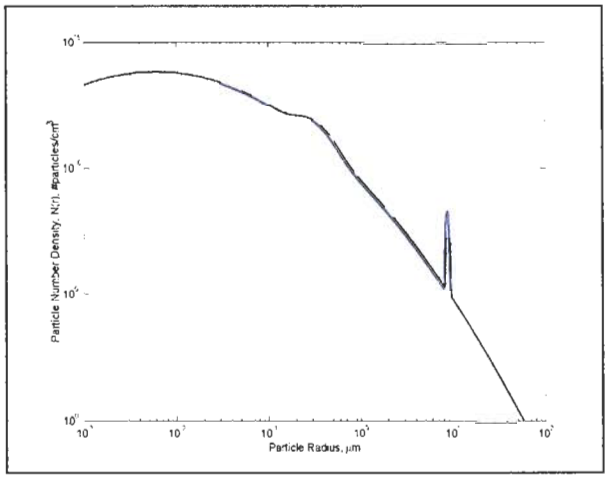

Figure 2-12: Particle number density distribution of trimodal aerosols.

2.5 HIGHER MOMENTS OF THE LOGNORMAL FUNCTION

Aerosol studies center around the measurement of particle sizes in terms of their radius (or diameter). From this primary measurement, additional information, notably surface area and volume distributions of the particles can also be obtained. These additional distributions provide insights that would otherwise be obscured with a particle distribution alone (Whitby, figure 1, p. 179, 1972). For example, in light scattering experiments, the critical parameter is a particle's cross-section area (Whitby, pp. 612-617, 1974), while pollution studies deal with particle mass concentrations, which is related to volume (Whitby, p. 617 & p. 630, 1974).

Because the particles are assumed to be spheres, surface area and volume are simply related to the radius by $4\pi r^2$ and $\frac{4}{3}\pi r^3$ respectively. Using the mathematics established in section 2.3, the statistics of the area and volume distributions will be determined. However, there is a caveat: The (true) statistics of the area and volume distributions are not what is reported in the aerosol and small particle literature. This should not come as a surprise as we have already seen what aerosol and small particle scientists have reported as the geometric mean is actually the median[†] and the reported geometric standard deviation actually represents 69% of the distribution around the median.

Obviously, there must be a source for the differences and that is precisely what we will be examining. Since there are differences between the mathematical statistics and particle statistics of area and volume distributions, both approaches will be established as a point of reference (for understanding as well as continuity) since this is exactly what was done with Sections 2.3 and 2.4.

Although mathematical purists have been at odds with particle scientists with respect to the language used in describing lognormal distributions, (Aitchison & Brown 1957, Jordan and Lee 1964, Mage and Ott 1978, Crow and Shimizu 1988), the only real difference between the use of lognormal functions by mathematicians and small-particle physicists is a matter of terminology. Crow (Crow and Shimizu, p. 338), during his examination of particle statistics, stressed that the particle physicists must be specific in their definitions. Crow writes

> *The point has been belabored, but it has seemed necessary to do so to show that the proliferation of possible distributions and means thereof has led to confusion and that writers should be explicit in their definitions or references.*

Although Crow is correct in stating the true statistics of lognormal functions differ from the statistics reported by particle scientists[††], he failed to establish the origins of these statistics[‡] and thus could neither provide insight into their development nor recognize the simplicity of their use.

[†] Although many atmospheric scientists have transitioned to using the correct terminology of median, some have begun to also refer to the median as the geometric mode that is the peak of the lognormal function. However, the peak they refer to is the mode of the random variable **logr** or **lnr**, and not the true random variable **r**.

[††] The statistics are different but related (See Sections 2.3 and 2.4).

The first part of this chapter dealt with establishing the mathematical statistics of lognormal functions and to show how these statistical definitions are related to a different set of statistics used and reported by small particle physicists. In keeping with this examination between the mathematical and physical statistics, this section begins by first establishing the (true) mathematical statistics of surface area and volume distributions while the next part of this section shows how atmospheric scientists define the statistics of surface area and volume distributions. As will be seen, the difference lies once again in the choice of random variables.

2.5.1 The Small Particle Definition of Higher Lognormal Moments

The terminology "moment distribution" may at first seem nonsensical. How can a moment be distributed? Isn't a moment a calculated number? What is actually being referred to as a moment distribution is actually a redefinition of the ordinate of the statistics. We begin to show this by starting the derivation with a distribution of particle sizes as would be collected in the field.

In section 2.4, we began the derivation of the (particle) geometric mean and the (particle) geometric standard deviation by plotting a particle size density distribution as shown in Figure 2-13a. Since Figure 2-13a indicates the number of particles per unit volume, Δn_i, at a radius r_i then the total surface area[††], ΔA_i, of the particles within each class interval is found by

$$\Delta A_i = 4\pi\, r_i^2 \cdot \Delta n_i \tag{2-66}$$

and we now have a plot of total particle surface area, ΔA_i, at a radius r_i (Figure 2-13b). This is what is referred to in the small particle literature as a surface area distribution or the 2nd moment distribution. Notice that unlike the mathematical definition of surface area, here it is not the random variable, **r**, that has been changed but the ordinate that has been changed to represent area.

To obtain the statistics of the surface area distribution we proceed as was done in section 2.4 by first dividing each bin, ΔS_i, of Figure 2-13a by the bin interval, Δr_i, to obtain

$$\frac{\Delta S_i}{\Delta r_i} = 4\pi\, r_i^2 \cdot \frac{\Delta n_i}{\Delta r_i} \tag{2-67}$$

as shown in Figure 2-13b. As the number of bins are increased while the width of each bin is decreased, Eqn. 2-67 becomes the continuous expression

$$\frac{dS}{dr} = 4\pi\, r^2 \cdot \frac{dN}{dr}. \tag{2-68}$$

[‡] Crow did not show how small particle physicists derived the geometric mean and geometric standard deviation; he simply stated the definitions from the Herdan's book.

[††] To match the literature, S is used to represent surface area as opposed to A.

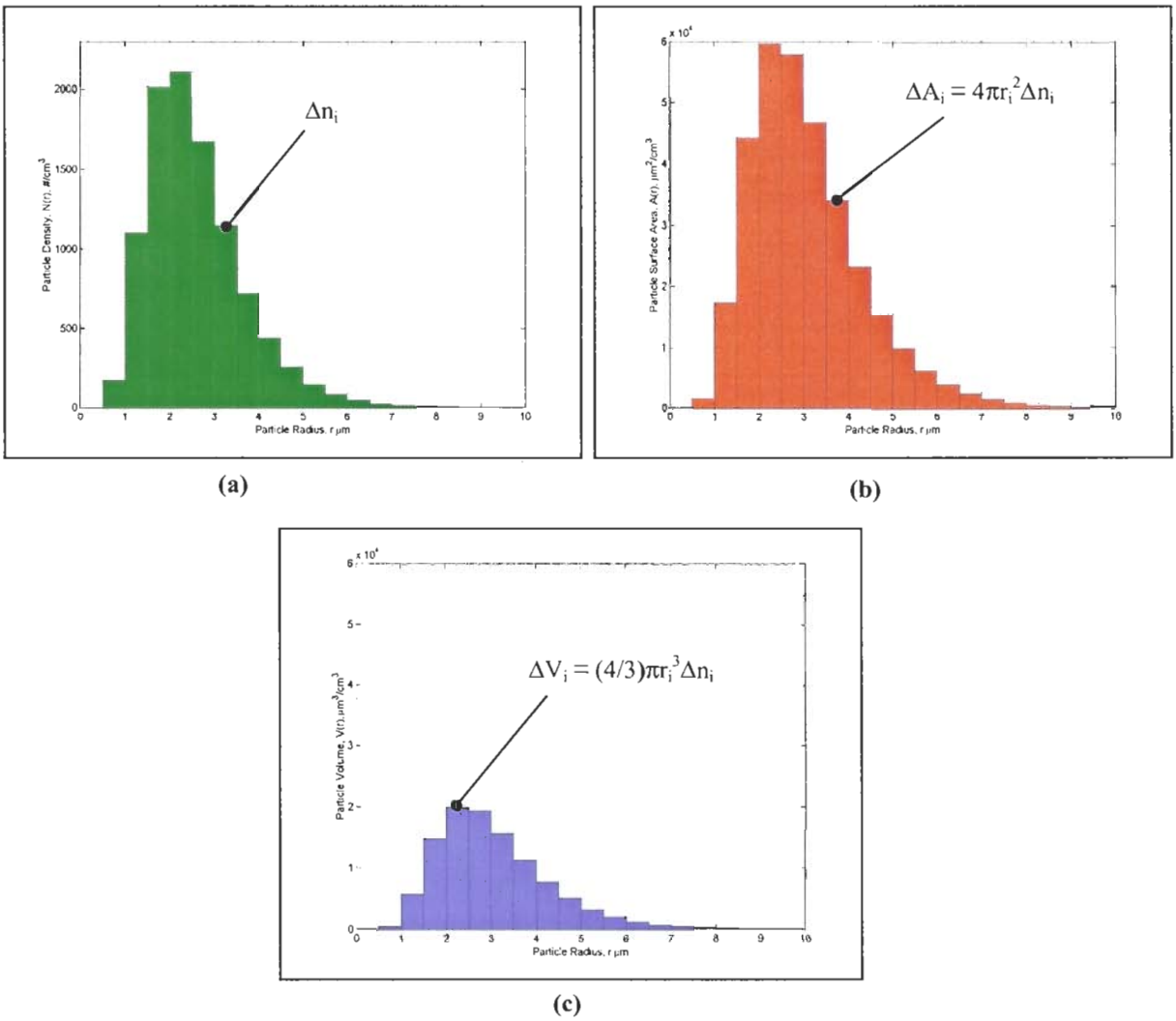

Figure 2-13: Distributions of (a) Particle number density, (b) Particle surface area density, (c) Particle volume density.

Substituting Eqn. 2-29, we have

$$\frac{dS}{dr} = 4\pi\, r^2 \frac{N_T}{\sqrt{2\pi}\cdot\sigma r}\exp\left(-\frac{1}{2\sigma^2}\left(\ln(r)-\mu\right)^2\right), \tag{2-69}$$

for which we still need to derive its statistics.

Similarly, the total volume, ΔV_i, of the particles within each class interval is found by

$$\Delta V_i = \frac{4}{3}\pi\, r_i^3 \cdot \Delta n_i \tag{2-70}$$

and a plot of the total particle volume at a radius r_i (Figure 2-13c) results. This is the volume distribution for particle physics and is also referred to as the 3rd moment distribution of the lognormal function. By dividing each bin, ΔV_i, by the bin interval, Δr_i, and allowing the bins to become continuous, yields

$$\frac{dV}{dr} = \frac{4}{3}\pi r^3 \cdot \frac{dN}{dr}. \tag{2-71}$$

The statistics of the area and volume distributions will be derived shortly but an important result must first be established.

2.5.1.1 Kapteyn's Transformation

As described above, particle physics defines area and volume distribution through multiplications of the lognormal pdf by appropriate powers of the random variable. For example, the lognormal pdf (Eqn. 2-28) is multiplied by $\mathbf{r}^2$ to obtain the area distribution and by $\mathbf{r}^3$ to obtain the volume distribution. In 1903, J.C. Kapteyn showed that multiplication of a lognormal function by powers of the random variable results in another lognormal function (Herdan, p. 85). Kapteyn, termed this effect as a distribution of moments. Aitchison and Brown did not specifically attribute this distribution of moments to anyone but do give Kapteyn's result as a theorem (Aitchison and Brown, eqn. 2.15, p. 12), and also provide a derivation. Since Aitchison and Brown's derivation uses a somewhat different mathematical language than used here and because of its importance in establishing the statistics of area and volume distributions used by small particle physicists, the derivation is worth showing.

The k^{th} moment distribution of a lognormal function, $f_{R_k}(r)$ is defined as

$$f_{R_k}(r) = \frac{r^k f_R(r)}{\int_{-\infty}^{\infty} r^k f_R(r) dr}, \tag{2-72}$$

where the integral in the denominator is needed to normalize $f_{R_k}(r)$ such that

$$\int_{-\infty}^{\infty} f_{R_k}(r) dr = 1. \tag{2-73}$$

However, the integral in Eqn. 2-72 is k^{th} central moment of the lognormal pdf and is evaluated as (see Appendix A)

$$\int_{-\infty}^{\infty} r^k f_{R_k}(r) dr = e^{\mu k + \left(\sigma^2 k^2 / 2\right)}. \tag{2-74}$$

Now, using Eqns. 2-15, 2-74 and

$$r^k = \exp\left(\ln\left(r^k\right)\right), \tag{2-75}$$

Equation 2-72 is written as

$$\begin{aligned} f_{R_k}(r) &= \exp\left(-\mu k - \sigma^2 k^2/2\right)\exp\left(\ln\left(r^k\right)\right)\frac{1}{\sqrt{2\pi}\cdot\sigma r}\exp\left(-\frac{1}{2\sigma^2}(\ln(r)-\mu)^2\right) \\ &= \frac{\exp\left(-\mu k - \sigma^2 k^2/2 + \ln\left(r^k\right)\right)}{\sqrt{2\pi}\cdot\sigma r}\exp\left(-\frac{1}{2\sigma^2}\left(\ln^2(r) - 2\mu\ln(r) + \mu^2\right)\right) \\ &= \frac{1}{\sqrt{2\pi}\cdot\sigma r}\exp\left(-\frac{1}{2\sigma^2}\left[\ln^2(r) - 2\mu\ln(r) + \mu^2 - 2\sigma^2\left(-\mu k - \sigma^2 k^2/2 + k\ln(r)\right)\right]\right). \end{aligned}$$

Since the terms in the [] form a perfect square,

$$f_{R_k}(r) = \frac{1}{\sqrt{2\pi}\cdot\sigma r}\exp\left(-\frac{1}{2\sigma^2}\left(\ln(r) - \mu - k\sigma^2\right)^2\right)$$

and defining,

$$\mu_k = \mu + k\sigma^2 \tag{2-76a}$$

$$\sigma_k = \sigma, \tag{2-76b}$$

we have the distribution of moments' lognormal probability density function given as[†]

$$\begin{aligned} f_{R_k}(r) &= \frac{1}{\sqrt{2\pi}\cdot\sigma_k r}\exp\left(-\frac{1}{2\sigma_k}(\ln(r) - \mu_k)^2\right) \\ &\equiv \Lambda\left(\mu_k, (\sigma_k)^2\right) \\ &= \Lambda\left(\mu + k\sigma^2, (\sigma)^2\right). \end{aligned} \tag{2-77}$$

Upon examining the relations of Eqn. 2-76, lognormal moment distributions all have the same σ_k and so will have the same width for a logarithmic random variable (such as **lnr** or **logr**). However, since each lognormal moment has a different μ_k, the position of each lognormal moment distribution will be different. Specifically, in terms of the (particle) median and (particle) geometric standard deviation of Eqns. 2-24 & 2-25, the corresponding lognormal moment parameters are

---

[†] The lognormal parameters μ, μ_k, σ and σ_k are for the natural log form of the lognormal pdf. Parameters for the $\log_{10}$ form of the lognormal pdf will be shown later and will use the subscript 10.

$$\boldsymbol{\sigma}_{g_k} = e^{\boldsymbol{\sigma}_k} = e^{\boldsymbol{\sigma}} = \boldsymbol{\sigma}_g \tag{2-78}$$

$$\begin{aligned} \mathbf{r}_{\text{median}_k} &= e^{\boldsymbol{\mu}_k} = e^{\boldsymbol{\mu}+k\boldsymbol{\sigma}^2} \\ &= \mathbf{r}_{\text{median}} e^{k\boldsymbol{\sigma}^2} \\ &\therefore \ \ln\left(\mathbf{r}_{\text{median}_k}\right) = \ln\left(\mathbf{r}_{\text{median}}\right) + k\boldsymbol{\sigma}^2 , \end{aligned} \tag{2-79}$$

and using Eqn. 2-78,

$$\ln\left(\mathbf{r}_{\text{median}_k}\right) = \ln\left(\mathbf{r}_{\text{median}}\right) + k \ln^2\left(\boldsymbol{\sigma}_g\right) \tag{2-80}$$

Although the plots in Figure 2-13 are not true lognormal moment pdfs, closer inspection of each plot's width and position show that even here, these results bear out. This will be an important point when we develop the trimodal model of atmospheric aerosols. We are now ready to establish the lognormal moment statistics for both surface area and volume distributions.

2.5.1.2 The Statistics of the 2nd Moment of the Lognormal Particle Size Density Distribution (Surface Area)

From Eqn. 2-77, the surface area distribution statistics are described by the pdf[†]

$$f_{R_2}(r) = \frac{1}{\sqrt{2\pi}\,\boldsymbol{\sigma}_2 r} \exp\left(-\frac{1}{2\boldsymbol{\sigma}_2^2} \left(\ln(r) - \boldsymbol{\mu}_2\right)^2 \right) \tag{2-81a}$$

$$= \frac{1}{\sqrt{2\pi}\cdot \ln\left(\boldsymbol{\sigma}_{g_2}\right) r} \exp\left(-\frac{1}{2\ln^2\left(\boldsymbol{\sigma}_{g_2}\right)} \left(\ln\left({}^{r}\!/_{\mathbf{r}_{\text{median}_2}} \right) \right)^2 \right) \tag{2-81b}$$

where,

$$\mathbf{r}_{\text{median}_2} = \mathbf{r}_{\text{median}} e^{2\boldsymbol{\sigma}^2} = e^{\boldsymbol{\mu}_2} \tag{2-82}$$

$$\boldsymbol{\sigma}_{g_2} = \boldsymbol{\sigma}_g = e^{\boldsymbol{\sigma}_2} \tag{2-83}$$

are the (particle) area geometric mean (median) and the (particle) area geometric standard deviation. Here, the random variable $\mathbf{r}$ is still used (as opposed to $\mathbf{r}^2$ for area) and the subscript 2 is used to denote that the parameters and statistics are for the 2nd lognormal moment. The various (true) statistics of the 2nd lognormal moment are found in Appendix A. In keeping with the particle size density distribution of section 2.4, the values of Eqns. 2-82 and 2-83 are the ones most often found in the literature.

[†] Herdan implied that the statistics of the particle surface area/volume distributions were identical to the mathematical statistics. See Herdan, eqn. 4-10, p. 34 and section 6.8, pp. 84-85.

Using Eqn. 2-68, we now show how to obtain expressions for the surface area distribution similar to those for the particle number expressions of Eqns. 2-29, 2-48b and 2-58b. To make Eqn. 2-68 into a pdf, we must integrate as

$$\int_{-\infty}^{\infty} \frac{dS}{dr} dr = \int_{-\infty}^{\infty} 4\pi r^2 \frac{dN}{dr} dr$$
$$= 4\pi N_T \int_{-\infty}^{\infty} r^2 \frac{1}{\sqrt{2\pi} \cdot \boldsymbol{\sigma} r} \exp\left(-\frac{1}{2\boldsymbol{\sigma}^2} (\ln(r) - \boldsymbol{\mu})^2 \right) dr .$$

Since the integral is the 2nd central moment of a lognormal distribution, we have

$$\int_{-\infty}^{\infty} \frac{dS}{dr} dr = 4\pi N_T e^{2\boldsymbol{\mu} + 2\boldsymbol{\sigma}^2}$$
$$\equiv S_T \tag{2-84}$$

and, therefore,

$$\frac{1}{S_T} \frac{dS}{dr} = f_{R_2}(r), \tag{2-85}$$

which is similar to the particle size expression of Eqn. 2-28. Although N_T represents the total number of particles of a lognormal distribution, S_T, is somewhat more difficult to interpret. Strictly, S_T represents the total surface area of all the particles in the distribution but does not provide one with any additional information. For now, the best way to interpret S_T is to simply state that is a normalizing factor used to obtain the statistics of a surface area distribution. Now, using Eqns. 2-81a, 2-84 and 2-85 with Eqn. 2-68, we have

$$\frac{dS}{dr} = \frac{A_T}{\sqrt{2\pi} \cdot \boldsymbol{\sigma}_2 r} \exp\left(-\frac{1}{2\boldsymbol{\sigma}_2^2} (\ln(r) - \boldsymbol{\mu}_2)^2 \right). \tag{2-86}$$

Also, using the (particle) area median and (particle) area geometric standard deviation of Eqns. 2-82 & 2-83, we have, for the random variable **lnr**,

$$\frac{dS}{d\ln r} = \frac{S_T}{\sqrt{2\pi} \cdot \ln(\boldsymbol{\sigma}_{g_2})} \exp\left(-\frac{1}{2\ln^2(\boldsymbol{\sigma}_{g_2})} \left(\ln\left(r / \mathbf{r}_{\text{median}_2} \right) \right)^2 \right) \tag{2-87}$$
$$= 4\pi r^2 \frac{dN}{d\ln r},$$

and for the random variable **logr**,

$$\frac{dS}{d\log r} = \frac{S_T}{\sqrt{2\pi}\cdot\log(\sigma_{g_2})}\exp\left(-\frac{1}{2\log^2(\sigma_{g_2})}\left(\log\left(r/r_{\text{median}_2}\right)\right)^2\right) \qquad (2\text{-}88)$$
$$= 4\pi r^2 \frac{dN}{d\log r}.$$

2.5.1.3 Statistics of the 3rd Moment of the Lognormal Probability Density Function (Volume)

From Eqn. 2-77, the volume distribution statistics are described by the pdf

$$f_{R_3}(r) = \frac{1}{\sqrt{2\pi}\cdot\sigma_3 r}\exp\left(\frac{1}{2\sigma_3^2}(\ln(r)-\mu_3)^2\right)$$
$$= \frac{1}{\sqrt{2\pi}\cdot\ln(\sigma_{g_3})r}\exp\left(\frac{1}{2\ln^2(\sigma_{g_3})}\left(\ln\left(r/r_{\text{median}_3}\right)\right)^2\right)$$

where,

$$r_{\text{median}_3} = r_{\text{median}} e^{3\sigma^2} \qquad (2\text{-}90)$$

$$\sigma_{g_3} = \sigma_g = e^{\sigma_3} \qquad (2\text{-}91)$$

are the (particle) volume geometric mean (median) and the (particle) volume geometric standard deviation. As with the (particle) surface area, the random variable here is still **r** (as opposed to $\mathbf{r}^3$ for volume). The subscript 3 is used to denote that the parameters and statistics are for the 3rd lognormal moment. In keeping with the particle size density distribution of section 2.4, the values of Eqns. 2-90 and 2-91 are the ones most often found in the literature.

To obtain expressions similar to those of the surface area above (Eqns. 2-86, 2-87, 2-88), we begin with Eqn. 2-71 and integrate as

$$\int_{-\infty}^{\infty}\frac{dV}{dr}dr = \int_{-\infty}^{\infty}\tfrac{4}{3}\pi r^3\frac{dN}{dr}dr \qquad (2\text{-}92)$$
$$= \tfrac{4}{3}\pi N_T\int_{-\infty}^{\infty} r^3\frac{1}{\sqrt{2\pi}\cdot\sigma r}\exp\left(-\frac{1}{2\sigma^2}(\ln(r)-\mu)^2\right)dr.$$

Since the integral evaluates as the 3rd central moment of a lognormal pdf, we have

$$\int_{-\infty}^{\infty}\frac{dV}{dr}dr = \frac{4}{3}\pi N_T e^{3\mu+9\sigma^2/2} \qquad (2\text{-}93)$$
$$\equiv V_T$$

and therefore,

$$\frac{1}{V_T}\frac{dV}{dr} = f_{R_3}(r)\,, \tag{2-94}$$

where the normalization factor V_T is the total volume of all the particles in the distribution. Now, using Eqns. 2-89a, 2-93, and 2-94 with Eqn. 2-71, we have

$$\frac{dV}{dr} = \frac{V_T}{\sqrt{2\pi}\cdot\boldsymbol{\sigma}_3 r}\exp\left(-\frac{1}{2\boldsymbol{\sigma}_3^2}(\ln(r)-\boldsymbol{\mu}_3)^2\right). \tag{2-95}$$

Further, using the (particle) volume median and (particle) volume geometric standard deviation of Eqns. 2-90 and 2-91, we have, for the random variable **lnr**,

$$\frac{dV}{d\ln r} = \frac{V_T}{\sqrt{2\pi}\cdot\ln(\boldsymbol{\sigma}_{g_3})}\exp\left(-\frac{1}{2\ln^2(\boldsymbol{\sigma}_{g_3})}\left(\ln\left(r/\mathbf{r}_{\text{median}_3}\right)\right)^2\right) \tag{2-96a}$$

$$= \frac{4}{3}\pi r^3\frac{dN}{d\ln r}\,,$$

and for the random variable logr,

$$\frac{dV}{d\log r} = \frac{V_T}{\sqrt{2\pi}\cdot\log(\boldsymbol{\sigma}_{g_3})}\exp\left(-\frac{1}{2\log^2(\boldsymbol{\sigma}_{g_3})}\left(\log\left(r/\mathbf{r}_{\text{median}_3}\right)\right)^2\right) \tag{2-96b}$$

$$= \frac{4}{3}\pi r^3\frac{dN}{d\log r}\,.$$

2.5.1.4 Trimodal Display of (Particle) Surface Area and Volume Distributions

Similar to Eqn. 2-87, we have for the surface area and volume distributions,

$$\frac{dS}{d\log r} = \sum_{i=1}^{3}\frac{S_{T_i}}{\sqrt{2\pi}\cdot\log(\boldsymbol{\sigma}_{g_i})}\exp\left(-\frac{1}{2\log^2(\boldsymbol{\sigma}_{g_i})}\left(\log\left(r/\mathbf{r}_{\text{median}_{2_i}}\right)\right)^2\right) \tag{2-97}$$

$$\frac{dV}{d\log r} = \sum_{i=1}^{3}\frac{V_{T_i}}{\sqrt{2\pi}\cdot\log(\boldsymbol{\sigma}_{g_i})}\exp\left(-\frac{1}{2\log^2(\boldsymbol{\sigma}_{g_i})}\left(\log\left(r/\mathbf{r}_{\text{median}_{3_i}}\right)\right)^2\right). \tag{2-98}$$

Using the data taken from Kelkar and Joshi (Kelkar and Joshi, table 1, p.532), shown in Table 2-2 below, which are parameters used to fit Whitby's 1972 Los Angeles smog data to a trimodal distribution, we obtain the plots of Eqns. 2-65, 2-97 and 2-98 (Figure 2-14).

Table 2-2: Parameters of a trimodal aerosol distribution (Whitby, 1972).

	N_{Ti} (#/m^3)	$r_{mediani}$ (μm)	σ_{gi}
Mode #1	$4\text{x}10^{11}$	0.002	2.7
Mode #2	$7.5\text{x}10^{9}$	0.05	1.7
Mode #3	$1.2\text{x}10^{7}$	0.25	2.25

We can obtain the probability density function for the number, surface area and volume density distributions of Eqns. 2-65, 2-97 and 2-98 by normalizing each expression with the appropriate value such that the area under each curve is unity. These new pdfs will not be lognormal but represent the pdf of a sum of three lognormal functions. Specifically, for the trimodal particle size density distribution, we have

$$\begin{aligned}\overline{N}_T &= \int_{-\infty}^{\infty} \frac{dN}{d\log r} d\log r \\ &= \int_{-\infty}^{\infty} \sum_{i=1}^{3} \frac{N_{T_i}}{\sqrt{2\pi}\cdot\log(\sigma_{g_i})} \exp\left(-\frac{1}{2\log^2(\sigma_{g_i})}\left(\log\left(r/r_{\text{median}_i}\right)\right)^2\right) d\log r \\ &= N_{T_1} + N_{T_2} + N_{T_3}.\end{aligned} \tag{2-99}$$

Therefore, the pdf for the trimodal particle size distribution is given by

$$f_N(r) = \frac{1}{\overline{N}_T}\frac{dN}{d\log r}. \tag{2-100}$$

Similarly, for surface area,

$$\begin{aligned}f_S(r) &= \frac{1}{\overline{S}_T}\frac{dS}{d\log r} \\ &= \frac{1}{(S_{T_1} + S_{T_2} + S_{T_3})}\frac{dS}{d\log r}\end{aligned} \tag{2-101}$$

and for volume,

$$\begin{aligned}f_V(r) &= \frac{1}{\overline{V}_T}\frac{dV}{d\log r} \\ &= \frac{1}{(V_{T_1} + V_{T_2} + V_{T_3})}\frac{dV}{d\log r}.\end{aligned} \tag{2-102}$$

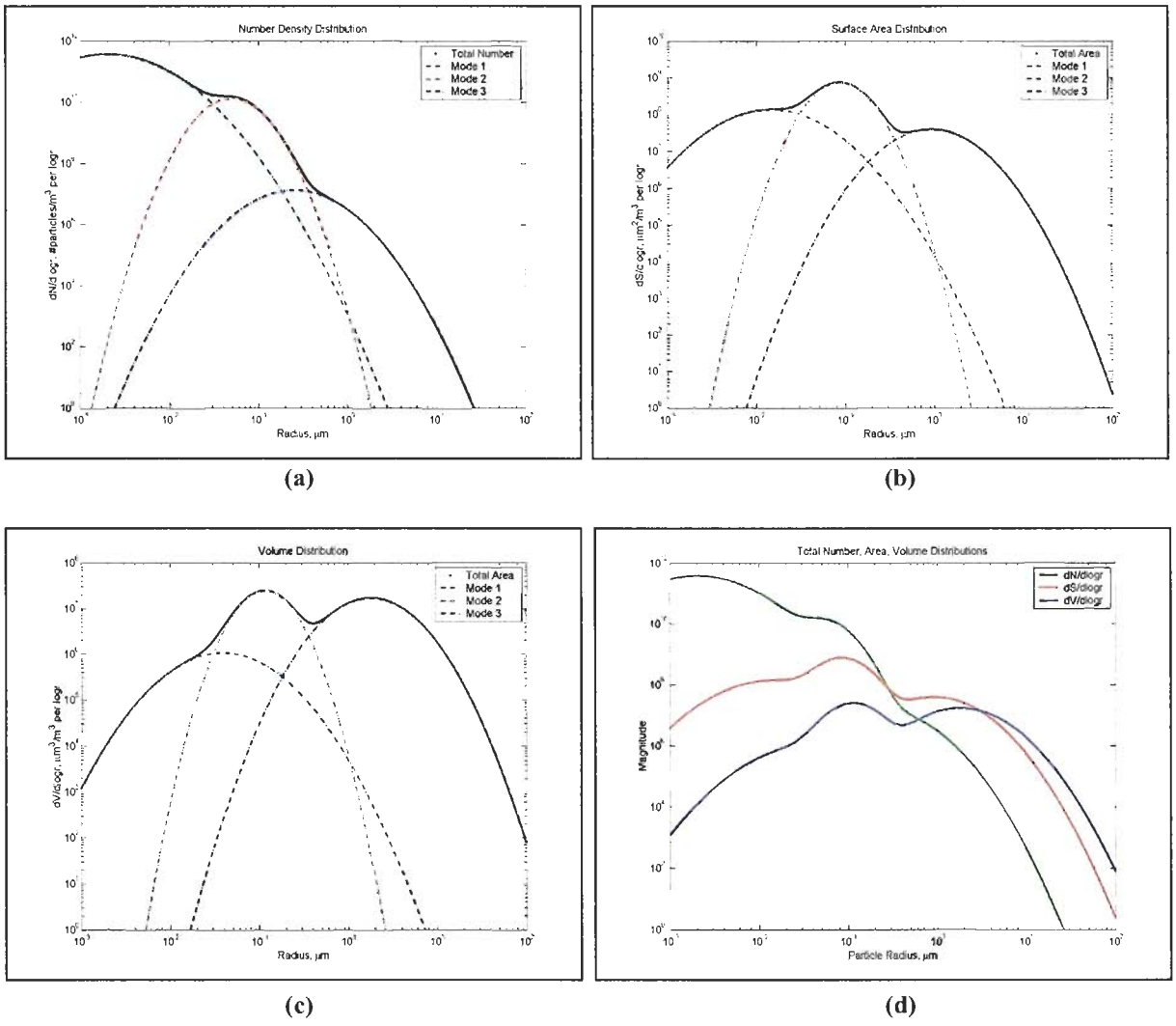

Figure 2-14: Plots of particle number, surface area and volume for a trimodal aerosol distribution (based on Whitby, 1972). Each plot shows different details of the same particle distribution and are used to enhance characteristics that would otherwise be obscured by viewing only one type of distribution alone.

Using the data of Figure 2-14, Eqns. 2-100, 2-101 and 2-102 are plotted in Figure 2-15 where we see some interesting information. The particle number is a maximum at different places from the surface area and volume. This figure indicates that for optical studies, which rely on the cross-section or surface area of the particle distribution, the range of interest is around 1 μm. Further, when we examine trimodal aerosol populations, we will find that mode 1 is the most numerous, mode 2 generally has the most area, and mode 3 generally has the most mass (volume).

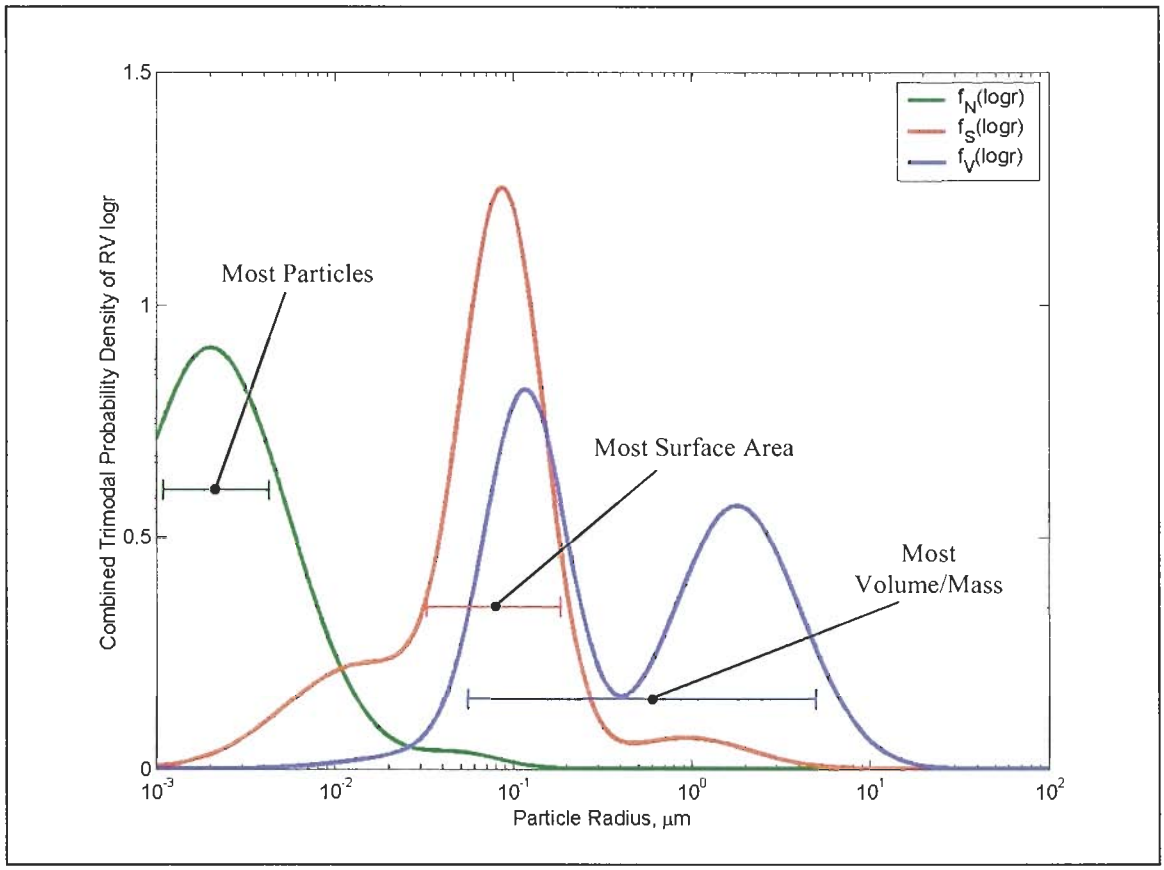

Figure 2-15: Total probability density functions of particle number, surface area and volume based on a trimodal aerosol model (See also Whitby).

2.5.1.5 Variations on a Theme: The Mass Density Distribution

In pollution studies, the primary measurement is of determining the mass of a particular species (such as sulfate compounds) or a collection of particles (such as $PM_{2.5}$ or PM_{10}). The mass of a sphere is given as

$$\begin{aligned} M &= \rho V \\ &= \rho \frac{4}{3} \pi r^3 , \end{aligned}$$

where ρ is the mass density in g/cm^3. However, since volume density distributions are typically given as a function of particle radius or diameter in μm, the mass density, ρ, must be converted to units of g/μm. We will not take the time to write out the statistics using for mass primarily because access to ρ is speculative at best. However, based on what we have presented here, the interested reader should have no trouble in working through the mathematics.

2.6 SUMMARY

In this chapter we have explicitly shown the use of the lognormal function in atmospheric and small particle physics. The true statistics, as shown in Appendix A, differ from the applied statistics based on the use of the random variable. In mathematics, the random variable **r** is used while in the physical application, the random variable **logr** or **lnr** is used. Although using **lnr** is more appropriate for mathematical analysis, **logr** is often chosen for display purposes because of the ease of working with powers of 10. However, regardless of what base is desired, the median, $\mathbf{r}_{\mathbf{median}}$, and the geometric standard deviation, σ_g, yield the same results. The only difference between using **lnr** or **logr** arises when one uses these functions for describing distributions (as opposed to probability density functions). In distributions, the two functions differ by a factor of $\ln(10) = 2.303$.

3

Chapter 3:
Scattering Theory

I hear, I forget.
I see, I remember.
I do, I understand.

Scattering theory describes the interaction of electromagnetic radiation with matter. This seemingly simple description belies an exceptionally complicated set of expressions, which, even in the simplest of cases, can pose great difficulties to their understanding, interpretation and application. However, the reward one receives for putting the time and energy into understanding these complicated expressions will be in having at their fingertips a fundamental, yet beautiful, grasp of the electromagnetic world in which we live.

At the very mention of Maxwell's equations, most peoples' eyes glaze over as they enter into a trance-like state, vacantly nodding every so often in the direction of the speaker just to be polite. Thankfully, there are many good sources showing the mathematics in all of its gory detail so the full derivation and exposition of scattering theory will not be given here. However, scattering theory forms a cornerstone of this thesis and so it would seem inadequate to simply quote formulas without giving some description of where they came from, of what other possible forms of the equations exist, and most especially, how these equations are used in this thesis. Additionally, it is important to establish the nomenclature and to be consistent throughout this thesis since just about every author uses a similar, yet somewhat different set of variables to describe the theory. The most significant point to placing scattering theory in this thesis however, is to give the reader a complete document where the significant terms are defined, derived and explained rather than leaving the reader to ferret out (or worse, assume) the exact research paper or text. It would be advantageous to the reader to have in front of them a document that explains the basics in detail but yet provides direct links to additional sources.

This chapter will establish the basic electromagnetic theory and the definitions to be used throughout this thesis. As with Chapter 2, this chapter is very mathematical and is simply meant to put forth the theoretical foundations to be used throughout the remaining chapters. Readers who are comfortable with scattering theory should be able to skip this chapter entirely and may only need to consult it to obtain various definitions. Those readers who already have a firm grasp of electromagnetics and only need to get a better feel of scattering theory are directed immediately to section 3.2.

3.1 BASICS OF ELECTROMAGNETICS

In this section, we establish the basic expressions governing the behavior of electromagnetic phenomena. While these expressions are considered basic, they are by no means simple. Indeed, it generally takes a person a lifetime of commitment to their understanding and application. It is not our intention here to give a lengthy exposition of electromagnetic theory. We simply wish to include enough of

the basics to refresh and direct the reader to our train of thought. This is necessary because while the equations themselves are not ambiguous, the various terminology and mathematical language employed by people to describe these equations have varied much over the years. What works and is comfortable for one person may be completely alien to another. The lack of continuity in the mathematical language employed by various authors has been one of the main difficulties in understanding electromagnetic theory.

3.1.1 Maxwell's Equations

Although the electromagnetic principles were known and had been investigated for some time, it was a mechanical engineer named James Clerk Maxwell, working in the field of fluid dynamics, who noticed similarities in the expressions he was using and in those being used by physicists working with electromagnetic waves. Indeed, those who study the fluid-governing Navier-Stokes equations will undoubtedly see the similarities to the electromagnetic equations since the mathematical language employed is rather transparent to the application. In 1848, Maxwell collected the expressions into a set of four basic equations, now called the Maxwell Equations (Table 3.1). Maxwell's insightful observations also helped him to identify a missing term in the equations (the displacement current).

Table 3.1: Point and Integral Forms of Maxwell's Equations

	Differential Form (Point Form)[†]	Integral Form (Large Scale Form)
Faraday's Law	$\nabla\times\vec{\mathbf{E}}=-\frac{\partial\vec{\mathbf{B}}}{\partial t}$	$\oint_C\vec{\mathbf{E}}\cdot d\mathbf{l}=-\iint_A\frac{\partial\vec{\mathbf{B}}}{\partial t}\cdot d\mathbf{S}$
Ampere's Law	$\nabla\times\vec{\mathbf{H}}=\vec{\mathbf{J}}_c+\frac{\partial\vec{\mathbf{D}}}{\partial t}$	$\oint_C\vec{\mathbf{H}}\cdot d\mathbf{l}=\iint_A\left(\vec{\mathbf{J}}_c+\frac{\partial\vec{\mathbf{D}}}{\partial t}\right)\cdot d\mathbf{S}$
Gauss' Electric Law	$\nabla\cdot\vec{\mathbf{D}}=\rho_V$	$\oiint_A\mathbf{D}\cdot d\mathbf{S}=\iiint_V\rho_V\,dV$
Gauss' Magnetic Law (no magnetic charges)	$\nabla\cdot\vec{\mathbf{B}}=0$	$\oiint_A\vec{\mathbf{B}}\cdot d\mathbf{S}=0$

From Table 3.1, the principal items of interest are the electric and magnetic fluxes ($\vec{\mathbf{D}}$ & $\vec{\mathbf{B}}$) and the electric and magnetic fields ($\vec{\mathbf{E}}$ & $\vec{\mathbf{H}}$). Although there are four equations, only two are independent (Faraday's and Ampere's laws). Thus two additional expressions are needed to specify a unique solution. These expressions are called the constituitive relations and are given by

---

[†] While it is erroneous to do so, the del operator can be used as the vector, $\vec{\nabla}=\hat{\mathbf{x}}\frac{\partial}{\partial\mathbf{x}}+\hat{\mathbf{y}}\frac{\partial}{\partial\mathbf{y}}+\hat{\mathbf{z}}\frac{\partial}{\partial\mathbf{z}}$.

$$\vec{D} = \bar{\bar{\varepsilon}}\,\vec{E} \tag{3-1a}$$

$$\vec{B} = \bar{\bar{\mu}}\,\vec{H} \tag{3-1b}$$

where $\bar{\bar{\varepsilon}}$ is the complex permittivity tensor and $\bar{\bar{\mu}}$ is the complex permeability tensor. For the remainder of this thesis, we will assume a homogeneous and isotropic medium (the atmosphere) and so we will drop the tensor notation to allow the permittivity and permeability to be scalar coefficients. Along with conductivity and the (complex) index of refraction, permittivity and permeability are collectively termed phenomenological parameters. The permittivity and permeability are expressed in complex terms as

$$\varepsilon = \varepsilon' \pm j\varepsilon'' \tag{3-2a}$$

$$\mu = \mu' \pm j\mu'' \tag{3-2b}$$

Having the +/- signs here is for completeness and later we will use (and show why) the '+' sign is preferred in this thesis. The constituitive relations are needed to obtain a unique electromagnetic solution within a medium but in solving the electromagnetic fields across two boundaries, one will also need to use boundary conditions.

3.1.1.1 Simplifications and Assumptions for the Atmosphere

Maxwell's equations are exceptionally powerful. In fact, they could be used for direct analysis of electronic circuits but, thankfully, simpler expressions such as Ohm's Law are available (which derives from Maxwell's equations). We will be using Maxwell Equations to describe the electromagnetic interaction with particles (assumed to be spherical) in the atmosphere. There are also a set of assumptions known as the free-space approximations that will help us to simplify our starting set of Maxwell Equations.

The free-space approximations directly impact the phenomenological coefficients (permittivity, permeability, and index of refraction). In the atmosphere, it is generally assumed that free-space conditions hold, i.e., the medium is linear, homogenous, isotropic, contains no free charges and the permeability is μ_0. Typically, conductivity is used to characterize free electrons in metals while permittivity is used to describe the bound electrons in dielectrics (Ramo, et al., p. 284). Since both contribute to the absorption, it is difficult to distinguish between free and bound charges in a medium (Bohren & Huffman, p. 19). For the atmosphere, the conductivity, σ, is assumed zero. However, to account for particles with high absorption that may be present in the atmosphere, such as carbonaceous compounds, the permittivity is allowed to be complex (its exact form will be found in the next section). The Maxwell Equations for the atmosphere are given in Table 3.2.

Table 3.2: Reduced, Point-Form of the Maxwell Equations for Atmospheric Propagation.

Faraday's Law	$\nabla \times \vec{\mathbf{E}} = -\frac{\partial \vec{\mathbf{B}}}{\partial t}$
Ampère's Law	$\nabla \times \vec{\mathbf{B}} = \varepsilon \mu_0 \frac{\partial \vec{\mathbf{E}}}{\partial t}$
Gauss' Law	$\nabla \cdot \vec{\mathbf{E}} = 0$
Gauss' Law (no magnetic charges)	$\nabla \cdot \vec{\mathbf{B}} = 0$

3.1.1.2 Plane Wave Solution for the Atmosphere

Let us solve the electromagnetic equations to obtain a solution applicable to propagation in free space. There is a very important, often overlooked, yet subtle point concerning the sign convention used in electromagnetic texts that emerges from the following solution. Taking the curl of both sides of Faraday's law yields

$$\nabla \times \left(\nabla \times \vec{\mathbf{E}}\right) = -\frac{\partial}{\partial t}\left(\nabla \times \vec{\mathbf{B}}\right). \tag{3-3}$$

Using the vector identity

$$\nabla \times \left(\nabla \times \vec{\mathbf{A}}\right) = \nabla\left(\nabla \cdot \vec{\mathbf{A}}\right) - \nabla^2 \vec{\mathbf{A}}$$

where

$$\nabla^2 \vec{\mathbf{A}} = \frac{\partial^2 \vec{\mathbf{A}}}{\partial x^2} + \frac{\partial^2 \vec{\mathbf{A}}}{\partial y^2} + \frac{\partial^2 \vec{\mathbf{A}}}{\partial z^2}$$

is the Laplacian operator and $\vec{\mathbf{A}}$ is some vector. Rearranging and simplifying, we have the 3-dimensional wave equation

$$\nabla^2 \vec{\mathbf{E}} = \mu_0 \varepsilon \frac{\partial^2 \vec{\mathbf{E}}}{\partial t^2}. \tag{3-4}$$

A similar result can be found for the magnetic flux, $\vec{\mathbf{B}}$. The expression that satisfies Eqn. 3-4 must be a function of position and time, specifically, one that is twice differentiable with respect to both position and time (Hecht, p. 14). The most general solution to Eqn. 3-4 is an $\vec{\mathbf{E}}$ field of the form

$$\vec{\mathbf{E}} = E_x(x,y,z,t)\hat{\mathbf{x}} + E_y(x,y,z,t)\hat{\mathbf{y}} + E_z(x,y,z,t)\hat{\mathbf{z}}. \tag{3-5}$$

To make the solution easier to obtain and visualize, we'll restrict the $\vec{\mathbf{E}}$ field to have only a $\hat{\mathbf{x}}$ component and that component to only be a function of $\hat{\mathbf{z}}$, i.e., the field is propagating in the $\hat{\mathbf{z}}$ direction. Therefore, Eqn. 3-4 reduces to

$$\frac{\partial^2 E_x(z,t)}{\partial z^2} = \mu_0 \varepsilon \frac{\partial^2 E_x(z,t)}{\partial t^2}. \tag{3-6}$$

Equation 3-6 is the one-dimensional wave equation whose solution is periodic in both space and time. Since any real, physical pulse shape can be decomposed into harmonics, the simplest expression that satisfies Eqn. 3-6 is a sinusoid given by

$$\vec{\mathbf{E}} = \vec{\mathbf{x}} A \cos(\pm kz \pm \omega t) \tag{3-7}$$

under the condition that

$$k^2 = \mu_0 \varepsilon \omega^2 . \tag{3-8}$$

Equation 3-7 indicates that there are four possible solutions to Eqn. 3-4. However, only two of the solutions represent a wave propagating in the positive $\hat{\mathbf{z}}$, or forward, direction. The phase velocity, v, is given by (Hecht, eqn. 2.32, p. 18)

$$\mathrm{v} = -\frac{\left(\partial\phi/\partial t\right)}{\left(\partial\phi/\partial z\right)} = -\frac{\partial z}{\partial t}, \tag{3-9}$$

where ϕ is the argument, or phase, of the wave solution (Eqn. 3-7). The phase velocity is positive for a wave traveling in the positive direction and so the wave solutions that satisfy this are

$$\vec{\mathbf{E}} = \hat{\mathbf{x}} A \cos(kz - \omega t) \tag{3-10}$$

or

$$\vec{\mathbf{E}} = \hat{\mathbf{x}} A \cos(\omega t - kz). \tag{3-11}$$

As can be seen from Eqns. 3-10 and 3-11, the fields are simply out of phase by 180°. Because complex exponentials are easier to manipulate, the complex representation of the field is

$$\vec{\mathbf{E}} = \hat{\mathbf{x}} A e^{j(kz-\omega t)} = \hat{\mathbf{x}} A e^{jkz} e^{-j\omega t} \tag{3-12a}$$

or

$$\vec{\mathbf{E}} = \hat{\mathbf{x}} A e^{j(\omega t-kz)} = \hat{\mathbf{x}} A e^{-jkz} e^{j\omega t} \; . \tag{3-12b}$$

We are generally concerned with a single (temporal) frequency, the time harmonic part of the above equations can be suppressed for the sake of convenience. Since either solution represents a wave traveling in the positive direction, which do we choose? Either will do since being out of phase by 180° makes no difference to the wave expression - phase is only an indication of the starting point. However, the impact of choosing one solution or the other manifests itself in the mathematical definitions of the underlying parameters and coefficients. In keeping with the Mie theory shown in Section 3.4, this thesis uses Eqns. 3-10 and Eqn. 3-12a for the $\vec{\mathbf{E}}$ field solutions.

In the solution of the Maxwell equations, a simplification to the analysis method is often made using the assumption of time-harmonic fields. This assumption indicates that the frequency is constant with time and therefore the quantity, ωt, repeats, i.e. time-harmonic (Shen & Kong, p. 36). Time-harmonic means that the electromagnetic wave varies sinusoidally or periodically (subject to Dirchlet conditions) with time, but not necessarily with space. The assumption of time-harmonic waves allows one to simplify the time-domain differential Maxwell Equations of Table 3.2 into frequency-domain algebraic equations of Table 3.3. One is cautioned however, that the Fourier Transform pair,

$$\frac{d^n}{dt^n} \Leftrightarrow (j\omega)^n$$

was NOT used in the conversion (see Shen & Kong, problems 2.18 & 2.19, p. 43).

3.1.1.3 Phenomenological Parameter Definitions and the Complex Index of Refraction

Generally, microwave frequencies use epsilon notation, while optical frequencies use the index of refraction (Ramo, et al., p. 682; Bohren & Huffman, p. 228) to describe the propagating medium. However, these constants are neither equal to each other nor or are they independent (Bohren & Huffman, p. 227). Further, the real and complex parts of either epsilon or the refractive index are not completely independent (Bohren & Huffman, p. 265, p. 279). In bulk matter, the optical coefficients are obtained through reflected and transmitted waves. In particles, the optical coefficients are obtained through the scattered field (Bohren & Huffman, section 2.10, p. 42).

Table 3.3: Time-Harmonic Forms of the Atmospheric Maxwell Equations

Phase Front Quantity	$e^{j(kz-\omega t)}$ (Bohren & Huffman)	$e^{j(\omega t-kz)}$ (Shen & Kong)
Faraday's Law	$\nabla\times\vec{\mathbf{E}} = j\omega\vec{\mathbf{B}}$	$\nabla\times\mathbf{E} = -j\omega\vec{\mathbf{B}}$
Ampère's Law	$\nabla\times\vec{\mathbf{H}} = \vec{\mathbf{J}}_c - j\omega\vec{\mathbf{D}}$	$\nabla\times\vec{\mathbf{H}} = \vec{\mathbf{J}}_c + j\omega\vec{\mathbf{D}}$
Gauss' Law	$\nabla\cdot\vec{\mathbf{D}} = \rho_V$	$\nabla\cdot\vec{\mathbf{D}} = \rho_V$
Gauss' Law (no magnetic charges)	$\nabla\cdot\vec{\mathbf{B}} = 0$	$\nabla\cdot\vec{\mathbf{B}} = 0$

Because epsilon is complex, the wave number, k, is also complex and since we are using the form of Eqn. 3-12a, k must be of the form

$$k = k_{\mathrm{Re}} + jk_{\mathrm{Im}}. \tag{3-13}$$

The reason for this can be seen by substituting Eqn. 3-13 into Eqn. 3-12a, yielding

$$\begin{aligned}\vec{\mathbf{E}} &= \hat{\mathbf{x}}Ae^{j(k_{\mathrm{Re}}+jk_{\mathrm{Im}})z} \\ &= \hat{\mathbf{x}}Ae^{jk_{\mathrm{Re}}z}e^{-k_{\mathrm{Im}}z}\end{aligned}, \tag{3-14}$$

where the harmonic term, $e^{j\omega t}$ is understood to be present. It is immediately seen that the complex exponential term in Eqn. 3-14 represents the sinusoidal wave function while the real exponential term represents attenuation. Converting Eqn. 3-14 into its real form yields

$$\begin{aligned}\vec{\mathbf{E}} &= \mathrm{Re}\left\{\hat{\mathbf{x}}Ae^{jk_{\mathrm{Re}}z}e^{-k_{\mathrm{Im}}z}\right\} \\ &= \hat{\mathbf{x}}Ae^{-k_{\mathrm{Im}}z}\cos(k_{\mathrm{Re}}z-\omega t).\end{aligned} \tag{3-15}$$

The result indicates that the imaginary part of the wave number represents attenuation of the wave as it propagates. The phase velocity of the wave is dependent only on the real part of the wave number (Hecht, p. 110). By expanding Eqn. 3-8 as

$$k = \omega\sqrt{\mu_0\varepsilon} \tag{3-16a}$$

$$= \frac{2\pi c}{\lambda}\sqrt{\mu_0\varepsilon}, \tag{3-16b}$$

where c is the speed of light in a vacuum given by

$$c = \frac{1}{\sqrt{\mu_0 \varepsilon_0}},$$

and neglecting for the moment that k and ε are complex, we have

$$k = \frac{2\pi}{\lambda}\frac{c}{v} \tag{3-17}$$

where v is the speed of the electromagnetic wave in the medium. For an isotropic medium, the index of refraction is defined as the ratio of velocities in free-space to that in the medium (Hecht, eqn. 3.58, p. 56; Bohren & Huffman, eqn. 2.47, p. 27),

$$n(\lambda) = \frac{c}{v} = \frac{\sqrt{\mu_0 \varepsilon}}{\sqrt{\mu_0 \varepsilon_0}}. \tag{3-18}$$

What may cause one to wonder is, if the permittivity and wave number can be and are complex quantities, then this would seem to indicate that the wave velocity is also complex, a seemingly physical impossibility, or at least a physically meaningless term. The answer is that the wave velocity (phase velocity) is always a real number and is found by using only the real parts of the complex index of refraction, permittivity or wave number (Hecht, p. 110). Although wavelength is not explicitly present in Eqn. 3-18, it must be present to indicate that the propagation properties of materials and mediums change over wavelength (or frequency).

Combining Eqns. 3-13, 3-17, & 3-18, yields the complex expressions

$$k = k_{\mathrm{Re}} + jk_{\mathrm{Im}} = \frac{2\pi}{\lambda}\left(n_{\mathrm{Re}} + jn_{\mathrm{Im}}\right). \tag{3-19}$$

Now, using the atmospheric free-space parameters (specifically, conductivity is assumed to be zero), Eqn. 3-2a is generalized as

$$\varepsilon = \varepsilon' + j\varepsilon''. \tag{3-20}$$

To relate the real and imaginary parts of the complex constants, Eqns. 3.19 & 3.20 are substituted into Eqn. 3-18 to yield

$$n_{\mathrm{Re}} + jn_{\mathrm{Im}} = \sqrt{\frac{\varepsilon'}{\varepsilon_0} + j\frac{\varepsilon''}{\varepsilon_0}}. \tag{3-21}$$

Squaring both sides and equating like terms yields two equations (Bohren & Huffman, eqn. 9.1, p. 227)

$$\frac{\varepsilon'}{\varepsilon_0} = n_{\mathrm{Re}}^2 - n_{\mathrm{Im}}^2 \tag{3-22a}$$

$$\frac{\varepsilon''}{\varepsilon_0} = 2n_{\mathrm{Re}}n_{\mathrm{Im}}\,, \tag{3-22b}$$

which can be rearranged with respect to the index of refraction components as (Bohren & Huffman, eqn. 9.2, p. 227; Ramo et al., eqns. 5 & 6, p. 284)

$$n_{\mathrm{Re}} = \sqrt{\frac{\sqrt{(\varepsilon')^2 + (\varepsilon'')^2} + \varepsilon'}{2\varepsilon_0}} \tag{3-23a}$$

$$n_{\mathrm{Im}} = \sqrt{\frac{\sqrt{(\varepsilon')^2 + (\varepsilon'')^2} - \varepsilon''}{2\varepsilon_0}}\,. \tag{3-23b}$$

Sometimes, the complex index of refraction is given as (Kerker et al., 1978; Bohren & Huffman, p. 136; Handbook of Chemistry and Physics, 67th ed.)

$$n = n(1 + j\kappa)\,, \tag{3-24}$$

where κ is called the absorptivity. Here, we will strictly use Eqn. 3-21 for denoting the complex index of refraction.

A subtle, but important point must be made regarding the optical constants† in Eqns. 3-19, 3-20 & 3-21. All of these constants are of the form a + jb due to the choice of the time harmonic $e^{-j\omega t}$ used in the solution of the wave equation. Having the constants of this form gave the physically realizable solution in Eqn. 3-15. If, instead, the time harmonic $e^{j\omega t}$ had been used in the solution of the wave equation, then each of the optical constants would have the form a – jb in order to obtain a tractable solution to the wave equation. The sign is simply an indication of the harmonic function used and is present because complex exponentials must always exist as complex conjugate pairs. Therefore, the imaginary part of each optical constant is always reported as a real, positive number. There is no such thing as a negative optical constant.

It is somewhat more difficult to understand the effects of the imaginary part of the refractive index. Although it is responsible for attenuation or absorption, it often manifests itself as a highly reflecting medium in metals. A medium that is very strongly absorbing at a given frequency doesn't actually absorb the incident light because of the small skin depth but rather selectivity reflects it (Hecht, p. 111). It is this mechanism of selective absorption (reflection) that gives objects their distinctive visual appearance (Hecht,

† Again, it must be stressed that these optical "constants" are not constant but vary with wavelength. The word "coefficient" is preferred.

p. 57). In the atmosphere, absorption is due not only to the *material* composition of the particles present but also due to the scattering by the *size and shape* of the particles. We will expand on this point in section 3.4.

3.1.2 Polarization

Using a polarization description is often more useful and advantageous in describing the scattering process and, more importantly, can circumvent some of the bulky and unwieldy field expressions. We make heavy use of polarization in this thesis.

A good source for additional information on polarization can be found in the Handbook of Optics, Vols. I and II, 1995.

3.1.2.1 Meaning between x,y and perpendicular and parallel polarization

Often, electric fields are described as being out-of-plane (perpendicular or normal) or in-plane (parallel) with respect to the plane of incidence. In a strict sense, polarization does not have to be identified with respect to an interface or boundary. Many introductory electromagnetic texts initially define and describe polarization in generic, mathematical terms but later convert to the more widely used boundary-specific definitions of parallel/perpendicular polarization. We must make clear exactly what this terminology means as it could be confusing to the uninitiated. The terminology in describing an electric field in terms of its seemingly arbitrary parallel and perpendicular components came from the analysis of electromagnetic reflection and refraction at an interface. An interface is a plane surface that connects two different mediums (Figure 3-1). If we consider the simple case of two mediums with purely real constants, then a wave incident at the interface of the two mediums will reflect and transmit according to Snell's Law. The plane of incidence, different from the interface plane, is defined as the plane that contains both of the directional wave vectors in medium 1 and medium 2 (Hecht, figures 4.20, p. 94 and 4.21, p. 96; Bohren & Huffman, p. 33). As shown in Figure 3-1a, the $\bar{\mathbf{E}}$ field is entirely in a plane parallel to the plane of incidence while in Figure 3-1b, the $\bar{\mathbf{E}}$ field is perpendicular to it. It takes two orthogonal planes to uniquely specify a volume.

Many texts introduce polarization using the familiar $\hat{\mathbf{x}}\hat{\mathbf{y}}\hat{\mathbf{z}}$ coordinate system without establishing an interface or plane of incidence (Ramo et al., p. 280; Shen & Kong, p. 56; Hecht, p. 270). However, it is often much more desirable to describe polarization in terms of components that are either parallel or perpendicular to the plane of incidence. One cannot and should not simply assume that the $\hat{\mathbf{x}}$ component is the perpendicular component and the $\hat{\mathbf{y}}$ component is the parallel component. In doing so, an ambiguity arises, especially in the case of normal incidence (Bohren & Huffman, p. 61). For example, consider an electromagnetic wave propagating in the $\hat{\mathbf{z}}$ direction with its $\bar{\mathbf{E}}$ field entirely in the $\hat{\mathbf{x}}$ direction (Figure 3-2), which encounters some interface, shown as a dotted blue rectangle. This would be the case of normal incidence. Now, if one rotates the interface around its local x-axis, according to Snell's law, the

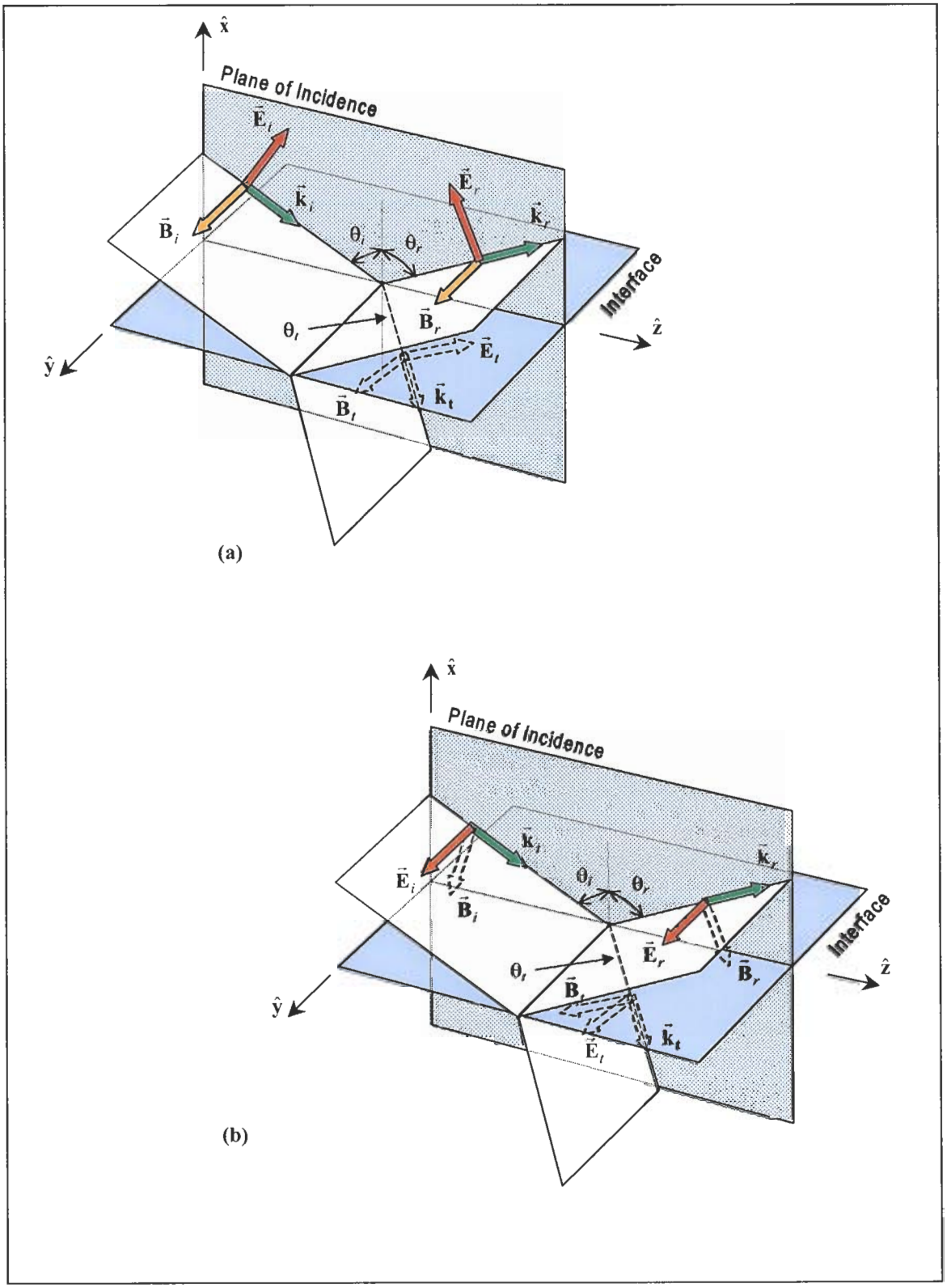

Figure 3-1: Definition parallel and perpendicular components and plane of incidence. (a) Electric field perpendicular to plane of incidence. (b) Electric field parallel to plane of incidence. From Hecht, p. 94 and p. 96.

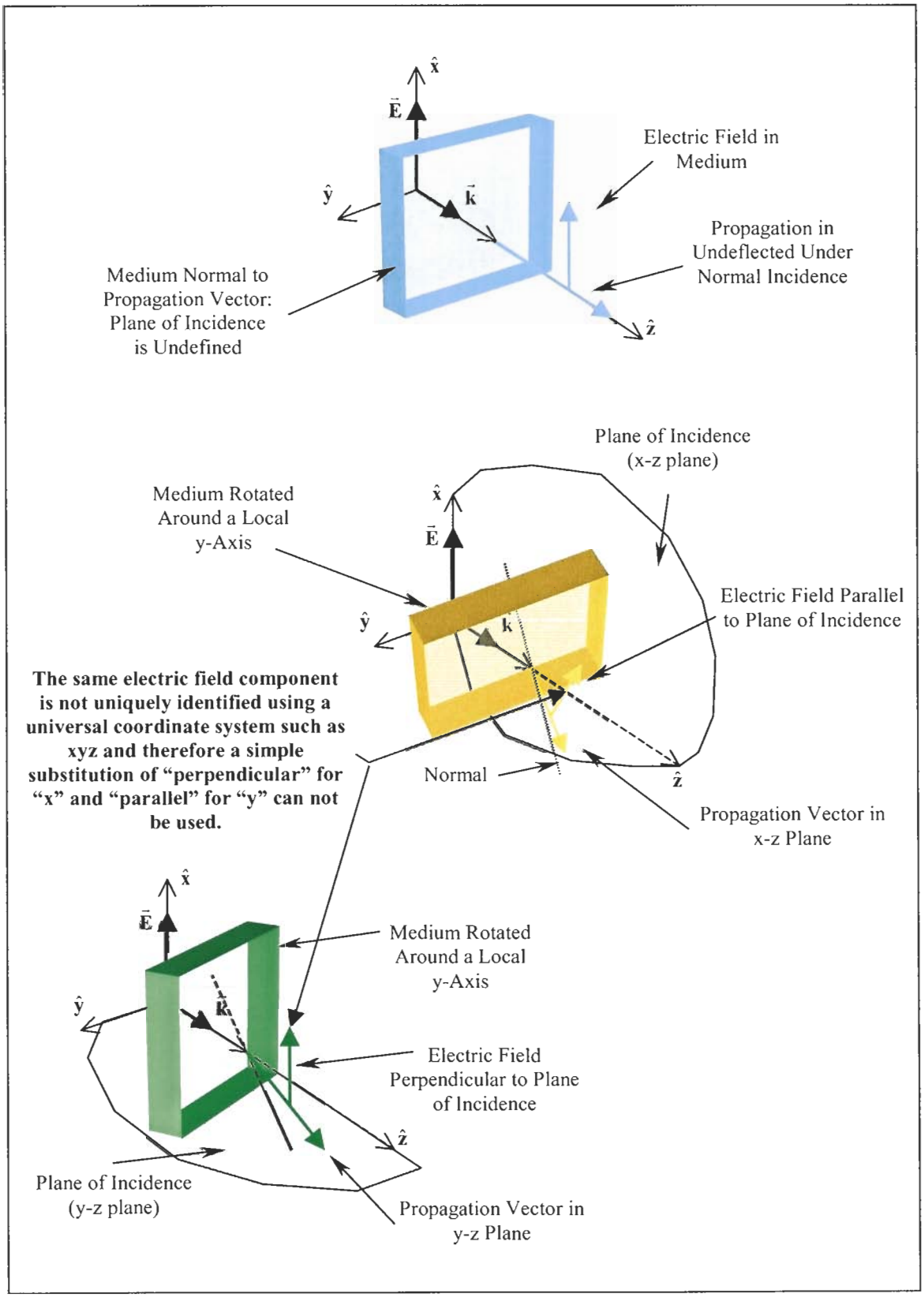

Figure 3-2: Illustration of ambiguity in using a fixed coordinate system to describe polarization components as being perpendicular or parallel.

propagating wave inside the medium remains in the y-z plane and thus the y-z plane is the plane of incidence. However, if the interface is rotated about its local y-axis, the refracted wave propagates in the x-z plane. The former case indicates the $\hat{\mathbf{x}}$ directed $\vec{\mathbf{E}}$ field is perpendicular to the plane of incidence while the later case indicates the $\hat{\mathbf{x}}$ -directed $\vec{\mathbf{E}}$ field is parallel to the plane of incidence. Similarly, a $\hat{\mathbf{y}}$ -directed $\vec{\mathbf{E}}$ field could also be given dual descriptions of being parallel or perpendicular depending on the orientation of some interface. Thus, one cannot assign the terms perpendicular (vertical) or parallel (horizontal) to the components of an electric field without first explicitly identifying the plane of incidence. One should only use $\hat{\mathbf{x}}\hat{\mathbf{y}}\hat{\mathbf{z}}$ vectors for describing the polarization of an electromagnetic wave within a medium, not between two mediums.

3.1.2.2 Descriptions of Polarization

Interestingly, there are several mathematical descriptions that can be used to define the polarization state of a wave. The most widely used are ellipsometric and polarimetric terminology. The use of these approaches is basically determined by tradition and somewhat on the application itself. However, the ellipsometric and polarimetric approaches are related and can be interchanged. As is the case throughout electromagnetics, there is no one universally accepted set of polarization parameters because there is not one universally used set of Maxwell equations and sometimes one set is easier to use in certain applications than the other.

3.1.2.2.1 Ellipsometric

Although in this thesis the polarimetric parameters are used, the ellipsometric parameters are another set of widely used polarization parameters (Watanabe, et al., 1992; Tachibana, et al., 1994; Swinkels, et al., 1998; Stoffels, et al., 2000).

As shown in Figure 3-3, the polarization state of an electromagnetic wave is visualized by tracing out the time harmonic rotation of the transverse components of the electric field in a constant plane ($z = 0$ for convenience) (See Shen and Kong, p. 56 for a good definition of the vibrational ellipse). The most general polarization state is elliptical and so the analytical parameters that describe an ellipse are used to describe the state of polarization. The parameters are irradiance, azimuth, ellipticity and handedness and are collectively known as the ellipsometric parameters. The ellipsometric parameters completely characterize the polarization state of an electric field.

The first ellipsometric parameter, irradiance is a very useful and physically identifiable parameter. Irradiance, also termed the time-averaged Poynting vector, is defined as (Shen & Kong, p. 40)

$$\langle S \rangle = \frac{1}{2\pi} \int_0^{2\pi} \vec{\mathbf{E}}(x,y,z,t) \times \vec{\mathbf{H}}(x,y,z,t)\, d(\omega t) \tag{3-25}$$

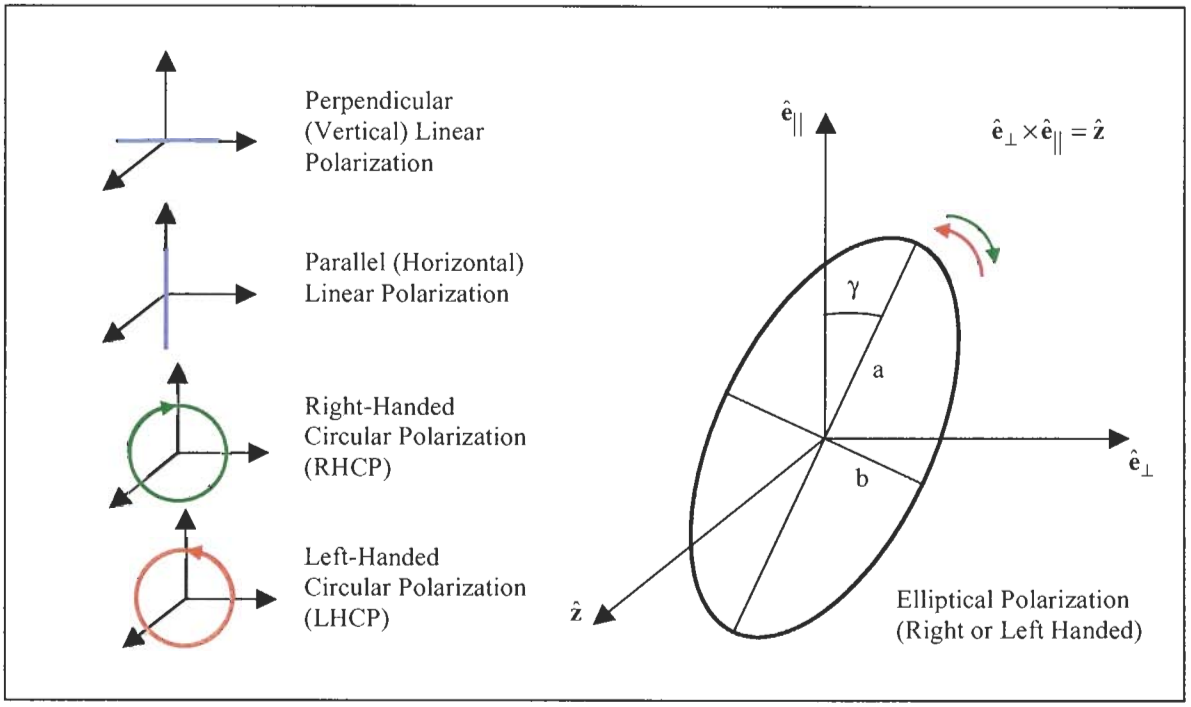

Figure 3-3: Polarization vibrational ellipse.

and has units of W/m^2. To show the determination of irradiance, we must include the time-harmonic part with the generic plane wave and write the electric field as

$$\begin{aligned}\vec{\mathbf{E}} &= E_{0\perp}\cos(kz-\omega t)\hat{\mathbf{e}}_{\perp} + E_{0||}\cos(kz-\omega t+\varphi)\hat{\mathbf{e}}_{||} \\ &\equiv E_{\perp}\hat{\mathbf{e}}_{\perp} + E_{||}\hat{\mathbf{e}}_{||}.\end{aligned} \tag{3-26a}$$

From Table 3-2 and the constituitive relationship of Eqn. 3-1b, the magnetic flux density is determined from

$$\mu\frac{\partial\vec{\mathbf{H}}}{\partial t} = \nabla\times\vec{\mathbf{E}}. \tag{3-26b}$$

Substituting Eqn. 3-26a into Eqn. 3-26b yields two equations

$$\begin{aligned}\hat{\mathbf{e}}_{\perp}\left[-\frac{\partial E_{||}}{\partial z}\right] &= \hat{\mathbf{e}}_{\perp}\left[\frac{kE_{0||}}{\mu_0}\sin(kz-\omega t+\varphi)\right] \\ &= \hat{\mathbf{e}}_{\perp}\left[\frac{\partial H_{\perp}}{\partial t}\right]\end{aligned} \tag{3-27a}$$

$$\begin{aligned}-\hat{\mathbf{e}}_{||}\left[-\frac{\partial E_{\perp}}{\partial z}\right] &= \hat{\mathbf{e}}_{||}\left[-\frac{kE_{0\perp}}{\mu_0}\sin(kz-\omega t)\right] \\ &= \hat{\mathbf{e}}_{||}\left[\frac{\partial H_{||}}{\partial z}\right],\end{aligned} \tag{3-27b}$$

where we have used the free space permeability, $\mu \approx \mu_0$. Using the intrinsic impedance† defined as

$$\eta = \sqrt{\frac{\mu_0}{\varepsilon_0}} \tag{3-28}$$

and the plane wave condition of Eqn. 3-12, Eqns. 3-27a & 3-27b are easily solved to obtain the magnetic field

$$\vec{\mathbf{H}} = -\frac{E_{0||}}{\eta}\cos(kz-\omega t+\varphi)\,\hat{\mathbf{e}}_{\perp} + \frac{E_{0\perp}}{\eta}\cos(kz-\omega t)\,\hat{\mathbf{e}}_{||}\,. \tag{3-29}$$

The Poynting vector, $\vec{\mathbf{S}}$, is the power flux (W/m^2) of an electromagnetic wave and is given by

$$\vec{\mathbf{S}} = \vec{\mathbf{E}} \times \vec{\mathbf{H}} \tag{3-30}$$

and points in the direction of propagation. Here, the Poynting vector is

$$\vec{\mathbf{S}} = \hat{\mathbf{z}}\left[\frac{E_{0\perp}^2}{\eta}\cos^2(kz-\omega t) + \frac{E_{0||}}{\eta}\cos^2(kz-\omega t+\varphi)\right]. \tag{3-31}$$

Using,

$$\frac{1}{2\pi}\int_0^{2\pi}\cos^2(kz-\omega t+\varphi)\,d(\omega t) = \frac{1}{2}\,,$$

the time-averaged Poynting vector (irradiance) is

$$\left\langle \vec{\mathbf{S}} \right\rangle = \hat{\mathbf{z}}\frac{1}{2\eta}\left[E_{0\perp}^2 + E_{0||}^2\right]. \tag{3-32}$$

The time-averaged Poynting vector is often obtained by using

$$\left\langle \vec{\mathbf{S}} \right\rangle = \frac{1}{2}\mathrm{Re}\left[\vec{\mathbf{E}} \times \vec{\mathbf{H}}^*\right] \tag{3-33}$$

and for a plane wave,

---

† The intrinsic impedance can be complex if the permeability or the permittivity parameters are complex.

$$\left\langle \vec{\mathbf{S}} \right\rangle = \frac{\left|\vec{\mathbf{E}}\right|^2}{\eta}. \tag{3-34}$$

The ellipticity parameter simply describes the relative shape of the vibrational ellipse traced out by the electric field in a constant plane. Ellipticity is given by[†]

$$\frac{b}{a} = \tan(\beta) \tag{3-35}$$

where a, the major axis, is <u>always</u> larger than b, the minor axis. Ellipticity can range from 0 (linear polarization) to 1 (circular polarization); therefore, $0 \le \beta \le \pi/4$. It may not seem obvious but because the ellipticity is rotationally invariant, we can write it as

$$\frac{E_{0||}}{E_{0\perp}} = \tan(\beta) \tag{3-36}$$

where we assume[‡] $E_{0||} \le E_{0\perp}$ and $\varphi \neq 0°$ or 180°.

The azimuth parameter, γ, indicates the orientation of the polarization ellipse. As shown in Figure 3-3, γ is the angle between the $\hat{\mathbf{e}}_{||}$ axes and the major axis a. We can determine the azimuth angle by choosing a constant plane ($z = 0$) and finding the time at which the electric field reaches a maximum.

Of all the ellipsometric parameters, the handedness is the most confusing as it is often defined in a qualitative manner and subject to the perspective of the observer. Here, we shall provide the reader with an unmistakable way of determining the handedness independent of the observer's viewpoint. The primary reason for the confusion in obtaining handedness is that it is often confused with rotation (either clockwise or counterclockwise). Handedness and rotation are not the same thing. Handedness refers to the temporal rotation of the transverse electric field components while rotation refers to the spatial rotation. We can illustrate this with two examples.

We will simplify things by making $E_{0\perp} = E_{0||} \equiv E_0$ and $q = kz - \omega t$ since plane waves have constant phase fronts. Therefore, we can write the electric field as

$$\vec{\mathbf{E}} = E_0 \cos(q)\,\hat{\mathbf{e}}_{\perp} + E_0 \cos(q+\varphi)\,\hat{\mathbf{e}}_{||}. \tag{3-37}$$

[†] Here, β is not allowed to be negative since a geometrical ellipse must have positive axes lengths.
[‡] We stress that the smaller component is always the minor axes and, here, we assume that $E_{0||}$ is.

Using $\varphi = \pi/2$, we immediately see that $\hat{\mathbf{e}}_{||}$ leads $\hat{\mathbf{e}}_{\perp}$ and therefore traces out a left-handed helix (Figure 3-4a). The terminology "left-handed" comes from curling the fingers of one's left hand in the direction of the resultant electric field rotation while pointing the thumb in the direction of propagation. In this case,

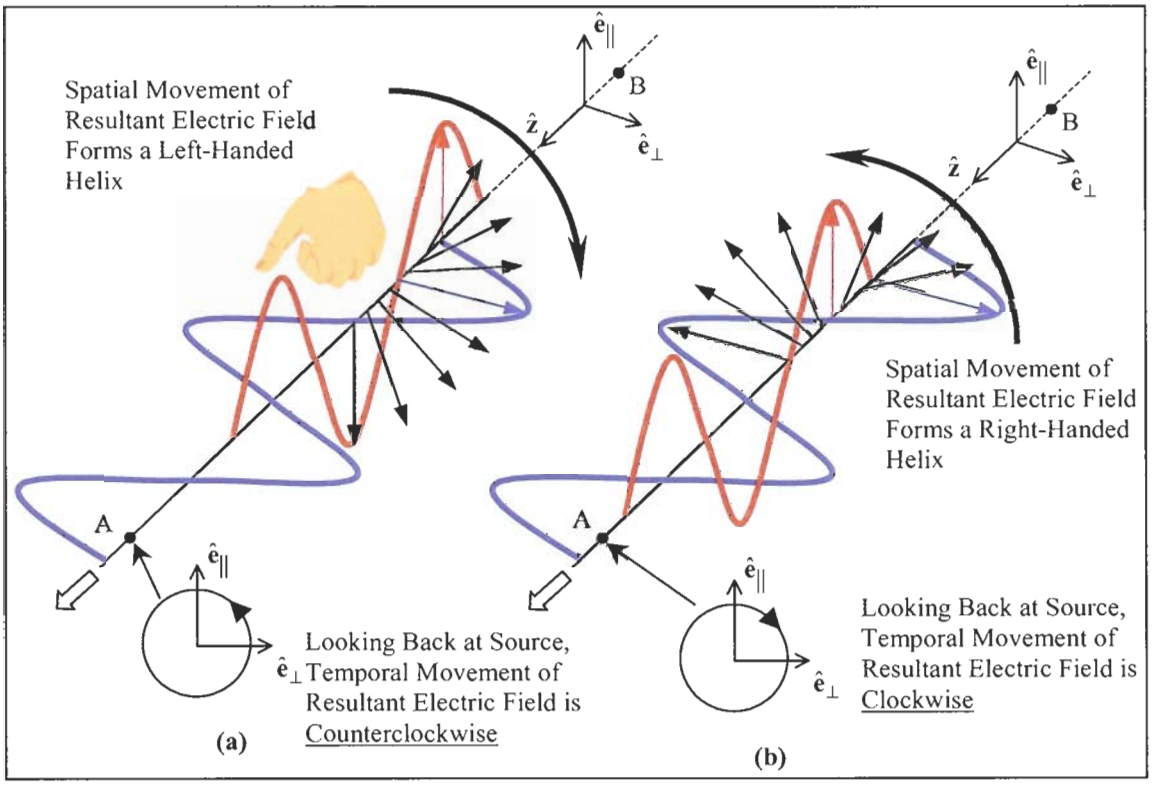

Figure 3-4: Definition of polarization handedness. a) Left-handed polarization. b) Right-handed polarization.

only the left hand wraps correctly around the z-axis with the thumb pointing in the positive direction. It is your hand that forms a helix. From a spatial perspective, the $\vec{\mathbf{E}}$ field seems to be rotating clockwise as it propagates down the z-axis as one looks back at the source. However, suppose you are at point A and looked back at the source. It now actually appears that the $\vec{\mathbf{E}}$ field is rotating in the counterclockwise direction as it passes you. What you are doing is watching the progression of the wave on a constant plane (say $z = 0$) and therefore watching a temporal evolution of the wave. This is the definition of rotation. If one observes the wave from point B (looking from the source), the wave would actually appear to rotate clockwise. We can backup our qualitative argument with some mathematics by setting $z = 0$ and using the simplified electric field

$$\begin{aligned}\vec{\mathbf{E}} &= E_0 \cos(-\omega t)\,\hat{\mathbf{e}}_{\perp} + E_0 \cos\left(-\omega t + \pi/2\right)\hat{\mathbf{e}}_{||} \\ &= E_0 \cos(\omega t)\,\hat{\mathbf{e}}_{\perp} + E_0 \sin(\omega t)\,\hat{\mathbf{e}}_{||}\,. \end{aligned} \tag{3-38}$$

To see the vector this electric field traces out in time, we write the resultant electric field in the form

$$\vec{\mathbf{R}} = |R| e^{j\theta_R} \hat{\mathbf{r}} \tag{3-39}$$

where

$$|R| = \sqrt{\vec{\mathbf{E}} \cdot \vec{\mathbf{E}}^*} = E_0 \tag{3-40}$$

and

$$\begin{aligned} \theta_R &= \tan^{-1}\left(\frac{\sin(\omega t)}{\cos(\omega t)}\right) \\ &= \omega t \,. \end{aligned} \tag{3-41}$$

Here, we have defined the instantaneous angle, θ_R, as shown in Figure 3-5. Thus, θ_R is rotating at an angular rate of ω radians/s in the counterclockwise direction, as expected, for the observation point A.

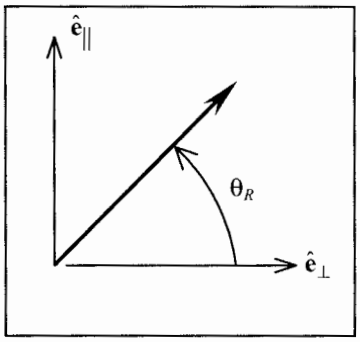

Figure 3-5: Definition of instantaneous angle.

Similarly, if $\varphi = -\pi/2$, then $\hat{\mathbf{e}}_{\perp}$ leads $\hat{\mathbf{e}}_{||}$ and therefore the $\vec{\mathbf{E}}$ field traces out a right-handed helix (Figure 3-4b). In this case, if one looks back at the source, the polarization rotation would be in the clockwise direction while if one looked from the source, the polarization rotation would be in the counterclockwise direction.

Therefore, in defining polarization with respect to rotation, one would have to introduce another parameter, the observation point. This is unnecessary and should be avoided at all costs as the simpler solution is generally the preferred solution. Thus, handedness is described simply as being left-handed (-1) or right-handed (+1). In the case of linear polarization, the handedness is 0.

One last point should be made with respect to ellipsometric parameters and that is there are more than one unique way in which to specify the analytical dimensions and properties of an ellipse (See Handbook of Optics, Vol. II, polarimetry). However, each set of ellipsometric parameters will yield the identical Stokes parameters.

3.1.2.2.2 Stokes (Polarimetric)

Like the ellipsometric parameters, Stokes parameters are a way of describing the polarization state of an electric field. However, since ellipsometric parameters are directly dependent on the electric field vector and since the electric field vector is traveling at the speed of light, direct observation and measurement of the ellipsometric parameters are not feasible with any currently known electronic measuring device. On the other hand, Stokes parameters are readily obtained through a set of irradiance measurements from which the ellisometric parameters can be derived. Despite their relationships, one will quickly find out there is no need to obtain the ellipsometric parameters once the Stokes parameters have been obtained as the Stokes parameters themselves uniquely define the polarization state of an electric field and are actually easier to use in most cases. There are four Stokes parameters: S_0, S_1, S_2, and S_3 but we will also substitute the parameters, I, Q, U, and V when we get to the sections describing electromagnetic scattering by a sphere (section 3.2). This is strictly a matter of preference and terminology. The author of this thesis was introduced and became accustomed to using $S_{1\text{-}4}$'s for the Stokes parameters but for consistency, we will use the I, Q, U, and V descriptors. In our definitions, these variables are identical and can be freely substituted for each other. The derivation of the Stokes parameters is straightforward and a very nice exposition is shown in Bohren & Huffman (Bohren & Huffman, p. 46) so it will not be shown here. The reader is encouraged to review this derivation. The interpretation of each Stokes parameter, however, is worth mentioning. The Stokes parameters lend themselves readily to, and are well suited for, matrix manipulation.

The easiest of the Stokes parameters to understand is the S_0 parameter, which represents the total irradiance of the electromagnetic wave and is equal to the magnitude of the time-average Poynting vector. The S_1 parameter is a measure of the irradiance in the vertical and horizontal directions[†] while the S_2 parameter is a measure of the irradiance in the +45° and a –45° directions. Both the S_1 and S_2 parameters measure the linear characteristics of a polarization state. The last parameter, S_3, the most difficult to understand, provides direction information on the circular polarization characteristics of an electric field. If S_3 is positive, then the wave is right-handed and if S_3 is negative, the wave is left-handed. The Stokes parameters are related to the ellipsometric parameters by (Bohren & Huffman, eqn. 2-81, p. 50):

$$S_0 = \left|\left\langle \bar{\mathbf{S}} \right\rangle\right| \tag{3-42a}$$

$$S_1 = \left|\left\langle \bar{\mathbf{S}} \right\rangle\right| \cos(2\beta)\cos(2\gamma) \tag{3-42b}$$

$$S_2 = \left|\left\langle \bar{\mathbf{S}} \right\rangle\right| \cos(2\beta)\sin(2\gamma) \tag{3-42c}$$

$$S_3 = \left|\left\langle \bar{\mathbf{S}} \right\rangle\right| (h)\sin(2\beta), \tag{3-42d}$$

[†] As shown in Bohren & Huffman, these parameters are a measure of the difference between their respective components. For this thesis, this point is not very important but the reader should be aware of the true meanings of the parameters.

where we have taken the liberty of using h to represent handedness (h = ± 1 or 0). If the light is 100% polarized, then we have the important relation

$$S_0^2 = S_1^2 + S_2^2 + S_3^2 \,. \tag{3-43}$$

Typically, the Stokes parameters are normalized to the total irradiance:

$$\mathbf{S}_0 = \frac{S_0}{S_0} = 1$$
$$\mathbf{S}_1 = \frac{S_1}{S_0}$$
$$\mathbf{S}_2 = \frac{S_2}{S_0}$$
$$\mathbf{S}_3 = \frac{S_3}{S_0}$$

where bold face denotes that the Stokes parameters are normalized. Therefore, Eqn. 3-43 can be written as

$$1 = \mathbf{S}_1^2 + \mathbf{S}_2^2 + \mathbf{S}_3^2 \tag{3-44}$$

which is the equation of a unit sphere. Various polarization states are summarized in Figure 3-6. Equation 3-44 leads directly to displaying the Stokes parameters as a 3-D display on a sphere, formally termed the Poincaré sphere. The Poincaré sphere is a very elegant and powerful way of visualizing polarization not as a conglomeration of bulky mathematics but rather as a simple graphical display. One should make every effort to visualize polarization as a graphical display rather than dealing with the cumbersome mathematical field components. For the uses of the Poincaré sphere and the Stokes parameters, see Agilent Technology corporation's line of fiber optic sensing equipment.

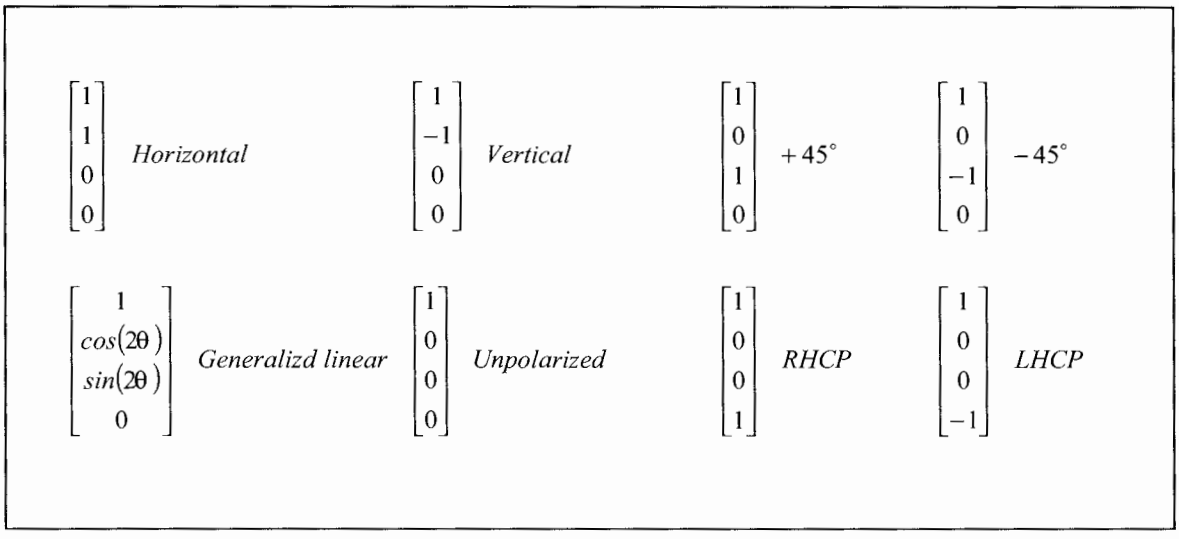

Figure 3-6: Stokes representations of several polarization states.

3.1.2.3 Use of Polarization in Linear System Theory (Mueller Matrices)

The Stokes parameters provide a simple yet very powerful way of condensing the cumbersome field expressions into simple matrices that readily identify the polarization state of an electromagnetic wave. Additionally, the visualization of the Stokes parameters is enhanced as a graphical display on a unit sphere, termed the Poincaré sphere. Now that we have a feeling for what the Stokes parameters convey, we now have a simple formalism with which to analyze not only electromagnetic waves, but also optical systems. Where the Maxwell equations are oriented to describe waves and systems analytically, the Stokes parameters are oriented to describe waves and systems using matrices.

By using Stokes parameters, the complex electromagnetic fields can be reduced to 4x1 matrices (Stokes parameters). We make the only condition that the fields must be linear. Further, in describing how fields travel through mediums or devices, such mediums or devices can be expressed as a 4x4 matrix, called a Mueller matrix. In Figure 3-7, we show how the Stokes parameters can be conceptualized using linear system theory. Further, this type of approach is not limited to just the Stokes parameters as the electric fields themselves can also be written in matrix form. When using complex field notation, the matrices are 2x2 and termed Jones matrices. There are advantages to using one over the other.

The use of Stokes parameters and Mueller matrices is very beneficial and is quite useful in streamlining analysis of systems. Figure 3-8 lists several useful Mueller matrices for often-used optical components and devices. See also the Handbook of Optics, Vol.2, Chapter 22 (polarimetry).

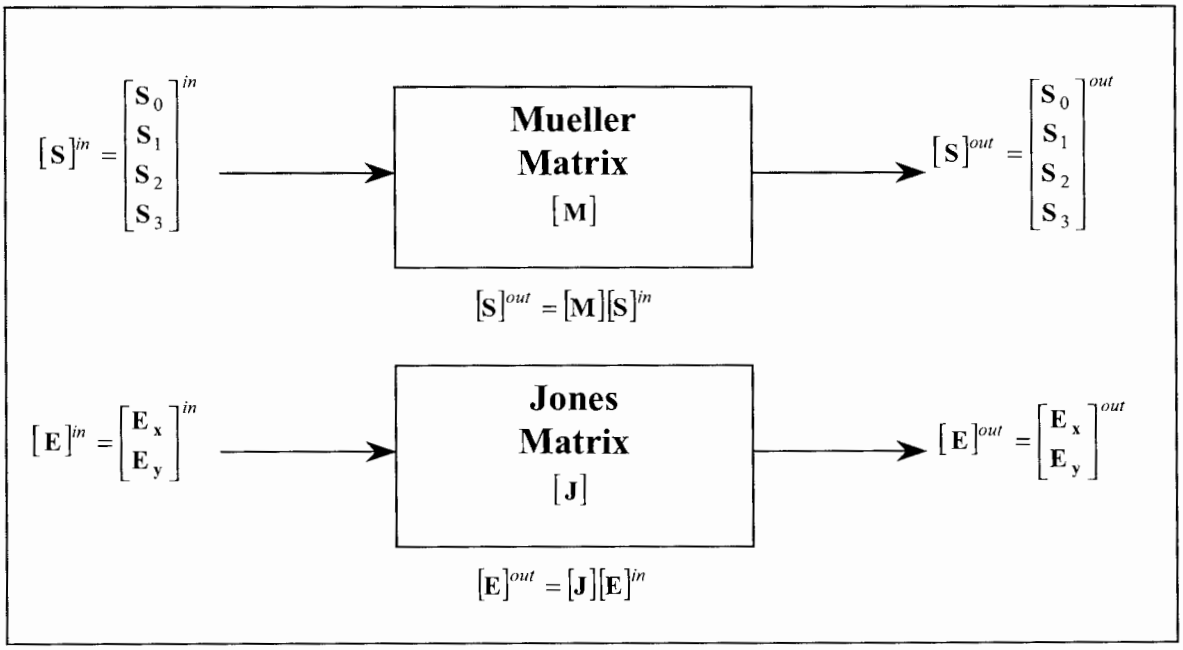

Figure 3-7: Linear system approach of Mueller and Jones matrices.

General linear retarder, fast axis θ, retardance δ:

$$\begin{bmatrix} 1 & 0 & 0 & 0 \\ 0 & cos^2(2\theta)+sin^2(2\theta)cos(\delta) & sin(2\theta)cos(2\theta)\{1-cos(\delta)\} & -sin(2\theta)sin(\delta) \\ 0 & sin(2\theta)cos(2\theta)\{1-cos(\delta)\} & sin^2(2\theta)+cos^2(2\theta)cos(\delta) & cos(2\theta)sin(\delta) \\ 0 & sin(2\theta)sin(\delta) & -cos(2\theta)sin\delta & cos(\delta) \end{bmatrix}$$

Horizontal Polarizer

$$\begin{bmatrix} 1 & 1 & 0 & 0 \\ 1 & 1 & 0 & 0 \\ 0 & 0 & 0 & 0 \\ 0 & 0 & 0 & 0 \end{bmatrix}$$

Vertical Polarizer

$$\begin{bmatrix} 1 & -1 & 0 & 0 \\ -1 & 1 & 0 & 0 \\ 0 & 0 & 0 & 0 \\ 0 & 0 & 0 & 0 \end{bmatrix}$$

+45° Linear Polarizer

$$\begin{bmatrix} 1 & 0 & 1 & 0 \\ 0 & 0 & 0 & 0 \\ 1 & 0 & 1 & 0 \\ 0 & 0 & 0 & 0 \end{bmatrix}$$

$\lambda/2$ plate – linear retarder (polarization rotator):

$$\begin{bmatrix} 1 & 0 & 0 & 0 \\ 0 & cos^2(2\theta)-sin^2(2\theta) & 2sin(2\theta)cos(2\theta) & 0 \\ 0 & 2sin(2\theta)cos(2\theta) & sin^2(2\theta)-cos^2(2\theta) & 0 \\ 0 & 0 & 0 & -1 \end{bmatrix}$$

$\lambda/4$ plate – circular retarder:

$$\begin{bmatrix} 1 & 0 & 0 & 0 \\ 0 & \cos^2(2\theta) & \sin(2\theta)\cos(2\theta) & -\sin(2\theta) \\ 0 & \sin(2\theta)\cos(2\theta) & \sin^2(2\theta) & \cos(2\theta) \\ 0 & \sin(2\theta) & -\cos(2\theta) & 0 \end{bmatrix}$$

Figure 3-8: Mueller matrices of several optical devices.

3.2 MIE THEORY – SCATTERING BY A SPHERE

With our opening salvo of electromagnetic equations and assumptions whizzing by the reader, we are now ready to open a full-scale assault on the major theory behind this thesis: electromagnetic scattering by a sphere. However, our attack will be more of a hit-and-fade than invasion as we are not going to go through the full derivation of what is known as Mie theory. The reason for this is simply that others have already performed the derivation (namely Mie himself) so why should we do what has already been done? However, we have gone through the entire derivation and while it was not simple, it was certainly instructive. Further, more advanced derivations involving non-spherical particles rely on many of the core concepts used in the Mie theory derivation and so the effort was not wasted. The real reason the derivation is not presented here however is simply because it takes an incredible amount of time to type in all the equations needed and so we will simply outline the important steps.

Although the derivation and explanation of Mie theory presented here is of somewhat a qualitative nature, one may find even this presentation difficult to understand without at least an introductory knowledge of electromagnetic theory. This was the main reason for presenting the material in section 3.1. For those who may want to refresh their understanding of electromagnetic theory beyond what has been

presented, the texts by Shen & Kong, Ramo et al., and Hecht provide good descriptions of elementary electromagnetic concepts. However, reading a book or attending lectures is generally not enough for people to get a good understanding of the physical processes described by the mathematics. The interested reader is urged to simulate the given expressions with a computer and to perform their own investigations of the mathematics. The central idea behind this chapter is that in doing something, one will learn things that no one can teach you. One can sit in a lecture or read scientific papers but until you do it yourself, everything is just academic. To do is to understand.

Our approach follows Bohren & Huffman's but we also consulted Kerker and van de Hulst. Kerker may be a bit dated, but it is still a very good read while van de Hulst, given credit for fathering modern scattering theory, is somewhat lacking in the details and a bit harder to decipher his terminology. The derivation of Mie theory was primarily for our own benefit but we were also interested in several items. For example, we wanted to determine where the index of refraction manifests itself and to identify where the angular scattering dependency occurs. Basically, our derivation fills in the details that were not included in Bohren and Huffman, most likely due to the same time and space constraints we have. We will however provide the briefest of outlines as it is the resulting equations that we are after and will use extensively throughout this thesis. It is simply nice to know where our equations came from and to not over extend their interpretation and use (ignorance is not bliss in science). Let us first begin with the basic definitions used in scattering that are applicable to all objects, not just spheres. Hopefully, this brief introduction to scattering theory will be sufficient as a top-level overview (albeit rather limited) to at least get one indoctrinated into the field rather than thrown directly into the deep end.

There are several sources of information that can and should be consulted for more information. The primary source, and the source used throughout this thesis, is the book by Bohren and Huffman. Although almost 20 years old, this book is still by far one of the most well-prepared and well-written manuscripts on electromagnetic scattering and its practical difficulties. This book is not for the faint of heart because it is written in a very condensed format which means that it usually takes one several read-throughs in order to understand the points being made. About the only downside is that the book, being 20 years old, perhaps lacks some of results of recent research made in electromagnetic scattering. To supplement the book, the text by Mischenvko is a decent starting point for additional study and contains references for even more information. All of our scattering terminology and expressions are identical to those used in Bohren & Huffman.

3.2.1 General Definitions of Scattering (Absorption + Scattering = Extinction)

Collectively, the interaction of electromagnetic waves with a particle is composed of two processes: absorption and scattering. Absorption is the process of converting incident electromagnetic energy into other forms of energy (typically thermal) thereby removing some of the propagating electromagnetic radiation. On the other hand, scattering does not remove the incident electromagnetic radiation but rather

redirects it along some new path. Together, absorption and scattering contribute to extinction, which is an indication of the radiation removed by an object or collection of particles (in a non-absorbing medium). Figure 3-9 illustrates the processes of absorption, scattering and extinction for a collection of particles. Absorption, scattering and extinction are important topics in their own rights but a simple, qualitative description of each is warranted here.

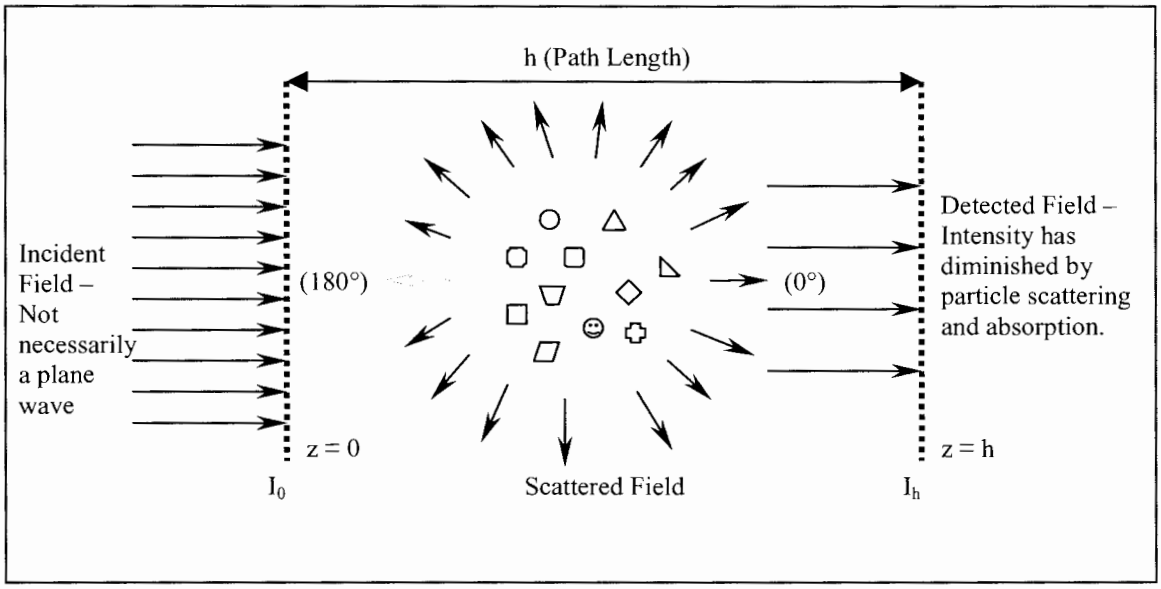

Figure 3-9: Conceptualization of absorption, scattering and extinction in a non-absorbing medium by a collection of particles (not necessarily spherical).

An important aspect of scattering is its angular dependence, *i.e.*, scattering intensity as a function of angle, θ. Shown in Figure 3-9 are two specific cases of scattering: 0° or forward scattering and 180° or backscattering. The backscattering component of the scattered field is what is measured by monostatic lidars. However, with respect to this thesis, many scattering angles will be measured and it will be shown that the scattering angles provide information about particle sizes and densities. At first, the forward scattering component may seem to be mislabeled. After all, the incident field was already traversing in this direction so how can one distinguish between forward scattering and the incident wave? The answer is that you can't (Bohren & Huffman, p. 68). The mathematical derivation does not preclude radiation from being scattered forward but in fact establishes its existence.

The principal parameter in describing scattered radiation due to a particle or a collection of particles is the scattering cross section, C_{sca}, which has units of area. The scattering cross section represents a virtual area whose effect is to reduce the light intensity seen by a detector in the forward path. The term "virtual area" is used because C_{sca} does not represent a physical area. For example, a sphere of radius r has a physical cross sectional area of πr^2 but its scattering cross sectional area can be up to twice as large. Bohren & Huffman address this apparent paradox (Bohren & Huffman, p. 107).

The scattering cross section is given by (Bohren & Huffman, eqn. 3.26, p. 71)

$$
\begin{aligned}
C_{sca} &= \int_S \vec{\mathbf{E}} \cdot \hat{\mathbf{n}}\, dS \\
&= \int_0^{2\pi} \int_0^{\pi} \vec{\mathbf{E}} \cdot \hat{\mathbf{n}}\, r^2 \sin(\theta)\, d\theta\, d\phi \\
&= \int_0^{4\pi} \vec{\mathbf{E}} \cdot \hat{\mathbf{n}}\, r^2\, d\Omega\,,
\end{aligned}
$$

where dS is the differential spherical surface element and $d\Omega$ is the differential solid angle.

Extinction is due to both absorption and scattering and its cross section is given by

$$C_{ext} = C_{abs} + C_{sca}\,. \tag{3-45}$$

In the absence of multiple scattering, light attenuates as it propagates according to the Beer-Lambert Law

$$I = I_0 e^{-\alpha_{ext} h} \tag{3-46}$$

where α_{ext}, the extinction coefficient is given by

$$
\begin{aligned}
\alpha_{ext} &= N\left(C_{abs} + C_{sca}\right) \\
&= \alpha_{abs} + \alpha_{sca}
\end{aligned} \tag{3-47}
$$

and N is the particle number density (#/m^3). Here, the extinction coefficient operates the same as the absorptivity or attenuation coefficient found in Section 3.1 with a complex index of refraction but here, extinction is due to both absorption AND scattering. The Beer-Lambert Law directly relates to visibility (see Stevens p. 72).

Since absorption, scattering and extinction are related, it is a simple matter of measuring for two of the three parameters and then solving for the third. This is precisely what is done for absorption because absorption requires the measurement of fields inside the particle(s) (which are inaccessible to the experimentalist).

3.2.2 Outline of Derivation of Scattering by a Sphere

As we have already mentioned, the outline of Mie theory follows that given by Bohren & Huffman. While we have done every step in the derivation, the gory details will not be shown here due primarily to a lack of space, time and necessity. A simple framework of the basic theory will suffice as we are much more interested in the physical application and results that stem from the theory.

The basic coordinate system and unit vector definitions are shown in Figure 3-10. Here we use a non-spherical particle to make the initial setup generic but we will later use a spherical particle to make several simplifying conditions.

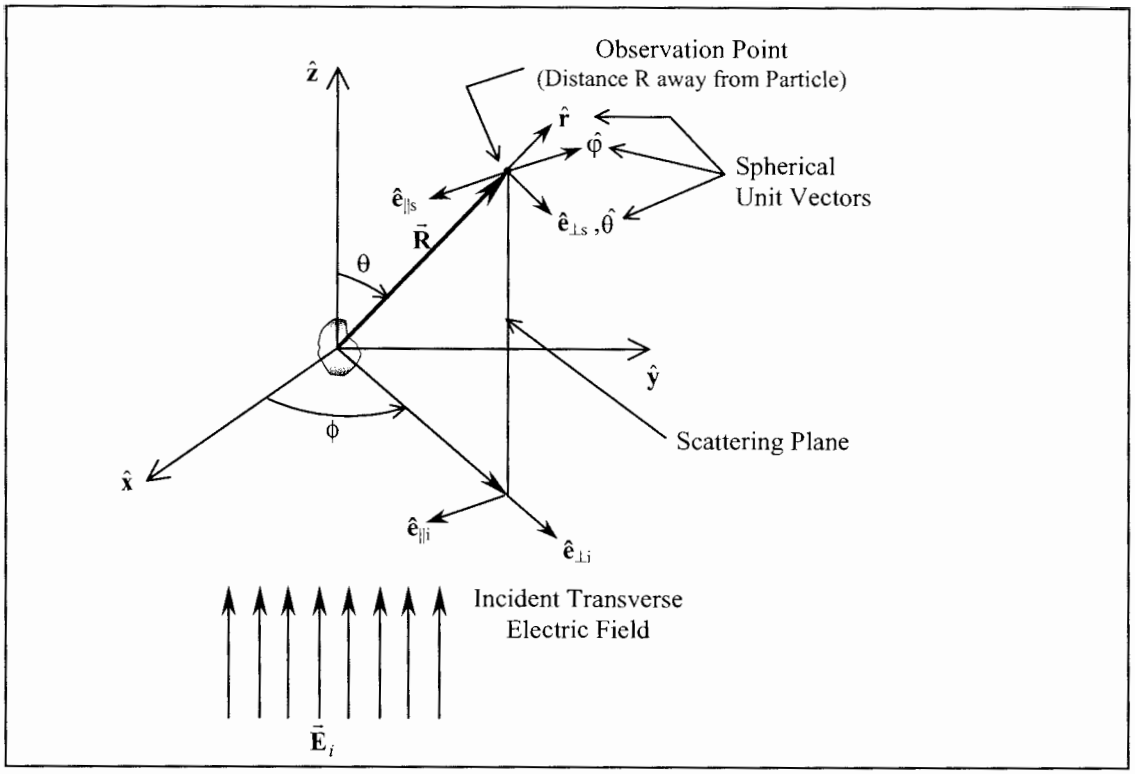

Figure 3-10: Coordinate system for electromagnetic field solution surrounding an arbitrary particle.

In the strictest sense, the electric field may be completely arbitrary and therefore it need not be transverse. However, it can be shown that any arbitrary electric field can be expanded into an infinite series of harmonic plane waves in much the same way as a temporal periodic signal can be decomposed into a Fourier Series (Bohren & Huffman, p. 22 and 57). Therefore, we take the fundamental case that the electric field is a plane wave and has no component along the direction of propagation. Additionally, the electric field can be of arbitrary polarization where the most generic polarization is elliptical. This is allowed since any polarization state can be decomposed into two orthogonal polarization states. For example, elliptical polarization can be written as a linear combination of right-hand and left-hand circular polarization while linear polarization can be written as a linear combination of parallel and perpendicular polarization (Bohren & Huffman, p. 47 & 61).

Since an arbitrarily polarized electric field can be decomposed into two orthogonal polarization states, the incident electric field can be written as composed of a parallel and perpendicular scattering component, $\hat{\mathbf{e}}_{\parallel}^{\mathbf{i}}$ and $\hat{\mathbf{e}}_{\perp}^{\mathbf{i}}$. Our job then becomes one of determining what the resultant electric field is in terms of the scattered components, $\hat{\mathbf{e}}_{\parallel}^{\mathbf{s}}$ and $\hat{\mathbf{e}}_{\perp}^{\mathbf{s}}$. Because the scattering is assumed linear (and it is), we formalize the scattering field relationship as (Bohren & Huffman, eqn 3.12)

$$\begin{bmatrix} \vec{\mathbf{E}}_{\parallel} \\ \vec{\mathbf{E}}_{\perp} \end{bmatrix}^{s} = \frac{e^{jk(R-z)}}{-jkR} \begin{bmatrix} S_2 & S_3 \\ S_4 & S_1 \end{bmatrix} \begin{bmatrix} \vec{\mathbf{E}}_{\parallel} \\ \vec{\mathbf{E}}_{\perp} \end{bmatrix}^{i}, \tag{3-48}$$

where S_{1-4} are the complex valued amplitude scattering coefficients (not Stokes parameters). It is the whole point of the derivation to determine the exact expressions for these amplitude coefficients and subsequently, the supporting mathematics are not easy. By building on the concepts we showed in our discussion of polarization, we can convert Eqn. 3-48 into polarization form. Bohren & Huffman show the process in section 2.11 and 3.3. Here, we present the result as (Bohren & Huffman, eqn. 3.16, p. 65),

$$\begin{bmatrix} I_s \\ Q_s \\ U_s \\ V_s \end{bmatrix} = \frac{1}{k^2 R^2} \begin{bmatrix} S_{11} & S_{12} & S_{13} & S_{14} \\ S_{21} & S_{22} & S_{23} & S_{24} \\ S_{31} & S_{32} & S_{33} & S_{34} \\ S_{41} & S_{42} & S_{43} & S_{44} \end{bmatrix} \begin{bmatrix} I_i \\ Q_i \\ U_i \\ V_i \end{bmatrix} \tag{3-49}$$

where S_{ij} are the Mueller Matrix parameters. Expressions relating the amplitude scattering coefficients and the Mueller Matrix parameters are given on p. 65 of Bohren & Huffman. While we can use these general expressions, by choosing to analyze the scattering from a sphere, the set of coefficients and parameters reduces significantly.

As it turns out, the derivation of scattering from a sphere will produce $S_3 = S_4 = 0$. The result of this is that incident parallel polarized light remains parallel polarized under scattering and the same is true for perpendicular polarized light. However, one need not proceed through a lengthy derivation to find such a simplification. Bohren & Huffman (section 13.6) and van de Hulst have shown that such simplifications can also be made with a little help from the theorem of reciprocity. This approach relies on intuition and a good deal of abstract thought, but the result is a beautiful way of circumventing the mathematics in favor of some insightful physics (a worthwhile goal of any discipline).

One last item needs to be mentioned. Colleagues of Van de Hulst wrote an excellent set of papers (see all papers by Hovenier et al. listed in References) in which they explicitly examine Eqn. 3-49 using polarization concepts. These references are definitely worth reading. However, these papers were found after we had completed our derivation and while the papers did not provide any details about the derivation itself, they are very instructional in setting up the polarization characteristics and very useful in interpreting the results.

3.2.3 Main Scattering Expressions used in this work

Using the simplification for spheres, Eqns. 3-48 and 3-49 reduce to

$$\begin{bmatrix} \vec{\mathbf{E}}_{\parallel} \\ \vec{\mathbf{E}}_{\perp} \end{bmatrix}^s = \frac{e^{jk(R-z)}}{-jkR} \begin{bmatrix} S_2 & 0 \\ 0 & S_1 \end{bmatrix} \begin{bmatrix} \vec{\mathbf{E}}_{\parallel} \\ \vec{\mathbf{E}}_{\perp} \end{bmatrix}^i \tag{3-50}$$

and

$$\begin{bmatrix} I_s \\ Q_s \\ U_s \\ V_s \end{bmatrix} = \frac{1}{k^2 R^2} \begin{bmatrix} S_{11} & S_{12} & 0 & 0 \\ S_{21} & S_{11} & 0 & 0 \\ 0 & 0 & S_{33} & S_{34} \\ 0 & 0 & S_{43} & S_{33} \end{bmatrix} \begin{bmatrix} I_i \\ Q_i \\ U_i \\ V_i \end{bmatrix}. \tag{3-51}$$

Bohren & Huffman provide a FORTRAN code to calculate the scattering from a sphere, subject to the user's desired parameters. We took this code and adapted it into a MATLAB function that would also accept arrays of particle radii, indices of refraction (real and imaginary) and desired scattering angles. Because of a sphere's symmetry, all of the necessary scattering parameters are obtained from the determination of S_1 and S_2.

From Bohren & Huffman, we also have several notable results from the derivation of the amplitude scattering coefficients. The first result is

$$S_1(0^\circ) = S_2(0^\circ), \tag{3-52}$$

which indicates that the scattering in the forward direction is independent of the incident polarization state. It takes some time to prove to oneself but this relationship also indicates that scattering in the forward direction is independent of the index of refraction. This has led some to suggest that this could be viewed as a diffraction process but Bohren refutes this since the physical model indicates that the scattering in the forward direction does indeed impact on the sphere and it is simply directed in the forward direction.

Another result is

$$S_1(180^\circ) = -S_2(180^\circ), \tag{3-53}$$

which indicates that scattering in the backward direction is also independent of polarization (but the scattered wave does retain the incident state of polarization). Although we have no access to the forward direction, we do have access to the backward direction and we will use this result to validate our theoretical results.

To make use of these expressions, we need to have the expressions for the scattering resulting from parallel incident polarization and also for scattering due to perpendicular incident polarization. The parallel scattering intensity per unit intensity is

$$i_{\parallel} = S_{11} + S_{12} = |S_2|^2 \tag{3-54}$$

and the perpendicular scattering intensity per unit intensity is

$$i_{\perp} = S_{11} - S_{12} = |S_1|^2 \tag{3-55}$$

The reader is cautioned that these are not scattering intensities (the units are incorrect). These expressions are actually unitless but are the principal functions used in the polarization ratio method (see section 3.4) that forms a cornerstone of this thesis.

Interestingly, the matrices of Eqns. 3-50 and 3-51 above do not change in form for particles that are non-spherical, but still have spherical symmetry. Specifically, in the case of prolate (cigar-shaped) and oblate (pancake-shaped) spheroids, the Mueller matrix has the form

$$\begin{bmatrix} I_s \\ Q_s \\ U_s \\ V_s \end{bmatrix} = \frac{1}{k^2 R^2} \begin{bmatrix} S_{11} & S_{12} & 0 & 0 \\ S_{21} & S_{22} & 0 & 0 \\ 0 & 0 & S_{33} & S_{34} \\ 0 & 0 & S_{43} & S_{44} \end{bmatrix} \begin{bmatrix} I_i \\ Q_i \\ U_i \\ V_i \end{bmatrix}, \tag{3-56}$$

showing that the elements retain their individuality. This is one of the reasons why Mie theory may still be applicable to atmospheric particles (other than dust). Mishchenko (Mishchenko, et al.., 1995) used a T-matrix computing algorithm to simulate the scattering from various sphere-like objects. His results showed that, in the limit, as the spheroid become more needle-like or more plate-like, the scattering parameters resembled those due to a sphere. Thus, scattering by a sphere is not unique and ambiguity as to its shape, size and composition may exist. This by no means invalidates the results here as one simply has to know the limitations and applicability of any theory used.

At this point, we have not yet identified the polarization ratio methodology that we will use throughout the remainder of this work (see Section 3.4). For now, the amplitude coefficients are actually functions of wavelength, index of refraction (medium and particle), particle size (radius), and scattering angle, i.e.,

$$S_{1,2}(\lambda, n, r, \theta).$$

We can see from Eqn. 3-51, that the polarization approach yields some quick results. For example, incident 100% arbitrarily polarized light remains 100% polarized light upon scattering with a sphere. But interestingly, when unpolarized light is incident on a sphere, the sphere actually partially polarizes the light. Thus scattering is one of the primary mechanisms for polarizing light (see Hecht for others).

3.3 RAYLEIGH THEORY

Rayleigh (scattering) theory was the first attempt at trying to provide a framework as to why sunlight was found to be polarized at 90° from the forward direction. Simply, Rayleigh theory applies to particles much smaller than the wavelength of incident radiation but there is another, equally important qualification

that also must be made. Two basic assumptions need to be made in order for Rayleigh theory to apply. The first is the well-known small particle limit given as

$$\frac{2\pi r}{\lambda} << 1, \tag{3-57a}$$

which indicates simply that the size of the particle must be small compared to the wavelength. The second criteria is somewhat less known and is given as

$$m\frac{2\pi r}{\lambda} < 1, \tag{3-57b}$$

where m is the (relative) refractive index of the sphere. The condition given by Eqn. 3-57b results from the requirement that the resulting scattered field needs to be established on a time scale that is small compared to the period of the incident wave. A very good (and short) reference is Kerker, et al., 1977. Collectively, Eqns. 3-57a & 3-57b are written as

$$m\frac{2\pi r}{\lambda} < 0.05. \tag{3-57c}$$

Once the complete scattering due to a sphere is obtained, it is a very simple matter to apply the above simplifications to arrive at Rayleigh scattering expressions. Indeed, Bohren & Huffman take such an approach (see Bohren & Huffman, chapter 5, section 5.2, p. 136).

3.4 APPLICATION OF MIE THEORY TO ATMOSPHERIC SCATTERING – THE POLARIZATION RATIO

This is the section in which we take all of the mathematics from Chapter 2 and the previous sections of this chapter and show the mathematical form of the polarization ratio (PR), which is the central analytical tool we are going to be using from here on out. While we are primarily examining the mathematical nature of the polarization as it applies to atmospheric scattering, underpinning our examination are physically observed aerosol lognormal parameters. At this point, however, we are not going to discuss the physicality of the aerosol parameters, as we will leave that topic for subsequent chapters. This viewpoint of using physical parameters in our investigation of the mathematics simply cannot be overstated because, while any numbers of mathematical combinations are possible, such combinations may not be physically plausible. Mathematics, ungrounded in physics, has its merits but is fraught with danger.

3.4.1 Mathematical Expression of the (Linear) Polarization Ratio

The mathematical expression of the polarization ratio is given by

$$PR(\theta) = \frac{I_{\text{TOTAL}\,\parallel}(\theta)}{I_{\text{TOTAL}\,\perp}(\theta)} = \frac{\int |S_2(r,\theta)|^2\, y(r)dr + \text{Molecular}_{\parallel}}{\int |S_1(r,\theta)|^2\, y(r)dr + \text{Molecular}_{\perp}}, \tag{3-58}$$

where,

$I_{TOTAL\parallel}(\theta)$ is the total scattering intensity from incident parallel polarization,

$I_{TOTAL\perp}(\theta)$ is the total scattering intensity from incident perpendicular polarization,

$|S_{1,2}(r,\theta)|^2$ are the pre-calculated scattering matrices (for a given wavelength and index of refraction),

$y(r)$ is the total lognormal number density distribution (#/m^3 or #/cm^3 vs. particle radius) (See Eqn. 2-147)

and the required molecular components. At first, this expression seems rather complicated but we will find that it is actually quite easily understood if we break it into smaller, more digestible pieces. Each piece plays a crucial part in this work so we should spend a little time explaining each term in a little more detail. The last part of this section reveals how to calculate the polarization ratio.

3.4.1.1 The Molecular Component - Equivalent Dielectric Spheres

One of the major components included in the polarization ratio is molecular scattering. By far, molecules in the atmosphere (10^{25} /m^3 at sea level) are the most numerous of all the scattering components. Generally molecules are not called particles or aerosol particles but are rather left as a separate group, specifically gases. Individually, molecules contribute little to atmospheric scattering compared with aerosol particles. However, due to their enormous number, they cannot be neglected and must be included in our scattering model. The question, of course, is how to include them.

Nitrogen (N_2) and Oxygen (O_2) exist as diatoms, rather than spheres, in the atmosphere. In order for us to make use of the Mie calculating routines, we will convert non-spherical molecular scatterers to equivalent dielectric spheres. Stevens has already shown how to do this so (section 4.2.2, Stevens) so we will not go into great detail here. Essentially, because molecules are so small compared to the wavelength, they appear to scatter similar to spheres. What we need to determine is the equivalent spherical radius that will give us this same scattering. The expression is

$$radius_{\text{equivalent}} = \left[\frac{3\sigma_{\text{section}}}{8\pi} \left(\frac{\lambda}{2\pi} \right)^4 \frac{n_{\text{real}}^2 + 2}{\left(n_{\text{real}}^2 - 1 \right)^2} \right]^{1/6} \tag{3-59}$$

where σ_{section} is the Rayleigh cross-section at 532 nm. This equivalent radius is then sent to the scattering program which will return the scattering parameters versus scattering angle. From the above equation, we see the presence of the index of refraction, n_{real}. It is the presence of the index of refraction that is the meaning behind 'dielectric' in our description. One of our themes in this work is to investigate and include the index of refraction in our analysis. Figure 3-11 shows how the equivalent dielectric radius changes for a change in the index of refraction. Since these radius values are very small (in the nanometer range), the resulting scattering components S_1 and S_2 are identical for each radius and so the resulting polarization

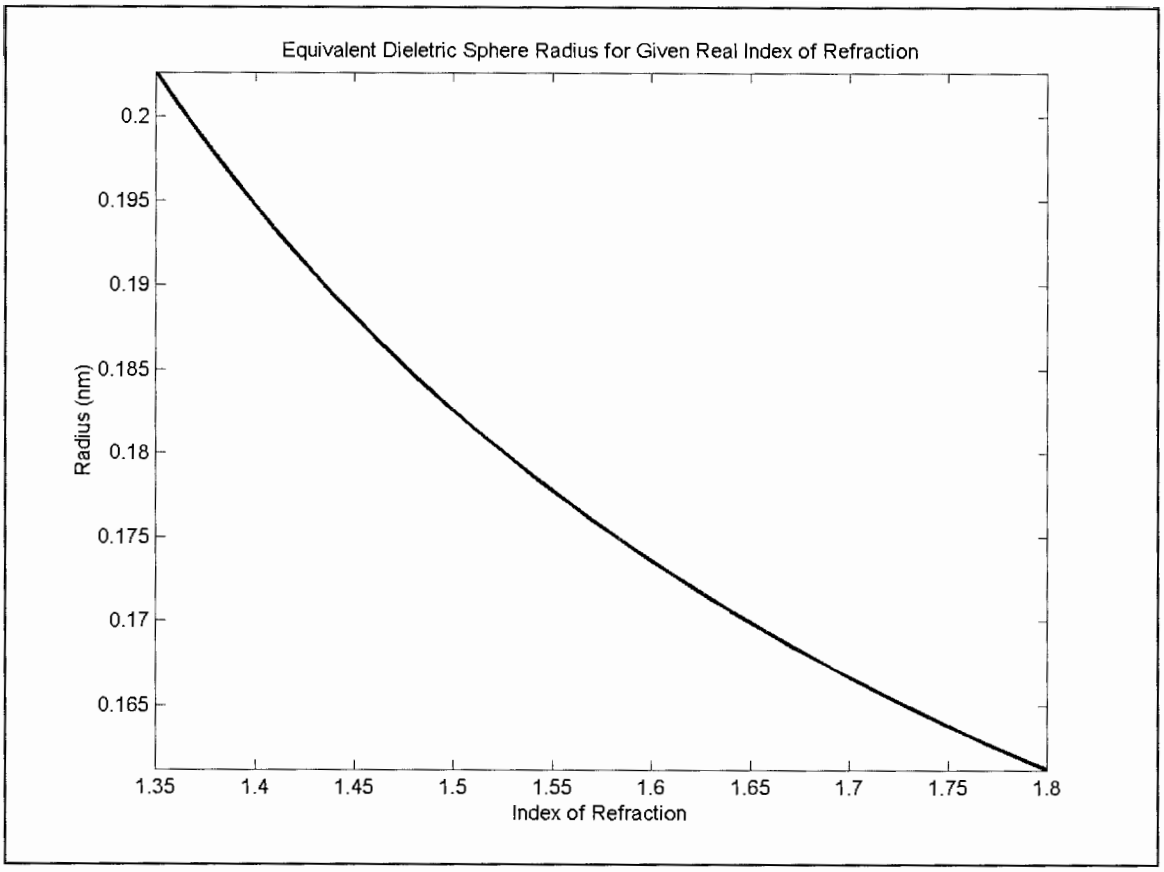

Figure 3-11: Equivalent dielectric radius as a function of index of refraction.

ratio is also identical. Thus, the index of refraction has no consequences for us with respect to molecular scattering components. But as we will see, the same cannot be said for all of the particles in the atmosphere, which undoubtedly have varied indices of refraction.

In our polarization ratio expression (Eqn. 3-58), the molecular components are simply the resulting scattering due to equivalent dielectric spheres for a given incident polarization. In section 3.4.1.3, this will become clearer when we describe the calculation procedure.

3.4.1.2 Lognormal Modes and Number Density Determination

In the polarization ratio expression of Eqn. 3-58, the function, y(r), represents the total aerosol number density concentration versus particle radius. From Chapter 2 (see section 2.4), we indicated that this distribution is generally composed of a trimodal lognormal distribution in the atmosphere. There are a number of ways in which we can proceed to achieve its calculation but the one we show here is what we have used throughout this work.

The first step is to identify each of the distribution's parameters. For a trimodal distribution, there are a total of nine parameters, three for each mode. Thus, each mode can be individually expressed as (from Chapter 2)

$$\frac{N_{Ti}}{\sqrt{2\pi}\, r\sigma_{gi}}\exp\left(-\frac{1}{2\sigma_{gi}^2}\left(r-\mathbf{r}_{\text{median}\,i}\right)^2\right)$$

where *i* represents the appropriate modal number (1, 2 or 3). The above expression is the mathematical expression for the number density distribution of a specified aerosol mode. Most of the aerosol literature, however, expresses the number distribution in the more compact notation of dN/dlnr vs dlnr or, dN/dlogr vs. logr for display purposes[†]. In keeping with this convention, we convert to the differential form simply by taking the desired logarithm. For display purposes, generally the base 10 logarithm is preferred, but for calculations the natural logarithm is more often employed. Our model sets up an array of 250 particle radii, logarithmically distributed, from 1 nm to 35 μm. After the natural logarithm of r, $\mathbf{r}_{\text{median}}$ and σ_g are taken, we have

$$\frac{dN_i}{d\ln r}=\frac{N_{Ti}}{\sqrt{2\pi}\,\ln(\sigma_{gi})}\exp\left(-\frac{1}{2\ln^2(\sigma_{gi})}\left(\ln(r)-\ln(\mathbf{r}_{\text{median}\,i})\right)^2\right).$$

To obtain the number density distribution, $N_i(r)$ versus particle radius, all one needs to do is to multiply by the logarithmic bin width, $d\ln r$. Since we specified a logarithmic distribution of radii, each bin is the same width. Thus, the number density of an aerosol mode, $y_i(r)$, is determined as

$$y_i=\frac{dN_i}{d\ln r}\,d\ln r\,.$$

Extending to the total particle distribution across all modes is simply obtained through summation as

$$y_{TOTAL}=y_1+y_2+y_3\,.$$

In the calculation, the final total number density distribution will be an array of 250 rows by 1 column. The array is then multiplied by the appropriate scattering matrix (described in the next section). As a side note, if during an investigation/inversion it is desired to remove a mode, the corresponding total number density parameter, N_T, is set to zero. There is no need to set the other parameters to zero.

A final note regarding the calculation of the number density distribution must be made. Our model

---

[†] It would be bad form to use dN/dlnr and plot vs. logr (i.e., base 10).

used fixed logarithmic bin intervals, $d\ln r$. However, as the particle size increases, the polarization ratio changes considerably over scattering angle and so a logarithmic bin width would be lumping together large particle sizes into one size for calculation of the scattering matrices and yielding errors in the final polarization ratio. To overcome this, one has two choices. First, one can use a linear bin width, dr but this choice will cause the computation of the scattering matrices to take considerably longer time. For example, if one chose a 1nm dr increment, then one would need to calculate the scattering matrices for 35,000 different particle radii (from 1 nm to 35 μm). The second choice, and the more preferred one, is to increase the total number of particles or decrease the logarithmic bin width. For example, we could have used 1000 particle radii instead of 250 and this would have decreased our logarithmic bin width. For future studies using the polarization ratio, especially in environments that have large particles present, we recommend using more particle radii or smaller logarithmic bin widths.

3.4.1.3 Calculation of the Complete Polarization Ratio

With the molecular and particle size density contributions to the polarization ratio outlined in the previous sections, we now combine these elements to set down the complete polarization ratio.

In calculating the polarization ratio, one must obviously calculate the amplitude coefficients, S_1 and S_2. Stevens pre-calculated these coefficients because the scattering routine took several days to run on a 90-MHz Pentium computer (the larger particle sizes take a long time to compute). As we will discuss further in Chapter 4, we were able to cut a significant number of larger particles out of our calculation and shorten the processing time considerably. However, although we were running on a 1-GHz Pentium machine, each run took slightly more time (about 5 minutes) than was practical during an inversion investigation so we also resorted to using pre-calculated amplitude scattering matrices. We pre-calculated all of the scattering matrices for indices of refraction from 1.33 to 1.8 in steps of 0.002. This took about an evening to run, and once completed, no further lengthy processing was needed.

The pre-calculated scattering matrices are arrays of 175 rows by 250 columns, where the rows correspond to the scattering angles (150° to 180°, in steps of 1/5 of a degree) and the columns correspond to particle radii (1 nm to 35 μm, logarithmically separated). Because the first particle radius, 1 nm, has no corresponding bin width with which to multiply by, this radius is omitted prior to the final calculation of the polarization ratio. Early on, we were using very strict mathematical rules for our calculations but found we could ease these rules. Thus we found that it is no problem to include the 1 nm particle radius but there is also no appreciable effect resulting from its absence since the 1 nm starting point is arbitrary. If this is upsetting to some, it can be easily fixed. We only mention this point so that the interested reader knows the specifics of our implementation of the polarization ratio.

The complete polarization ratio is determined by first reading in the desired scattering matrix. For example, the parallel component is determined by,

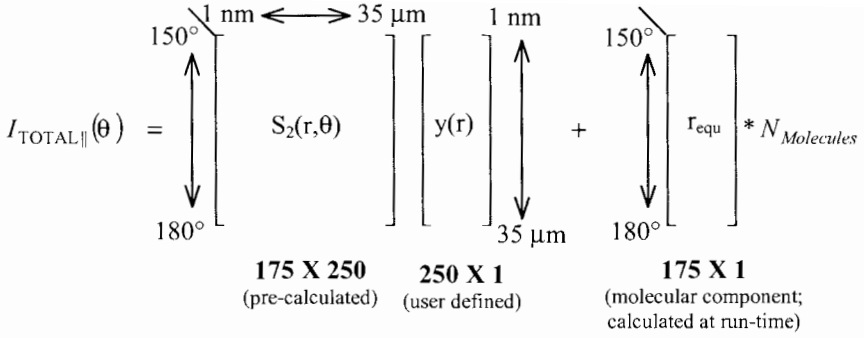

The perpendicular component, $I_{TOTAL\perp}(\theta)$, is determined in a similar fashion. Note that here, the integration of Eqn. 3-58 is taken care of by the matrix multiplication of the pre-calculated scattering matrix and the number distribution. Thus, $I_{TOTAL\parallel}$ and $I_{TOTAL\perp}$ will contain 175 elements, each element representing the total scattering of all of the particles for the given incident polarization. Finally, the polarization ratio, PR, is

$$PR(\theta) = \frac{I_{TOTAL\parallel}(\theta)}{I_{TOTAL\perp}(\theta)}. \tag{3-60}$$

As a final reminder, the determined polarization ratio is for a given index of refraction. In the next sections, we will see how the polarization ratio changes for various changes in the underlying aerosol parameters as well as the index of refraction.

3.4.2 Indifference to Complex Part of Refraction

In the modeling of atmospheric scatterers, the index of refraction can and should be included. As we will see in Chapter 4, most substances have an imaginary refractive component, indicating absorption. However, most gases and particles have extremely small complex parts of refraction ($\sim 10^{-8}$), the notable exceptions being carbonaceous compounds (10^{-3} to ~ 0.1. We now show what effect the complex part of the index of refraction has on the polarization ratio.

The simplest way to see how the complex refractive part manifests itself is by examining how the polarization ratio changes (over angle) for a monodispersed (*i.e.*, single aerosol mode, small σ_g) particle distribution. Extending the analysis to a polydisperse (*i.e.*, more than one mode) distribution is then a simple matter.

The monodispersed distribution is shown in Figure 3-12. In Figure 3-13, the polarization ratio is shown as the index of refraction is varied from $1.35 + j10^{-8}$ to $1.35 + j1$. This range will be suitable for our purposes of demonstration but we do realize that such a range is probably not physically possible since the real and imaginary indices of refraction are not entirely independent of each other especially for visible wavelengths (see Kramers-Kronig relations, Bohren & Huffman, p. 19). From Figure 3-13, we see that the

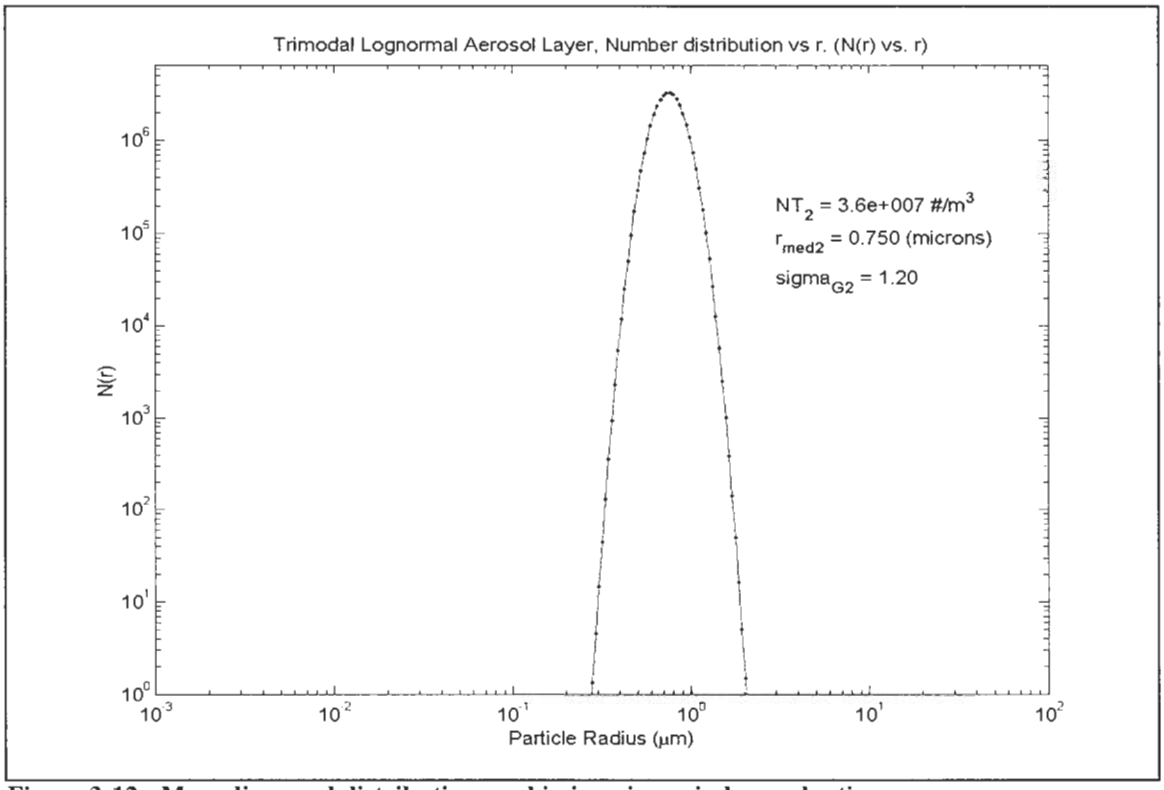

Figure 3-12: Monodispersed distribution used in imaginary index evaluation.

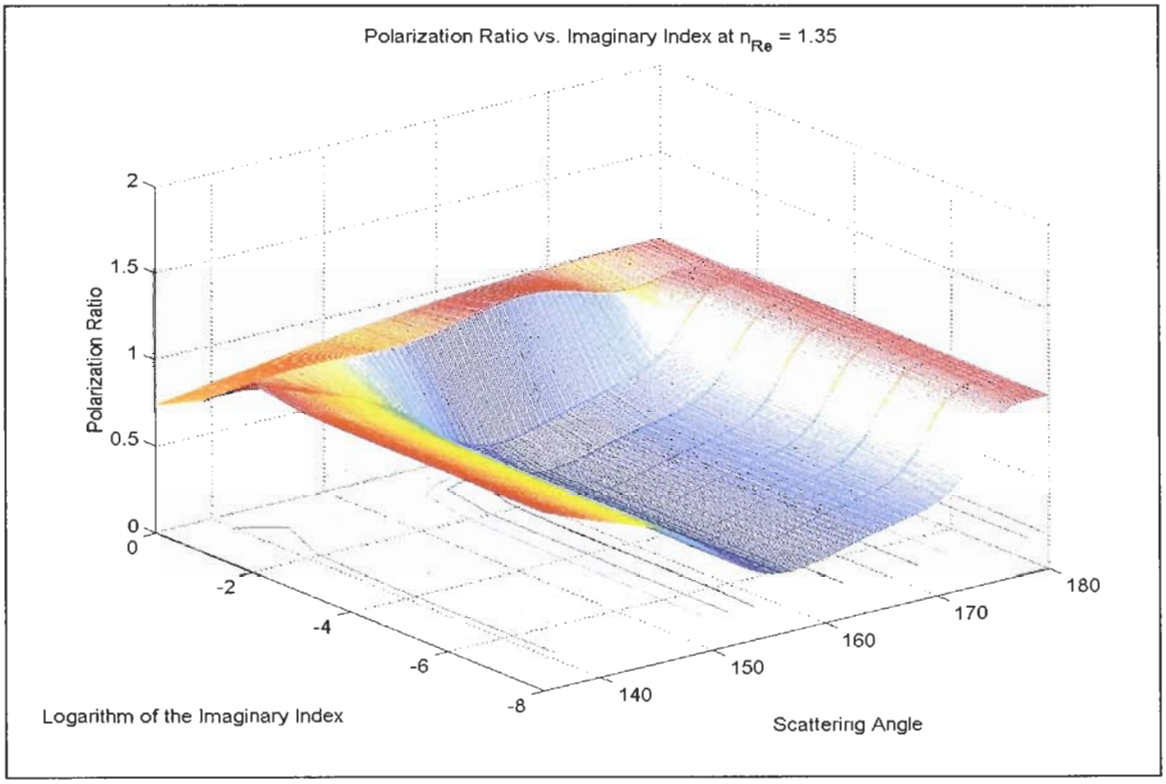

Figure 3-13: Polarization ratio over (logarithm of) the imaginary index for the above distribution.

higher complex refractive part dampens the scattering lobes. This then is the effect of the imaginary index: It removes the internal fields of the particle (by absorption) thus preventing them from interfering and recombining. Of greater interest, however, is noticing how little the polarization ratio changes in the range 10^{-8} to 10^{-3}. Because there is almost no change in the polarization ratio over this range, we say that the polarization ratio is indifferent with respect to the imaginary index of refraction. This is not due to the polarization ratio, but rather is due to Mie theory itself. Thus, the imaginary index should not and will not be included in our models or in our inversion routines. This is an example of being able to understand the theory in order to apply it correctly. We could not have done so if we had not taken the effort to go through the theory in depth and reproduced the derivation.

Extending the analysis to a polydispersed (i.e., trimodal) lognormal distribution, the dampening effect of the imaginary index is compounded with the smoothing effect produced by a wide and varied distribution of particles further dampening the magnitude of the scattering lobes.

3.4.3 Atmospheric Examples/Simulations

The polarization ratio methodology with which we are modeling the scattering of atmospheric gases and particles contains 9 lognormal parameters and 1 (real) index of refraction[†]. Ten parameters give us a large degree of possibilities from which to choose from. This has a significant impact on our being able to find possible inversion solutions when we try to fit the experimental data with the theoretical model.

While the number of available parameters provides us with considerable latitude in our mathematical analysis, only physically observed solutions should be tried. The reason for this is simple: Our methodology, principally light scattering, is an inference of the particle sizes present and not a direct measurement. While we refrain from using the word "guess", this is as good a description as any. However, we do not wish to imply to the reader that we are just pulling numbers out of thin air. We obviously want to make "best guesses" and not embark on untamed ornithoid excursions[‡]. Thus, during our inversions, we will only pursue solutions that are based in physical reality. Illustrations of the polarization ratio for several environments are shown in Figure 3-14. However, the index of refraction is an unknown parameter that makes the shown ratios somewhat suspect. Despite this speculation, it is still instructive to see how the polarization ratio is affected from a mathematical standpoint.

[†] It is understood that the wavelength is fixed at 532 nm.
[‡] Wild goose chases.

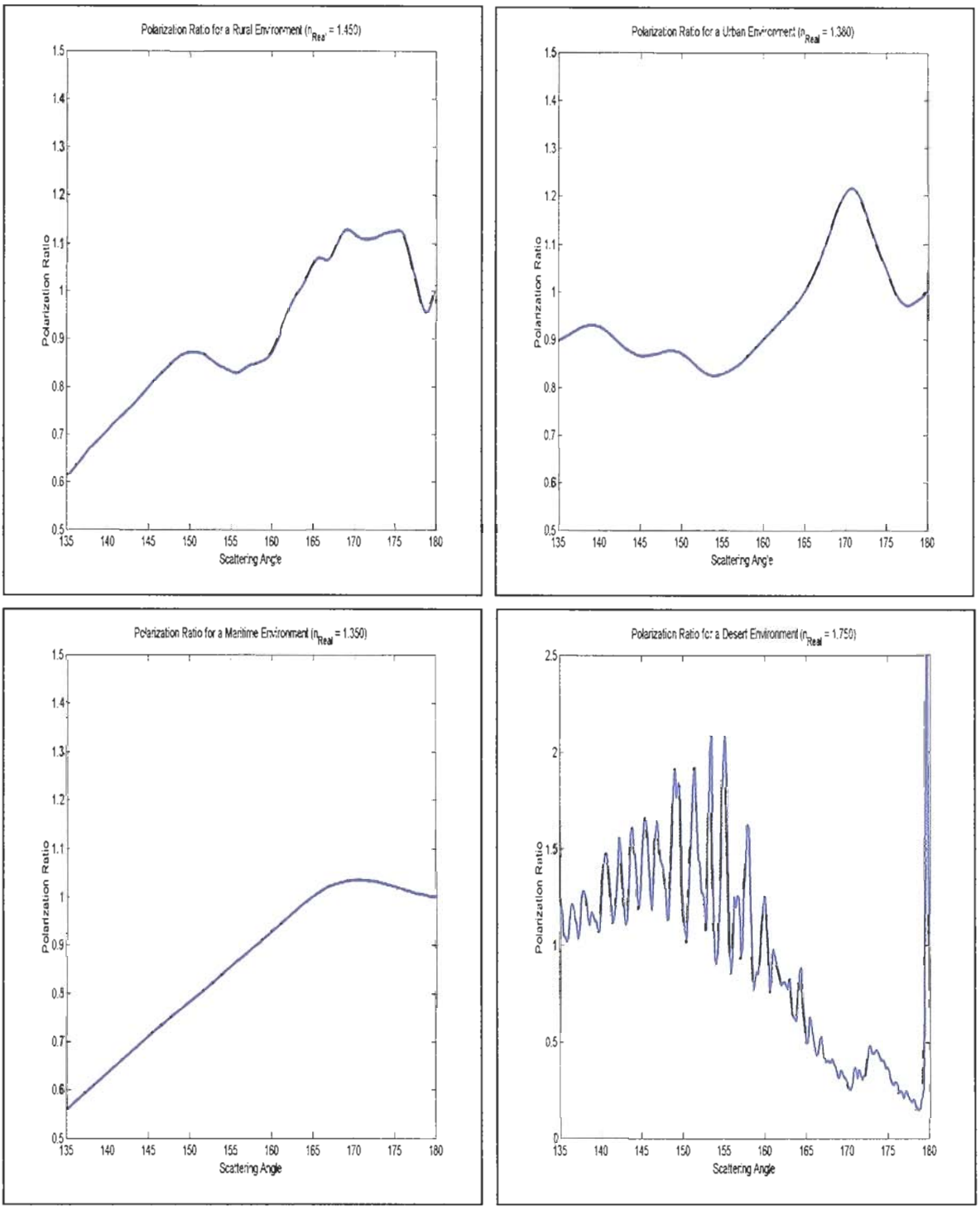

Figure 3-14: Polarization ratios for several environments. The figures show that the polarization ratio can change dramatically for changes in the underlying aerosol and optical parameters.

3.4.3.1 Polarization Ratio Change for Changes in Aerosol Parameters

Eventually (in Chapter 5), we will need to figure out which are the best sets of parameters that will fit a particular set of data. Given that we essentially have 1 equation (the polarization ratio) and 10 unknowns (9 lognormal parameters and an index of refraction), there appears to be a limitless set of possible solutions. Thankfully, this is not the case and here is why.

We mentioned in the previous section that although a solution may be mathematically possible, it may not be physically observable. This still leaves us with a lot of possible solutions. Although we can (and will) rely on the solutions obtained by Stevens and others, we still need to address a simple question: How sensitive is the polarization ratio to a change in a particular parameter? This question, which emerged after we began fitting our model to the data, is formalized as trying to determine the differentiation of the polarization ratio (Eqn. 3-58) with respect to a desired parameter. Taking the differential of the polarization ratio is not recommended at this point as we have found an approach that is somewhat easier to manage and even easier to implement with a computer. We will discuss the specifics in Chapter 8. At this point, we are not going to take the differential of the polarization ratio but simply see how the polarization ratio changes for changes in the ten modeling parameters.

In order to understand the effect a particular parameter has on the polarization ratio, we need some way of visualizing the polarization ratio as it changes. It turns out that this is no easy task as there is no understood way of visualizing a 10^{th} dimensional function. We will have to settle for a lesser dimension. Figure 3-15a shows a lognormal distribution and how the polarization ratio changes as a single parameter is varied (here, $\mathbf{r}_{median1}$ is changed). Admittedly, it is somewhat difficult to get a good feel for the results from this display. However, we hit upon a slightly better approach when we viewed the data from below, or, specifically, projected the data from 3-D to 2-D. Figure 3-16 shows the projection plot of Figure 3-15b. Here, the change in the polarization ratio is much more conducive to understanding as we see the values of the polarization ratio are color-coded into contours[‡]. These contour plots were found to be very valuable in our investigations. Figure 3-17 is a collage of how the polarization ratio changes as each of the 9 parameters are changed individually. We will address the change in the polarization ratio for a change in the index of refraction in the next section.

A few comments must be made on these contour plots. The first is to identify that 2^{nd} mode's geometric median radius, $\mathbf{r}_{median2}$ and the total number density of the 3^{rd} mode, N_{T3}, appear to cause the most amount of fluctuation in the polarization ratio. While this is true for the most part, one has to realize that these changes are specific to a starting set of lognormal parameters and a fixed index of refraction. So although these figures are useful, they should not be taken as universal. In order for the interested reader to get a true appreciation of how the polarization ratio changes for various parameters, one has to play with the expressions themselves. There is simply no substitute for experience.

[‡] Figure 4.9, 4.10, and 4.11 from Stevens are not contour plots but contain a pseudo-color contour map and can be misleading.

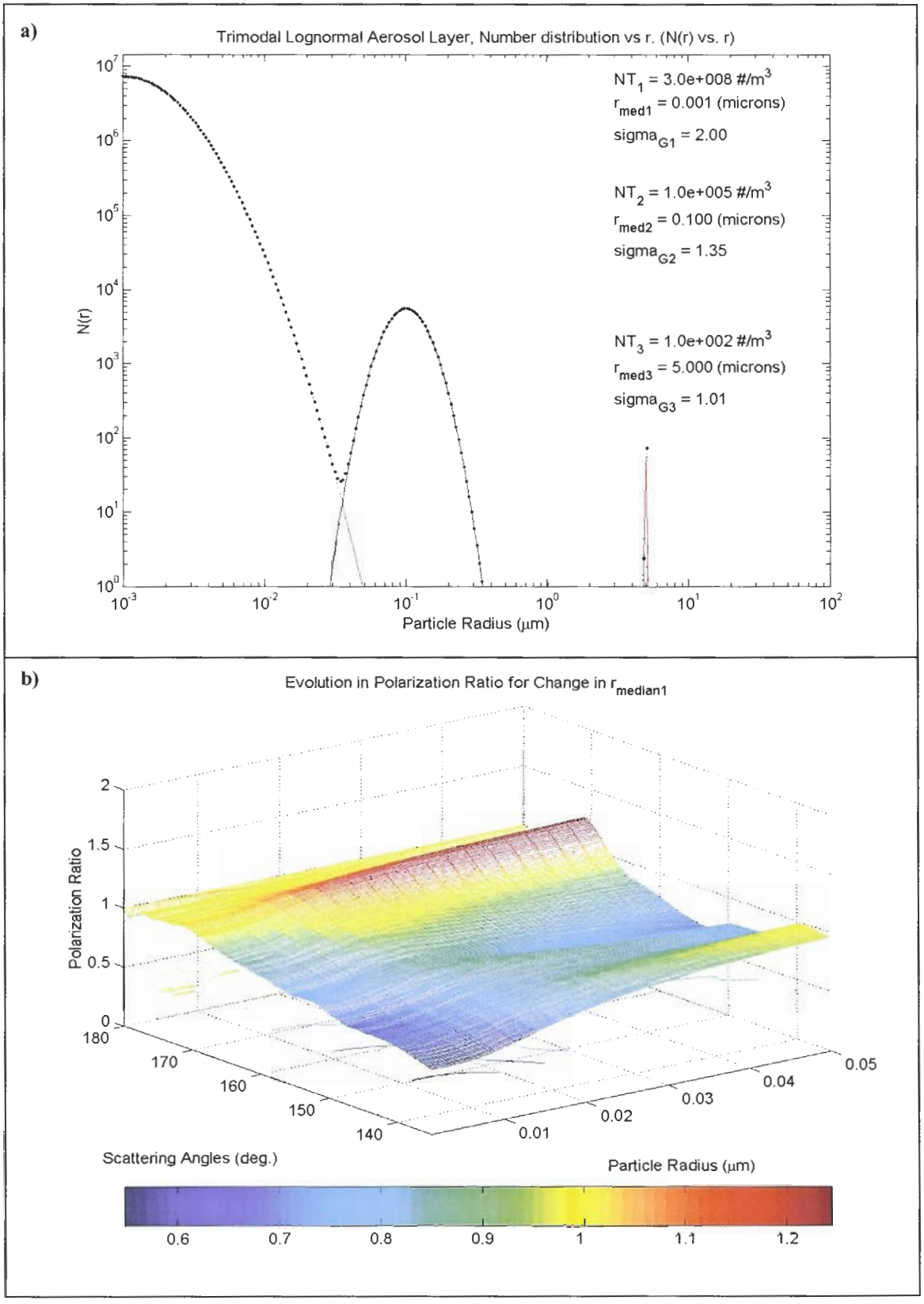

Figure 3-15: (a) Initial trimodal lognormal distribution. (b) 3-D plot of the change in the polarization ratio for a change in the 1st mode's geometric median radius.

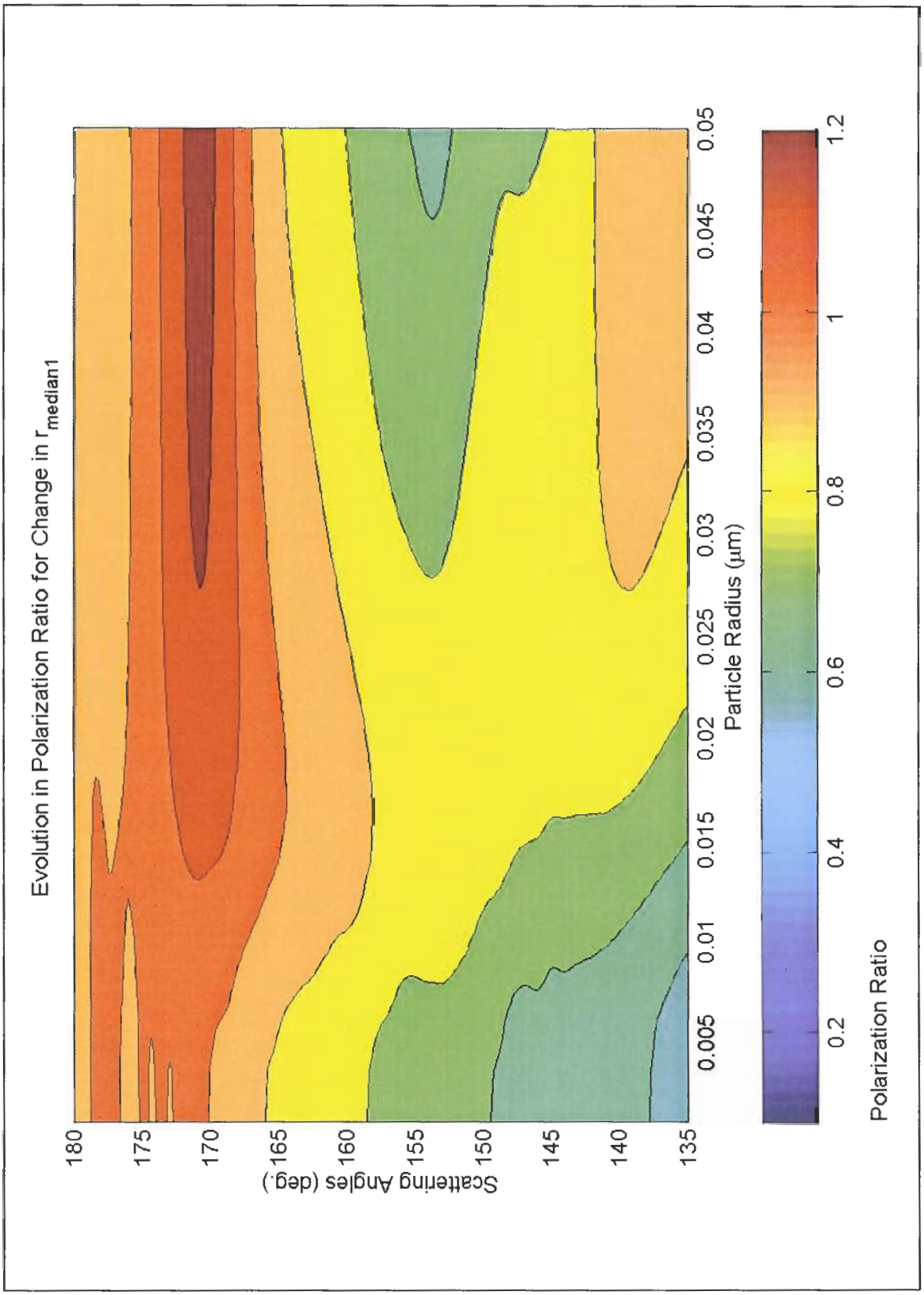

Figure 3-16: Contour plot showing evolution of polarization ratio with respect to $r_{median1}$.

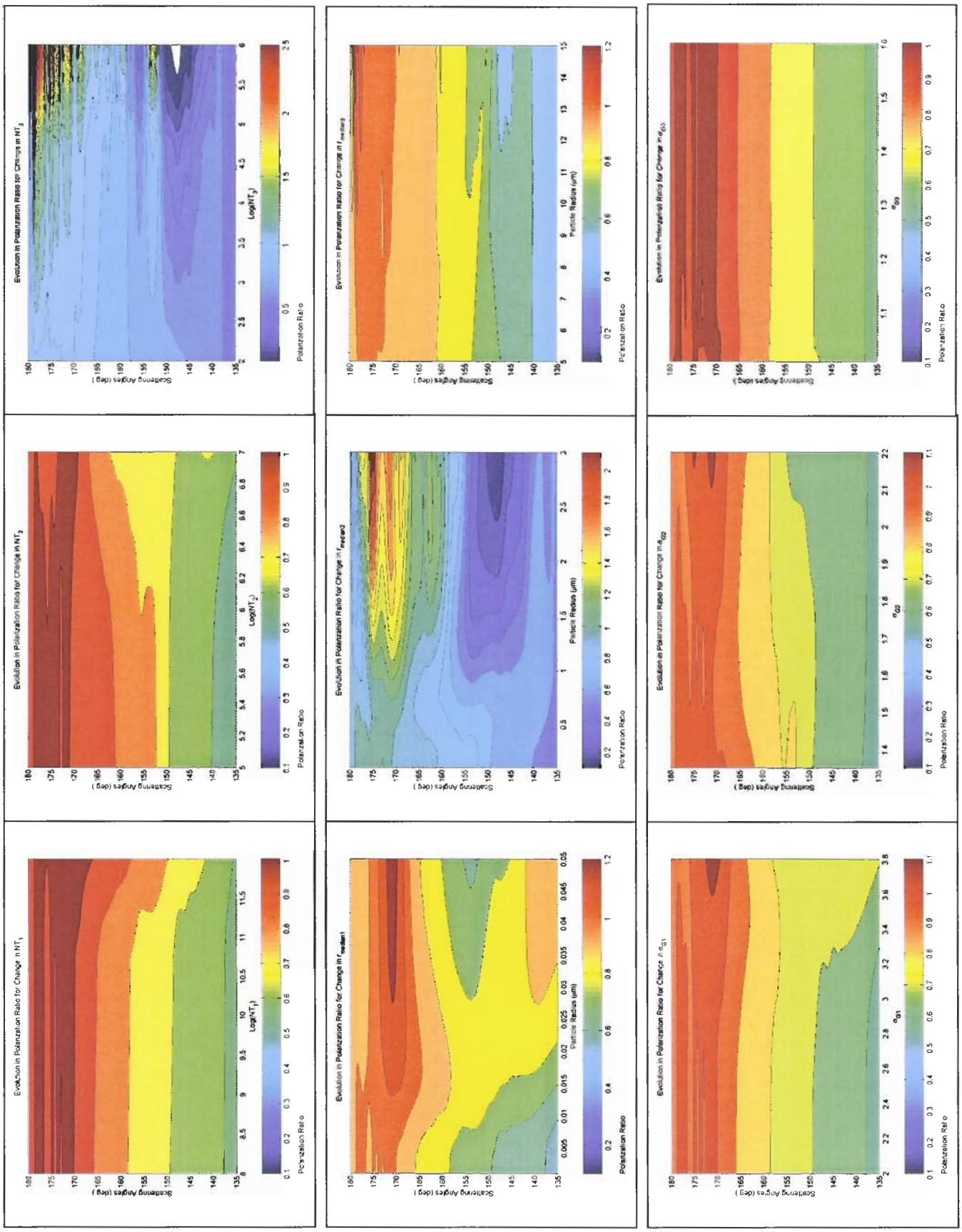

Figure 3-17: Collage of the evolution of the polarization ratio with respect to each of the nine lognormal parameters. The index of refraction used is 1.38.

The second point about these figures refers to the values of the parameters used in these calculations. While we started with a physically observable set of parameters (from Stevens), we allowed each parameter to take on values while the others were fixed. It has been observed, however, that these parameters, while being mathematically independent, are not physically independent. Thus, while we freely admit we have violated a tenet of our approach to maintain its physicality, it was a necessary evil to allow the mathematics to express itself unhindered. There was simply no other viable alternative.

3.4.3.2 Polarization Ratio Changes for Change in Index of Refraction – Practical Angular Limit

In this section we wish to see how the polarization ratio changes for a change in the index of refraction. Starting with the trimodal lognormal size number density distribution of Figure 3-15a, the (real) index of refraction was allowed to vary from 1.33 to 1.8 in steps of 0.002. Again, as with the 9 lognormal parameters, the contour plot was far better in visualizing how the polarization ratio changes as the index of refraction changes. Plots for combinations of aerosol parameters are shown in Figures 3-18 and 3-19. The aerosol parameters used in these plots are given in Table 3.4.

These plots are not just pretty filler. It was actually these plots that answered several critical questions that emerged after we took data and tried to fit the model to the data. Specifically, these plots suggest a minimum set of scattering angles and what values these scattering angles are in order for a unique solution to be obtained. For example, if one examines Figure 3-19 at n = 1.38 between 135° and 150° and then also examines the same angles but with n = 1.8, one would get essentially the same polarization ratio experimentally. Further, Bohren (1986) commented on the use of "effective index strategies" and so obtaining a solution of 1.8 would be non-physical for all three aerosol modes which have been shown to be chemically diverse. We do not discount higher indices altogether since, as will be shown in Chapter 5, with only one mode such indices are still plausible.

Table 3-4: Lognormal parameters for the given figures.

	N_{T1} ($\#/m^3$)	$r_{median1}$ (μm)	σ_{G1}	N_{T2} ($\#/m^3$)	$r_{median2}$ (μm)	σ_{G2}	N_{T3} ($\#/m^3$)	$r_{median3}$ (μm)	σ_{G3}
FIGURE 3-18	4e11	0.01	3.85	3.6e6	2.5	1.85	4.5e3	12.5	1.3
FIGURE 3-19	4e10	0.005	3.45	———	———	———	———	———	———

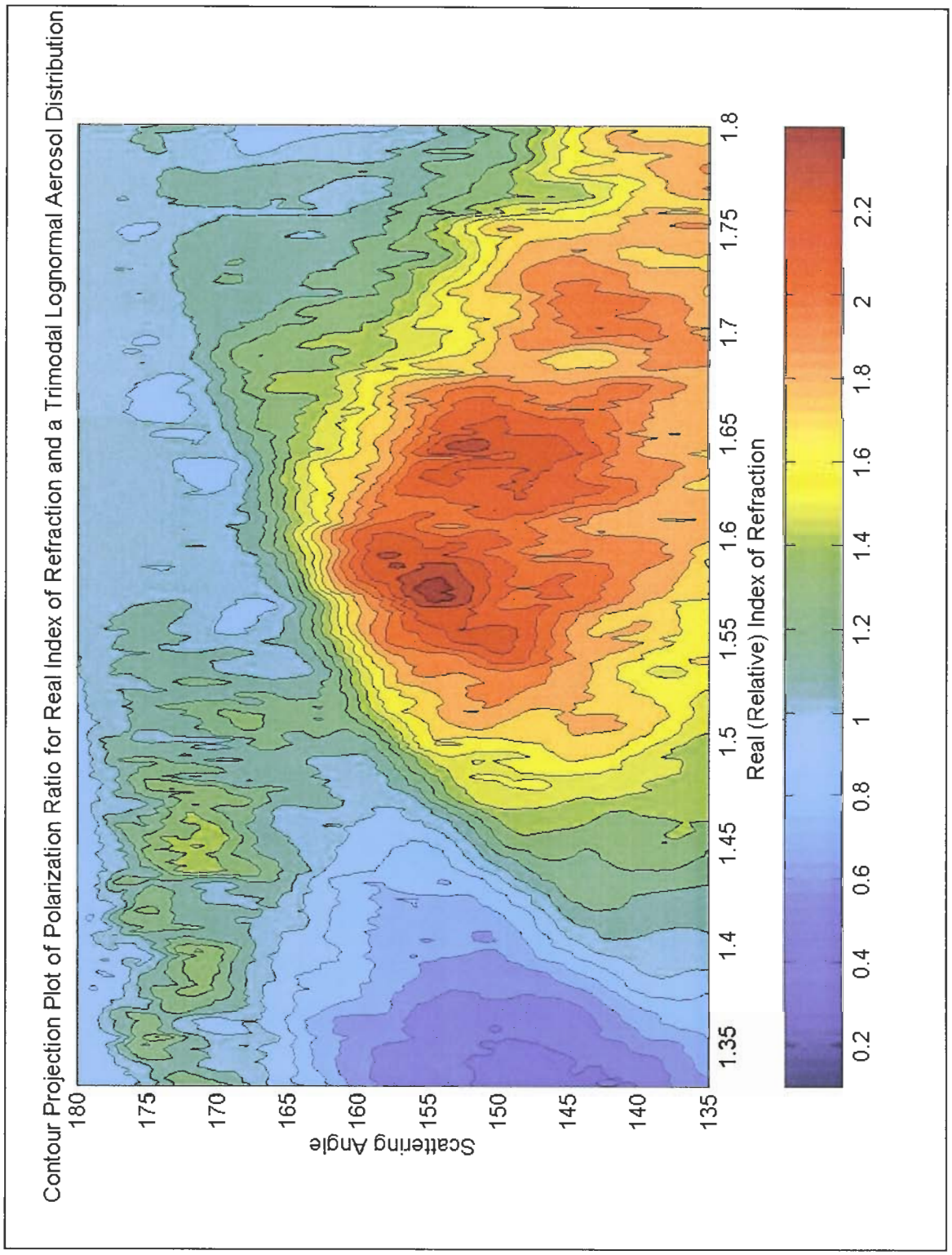

Figure 3-18: Polarization ratio change for a change in the index of refraction.

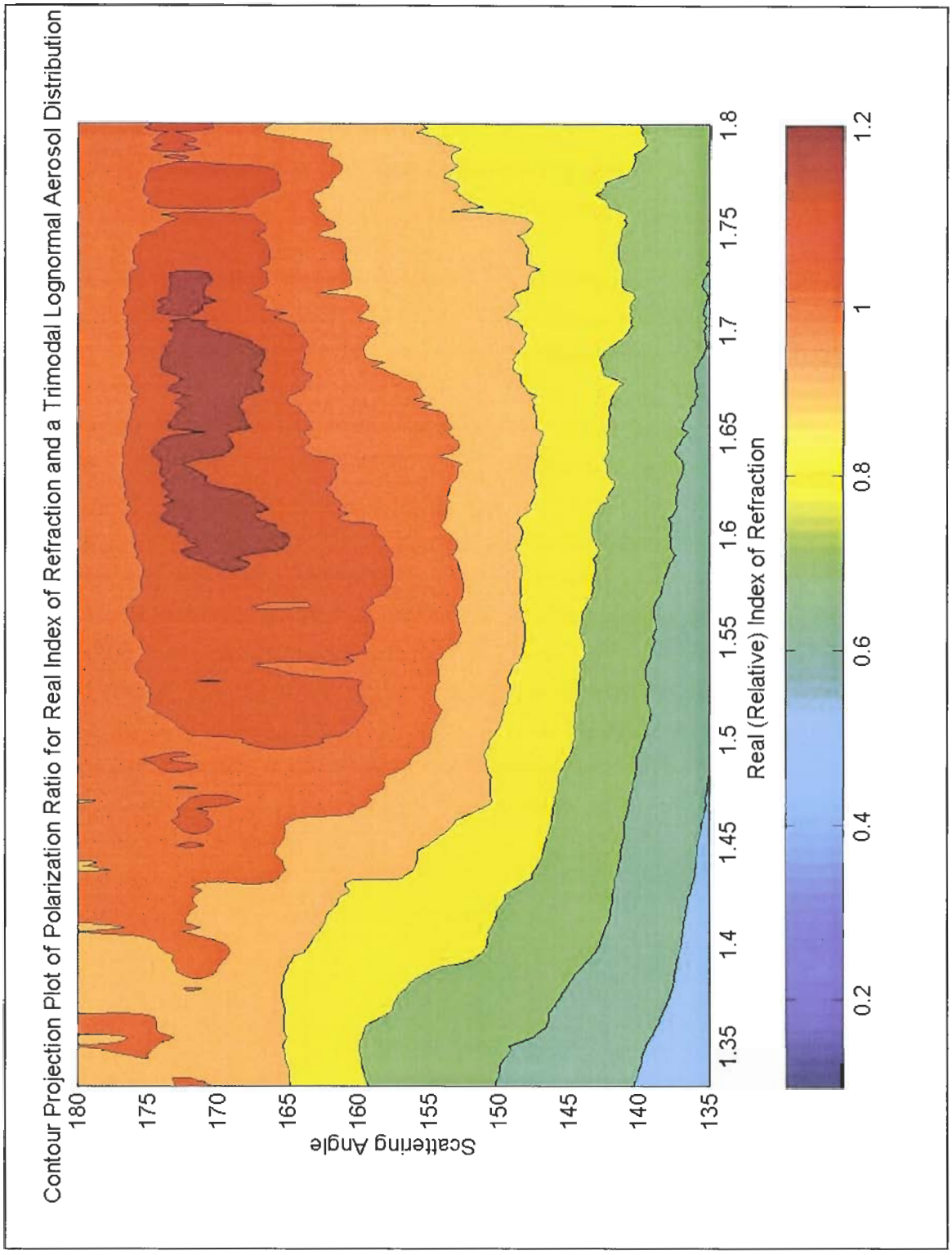

Figure 3-19: Change in the polarization ratio for a change in the index of refraction.

3.5 SUMMARY

In this chapter we put forth the basic scattering theory to be used throughout this thesis. Specifically, we are assuming that the atmospheric aerosols and particulates can be modeled as spheres. Our primary methodology is to use the ratio of the parallel and perpendicular scattered components. This methodology is much more conducive to experimental studies since it eliminates many instrument-related errors from corrupting the results. However, we also showed that the polarization ratio, and more specifically, Mie theory, is insensitive to the imaginary index of refraction and thus should not be included in our model.

We concluded this chapter by putting the polarization ratio through its paces by allowing the aerosol modal parameters and the index of the refraction to vary. Such investigation yielded a better understanding of the polarization ratio and also brought forth practical limits in the use of the polarization ratio as a tool in obtaining particles size density information from light scattering measurements.

4

Chapter 4:
The Atmosphere

Occam's razor can't cut air.

To say that the atmosphere is a complicated place is an understatement of staggering proportions. Thus, we will not presume to be able to discuss all of the complexities of the atmosphere in a single chapter. But since the atmosphere is the laboratory of this thesis, to not discuss it would be a serious error. Simply put, we have to describe the part of the atmosphere that pertains specifically to this thesis yet still provide enough of an overview of the atmosphere as a whole. What we write here is to aid the reader in developing a better mental idea of some of the processes that occur in the atmosphere and how our scattering experiments can be arranged to avoid errors but still yield credible results. This chapter needed to be set apart from other chapters as it contains a plethora of information. This chapter is placed prominently up front not to let the reader think the author is an expert on the atmosphere but for a more important reason: The physics of the atmosphere is the driver of this work. Specifically, electromagnetic scattering theory does not dictate the atmosphere, the atmosphere dictates scattering behavior. If we simply delved straight into scattering theory and all of its mathematical glory we may be misled by the results since we would be allowing the mathematics to drive the physics. However, the physics and chemistry of every atmospheric constituent will not be fully explored here as this chapter is primarily focused on general results and processes. For an in-depth examination of the atmosphere, it is highly recommended that one begin with Seinfeld and Pandis 1999 (it is a mere 1326 pages). This reference is exceptionally complete and highly scientific yet has managed to remain accessible to those outside of atmospheric chemistry and physics.

The information contained in this chapter is accurate but admittedly it is limited (there simply is not enough space to do a thorough examination) and so the reader may be unsatisfied with the portion of the atmospheric picture presented here. The only real way to satiate one's appetite in atmospheric chemistry and physics is to investigate ideas and perform analysis one self. However, no matter how much one knows about the atmosphere, there is always something new to learn. We thus start with describing the basic picture of the atmosphere and subsequently refine it for use in this thesis. This work is specifically interested in the lower troposphere (about 1 km from the ground) and so we will focus our efforts in developing a mental picture of that particular portion of the atmosphere. Unfortunately, this is also the portion of the atmosphere that is the most chemically active and diverse in its particulate composition. We could not have chosen a more complicated region of the atmosphere and, as we have found out, this diversity and uncertainty will come back to haunt us later. In this case, the simplest solution may not be the correct one.

4.1 THE BASIC STRUCTURE OF THE ATMOSPHERE

We start here with the basics of the atmosphere, namely its pressure, temperature and molecular number profiles, *i.e.*, variations with altitude. All data, expressions and figures in this section are based on the U.S. Standard Atmosphere 1976 (the molecular component does not change radically from year to year). In our atmospheric model, of which aerosols are of primary importance, we must include the molecular component. The data given here are based on world averages and can certainly change depending on geographical location. Later, we will find that it will take significant changes in the background properties of the atmosphere (i.e., the molecular and ultrafine particles) to effect any noticeable change in our atmospheric scattering calculations. Thus, it will be valid to hold our molecular number density constant for our scattering calculations. With respect to the polarization ratio, a change in the number of molecules will have no effect on the angular scattering diagram[†] as the molecules and ultrafine particles are very much smaller than the wavelength of light and so the Rayleigh criteria applies (See Chapter 3).

4.1.1 Temperature

The (average) temperature profile is approximated by seven straight-line segments as shown in Figure 4-1 (the 1976 Standard Atmosphere is missing one segment in its figure 3 but provides the data for it in table 4[‡].) The temperature profile results from observational data and is perpetuated by tradition. It is the temperature profile that has been used to categorize the atmosphere into layers. Although Figure 1 only shows the temperature profile up to about 90 km, Earth's atmosphere is considered to extend to more than 500 km. However, we are most interested in the region from the ground to the tropopause, or, simply, the troposphere. Because of its importance, a few words should be mentioned specifically about this region.

The troposphere, aptly coined from the Greek word *tropos*, meaning turning, is a dynamic and turbulent region of the Earth's lower atmosphere. Typically, the height of the top of the troposphere is a maximum over the equator and a minimum over the poles. Despite being a small fraction of the Earth's total atmospheric thickness, the troposphere accounts for approximately 80% of the total atmospheric mass (Seinfeld and Pandis, 1998, p. 8). Because of the turbulence of the troposphere, we assume this region to be well-mixed which means that the same percentage by volume (mass) of any particular constituent is constant throughout the region (U.S. Standard Atmosphere, 1976, p. 12). For molecular concentrations, the same fractional composition is constant until about ~90 km and so the molecules are assumed well-mixed up to ~90 km. Of course, the total number density (or volume) of any particular constituent is allowed to vary with altitude, *i.e.*, we expect more N_2 molecules near the ground than at 10 km but the fractional component of N_2 will be the same at each altitude up to ~90 km. Finally, the troposphere itself can be further partitioned into the planetary boundary layer (PBL) and the free troposphere. The sun drives the dynamics of the Earth's atmosphere and the height of the PBL changes from about 0.5 km during

---

[†] Of course, the scattering intensity will change.
[‡] This was later corrected in an errata sheet.

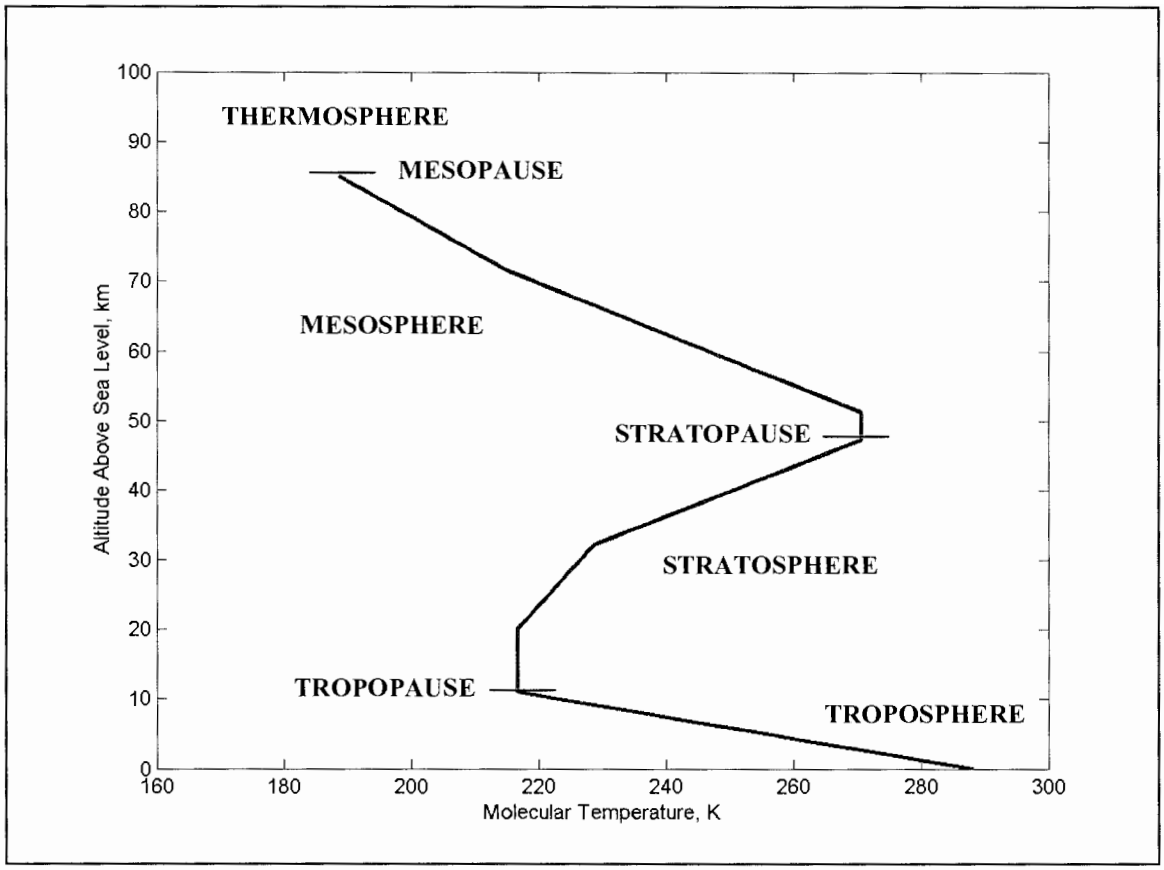

Figure 4-1: Temperature profile and definitions of the atmospheric layers.

the night to about 2.5 km during the day. The free troposphere extends from the PBL to the tropopause.

4.1.2 Pressure

Determination of the pressure profile begins with the assumption that a region of the atmosphere is in hydrostatic equilibrium. This assumption means that the force due to gravitational acceleration and the force due to pressure balance. Quantitatively, this is given by

$$-\frac{1}{\rho(z)}\frac{dP(z)}{dz} = g\,, \tag{4-1}$$

where $P(z)$ is the pressure (Pascals, Pa)[†] at some altitude z, $\rho(z)$ is the mass density (g/m^3) of air at the same altitude, and g is the acceleration due to gravity (9.8 m/s^2). While considering the troposphere, a reasonable

[†] 1 atm = 760 mm Hg = 760 Torr = 1013.25 mb = 101.325 x 10^3 Pa = 101.325 x 10^3 N/m^2.
Standard temperature and pressure is considered 273.15 K and 1 atm.

approximation allows us to neglect the variation of g with altitude (U.S. Standard Atmosphere, 1976, fig. 2, p. 8). Rearranging Eqn. 4-1, we have

$$\frac{dP(z)}{dz} = -\rho(z)g\,, \tag{4-2}$$

which is the familiar hydrostatic equation (Seinfeld and Pandis, eqn. 1.1, p. 9). To solve explicitly for *P(z)*, we introduce the ideal gas law. The ideal gas law is given as

$$P(z)V = NR^*T\,, \tag{4-3}$$

where

P(z) – Pressure (N/m^2)
V – Volume (m^3)
T(z) – Temperature (K)
N - mols
R^* – Universal Gas Constant = 8.314 N·m/mol·K
= 0.08206 L·atm/mol·K.

Now if we rearrange the ideal gas law as

$$\frac{N}{V} = \frac{P(z)}{R^*T} \tag{4-4}$$

and after multiplying both sides by the molecular weight, M (g/mol), of a substance, we have

$$\rho(z) = \frac{NM}{V} = \frac{MP(z)}{R^*T}\,. \tag{4-5}$$

The mean molecular weight for air is taken to be M_{air} = 28.96 g/mol (or kg/kmol) and the calculation for M_{air} is shown in Section 4.1.3. Thus, we can express the ideal gas law as

$$\rho(z) = \frac{M_{air}P(z)}{R^*T(z)}\,. \tag{4-6}$$

Substituting Eqn. 4-6 into Eqn. 4-2 and rearranging for *P(z)*, we have

$$\frac{dP(z)}{P(z)} = -\frac{gM_{air}}{R^*T(z)}dz\,,$$

which is solved as

$$\frac{dP(z)}{P(z)} = d\ln P(z) = -\frac{gM_{air}}{R^*T(z)}dz$$

$$\int_{P_0}^{P} d\ln P(z) = -\frac{gM_{air}}{R^*T(z)}\int_0^z dz$$

$$\ln P(z) - \ln P(0) = -\frac{gM_{air}}{R^*T(z)}z$$

$$\ln\frac{P(z)}{P_0} = -\frac{gM_{air}}{R^*T(z)}$$

$$P(z) = P_0\exp\left(-\frac{gM_{air}}{R^*T(z)}z\right), \tag{4-7}$$

where P_0 is the pressure at sea level, taken to be standard pressure (760 mm Hg) at standard temperature (273.15 K). If we define the atmospheric scale height as

$$H_{ATM}(z) = \frac{R^*T(z)}{gM_{air}}, \tag{4-8}$$

then Eqn. 4-7 simplifies to

$$P(z) = P_0\exp\left(-\frac{z}{H_{ATM}(z)}\right). \tag{4-9}$$

A plot of the pressure profile is shown in Figure 4-2. Upon comparing the temperature and pressure profiles of Figures 4-1 and 4-2, respectively, we see that the temperature changes by roughly a factor of 2 whereas the pressure changes by several orders of magnitude. The atmospheric scale height, also known as the e-folding distance, has a value of $H_{ATM} \approx 8$ km. This is the altitude where the pressure falls to $1/e$ of its sea-level value or 37% of its initial value and is often a basic parameter in describing the conditions of the atmosphere.

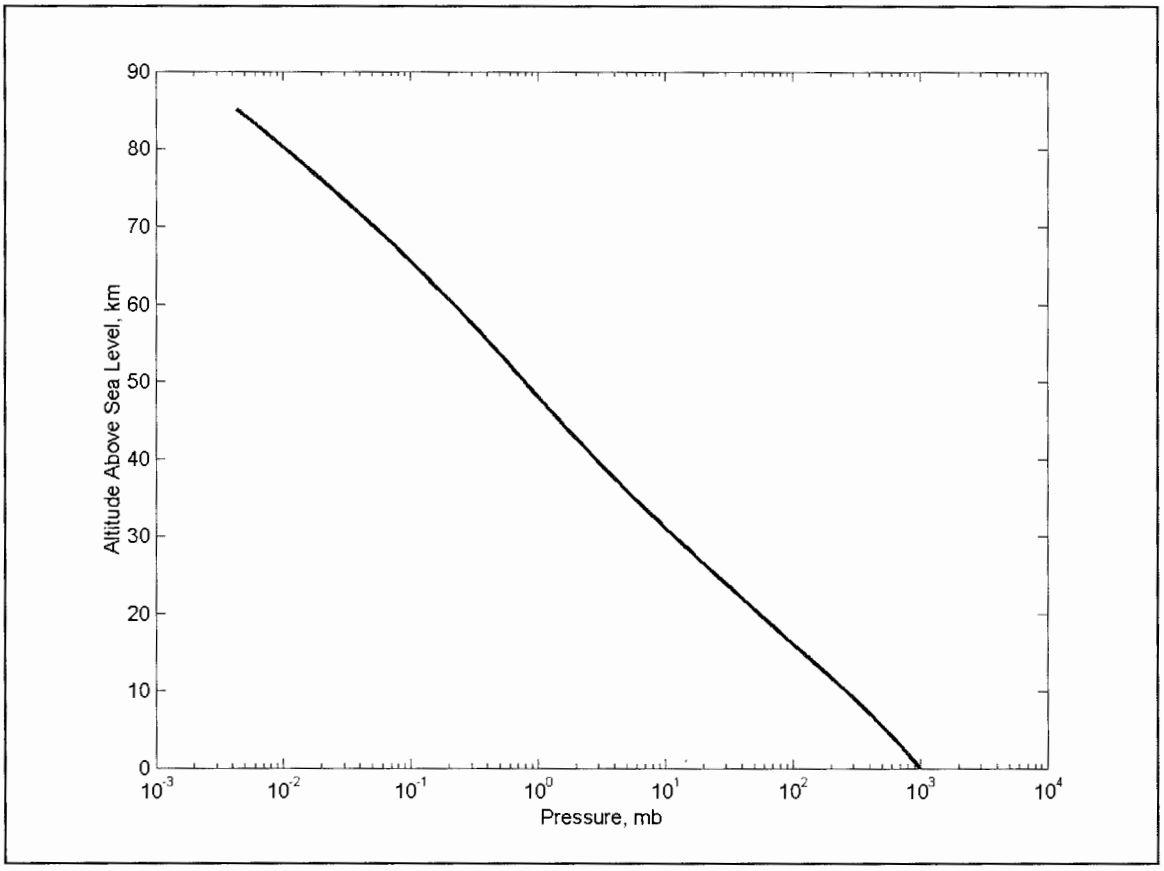

Figure 4-2: Pressure profile of the atmosphere.

4.1.3 Molecular Constituents and Profiles

In terms of shear numbers, the molecules in the atmosphere far outnumber the most abundant particles and aerosols by nearly 15 orders of magnitude. Although we have indicated in Chapter 3 that a single molecule scatters very little compared to a single aerosol particle, the total molecular abundance indicates that their effect on our atmospheric scattering model cannot be neglected.

The basic molecular constituents of the atmosphere are given in Table 4-1 (U.S. Standard Atmosphere, 1976, p.3). It is assumed that up to approximately ~90 km each molecule exists in the same fractional volume (although their number density does change with altitude). We can show the altitudinal variation by first introducing Avogadro's number, $N_A = 6.022 \times 10^{23}$ #/mol, which defines that 1 mole of something (atoms, molecules, ions, etc.) has 6.022×10^{23} members, regardless of its composition. Starting with Eqn. 4-4 and multiplying both sides by N_A, we have (eqn. 41, p. 15, U.S. Standard Atmosphere, 1976),

$$\frac{N_A N}{V} = N_T(z) = \frac{N_A P(z)}{R^* T(z)} = \frac{P(z)}{k_B T(z)}, \tag{4-10}$$

Table 4-1: Molecular constituents of the Earth's atmosphere

Gas Species	Molecular Weight M_i, (kg/kmol)	Fractional Volume f_i
N_2	28.013	0.78084
O_2	31.999	0.209476
Ar	39.948	0.00934
CO_2	44.010	0.000314
Ne	20.183	0.00001818
He	4.003	0.00000524
CH_4	16.043	0.000002
Kr	83.800	0.00000114

where $N_T(z)$ is the total number of molecules per cubic meter at some altitude z and k_B is Boltzman's constant. Thus, using the fractional volumes given in Table 4-1, the number density of some molecular component, i, at some altitude, z, is given by

$$n_i(z) = f_i N_T(z), \tag{4-11}$$

where $i = N_2$, O_2, Ar, etc. A plot of the total number density and the number density of the three most abundant molecular components in the atmosphere is given in Figure 4-3.

The mass density profile of a molecular component can be found by

$$\rho_i(z) = \frac{n_i(z) M_i}{N_A} \tag{4-12}$$

and so the total mass density is

$$\rho(z) = \sum_i \rho_i(z), \tag{4-13}$$

which is equivalent to Eqn. 4-6. A plot of the mass density profiles for several molecular components, as well as the total mass density profile, is shown in Figure 4-4.

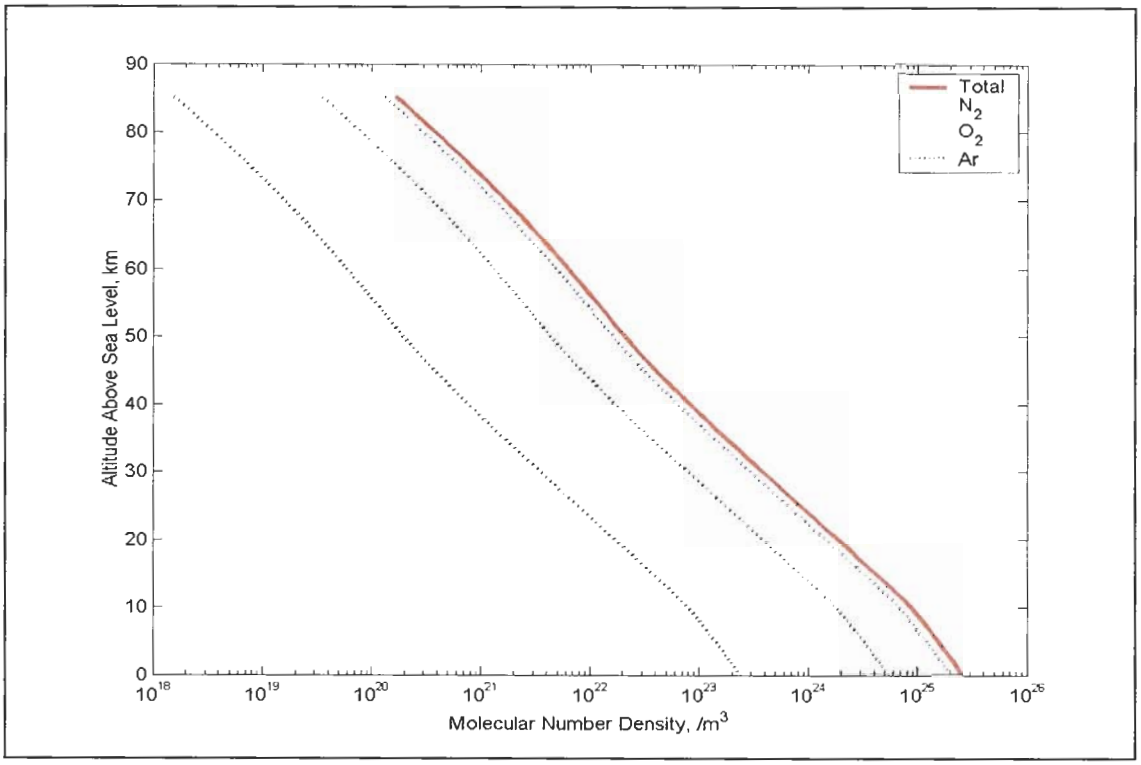

Figure 4-3: Number density profile of several molecular species. At sea level, the total number density is 2.55 x 10^{25} /m^3 (1 atm, 15 °C).

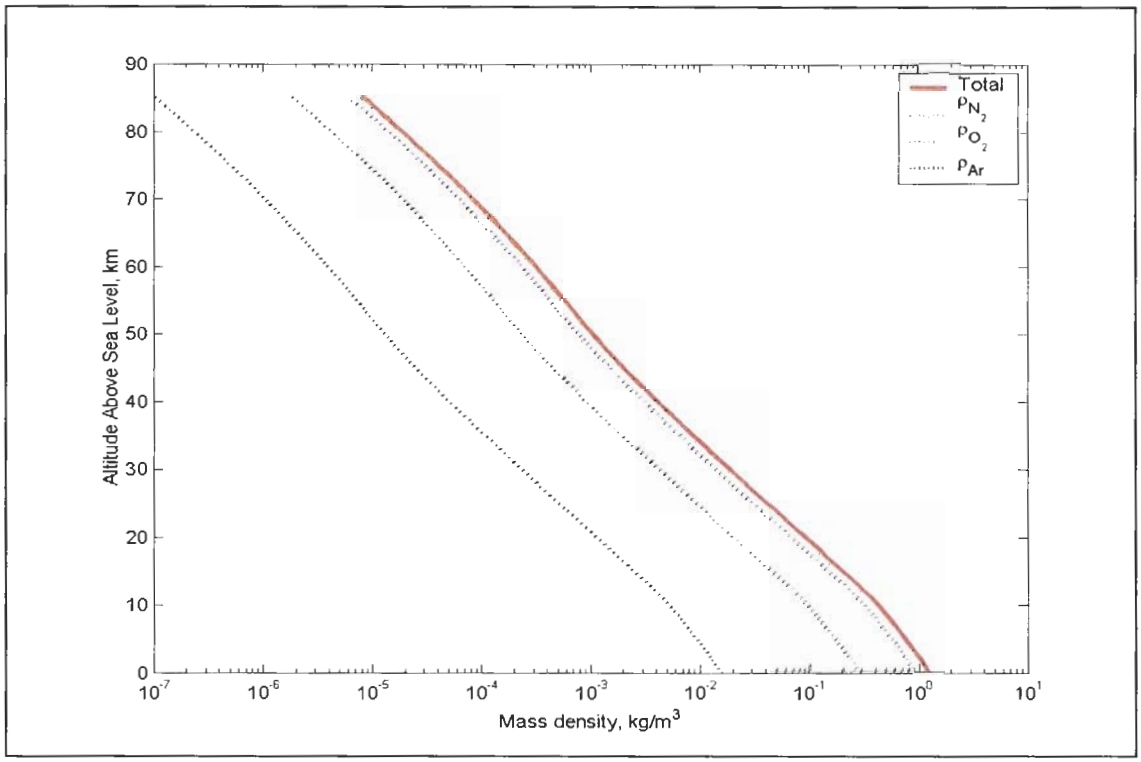

Figure 4-4: Mass density profile of several molecular species.

The summation of the individual molecular densities to yield the total molecular density stems from the law of partial pressures, which states that the total pressure is due to the sum of the pressures of each individual gas component under the assumption of constant temperature and volume. By expanding the total pressure into its partial pressure components and keeping temperature and volume constant, we have,

$$P(z) = P_1(z) + P_2(z) + P_3(z) + \ldots \tag{4-14a}$$

$$= \frac{RT}{V}(N_1 + N_2 + N_3 + \ldots). \tag{4-14b}$$

Using Table 4-1 and the law of partial pressures, it immediately follows that the mean molecular weight of air must be

$$M_{air} = \sum_i f_i M_i \tag{4-15}$$

$$= 28.96 \text{ g/mol} \quad .$$

4.1.4 Conversion of Gas Quantities to Aerosol Quantities

In the literature, gas quantities are reported in parts-per-million (ppm), -billion (ppb), or -trillion (ppt), while aerosol quantities are typically reported as number densities (#/m^3) or mass densities ($\mu g/m^3$). This is an important point to keep in mind because it is often found that one article may be speaking of a compound such as SO_2 like a gas and another article may be speaking of SO_2 as an aerosol. The units on the quantities are helpful identifiers of how those quantities are being analyzed and interpreted. Further, gas quantities like ppm, are generally given as ppmv, which indicates parts-per-million-by volume (m^3 or cm^3) and so are also called mixing ratios. In most instances, volume is understood and so the quantities are simply reported as ppm, ppt and so on. Occasionally, some quantities are reported with respect to mass (ppmm, ppbm, pptm). See Seinfeld and Pandis for additional conversion information (p.19, Seinfeld and Pandis, 1998). Here, we assume the quantities are with respect to volume.

Because our scattering model encounters number and mass densities, it is desirable to be able to convert between gas quantities and aerosol quantities. Although it is a very simple matter to accomplish the conversion, it is important to know how to do in order to make better use of the various data on the atmosphere in our scattering models. Let us assume we are given a quantity of some gas in units of ppt, specifically we assume 1 ppt. (There is no change in the following calculations if one has ppm or ppb, except in the proper use of the million and billion exponent identifier.) Generally, standard temperature and pressure conditions are assumed (1 atm, 0° C) but often the global mean temperature at sea level of 15 °C is used and so we will also use this global mean temperature. Using Eqn. 4-10, the total number density, N_T, at sea level is found to be $2.55 \times 10^{25}/m^3$. Thus, if a gas is reported as 1 ppt, the corresponding number density is determined as

$$n_i = \frac{N_T}{(1\ ppt)} = \frac{N_T}{\left(1\ x\ 10^{12}\right)}, \tag{4-16}$$

where n_i has the units of $\#/m^3$. If the gas were given in ppm or ppb, then the exponent in the denominator of Eqn. 4-16 would be changed to 6 and 9 respectively. To convert to mass density, we determine the molecular weight, M_i, of the gas (in units of g/mol), and, using Avogadro's number, we have

$$\rho_i = \frac{n_i\ M_i}{N_A}, \tag{4-17}$$

where ρ_i has the units of mass density, g/m^3. At this point, it is a simple matter to convert to $\mu g/m^3$.

4.2 THE ATMOSPHERIC AEROSOL

We would like to answer some basic questions about aerosols. Invariably, those new to the science of aerosols ask basic questions about the nature and classification of aerosols. Some may seek simple understanding as to what is the composition of an aerosol and what will be its ultimate impact on the Earth's climate. Much research has been done and so there are answers to many basic questions. Unfortunately the answers typically begin with conditional statements such as *generally*, *in most instances*, *sometimes*, *may*, and so on. In other words, when talking about aerosols, seldom are absolutes encountered. We should, however, know some background about the aerosols we studying since it will help us to avoid applying mathematical formulas whose parameters may have non-physical values. Thus, if we know about the physical properties of aerosols before hand, we can judge the validity of our solution's parameters and thus place constraints on our inversion techniques. As it turns out, light-scattering experiments of the atmosphere must have *a priori* knowledge of the environment under examination as there is no single electromagnetic theory that can account for every constituent of the atmosphere.

There are several reasons for the vagueness of answers when trying to describe the physics of aerosols. First, the atmosphere itself is a dynamic place. Not only is man contributing to its makeup through pollution brought about by travel and industrial processes, but there are also naturally occurring components being added to the atmosphere (for example, due to wind erosion and from organic compounds emitted from trees). Thus, from one instant to the next, the makeup of the atmosphere can change in a rapid and unpredictable manner. We have witnessed such transitions from the experiments conducted in this thesis (see Chapter 6). A secondary effect, which comes directly from the first above, is that our models of the atmosphere are incomplete as we have no way of identifying and tracking each and every particle in the atmosphere so we must rely on probabilistic methods, which directly leads to uncertainty. We never quite know exactly what is in the atmosphere at any given time at any given locale around the globe, which means that the answers we give with respect to aerosols must be conditional. This is an

important point to keep in mind because with so much research going on around the globe, seldom is the research being done at one location and so trying to compare results from one locale and time period to another is generally not advisable. Often, correlation is made between locales but not corroboration.

Knowing that aerosols vary widely in size and composition is the first lesson any researcher in the field of aerosols must come to understand. Such a lesson is especially important when using optical scattering as a means of determining size and number density of aerosols. Although any driver knows that one cannot see as well as in a fog as on a clear day, as a point of comparison, optical scattering tries to distinguish *between* clear days. Unfortunately, a comprehensive scattering theory does not exist which can take into account the myriad of aerosol configurations and so there will undoubtedly be instances where the model will not fit the observed data. Thus, the greatest source of error in light scattering measurements is misapplying a particular theory or model to all cases. In order to give a particular theoretical scattering model any chance of successfully working, we need to know something about the quarry we are seeking *i.e.*, we need to know what aerosols we are hunting. The scattering theory that we have adopted (Mie theory) cannot be used on just any aerosol, but only on a specific class of aerosol, i.e. instances where we may find homogenous spheres. We now embark on giving basic definitions and generalizations of aerosols and showing how others have dealt with the problem of using optical scattering to ascertain the properties of aerosols.

4.2.1 Definition of an Aerosol

If we had started this section as, "An aerosol is …", we'd be breaking our own mantra of not using absolutes when describing aerosols because there is no universally accepted definition of what an aerosol actually is. Although this may seem like we can write a blank check and describe an aerosol in any way we see fit, we will use a widely accepted definition. So, we preface our definition of an aerosol by providing the condition that we are defining an aerosol as it pertains to this thesis, but the definition used here is also used by others (see Seinfeld and Pandis).

Due to the large spatial and temporal variability of an aerosol in both its composition and distribution, the only conventional means of classifying an (atmospheric) aerosol is by its size range. Typically, an aerosol whose particles lie in the range from about a few nanometers to tens of micrometers in diameter, are defined as the suspension of any solid or liquid particles suspended in a gas (Seinfeld and Pandis, 1998, p. 97). The current classification of an aerosol is principally by its solid component and thus an aerosol is often referred to as particulate matter. An aerosol is also distinguished between being primary (directly entrained into the atmosphere such as from erosion) or secondary (formed by gas-particle conversion). We do not wish to overrule conventional wisdom in our definition of an aerosol, but we do need to be more specific as to what an aerosol is with respect to this work.

In this work, an aerosol is any object[†] (which includes organic and biological entities such as bugs and viruses) in the atmosphere in the size range from 1 nm to 35 μm in radius. Our definition of an aerosol is consistent with the scientific community and only differs in that we make no distinction between a liquid (wet) particle and a solid (dry) particle. The principal reason for this is obvious: Our scattering model cannot readily distinguish between two spheres of different composition much as one could not determine the colors of two billiard balls from touch alone. The second reason for not wanting to separate an aerosol into wet and dry components is that we are after the optical scattering of the entire collection of particles in the atmosphere and not individual components. This collective scattering idea is embedded in our use of an effective index of refraction. Lastly, and most importantly, we expect to find good agreement between the experiment and theory when the relative humidity exceeds 80%. Due to their hygroscopic nature, most particles have a high water content and so tend to be spherical.

The size range of our aerosols does require a bit more explanation. The choice of an upper limit of 35 μm, albeit somewhat arbitrary and considerably different from the upper limit of 250 μm (in radius) used by Stevens, has been chosen due to a number of practical considerations. The first consideration is the (wet or dry) deposition rate. The particle size is the most influential factor in determining the residence time of an aerosol in the atmosphere but other factors such as particle density, coefficients of drag and diffusion, and aerodynamic resistance also play a (complicated) role (see Chapters 19 and 20, Seinfeld and Pandis, 1998). For particles < 0.5 μm in radius, Brownian motion generally governs their movement while gravitational settling governs particles > 10 μm in radius (p. 969, Seindfeld and Pandis, 1998). Figure 4-5 (fig. 8.6, p. 467, Seinfeld and Pandis), below shows how the settling velocity varies with particle diameter. This plot is somewhat of an over simplification as the settling velocity of the small particles actually has a minimum value. More exact settling velocities are found elsewhere (figs. 19.3, 19.4, Seindfeld and Pandis, pp. 970-971, 1998), however, for our purposes, Figure 4-5 will suffice. A particle of 50 μm in diameter has a settling velocity of about 50,000 cm/hr. As we discuss in Chapter 5, our measurements may be 30 seconds apart. Thus, a 25 μm particle (in radius) may fall by 4.2 m and so between measurements, this particle may move between scattering volumes and yield error. At 15 μm (in radius), the settling velocity is estimated at 25,000 cm/hr corresponding to a distance of 2.1 m, a slightly more useable result. After taking into account a variety of factors (including settling time), aerosols and various gaseous species can be classified according to their mean residence times in the atmosphere and ultimately impact the distribution of these species on a global scale. Figure 4-6 (fig. 1.17, Seinfeld and Pandis, p. 41) shows the temporal and spatial scales of several atmospheric constituents.

[†] Since we are using Mie theory, our "objects" are assumed to be homogeneous spheres.

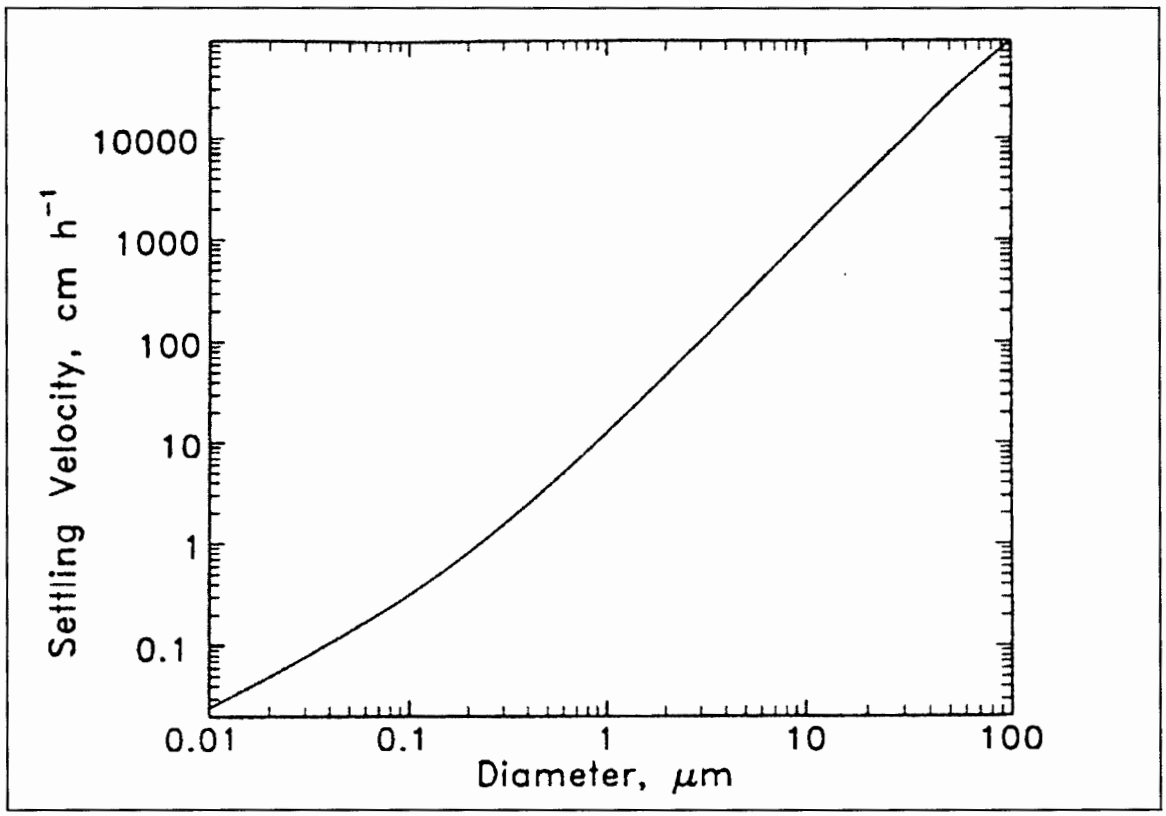

Figure 4-5: Settling velocity versus particle diameter (fig. 8.6, p. 467, Seinfeld and Pandis, 1998).

Gravitational settling is a nice way of visualizing the physics of larger sized particles but with respect to our scattering work it is not the only consideration. As particles increase in size (especially dry particles that result from grinding and crushing) they become less and less spherical and thus Mie theory becomes less applicable. Combining gravitational settling with nonsphericical particles makes it reasonable to set an upper limit of about 30 μm in particle size. Any larger than that, and even wet particles fall too fast to capture in the allotted time.

Just in case the reader is still not convinced about the upper limit, we have two more convincing cards to play. In the Mie calculation, as the radius of the sphere is increased, the number of terms needed to have a convergent solution also increases. The result of this is that one can obtain two different results from two different computers running the same program due to round off error. It was found that at about 35 μm, the calculated scattering values began to deviate in value. Finally, Steven's own data shows that he never had particles in any quantity much above 25-35 μm in radius so there is no need to calculate the scattering matrices for particles above 35 μm.

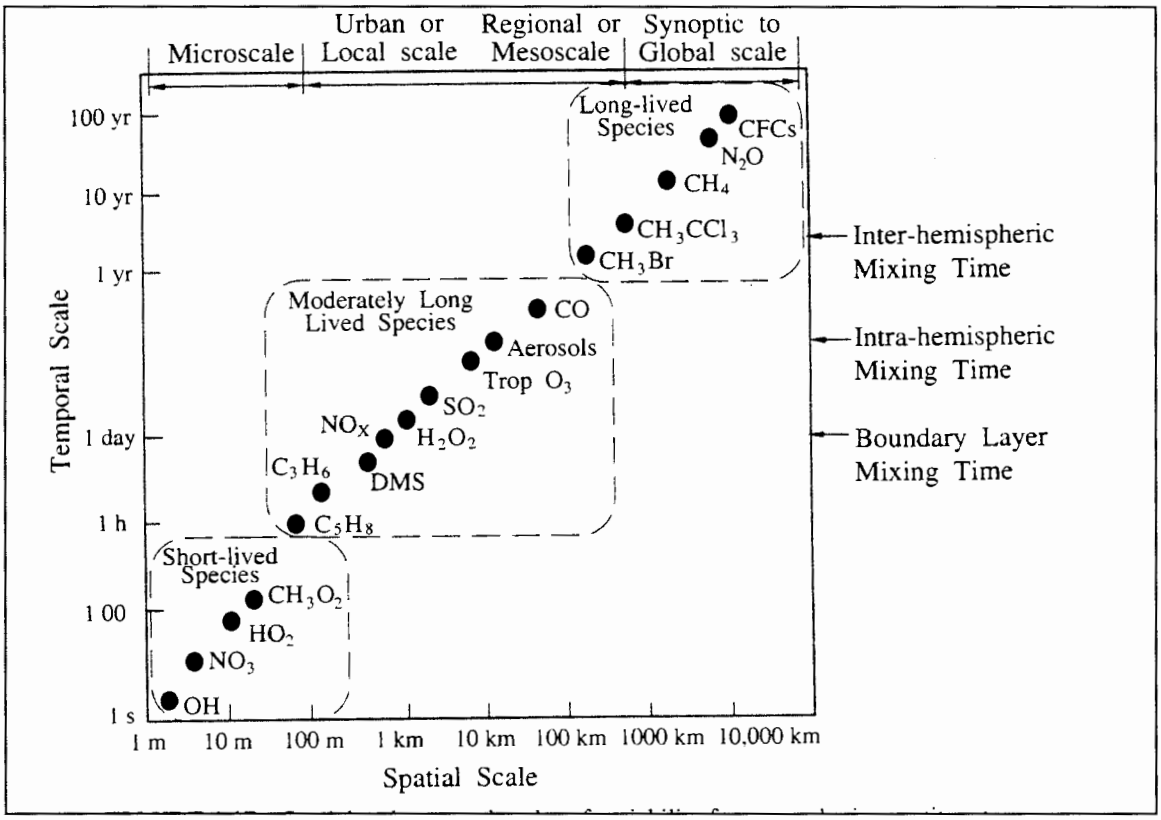

Figure 4-6: Spatial and temporal residences of several atmospheric species (fig. 1-17, p. 41, Seinfeld and Pandis, 1998).

The choice of the lower size limit is considerably less rigorous. The principal reason is that accurate particle size information does not exist below 10 nm. This thesis is primarily concerned with interpreting the optical scattering due to a distribution of particles and so it is not trying to establish or refute any particular size distribution model(s). To do so would require instruments that have been specifically designed and calibrated to accomplish such a task. The best course of action for this thesis is to choose a particular model and stick with it instead of using a slew of different models. This is precisely what Stevens has done and what others have also done when investigating scattering processes. We also will adopt this approach. The only real consideration in choosing a lower size limit of 1 nm is that we do not want to include molecular gases as an aerosol. Gases and aerosols are separate entities.

4.2.2 Aerosol Size Distributions

Not only can we classify aerosols in terms of size but also in the way aerosols are distributed over a size range. We have presented size density distributions in Chapter 2 (specifically the lognormal) but we will recap some of the important points here in this chapter and will provide explicit examples of aerosol size density distributions in the lower troposphere.

Typically, aerosols are collected by particle sizing instruments and displayed as the number of particles per cubic centimeter (or per cubic meter) within a specified size range. Quantitatively, distributions are expressed as

$$\frac{\Delta N}{\Delta D_p} \tag{4-18}$$

where ΔN represents the number density of particles within a size range, ΔD_p (μm). Thus, the overall units of the number density expression of Eqn. 4-18 are $\mu m^{-1}\ cm^{-3}$. Here, the size range or bin, ΔD_p, refers to particle diameter. This work uses particle radius as an input to the Mie scattering routines so we will express our aerosol size density distributions as a function of particle radius. Thus, Eqn. 4-18 is simply restated as

$$\frac{\Delta N}{\Delta r}. \tag{4-19}$$

Because the size of aerosols vary over several orders of magnitude, inequalities in displaying the size number density distribution will arise if one uses a fixed Δr size bin (Seinfeld and Pandis, p. 415, 1998). To compensate for this, particle size density distributions are made with respect to logarithmic size ranges, $\Delta \ln r$ or $\Delta \log r$. For our purposes we will use the base 10 logarithm so Eqn. 4-19 is typically expressed as

$$\frac{\Delta N}{\Delta \log r}. \tag{4-20a}$$

However, when plotting Eqn. 4-20a vs. the particle radius r, the resulting area under the curve no longer corresponds to the particle number size density. This is easily seen since the area under the curve would be

$$\begin{aligned} \text{Area} &= \{\text{height}\}\{\text{width}\} \\ &= \frac{\Delta N}{\Delta \log r} \cdot r, \end{aligned}$$

which does not correspond to particle number density as the units are completely wrong. Obviously, to make the units correct all we need to do is multiply Eqn. 4-20a with logr, i.e., we should plot $\Delta N/\Delta \log r$ vs. $\Delta \log r$ and so the area under the curve will correspond to the number density of particles. In the mathematical limit, the aerosol size density distributions are displayed as

$$\frac{dN}{d\log r} \quad \text{vs.} \quad d\log r\,. \tag{4-20b}$$

At this point, we have not attached any mathematical function to describe our aerosol size distributions. All we have done is stated how we should take raw data and display it properly to take into account the large size range of aerosol particles. Since reporting all of the particle size data would necessitate specifying a particle number density for each logarithmic bin size, mathematical functions have been used to curve-fit to the particle size density data as a means of efficiently reporting and analyzing results.

One of the first mathematical functions employed to describe aerosol size density distributions is the power law[†] expressed as

$$\frac{dN}{d\log r} = \frac{C}{r^{-\beta}}$$

where C and β are constants but are dependent on the specific size range investigated. The power law was accepted for many years as it seemed to fit typical aerosol size density distributions like the one shown in Figure 4-7 (figure 1, Willeke and Whitby, 1975, p. 530).

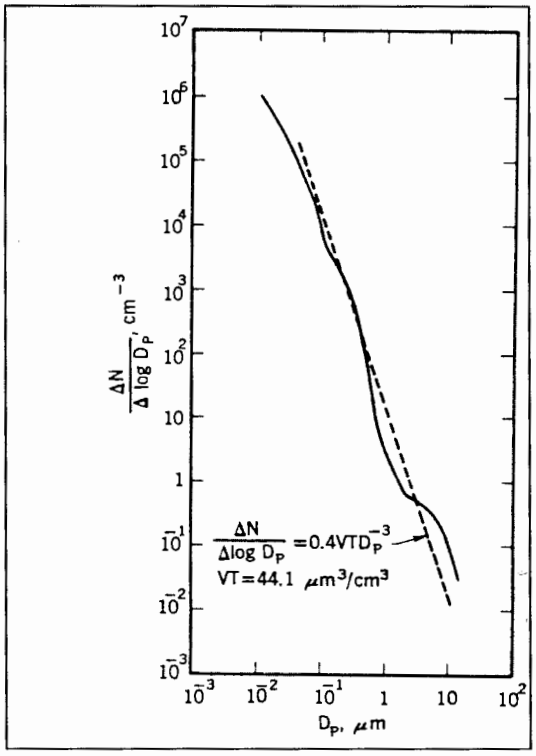

Figure 4-7: Aerosol size density data and the corresponding power law fit (figure 1, , p. 530, Willeke and Whitby, 1975).

[†] Also known as the Junge power law to honor Christian Junge who did some of the earliest aerosol sizing work.

As we can see from Figure 4-7, the power law does a reasonably good job at fitting the aerosol distribution around 0.1 μm but near the ends of the size ranges, the power law deviates noticeably. At the time, it was thought that instrument error was the principal cause of the discrepancy but as instrumental errors were reduced, more scrutiny fell on the power law itself. A new model was needed.

4.2.2.1 Trimodal Lognormal Model of Aerosol Size Distributions of the Lower Troposphere

Whitby et al. (1972) published data on the aerosol size distributions of Los Angeles smog. It was this paper that was the beginning of the end of using the power law to describe aerosol size density distributions. In its place would emerge the use of the lognormal distribution, which we will describe momentarily. Although Whitby is usually given credit for establishing the use of lognormal functions to describe aerosol distributions, he never mentioned lognormal functions in this 1972 work. What Whitby did do was actually something better than suggesting a new mathematical function.

In examining the aerosol number size density data, Whitby also began to evaluate plots of surface area distributions,

$$\frac{dS}{d\log r} = 4\pi r^2 \frac{dN}{d\log r}$$

and volume distributions,

$$\frac{dV}{d\log r} = \frac{4}{3}\pi r^3 \frac{dN}{d\log r},$$

as shown in Figure 4-8. Upon examining reams upon reams of aerosol data and obtaining plots similar to the ones shown in Figures 4-7 and 4-8, Whitby began to see the same patterns emerge. Principally, he noted that his number, area and volume plots were showing humps in the same general locations. These recurring markers in the distribution plots indicated to Whitby that the aerosols should not be lumped together over the entire size range but should be decomposed and placed into distinct size ranges. Whitby states (pp. 78-79, Whitby *et. al.* , 1972),

> *"...it soon became apparent that no single distribution function could or should describe more than about a one-decade range of particle sizes...The realization that the size distributions should be broken up into subranges of about one decade for description was a real breakthrough."*

This may indicate that all one needed to do with the power law was to apply it to specific size ranges in a piecewise continuous manner. However, in a very simple and elegant paper, Davies (1974), building on the idea of using subranges as proposed by Whitby, showed that the power law should not be used to

describe large particle sizes at all. Davies then went on to suggest using lognormal functions for each subrange as needed and he proceeded to fit Whitby's Los Angeles smog aerosol size density data with seven lognormal functions, or modes (Figure 4-9). Davies, however, gave no rationale for choosing lognormal functions.

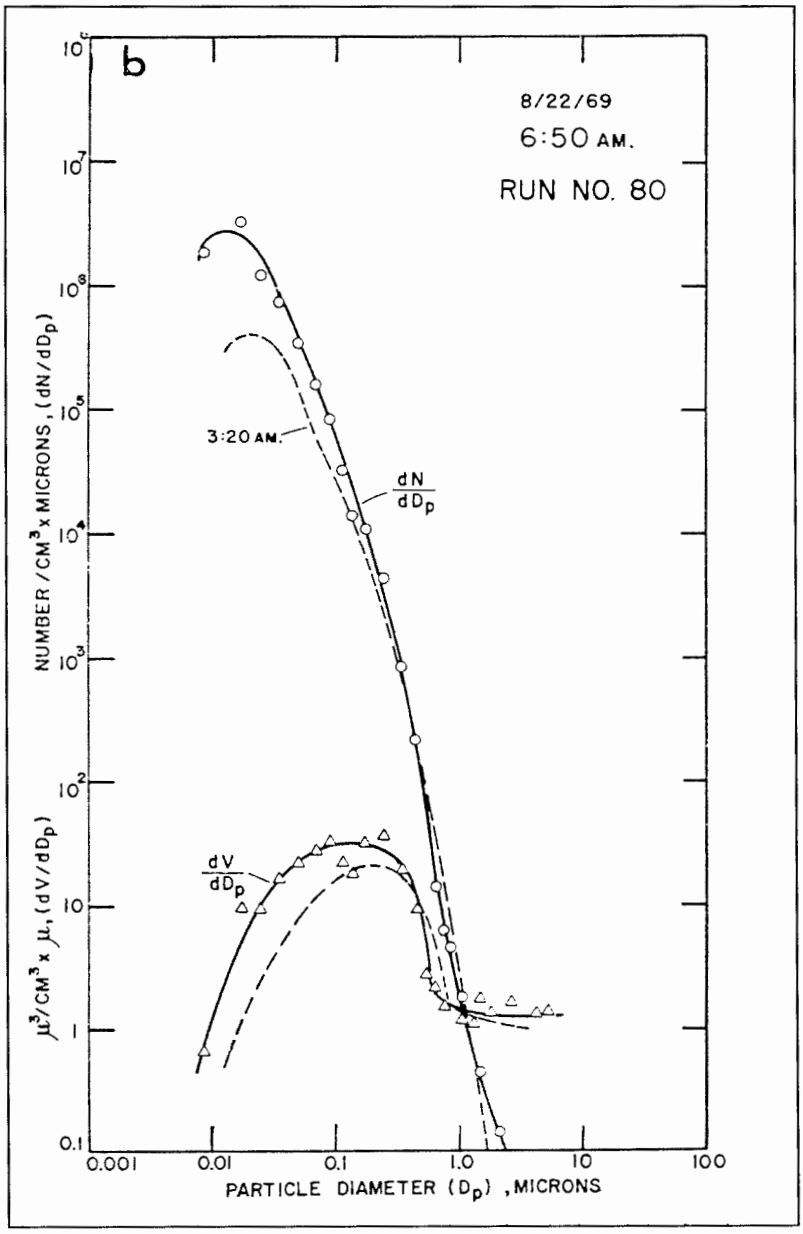

Figure 4-8: Plots of aerosol size number density and volume distributions (Whitby et al., 1972). It was these types of plots that lead to the decomposing aerosols into size ranges.

It was widely known in small particle physics that particles produced by a single mechanism such as erosion or communition (grinding) often follow a lognormal distribution. This fact was known by Hatch and Choate, Krumbein, Epstein and others (see Chapter 2). At about the same time that Whitby was evaluating his Los Angeles smog data, researchers were making the connection that aerosols were produced

from specific mechanisms. In 1975, Kelkar and Joshi (1977), based on the work done by Heisler et al. (1973) suggested that three principal mechanisms produced the aerosol size distributions obtained by Whitby and so they used three lognormal functions to describe Whitby's data. These three mechanisms are: 1) Gas-particle conversion (produces ultrafine particles in the range 1 nm – 0.1 μm); 2) Condensation of vapors onto existing particles (produces fine particles in the range 0.5 μm – 2.5 μm), and 3) Disruption of bulk

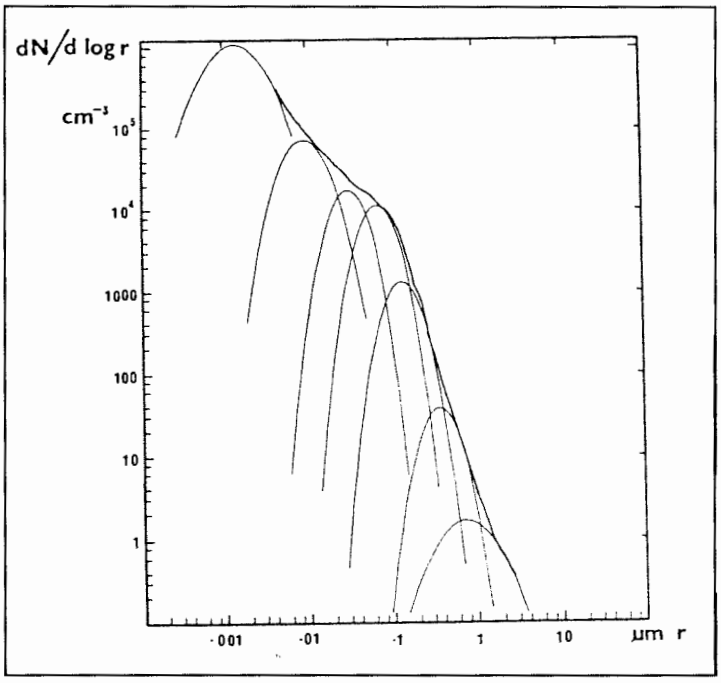

Figure 4-9: Davies' use of seven lognormal components to fit to Whitby's Los Angeles data (Davies, 1974).

material and resuspension of the settled particles (produces coarse particles in the range 2.5 μm – 25 μm). The trimodal lognormal size number distribution is formally expressed as

$$\frac{dN}{d\log r} = \sum_{i=1}^{3} \frac{N_{T_i}}{\sqrt{2\pi}\cdot\log(\sigma_{g_i})} \exp\left(-\frac{1}{2\log^2(\sigma_{g_i})}\left(\log\left(\frac{r}{\mathbf{r}_{\text{median}_i}}\right)\right)^2\right) \tag{4-21}$$

For the i[th] mode, the principal reported parameters are the total number concentration, N_{T_i} (#/cm^3), the median radius[†], $\mathbf{r}_{\text{median}\,i}$ (μm) and the geometric standard deviation, $\sigma_{g\,i}$ (unitless). The trimodal lognormal model of aerosol size number density distributions is the most widely accepted model of lower tropospheric

[†] Also known as the geometric mean radius.

aerosols not only because it fits the observed data well under most circumstances, but also because the lognormal function is tied to physical mechanisms.

There is often much discussion between using the base 10 log and the natural log, ln, for lognormal functions. We have rigorously related the statistical parameters for both lognormal functions based on base 10 and on base *e* in Chapter 2 and Appendix A. We briefly summarize the results here. Using the conversion,

$$\log(x) = \frac{\ln(x)}{\ln(10)} = \frac{\ln(x)}{2.303} \tag{4-22}$$

we can express Eqn. 4.21 using the natural log, ln, as,

$$\frac{dN}{d\log r} = \sum_{i=1}^{3} \frac{N_{T_i}}{\sqrt{2\pi}\cdot 2.303\cdot \ln(\sigma_{g_i})} \exp\left(-\frac{1}{2\ln^2(\sigma_{g_i})}\left(\ln\left(r/r_{median_i}\right)\right)^2\right)$$

$$2.303\cdot\frac{dN}{d\log r} = \sum_{i=1}^{3} \frac{N_{T_i}}{\sqrt{2\pi}\cdot \ln(\sigma_{g_i})} \exp\left(-\frac{1}{2\ln^2(\sigma_{g_i})}\left(\ln\left(r/r_{median_i}\right)\right)^2\right)$$

and so we have

$$\frac{dN}{d\ln r} = \sum_{i=1}^{3} \frac{N_{T_i}}{\sqrt{2\pi}\cdot \ln(\sigma_{g_i})} \exp\left(-\frac{1}{2\ln^2(\sigma_{g_i})}\left(\ln\left(r/r_{median_i}\right)\right)^2\right). \tag{4-23}$$

From this simple conversion, we have the relation

$$\frac{dN}{d\log r} = 2.303\frac{dN}{d\ln r} \tag{4-24}$$

and we see that the statistical parameters do not change, only the number density concentrations need to be converted between the different mathematics. To show this, one need only pick the same parameters and use them in Eqns. 4-21 and 4-24.

4.2.2.2 Aerosol Modes

As discussed in the previous section, no one mathematical function can be, nor should be, made to fit the entire particle size spectrum from 1 nm to around 35 μm. However, one of the significant achievements in particle and aerosol science has been the understanding that the total aerosol size distribution range is

actually the cumulative result of several particle-generating mechanisms. Each mechanism shows a propensity for being described by lognormal functions and covers roughly 1 to 2 decades. Thus, from 1 nm to 100 μm (5 decades), there are typically 3 aerosol-generating mechanisms, or aerosol modes and a trimodal lognormal aerosol size density distribution, given by Eqn. 4-21 or Eqn. 4-23, is generally used to describe the particles within this size range. Each mode requires three parameters for complete characterization: median radius, r_g, geometric standard deviation, σ_g, and the total number density, N_T. Thus, for three modes, a total of nine modal parameters are needed.

Figure 4-10 shows a typical aerosol mass distribution found in the lower troposphere (Watson and Chow, 1999). We will explain the presence of the two submodes in the accumulation mode shortly. We notice that the three major modes (the ultrafine, the accumulation and the coarse) each cover roughly 1 – 2 decades. Further, while the fine mode dominates the other two major modes in terms of number density, the second and third modes contain the most mass. As we have indicated in Chapter 3, it is the accumulation mode that is most efficient in terms of optical scattering. The coarse mode can be a significant source of error in optical scattering studies as this mode typically contains non-spherical particles and can vary much more than the other two modes from one instant to the next.

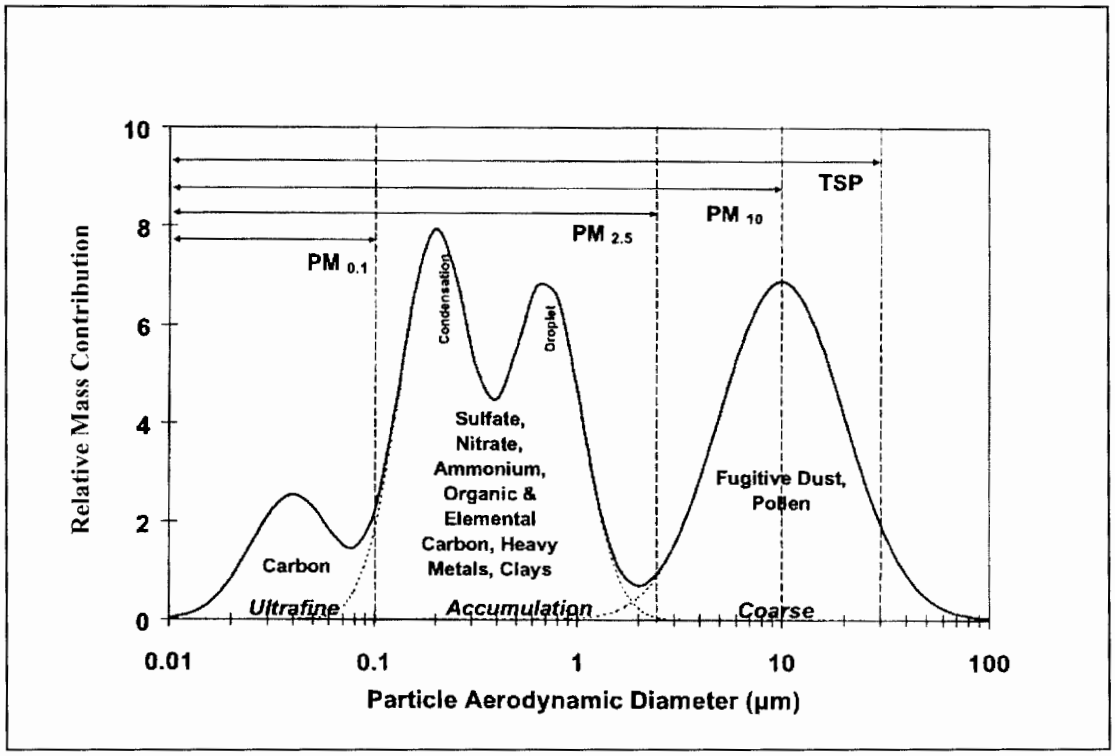

Figure 4-10: Aerosol modes in the lower troposphere (adapted from Watson and Chow, 1999).

The definition between the modes is most pronounced as the aerosols age, i.e., the inflection, which denotes the separation between aerosol modes is most pronounced for aerosols with long residence times and least pronounced with aerosols of recent origin (p. 608, Leaitch and Isaac, 1991).

The major geographic regions on the earth, such as the polar ice caps, deserts and maritime environments, have been examined for their aerosol composition and distribution. Jaenicke gives a nice summary of the aerosol modal parameters for each region (Hobbs, 1993), which was also summarized in Seinfeld and Pandis (1998). Stevens also included the table found in Hobbs in his thesis (Stevens, 1996, p. 81). However, given the large spatial and temporal variability of aerosol size density distributions, making use of such representative modal parameters is difficult even to serve as a guide. Although it is certainly important to understand what a particular environment's representative modal parameters are, it is also important to understand any additional nearby factors that may influence their departure from representative values.

We would like to take a slightly different approach and instead of examining aerosols with respect to a particular location, we will examine each mode individually, with emphasis on urban aerosols. This section delves deeper into each mode itself so that the reader will have a better feel for the type of modal parameters that are found and what we should expect in the environment in which we are operating. For additional information on aerosols of different geographic regions, see Hobbs, 1993, pp. 12 – 26 and Seinfeld and Pandis, 1998, pp. 429 – 446.

4.2.2.2.1 Mode #1: Ultra Fine Mode/Aitken Mode (1 nm – 0.1 μm)

By far, the most numerous particles (not molecules) in an urban environment are the number of particles contained in the ultrafine mode. In most regions of the Earth, the number density of this first mode is at least equal to but is often several orders in magnitude greater than either the 2nd or 3rd major aerosol modes. The size range given here is with respect to size density distributions but may change if one wishes to examine surface area or volume distributions using the transformations given in Chapter 2. For this work, all sizes are with respect to the number density distribution.

The sources of the ultrafine aerosols are varied, especially in an urban environment. Combustion processes from automobiles and heavy industry contribute significantly to the population of the ultrafine mode. This is important to keep in mind since locations within a city may give drastically different aerosol size density parameters depending on what local influences may be present. The ultrafine particles also result from chemical reactions.

Although the ultrafine mode generally contains the most particles, it frequently contains nearly negligible mass (volume) and very little surface area and so it takes many particles in this mode to affect the optical scattering intensity. Typically, the ultrafine particles will grow and enter the 2nd aerosol modal region by coagulation or condensation. In this study, we are not interested in a temporal evolution of the aerosols but rather in their spatial distribution. We are taking snapshots of the atmosphere and not making movies.

The chemical composition of the ultrafine varies but is typically predominately sulfate $\left(SO_4^{-2}\right)$, nitrate $\left(NO_3^{-1}\right)$, ammonium $\left(NH_4^{+1}\right)$, and organic and elemental carbon. Many of these compounds eventually end up in the accumulation mode.

4.2.2.2.2 Mode #2: Fine Mode/Accumulation Mode (0.1 μm – 2.5 μm)

In general, the fine/accumulation aerosol mode has fewer particles than the ultrafine mode but has the most surface area of the three major aerosol modes. It is this 2nd aerosol mode that is arguably the most important mode in scattering experiments. There are several reasons for such an argument.

First, the removal of the 2nd mode's particles form the atmosphere is inefficient with respect to the 3rd mode and so the aerosols in this mode typically have large residence times. A large residence time allows these aerosols to reach greater altitudes (and be transported over longer distances) and so this mode is the major component of what is termed the background aerosol (Hobbs, p. 13 and p. 25; Seinfeld and Pandis, p. 436). The background aerosol is found in the free troposphere, above the clouds, and so is also referred to as the free tropospheric aerosol (Leaitch and Isaac, 1991).

Second, although the 1st aerosol mode has the most number of particles, the 2nd aerosol mode has the most surface area (see Chapter 2) and is thus the most influential with respect to optical scattering and propagation studies of the atmosphere, becoming quite important in describing global energy budget and regional haze issues.

Finally, there is increasing concern about the health effects associated with inhalation of particles in the fine mode region as human respiratory and circulatory systems cannot adequately filter out such small particles. Understanding the particles in this size range, both in terms of their constituents and their dynamics, have become increasingly important in environmental and biological studies (Magari et al., 2001; Peters et al., 2001).

As indicated in Figure 4-10, however, there seems to be two submodes within the accumulation mode. Investigations of this region have confirmed the existence of these two submodes and labeled them the condensation mode (median diameter ~ 0.2 μm) and the droplet mode (median diameter ~ 0.7 μm). If we count the condensation and droplet modes as two separate modes, then we actually have a quadramodal lognormal aerosol distribution. Stevens neglected using four aerosol modes by simply stating that he was not using four modes in his model because of the complexity of inverting a data set with a total of 12 (nearly) independent parameters. We would like to inform the reader with a little bit more information on these two submodes.

Both submodes have been found in urban, rural and maritime environments (Seinfeld and Pandis, p. 821). The important point, however, is under what *conditions* these sub modes have been found. Initially, these two submodes were first discovered by Hering and Friedlander from their examination of the sulfate-laden aerosol in the Los Angles basin (Hering and Friedlander, 1982). Interestingly, their measurements showed that 90% of the time, only one submode was present and the majority of this was the droplet mode. Hering and Friedlander went on to attribute sulfate-generating mechanisms to these submodes and showed that the modes appeared to be independent of each other (Table 2, p. 2655, Hering and Friedlander). Thus, there were two separate sulfate-generating mechanisms, each responsible for a submode. Their calculations indicated that the condensation mode formed from gas-phase reactions while the droplet mode formed from aerosol phase reactions (Hering and Friedlander, p. 2655). Thus, episodes of low relative humidity allow

the gas phase reactions to dominate and so the condensation submode is formed. During episodes of high relative humidity, aerosol phase reactions dominate giving rise to the droplet mode. These findings were later confirmed by John et al., and Meng and Seinfeld (Seinfeld and Pandis, p. 821). Thus, to avoid having to model four separate aerosol modes, we will want to be operating under conditions of extreme relative humidity but away from clouds, which is precisely where we want to operate anyway. We can now justify why Stevens could use three lognormal aerosol modes in his model and exclude a fourth: Stevens was operating in a warm humid marine environment (he reported relative humidities about 90%) and thus we expect to have only the droplet mode present. We also will use only three lognormal modes in this thesis.

4.2.2.2.3 Mode #3: Coarse Mode (5 μm – 25 μm)

The coarse mode is typically very different in composition, number density and origin than both the ultrafine and fine modes. In aerosol studies, it is often found that when one speaks of aerosols, all particles with diameters greater than about 2.5 μm are classified as coarse particles while particles with diameters less than 2.5 μm are collectively classified as fine particles.

The primary reason for the differences between the 3rd mode and the others is the generating mechanism behind their production. In general, the mechanism is primarily mechanical in nature such as erosion, mining, soil tilling, and resuspension through impact. Although the least plentiful in number, the coarse mode is responsible for the majority of mass (volume) of aerosol in the atmosphere and significantly contribute to the degradation of visibility. However, due to their larger size, coarse mode particles generally fall out rapidly from the atmosphere.

The chemical composition of the coarse mode is largely that of crustal elements, minerals and salts but it also includes pollen and mode spores. The part of the coarse mode that is anthropogenic (man-made) is referred to as fugitive dust and often result from the use of heavy industrial or agricultural processes.

One of the major concerns with the coarse mode is that the particles that make up its population are generally nonspherical in nature and so pose a problem for using Mie theory to describe the scattering processes. Further, many of these particles are insoluble in water and thus even in conditions of high relatively humidity will remain dry. Fortunately, the coarse mode particles do not stay in the atmosphere very long nor do they reach very high altitudes. Only particles less than about 10 μm can stay aloft long enough to transport over long distances such as been found with Saharan desert dust depositing in Florida (p. 440, Seinfeld and Pandis, 1998; Watson and Chow, 2000).

The sources of coarse mode particles are highly variable. For example, the wind itself may kick up large amounts of coarse mode particles (p. 434 and 438, Seinfeld and Pandis, 1998; Watson and Chow, 2000). It is wise to take measurements in a stable environment with low wind speeds.

While we have implied that the ultrafine and fine aerosol modes stay relatively independent of the coarse mode, this is not a steadfast rule, as fog and clouds typically grow from very small particles. As with just about everything in the atmosphere, there are exceptions to every rule.

4.2.3 Aerosol Profiles

There is surprisingly little information on the variation of aerosols (number density, mass and composition) with altitude. Recently, however, there has been increasing interest in aerosol profiles and calls have been made for intensive investigations (Watson and Chow, 2000; p. 17, Hobbs, 1993). The principal reason for the lack of aerosol profile information is very simple: It is both expensive and difficult to acquire information on aerosols through the use of aircraft or balloons. By using remote sensing, it is intended that this study begin to help to uncover the vertical profile of aerosols for the first kilometer of the atmosphere (where most of the aerosols are located).

As anticipated from the exponential decrease of pressure with altitude (Eqn. 4-9), the aerosol mass and number concentrations also exhibit an exponential decrease with altitude. Based on aerosol data from various regions, Jaenicke (Hobbs, 1993) suggested that the aerosol mass ($\mu g/m^3$) profile varies as

$$M(z) = M(0)\exp\left(-\frac{z}{H_m}\right), \tag{4-25}$$

where *M(0)* is the ground level mass concentration and H_m is the mass scale height (eqn. 7.59, p. 444, Seinfeld and Pandis, 1998; eqn. 6, p. 20, Hobbs, 1993). From the data, Jaenicke estimated that $H_m \sim 730$ m for remote continental aerosols while he estimated that $H_m \sim 2000$ m for desert aerosols owing to increased atmospheric convection in these regions. Jaenicke gave no information on urban or rural aerosol mass density profiles.

For the number density ($\#/cm^3$) profile, Jaenicke suggested a slightly more complicated expression as (eqn. 7.60, p. 444, Seinfeld and Pandis; eqn. 5, p. 20, Hobbs)

$$N(z) = N(0)\left[\left(\frac{N_B}{N(0)}\right)^{H_m/|H_m|} + \exp\left(\frac{-z}{|H_m|}\right)\right]^{H_m/|H_m|}, \tag{4-26}$$

where $N(0)$ is the ground level number concentration, N_B is the background aerosol concentration aloft (*i.e.*, in the free troposphere) and H_m is the number concentration scale height. To account for instances where the aerosol number density may increase with altitude, H_m can be negative. Such conditions have been found over the ocean and remote continental sites. Again, Jaenicke provided no information on urban or rural number density profiles.

It is important to restate that these expressions and numbers are estimates based on average conditions as well as sparse profile data. However, in clouds or during atmospheric instability (storms), significant changes in the profiles can and do occur. Thus, we should not use Eqns. 4-25 or 4-26 since it is intended that this work produce representative profiles during our inversion process (see Chapter 6). However, as

with every aspect of optical scattering by small atmospheric particles, one needs to be aware of the environment in which the measurements are being conducted.

4.2.4 Aerosol Dynamics

Aerosols are affected by a myriad of environmental and atmospheric conditions and so it should come as no surprise that aerosols seldom remain in the same state in the same location at the same time for very long. However, despite the seeming randomness of aerosol sizes, concentrations, production mechanisms, and composition, aerosols are predictable with respect to one universal condition: All physical systems tend toward the least energetic state[†]. In other words, chemical potential energy governs the dynamics of aerosols. To understand why a particular species wants to be in a gaseous state, an aqueous state, or a solid state requires the application of thermodynamic principles (Chapter 9, Seinfeld and Pandis). However, an in-depth examination of such principles is not warranted for this work. We simply wish to convey to the reader an idea of how aerosols form and evolve in the atmosphere and that idea is based on free energy. Although we do not use thermodynamic principles directly in our analysis, having knowledge of the dynamics of aerosols and aerosol populations can prevent one from over-reaching conclusions from optical scattering measurements.

The major processes between the three states of matter are illustrated in Figure 4-11. Of all the processes, it is the processes of condensation/deliquescence and freezing/crystallization that are of major

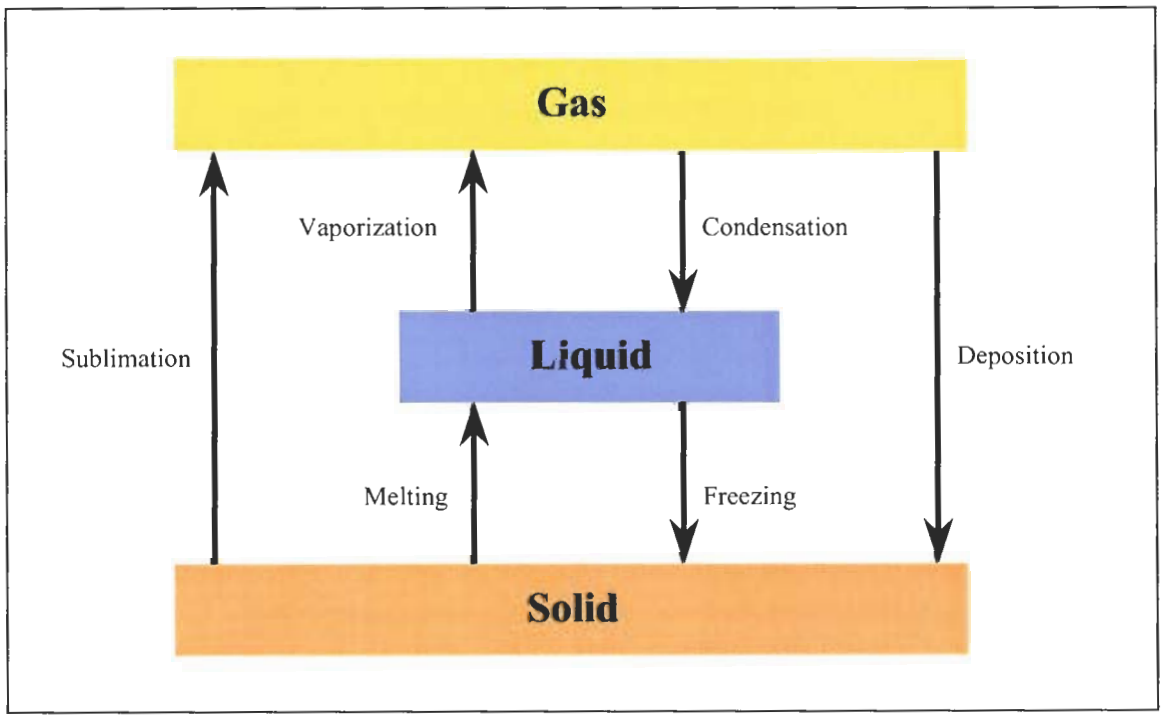

Figure 4-11: Transition processes of matter (adapted from figure 11.4, p. 343, Brown and Lemay)

[†] Entropy, which indicates randomness, and energy have different units. The least energetic state is not necessarily also the most entropic (e.g., solids vs gases).

consequence to the formation of the second aerosol mode. It is the second aerosol mode that changes the most dynamically with respect to temperature, pressure and atmospheric water content (relative humidity). Since water is the most important solvent in the atmosphere, our attention is focused on the properties of aqueous solutions. As it turns out, sulfates, nitrates and various other salts can exist in both the gaseous and aqueous states and these species generally end up in the second aerosol mode via growth by condensation/deliquescence and subsequent (re-) crystallization.

Water plays an important role in the atmosphere out of proportion to its presence (Seinfeld and Pandis, 1999). Although the processes of condensation and deliquescence are similar in that they both represent a particle's ability to acquire water, deliquescence differs in that it represents a transition from the solid state to the liquid state whereas condensation represents the phase transition from the gas state to the liquid state. Additionally, deliquescence is a function of particle properties, relative humidity and temperature (eqn. 9.72, p. 511, Seinfeld and Pandis, 1998). These processes are directly responsible for the growth and evolution of many nitrate and sulfate aerosols into the second aerosol mode and thus impact optical scattering studies. We will see that high relative humidity is our friend in this work and is our ally. Why? Because a high relative humidity means that there is large water content and that the water droplets that form are going to be spherical due to surface tension of water. Spherical or near-spherical particles are required in order for us to reasonably apply Mie scattering theory. Further, the more water, the more dilute is the solution and in effect, the solution appears to be homogeneous, even with more than one salt component. Thus, this 'effective' solution approaches a known 'effective' index of refraction[†] (a good source for optical coefficients is the five-volume set edited by Palick). Having a particle that is homogeneous is the other major requirement of Mie theory. Thus high relative humidity not only increases the scattering efficiency of light (because the particles are growing into the optically efficient region of the 2nd aerosol mode), but also gives Mie theory a much firmer footing to yield good results than in a dry and or dusty region. The results of Stevens have confirmed these conditions.

4.2.4.1.1 Deliquescence

Deliquescence is the ability of a solid particle to take on sufficient water to become liquid. In many cases, electrolytes and salts exhibit deliquescent behavior. The defining characteristic of deliquescent particles is that they only begin to take on large amounts of water above certain relative humidities, generally above 70%. As the relative humidity in the atmosphere begins to rise, solid particles in the atmosphere need additional energy to stay solid and not enter an aqueous state. Since thermodynamic principles require that species be in their lowest energy state, such species find that it is easier to become liquid and thus the particle absorbs water to form a saturated electrolytic (salt) solution. For such species there is a marked relative humidity transition, where a significant increase in the particle's mass occurs.

[†] We have already cautioned the reader on using effective indices of refraction (see Chapter 3).

This relative humidity is termed the deliquescence relative humidity (DRH) and marks the particles' transition between the solid state and the liquid state.

Some species do not exhibit deliquescent behavior but nonetheless absorb water hygroscopically. Hygroscopic species do not show a marked mass increase at a given relative humidity but rather acquire water continuously and smoothly as relative humidity increases.

Interestingly, as the relative humidity decreases below the DRH, the solution does not immediately give up its water content and re-crystallize (Tang and Munkelwitz, 1994). Again, due to energy concerns, as the relative humidity drops substantially below the DRH point, water evaporates thereby leaving an increasingly saturated solution (p. 508, Seinfeld and Pandis, 1998). At critical supersaturation, crystallization finally takes place, forming a solid particle. Thus, deliquescent particles have a relative humidity hysteresis. From Figure 4-12, we see that ammonium sulfate ($(NH_4)_2SO_4$)has a DRH at 80% and reforms at a RH of about 40% while sulfuric acid (H_2SO_4) exhibits hygroscopic behavior. The reader is reminded that DRH is a function of temperature so perhaps dew point is a better descriptor.

The effects of relative humidity have been observed in optical scattering and extinction studies. Stevens attributed the good degree of fit between his model and his experimental data to the effects of particle growth due to relative humidity (figures 5-14 through 5-18, Stevens, 1998). Additionally, backscatter measurements taken during episodes of relative humidity transitions show a marked increase in extinction due to particle growth.

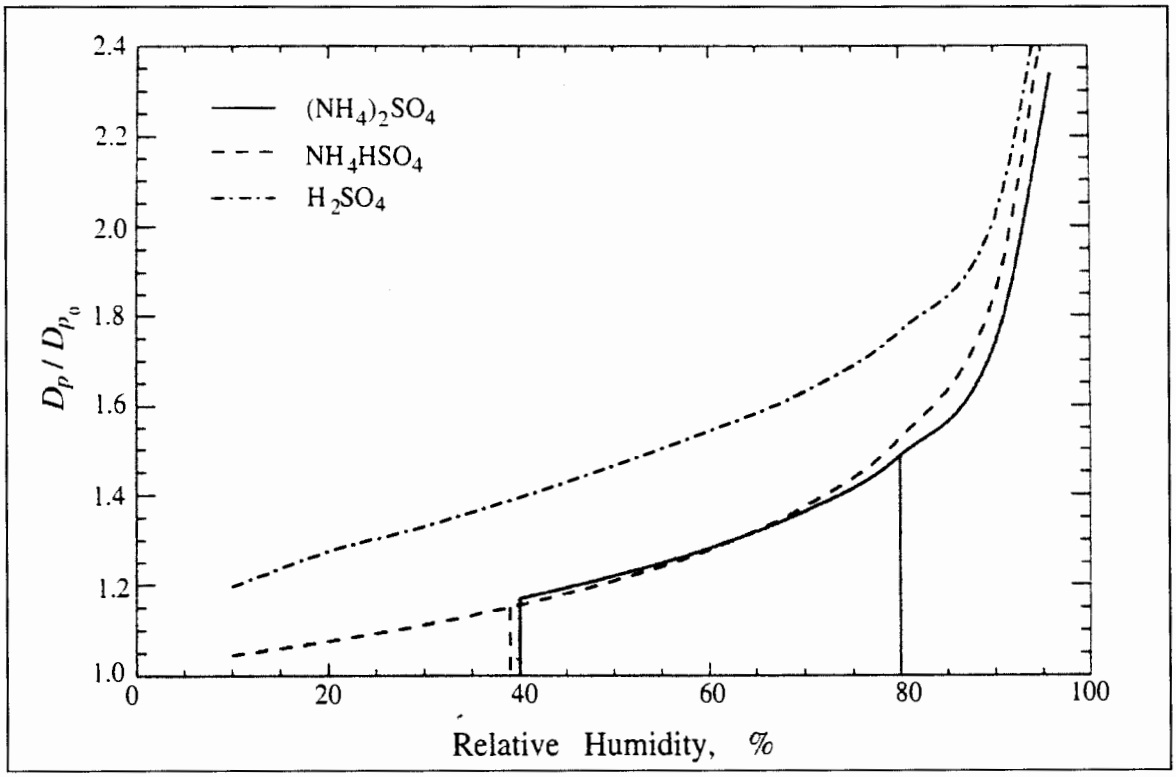

Figure 4-12: Example of diameter change on several species for a given relative humidity (figure 9.4, p. 507, Seinfeld and Pandis, 1998).

4.2.4.1.2 Deliquescent Behavior of Multicomponent Solutions

Because of the diversity of species in the atmosphere, seldom does one find only one salt or one deliquescent species. More often, several aerosol components are found, each with its own DRH point. Table 4-2 lists the DRH of several salt compounds. Studies have been done (Tang and Munkelwitz, 1994)

Table 4-2: DRH points of several salt compounds (adapted from Seinfeld and Pandis, table 9.4).

Compound 1	DRH_1 (%)	Compound 2	DRH_2 (%)	Overall DRH
NH_4NO_3	59.4	$NaNO_3$	72.4	46.3
$NaNO_3$	72.4	NH_4Cl	77.2	51.9
NH_4NO_3	59.4	$(NH_4)_2SO_4$	79.2	52.3
NaCl	75.2	NH_4Cl	77.2	68.8
NH_4Cl	77.2	$(NH_4)_2SO_4$	79.2	71.3

regarding the effect of multicomponent solutions and have showed that such solutions exhibit behavior similar to single component solutions. A multicomponent solid particle always has a lower DRH than the individual components (Seinfeld and Pandis, p. 516). An example of the effect of a multicomponent solution is shown in Figure 4-13. Here, the mixed solution is composed of potassium chloride (KCl) and sodium chloride (NaCl). Using Table 4-2 and Figure 4-13, we see that deliquescence begins below the DRH for both salts but the overall deliquescent behavior of the mixed solution shows transition points as marked.

These transition points are an indication of the salt that is being deliquesced and can act as identifiers of the particular salt. This may even allow optical scattering programs to identify a particular aerosol species. As the relative humidity begins to drop, again we see step transitions as KCl first begins to re-crystallize (at about 65% RH) and then NaCl (at about 62% RH) (p. 519, Seinfeld and Pandis, 1998) and thus offers the possibility of using optical scattering to identify chemical species. However, not all salts can be identified through re-crystallization as their crystallization RH ranges between 10% and 40% thus indicating that they cannot be dried in the atmosphere (the atmosphere's RH in many regions never gets that low) (p. 519, Seinfeld and Pandis, 1998). Thus, one cannot simply determine the salt content based on a direct RH measurement but, because of the hysteresis, one has to know the history of the salt.

4.2.4.2 Condensation

Condensation refers to the process by which a vapor becomes a liquid or a solid. Although technically a gas-to-particle conversion process (see Section 4.2.4.5), condensation does not include nucleation in its

definition. When gases dissolve in liquids, condensation is not the process responsible for particle growth. Further, condensation is also not a coagulation process, as coagulation is defined differently[‡] (see Section

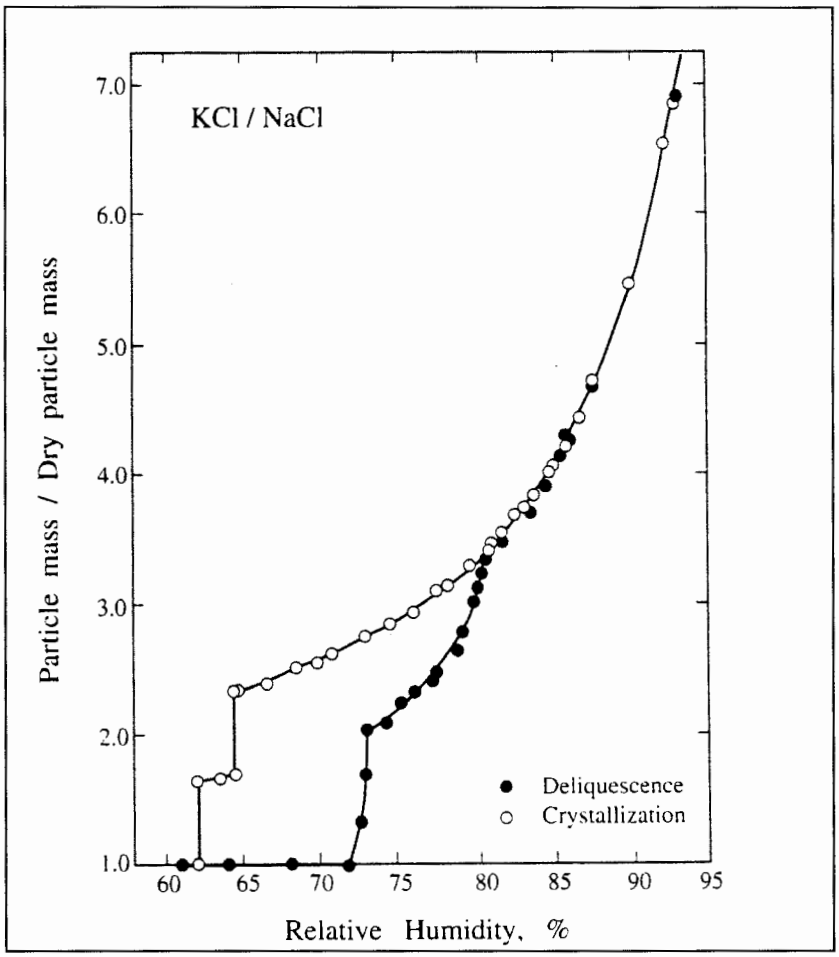

Figure 4-13: Example of hysteresis in the hygroscopic growth and evaporation of a mixed-salt particle (figure 9.7, p. 515, Seinfeld and Pandis, 1998).

4.2.4.3). Our description follows Chapter 12 of Seinfeld and Pandis (1998).

To understand the effects of particle growth solely due to condensation, we assume that there are no particle sources or sinks and so the total particle number is preserved. However, the volume, mass and particle diameter will change over time. With respect to particle diameter, the basic equation governing particle growth due to condensation is (eqn. 12.10, p. 651, Seinfeld and Pandis, 1998)

$$\frac{\partial n_D(D_p,t)}{\partial t}+\frac{\partial}{\partial D_p}\left[I_D(D_p,t)\,n_D(D_p,t)\right]=0\,, \tag{4-27}$$

where n_D is the number density size distribution with respect to particle diameter, D_p, and I_D is

[‡] Science and technology are not difficult to understand. It is the terminology that is the challenge.

$$I_D(D_p,t) = \frac{dD_p}{dt},$$

which represents the rate of diameter change. When I_D is positive, condensation is occurring and when I_D is negative, evaporation is taking place. To a first order approximation, I_D takes the form (eqn. 12.13, p. 652, Seinfeld and Pandis, 1998)

$$I_D(D_p,t) = \frac{A}{D_p},$$

where A is a constant. Thus smaller particles grow faster than larger particles as illustrated in Figure 4-14.

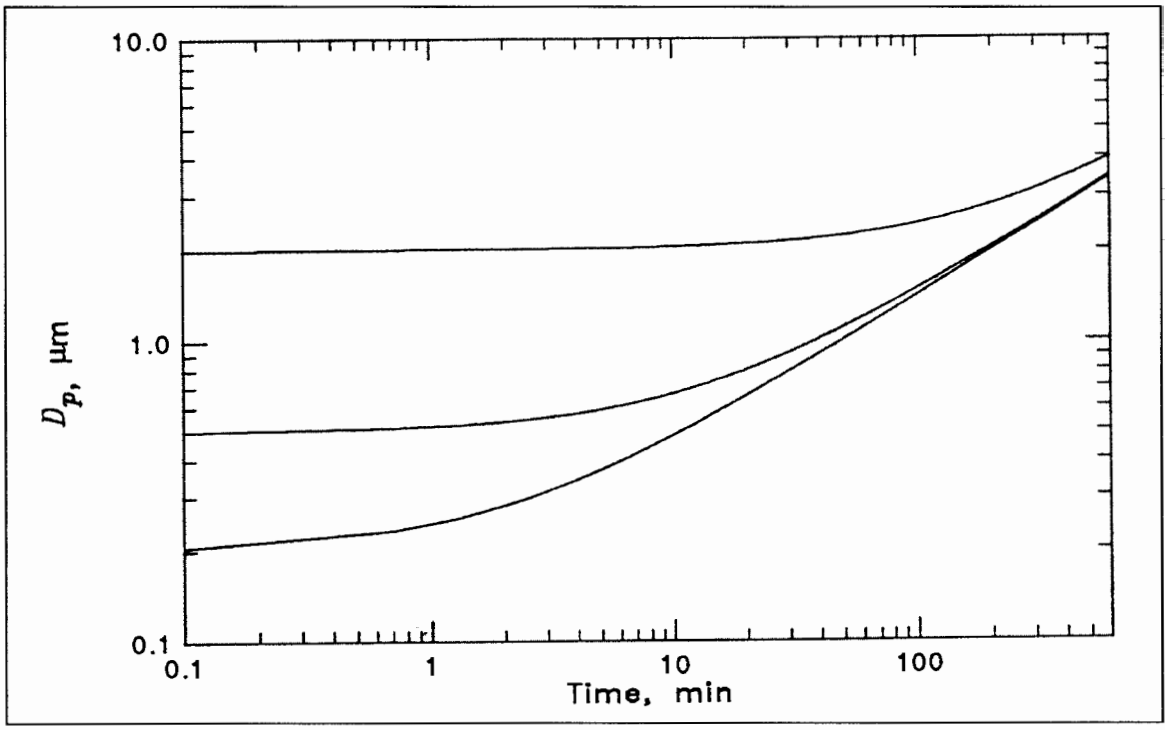

Figure 4-14: Illustration of particle growth during condensation (figure 12.2, p. 653, Seinfeld and Pandis, 1998).

We can modify the lognormal aerosol distributions of Chapter 2 to show the evolution of the aerosol distribution under the influence of condensation. Seinfeld and Pandis solve the condensation equation (Eqn. 4-27) and incorporate the solution into the lognormal distribution as (eqn.12.27, p. 654, Seinfeld and Pandis, 1998)

$$n_D(D_p,t)=\frac{dN}{dD_p}=\frac{D_p}{\left(D_p^2-2At\right)^{1/2}}\frac{N_T}{\sqrt{2\pi}\cdot\log(\sigma_g)}\exp\left(-\frac{1}{2\log^2(\sigma_g)}\log^2\left[\frac{\left(D_p^2-2At\right)^{1/2}}{D_{pg}}\right]\right). \quad (4\text{-}28)$$

The impact of condensation on the aerosol number density distribution is shown in Figure 4-15. As can be seen, the smaller particles grow faster than the larger particles resulting in a compression of the distribution. As $t \rightarrow \infty$, the aerosols approach a monodisperse distribution.

We now have a partial answer to what Stevens measured during a radiation fog event. In his curve fitting, the 3rd aerosol mode seems almost unnaturally thin, just about approaching the mathematical limit of $\sigma_g = 1$. With the preceding discussion of condensation in hand, we suggest that Stevens was observing particle growth by condensation. Again, this is a partial answer and may be incomplete because the temporal evolution of the measured data set was not directly corroborated with particle sizers (no particle sizers were employed during the Wallops measurement campaign). We also have to balance this interpretation with fog growth and nucleation so it is difficult to substantiate the results.

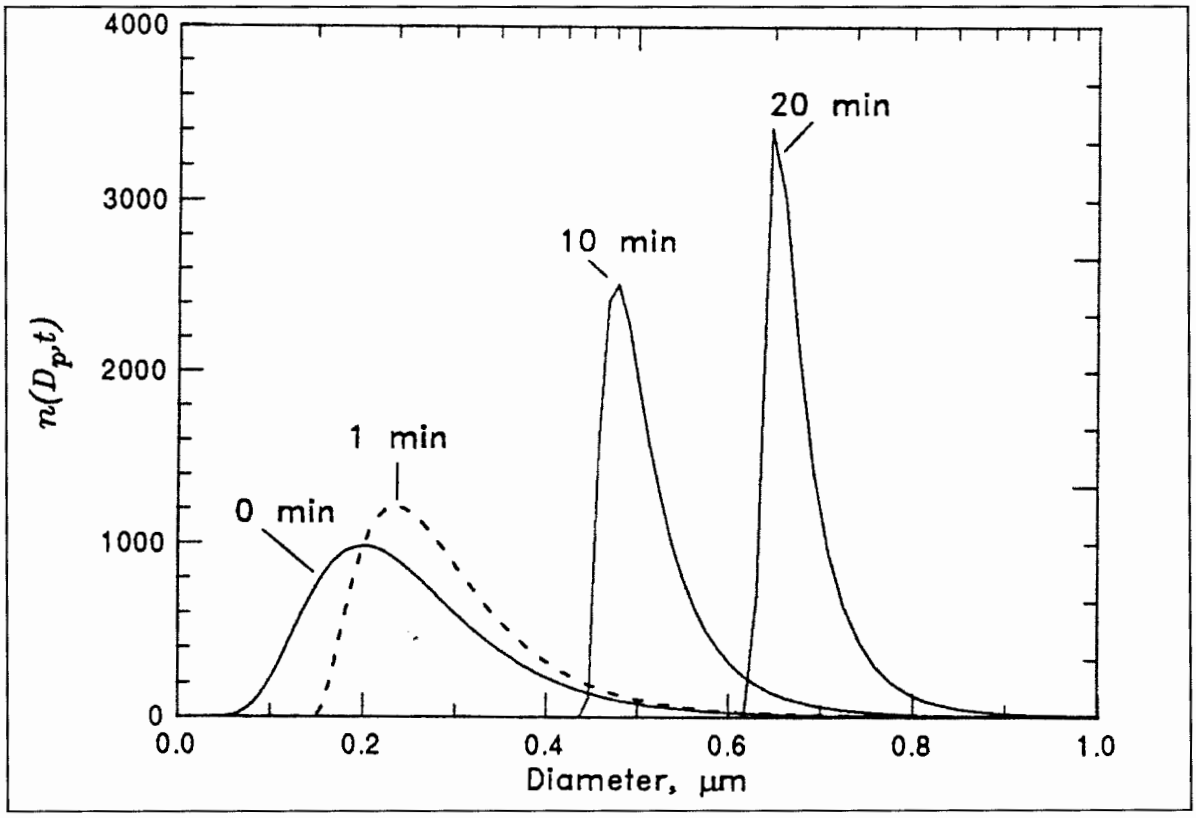

Figure 4-15: Illustration of a lognormal distribution growth under condensation (figure 12.3, p. 655, Seinfeld and Pandis, 1998).

4.2.4.3 Coagulation

Coagulation refers to the process by which two solid particles collide and stick to each other (adsorption). The overall effect of coagulation leads to a reduction in the total particle number while keeping the total volume fixed. Again, in keeping with the style of Seinfeld and Pandis, we take a simplified approach to the theory of coagulation and present trends and results. More detailed information can be found in Seinfeld and Pandis, pp. 656-680.

Particles coagulate due to a variety of influences such as interparticle forces, gravitational settling, turbulence, and Brownian motion. Of these, coagulation by Brownian motion generally dominates the submicrometer size region while coagulation by turbulence generally dominates the larger particles (Seinfeld and Pandis, p. 665). The influence due to gravitational settling is most pronounced in the scavenging of particles by rain, a situation we wish to avoid lest the equipment short circuit. A critical parameter describing coagulation rates is the coagulation coefficient, K (Seinfeld and Pandis, pp. 659–662). The coagulation coefficient increases in magnitude as the ratio between the diameters of the colliding particles increase, thereby increasing the coagulation rate. This intuitively makes sense since a slow-moving large particle provides a large target (cross-sectional area) for a fast moving smaller particle. Alternatively, two small particles would tend to miss each other (thus have low coagulation rates) because of their speed and small cross-sectional areas while two large particles will also have low coagulation rates due to their slow speed (they do not impact as frequently). This qualitative description of coagulation is admittedly somewhat oversimplified but it nonetheless gets across the idea of coagulation.

Unlike the condensation equation (Eqn. 4-27), the coagulation equation is somewhat more involved and will not be presented here (see section 12.3.6, p. 672, Seinfeld and Pandis for more information). However, extending our qualitative description of the coagulation process from the previous paragraph will be sufficient for our needs in illustrating the effect of coagulation on aerosol distributions. In a trimodal lognormal aerosol size density distribution, coagulation principally occurs as the 1^{st} and 2^{nd} modes collide with each other and with the 3^{rd} aerosol mode. Since the 3^{rd} mode has a substantial amount of mass (volume), the impact of the 1^{st} and 2^{nd} modes has little or no effect on the distribution of the 3^{rd} mode. In effect, the 1^{st} and 2^{nd} modes are removed (Seinfeld and Pandis, p. 679). Figure 4-16 illustrates the time scale and effect of the coagulation process.

4.2.4.4 Gas-To-Particle Conversion

The previous sections discussed particle growth and evolution due to relative humidity effects, condensation, coagulation and nucleation. These processes, however, can be more or less grouped under the heading of gas-to-particle conversion. For example, condensation involves the transfer of a vapor (gas) to the surface of a solid particle. Coagulation, although typically involving the collusion of two particles, can also be extended to include the impact of a solid (or liquid) particle by a gas. Thus, gas-to-particle conversion is a somewhat ubiquitous phrase and has rather broad meaning. However, its effects are very

specific and are typically revealed by an increase in some aspect (number, mass, volume) of the 1st and 2nd aerosol modes (Seinfeld and Pandis, p. 684).

The gas-to-particle production rates are controlled by three main mechanisms: 1) The rate of diffusion, 2) The rate of surface reaction, and 3) The rate of volume reaction. Each mechanism or combination of mechanisms can limit the particle production rates and may serve as identifiers of the chemistry in the atmosphere through an examination of aerosol distribution evolution (Seinfeld and Pandis, p. 684). It was these mechanisms that aided researchers in the development of the trimodal lognormal aerosol model.

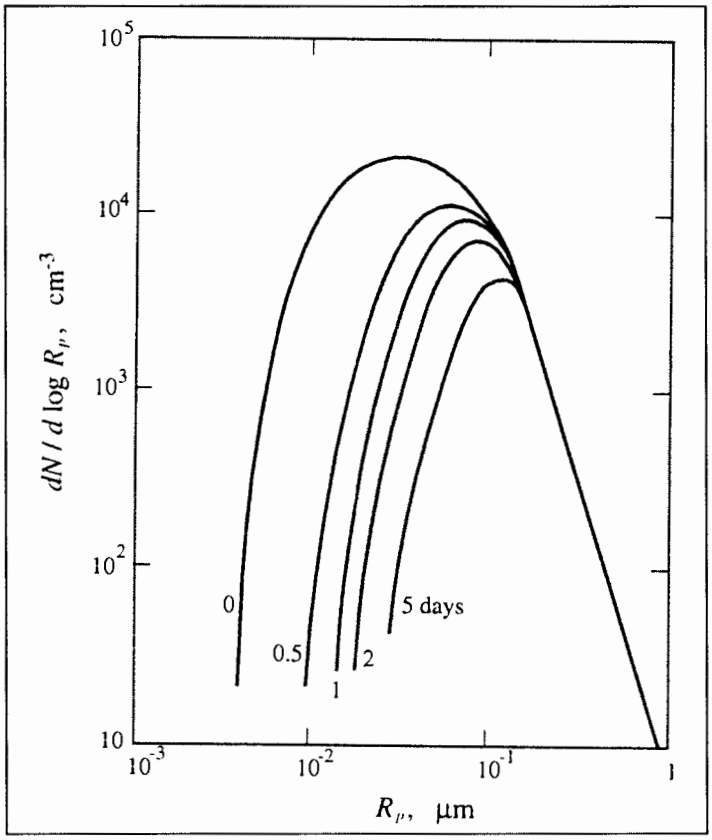

Figure 4-16: Particle size distribution undergoing coagulation over several days (figure 12.13, p. 680, Seinfeld and Pandis, 1998).

Particle growth by diffusion is very much like condensation/evaporation in that gases diffuse into or out of a solid particle resulting in a change in particle mass. The diffusional growth rate is proportional to D_p^2 for small particles but proportional to D_p for larger particles (eqn. 12.122, p. 686, Seinfeld and Pandis, 1998) and so diffusional growth is important for small particles. Particle growth by surface reaction makes no such distinction between particle sizes as all particles subject to this growth mechanism do so in proportion to their square diameters, D_p^2 (p. 689, Seinfeld and Pandis). Finally, particle growth by volume reaction is proportional to D_p^3 and so large particles are greatly affected by this mechanism (p. 689, Seinfeld and Pandis). Because most of the particles subject to gas-to-particle mechanisms are generally in

the 1st and 2nd aerosol modes, volume reactions show the most pronounced change in aerosol mass distributions while diffusion and surface reaction mechanisms are somewhat more difficult to distinguish from each other. (See Figure 4-17).

In our atmospheric model, we have included molecules (gases) and aerosols. As discussed in Chapter 3, the equivalent dielectric spheres that represent molecules are approximately 0.2 nm in radius while our aerosol size range begins at 1nm. From the standpoint of gas-to-particle conversion, there should be a transition between the two rather than a molecular spike followed by a vacuum. While we are not trying to circumvent physical reality, practical investigations showing explicit particle concentrations in this subnanometer region have not been found. Further, our investigation is on light scattering effects and not on gas/particle distributions (we are doing inferences, not direct measurements). As it turns out, the

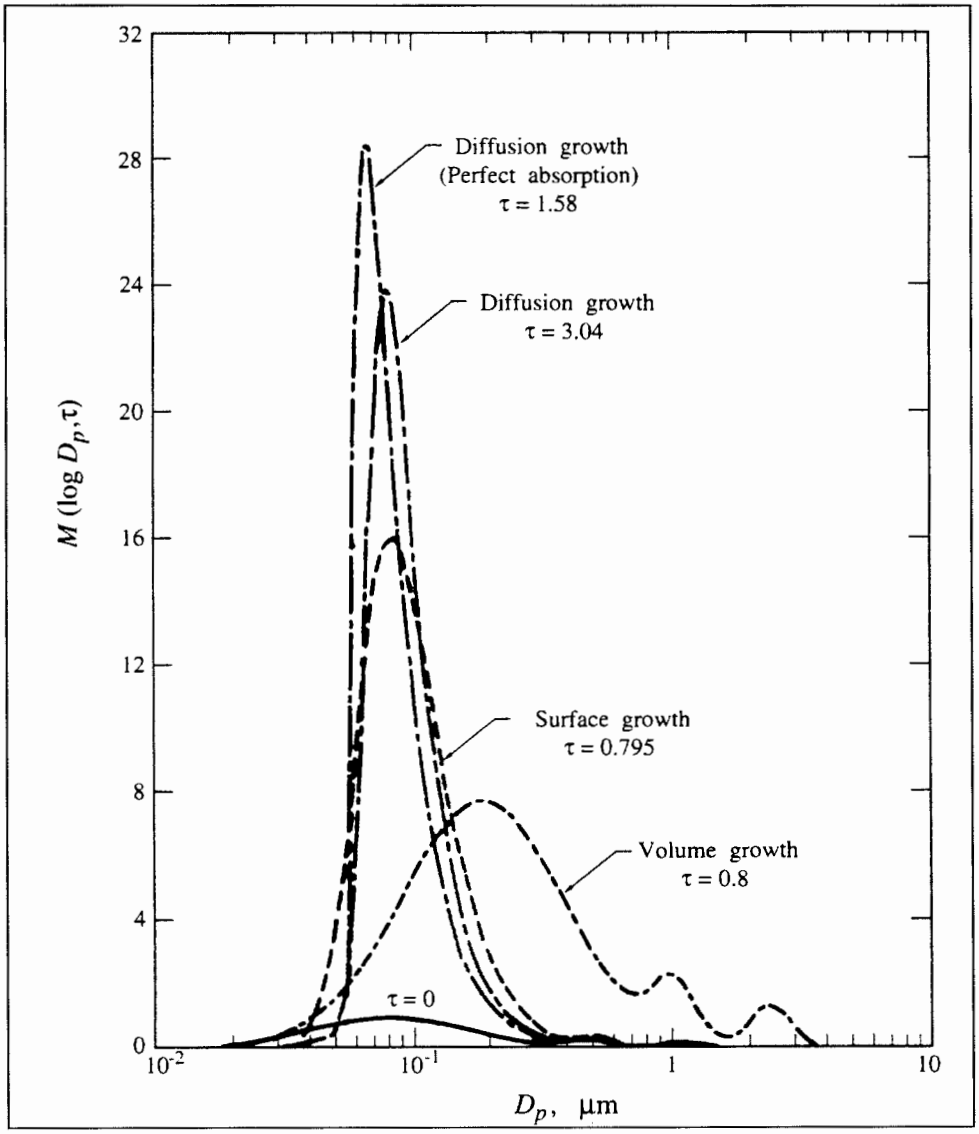

Figure 4-17: Aerosol mass distribution growth by gas-to-particle conversion (figure 12.16, p. 692, Seinfeld and Pandis, 1998).

scattering contribution from these extremely small particles is essentially negligible since scattering varies along the sixth power of the radius (i.e., r^6). In effect, while we are not being physically accurate, we are being pragmatic in our approach. The scattering model used in this thesis can and should be updated once better particle information is obtained.

4.2.4.5 Nucleation

Nucleation increases both the particle number and volume whereas condensation increases the volume but leaves the number fixed and coagulation decreases the number but leaves the volume fixed (table 12.6, p. 683, Seinfeld and Pandis, 1998). Stevens' results contained a particular episode where there was a very pronounced aerosol growth period (radiation fog). However, since we wish to avoid heavy fog and clouds in our endeavor (principally to avoid multi-scattering events and having the presence of a 4^{th} aerosol mode), we will not expand further on this subject. As we have been indicating to the reader throughout this chapter, Seinfeld and Pandis should be consulted for more information.

4.2.4.6 Mechanical Effects

Wind erosion, mining operations, automobile travel, heavy industry, etc. contribute large particles to the atmosphere. In the absence of a cataclysmic event to send the particles into upper regions of the atmosphere (major volcanic eruption, asteroid impact, desert wind storms), most of these larger sized particles remain local. For example, tire particles and brake pad linings from automobiles typically stay within a few meters of a roadway (Watson and Chow, 1999) but sand and dust sent high aloft into the atmosphere from the Sahara Desert has been found in the U.S. (Florida). Collectively, these man-made and non-local large particles are termed fugitive dust. Since these particles are non-spherical and generally contain a variety of minerals[†], Mie theory will not be as applicable to predicting observed scattering effects.

4.2.5 Aerosol Studies

Up to this point, the reader is hopefully getting a feel for just how diverse the aerosol content of the atmosphere is. It is precisely this diversity that makes studying the atmosphere rather challenging. Since the atmosphere is so difficult to understand, one study will not answer all question but there have been several good studies that have been made.

Because the atmosphere is so vast, it makes sense to segment the atmosphere into more manageable portions. This means that not only is a geographic region or locale important but an altitude region is also important. However, in the initial investigations, researchers (Junge and van de Hulst, 1950s) were not aware that the atmosphere contained such diversity. It was only through subsequent investigations that the diversity of the atmosphere became more understood. Thus, today's research has primarily concentrated into more specialized interests. This is seemingly the correct approach to take when confronted with such a

---

[†] We wish to avoid effective indices of refraction.

large problem. In any event, today's research into atmospheric particles is typically interested in total mass and volume concentrations rather than measuring the spectrum of number densities. These types of measurements (as outlined in Chapter 2) are not conducive to light scattering measurements. It is increasingly difficult to find good quality data that list lognormal parameters.

In the 1950s and 1960s, researchers were taking a lot of particle size density data. The problem with these data is not so much that it is dated (the atmosphere never stays the same) but some of the instruments of the time could only handle limited regions of the particle spectrum. However as time went on, instrumental limitations were overcome, allowing scientists to see a more complete picture. Attaching physical significance and backing it up with mathematical predictive models has been the main course of action ever since. The study that really set things into motion was by Whitby et al. in 1971. It was in this study that Whitby and his team recognized that the aerosols seemed to be better grouped in size-segmented areas. Although Whitby did not attach lognormal modes to his data, this was a significant realization. Researchers previously would use one curve or function to fit the entire size spectrum (the Junge power law). But Whitby was using instruments that provided larger coverage of the particle spectrum and he found significant changes in the curves that were not due to instrument malfunction. He concluded that there was some physical generating mechanism responsible for the size structure present. Later, Davies and then Kelkar established the use of lognormal modes to describe aerosol size density populations. Throughout the 1970s, Whitby continued to make a series of substantial measurements (1973 and 1977) that further corroborated his findings of the presence of physical mechanisms generating aerosols. His 1977 study of sulfur in the plumes of coal-fired power plants firmly established physical mechanisms in the generation of atmospheric aerosols. This was one of the first studies that concentrated on a particular aspect of the aerosol content in the atmosphere.

After Whitby, there are several other studies that took his idea of focusing on a particular region or aspect of aerosol particle generation. In 1981, Gras et al. made measurements of stratospheric aerosols and showed that there was a large, uniform concentration of sulfur compounds present[†]. Later studies would attribute this layer not only to anthromorphogenic sources but was also highly influenced by volcanic eruptions[††] since sulfur compounds scatter light effectively (compared to carbonaceous compounds that absorb light and tend to heat the atmosphere).

There have also been a plethora of lower troposphere studies made (Fitch and Cress, 1983; Hobbs, 1985; Kim, 1988; Leaitch, 1991; Malm,1994; Ansmann et al., 2000). These studies have been made over the continental U.S. and western Europe and deployed a variety of instruments. Some of these studies have been extensive (Malm, 1994) and have tried to obtain a vertical profile of aerosols. Vertical profiles have not been done conclusively primarily because aircraft cannot stay aloft indefinitely so the altitude distribution is roughly known.

[†] Junge did the first aerosol examination of the stratosphere (1961) and this layer bears his name.

[††] Winters after eruptions by Mt. St. Helens and Mt. Pinotubo were characterized by colder than normal temperatures and heavier snow falls.

A final study that we would like to mention took place in 1989 in the deserts of south central U.S.S.R. This study was comprehensive and focused on studying dust, its generation and its transport. A whole series of papers came out of this study, which discussed the physical makeup, the size density distributions, and the movement of the particles. These papers provide a good read for investigation of dry and/or desert aerosols.

4.3 SUMMARY

In this chapter, we strived to provide the reader with a picture of the constituents and processes found in the lower troposphere. Due to the dynamic nature of the atmosphere as a whole, it was not our intention to give a comprehensive explanation but rather to focus on some of the basics that may influence our experiment and help us to understand our results. Of primary importance to us in this work are aerosol populations, their chemical and physical makeup, and basic mechanisms that influence their behavior. The result of our exposition led us to modeling aerosols of the lower troposphere as homogeneous spheres in the size range of 1 nm to 35 μm. However, as indicated, we could not and will not neglect the contribution molecules have on our scattering model. Lastly, we believe the urban environment we will be operating in (east coast, U.S.) will afford us the type of conditions (humid, stable atmosphere) that will enable us to successfully apply the scattering theory of Chapter 3.

5

Chapter 5:
The Multistatic Receiver

Any sufficiently advanced technology is indistinguishable from magic.

This chapter describes the instrumentation to be used to investigate the vertical distribution of atmospheric aerosols via light scattering. Although there are certainly other ways to implement such a design, it was pointed out to the author that after the technology becomes obsolete (and it will), what remains must be the science. Thus, the instrumentation is not the focus of our attention, but is simply a tool to be employed in our research endeavor. However, we cannot neglect the impact the instrumentation and its operation may have on our analysis and results. Since we are not manufacturing multistatic receiver units at the moment, the configuration and operation of the equipment used in this thesis will undoubtedly undergo several evolutionary changes as the science behind our research becomes better established.

The main pieces of equipment used in this thesis were three CCD cameras (described in more detail below). The decision to use CCD cameras, instead of linear diode arrays used by Stevens was principally one of economics as two cameras were previously used in another measurement campaign and were already available. As we'll see, the inclusion of a third camera was necessary to provide additional scattering angles along the length of the vertical beam, which became useful during episodes when the atmospheric content changed rapidly in altitude. In addition to the cameras, a high-power lidar, the Lidar Atmospheric Profile Sensor (LAPS), was used to supply the desired polarized beam.

We now wish to examine the design criteria and requirements used in this experiment. In our proceedings, we will also compare and contrast what Stevens has done in order for the reader to get a better feel for the context of our experiments. Initial results of our experiment are presented here only as a means of showing data. Analysis of the data will be presented in Chapter 6.

5.1 BASIC CONFIGURATION AND LAYOUT

The term "multistatic" refers to the use of several receivers (here, the CCD cameras) that are at a separate location from the transmitter (LAPS). In Stevens, a bistatic configuration was used (one receiver, one transmitter). Here, a multistatic configuration was used (three receivers, one transmitter). While monostatic configurations (such as LAPS) collect a single scattering angle of 180° (which is all that is needed for Raman spectroscopy and monitoring of molecular species) one scattering angle is inadequate for use in aerosol particle sizing and determination (See Chapter 3). Thus the need to examine off-axis scattering angles, especially in the range of 145° to 175° becomes necessary and only realizable with receivers set apart from the transmitter. The basic configuration is shown in Figure 5-1. Each camera is in-

line with the laser and so forms the scattering plane. A polarization rotator, remotely-controlled, was inserted to change parallel to perpendicular polarization. In essence, the configuration used in this thesis amounts to an open-air nephelometer.

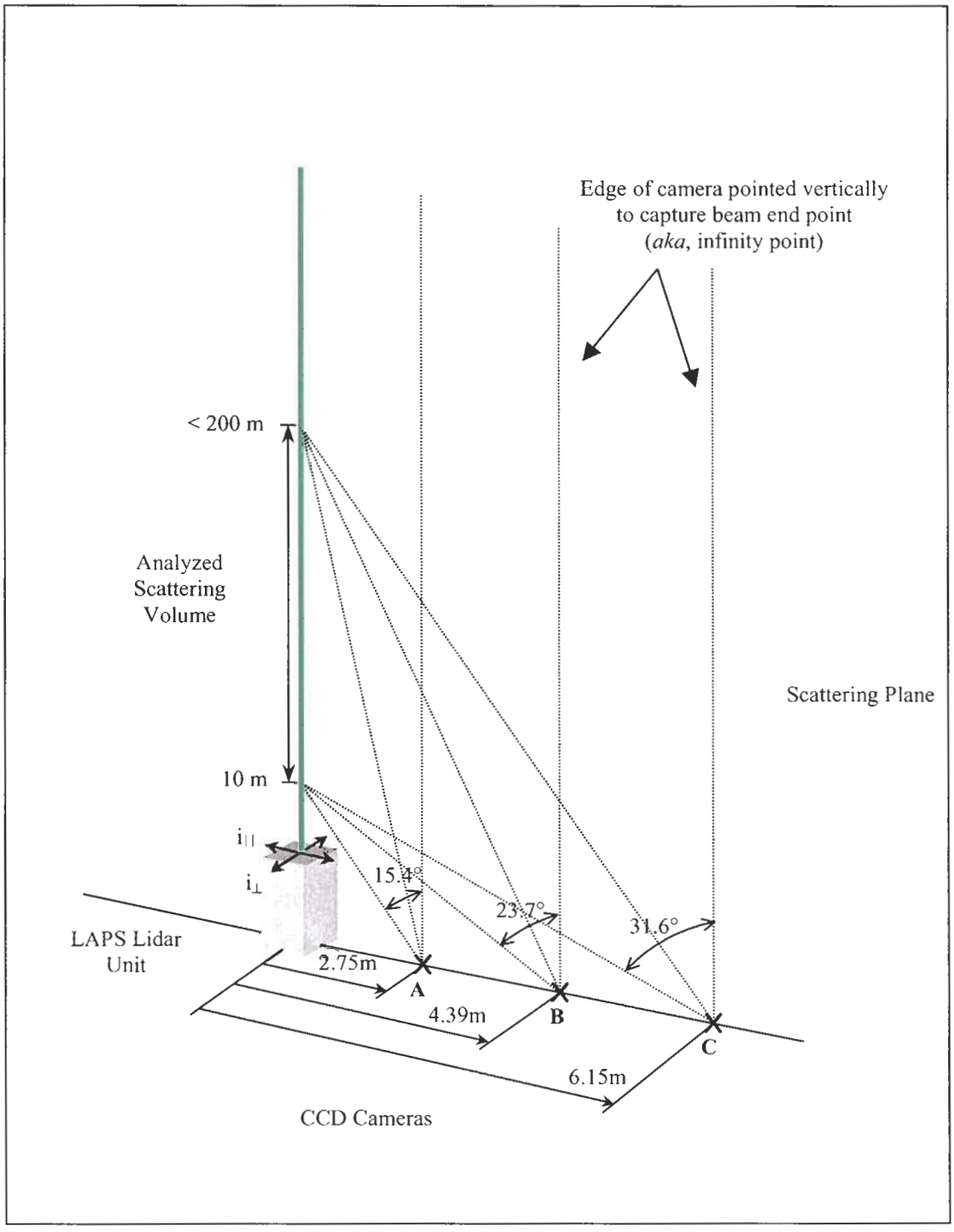

Figure 5-1: Multistatic receiver equipment and configuration.

The cameras used in this thesis were Pictor 416XTE CCD cameras from Meade Instruments Corporation (www.meade.com). The CCD array chip in each camera was the KAF-0401E manufactured by Kodak. This particular CCD array is a 16-bit blue-enhanced, 768 x 512 array made up of 9 μm square pixels giving it dimensions of 6.9 mm x 4.6 mm. Its response curve, provided by Kodak, is shown in Figure 5-2. Additionally, these cameras were thermo-electrically cooled which made them substantially less noisy than the air-cooled linear diode array used by Stevens.

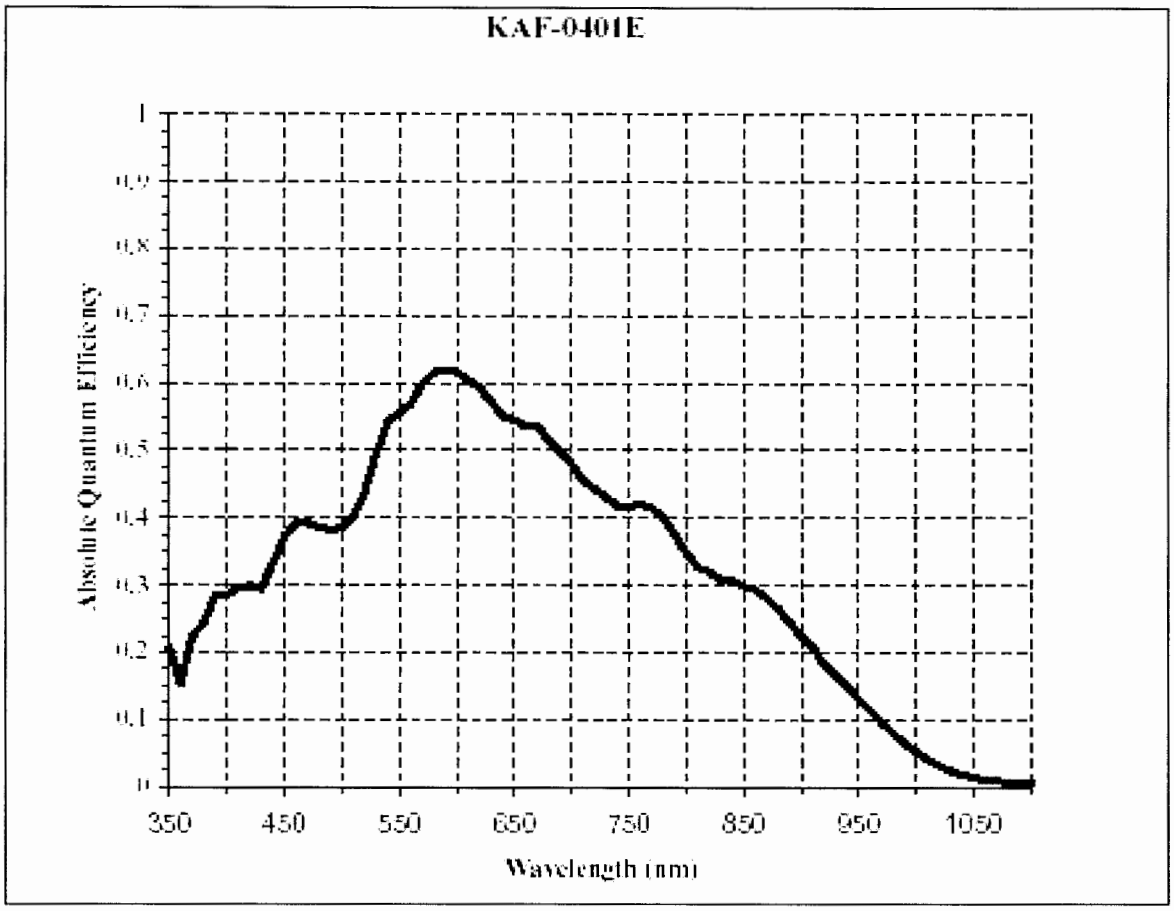

Figure 5-2: Spectral response curve of the KAF-0401E Kodak CCD chip (from Kodak, Corp.).

Each camera was connected to a desktop computer via a SCSI connection that made the downloading of the image data much faster than a serial cable. The controlling software, included from Meade, allowed exposures from 10 ms and up. A network was configured that enabled the control of all three cameras from a single computer. However, because the Meade software is not an open software package (and Meade was unwilling to allow us access to their source code), the cameras could not be operated by a single command but rather had to be initiated in sequence. Nevertheless, we were able to have all of the cameras take an image with less than one-quarter second between them.

A data set sequence consisted of taking a dark image, a background image, a parallel polarization image and a perpendicular polarization image for a total of 12 images (4 for each camera). In all, we were able to complete the entire data acquisition cycle in less than 2 minutes, including the time for the images to download. In comparison, Stevens, took 2 minutes to run his data acquisition cycle with a single linear diode array. The main difference between our implementation and Stevens' lies in the way the parallel and perpendicular images were being taken. In our experiments, the parallel and polarization images were each taken within 30 seconds (including download) from the initial polarization image captured. In our experiments we used 1 second integration times principally because we had a substantially higher-powered laser than what Stevens had available (using LAPS, exposures of greater than 5 seconds typically led to saturation, even on clear nights with little backscatter). In comparison, Stevens used a 15 second integration time and took up to 1 minute between polarization images. Our approach needed to be as fast as possible because we also had to limit possible changes in atmospheric concentrations that might occur during longer integration intervals. Stevens did not need to rely on this as much because he was looking at a horizontal path which is generally more stable than a vertical path because of atmospheric stratification.

5.1.1 Design Criteria

As already mentioned, we wish to examine the vertical profile of aerosols within the first kilometer of the atmosphere. Further, because of the anticipated vertical variation of the aerosols in both number density concentration and composition, a single camera could not provide enough information. Thus, several cameras were needed to provide enough overlap in the scattering angles at the desired altitude.

The first criteria to determine is the scattering angle range to be examined. From Chapter 3, we have shown the structure of the polarization ratio for the scattering angles of around 145° to 175°. Indeed, the scattering angles examined by Stevens were from 155° to 175° and so these angles are where we will start. The desired scattering angles observed are dependent on how the cameras are arranged and the field-of-view (FOV) of the lenses used.

In addition to knowing the scattering angles, we also need to know the altitude that corresponds to each scattering angle. In order to accomplish this, we need a fixed point with a known altitude. Stevens had a target board located at around 3 km from his bistatic receiver. Obviously, when vertically pointed, we do not have such a target. However, the laser beam itself can be (and was) used as an altitude reference point. Specifically, the endpoint of the laser beam, *aka* the infinity point, is assigned an altitude of infinity. Thus, the laser is aligned on the CCD array such that the endpoint of the laser beam is on or near the last pixel in the array. This pixel, assigned an altitude of infinity, corresponds to a scattering angle of 180°. All of the other pixels are processed from the infinity point by simple geometry. Next, using the infinity point, the observed scattering angles are independent of the distance the cameras are from the laser because it is the FOV that determines the scattering angles to be observed. Figure 5-3 shows the scattering angles each camera observes in this experiment versus pixel and versus altitude. Notice that each camera sees the 180° scattering angle on the last pixel, as expected.

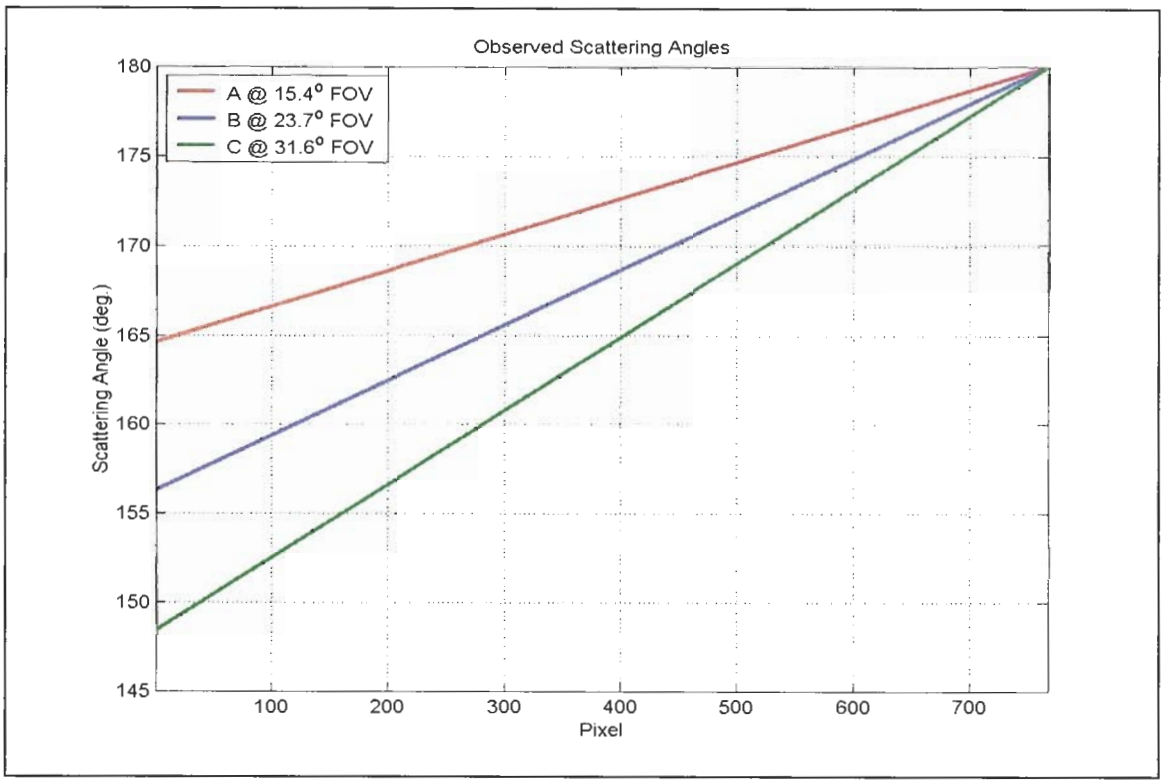

(a)

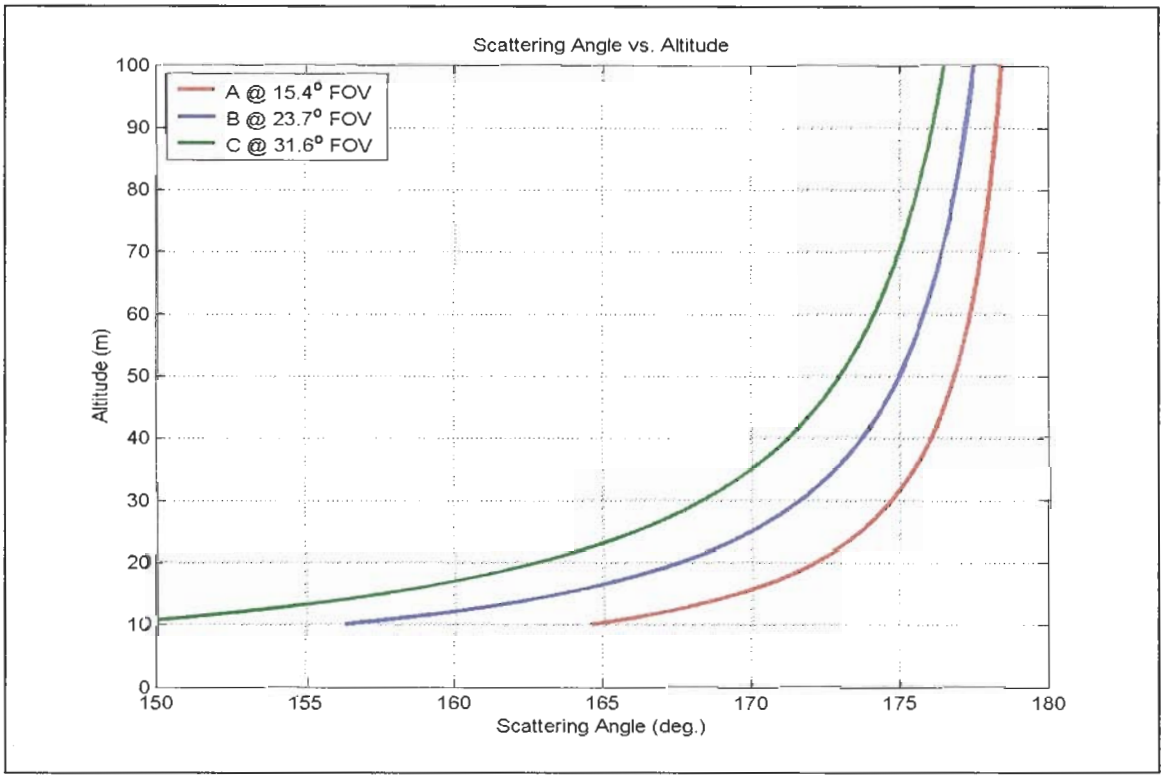

(b)

Figure 5-3: Observed scattering angles of the three CCD cameras (a) vs. pixel and (b) vs. altitude.

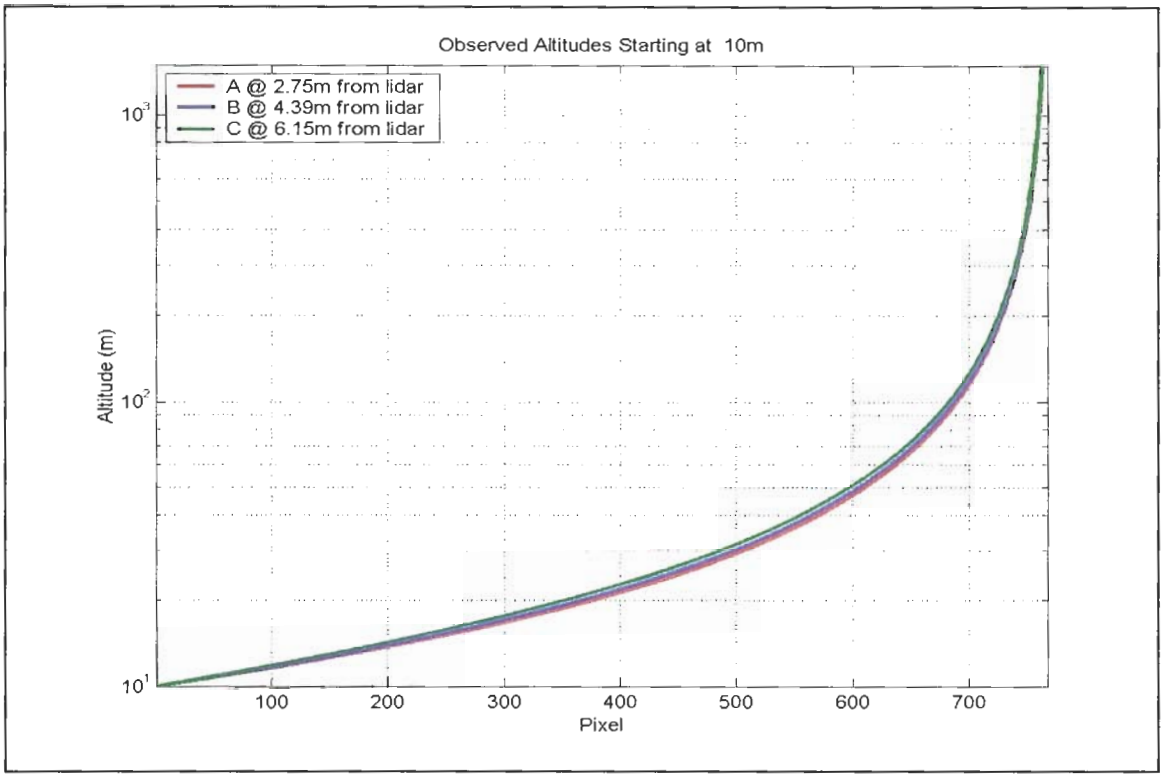

(a)

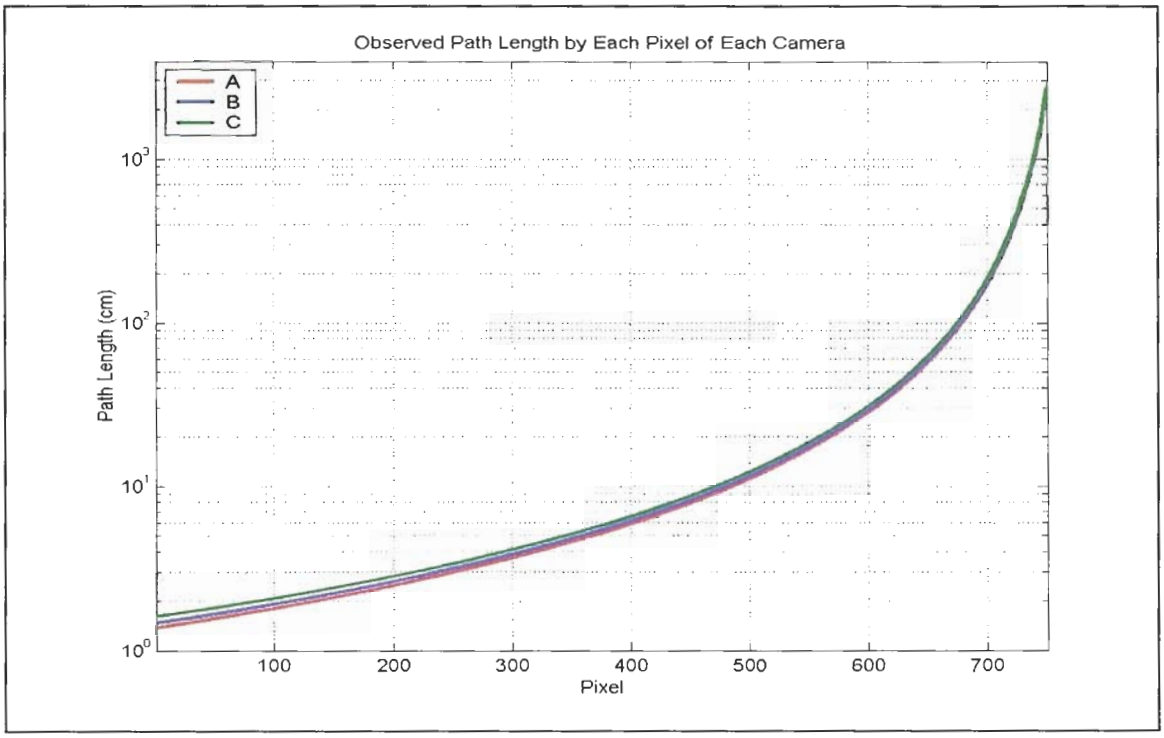

(b)

Figure 5-4: (a) Altitude observed at pixel, (b) Path length observed. The overlap indicates each camera sees (approximately) the same portion of the beam.

The last item that needed to be determined was the location of the cameras from the lidar itself. The overriding criterion here is that each camera must see the same altitude path as the others. To achieve this, the three cameras required three different FOV lenses and are set at three different locations. If each camera had the same FOV lens, then each would see the same scattering angles and there would be no diversity in the angles. Further, if each camera had the same FOV and were placed at different locations, then some of the altitude path would be missing overlap. Here, because we were primarily interested in very low altitudes, 10 meters was set as the minimum observed altitude. Figure 5-4 shows the observed altitudes by the three cameras. Notice that most of the pixels of each camera correspond to altitudes under 200 meters. This is the tradeoff that must be made, i.e., the lower the desired altitude, the closer the cameras have to be to the lidar thereby sacrificing upper altitudes. However, it is these very low altitudes, especially at night when the planetary boundary layer falls to under 500 meters, which are of more importance in particulate and pollution studies.

5.1.2 Filter and FOV Considerations

Each camera was fitted with a 2-inch diameter, 532 nm laser-line interference filter, with a 10 nm bandwidth, from Oriel (P/N 53051). Such filters exhibit an angular response that affects the central wavelength, the transmittance, and bandwidth. Oriel states that for off-normal angles < 25°, the effect on transmittance and bandwidth are negligible (Oriel 2001 catalog, p. 10-30). However, due to the increase in apparent thickness (i.e., an increase in the optical path through the filter), off-normal incidence will move the central wavelength towards shorter wavelengths. To a good approximation, Oriel suggests the angular response of such a filter is given by

$$\lambda_\theta = \lambda_o \left[1 - \left(\frac{n_0}{n_*} \right)^2 \sin^2(\theta) \right]^{1/2} \qquad 5\text{-}1$$

where θ is the angle of incidence (valid for $\theta < 25°$), λ_θ is the resulting shifted central wavelength, λ_o is the central wavelength at normal incidence, n_* is the effective index of refraction of the filter, and n_o is the index of the refraction of the surrounding medium (typically air). A somewhat more rigorous analysis of single- and multi-layer interference layers can be found in Hecht (Hecht, chapter 9). Because of the angular dependence of the interference filter, arbitrary FOV lenses could not be used. A simple calculation can be done to determine a reasonable upper limit of the maximum FOV that could be used. If we assume that the bandwidth is still around 10 nm for off-normal angles of incidence (good for a rough approximation), then using $\lambda_\theta = 527$ nm, $\lambda_o = 532$ nm, $n_* = 2.0$, and $n_o = 1$, we can re-arrange Eqn. 5-1 to solve for the angle incidence and find $\theta = 15.9°$. Thus, the upper FOV that could be used is 31.8°.

The angular response of various FOV lenses is shown in Figures 5-5 and 5-6. These images were taken in State College on the night/morning of 7th/8th August 2001 with a 532 nm Nd:YAG laser (Surelite -

lower power than LAPS). The left side of the beam in each image is the laser unit and the right side of each beam is the upper altitude (infinity) point. These images are displayed here as they appeared on the computer screen. From the calculation in the previous paragraph, we see that we are right on the edge of using the 31.6° FOV. Because we were using a lower power laser but with the same integration times, the 10nm interference filter's cutoff is starting to appear in Figures 5-5 e and f. In our initial tests with the

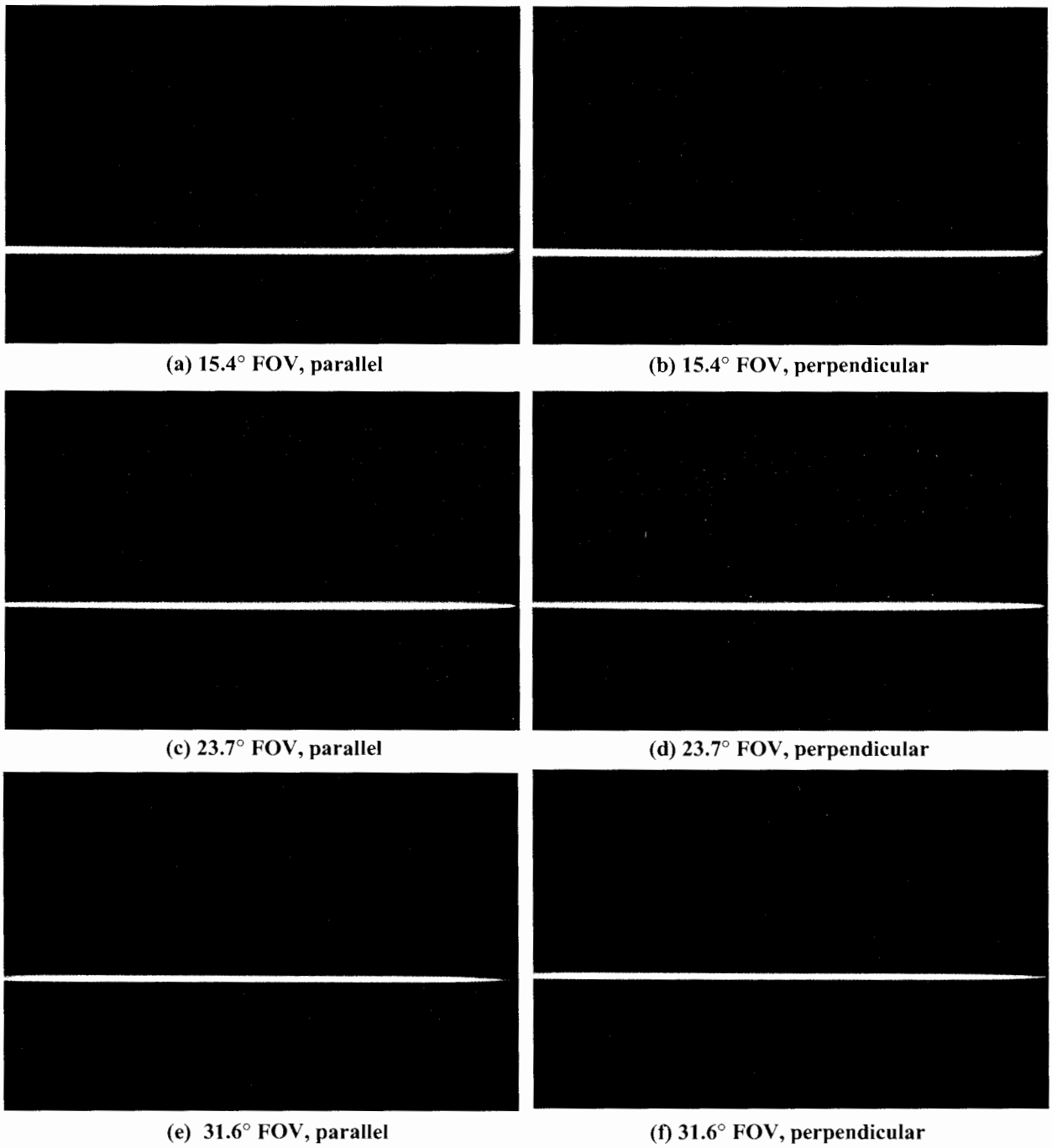

(a) 15.4° FOV, parallel **(b) 15.4° FOV, perpendicular**

(c) 23.7° FOV, parallel **(d) 23.7° FOV, perpendicular**

(e) 31.6° FOV, parallel **(f) 31.6° FOV, perpendicular**

Figure 5-5: Polarization response using 10 nm interference filter and various FOV lenses.

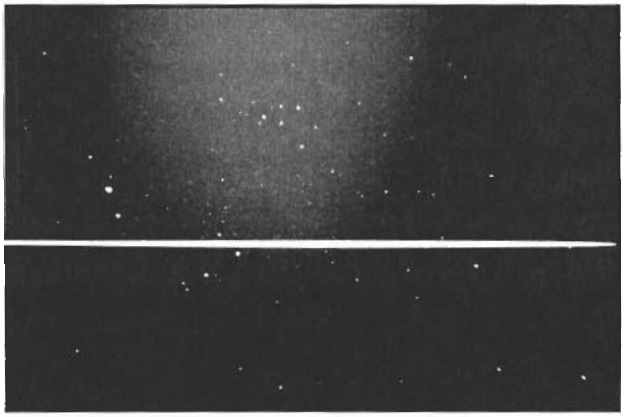

(a) 46.5°, unfiltered parallel

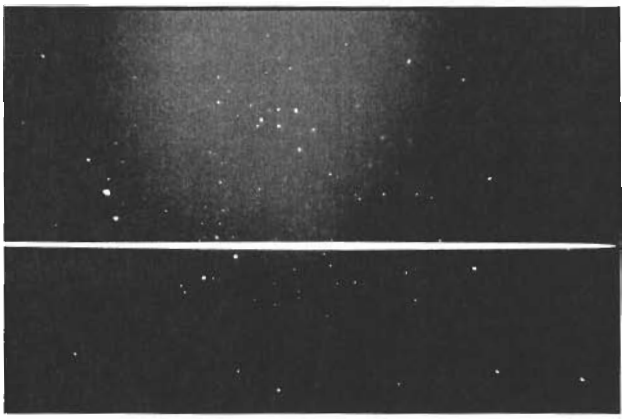

(b) 46.5°, unfiltered perpendicular

(c) 46.5°, filtered parallel

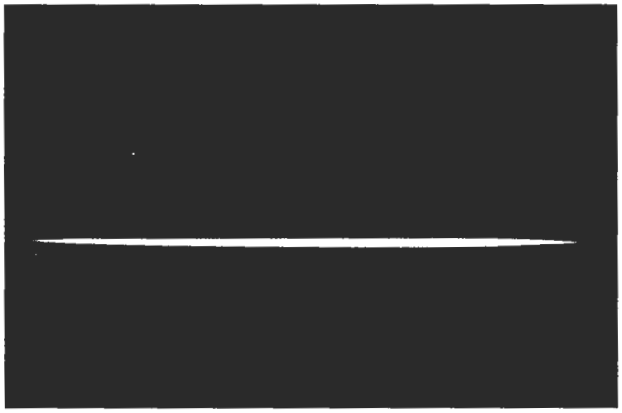

(d) 46.5°, filtered perpendicular

Figure 5-6: Polarization effect of 10 nm interference filter with large incident angles.

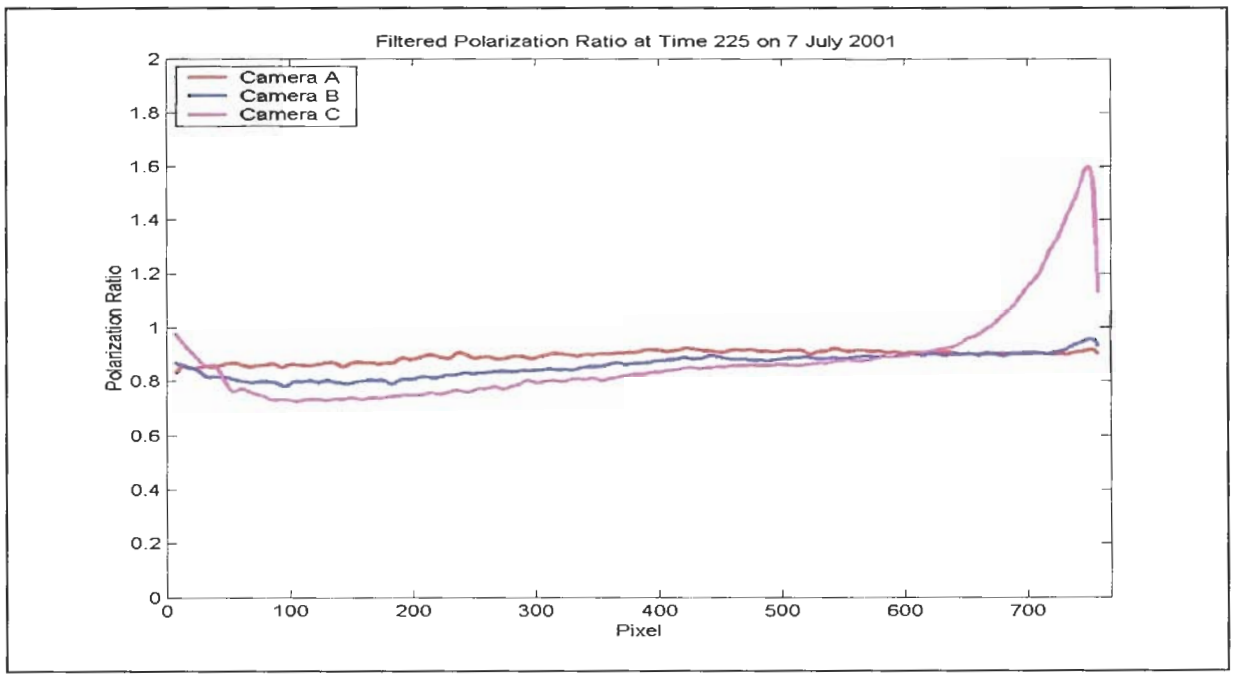

Figure 5-7: Polarization dependency evident with camera C (from Philadelphia data).

10 nm filter and 31.6° FOV lens, we were using the higher power LAPS unit and such an effect was not immediately identified. Using a 46.5° FOV lens, Figure 5-6 dramatically shows the effect of the interference filter's cutoff and polarization dependency. From Oriel (p. 10-31), "When the angle of incidence is large, > 30°, the spectral pass band characteristics of the filter can be so degraded as to yield two distinct peaks and transmittance becomes dependent on polarization." We did not realize that this polarization dependency was neither significant nor evident until we began processing the data from Philadelphia (experience is the best teacher). Figure 5-7 clearly reveals the polarization dependency of camera C in the polarization ratio measurements. Despite the polarization errors introduced by the interference filter, a large portion of the data from camera C was still useable[†]. The reason for this is that the polarization errors were most pronounced for the upper altitudes (which were not inverted due to an inhomogenous path length) and, for the first 4 meters of the lower altitudes, observed by camera C, we had a sufficient number of scattering angles from the other two cameras to compensate. If the data warranted it, altitudes 10 m to 14 m were neglected in the analysis.

5.1.3 Camera Comparison

Although the polarization ratio technique can eliminate or even significantly reduce many instrumental errors, the one thing that it cannot accommodate is the camera's polarization sensitivity. Eventually, the data collected by the three cameras will have to be combined into one data set and so it becomes necessary to understand how each camera performs with respect to each other. A series of tests was conducted to answer just such a question. As it turns out all three cameras give very similar results (though obviously not exact) using the polarization ratio and thus adds reassurance to the overall methodology and measurements.

One of the comparisons that must be done is to attempt to quantify how well the cameras take measurements with respect to each other. This is not an easy task, even in industry, because one needs a uniform, calibrated background image with which to take measurements. External noise, surface variations, temperature influences and spatial differences all make scientific comparisons difficult to obtain. A possible way to reduce these effects is to take images with the aperture of each camera closed (i.e., a constant input). Stevens used this approach and so we too will use it here. Unlike Stevens' instrument, all of our cameras are temperature stabilized with thermoelectric coolers, which have the effect of significantly reducing dark counts and noise. With the lens aperture closed, one hundred images were taken with each camera and subsequently processed to find the background level and standard deviation. We found that the cameras were extremely close to each other. Figure 5-8 summarizes the results from each camera.

A second test that needed to be performed was to identify any polarization dependence due to the CCD array itself (not due to the filters). Here, unfortunately, we had to compare images from a common

---

[†] As it turns out, camera B's filter also exhibits a very small amount of polarization dependency.

source. An overhead projector was used to illuminate a wall and a camera was placed relatively close in order to get as uniform an image as possible. Because of the sensitivity of the cameras, we were forced to use a filter to avoid saturating the CCD array[†]. All cameras used the 15.4° FOV lens. A linear polarizer was placed in front of the camera and two images were taken, one with the polarizer oriented horizontal and one oriented vertical. After a series of images were taken, the images were processed to obtain average values. Table 5-1 summarizes the results and shows that the polarization dependency of each camera is low. The data should serve as a reminder of the difficulty of comparing polarization images. Since Stevens did not perform a polarization dependency measurement, we cannot compare equipment polarization sensitivity.

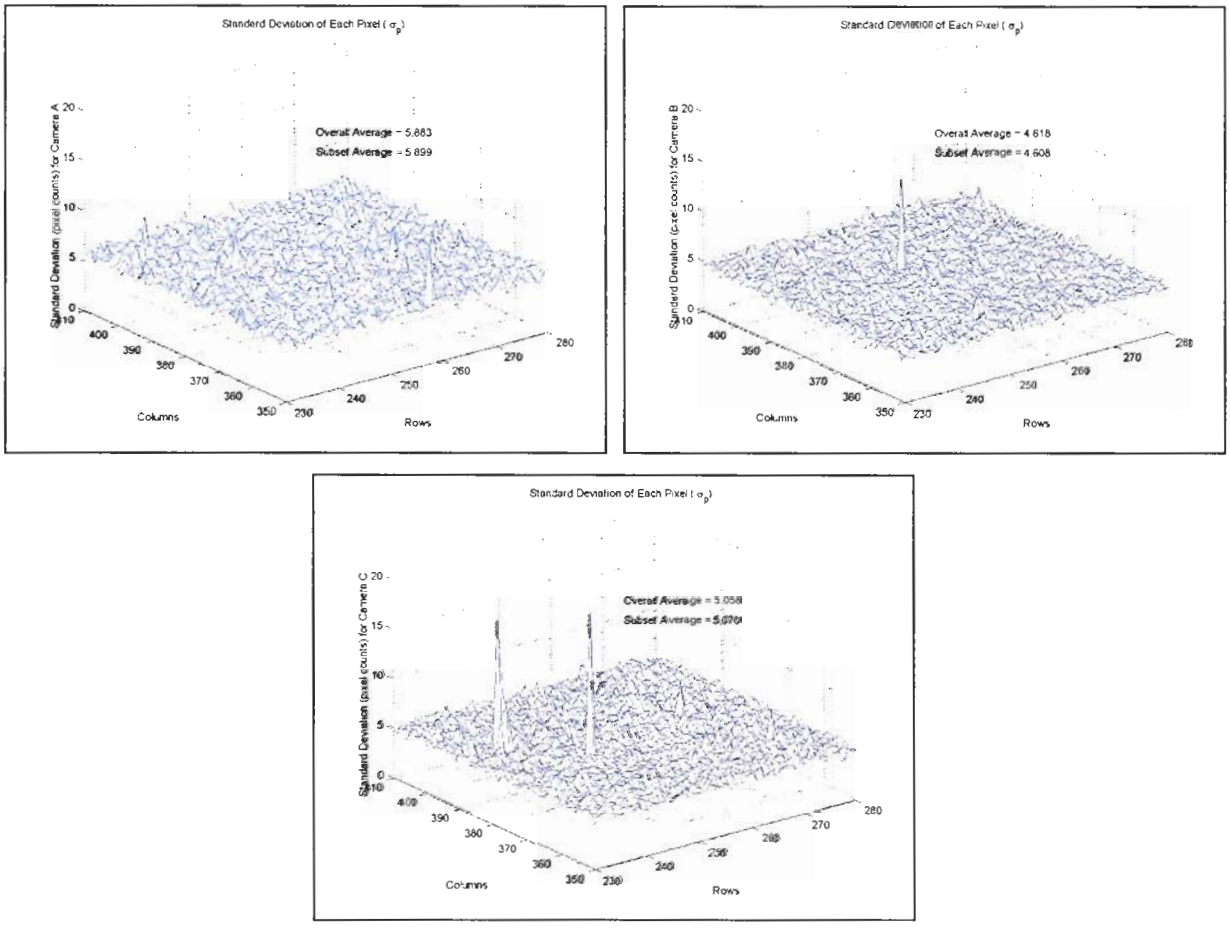

Figure 5-8: Standard deviation of each camera under dark conditions. The overall average covers the entire array (512x768) while the subset average covers the plotted rows and columns.

[†] Saturation occurred even with very low exposure times.

Table 5-1: Polarization results of each camera

Camera - Polarization	Average Maximum	Average Minimum	Average Maximum Std	Average Minimum Std
A – Horizontal	12999	3034.1	502.4	3.8
– Vertical	12728	3038.1	545.7	4.8
B – Horizontal	9263.8	3007.6	448.9	2.5
– Vertical	9009.5	3007.1	445.7	2.8
C – Horizontal	13270	3097.6	357.8	2.9
– Vertical	14432	3094.7	368.5	3.8

5.2 OPERATION AND INITIAL RESULTS

In this section, we describe the basic operation of the multistatic receiver array, including focusing, imaging, and data processing.

5.2.1 Procedure for Taking Images

As described in section 5.1.1, each camera was placed at a set distance from the laser beam which will establish the minimum observed altitude. Separate power supplies and desktop computers provided the necessary control of each camera. A network was configured to operate the cameras from one computer but the images from each camera were stored to each computer's hard drive.

As a note to future researchers who may wish to use the Meade cameras, we wish to convey that we had a rather difficult time getting the cameras to connect to the computers via the SCSI cards. There were two very common errors. The first, and most correctable, was that the software could not connect to the camera because it could not detect the SCSI card. Typically, the remedy for this was to try various settings within the Meade PictorView software until the camera connected. The reason for this error was basically a SCSI card incompatibility (Meade only recommends to use Adaptec SCSI cards, and further, only one specific type of Adaptec card. Adaptec SCSI cards are not cheap). We did purchase the correct SCSI cards and found that the cameras would connect quite readily, but once in a while, the software would not be able to find the SCSI card and various settings would have to be tried for it to finally connect. Sometimes, re-booting the whole computer was the only way to get the camera software to find the SCSI cards. The second error was, however, much more troublesome. After the software detects the SCSI card, commands are sent to the CCD camera head to start its cooldown. Apparently, there is a conflict between the SCSI card, the Windows operating system and the software itself, which would result in a "mode select error." In other words, the software could not control the camera and would crash the program. After we installed the latest version of the software, downloaded all of the most up-to-date SCSI drivers, and re-installed Microsoft Windows 98, this error was seldom seen. Unfortunately, it did crop up once in a while and the only way to circumvent it, was to shut the computer and camera down for a period of time and reboot. These problems cost a lot of time because the cameras should not be run for 20 minutes at start up to

stabilize the temperature. Our best guess is that the source of the mode select error was that the computer was too fast for the software. The remedy to these problems is perhaps to use laptops, instead of desktops as laptops are designed for outdoor use and the Meade cameras were primarily designed for use with laptops. However, as we mentioned at the start of this chapter, we are primarily interested in the science at this point and not the engineering. The point is, if one needs to use these cameras and comes across such errors, they are encouraged to keep trying to get the cameras to connect, because in our experience, they always did connect, eventually[†].

Once the cameras were in place and connected, the next step was to focus each camera. Because these cameras and lenses do far-field focusing (or infinity imaging), a suitable distant object was used, such as a distant tree or building. The best objects to use, however, were objects with writing on them. Focusing was not automated and did require some time to get it right. Once focusing was completed, the cameras were swiveled to image the beam and filters were placed over the lenses.

By far, the most difficult and often tedious job of using the cameras was aligning them with the beam. The beam's endpoint was typically positioned between pixels 760 and 767 on the camera. A range was used because getting the endpoint to appear on the same pixel each time was difficult since the tripods did not permit very fine angular movement (slight adjustments could translate in tens of pixels). We also wished to avoid positioning the end point of the beam on the last pixel because we had to be sure that the laser did not extend past the last pixel. Horizontal alignment also posed challenges, as it is advisable to have the beam parallel to a CCD array's rows, rather than transgressing diagonally across the array. With some care, we were able to have the beam aligned within 3 pixels of horizontal, and many times it was within 1 pixel.

After the focusing and alignment steps were completed, data were taken in the following manner. At the start of a data set, each camera would take a dark image, a background image, and a parallel polarization image. While the data from the parallel polarization image was being downloaded, the beam would be shut off, a polarization rotator would be inserted, and the beam would be turned back on. In many cases, the beam would be back up before the parallel polarization image was completely downloaded by all three cameras. As soon as the cameras were ready, a perpendicular image was snapped. The entire process typically took under 2 minutes. The critical time however, was to reduce the time between the parallel and perpendicular images since we did not want the atmosphere to change drastically between images. We were able to take the perpendicular image within ~10-15 seconds after the parallel image was taken. (Stevens had to wait up to 1 minute between polarization images and we believe that this length of time could account for some of the errors and differences he had in his data sets.) Only after all 12 images were taken were they finally saved. Data sets were separated by 10, 15 or sometimes 30 minutes, depending on whether anything interesting, such as a pollution event or fog formation, was occurring.

[†] Some swearing and threatening the computers with bodily harm usually resulted in a correct connection. Pleading and begging never did.

5.2.2 Processing of Data

Because of the amount of data that was taken, several Matlab scripts were created to automatically process the data (we did not want to be latched to our computer for days on end). The first step was to pre-process the data by finding the beam in the polarization images. The scripts that accomplish this task are *get_data.m* and *process_data.m*[†] and both can be found within the *Processed Data* folder of any day in which data was taken. Processing begins by loading in the parallel polarization image and subtracting the background. Since the laser beam will be the brightest source of light in the image (the moon was never in any image), the beam itself is found by examining the maximum of each of the 767 columns. Due to the high power of LAPS, the program generally had no problem finding the beam. But with lower power lasers, the program occasionally detected a maximum that was not the beam. Because the script had been initially written to analyze the data from an Argon-Ion laser (see below), the script contains code to correct such erroneously detected maxima. There is a lower limit, however, that we found when we first used a 532 nm laser. At the time, this 532 nm laser emitted very low power due to a variety of effects (most notably, beam misalignment of the cavity). From this data, it became evident that the program could not accurately find the beam and so was thrown out. Continuing with the processing, the script also determines the width of the beam (in terms of number of pixels) that is present on the CCD array. After some experience and examination of the data, the code has been hard-wired to accept a fixed-width number of pixels at 8[‡]. A smaller number should be used if exposure times were considerably shorter (since readout noise would dominate). After the data is pre-processed, the resulting data are saved to separate files for further examination by other programs.

There are two main ways of visualizing the data. First, a profile can be obtained using the Matlab script, *get_profile.m*, which takes the pre-processed data obtained by *get_data.m* and obtains the desired polarization profile. An example of a polarization profile is shown in Figure 5-9a. The profile is a good way of examining how the atmosphere has changed between polarization images (see Figure 5-9b). All profiles for each camera at each time are saved as individual files.

The second way of visualizing the data, and the more important with respect to this thesis, is the polarization ratio profile. Another Matlab script, *get_ratio.m* performs all the necessary calculations needed to obtain the polarization ratio for each camera, including filtering. Figure 5-10 shows an example of the polarization ratio profile data. As with the polarization profiles (i.e., the intensity profiles), all results for each camera's ratio data are saved individually.

Finally, the last piece of processing is to combine the polarization ratios from all three cameras at a specified time, into one composite polarization ratio file. The Matlab script, *get_composite.m* accomplishes this and performs all necessary calculations. It is these composite files that are used in the inversion process. Basically, the composite data files are convenient packages of the ratio and profile data.

[†] The main script, *process_data.m*, is the workhorse and is provided in Appendix B.
[‡] Beam widths of 3, 5 and 10 pixels were also examined in the processing and no appreciable difference was found.

As a final processing note, an entire night's worth of data (250 – 300 image files), can be completely processed by all four Matlab scripts in under 15 minutes on a 1 GHz Intel computer. Thus, although we had significantly more data to process than Stevens, we used a substantially faster computer. The inversion of the data however, typically takes considerably longer.

5.2.3 Initial Use of an Argon-Ion Laser

An Argon-Ion laser was initially used to test the cameras and the image processing programs. This laser is a relatively low-power (< 5 W) continuous-wave laser and so integration times of 5 seconds were used in taking the images. At the time of these initial tests, we only had two cameras (A & C) in our possession as camera B was sent back to Meade to be updated with the latest CCD chip (Cameras A & B were used in previous field campaigns and exhibited some wear-and-tear). All data taken with the Argon-Ion laser was collected at the PSU Lidar Laboratory in State College, PA. Although the data were not inverted, using the Argon-Ion laser did provide us with a better understanding of the overall processing that needed to be done with the data. Also, it was with the Argon-Ion that we encountered most of our connection problems with the Meade cameras and the SCSI cards.

5.2.4 Initial Results Using LAPS

Although the Argon-Ion laser served admirably in its role as a test laser, there were still a few items that revealed themselves during the use of the much more higher powered laser, LAPS. It was very good to use two different lasers because it helped to flush out bugs that would have otherwise been missed. There are no any major differences in the programs used to process the data from LAPS as those for the Argon-Ion laser. Actually, using the two different lasers made the processing algorithms much more versatile and stable. These programs are of by no means infallible as the presence of the moon or an over eager insect could cause the program to misinterpret the data. Thankfully, no images were taken which included the moon, but bugs did manage to disrupt several data sets.

Using LAPS however did not proceed smoothly as it had problems of its own to contend with. Due to the delay in getting LAPS to work, we were not able to adequately test the multitstatic receivers with the laser prior to deployment in the field in Philadelphia. However, the only real problem that was found was with camera C's polarization dependency. Once the Matlab scripts were refined, processing the data became easy. Figure 5-9 and 5-10 are processed data taken from LAPS.

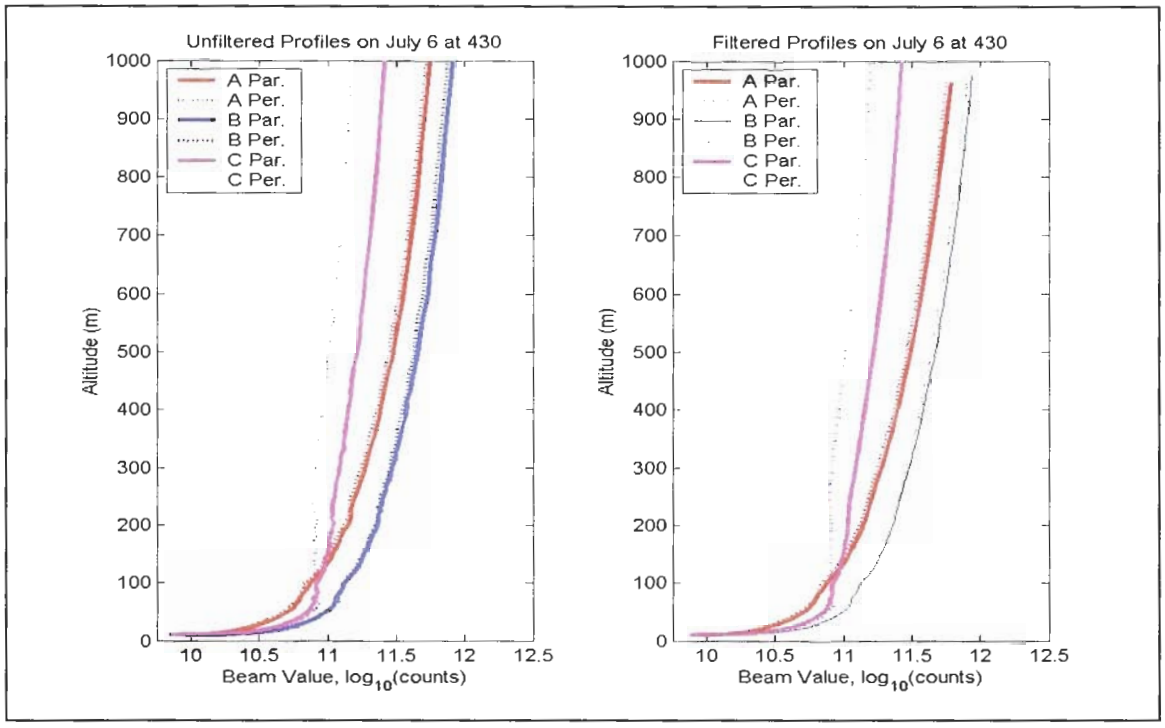

(a)

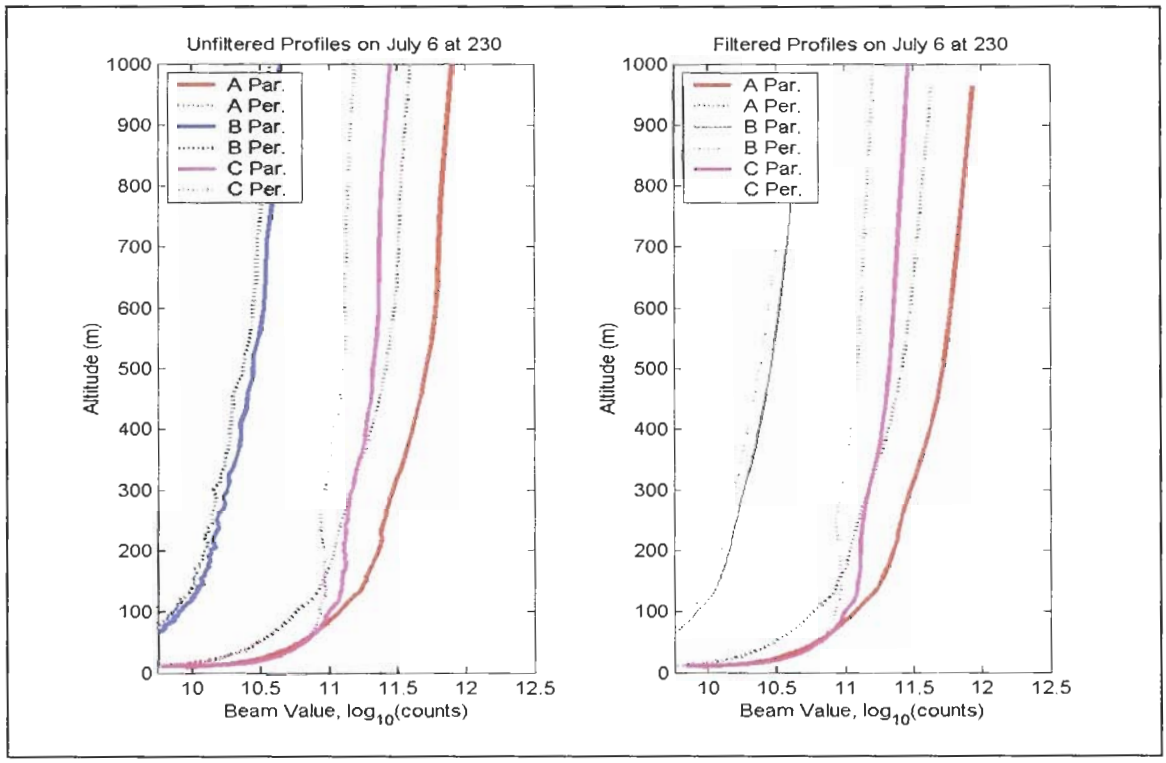

(b)

Figure 5-9: Sample polarization profiles. (a) The parallel and perpendicular curves are relatively close but in (b), the curves are further apart giving a possible indication that the atmosphere changed significantly between measurements.

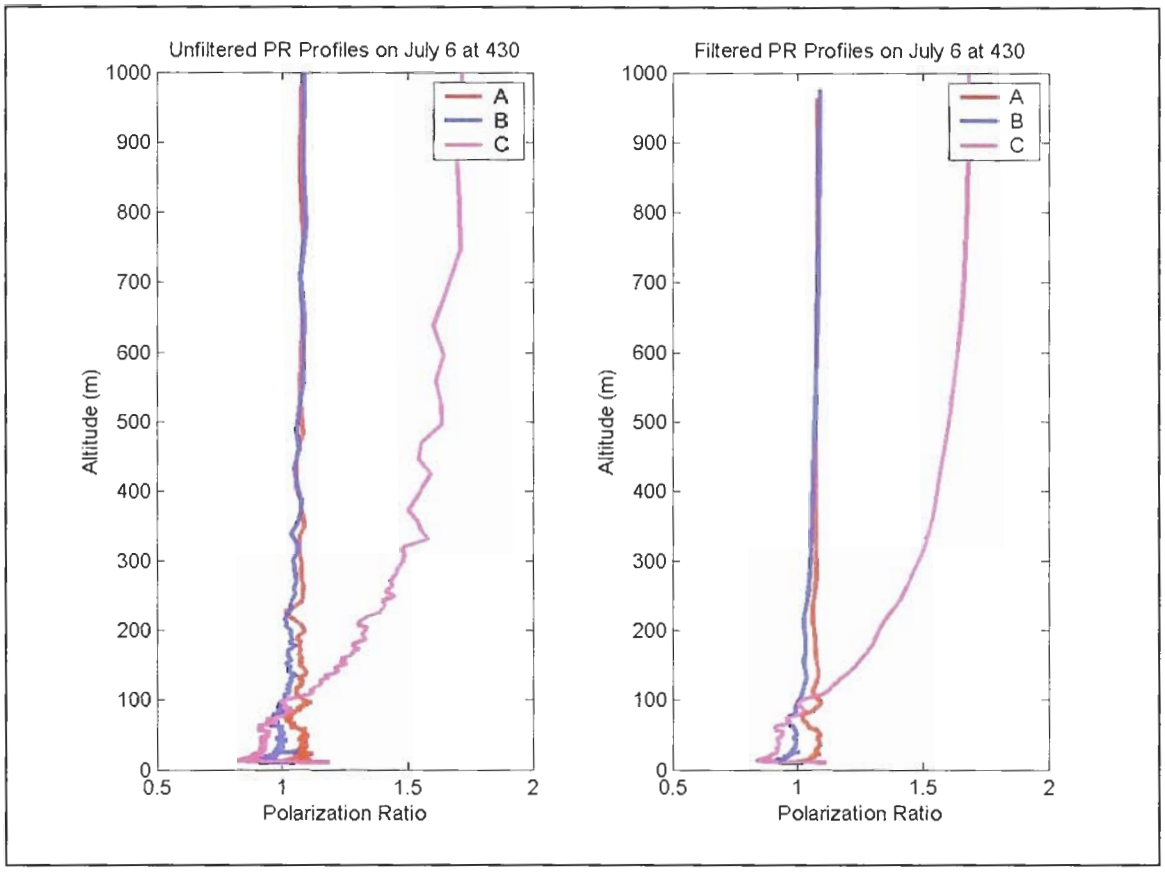

Figure 5-10: Sample polarization ratio profiles. Camera C is showing polarization dependence due to the angular response of the 10nm interference filter.

6

Chapter 6:
Results and Analysis

Analysis leads to paralysis.

In this chapter, we present the experimental results and describe the required analysis. Our intent here is to establish the particulate concentrations as a function of altitude and, if possible, to discern the physical composition of such concentrations. Our experiment was part of the North East Oxidant and Particulate Study (NE-OPS) funded by the U.S. Environmental Protection Agency and conducted in Philadelphia in the summer of 2001. In conjunction with our own investigation, we also make use of additional information available from other research groups that were present during this time (although the information is rather limited and difficult to correlate). We will also make use of and draw comparisons to the work presented by Stevens. It was only through the present work that we were able to critically examine Stevens' work and to offer possible explanations to some of his questions and experimental uncertainties. While this work and Stevens' work stand on their own individual merits, there are still several major questions that must be left unanswered for future studies. This is the nature of the beast: The atmosphere's complexities pose significant challenges for any single work to overcome as there seems to be a never-ending supply of questions and possible solutions. But together, these works begin to provide more information and suggest plausible explanations.

This chapter begins by establishing how the data was processed[†] and then proceeds to discuss the initial observations. From the initial examination of the data, several questions arose that caused us to further investigate the equipment setup, measurement procedures and underlying atmospheric assumptions in order to better understand and interpret the data. Our findings are detailed below. We have determined that the nighttime aerosol number density distribution is strongly altitude-dependent, much more so than was anticipated. Although it was anticipated that the nighttime vertical path would not be completely uniformly distributed, it was hoped that the path would contain stratified layers that could be analyzed individually. However, we have found a strong altitude dependence present in nearly all of our data sets. This is in sharp contrast to Stevens who found his observed horizontal atmospheric path to be (nearly) uniformly (lognormally) distributed. Although, the aerosol number density altitude dependence is a major finding of this work, its presence all but precluded us from performing an inversion analysis on the data to determine number density distributions. While we were still able to perform several inversions and obtain reasonable results, detailed, rigorous and stable inversions of remote sensing data will continue to be a

[†] Collection of the data was presented in Chapter 5.

daunting task for researchers. For now, one simply has to be honest and do the best with the data as they possibly can. A summary of our analysis and findings concludes this chapter.

6.1 DATA PROCESSING

As outlined in Chapter 5, the processing of the data is straightforward. Again, we wish to make a line of demarcation between data processing, which is easy, and data inversion, which is much more difficult. It is our intention that we clearly indicate how the data was processed so that someone else may reproduce our results and/or incorporate our approach into future work.

6.1.1 Procedures and Algorithms

The processing of the data was completed on a 1GHz Intel processor running Matlab, version 6. It took some time to develop an adequate and stable set of algorithms to process the image and data files for the desired information. Each data set consists of twelve image files (FITS format), split equally between the three cameras: a background image, a dark count image, and the two polarization images. These image files were used to obtain not only the polarization ratio, but also the individual polarization profiles and composite data files. An entire night's worth of data took less than 15 minutes to completely process, and with faster computers in the future, the algorithms could process the data in near real-time. The processing of the data was arranged to be nearly autonomous so as not to require constant attention from an operator.

The first stage in the processing procedure was the most computer-intensive, as it required manipulation of each 512x768 16-bit image file. The basic procedure was to open each image file, remove the header, and find the laser beam. There are several approaches that could have been used. Since we knew that the polarization images would consist of a very bright line on a relatively dark background, we wrote a Matlab script to look for the maximum in each of the 768 columns[†]. In contrast to our initial use with an Ar-Ion laser, LAPS was such high power that we had little problem finding the beam. However, some problems were encountered in obtaining the beam endpoint and checks had to be employed to acquire the beam end point consistently. Additionally, each camera's data was processed independently of the other cameras. Also, problems not found with the Ar-Ion laser were corrected with LAPS, insects being the main culprit as the Ar-Ion laser was used in March and April, 2001 and LAPS was used during July 2001.

After the maximum of each column was found, surrounding pixels were summed in order to get the total measured scattering volume at each altitude. The beam width was found to be approximately 8 pixels in width for the entire length of the beam and so was fixed in the program. However, this parameter could and was changed to see what effect it had on the processing. If the beam width was too large, the program would crash as it neared the end of the beam (higher altitudes) because the beam tapers (in the image) at

---

[†] The laser beam was imaged on the long length of the CCD array, *i.e.*, over 768 pixels.

these altitudes. Thus noise would be added to the beam instead of the beam itself. Although there is a practical upper limit to the beam width, a lower limit had little effect on the results with the most noticeable effect being that the resulting data plots fluctuated more indicating a larger noise component at lowered signal strengths. Beam widths of 1, 3, 5 and 10 pixel widths were tried. The algorithm also has checks to find the beam near daybreak and to reduce the influence of the presence of bugs in the beam (they leave a very bright spot in the images).

Once the beam was located and summed, the results from both polarization components for each camera for each time was saved to an individual file for closer inspection (if warranted) and for future use by other processing scripts. Typically, the polarization image files of 1.5 MB would be reduced to a single text file of about 24 KB. After the initial processing and beam determination, the polarization profile could be obtained easily. Data output from the initial processing was used as input in determining the polarization profiles as well as the ratios. The profiles were corrected for background signal, range and volume. The ratios were simply determined by dividing the output from the initial processing but as a check, the corrected polarization profiles were also divided to obtain the polarization ratio. Both approaches yielded the same result. Attached to the polarization profiles and ratios were the assigned altitudes and scattering angles. It was easier to read-in the processed data than having to reprocess the data each time it was needed.

Up to this point, the processing of the data is similar to what Stevens performed, although the implementation had to be done differently to account for imaging of the laser beam and that there were three imaging systems to consider rather than one linear diode array. The last piece of processing was directed at getting a composite data file. The principal impediments to overcome in this processing were to rectify the different beam end points and to zero-pad the files. The cause of the zero-padding was that is was very difficult to have the laser to fall on the same pixel for each camera (the Matlab routines prefer matrices that are of the same size). Having slightly different beam end points are of no concern since we did not invert any data above 200 m.

6.1.2 Presentation of Data & Initial Observations

In addition to our difficulties in analyzing and interpreting the data, we also struggled with how to present the information in such a way that would be conducive to scientific thought and reason. Obviously, we most desired plots that showed the measured polarization ratio as a function of scattering angle since this has been or primary focus throughout this thesis. However, additional plots showing both the polarization ratio as well as the individual polarization components (i.e, parallel and perpendicular) as a function of altitude and scattering angle also proved useful in our analysis. Without any further delay, we now begin to present and examine the data. However, we are going to proceed with our discussion in a slightly different manner than most discourses and manuscripts in that we are going to attempt to make the reader an active participant rather than a passive spectator. It is our hope that the reader will begin to understand the history behind our approach because it is the history that contains the learning and

experience behind much of what we are trying to accomplish here. How something is learned may be just as important as what was learned.

After careful examination of the data, we selected four representative dates that we will analyze throughout the remainder of this chapter. Shown in Figure 6-1 are the processed polarization profile components of these dates for the first 1km of the atmosphere. One particular point regarding the listed dates must be made. The given day indicates the night the data run was started (typically started around 11pm) while the given time is local time. For example, the date, July 6 at 257, shown in Figure 6-1a indicates that this data was taken on July 7^{th} at 2:57 am. The date could have been changed with additional code in the Matlab scripts; however, at the time, we were more interested in analyzing the data than making the pictures pretty. Such dates are simply a remnant of workable code and will be corrected for publications and journal articles. Let us now briefly turn to discuss each date.

Due to difficulties in getting LAPS ready for use in the NE-OPS campaign, the night of July 6^{th}, morning of July 7^{th} was the first time all three cameras were used in the field. However, the only technical problem we had was in keeping all three cameras connected over a network. After several hours, we finally abandoned trying to maintain a stable network connection and instead opted to acquire data by physically commanding each computer individually rather than from one single terminal as had been planned. For this reason, more time elapsed between images and between cameras than what we wanted. However, we were able to maintain the network on all future data runs. Thus, we viewed the July 6^{th}/7^{th} data with more skepticism than the other nights and we were not overly concerned if the data showed more variation among the cameras.

Upon examining Figure 6-1a, we see the presence of an atmospheric disturbance, possibly an aerosol layer, around 100m-200m as not only does each camera track the change but so does each polarization component. Also, cameras A & B track each other well for higher altitudes, as they should since upper altitudes have more homogenous atmospheric constituents (mostly gases). However, camera C reveals the polarization dependence caused by the interference filter (See Chapter 5). From our filter analysis of Chapter 5 and using the simple results from the Fresnel equations, this is to be expected. However, during our initial examination of the data, our first data sets showed the polarization components to be reversed. After carefully checking the laser, we were able to rectify the polarization and the data was subsequently re-processed. This was a very easy fix to accomplish and in fact, we actually needed the interference filter to exhibit a polarization response for us to have recognized the polarization problem.

The polarization profile components taken on July 12/13 at 2:57am shown in Figure 6-1b are similar to those in Figure 6-1a. Again, there is indication of a possible aerosol layer but here it is located below 100m. The polarization components match well for cameras A and B while C continues to show polarization effects from the interference filter. It turns out that the data taken on the night/morning of July 12/13 captured and monitored the progression of an aerosol layer from its beginning to its dissipation. We will examine features of this data later.

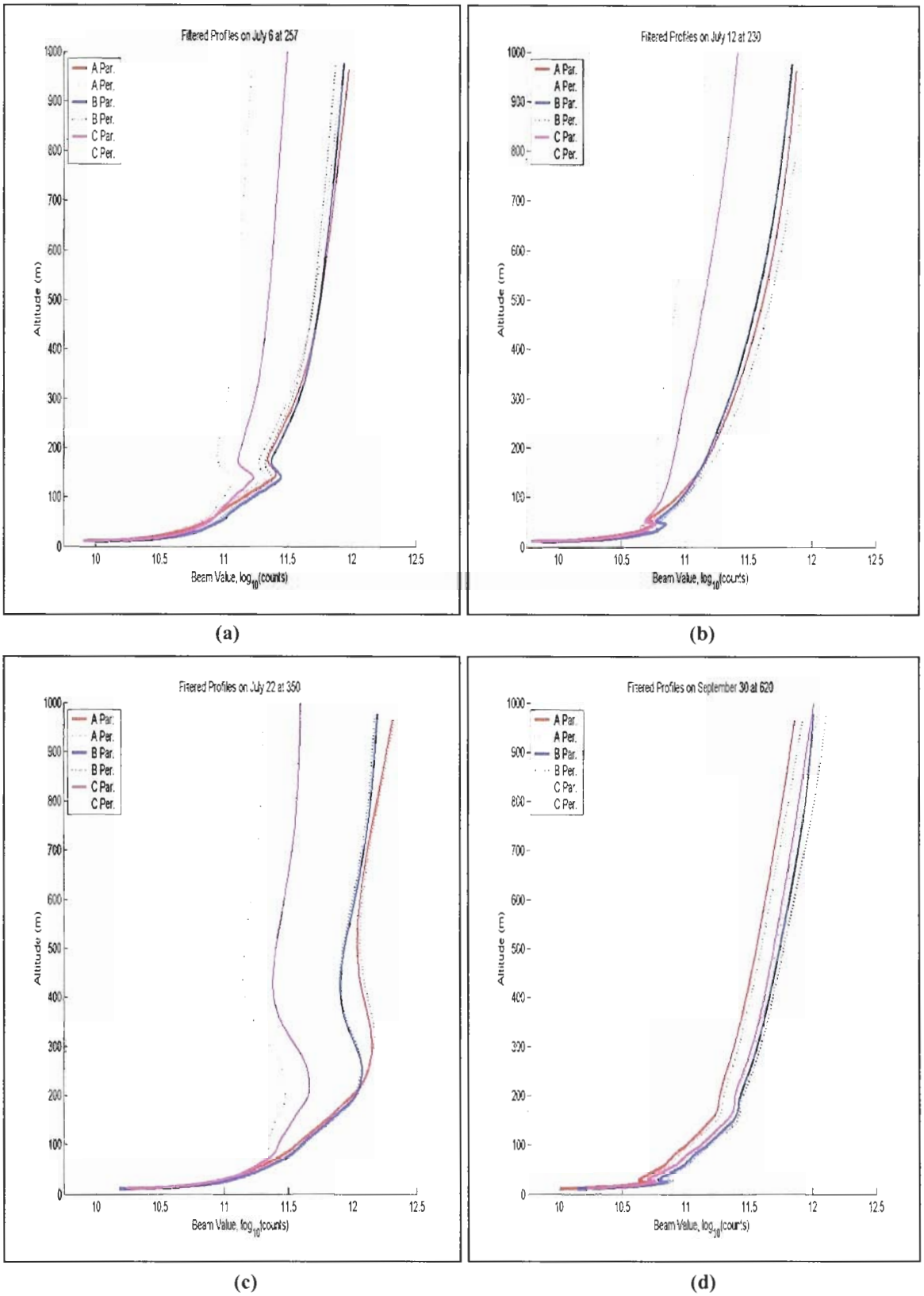

Figure 6-1: Polarization profiles for selected dates. (a) July 6/7, 2:57am, (b) July 12/13, 2:30am, (c) July22/23, 3:50am, (d) September 30/October 1, 6:20am (taken in State College, PA).

Although Figures 6-1a and b suggest that the more interesting aerosol features of the nighttime sky are located within the first 200m of the earth's atmosphere, Figure 6-1c easily counters such a generalization. It appears from the figure that there is a rather large aerosol layer from 200m-500m but this is somewhat deceiving because above ~150m, we have less and less pixel resolution for each altitude. Here, on the night/morning of July 22nd/23rd, we did not observe a strong aerosol layer or atmospheric disturbance as we found in the previously mentioned dates. However, this particular data set did show that the atmosphere was much more stable and uniform than on other nights and so is a good candidate for inversion. Also, the dates of July 22 through the 25 saw nearly every fielded instrument package operating and so there is much additional information to draw upon.

The last figure, Figure 6-1d, was taken in State College, PA. After seeing the same polarization dependency present in camera C, performing a multi-layer interference analysis and tracing the problem to the interference filter itself (see Chapter 5), we acquired data using wide-band filters. Figure 6-1d shows that not only have we corrected the polarization dependence problem of camera C but, in State College, a pronounced aerosol layer was also captured around 30m above the ground.

Based on results in Figure 6-1 and from examining other dates and times, we decided to focus our efforts on the first 100m of the atmosphere. This was primarily due to three main reasons. First, camera C's data could not be used above 100m because of the polarization dependence. At first this may seem to be a major setback but thankfully, we are not losing many angles above 100m (we also lose about 1-3m of altitude on the low side). Thus, the altitude range we will be examining for the remainder of this thesis is primarily between 13m and 100m from the ground. The second reason why we are concentrating on the first 100m of the atmosphere results directly from our initial observations which showed that nighttime aerosol layers appear to be most likely located below ~300m, i.e., below the nighttime planetary boundary layer. The last reason however is a consequence of our measurement approach and equipment setup. Higher altitudes correspond to scattering angles approaching 180°. However, from Mie theory, these angles become less and less polarization dependent and thus distinguishable information is not available. Figure 6-2 contains the same figures as in Figure 6-1 but here, the altitude has been re-set to an upper range of 300m so that the reader can see more details of the polarization profiles.

Examination of the upper altitudes of all of the data sets from the three cameras does show one important point: The polarization components do not have identical values at these altitudes. The question to the reader is, why not? After all, each camera is examining basically the same part of the atmosphere, i.e., above the PBL and at night. We expect that these altitudes contain primarily atmospheric gases and yield scattering angles that are relatively polarization independent and so each camera should measure the same value. Based on Figure 6-1, especially plot (d), we see that this is not the case. There are many reasons why the cameras do not provide identical data but principally because absolute measurements, i.e., direct measurements of either the parallel or polarization component, can be corrupted by instrumental

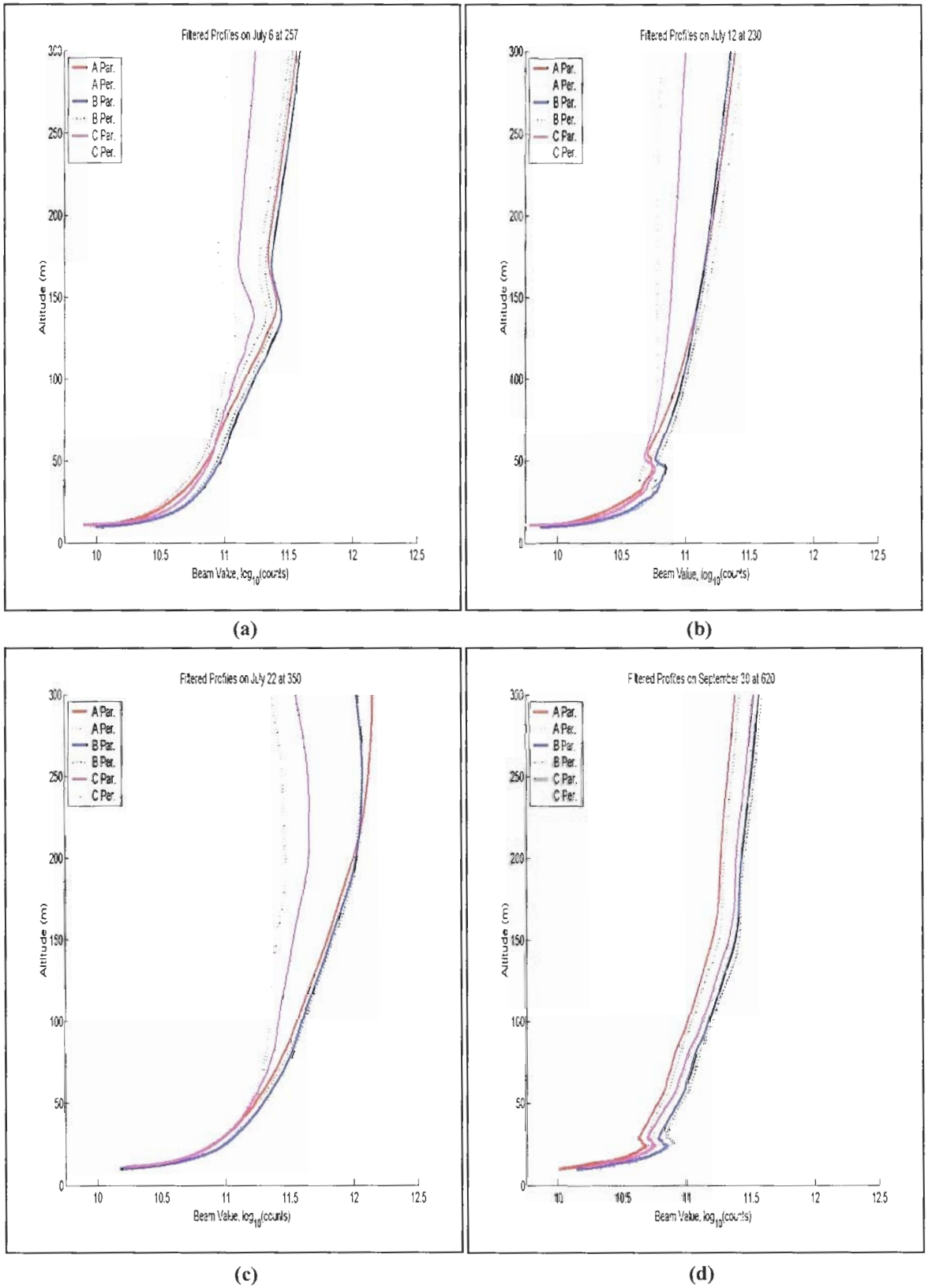

Figure 6-2: Same as Figure 6-1 except altitude range has been reduced to allow for more detail.

irregularities, differences in observed atmospheric path, and varying atmospheric concentrations. Because absolute measurements are so difficult to make with any reliability, most researchers, in a variety of fields, generally take normalized measurements, i.e., relative measurements (Bohren and Huffman, p. 135, p. 402). This is one of the primary reasons for using the polarization ratio method.

As we have already alluded to, the type of plots we are most interested in are those that show the polarization ratio as a function of scattering angle as well as altitude. Shown in Figure 6-3 and 6-4 are the polarization ratios corresponding to the dates and times of Figures 6-1 and 6-2. The polarization ratio is obtained simply by dividing the parallel component with the perpendicular component. It is these figures where the real analysis begins and so we will briefly discuss each before pursuing additional avenues of investigation.

In the left-hand plot of Figure 6-3a, we see evidence of the aerosol layer/atmospheric disturbance we noticed in our initial examination of the polarization component profiles of Figures 6-1a and 6-2a. Although we have said we will be focusing our efforts on the first 100m of atmospheric path, we have intentionally showed the first 200m of the polarization ratio for this date and time to illustrate a point. One can clearly see the bumps in the polarization ratio around 150m but with respect to the observed scattering angles, these bumps are squeezed together near 180°. Thus, due to our desire to observe a minimum altitude of 10m, we have sacrificed much of the upper altitudes. We will come back to this point later. Additional examination of the polarization ratio curves versus scattering angle for this date shows that while camera B and C appear to coincide over much of the atmospheric path, camera A is considerably different. Initially, we had attributed this difference to the approach we had used on this particular evening so we were not overly concerned. However, it was the date of July $12^{th}/13^{th}$ that caused considerable consternation.

In Figure 6-3b, we immediately see the striking presence of the aerosol layer we noticed from the polarization profiles discussed earlier. It was this plot that really stood out above the rest and began to make us re-evaluate our approach, setup and assumptions. If we had had only one imagine device as Stevens did, we would not have noticed any particular problem. However, the presence of three cameras gave us additional information to analyze and interpret, albeit at the expense of a much more complicated analysis. Upon examining the right-hand plot of Figure 6-3b, we see that the ratio peaks at a different scattering angle for each camera. However, under the assumption of a uniform nighttime atmosphere under the PBL, we would expect these peaks to be much more closely aligned. Curiously, the polarization ratio curves displayed versus altitude fit more to our expectations. It is the subject of the next sections to begin a more critical analysis in an effort to explain and interpret the data we were seeing in Figure 6-3b. For now, we continue with our initial examination of additional dates and times.

While we were in turmoil over interpreting the data from July $12^{th}/13^{th}$, the data from July $22^{nd}/23^{rd}$ had a very calming effect. The polarization ratio curves, shown in Figure 6-4a, are consistent with a stable and uniform atmosphere and we will be able to get a relatively good inversion to this particular date.

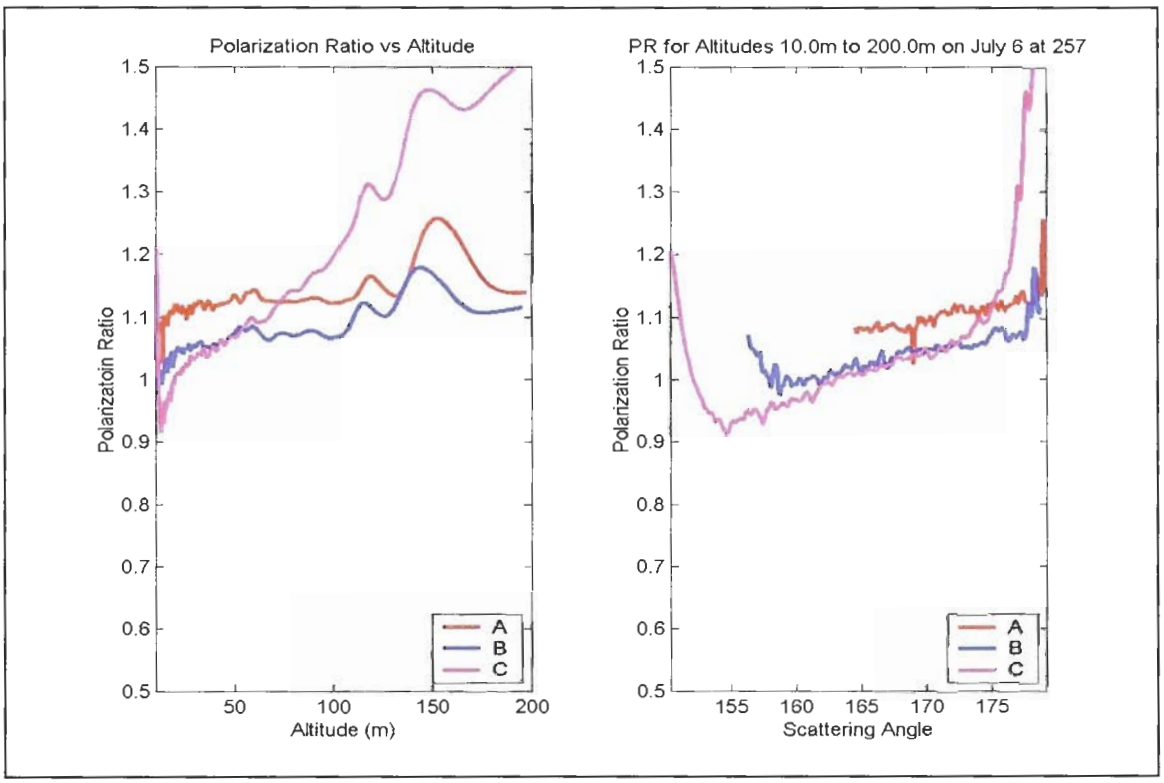

(a)

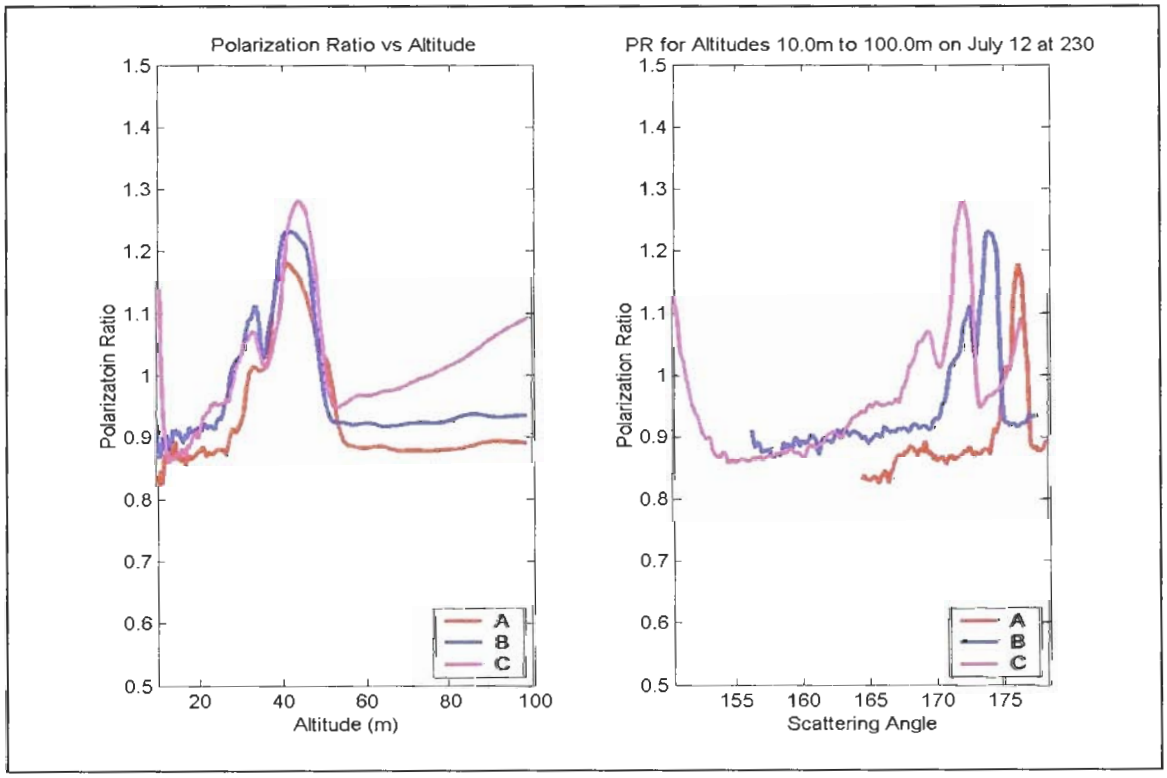

(b)

Figure 6-3: Polarization ratios for Figure 6-2 (a) and (b) respectively.

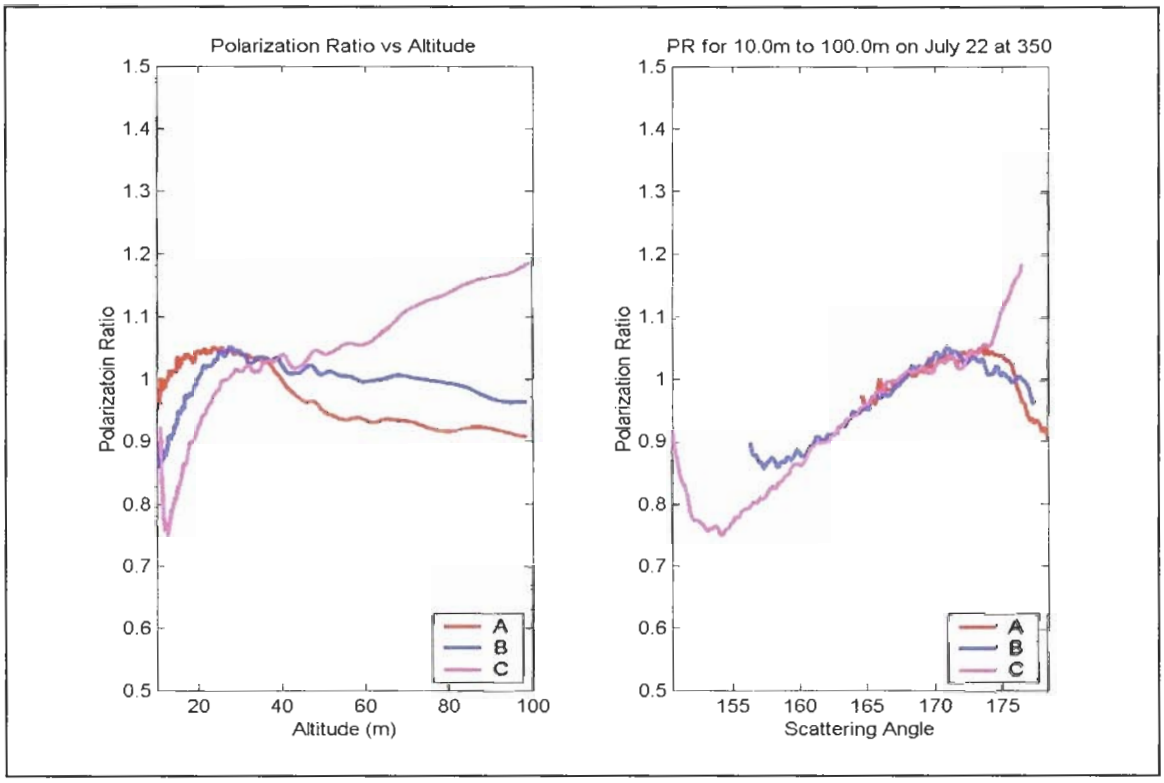

(a)

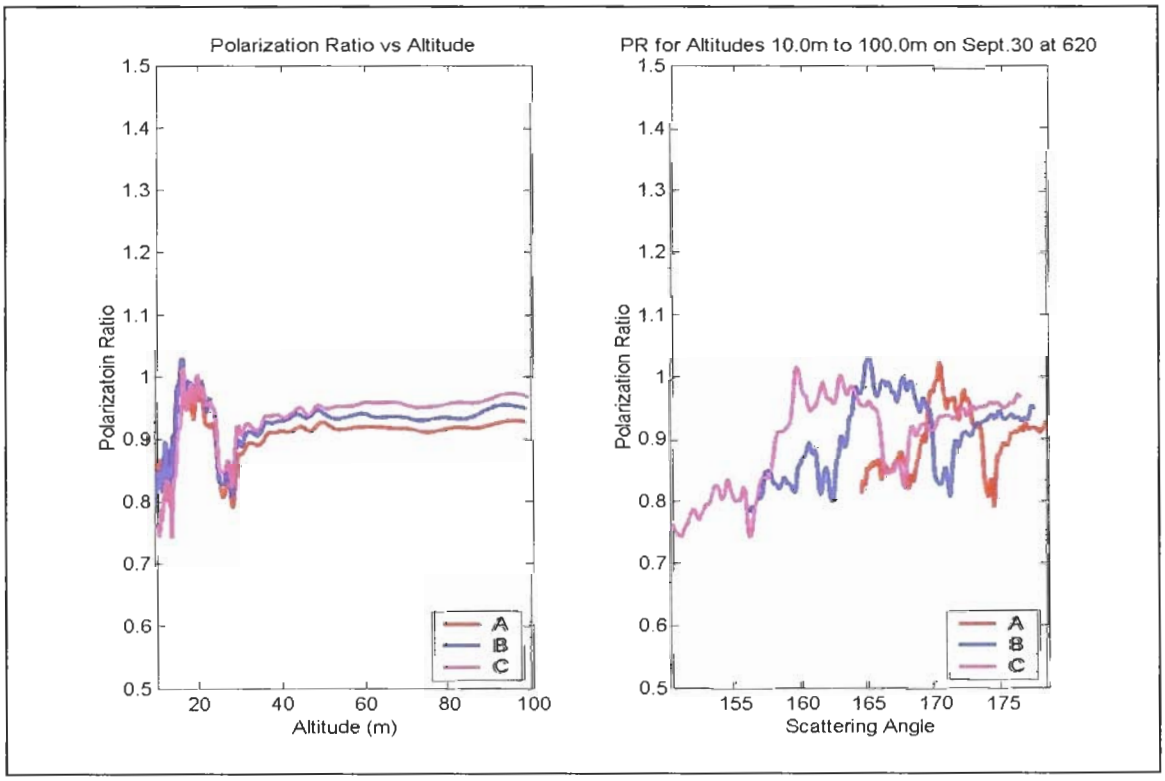

(b)

Figure 6-4: Polarization ratios for Figure 6-2 (c) and (d) respectively.

Finally, the polarization ratio curves for the State College date are shown in Figure 6-4b. The presence of the aerosol layer is clearly evident in these plots. There are two items for which the reader should take note. First, the curves track each other well over altitude but again, are translated over scattering angle, similar to the polarization ratio curves of Figure 6-3b. However, the second item to notice is that the ratio itself appears jagged, exhibiting more rapid variations than the curves of Figure 6-3b.

Because we cut off the displayed altitude to 200 m, one does not see the polarization ratio for upper altitudes. From Mie theory, because scattering becomes polarization independent near 180°, we expect the ratio to be near 1 at 180° degrees (i.e., at upper altitudes). In nearly all of our data sets, the polarization ratio was near 1, generally between 0.9 and 1.1. The reason for the difference is due to molecular anisotropy since the dominant molecular gases such as N_2 and O_2 are dumbbell shaped and not perfectly spherical. Overall, the depolarization due to atmospheric gases has been determined to be approximately 0.039, or ~4%. How the depolarization translates to the polarization ratio has not been explicitly determined. However, having the measured polarization ratio stabilize to a value near 1 was certainly an encouraging marker.

Our initial examinations of the polarization profiles and ratios for various dates caused us to re-examine our entire measurement campaign in the hopes of determining why the data was not as we expected and why there was so much variation present. Our next step is to search for possible sources of error both in our software and in our hardware.

6.1.3 Re-Evaluation of Equipment

After our initial inspection of the data, we had to ask ourselves: Did we make a mistake or overlook an important piece of information or make a bad assumption? If the atmosphere was truly uniformly distributed and the cameras were equal, then the same polarization ratio would be observed for each camera at the same scattering angle, at least to within the measurement error of each camera. From the data, this is obviously not the case. In fact the measured polarization ratios are quite different from each other. We now examine possible causes for the measured differences.

The very first item to be examined was of course the polarization dependency of the interference filters. While identifying, correcting and analyzing its impact was relatively straightforward, the polarization dependence was not the source of our problems. We have illustrated this from the data taken in State College, PA (Figures 6-1d, 6-2d, & 6-4b), which used filters that were not polarization dependent over the angles of interest. We had to look elsewhere for our answers.

Our investigation began by trying to determine what manipulation of the data would be needed for the measured polarization ratio versus scattering angle to be more closely aligned among the cameras. Our first thoughts suspected that the placement of the cameras with respect to the distance from the lidar unit could be causing an error in altitude assignment. In our setup, a square wooden board was secured to the ground and three holes were drilled to hold the feet of each camera's tripod. Thus, although the cameras were packed up each night, the boards were left so that all subsequent nights would take measurements at

the same place. Because altitude determination is based on simple geometry, it was found that the boards would have to be misplaced by a large amount for appreciable changes to occur in the location of the polarization ratio curves versus altitude and scattering angle. While we freely admit we were probably not at the precise distances from the lidar down to the ninth decimal place, we do not believe we were so inept as to misplace the cameras by up to several yards from the intended location. We concluded that the errors in distance from the cameras to the lidar were not to blame for our measurement differences.

Our next area to investigate revolved around the measurement accuracy of each camera. Our effort, documented in Chapter 5, showed that the cameras were providing measurements that were close to each other. Based on this evidence, we concluded that the cameras were yielding correct data.

At this point, we were a bit perplexed as to the source of the measured polarization differences. The filters had been corrected, the camera accuracy determined and the camera distances to the lidar examined but none of these causes were significant enough to change the polarization ratio curves. However, after staring at the polarization ratio curves versus scattering angle, we took a stab at determining angular errors. The only source of these errors that we had not yet examined was the field of views (FOVs) of the camera lenses. As it turns out, errors in FOVs can cause considerable change in the polarization ratio curves and this should be expected since it is the dependency on scattering angle in which we are most interested. We re-examined the FOVs of each lens and found that we were off in our measured values. Our initial FOVs for cameras A, B & C were found to be 15.4°, 23.7° and 31.6° and the corrected values were found to be 15.7°, 24.7° and 30.2° respectively. To illustrate our point, we left the FOVs of cameras A & B fixed and changed the FOV of camera C by a substantial amount. Shown in Figure 6-5a is camera C with a FOV of 25° while in Figure 6-5b, camera C has a FOV of 35° (we over-exaggerated the FOV for illustration only). After correcting the FOVs and re-running all of our data processing programs, we still obtained essentially the same curves. We conclude simply that while they certainly can have an impact on the polarization curves, FOVs can not account for the variation of the polarization ratio, especially since the shape of the curves are so similar.

After exhausting possible mechanistic errors, we started to think about our underlying assumptions, specifically that the atmosphere is uniformly mixed under the planetary boundary layer. We began to suspect that vertical aerosol layers must exhibit a strong altitude dependence. The first step to proving our hypothesis was to see if we could model an altitude-dependent aerosol distribution. Taking a cue from the July 12 data, we attempted to see how the polarization ratio changes by placing an aerosol layer in the altitude range of between 35m and 55m. For our first case, we decided to keep things simple so we changed only the number density of the first aerosol mode as a function of altitude and kept all other parameters constant. Also, without much reason given at this point, we also changed the index of refraction of the layer to 1.75 and kept the background aerosols at 1.38. The resulting polarization ratio is shown as a function of altitude (Figure 6-6a) and as a function of scattering angle (Figure 6-6b). While these figures are not similar in structure to our July 12 and September 30 examples, these figures do show two specific identifying factors. First, the polarization ratios for each camera show sharp transitions and

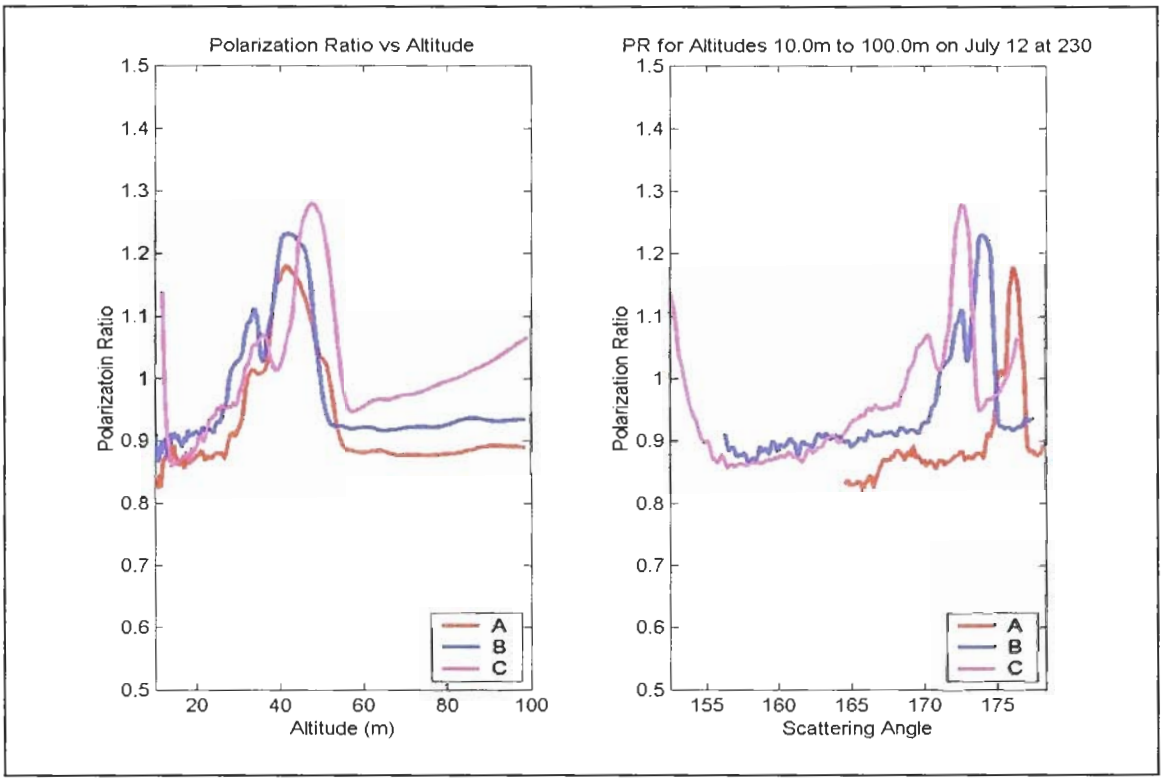

(a)

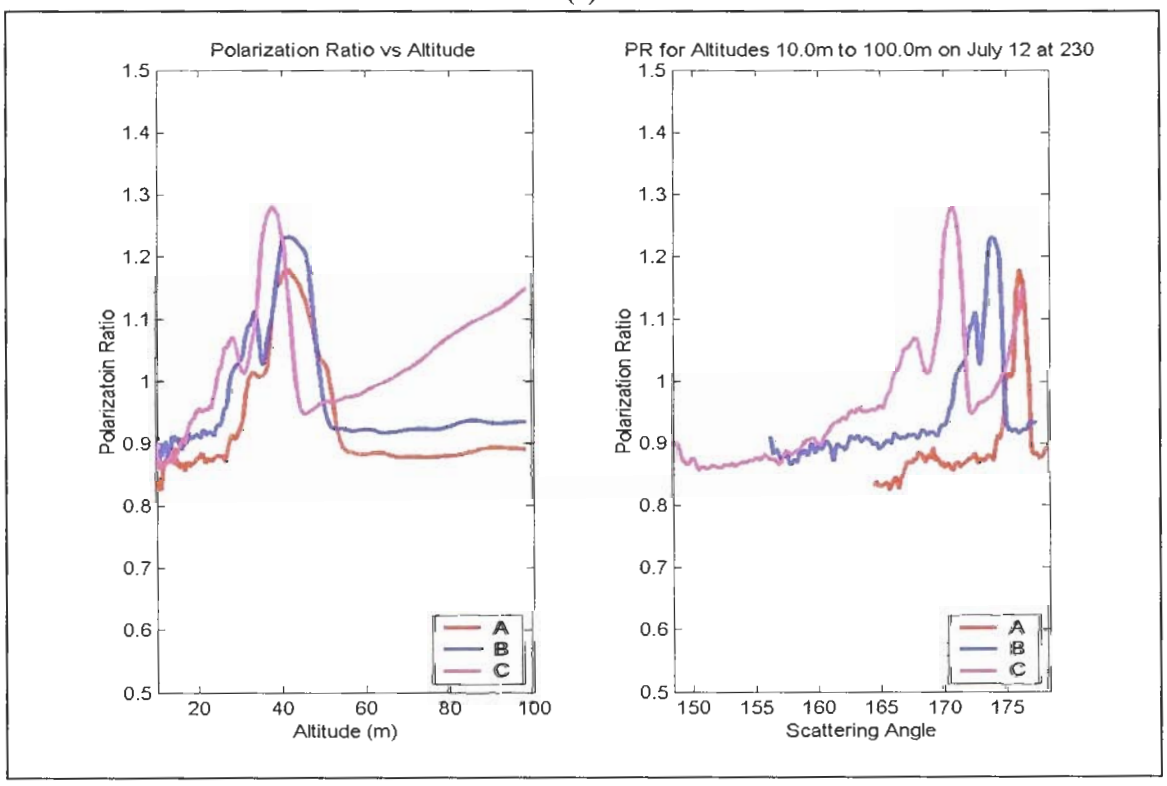

(b)

Figure 6-5: Depiction of change of camera C's polarization ratio for a FOV of (a) 25° and (b) 35°.

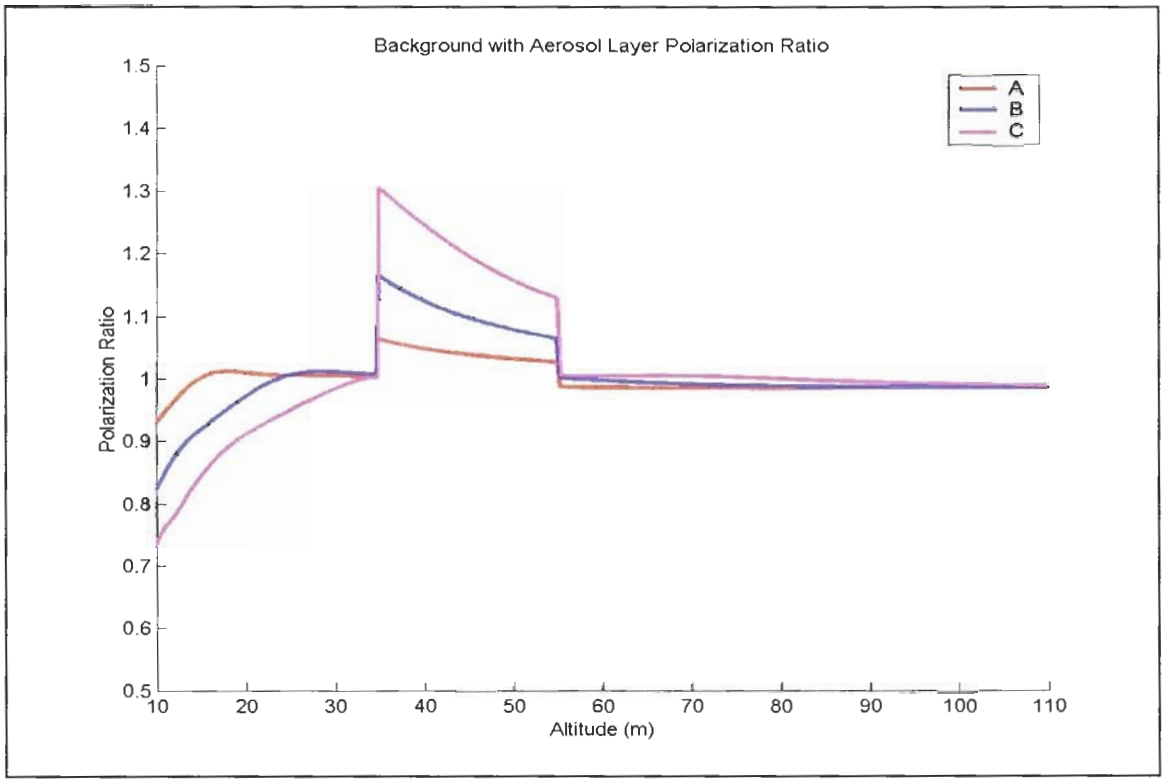

(a)

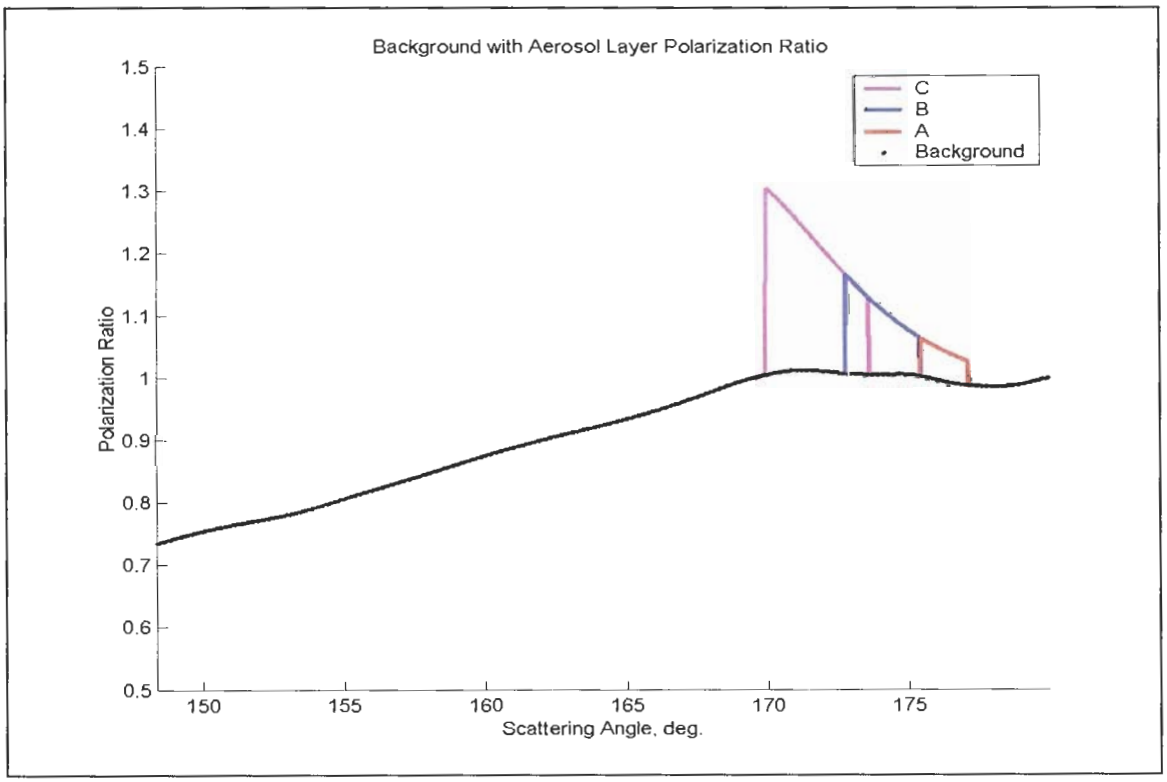

(b)

Figure 6-6: Modeled polarization ratio for a single, 20m thick aerosol layer (index = 1.75).

track each other well where the background and aerosol layers intersect in altitude. This is a common feature in the both the July 12 and September 30 data. Second, where there is overlap of the polarization ratio versus scattering angle, the polarization ratios coincide, exactly as expected. Since we did not see this particular overlap in our data, we surmise that the layer is even more variable over altitude. A second case should be examined which may be a better approximation to the observed data.

Returning to the same altitude range, we partitioned it into 1-meter segments giving for a total of 20 separate aerosol layers. Again, to keep things simple, we only changed the number density of the first mode and kept all other aerosol parameters constant (the index of refraction was also kept at 1.75). The results of this model are shown in Figure 6-7. Unlike Figure 6-6 where we used a single, 20m thick aerosol layer, here, 20, 1-m thick layers yield polarization ratio curves versus scattering angle for each camera that do not coincide where there is overlap. While these plots are certainly not conclusive, one can see that we are getting closer to approximating the altitude dependence of the aerosol layer.

We can provide additional explanation by re-examining the data from July 12 (Figure 6-3b). Let us first examine the right-hand plot. If the atmosphere was uniform, then the polarization ratio curves should be aligned, instead of translated as shown. For example, at the scattering angle of approximately 168°, camera C shows a small bump in its ratio, camera B is relatively flat at a value of 0.9 and camera A is also relatively flat at a value of ~0.88. Since these values are too different from each other and yet correspond to the same scattering angle, then the altitudes being examined contain differing aerosol distributions. While we were expecting such differences to be present, we were not prepared to see such marked difference between adjacent altitudes. Plots like those from July 22 (Figure 6-4a) were much more anticipated. From our model and from the data, we conclude that the nighttime vertical aerosol distribution under the planetary boundary layer is highly dependent on altitude. Having such a strong altitude dependence adds another undesired dimension to our analysis and makes the inversion of these aerosol layers highly suspect. We will examine the inversion process in section 6.2.

It should be noted, however, that we have not specified the exact nature of this altitude dependence. Specifically, we do not yet know if the altitude dependence affects the number density, geometric median radius, geometric standard deviation or some combination of these parameters. Truthfully, we may not have sufficient data from which to form a specific conclusion at this time.

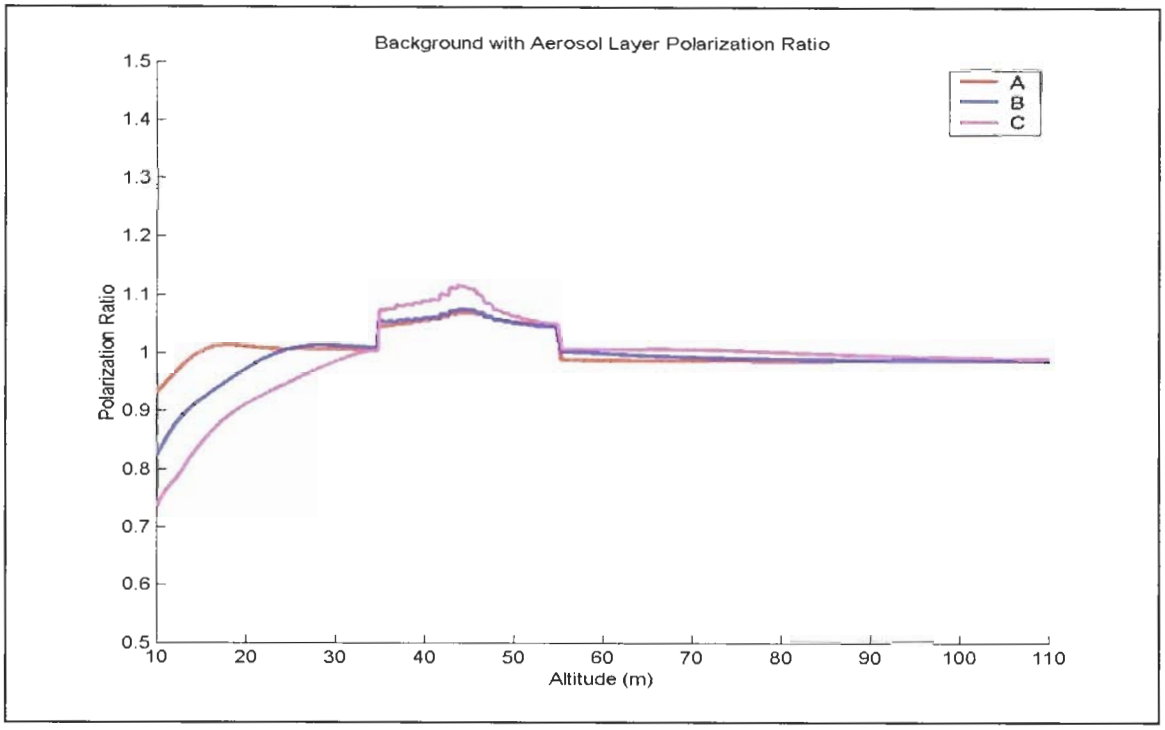

(a)

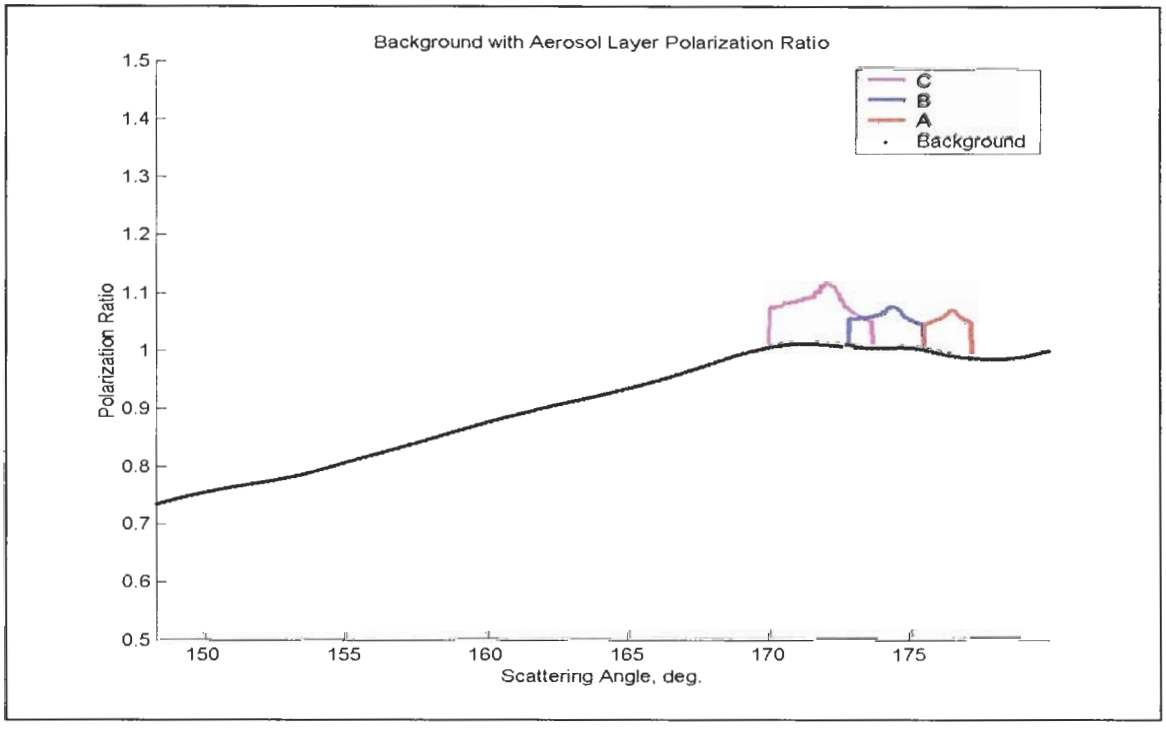

(b)

Figure 6-7: Modeled polarization ratio for 20, 1-m thick layers of varying total number density (mode 1 only, index = 1.75).

6.2 DATA INVERSION

One of the major goals of this thesis was to obtain particle size density distributions and, if possible, determine their physical makeup from the polarization ratio data. In this work, data inversion involves the determination of ten parameters (9 lognormal parameters, 1 index of refraction) that produces a polarization ratio that best fits the measured polarization ratio. Early in the course of our investigation, after an extensive review of the research literature, the difficulties we were up against in our attempt to obtain accurate particle size density distribution data from light scattering measurements became more and more clear. Such difficulties have been previously mentioned in Chapters 3 and 4 and truthfully, this work took a considerable amount of time because of our search for methods, models and approaches which may have been untried and could provide additional information. While we were not completely successful in our investigation and the effort we expended was not immediately fruitful, we were emboldened because the work was not completely in vain.

While the polarization ratio method is the focus of this work, from our research it became evident that and additional cast of supporting characters would be needed to at least corroborate, but hopefully validate, our data. Of particular importance to our work are particle samplers, which can yield particle size density distributions, and chemical sensors, which can determine the chemical makeup of the collected particulates. Additionally, basic meteorological data was also needed, such as humidity, wind speed and temperature. Although many of the instruments used during the NE-OPS campaign of 2001 were ground based, several instrument packages were either sent aloft using Millersville's tethersonde balloons or mounted on aircraft supplied by the University of Maryland and Brookhaven National Laboratory. However, over the altitudes we were examining and since we found a strong altitude dependence on the aerosol populations present, we had no hard evidence as to the distribution or chemical makeup of the aerosols we were examining. Thus, although we had additional equipment with which to draw upon, the only way we could be absolutely sure regarding our data would be to deploy sensors vertically along the laser's path, something that wasn't about to happen. Nevertheless, all hope is not lost and we can still make some inroads into the composition of the atmospheric aerosols under observation.

The results of the inversion process are not easy to obtain and while there is much uncertainty, the results nevertheless provide a quantitative analysis of the aerosol populations and even their chemical composition in such a way that hasn't been investigated previously. The reader is cautioned, however, not to expect perfect or even near-perfect results. Hopefully, the results from Stevens, combined with the results presented here, will find some benefit in future studies. Let us first start the inversion by examining more closely the results obtained by Stevens.

6.2.1 Prior Experiments

By far, the work done by Stevens has had the most influence on the work presented here as it is closest in overall methodology. All along we have used Stevens' work both as a fundamental basis for our work but at the same time, we have examined his work with a more critical eye. After all, there were several

major questions that arose during his investigation and that we have been providing answers to throughout the course of our research. However, the corroboration between Stevens' work and this thesis should not be taken too far as operating circumstances differ. In fact, we caution the reader to not make the same mistake we made early on and become overly fixated by the results present by Stevens. Expecting the data from Stevens to match the data here is a recipe for disaster.

It is assumed that the interested reader (in that we mean the reader who is going to build on this work or perform similar work) has already extensively read Stevens' thesis. The important chapter in that work as it pertains here is chapter 5. It was only through this effort and examining Stevens' work that we were able to truly appreciate both works together. Under no circumstances are we trying to disparage Stevens' work but rather, we truly appreciate the work as it is. While we cannot use Stevens' results to substantiate ours, we can still make useful comparisons so we would like to now bring in some of his results for illustration purposes.

Shown in Figure 6-8 is a representative casea from Stevens' results. The results in Figure 6-8 were reported by Stevens as a clear night example and he used only the first lognormal mode in his model. Of note however is how different the model is from the data. While we are not going to re-examine his data, we can certainly draw conclusions of our own. The reader most likely has noticed that the model curve generally stays above the data curve over most angles. Indeed, in our own data examples where we also encountered a clear night and low relative humidity, we had difficulty 'pushing' our polarization ratio

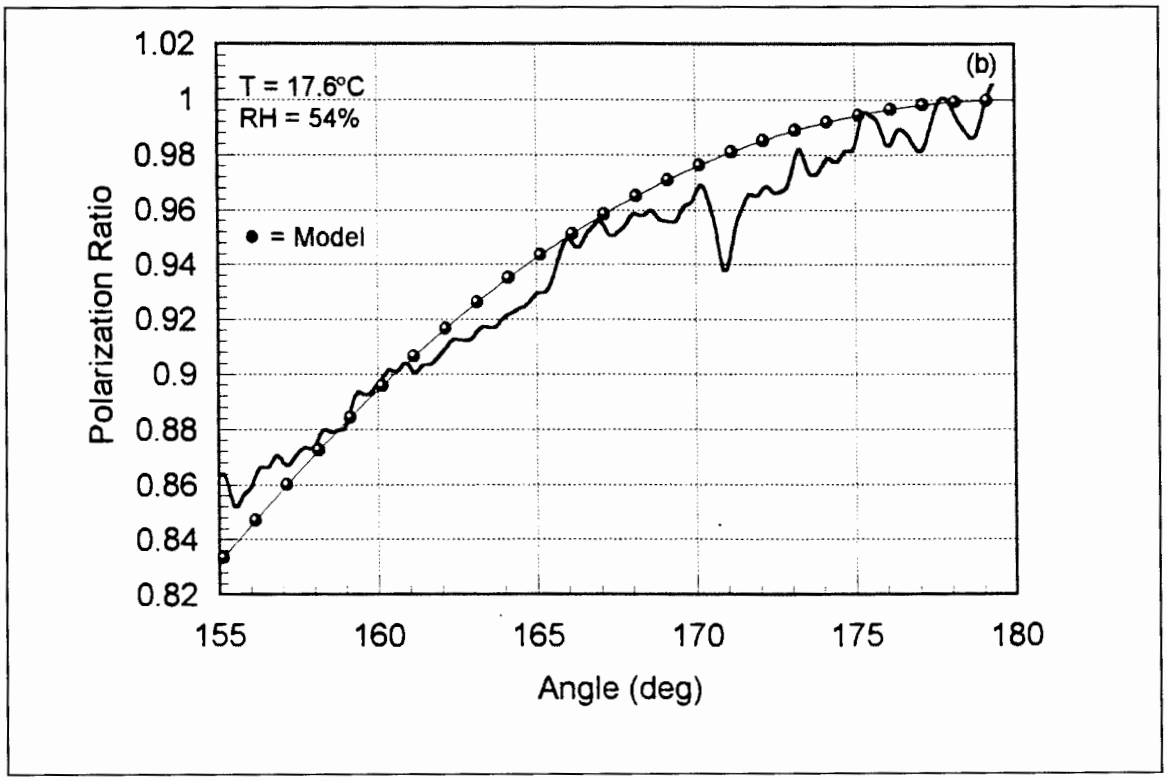

Figure 6-8: Results from Stevens (1996), figure 5.10, showing a clear night example.

model down to meet the observed data. While we do not know precisely why we had such difficulty, the similarity is still worth taking note.

Figure 6-9a is a most remarkable case from Stevens showing a rather striking fit of the model to the data, especially between 150° and 170°. Although the angles between 170° and 175° do have some noticeable differences between the model and the data, the fit is still quite good in this region as well. The fit between 175° and 180° is not good but this is certainly understandable given that the observed path length over this range was nearly 2 km and the atmospheric aerosols were undoubtedly not uniformly distributed over such a large range. Stevens goes on to indicate that this case validates using the polarization ratio method, but a single case hardly confirms the applicability of the method in the open atmosphere. This particular piece of data corresponded to the formation of radiation fog, an environment known to have large, third mode scatterers composed of water. Since these large aerosols dominate the scattering and because they are narrowly distributed, what Stevens' result actually showed experimentally was what we showed theoretically in Chapter 3: The more narrow and uniform an aerosol distribution, the easier it is to complete the inversion process (see Figure 6-9b). This should certainly come as no surprise to those who have used Mie theory and more general scattering theories extensively.

Upon comparison of Stevens' data with our own, we did find some similarities, especially in his attempt at suggesting possible curve fits. His data clearly showed that most attempts at the inversion will only be able to ballpark aerosol parameters but in circumstances where atmospheric conditions become uniform, the inversion can produce good results. With respect to our own data inversion, we should expect similar results.

6.2.2 Inversion of 23 July 2001, 3:50 AM

As we have previously mentioned, we have chosen to this particular date to perform an inversion because the polarization ratio curves (Figure 6-4a) among the three cameras show good agreement. We hypothesize that the atmosphere at this particular time was stable over the atmospheric path from the ground to approximately 100m. To prove this hypothesis, we must examine data from other sources. Such an examination will certainly add credibility to our analysis and may even aid us in our inversion process. Fortunately, most of the equipment for the NE-OPS campaign was up and running so there is a good deal of information available to us. The interested reader must understand that the polarization ratio method that we are using in the open atmosphere can not stand alone as an independent measuring technique (see Chapter 8 for more information) – It must be paired with several independent devices in order to form a complete picture.

6.2.2.1 Atmospheric Picture – Information from Supporting Instruments

The first pieces of information to be examined are the basic meteorological parameters such as temperature and relative humidity. At the onset of each data set, we recorded the above parameters and also made simple visual observations regarding local atmospheric conditions. For the date and time in

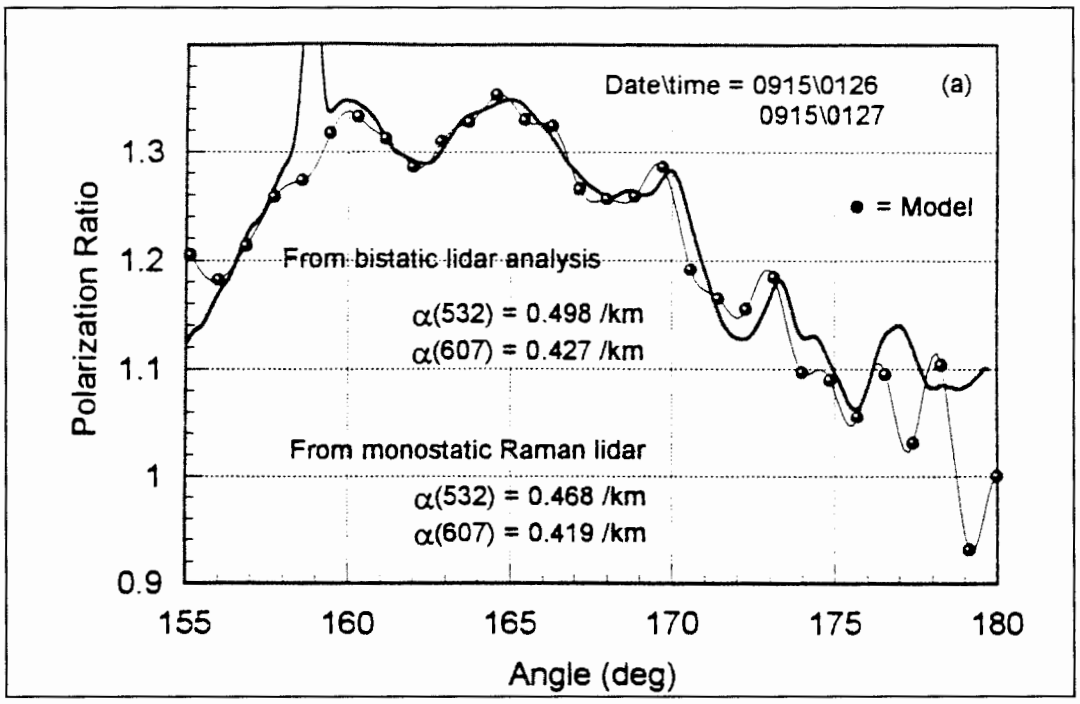

(a)

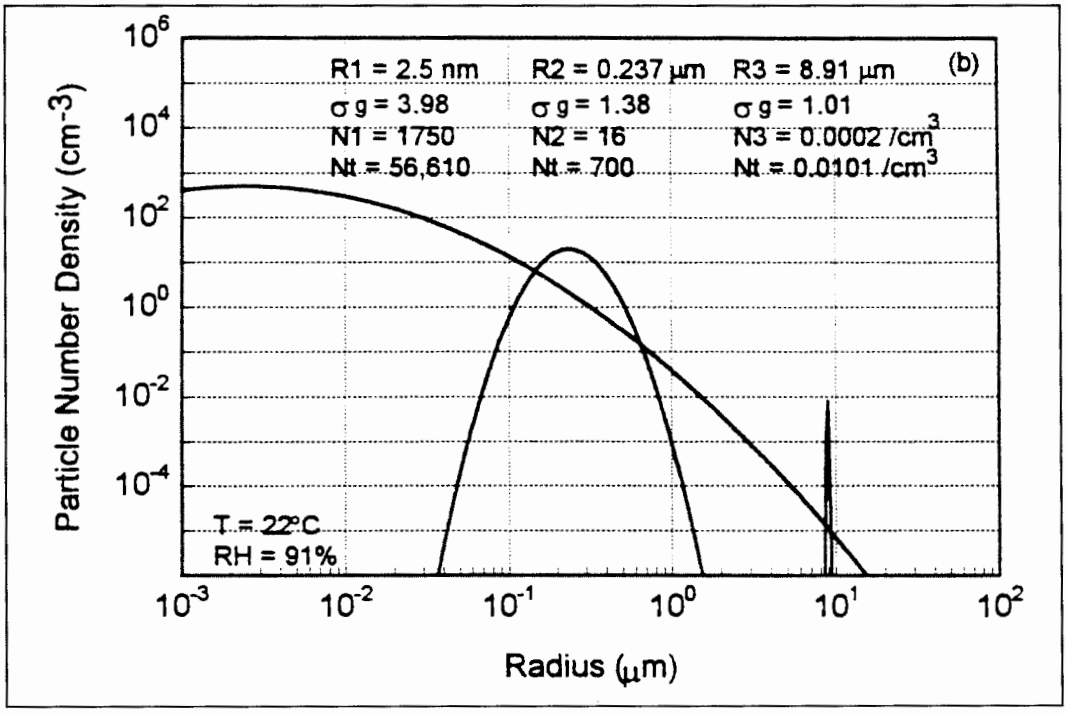

(b)

Figure 6-9: Results from Stevens (1996), figure 5.18, (a) showing a very good fit of the model to the data and (b) the corresponding lognormal number density distribution.

question, the relative humidity was measured to be ~91% and the temperature found to be 18.9 °C (66 °F). These measurements were obtained from the ground-based meteorological tower (Figure 6-10). Throughout the night of July 22 and into the early morning of July 23, the relative humidity exceeded 80%, a condition shown to be desirable for particle condensation into spheres (Philbrick and Li, 2000; Stevens, 1996).

Since we are examining a vertical atmospheric path, it is also advantageous to examine data from LAPS. Figure 6-11 shows the water vapor while Figure 6-12 shows the extinction for this time period. We will examine the water vapor and extinction at 3:50am on July 23 (UTC time 07:50). From the plots, we see a pronounced increase in the atmospheric content of water vapor in the lower altitudes (Figure 6-10) and at the same time, there is a sharp increase in the extinction (Figure 6-11). Taken together, these plots give a strong indication of the presence of wet aerosols. We realize, however, that the lidar instrument is a far-field device and so the data it collects for low altitudes (<500 m) may not be entirely accurate. Indeed, the first altitude provided by the lidar instrument begins above 100m (outside of our observation window). However, we feel that it can still provide useful information about the uniformity of the overall vertical path under the nighttime planetary boundary layer.

To overcome some of the measurement and near-field limitations of the lidar unit, additional assets in the way of balloons and aircraft were also used to obtain direct measurements of the properties of the vertical atmosphere. Of particular note was a large tethersonde balloon operated by Millersville University.

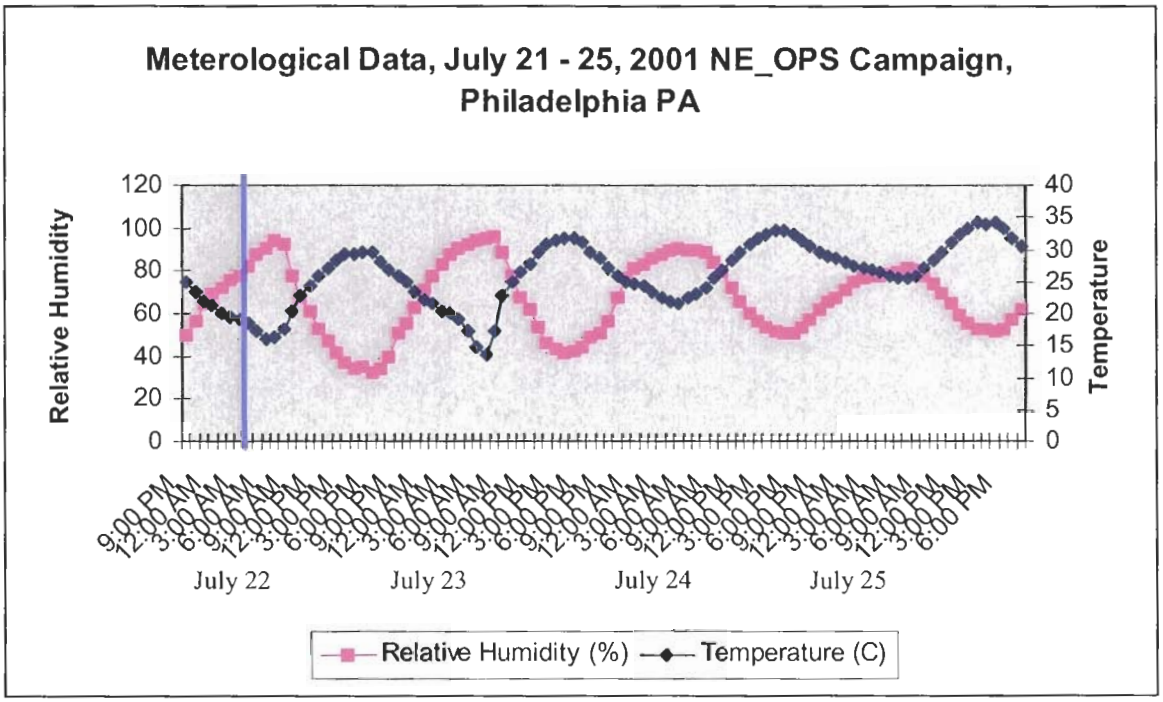

Figure 6-10: Basic meteorological data for the desired time period. The blue line indicates the time of our data set.

In addition to a ground based particle sampler, this large balloon was also outfitted with particle sampling devices that were used to measure particulate matter with an aerodynamic size less than 2.5 microns (i.e., $PM_{2.5}$) at altitudes of 100m, 200m, and 300m. A plot of the data for the time under consideration is shown in Figure 6-13.

From Figure 6-13, we see strong evidence of the differences between daytime and nighttime mixing. During the day, (UTC 10:00 to 20:00), the particle samplers match well over altitude but during the night, the atmosphere exhibits much more variation. For our interested time (July 23, 3:50AM or 7:50 UTC), there is a good deal of variation in $PM_{2.5}$ over the entire observed altitude range. However, from the ground to about 100m, the data shows less variation on this particular date. These results further substantiate our claim that the aerosol and particulate matter profiles are uniform during nighttime observations at this time.

While we have examined a good deal of information, the information that could have made the most impact would have been particle size distributions over altitude. However, no single instrument is capable of obtaining particle size information over the ranges we are most interested in (1nm to 35 μm). We have also found it difficult to obtain particle size information in the literature, as most researchers seem to settle for cumulative data such as that given by $PM_{2.5}$ and PM_{10} measurements. By far, the most difficult particle size information to obtain is that for very small particles (1nm – 100nm). Because, such small particles have shown to cause health risks to small children and the elderly, much research is begin conducted in

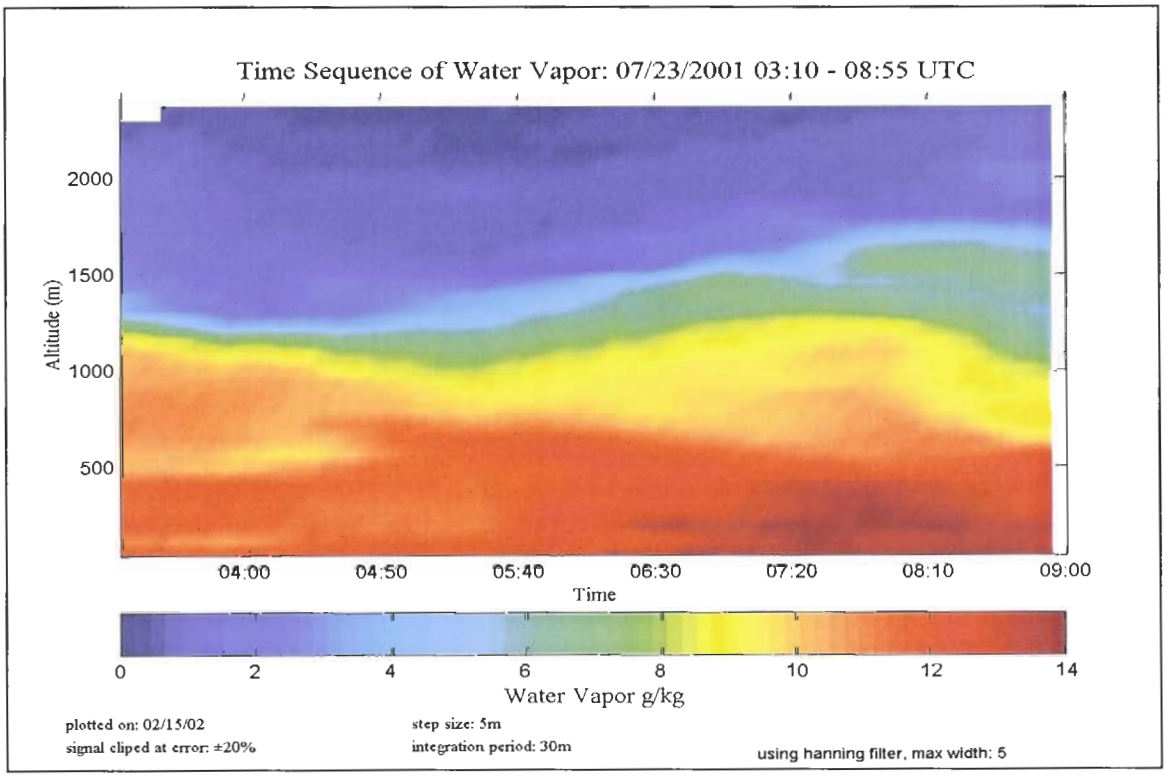

Figure 6-11: Evolution of water vapor for the given time period.

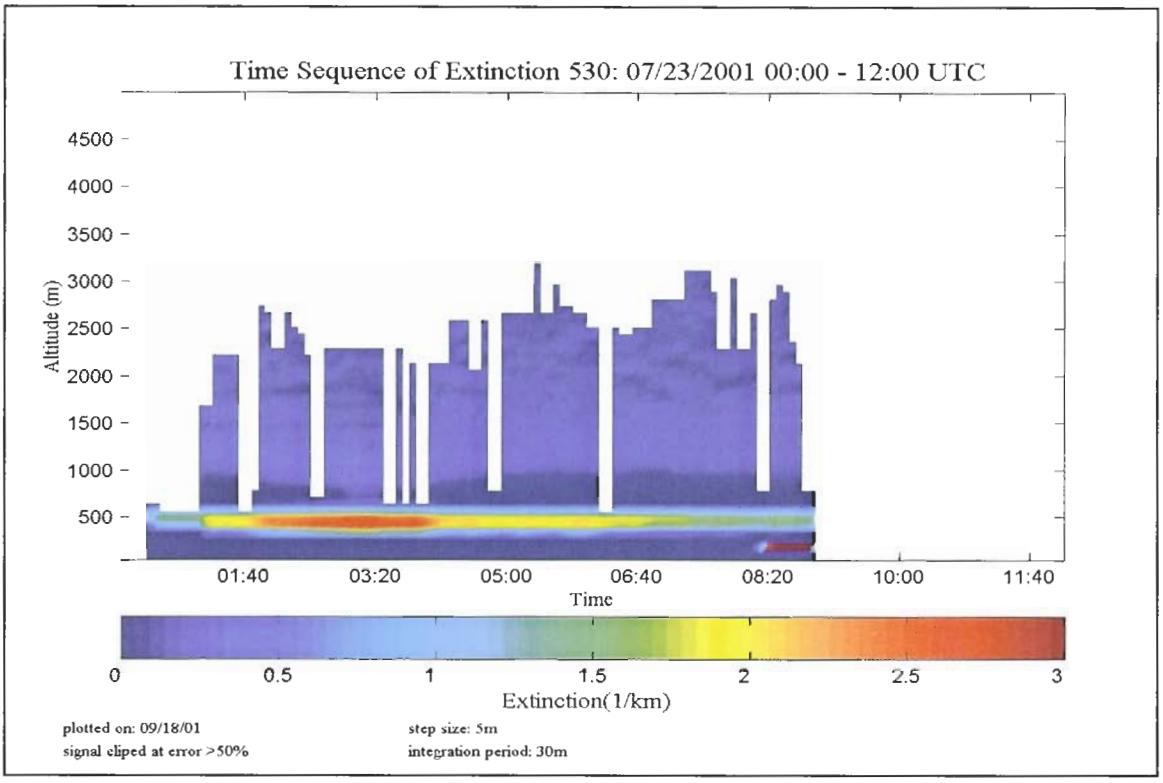

Figure 6-12: Summary of extinction for the given time period.

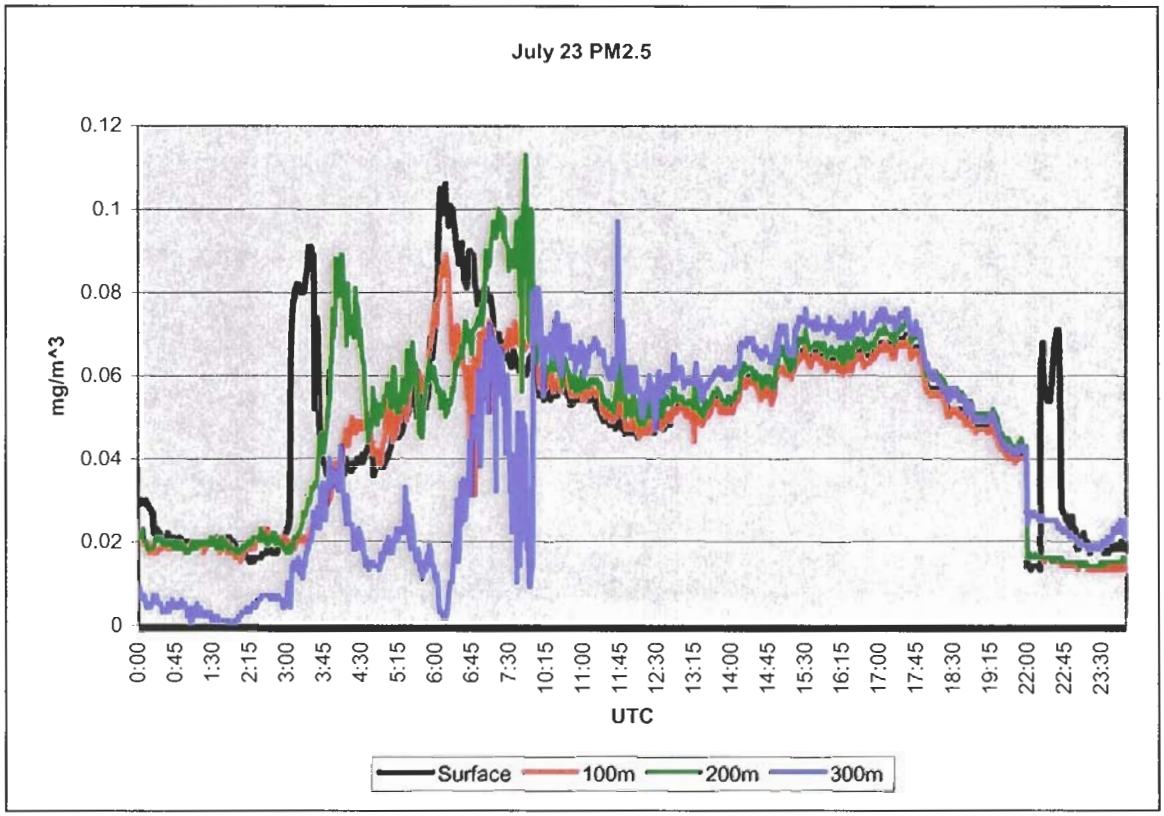

Figure 6-13: Collected particulate matter versus altitude obtained by Millersville large tethersonde balloon. UTC corresponds to local time of July 22, 8:00pm to July 23, 8:00pm.

understanding and analyzing these small particles. In the NE-OPS campaign, several ground-based small particle analyzers were deployed which yielded small-particle size-distributions. One of theses instruments was Carnegie Mellon's Scanning Mobility Particle Sizer (SMPS). Tim Raymond, a researcher developing and using the SMPS device, provided the author with the following description:

> *The SMPS is composed of a Differential Mobility Analyzer (DMA) and a Condensation Counter (CPC). The DMA has a central rod to which a voltage is applied. The incoming particles are charge-neutralized in a Krypton-85 particle neutralizer to attain a nearly Boltzmann distribution of charges centered around 0 charge with most particles having a 0, ± 1 or ± 2. The central rod has a negative voltage that attracts particles of positive voltage. There is a laminar flow of clear air around the rod. Particles of the correct mobility will travel through the air flow and out a narrow sampling gap to the CPC where they are counted. Particles that are too big or too small will exit in excess air or get stuck on the rod so that by choosing a particular voltage, only particles of a given size and +1 charge will be sampled at any given time. The instrument samples by ramping through voltages equivalent to about 10 nm to 300 nm diameter particles. All particles sampled are counted in the CPC which contains a 400% supersaturated butanol vapor and a laser for counting particles, under this supersaturation, every particle grows large enough to be seen by the laser. The data is resolved into 64 size bins on a logarithmic scale with the raw data being the total number of particles in each size bin which is then converted to #/cc or whatever else when the flow rates are known*

A sample of the data obtained by the SMPS for our interested date is shown in Figure 6-14. Additionally, the SMPS measures dry particles and since we know that water is a necessity to our scattering experiments (promotes sphericity) and has a large, identifiable effect on the polarization ratio (see Stevens), it is difficult for use to use the data taken from SMPS directly. Unfortunately, no lognormal curve fits were performed on the SMPS data at this time but the interested reader is directed to Chapter 8 for more information on a possible tool to accomplish such a task. As a note, the data given by SMPS is relative number concentration as a function of particle diameter, D_p and the time scale is local time (not UTC).

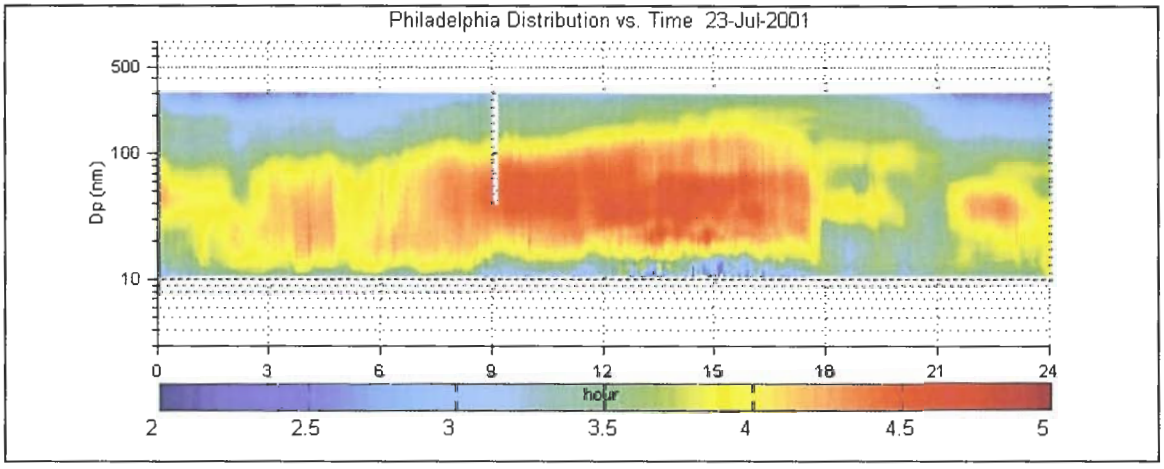

Figure 6-14: Relative concentration of small particles obtained by SMPS. Time shown begins midnight on July 23 and goes to midnight July 24.

The data from SMPS does show considerable variation over a typical 24-hour period and shows the presences of a substantial number of particles during afternoon hours, occasionally revealing a bimodal structure. However, we are obviously most interested in the nighttime hours. Initially, it was thought that perhaps the first aerosol mode could be essentially fixed primarily because its effect on the polarization ratio and scattering angles is very small in terms of structure. Indeed, our results of section 3.4.3 appear to suggest that changing the parameters of the first aerosol mode changes the polarization ratio but is not nearly as influential as the 2nd and 3rd modes. However, the data from the SMPS does show that the particles in the ultrafine and fine aerosol range can change significantly over the course of an evening, albeit slowly.

Examining the data from SMPS presents a question regarding Stevens' results. One of the troubling results was that Stevens fit his data using a very wide (large geometric standard deviation) first mode. It has been suggested that lognormal distributions are based on physical mechanisms where each mechanism may cover about 2 size decades, perhaps 3, but not more (Whitby and Davies). Stevens' first mode extended from 1 nm to nearly 100 μm, a range of about 5 decades. Perhaps he actually had a fourth mode which he discounted as being too difficult to model or perhaps another set of credible lognormal parameters could have been found. Indeed, in our own inversions, we too used an abnormally wide 1st aerosol mode in several instances and found this to fit the data adequately. In any event, while we may not be able to use the specific number density concentrations from SMPS (they exclude water content), we may be able to utilize the structure of the distributions and relative concentrations.

From Chapter 3, we know that the index of refraction has a large effect on the polarization ratio. Although we can not conclusively obtain the index, we can at least support our choice of index based on supporting evidence. Figure 6-15 shows the measured sulfate concentration for the two-week period of July 17, 2001 to August 1, 2001. On July 23, the sulfate concentration only began to rise near sunrise and although it peaked during the afternoon hours, the concentration again returned to very low levels by nightfall. Also, Figure 6-16 shows the measured elemental carbon (EC) and organic carbon (OC) concentrations for the same time period. Neither EC nor OC was found to be in abundance for the time period under investigation. It has been suggested that a useful index of refraction for a U.S. East coast aerosol that contains sulfates, nitrates and soot (carbon), is 1.45 + j0.005 (visible). The Air Force Geophysical Data Handbook (1986) lists an index of refraction for aerosols composed of sulfate to be 1.43 + j1e-8. Since our information shows neither sulfate nor carbon present[†] in appreciable amounts, we suggest that an index between 1.33 and 1.44 would be valid (no imaginary index). Unfortunately a better estimation of the index is not possible at this time and we are forced to examine a variety of cases in our inversion process.

From all of the data we examined, we indicate that we have justified our hypothesis that the atmosphere for the date in question, July 23 at 3:50am, was uniformly mixed and had a large moisture

---

[†] Nitrate is typically not found in the summer in the Northeastern United States and so was not measured.

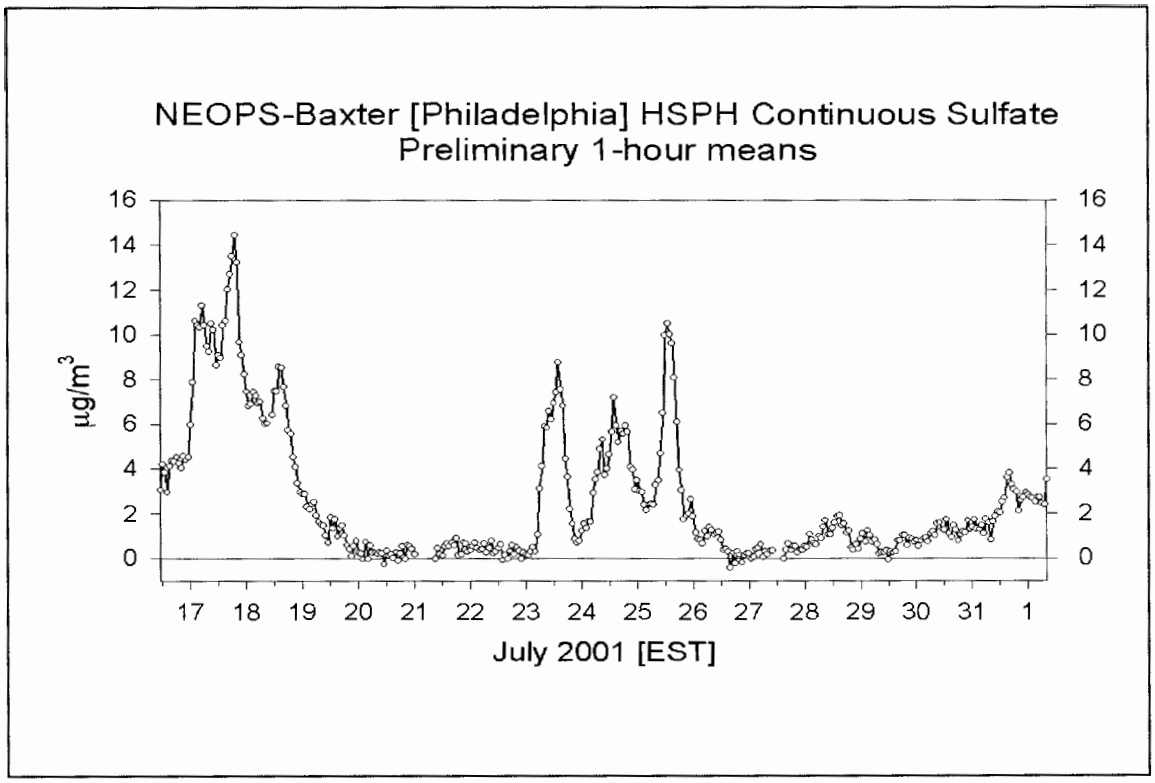

Figure 6-15: Sulfate concentration measurements, NE-OPS, Philadelphia, 2001 (Harvard).

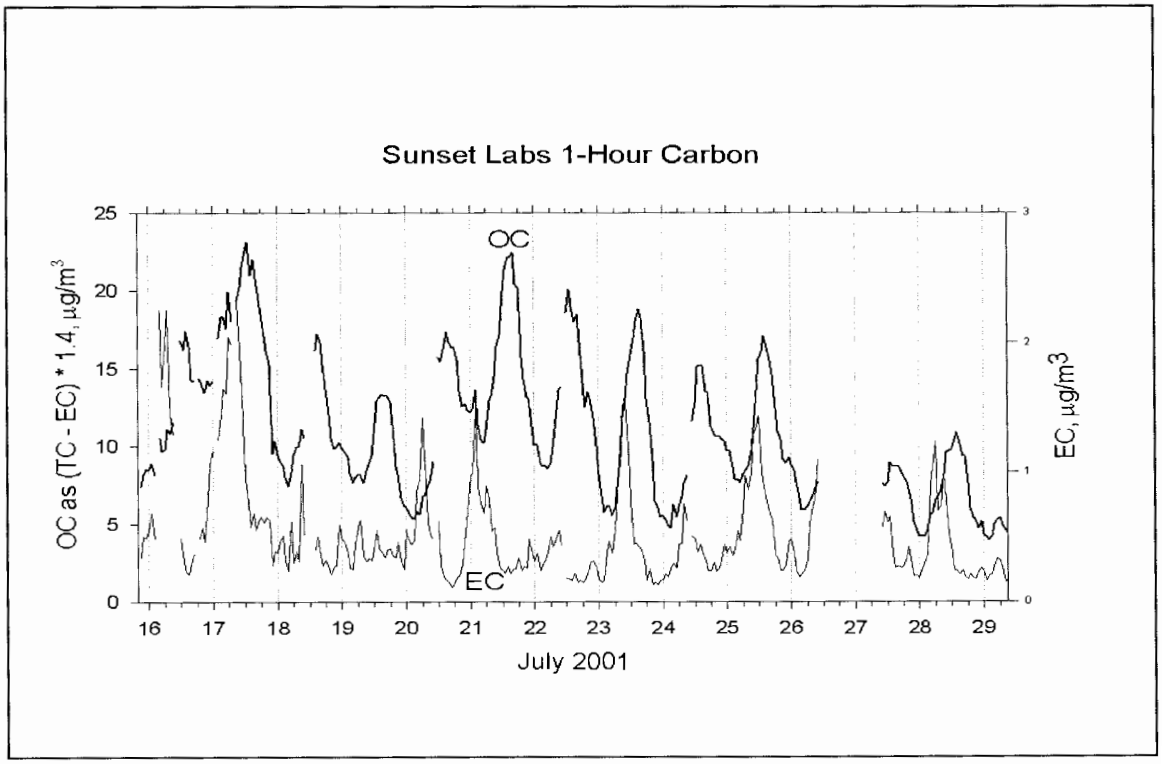

Figure 6-16: Elemental and organic carbon measurements, NE-OPS, Philadelphia, 2001 (Harvard).

content. Such an examination of separate and independent sources should serve to indicate two important points to the interested reader. First, it takes a significant amount of supporting information to substantiate our results. The reason for this is that we are still in the stages of scientific investigation and not in an engineering developmental stage. We simply do not have enough information to completely stand on our own at this point. Second, although one may have a lot of different sources of information, understanding and analyzing all of these sources is also quite difficult. Sometimes analysis can lead to paralysis.

6.2.2.2 Inversion Using Fixed Index of Refraction

Given all of the supporting information we examined in the previous section, one may think that the inversion process will be easy to perform. Unfortunately, inversion of data taken in the open atmosphere is never easy to perform since often one is dealing with incomplete information and is forced to make suppositions based on what little data is available. We have already encountered such supposition in our range estimation of the index of refraction. Ideally, we are trying to obtain a perfect fit of the data to the model. However, given the complexity, dynamics and uncertainty of the open atmosphere, we will consider it a success if we can find a reasonably close match.

We were hoping to have an automated program to perform the inversion for us. Stevens indicated that he used a "brute-force" method for his inversion that basically consisted of manually inputting the parameters, running the results and comparing the resulting curve with the data. Stevens repeated this excruciatingly tedious process until a reasonably close fit was obtained. Stevens also mentioned he used a Newton-Raphson inversion technique once he found a reasonably close fit. However, this particular method suffers from poor global convergence and we have doubts if Stevens actually had much success in obtaining optimized parameters.

Learning from the difficulties Stevens had in his inversion process, we, along with help from Dr. Hans Hallen of North Carolina State University, began to investigate using a non-linear least-squares (NLS) routine to aid us in inverting our polarization ratio data. Although much work was done on the NLS routine, we were unable to have it invert simulated polarization ratio data due to problems the routine has when it encounters very large numbers. Specifically, the NLS routines takes derivatives of the polarization ratio and evaluates the result for each of the parameters to be optimized (assuming a fixed index of refraction, for a trimodal distribution this would be 9 parameters). Thus, when the derivatives were evaluated near an inflection point, the result could lead to very large numbers thereby causing the NLS routine to crash. While we believe the NLS routine can eventually be made to invert the polarization ratio data, it will require serious efforts with computer science and mathematics principles, both outside the purview of this thesis. Chapter 8 contains much more information on the NLS routine we investigated. For now, we too had to resort to using a brute-force manual method to accomplish our inversions.

Figure 6-17a shows a reasonable fit of the model to the data using a refractive index of 1.33. For a point of comparison, we also included the polarization ratio due to a pure molecular[†] atmosphere. Since the data curves are very different from the molecular ratio curve, we conclude that there must be aerosols present. Building on the supporting information of the previous section, we kept the inversion simple by using only the first aerosol mode. The lognormal distribution and corresponding parameters are shown in Figure 6-17b. Our fit is similar to what Stevens reported for a clear night sky, although we differ in the choice of index of refraction.

Although Figure 6-17a suggests that the model and the data appear to match well, if we change the axis scale to zoom in on a portion of the data, as shown in Figure 6-18, we see that the model does deviate noticeably from the data. The question then becomes, how much can the model deviate from the data and still be considered a reasonable fit? The question is non-trivial and relies heavily on satisfying conditions of sphericity and homogeneity of the particles under observation. However, taking the simplified approach used by Stevens (Stevens, pp. 140 – 141), we can determine the standard deviation of the polarization ratio, σ_R, given the pixel standard deviation, σ_P, of each camera (See Chapter 5). The results for the data set of July 23 at 3:50am are shown in Figure 6-19. Immediately we recognize that such small standard deviations in the polarization ratio, σ_R, will not allow the range of each camera's measured data to overlap the other cameras. Thus, perfect fits of the model to the data, even under the best of circumstances, will not be possible. The best we can hope for is to estimate the range of the parameters we can use.

Figure 6-18 shows that there is a considerable amount of ripple in each camera's measured polarization ratio. Because the data of Figure 6-19 shows that the cameras are highly sensitive, these ripples can not be explained away as noise. Our examination of the polarization ratio in Chapter 3 suggests that these ripples could be due to the presence of larger sized particles. Figure 6-20a shows a suggested fit from including the 3rd aerosol mode and Figure 6-20b shows the corresponding lognormal distribution.

The question we would like to answer is: How well does the model fit the data? Since we cannot obtain a fit of the model to the data within the error range of each camera, we will not be able to perform a quantitative error analysis for each parameter. However, we can at least suggest to the reader the possible, yet reasonable, ranges of each parameter. Our process will be as follows. Starting with the given fit of the data, change one lognormal parameter while holding the others fixed. A limit is reached on the varied parameter when the resulting curve deviates noticeably from the measured data. For right now, we will hold the index of refraction constant (See section 6.2.2.3).

As an example, let us first consider the total number density of the first aerosol mode, N_{T1}. This particular parameter is generally most responsible for the overall magnitude of the polarization over scattering angle. In essence, N_{T1} may be considered a bias used to lift or raise the total polarization ratio curve to a desired level and while not always true, this approach has worked well for our atmospheric work. Figure 6-21a shows the polarization ratio with a value of $N_{T1} = 0.7e8$ #/m^3 while Figure 6.21b uses N_{T1} =

[†] Molecules were assumed spherical.

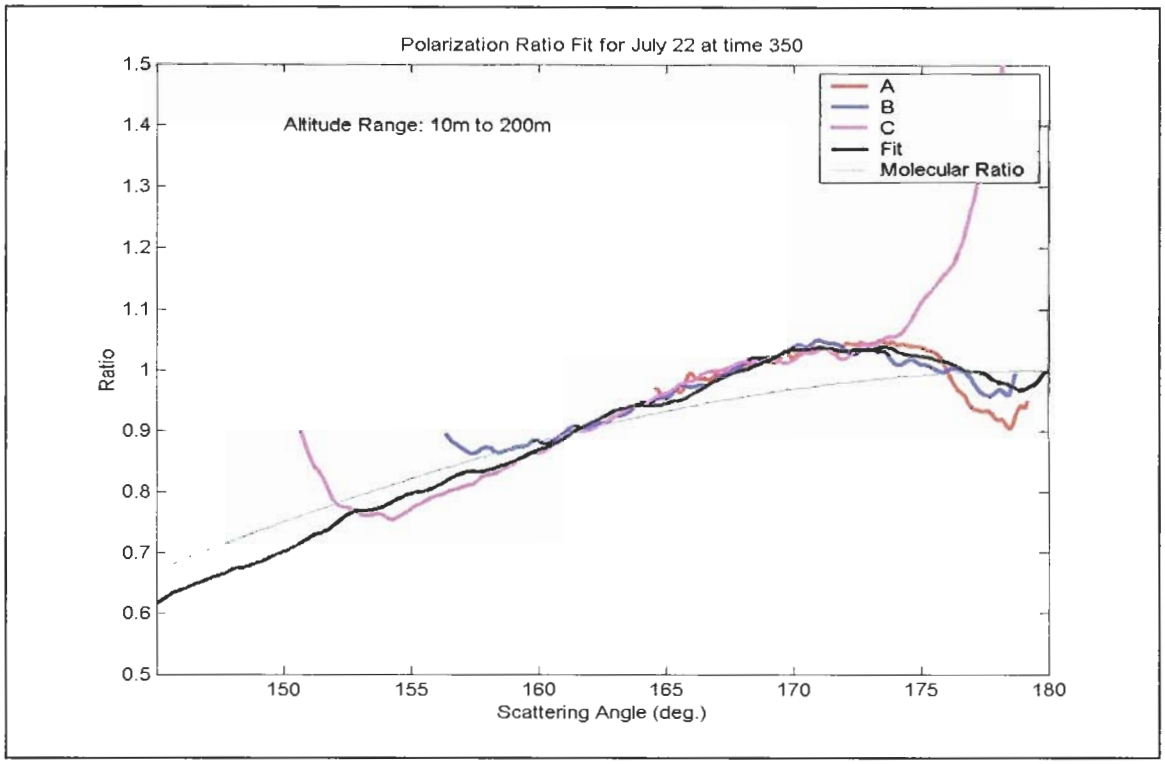

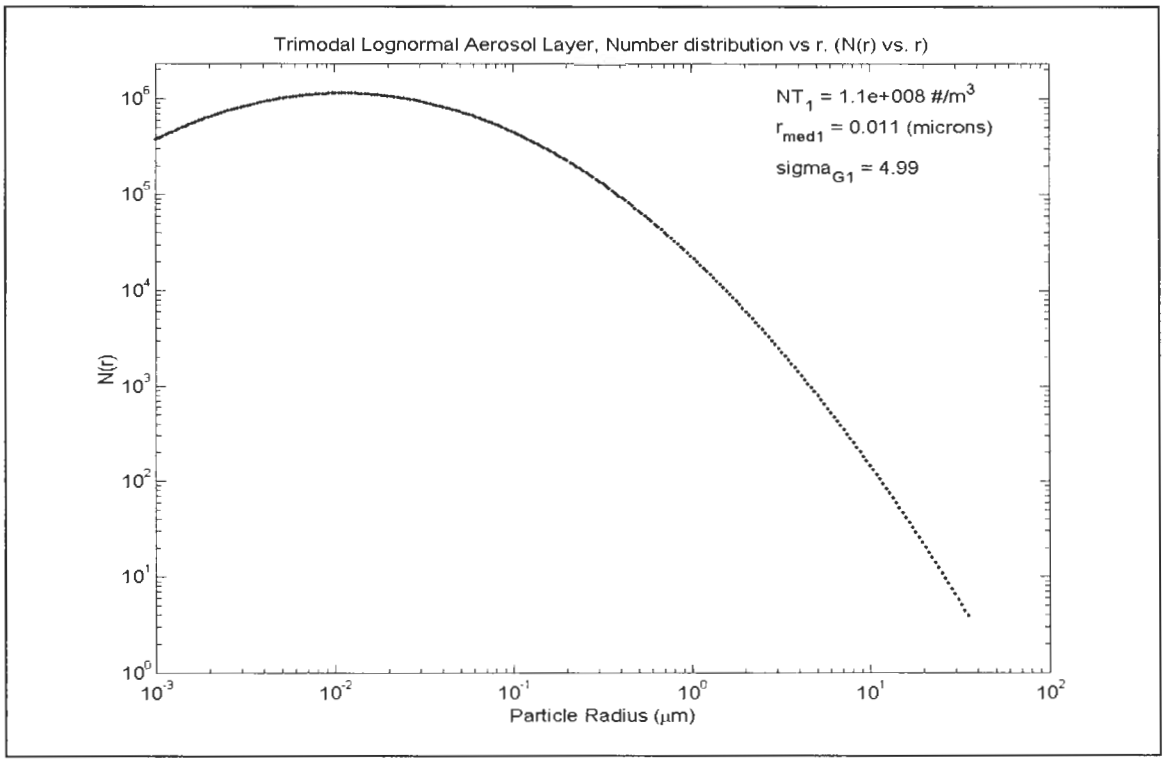

(b)

Figure 6-17: (a) Single mode lognormal fit of 3:50am, July 23, 2001. (b) Lognormal distribution.

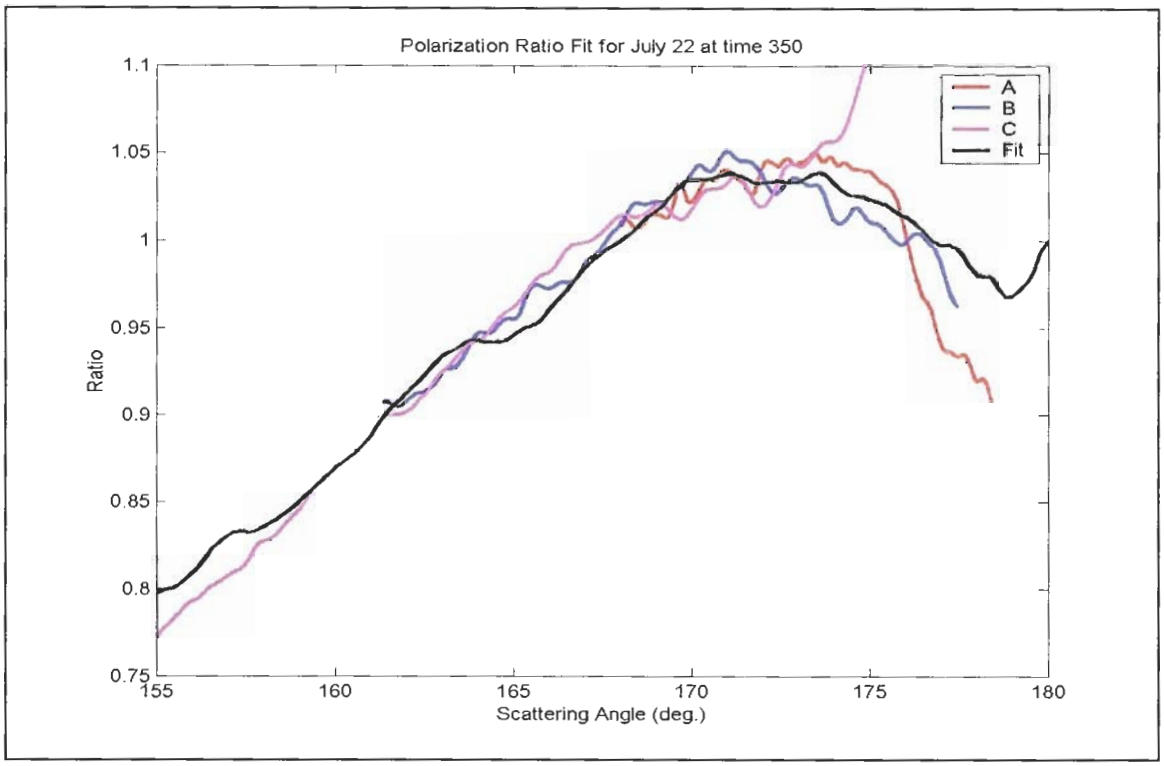

Figure 6-18: Closer view of the data and fit of Figure 6-17a.

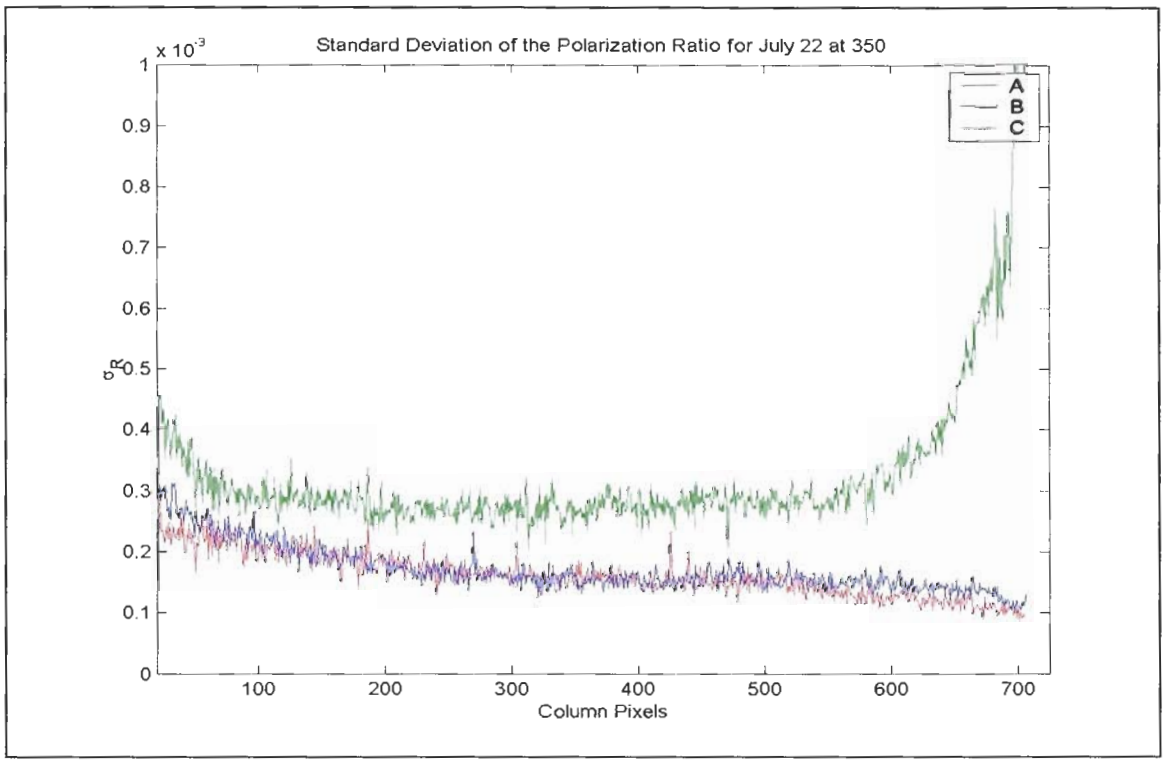

Figure 6-19: Standard deviation of the polarization ratio for 3:50am, July 23. Data shows cameras to be yielding highly accurate measurements.

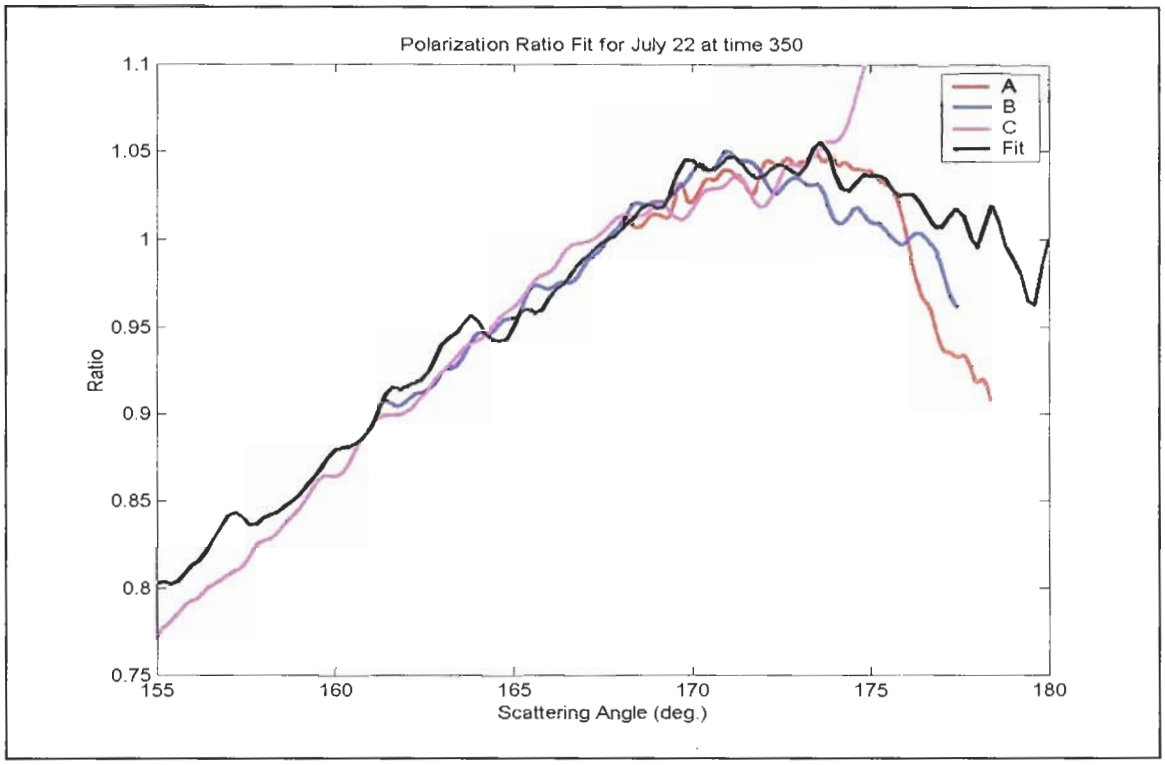

(a)

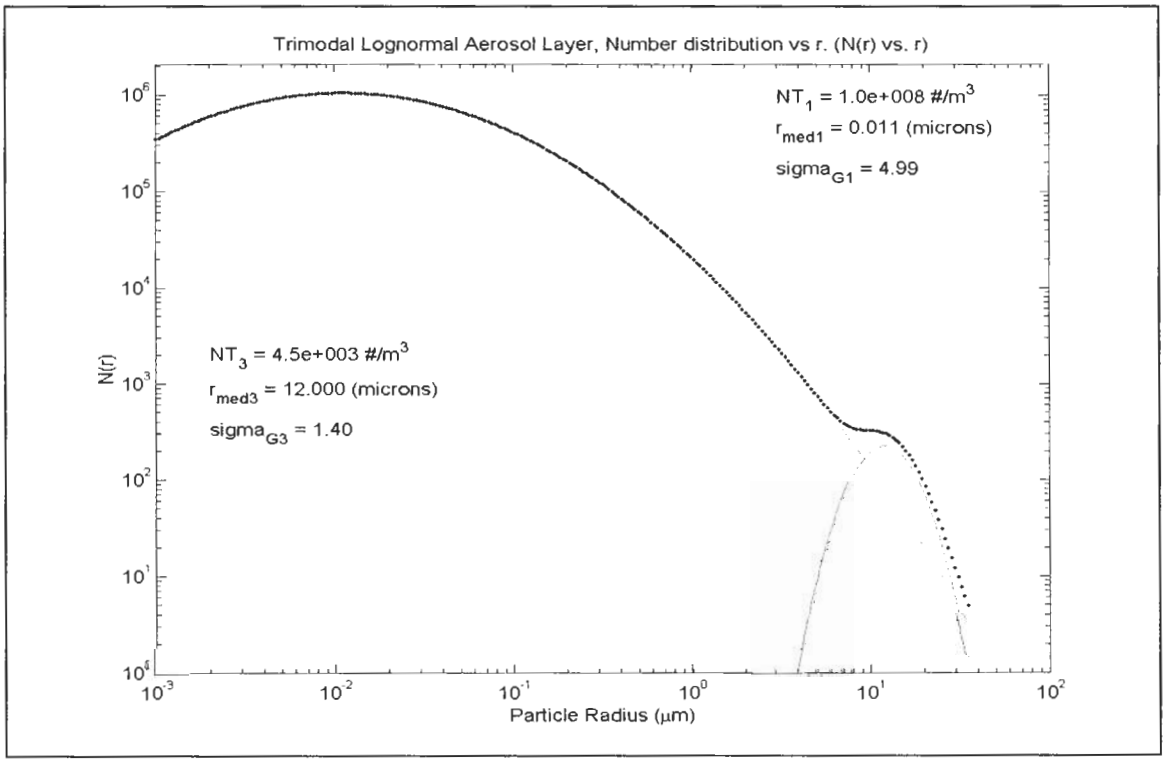

(b)

Figure 6-20: (a) Fit using 1st and 3rd aerosol modes (Index = 1.33). (b) Lognormal distribution.

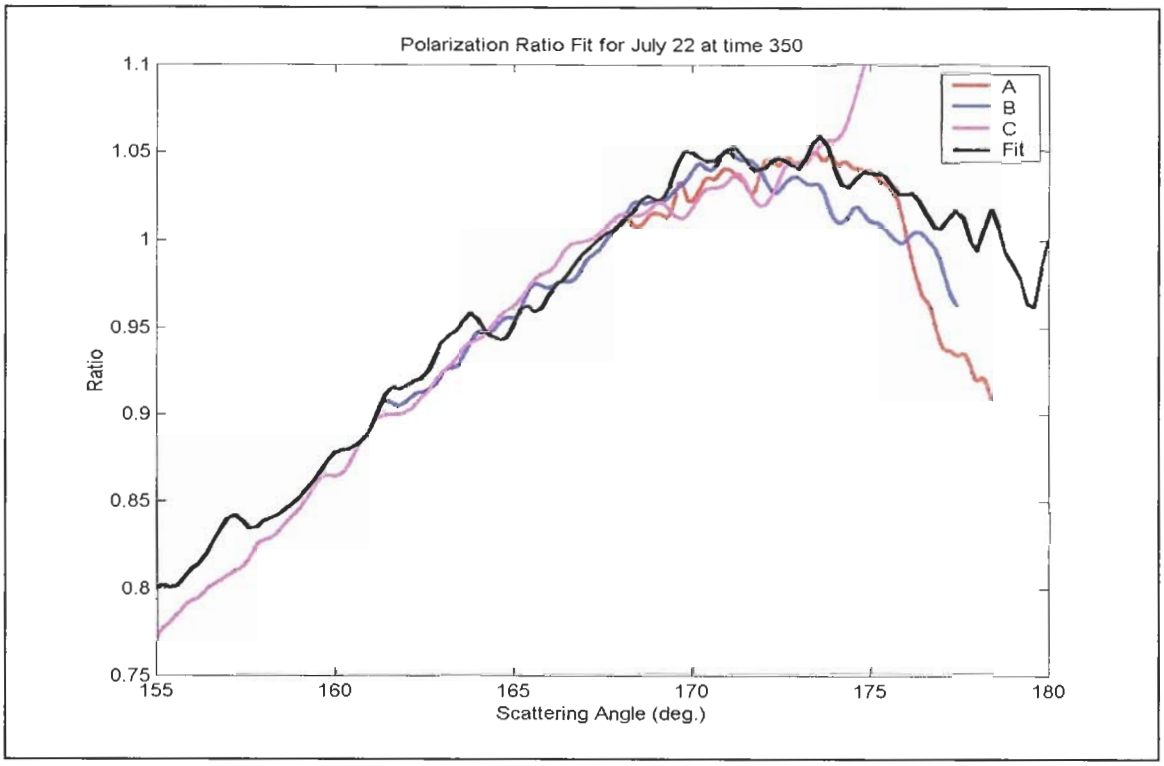

(a)

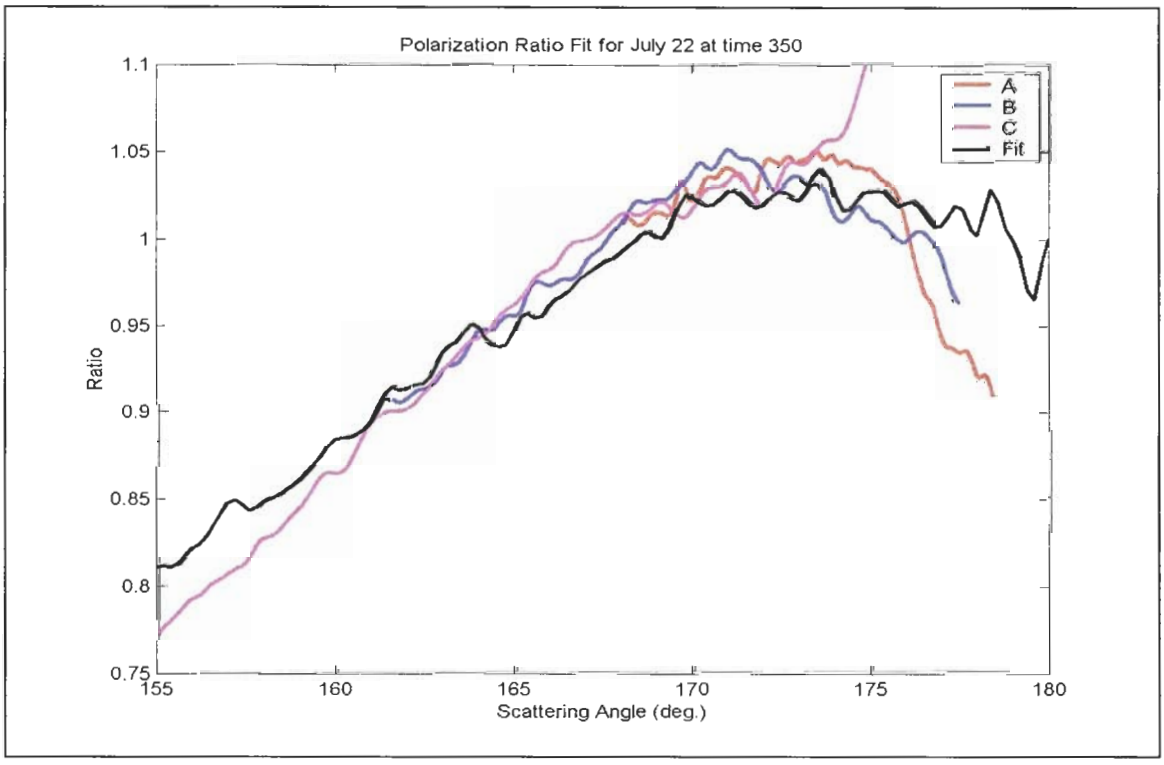

(b)

Figure 6-21: Range of the polarization ratio fit for (a) $N_{T1} = 0.7 \times 10^8$ and, (b) $N_{T1} = 1.2 \times 10^8$ #/m^3.

1.2e8 #/m^3. These values then become the range of N_{T1} for the given index of 1.33. For the remaining parameters, we found r_{med1} ranged between 9nm and 12nm, σ_{g1} ranged between 4.65 and 5.1, N_{T3} ranged between 1000 #/m^3 and 6000 #/m^3, r_{med3} ranged between 8μm and 13μm, and σ_{g3} ranged between 1.25 and 1.55. Along with the inversions using other indices of refraction, these ranges are tabulated in Table 6.1, in the next section.

6.2.2.3 Inversion Using Variable Index of Refraction

One of the main investigative points in this thesis revolved around the index of refraction, its effect on the polarization ratio and subsequent influence during the inversion process. Because of the environment in which he was working, Stevens used a fixed index of refraction of 1.38. Although he did attempt an inversion using an index of 1.53, he did not provide any reasoning behind his choice of this higher index. In the NE-OPS campaign, we were fortunate to have access to chemical information of the atmospheric constituents and so we are in a slightly better position to justify a choice of refractive index. However, as we now show, even with this additional information, it is possible to obtain more than one physically realizable inversion to a given data set.

Since Stevens used an index of 1.38, it may prove beneficial in the way of comparison to examine the inversion of our July 23 data using this index. Figure 6-22a shows a suggested fit of the polarization ratio data using the first and third modes and an index of 1.38 while Figure 6-22b shows the corresponding lognormal distribution. Upon comparing the parameters of Figure 6-22b with those using an index of 1.33 (Figure 6-20b), we see that the nominal values of the N_{T1} and σ_{g1} parameters are considerably different between the two cases. Additionally, while the rmed1 of Figure 6-22b is outside the range given for the 1.33 refractive index, all of the 3rd mode's aerosol parameters are within the same range.

Additional fits using indices of refraction of 1.40 and 1.44 are shown in Figure 6-23 and 6-24 respectively. Comparison of the lognormal parameters for each index shows that the 3rd aerosol mode's parameters are relatively close while the 1st mode's parameters can deviate appreciably. What remains is to determine the range each parameter has for each index of refraction. Table 6.1 summarizes the results for each case. Based on all of the information we have at our disposal, the best choice of index of refraction appears to be between 1.40 and 1.44 for the location, date and time of this particular data set.

We have still not yet determined which of the fits in Table 6.1 most represent the aerosol content in the atmosphere. Using the data of Table 3.4, we find that we have obtained values that are consistent with several atmospheric environments but not completely consistent for any one environment. While the values of Table 3.4 are representative and somewhat generic, we would expect our inversion parameters to be somewhat more in line with the given data. In order to better understand the quality of our fit, we must have access to particle distributions directly, taken at the time of measurement. Fortunately, we have such information for this particular time and date.

The Harvard research team operated a particle sizing instrument for the NE-OPS campaign of 2001. This instrument, unlike CMU's SMPS, had a somewhat larger range and also sized aerosols in their natural

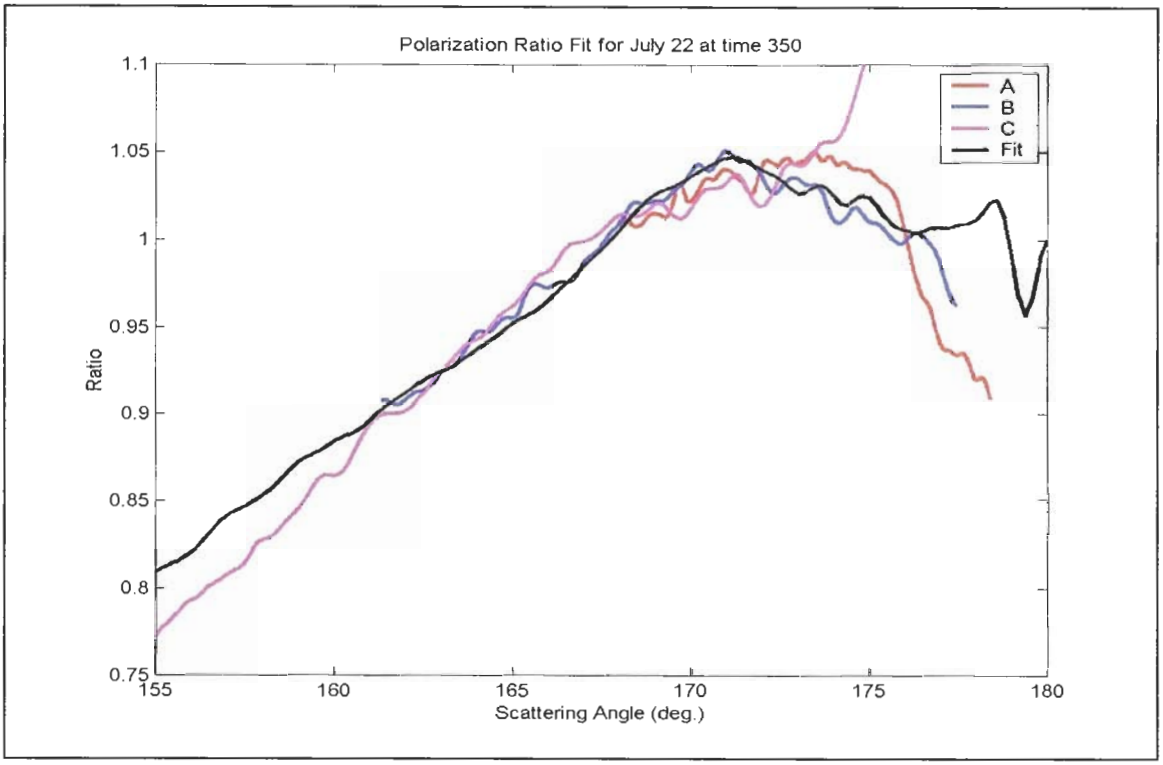

(a)

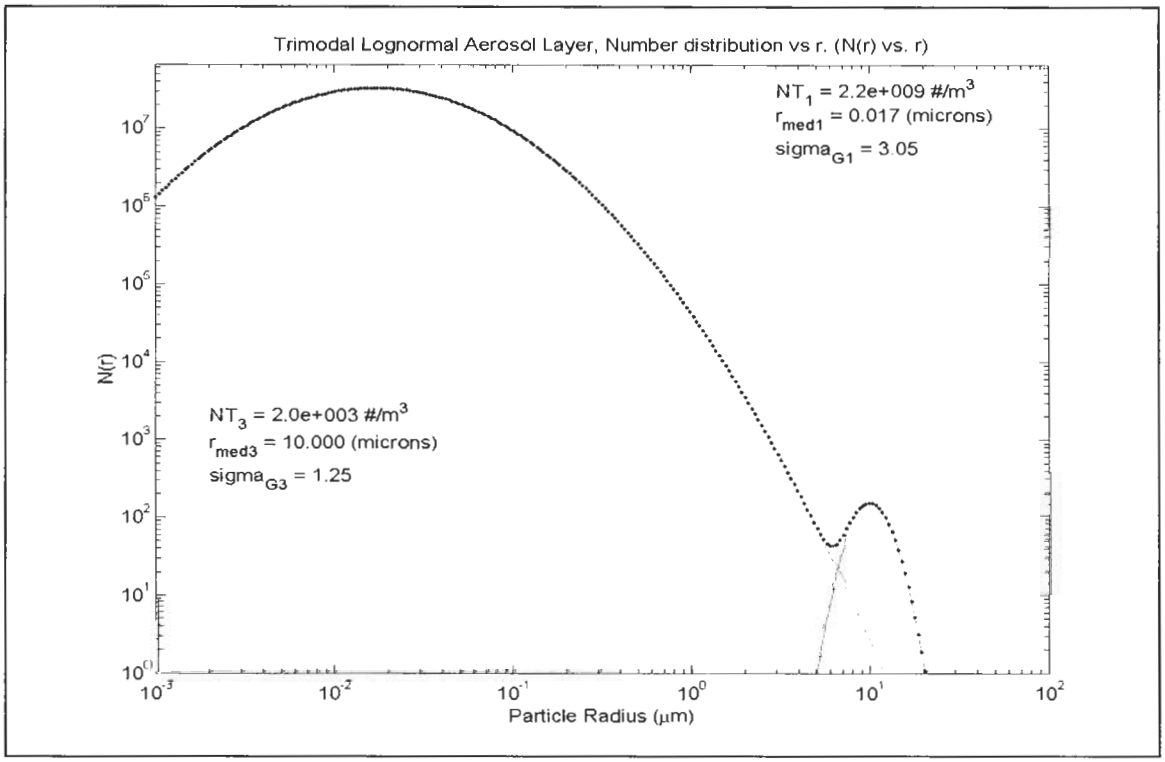

(b)

Figure 6-22: (a) Polarization fit using index of 1.38. (b) Corresponding lognormal parameters.

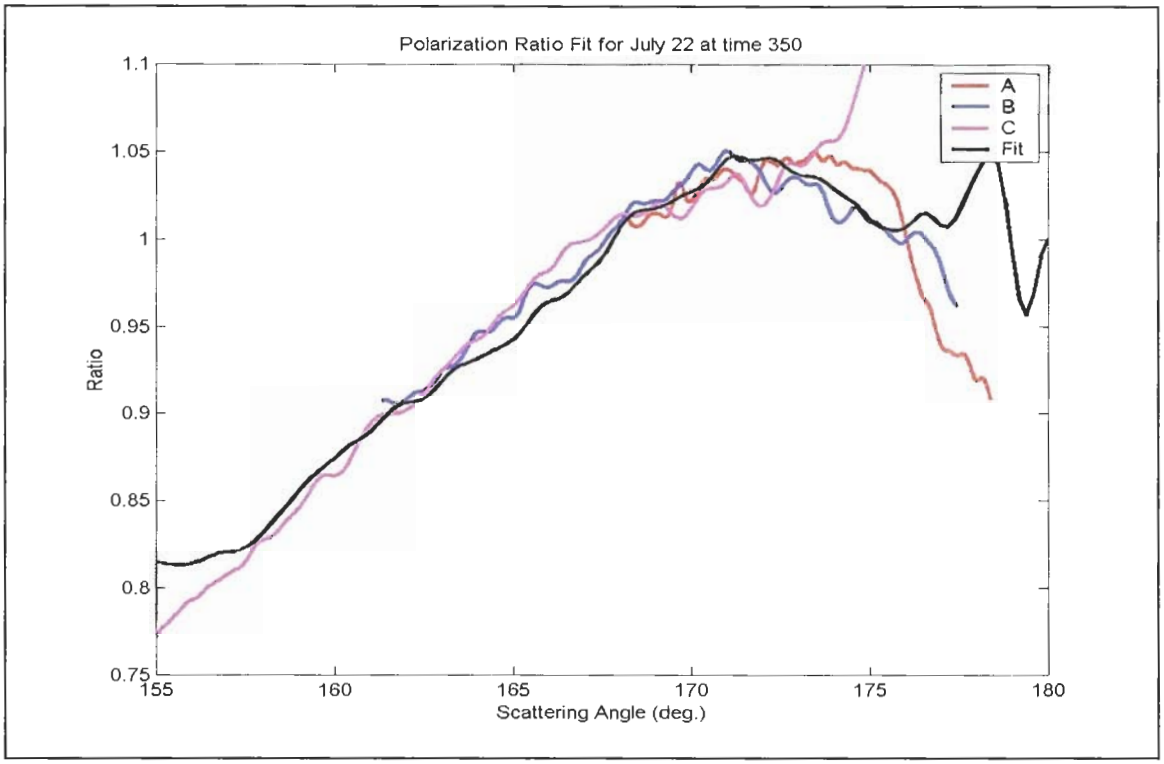

(a)

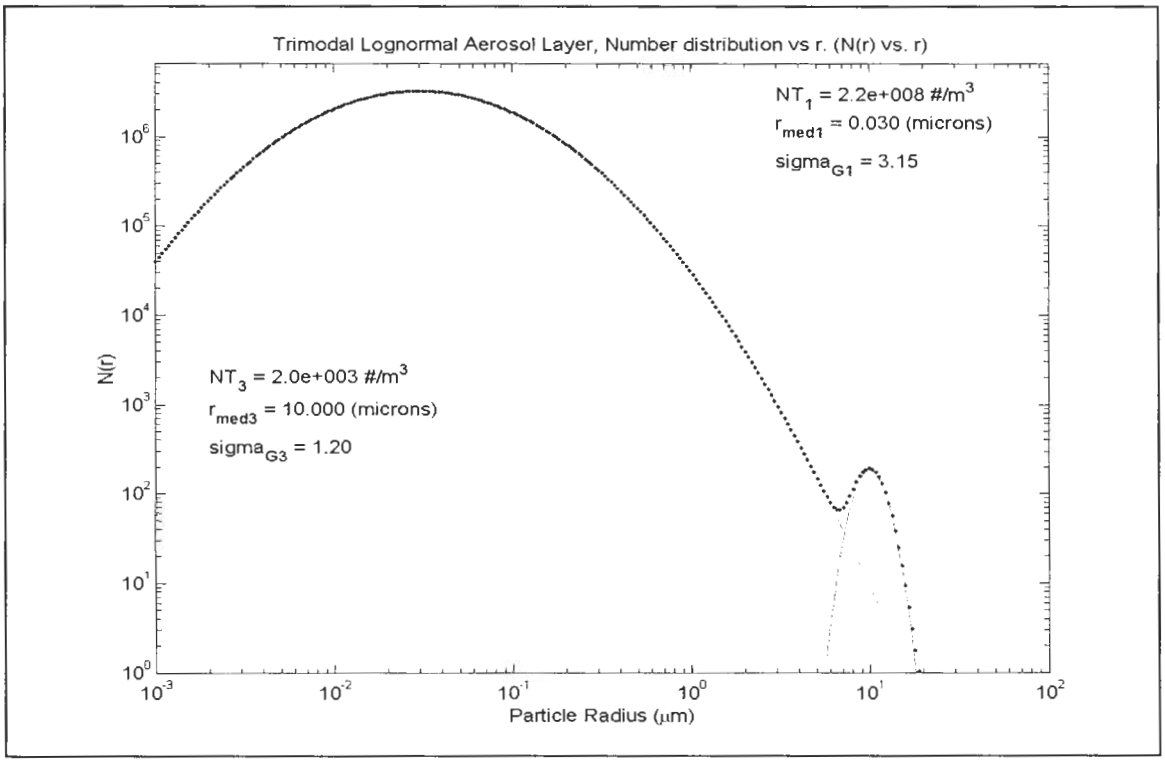

(b)

Figure 6-23: (a) Polarization ratio fit for index of 1.40. (b) Corresponding lognormal parameters.

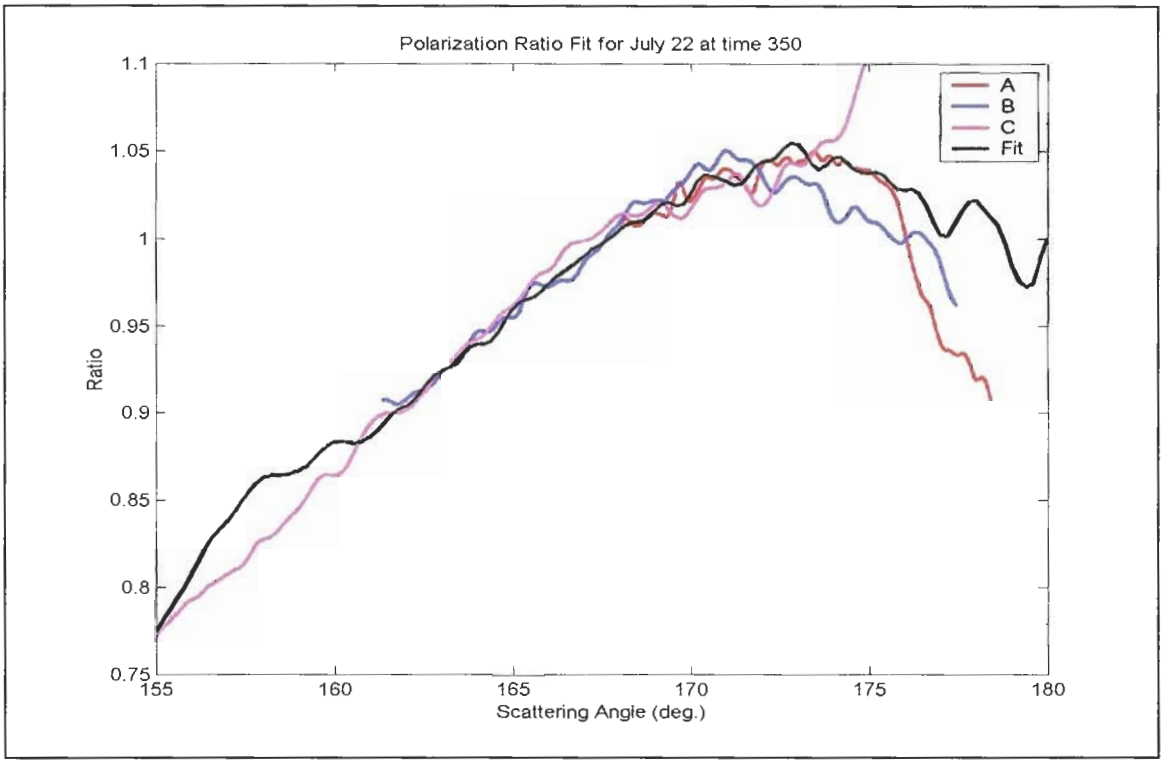

(a)

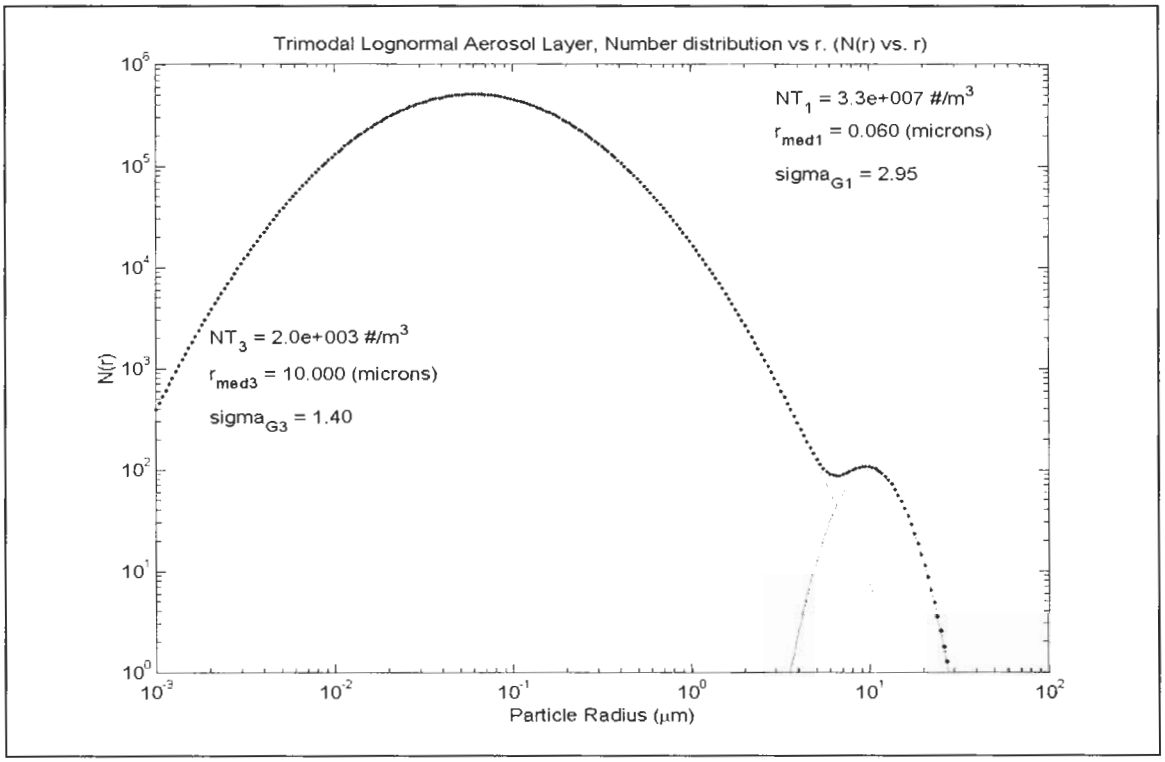

(b)

Figure 6-24: (a) Polarization ratio fit for index 1.44. (b) Corresponding lognormal parameters.

Table 6.1: Parameters for Polarization Ratio Fits of Data for 3:50am, July 23, 2001.

Index	N_{T1} (#/m^3) Nominal (Range)	r_{med1} (nm) Nominal (Range)	σ_{g1} Nominal (Range)	N_{T3} (#/m^3) Nominal (Range)	r_{med3} (μm) Nominal (Range)	σ_{g3} Nominal (Range)
1.33	1.1e8 (0.7e8 – 1.2e8)	11 (9 – 12)	4.99 (4.65 – 5.1)	4.5e3 (1e3 – 6e3)	12 (8 – 13)	1.4 (1.3 – 1.55)
1.38	2.2e9 (1.8e9 – 2.4e9)	17 (15 – 18)	3.05 (2.95 – 3.10)	2e3 (1e3 – 3e3)	10 (9 – 14)	1.25 (1.15 – 1.4)
1.40	2.2e8 (1.8e8 – 2.9e8)	30 (28 – 33)	3.1 (3.0 – 3.2)	2e3 (1.5e3 – 6e3)	10 (9 – 15)	1.2 (1.1 – 1.65)
1.44	3.3e7 (2.5e7 – 3.6e7)	60 (57 – 62)	2.95 (2.75 – 3.0)	2e3 (1e3 – 3e3)	10 (8 – 12)	1.4 (1.35 – 1.75)

state, i.e., this particular instrument did not dry the particles but left them "wet". In Figure 6-25, the green line shows the data obtained by Harvard while the underlying curve represents a good fit to their data. We immediately see that the total number density of the first mode, N_{T1}, which matches Harvard's data is considerably larger that what was used in most of our fits of Table 6.1. By keeping the lognormal parameters of Figure 6-25 fixed, we simply adjusted the index of refraction in steps of 0.01 to see which provided the closest fit. Shown in Figure 6-26 is the best fit found using an index of 1.35. Obviously, this does not truly represent a good fit and so the lognormal parameters were further adjusted using an index of 1.35 to come up with the polarization ratio fit of Figure 6-27a and subsequent lognormal distribution of Figure 6-27b. Along with the nominal and ranged values of each lognormal parameter for our fit of Figure 6-27a, we also compare the data from Hobbs 1993 and Whitby's ground-breaking 1972 Los Angeles aerosol distribution data in Table 6.2. Here, one can easily see the dangers of trying to generalize published aerosol distribution parameters and applying them to specific locations and cases. Direct particle size measurements at the time and location of an atmospheric light scattering experiment are an absolute necessity.

The examination we have done causes concern with the numbers Stevens reported, especially with respect to the percentage errors he provided for his obtained lognormal parameters[†]. However, we do note that Stevens had a considerably different case to examine in that he had very large scatterers present which were nearly monodispersed and dominated the scattering. Our results are more representative of the difficultly in obtaining accurate sizing information of ultra and very fine particles and are consistent with previous work done with fitting polarization components individually.

Our results also indicate that the index of refraction plays a critical role in the proper determination of the lognormal parameters. This finding should underline the difficulty in obtaining accurate particle size

[†] See Stevens, 1996, chapter 6.

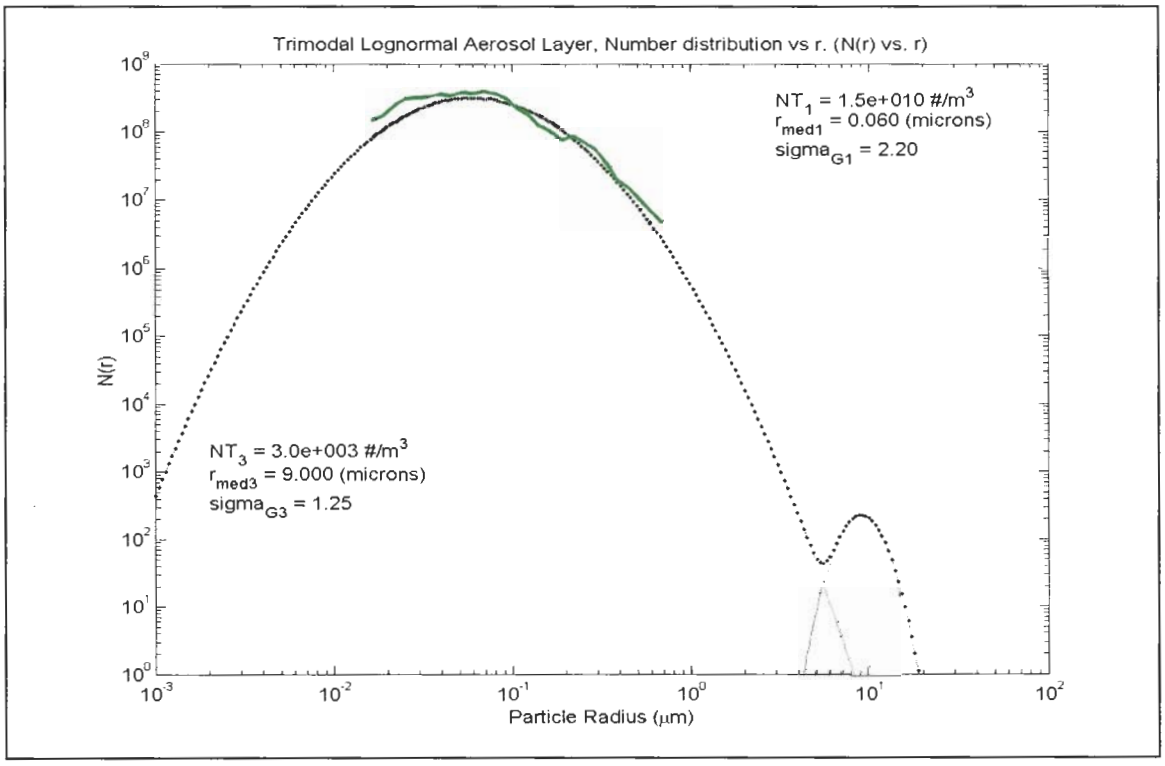

Figure 6-25: Harvard particle sizing information (green line) and corresponding lognormal distribution.

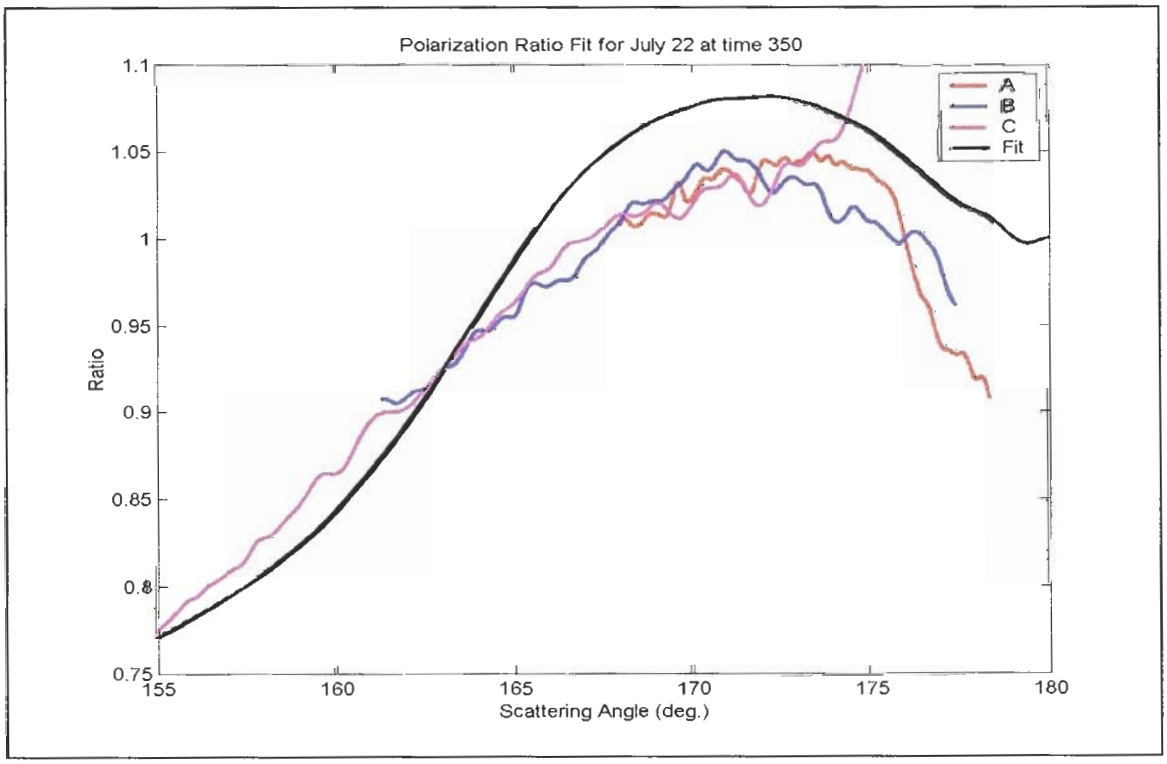

Figure 6-26: Fit using parameters of Figure 6-25 and index = 1.35.

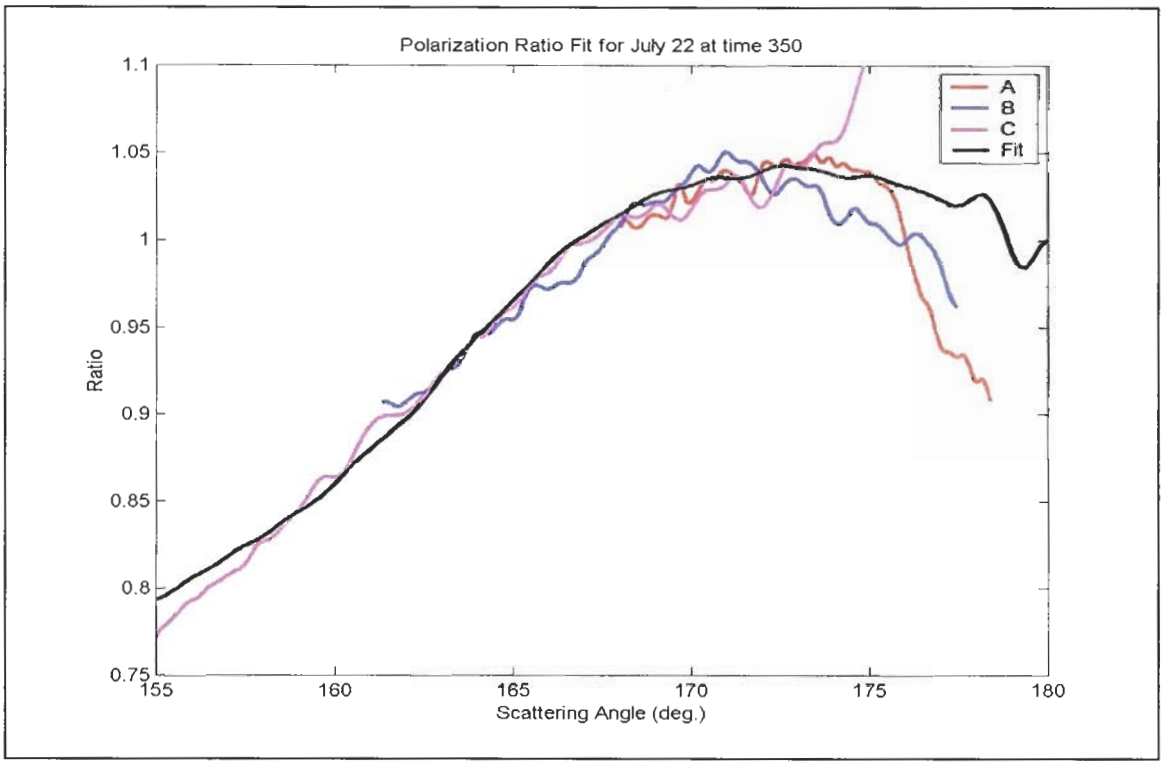

(a)

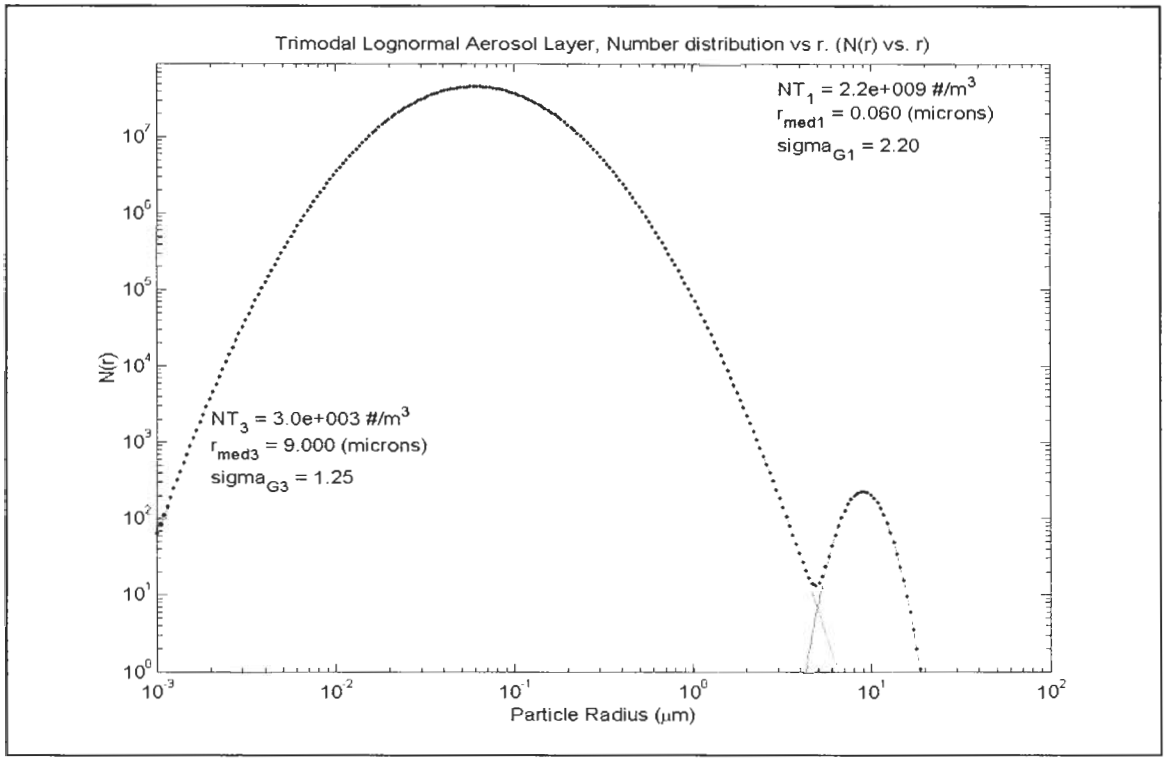

(b)

Figure 6-27: (a) Modified fit of Figure 6-26 using index = 1.35 and (b) corresponding lognormal parameters.

Table 6.2: Fitted parameters of Figure 6-27 along with parameters from Whitby (1972), Hobbs (1993), and Harvard (2001) data.

	N_{T1} (#/m^3) Nominal (Range)	r_{med1} (nm) Nominal (Range)	σ_{g1} Nominal (Range)	N_{T3} (#/m^3) Nominal (Range)	r_{med3} (μm) Nominal (Range)	σ_{g3} Nominal (Range)
Figure 6-27	2.2e9 (1.5e9 – 3.5e9)	60 (55 – 62)	2.20 (2.17 – 2.22)	3.0e3 (1e3 – 3.5e3)	9 (8.9 – 9.1)	1.25 (1.15 – 1.35)
Whitby	4.0e11	2	2.7	*	*	*
Hobbs (Urban)	9.93e10	6.57	1.76	*	*	*
Harvard	1.5e10	60	2.20	*	*	*

* Parameters given for the 3rd aerosol mode were not true coarse mode and were not applicable.

density and composition information from light scattering measurements alone. As it stands, additional and accurate independent information is always needed in order to give credence to the determined parameters, which obviates the use the methodology presented in this thesis. Otherwise, one is simply involved in a mathematical exercise.

6.2.3 Inversion of 13 July 2001, 2:30AM

Section 6.2.2 showed a best-case inversion and worked well because the available supporting information strongly suggested a uniformly mixed atmosphere at the time of measurement. However, as we have already seen, Figure 6-3b shows the presence of a pronounced aerosol layer situated between 35m and 60m in altitude. Although we could simply wash our hands of this particular data set, we would like to at least attempt an analysis in the hopes that future work may learn from our experience and formulate research plans to overcome the challenges we encountered.

This particular time period, 11:00pm July 22 to 5:00am July 23 was unique among the data sets we collected during the 2001 NE-OPS campaign. Although Figure 6-3b gives evidence of a strong aerosol layer, other times also showed the same level, although at different levels. Figures 6-28 and 6-29 shows selected time instances around the 2:30am data set. While we note that the aerosol layer varies in thickness from about 10m to 25m and exists in an altitude range of 25m to 60m, we do not have information on its width so we cannot comment on its overall size. Not only do these figures serve to illustrate that the vertical transport of aerosols can be monitored with a multistatic lidar approach, but that the vertical distribution of aerosols can change significantly within short periods of time.

6.2.3.1 Supporting Measurements

The first step of the analysis, of course, is to examine supporting information. Unfortunately, both the chemical analyzers and the tethersonde balloons were not operating at this particular time. However, given

the location of the aerosol layer under study, we doubt that even if such equipment were available that the measurements would be directly applicable at this instant in time.

At the 2:30am time, the atmosphere was observed to be clear and the conditions were cool and slightly damp. Shown in Figure 6-30 are the evolution of temperature and relative humidity for the overnight hours of July 12 and throughout the day of July 13.

Also operating at this time was the scanning mobility particle sensor (SMPS). Figure 6-31 shows the relative evolution of the particle concentrations for July 22 and July 23. From this information, it is difficult to determine the exact motion of the particles in the atmosphere and so making use of this information is difficult at best. Since the data from LAPS indicates a non-uniform atmosphere (corroborating the data from our multistatic receivers), data taken at the ground by the way of particle size analyzers and data taken at other altitudes would not be representative of the aerosol layer located between 10m and 100m.

6.2.3.2 Inversion

From the available information, we proceeded with the following assumptions. First, the aerosol layer we observe in our multistatic data (Figure 6-3b) is different from the aerosols and particulates found at ground level. Thus, we cannot make use of ground-based data. Further, we must also assume a particular atmospheric chemical composition is present in order to estimate a reasonable index of refraction. From the meteorological data and atmospheric observations, we will assume an index of 1.40 but we realize that this choice is somewhat arbitrary and circumstantial. To test our assumptions, we will attempt several inversion cases.

Our main goal in our inversion is not to try to fit a polarization ratio model to the data as the presence of the aerosol layer reduces the number of angles with which we have to work. However, we would like to investigate two distinct possibilities regarding the composition of the layer itself. Specifically, we wish to determine, if possible, whether the aerosol layer is simply the result of a changing concentration of the background aerosol, or whether the layer is completely different chemically from the background. In order to accomplish our analysis, we are going to concentrate solely on the peaks and troughs of the aerosol layer. We do this because we know that the aerosol layer is definitely changing with respect to altitude and so each altitude contains a different, though somewhat related, distribution than that of adjacent altitudes. Specifically, we are going to look at the peak at 34m, the trough at 36m and the large peak at 44m (the layer ends at 52m).

Figure 6-32a shows the model passing through the peak at 34m while Figure 6-32b indicates the distribution parameters used. The presence of the 3rd mode was found to be necessary as the 1st mode alone could not match camera A's data. Since the next altitude point at 36m appears to suggest a decrease in the particle concentration, we first attempted to find a fit by simply reducing N_{T1} and N_{T3}. Although the resulting curves did suggest that the total number densities of each mode were determining factors in achieving a fit of the data to the model at 36m, we did have to also adjust several of the other parameters in

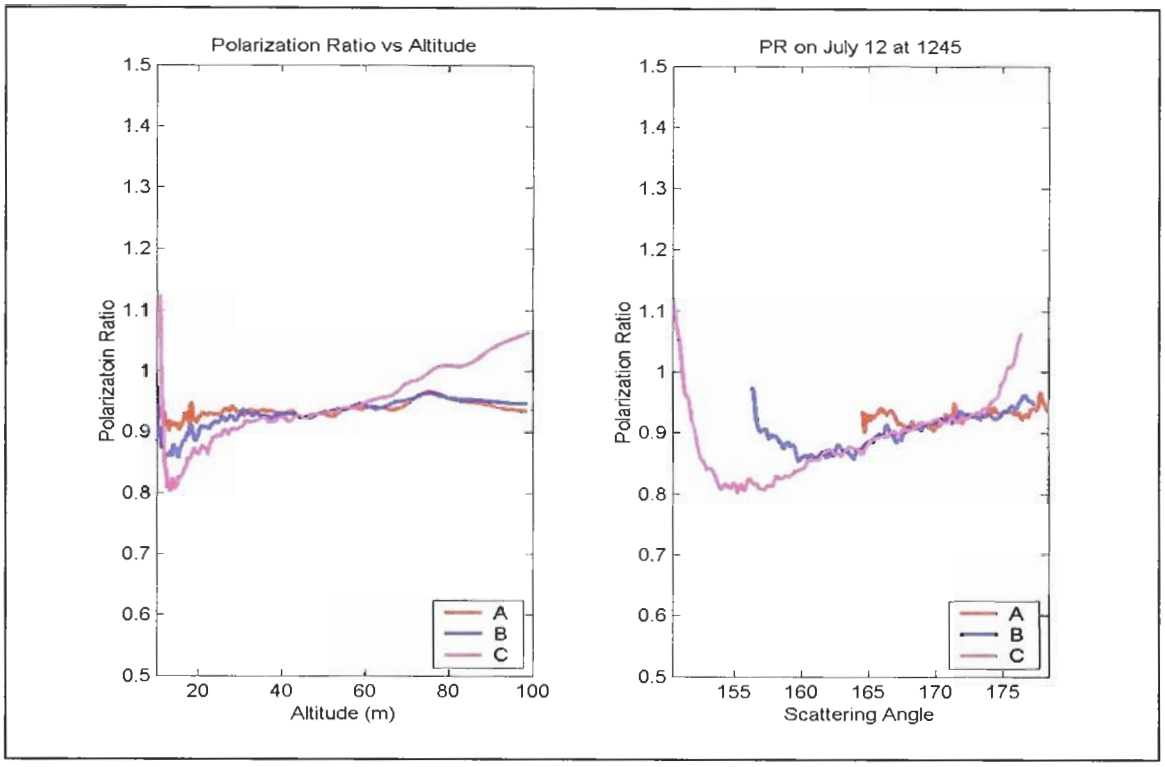

(a)

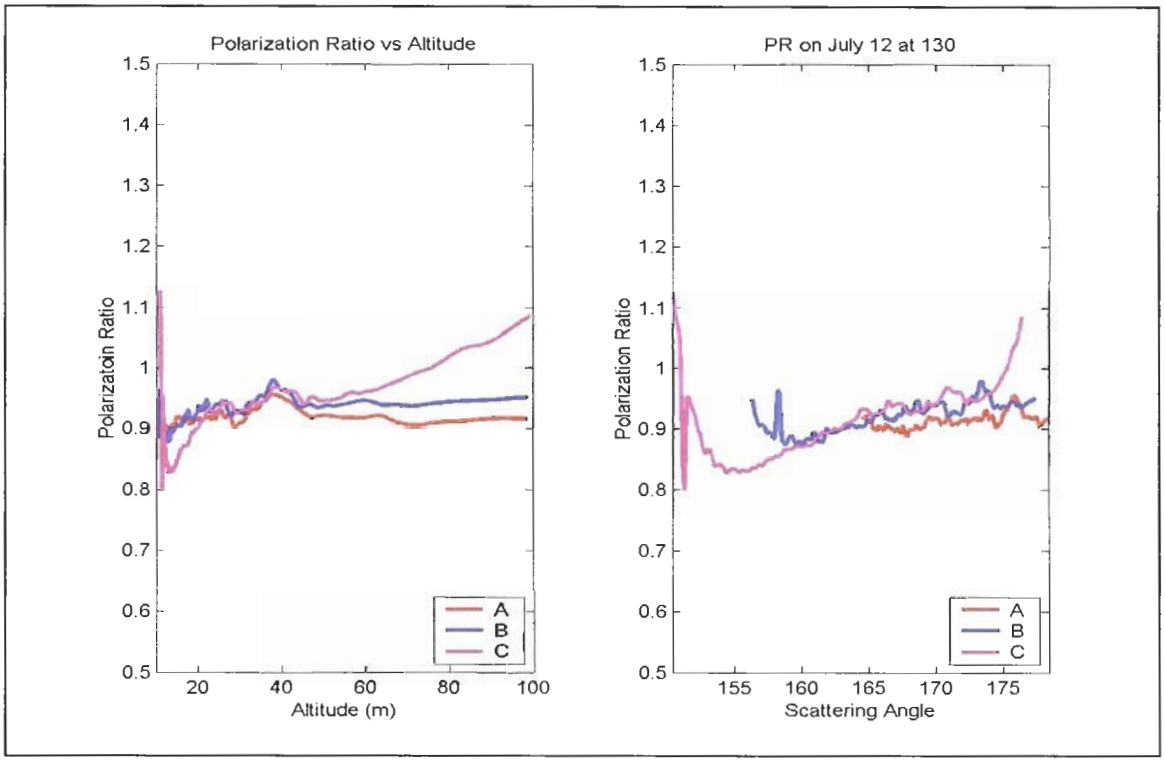

(b)

Figure 6-28: Polarization ratios for night of July 12, morning of July 13. (a) Aerosol layer not yet present. (b) Aerosol layer beginning to appear around altitude of 40m.

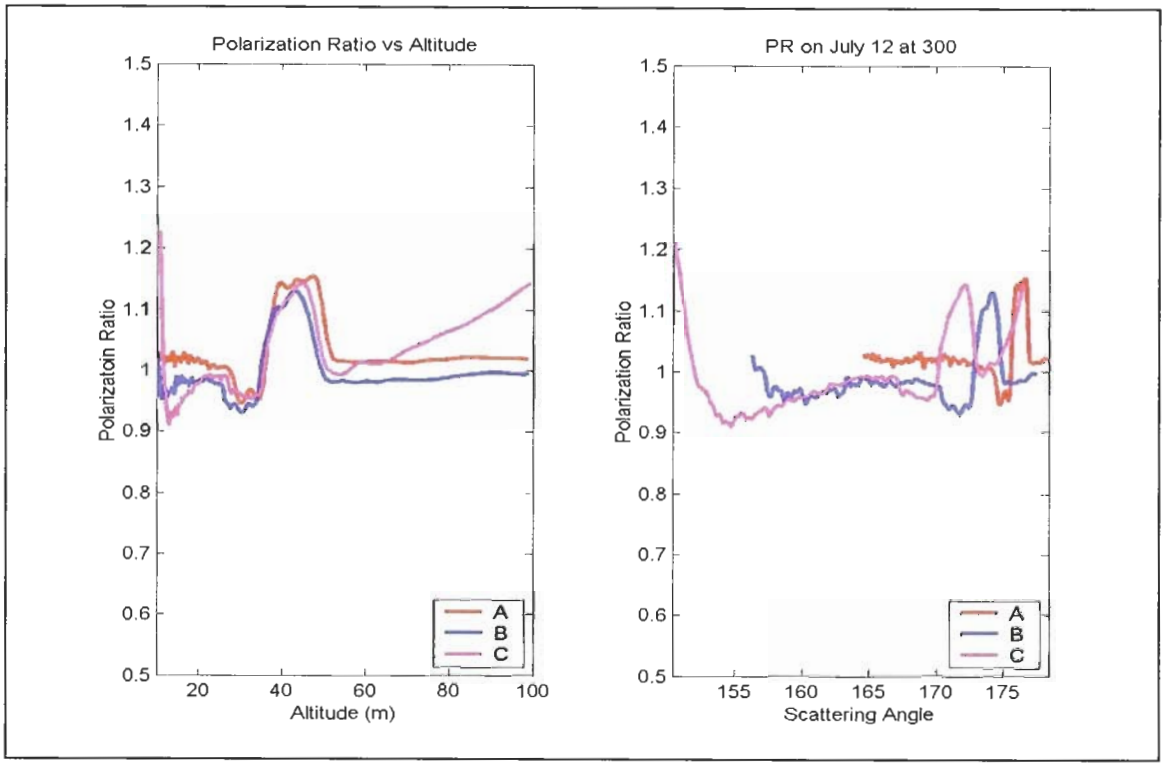

(a)

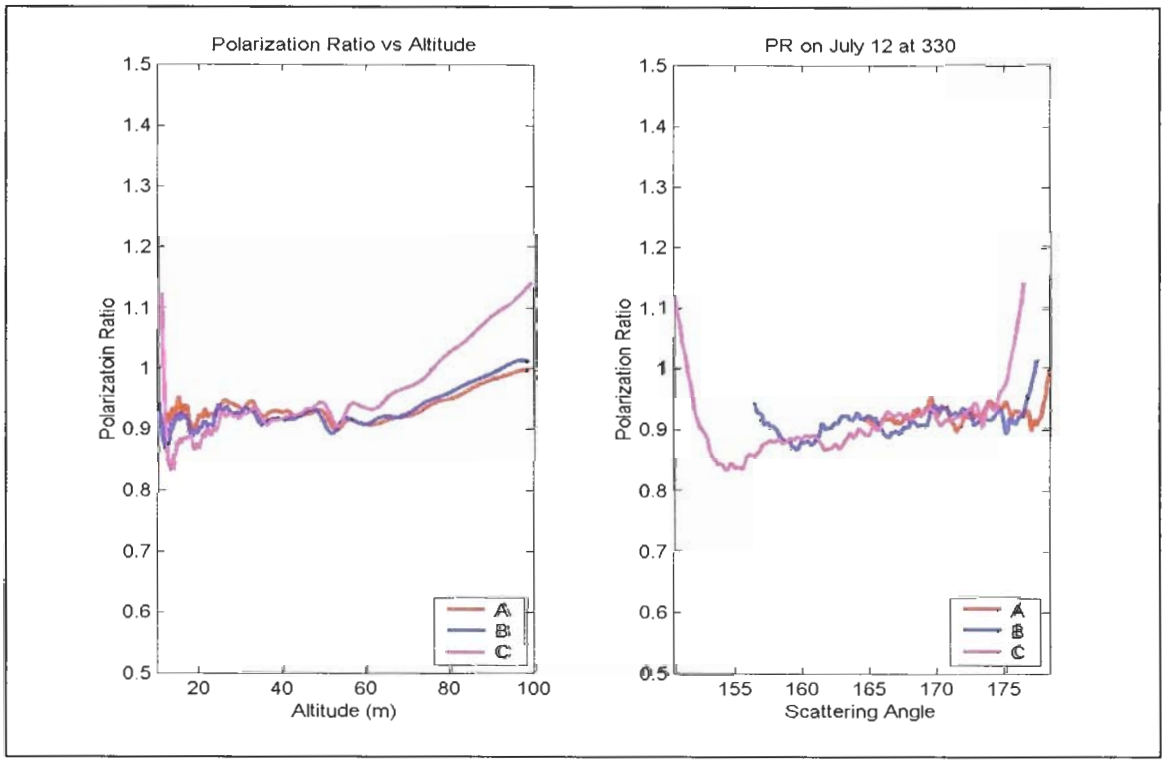

(b)

Figure 6-29: Polarization ratios for night of July 12, morning of July 13. (a) Presence of aerosol layer. (b) Aerosol layer has diminished.

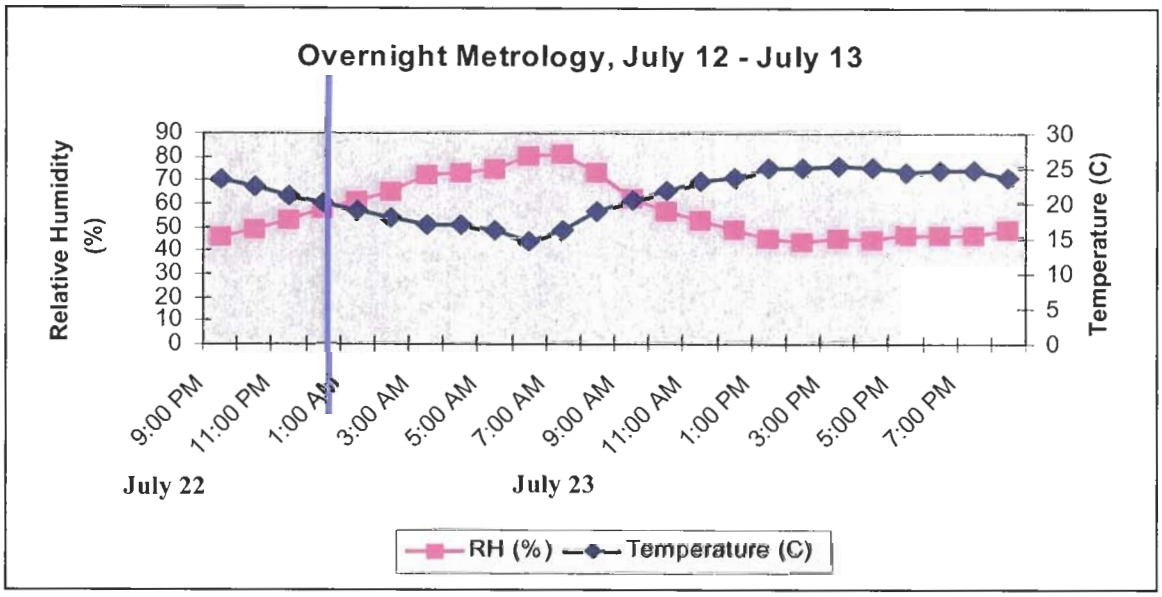

Figure 6-30: Evolution of temperature and relative humidity for given (local) time. The blue line corresponds to the time of the polarization data being examined.

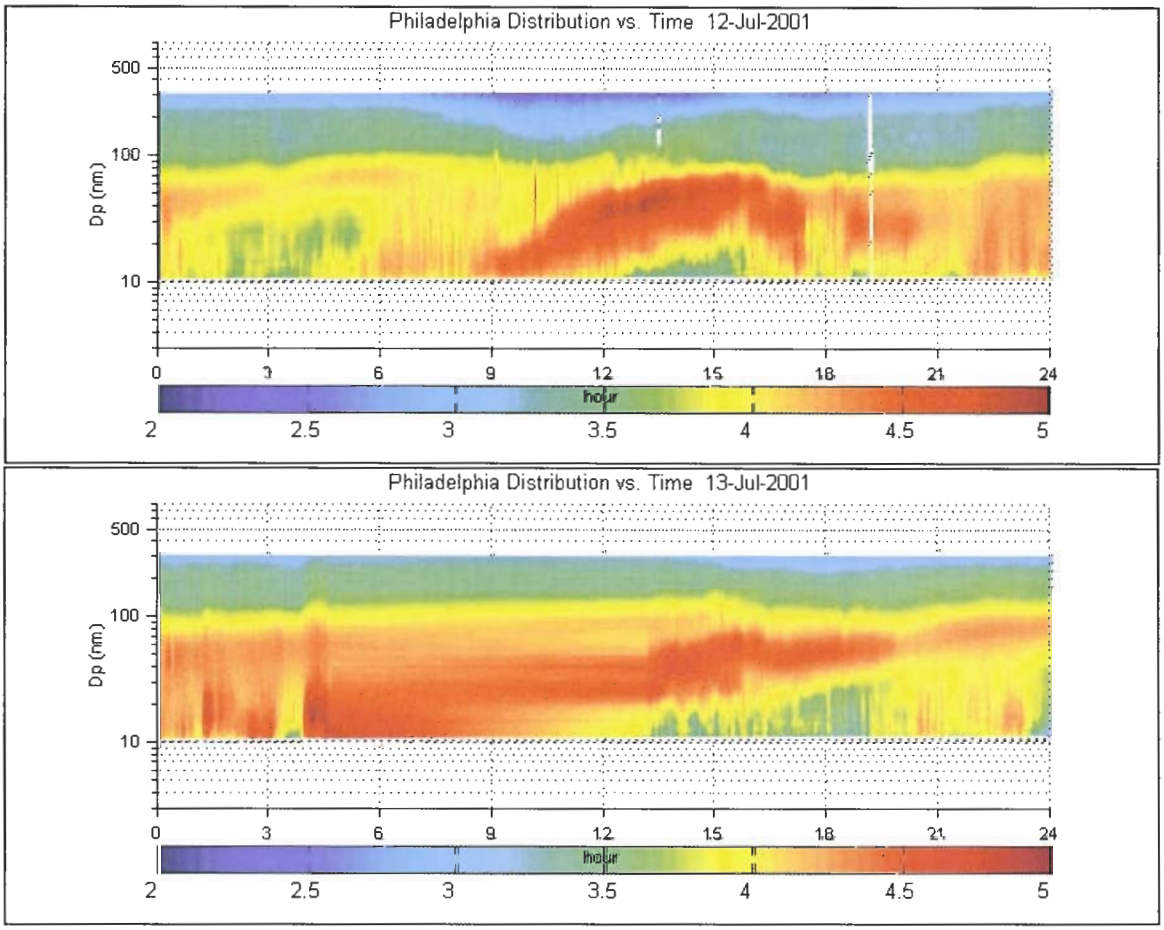

Figure 6-31: Results from scanning mobility particle sensor (CMU). Times given are local.

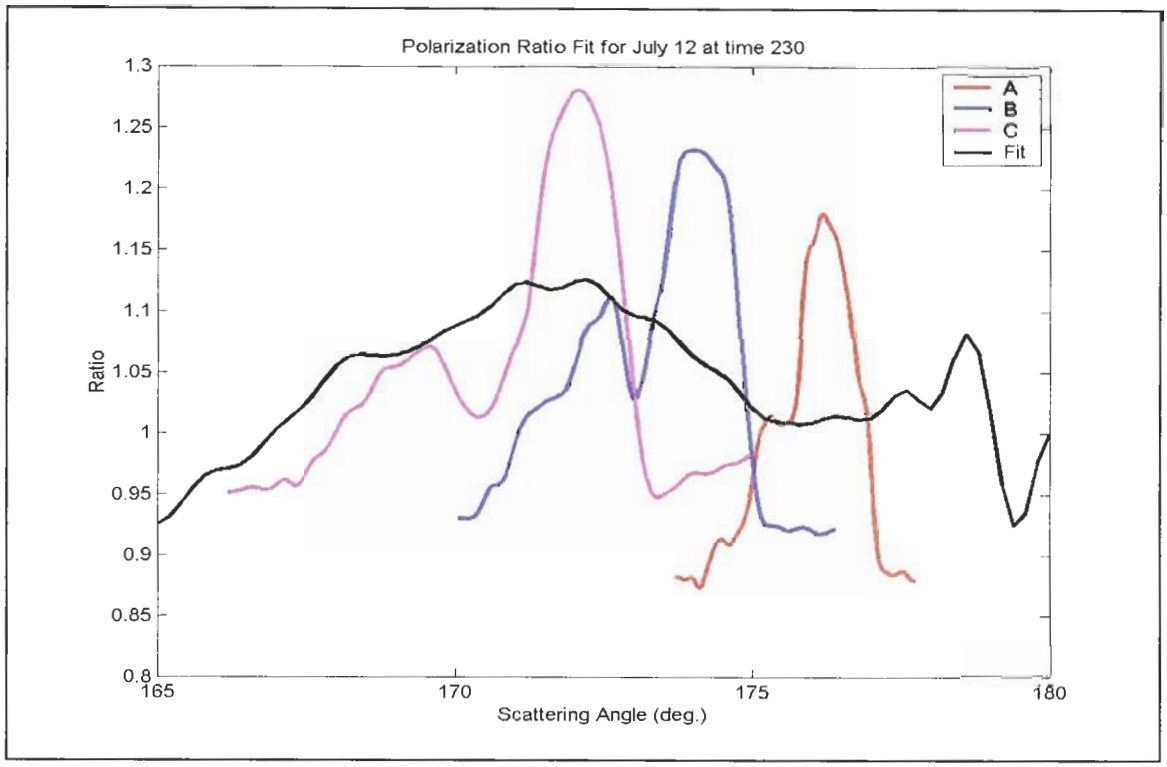

(a)

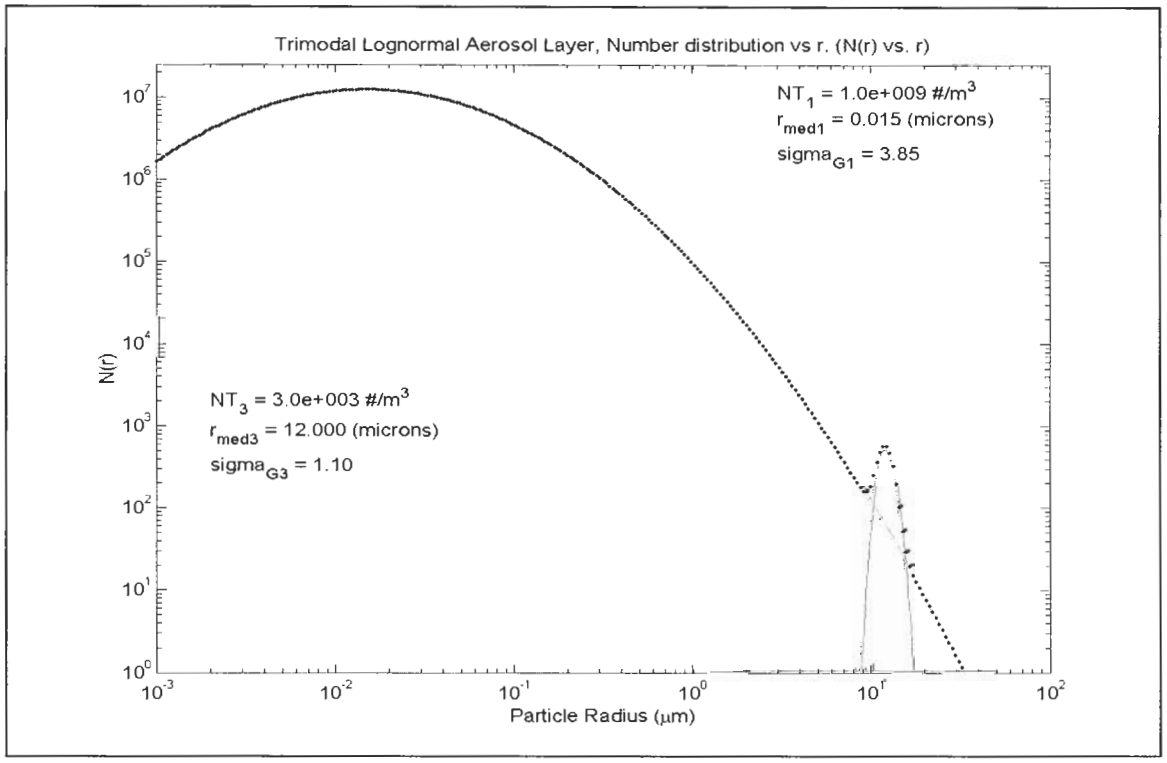

(b)

Figure 6-32: (a) Polarization ratio fit at the peak located at 34m altitude. (b) Lognormal parameters.

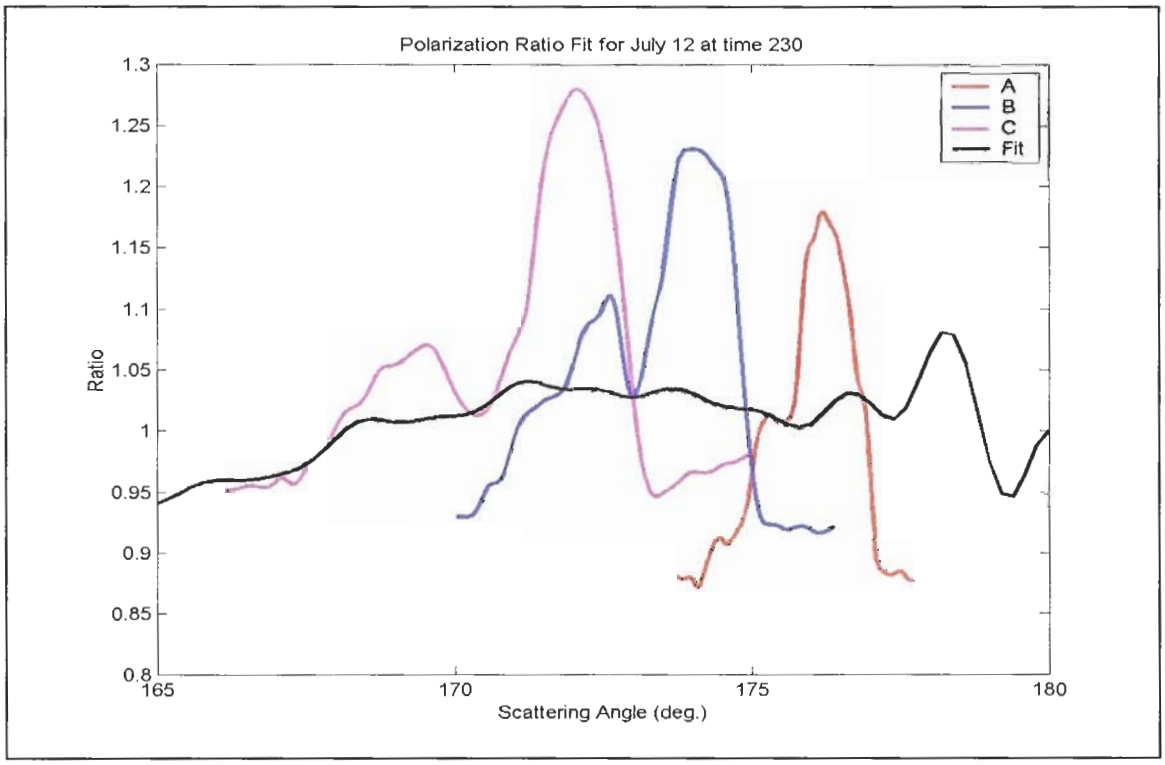

(a)

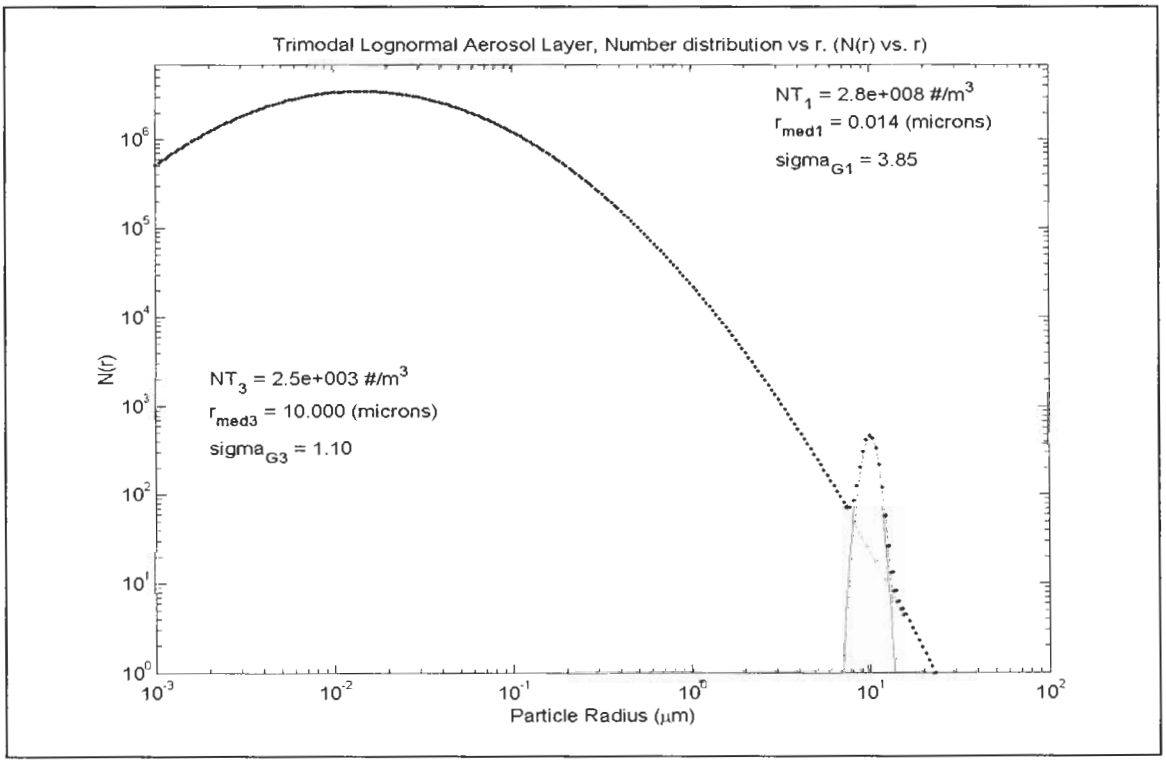

(b)

Figure 6-33: (a) Polarization ratio fit for the trough located at 36m altitude. (b) Lognormal parameters.

order to achieve better fits. Our results of the polarization ratio fit to the trough at 36m are shown in Figure 6-33.

Despite our success at finding a fit of the model to the data thus far, attempts at finding a suitable fit to the peak at 44m were unsuccessful. Assuming that our choice of index of 1.40 was incorrect, other indices in the range from 1.33 to 1.44 were also attempted without success. Additionally, we could not find a suitable set of parameters that would cause the polarization ratio model to pass through the end point of the aerosol layer at 52m.

At this point we were not discouraged because we suspected that the layer was actually composed of particles that were chemically different from the background and so perhaps a different choice of refractive index would assist us in the inversion. Given that we were in an urban environment, it seemed plausible that we could be witnessing a layer of fine carbonaceous particles. Using an index of 1.75 + j0.005, we again proceeded with finding fits to the peaks and troughs of the aerosol layer. However, due to the high absorptivity of the carbon and insensitivity of the polarization ratio to the imaginary refractive index, we were unable to obtain curves that would pass through the desired points. It should be pointed out that we did attempt inversions using a refractive index of 1.75 (i.e., no imaginary component) and it was very simple to produce curves that would fit the data but using such a high index over the entire size range represents a non-physical condition and should be avoided. We appear unable to proceed but there is still one other piece of information that we have not employed.

Our motivation for using the polarization ratio of the parallel and perpendicular scattering components was to avoid introducing instrument errors such as non-linear response across the lens and across the interference filters. However, another motivating factor was that other researchers had already tried to fit scattering data to one or the other scattering component and had found that the errors in the resulting particle size distributions could be quite large. Despite our misgivings of using the polarization components themselves, we can still make use of some of their characteristics.

Figure 6-2b shows the polarization components (parallel and perpendicular) for July 13 at 2:30am as a function of altitude. Using our altitude analysis of the polarization ratio, we can also examine the altitude dependence on the polarization components. Figure 6-34 shows the modeled polarization components for aerosol layers with an index of 1.4 and 1.75+0.005j, respectively. Upon comparing Figure 6-34 with Figure 6-2b, we see that the components do have similarities in the way of structure. However, in terms of magnitude, we see that the two figures are very much different. Measurement of absolute scattering intensities has proven to be very difficult and most researchers opt for normalized (or ratioed) data.

Of importance in Figure 6-34 is the relative magnitude due to the aerosol layer with an index of 1.4 and the layer with an index of 1.75+j0.005. Although Figure 6-34b contains a highly absorbing layer, we have no access to this absorption but, rather, we still have access to the scattered fields. From our introduction of basic electromagnetics, we know that it is the real part of the refractive index that is responsible for the propagation of a wave. Figure 6-34b's scattered polarization components are higher than those of Figure 6-34a's and Figure 6-34a's relative scattered field is more in line with the scattered

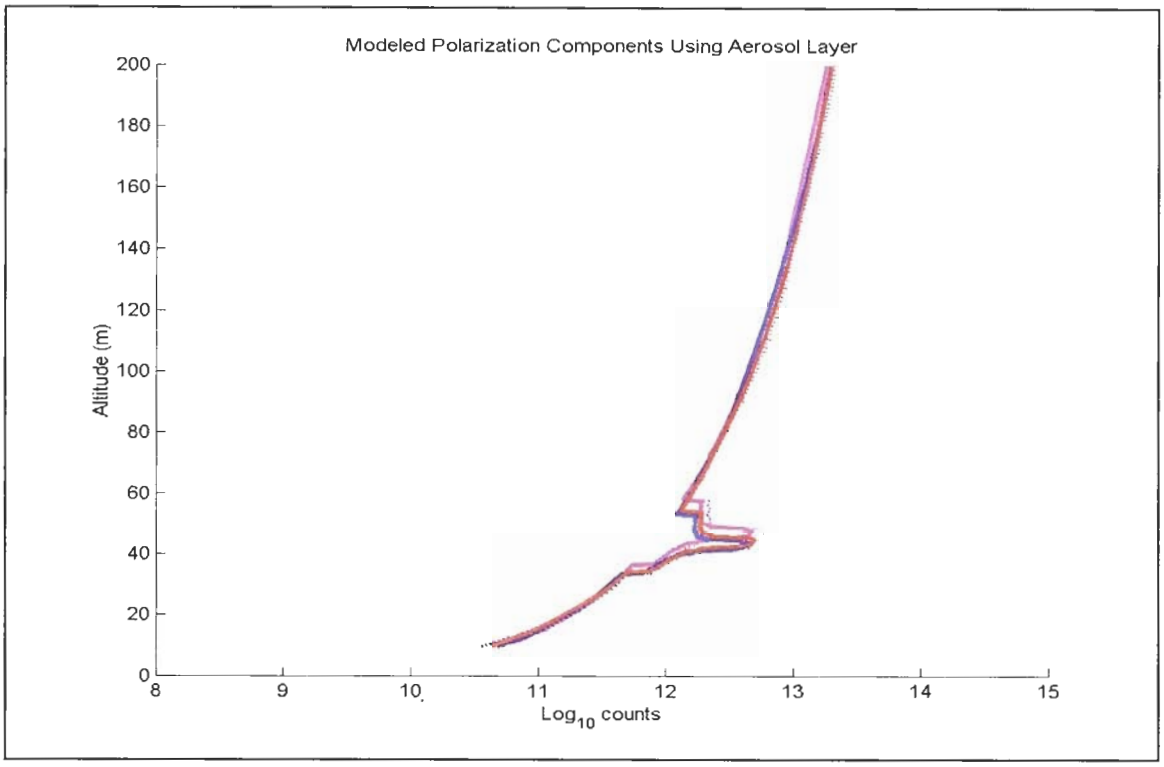

(a)

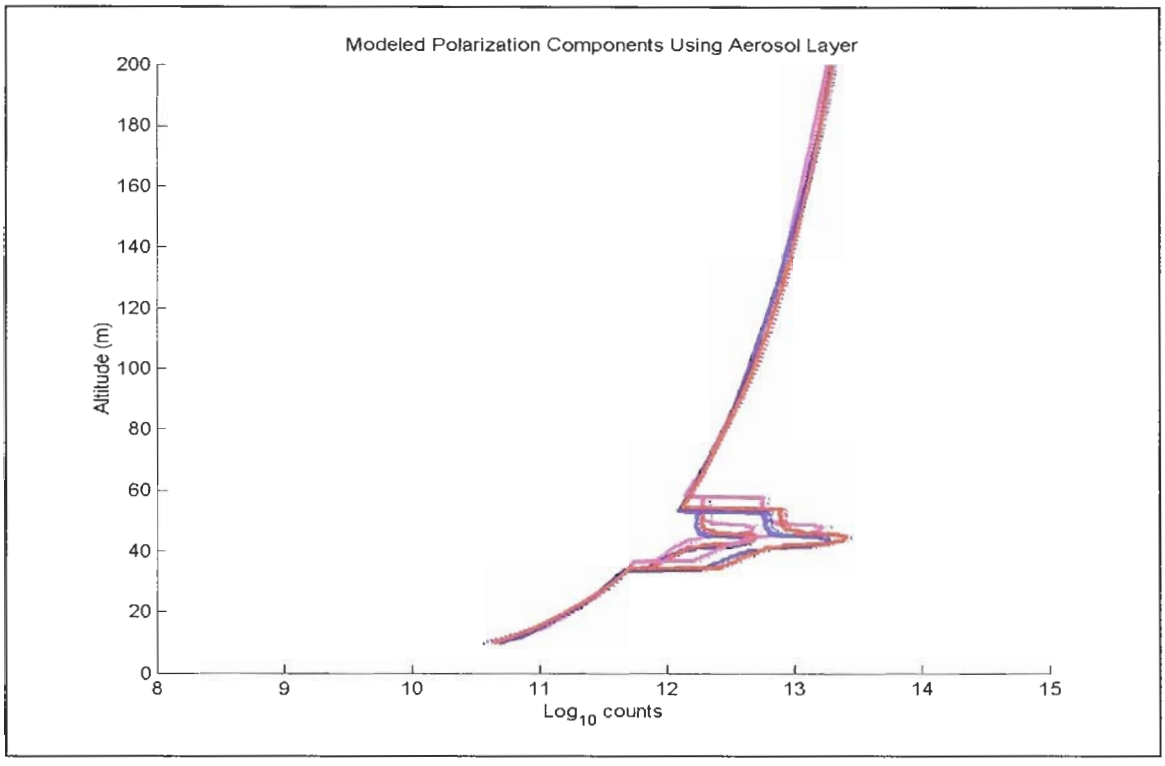

(b)

Figure 6-34: Modeled parallel and perpendicular components for (a) aerosol layer with index = 1.40 and (b) aerosol layer with index of 1.75 + j0.005. Plot has been range and volume corrected.

components of Figure 6-2b. Thus, we suggest that the observed aerosol layer is not likely carbonaceous but is composed of species that are more similar to the background aerosol, differing in number, size and distribution.

6.2.4 Inversion of 1 October 2001, 6:20am

The inversion of section 6.2.2 represented a best-case scenario while the inversion of section 6.2.3 represented a worst-case scenario. However, the inversion we perform here represents a middle ground and is representative of the data that we were expecting in our Philadelphia NE-OPS campaign. The data presented here was taken in State College, a small to mid-size town in rural central Pennsylvania. The primary reason for taking this data set was to have data that did not show polarization dependence due to the interference filters. On this date, 53nm bandwidth filters were used.

The purpose behind having more than one camera or imaging device to measure the scattering from a vertical atmospheric path was to ensure there were a sufficient number of angles present for a desired section of the altitude. However, as the July 12th-13th data showed, there was a much stronger altitude dependence present and we did not have enough angles for each altitude to uniquely specify an inversion. Our analysis in Chapter 3 indicated that around 10 degrees worth of scattering angles are needed when operating in an environment where three lognormal aerosol modes were present but that fewer angles would be required for more monodisperse atmospheric distributions. The location of the aerosols evident in Figure 6-4b provides us with more angles than we had to work with in Figure 6-4a.

Shown in Figure 6-35a is a closer examination of the polarization ratio for this date with respect to altitude. Due to the sharp transitions of the ratio exhibited by all three cameras at altitudes of 15m and 25m, we believe we have two distinct aerosol layers present. At this point, we do not know whether these layers are differentiated by chemical composition, size density distribution or simply the same aerosol but distributed in space. On this particular date, we did not have any supporting information in the way of chemical analyzers, particle sizers or tethersondes. We did note that this night's data was characterized by unseasonably cold and dry weather. Cross polarization tests were conducted, and although not a true test of sphericity, the tests did show that the parallel polarized light from the lidar unit remained primarily parallel polarized upon scattering with the atmosphere, as did the perpendicular component.

Of particular note from Figure 6-35a are the rapid and relatively large variations in the polarization ratio present. These variations are in contrast to the smooth ratios measured in the July 13th data. From our examination of the lognormal parameters' effect on the polarization ratio, we surmise that a significant number of larger particles are causing the scattering.

To start the inversion, we will first examine the layer between 15m and 25m. For simplification, we assume the index of refraction to be between 1.40 and 1.48. In Figure 6-36a, we show the inversion for altitudes 10m – 14m and in Figure 6-36b, the corresponding lognormal parameters. Unlike the previous cases, it was necessary to include the 2nd aerosol mode in the inversion in order to have the model flatten in

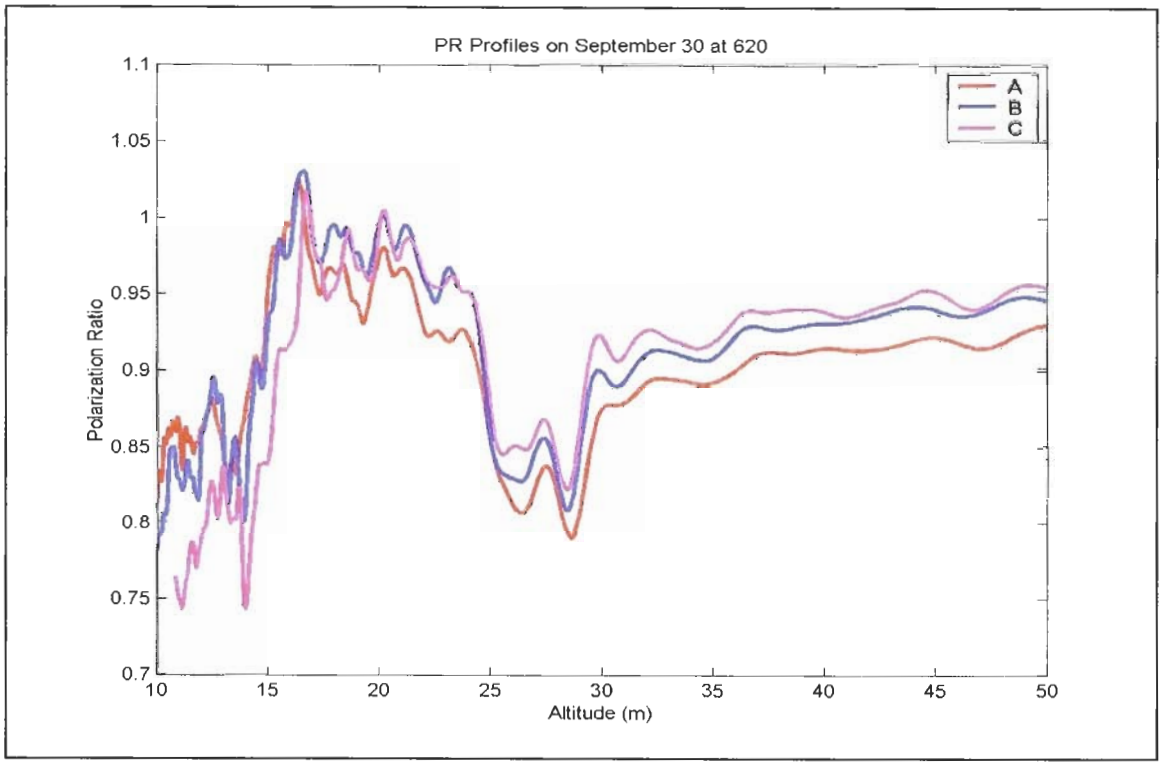

(a)

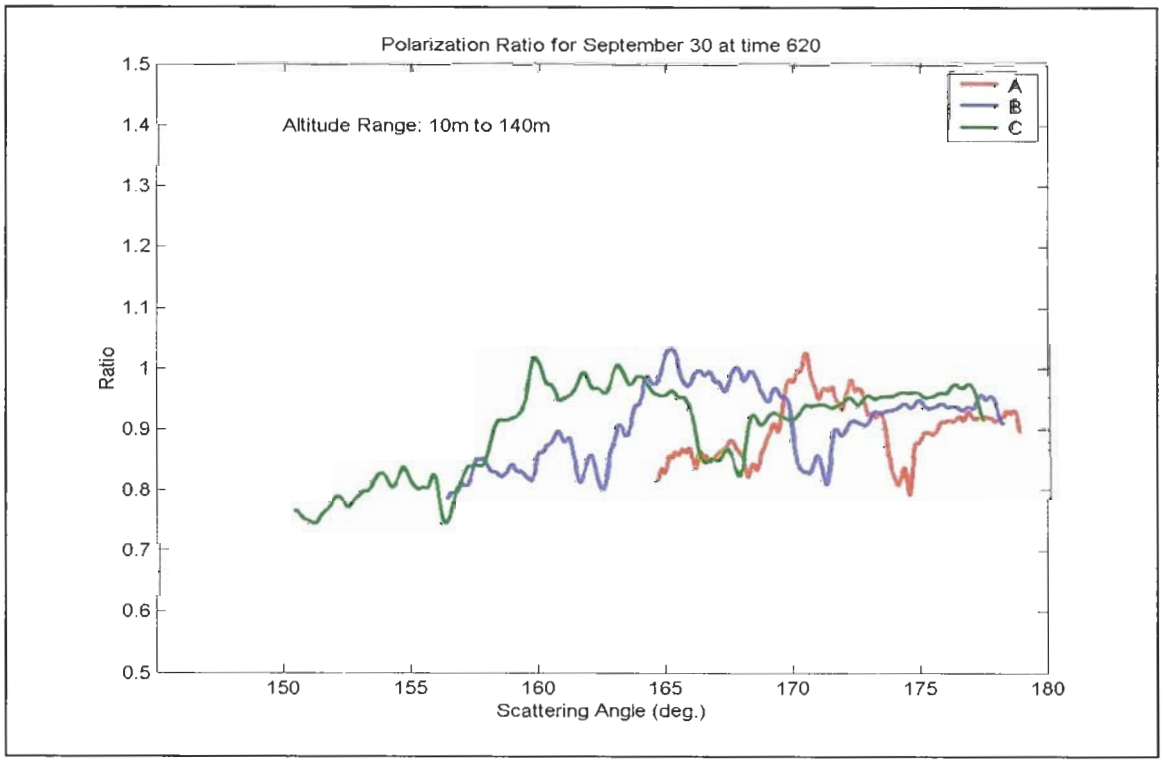

(b)

Figure 6-35: Polarization ratios as a function of (a) altitude and (b) angle for 1 October 2001, 6:20am, State College, PA.

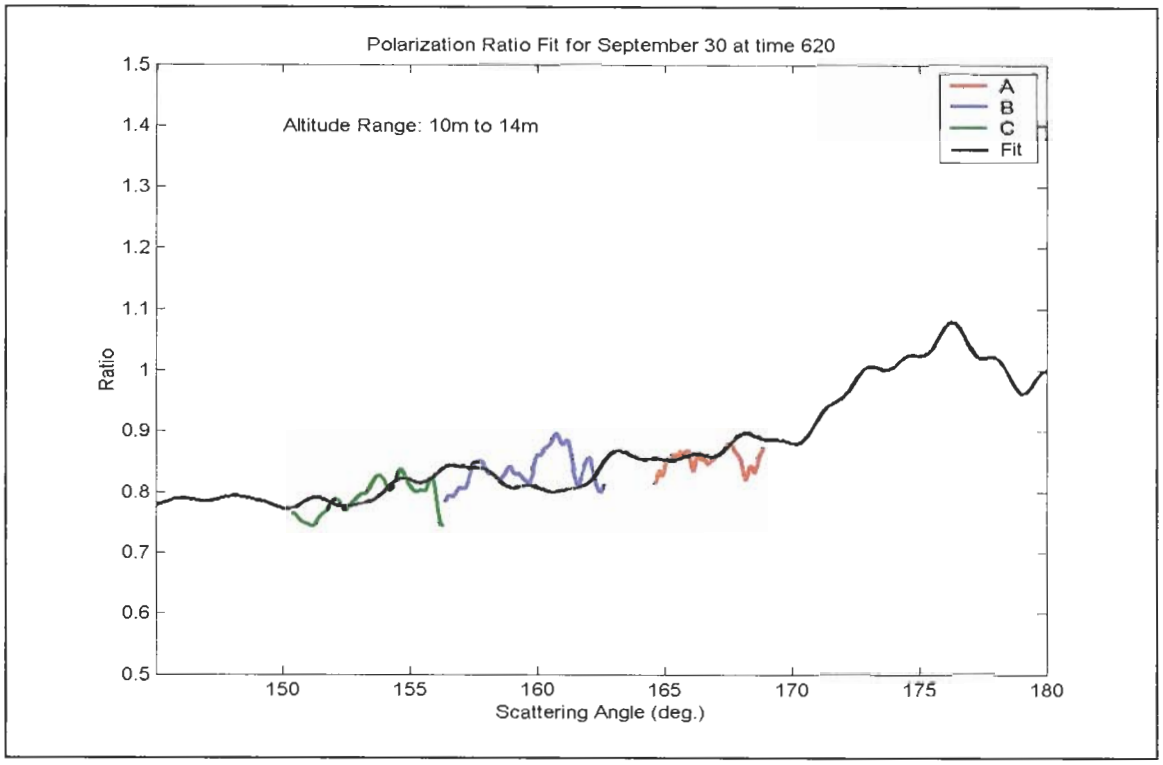

(a)

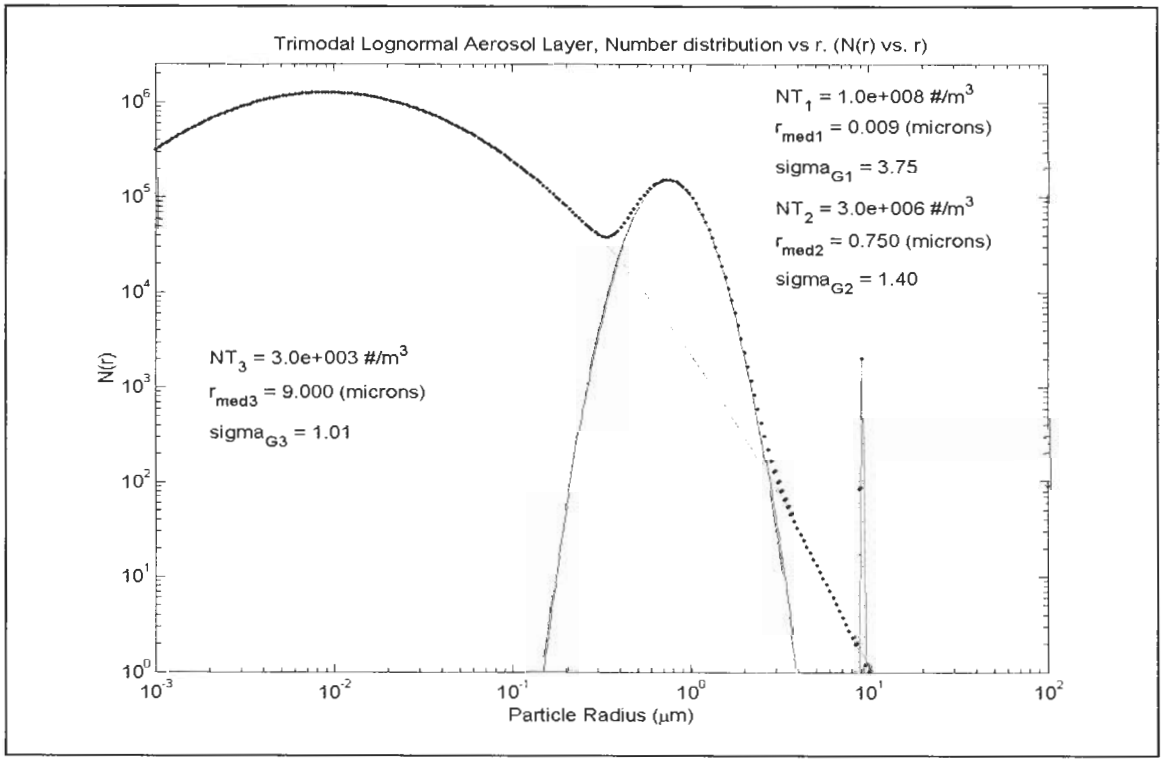

(b)

Figure 6-36: (a) Polarization ratio fit for 1 October 2001, 6:20am. (b) Lognormal parameters. The index used was 1.42.

certain angular regions. Such flattening of the polarization curve is consistent with Mie theory since interference patterns typically arise with particles near the size of the wavelength.

Since it is difficult to obtain an exact fit of the model to the data, the best we can do at this point is to place ranges on each of the lognormal parameters. A summary for this altitude and subsequent altitudes are tabulated in Table 6.3.

For altitudes 15m – 24m, the inversion and subsequent lognormal parameters are shown in Figure 6-37. These parameters, along with the index of refraction, suggest that the aerosols between 10m – 14m differ more so in space than in composition. With the given data, it is impossible to determine the exact nature of the differences.

Finally, for the aerosol layer occupying altitudes 25m – 29m, no adequate solution could be ascertained. A partial solution was found using an index of 1.5 and the first two aerosol modes, but it was still too far from the data to be considered as realistic. There are many of these cases where the model will not fit the data. Above 30m, the polarization ratio suggests that it is heading toward unity, consistent with a molecular atmosphere. Again, the measured polarization ratio will not and should not reach unity since molecules are not spherically shaped.

Table 6.3: Nominal and Range of Inversion Parameters for 1 October 2001, 6:20am.

Index (Alt.)	N_{T1} (#/m^3) Nom. & Range	r_{med1} (nm) Nom. & Range	σ_{g1} Nom. & Range	N_{T2} (#/m^3) Nom. & Range	r_{med2} (μm) Nom. & Range	σ_{g2} Nom. & Range	N_{T3} (#/m^3) Nom. & Range	r_{med3} (μm) Nom. & Range	σ_{g3} Nom. & Range
1.42 (10m-14m)	1e8 (1e7 – 2e9)	9 (1 – 25)	3.75 (3.25 – 3.95)	3e6 (2e6 – 4e6)	0.75 (0.72 – 0.80)	1.4 (1.3 – 1.5)	3e3 (2.5e3 – 3.5e3)	9 (8.0 – 9.1)	1.01 (1.01 – 1.10)
1.46 (15m-24m)	9e7 (1e7 – 2e8)	10 (1 – 15)	3.6 (3.0 – 3.9)	5.25e6 (9e5 – 9e6)	0.25 (0.15 – 0.30)	1.45 (1.25 – 1.60)	1.5e3 (1e3 – 3e3)	9 (8.0 – 9.2)	1.01 (1.01 – 1.05)

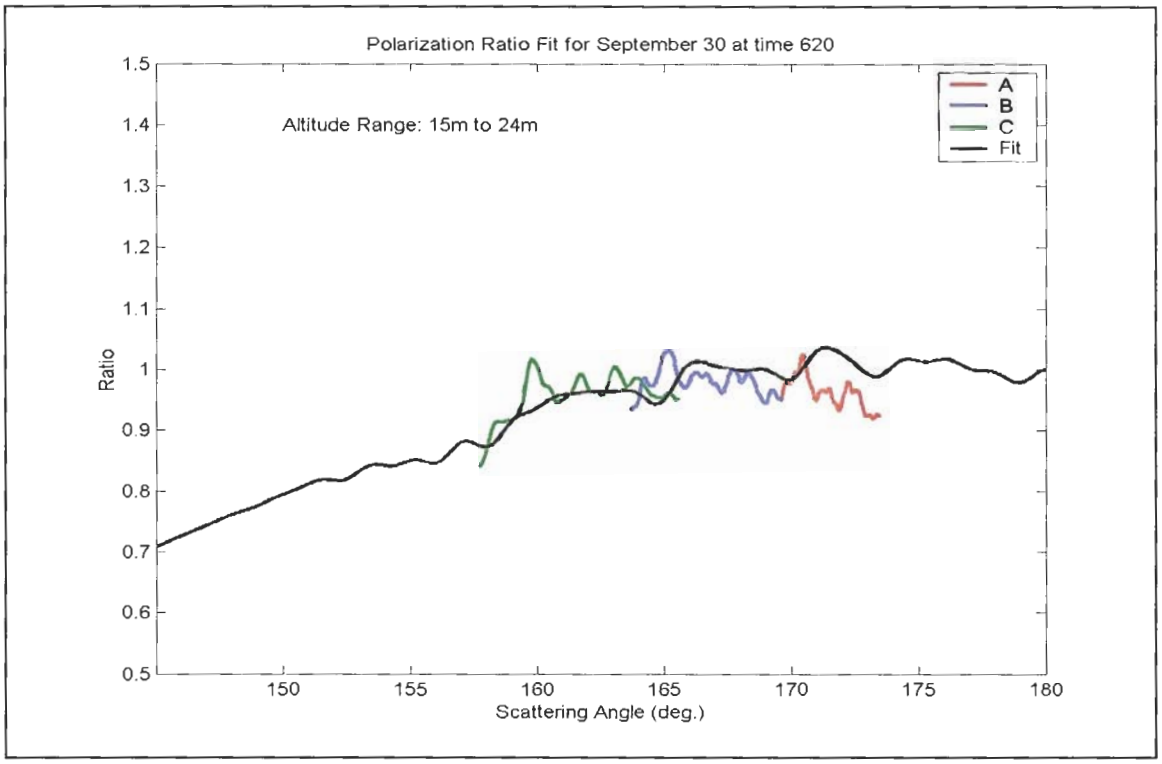

(a)

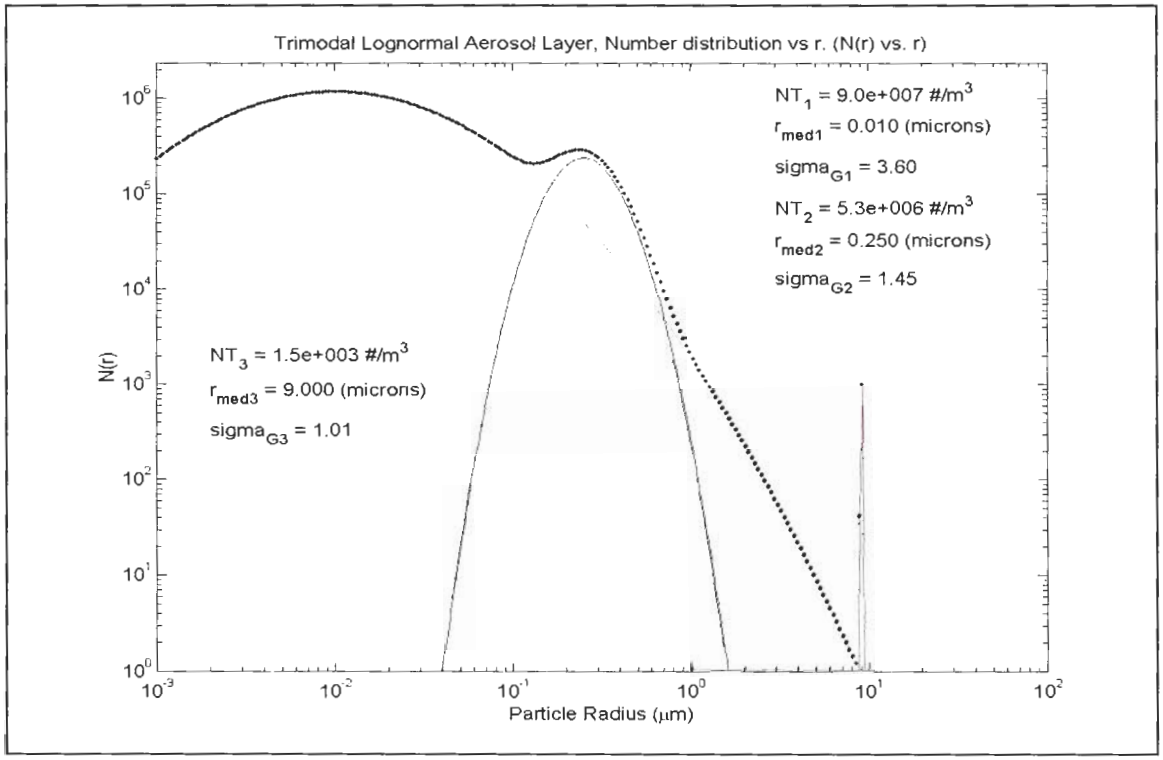

(b)

Figure 6-37: (a) Polarization ratio fit for 1 October 2001, 6:20am. (b) Lognormal parameters. Index used was 1.46.

6.3 SUMMARY

In this chapter, we analyzed polarization ratio data taken during the North East Oxidant and Particulate Study (NE-OPS) conducted during July 2001 in Philadelphia, U.S. Using a high power laser, our main goal was to be able to invert (i.e., infer) particle distributions and, if possible, particle composition, from the measured ratio of parallel and perpendicularly scattered radiation over altitudes from ground level to approximately 100m.

One of our main operating assumptions was that the nighttime atmosphere was uniformly mixed under the planetary boundary layer. While true some of the time, we found evidence of strong altitude variations of the aerosol concentrations. Such strong altitude dependence was unexpected and precluded rigorous inversions due to the lack of knowledge regarding the aerosol layers' spatial distribution and physical composition. However, in one instance, detailed in this chapter, we did encounter a relatively stable and uniform time period that could be inverted. Our results showed that the retrieved lognormal parameters were consistent with the available data but percent error could not be obtained due to lack of fit of the model to the data over a sufficient number of scattering angles. Additionally, an investigation of the role the index of refraction plays on the inversion process was also conducted. It was shown that the index of refraction could be changed significantly and yet reasonable lognormal parameters, inline with available data, could still be achieved. These results should serve to illustrate the difficulty in obtaining accurate particle data with open-air measurements, given the uncertainty of the parameters involved.

A case, which contained a strong and well-defined aerosol layer, was also investigated. Since the layer was above ground and not being directly monitored by any instrument or sensor, a true inversion was not possible. However, a model was constructed to allow for a more in-depth examination of the altitude distribution of the aerosol layer and inversion was conducted on several transition altitudes. Specifically, an attempt was made to determine whether the observed layer was carbonaceous in nature. Our results, while not conclusive, suggested that the layer was more likely related to the background than being composed of carbon particles.

A final case involved the examination of a data set taken in October 2001, in State College, PA. In comparing the data of this date to the data taken in Philadelphia, strong altitude-dependent aerosol layers were again observed. However, in the particular instance that was inverted, the aerosol layers appeared more stratified than those observed in Philadelphia thereby allowing an inversion of altitude sections.

Overall, although the data can be inverted to obtain particle size distribution parameters, the accuracy of the data is still in question. Based on this investigation and the one conducted by Stevens, further research using the polarization ratio must be conducted with known materials of known distributions.

7

Chapter 7: Summary

No thesis is ever finished.

We realize that the smart readers will immediately turn to this chapter and skip all of the discourse of the previous six chapters. Here, we will make an effort to summarize our efforts in a concise yet informative manner.

The focus of this thesis was to investigate and obtain particle (aerosol) concentrations within the first 1 km of the Earth's atmosphere by imaging the scattered light from a high-powered laser beam onto a set of three CCD digital cameras. The basic procedure began by first taking two images of the laser beam, one image with the laser emitting parallel polarization with respect to the scattering plane and one image with the laser emitting perpendicular polarization (see Chapter 5, Fig. 5-1). Once the images were taken, various programs and algorithms were used to ratio (divide) the two images to obtain the polarization ratio. By taking the ratio of a parallel polarized image with a perpendicular polarized image, the effect of instrumental errors could be alleviated. Upon obtaining the polarization ratio, an inversion process was used to attempt to find a possible, yet still reasonable, aerosol distribution responsible for the observed light scattering effects. The polarization ratio approach, first used by a former colleague of our laboratory, Tim Stevens, formed a cornerstone of this thesis. Although his equipment package and operating environment were different than what we presented here, Steven's work nevertheless provided us with a strong skeletal framework upon which to build this present work. Thus, it became a secondary goal of this thesis to not only expand upon Stevens' work but also to provide answers to several questions that he had left unanswered.

Our approach allowed us to investigate aerosol profiles at an altitude resolution that is not practical for other platforms such as balloons and aircraft. In recent years, there has been a call for further investigation of the vertical distribution and transport of aerosols. It was our intention to answer this call and to add information to the general body of knowledge regarding the vertical distribution of particulate matter and aerosols. We initially assumed that the atmosphere would be well mixed with uniformly distributed lognormal aerosol modes within the planetary boundary layer. However, we were able to show that the difference in the observed polarization ratios among the cameras for a given altitude range could not be attributed to measurement or instrumental errors but rather resulted from the presence of a rather pronounced altitude dependency. Thus, our experimental results would seem to suggest that the assumption that aerosols and particulates are uniformly mixed within the planetary boundary layer is not valid. It would, however, be more appropriate to say that the assumption of a uniformly mixed atmosphere within the planetary boundary layer is not valid within the spatial and temporal scales employed in this

thesis. In our review of the literature, information was difficult to obtain regarding the altitude distribution of aerosols, especially within the first 100-200 m of the atmosphere. Although the aerosol altitude dependence was a major finding of this thesis, it precluded us from obtaining more definitive results with regard to aerosol number density distributions.

While we encountered unforeseen difficulties on the experimental side of our work, our efforts on the theoretical side were well rewarded. Specifically, we put the polarization ratio itself under more analytical scrutiny in order to answer questions regarding its applicability and limitations. One of the more critical questions to answer was to try and understand how the polarization ratio itself changes for variations not only in aerosol number density distributions but also in the index of refraction[†]. We found that a practical angular viewing limit was approximately 10 degrees for a polydisperse atmosphere (more than 1 aerosol mode). However, with a more monodisperse distribution, a smaller range of angles could be used. Additionally, we also established that the polarization ratio is insensitive to the complex part of the index of refraction over nearly 6 orders of magnitude. Hence, the polarization ratio method (based on Mie theory) should not be used to obtain the complex index of refraction. Also from our investigation of the polarization ratio, we were able to answer a question posed by Stevens regarding the influence of the real part of the complex of refraction. Stevens suggested that changing the index of refraction might have provided him with better curve fits of his data to his model. Specifically, in one of his measurements, he was able to obtain a rather good curve fit over most of his observed angles but in other angular regions, the data and the theory deviated noticeably. Our investigation showed, however, that the real part of the refractive index has a large-scale effect on the entire polarization ratio curve and could not be used to accommodate certain parts of the curve while leaving other portions unaltered. Given our own data and investigation, we suggest that even in a horizontal configuration, the atmosphere may not be uniformly mixed.

For future studies, it must be stressed to the reader our extreme difficulty in obtaining verifiable results that are physically representative of the aerosols present at the time of measurement. In measuring atmospheric particle content using remote sensing techniques contains much uncertainty in the accuracy of the obtained distributions. If the monitoring of atmospheric particles and aerosols is to become practical, additional work must be accomplished first. In effect, one must step back from tackling the atmosphere as a whole and, instead, break it into more manageable parts. As it stands now, accurate monitoring of atmospheric particle concentrations is not practical with laser remote sensing.

Taken together, the work done by Stevens and this work have helped to demonstrate both the capabilities and limitations of the polarization ratio method as it pertains to the remote sensing of the aerosol constituency of the atmosphere. Hopefully one will learn from both the successes and failures of these studies and put them to good use in their own endeavors in using light scattering theory and techniques to investigate atmospheric aerosols, particulates and pollutants.

[†] Our wavelength was fixed so we did not investigate this parameter.

8

Chapter 8:
Future Work

Perfection is impossible therefore progress is infinite

In this work, we have encountered several problems that made our experimental analysis difficult and our data results somewhat uncertain. Specifically, we had unknown particle composition and distributions, scattering theory that was not universal, and inversion problems. Although we achieved a measured amount of success, there are still some glaring deficiencies that we would like to address. As we initially stated in Chapter 1, our ideal goal is to be able to completely identify the atmospheric makeup from the scattering of a laser beam. The next several sections identify the areas where we believe additional work can and should be done in order to reach this ideality. None of these suggestions are short term band-aids and it will take a significant amount of effort by many researchers in order to get a better handle on the science of scattering by atmospheric particles. We simply want to inform the reader some of the ideas that came about during the course of this investigation. Although we may not reach absolute perfection soon, there is certainly a lot of progress that can be done in the mean time.

8.1 THE USE OF KNOWN SCATTERING MEDIUMS

By far, the most difficult problem we encountered was that we simply did not know what the atmosphere contained in terms of its physical makeup and size distribution. We were forced to make assumptions about the particles' shape (spherical), their composition (via an index of refraction) and size distribution (lognormal and assumed uniformly distributed over a specified altitude segment). We do not want to sound overly adverse to our methodology but rather to simply point out the inherent difficulty in working in the open atmosphere.

We suggest that, before conducting another open-air investigation, the polarization ratio method should be applied to distributions of known index, size, shape and distribution. In essence, what is needed is a calibration step. Indeed, Stevens' own investigation appears to give credence to this suggestion. Specifically, Stevens' best data set was obtained when radiation fog moved into the observation area. Radiation fog contains a significant third aerosol mode, which yields identifiable structure in the polarization ratio. Although there were two other aerosol modes present, the scattering from this third mode dominated the other two and allowed Stevens to find very good curve fits to his data.

Once these experiments using known scattering mediums are completed and analyzed, the polarization ratio will have a much stronger footing in terms of both its theoretical and experimental aspects. We believe this is the only way to obtain a credible characterization of the polarization ratio method and will greatly aid the analysis of atmospheric scattering.

8.2 ELECTROMAGNETIC SCATTERING THEORY AND ATMOSHERIC MODELING

Electromagnetic scattering theory is exceptionally powerful if one knows how it is to be applied. It was originally thought that Mie theory (scattering by a sphere) is not applicable to atmospheric scattering but we found that under certain circumstances such as high relative humidity, the theory can explain experimental observations well. Mie theory only really begins to show problems in dust and desert situations where the particles are typically non-spherical and asymmetric. The question may come up as to whether there is something better than Mie theory. The answer is a resounding "probably".

The problem with various scattering theories is not that one is better than another but rather that one theory is better suited than another in certain situations. Mie theory is quite useful for predicting scattering in humid environments while other theories such as the T-Matrix and Charge Coupled Dipole methods may be better suited for arctic, desert or dry urban environments[†]. Basically, there is no ubiquitous theory that applies to all situations and conditions. One has to know something about the environment in which they are operating before applying any theory.

In addition to investigating the use of electromagnetic scattering theories, other aerosol size density distributions may also warrant further consideration. A lognormal function may not be desirable for profiling aerosol distributions. Although the lognormal function enjoys wide acceptance and use, another distribution that uses particle bins instead of analytical expressions is still used (see U.S. Environment Protection Agency, Models-3/4 software implementation). The benefit of this type of distribution is that it does not have the 9 lognormal parameters found in a standard trimodal lognormal function but instead uses the total number of particles within a size bin. On the surface, this may at first seem to be a somewhat more cumbersome approach since, if we had used a bin distribution in this work, we would need 250 bins to accommodate our 250 particle sizes. As it turns out, because there is no complicated expression, such an approach greatly reduces the complexity of the required computations needed for automated inversion processes such as a non-linear least squares approach (see section 8.4 below).

Lastly, we direct the interested reader's attention to the results of section 2.5, which discusses Kapteyn's transformation. When we first encountered this transformation, we were very impressed with its simplicity and results. The basic premise behind the transformation is to simply take the given data and mathematically manipulate it into another, more useful form in order to bring out details that would otherwise be obscured. For example, experimentally obtained particle size data generally does not readily show the presence of lognormal modes. However, by taking the data and converting it to a higher moment (such as area or volume), modal characteristics begin to appear. Although we did not investigate such an approach to our polarization ratio method, it is suggested that similar mathematical manipulation may help in uncovering details that would be of benefit during the inversion process.

[†] These theories are also highly successful in describing the scattering from a single particle or highly monodispersed distributions.

8.3 DAYTIME VIEWING

The sun has the single greatest effect of the earth's climate and meteorology. The method used in this work would be of greater use to pollution studies if it could be made to operate during daytime hours. To achieve this operation however requires ways to prevent the cameras[‡] from not only saturating but also from overheating during the day. Also, balance needs to be obtained between the need for a large number of scattering angles and the angular response of interference filters. The resulting equipment may need to operate in the UV region and use either neutral density filters or unique narrow band interference filters. In any event, daytime operation of the equipment is a desirable goal.

8.4 NON-LINEAR LEAST SQUARES (NLS) INVERSION

Aside from the interpretation of the data (*i.e.*, the aerosol distribution altitude dependence), the only major stumbling block encountered in this thesis was with the inversion process. When we read Stevens' work, he too had the greatest difficultly in inverting his polarization ratio data to obtain particle size density distributions. In fact, overcoming the difficulties with the inversion process was the single greatest motivating factor behind the intensive investigations of Chapter 2, 3 and 4 as we were looking for an approach or at least some insight as to how to manipulate the expressions in such a way to make them yield more readily useful information. Although we did not find such expressions during our investigations, we do believe that we have several tricks to play to aid us in the inversion process. The use of a non-linear least squares (NLS) routine has proven to be one of our aces (but it still needs some work).

If the inversion process could have been automated to avoid tedious repetition of guessing what set of parameters would best fit the data, not only would the overall interpretation of the data be easier but also the polarization ratio methodology would be that much more attractive in the remote sensing of particulates and aerosols in the open atmosphere. Stevens used a Newton-Raphson retrieval method to try and optimize his aerosol parameters. This inversion method did not work too well due to its lack of global convergence and so Stevens had to resort to a brute force, first guess, method. The NLS routine we used however does not suffer as much from a lack of global convergence, but it can still fail to converge if the initial guesses of the parameters are not good. We will show that, while the current version of the NLS routine we examined does have several significant challenges to overcome, it nevertheless performed beautifully in several trials. With work, the NLS routine has the potential to not only advance the interpretation and understanding of atmospheric scattering data but may also make real-time processing a reality.

The NLS routine used here was first coded by Hans Hallen and Brian Rasmussen from North Carolina State University. The core of the routine does not care about the significance or type of data it is processing but simply needs to know the mathematical rules (derivatives) with which to manipulate the

---

[‡] Linear diode arrays are just as good and a cost-effective substitute.

data. Thus, we had to come up with a front-end input algorithm that provided the data to be processed, initial guesses at the fitting parameters and the necessary derivatives. We also included steps that would allow us to follow the execution of the program and detail its success (or failure) in obtaining the desired solution. Several Matlab scripts were needed to display the results from the NLS routine.

Our goal, of course, was to use the NLS routine to fit data using the polarization ratio expression of Eqn. 3-58. Because we did not have a thorough understanding of the program and we still had to create the entire front-end interface, we first began investigating the NLS routine by using simple polynomials. Later, we graduated to multimode Gaussian and lognormal functions, finally arriving at the full-blown polarization ratio expression. While it took us a considerable amount of time to build up our understanding and knowledge of the NLS routine, taking a simpler approach first yielded results that we were able to directly use in more complicated investigations later.

In the next section, we will first examine the results of the NLS routine in fitting a 9th order polynomial function, including outlining the necessary derivatives. We will find that the NLS routine considers polynomial functions to be child's play as the routine barely breaks a sweat in finding the solution. In the next section, we start to stretch the capabilities of the NLS routine by fitting a single Gaussian function. The routine is further challenged when we introduce a trimodal Gaussian function. In fitting lognormal functions, we initially began by using the exact mathematical expressions as well as obtaining the analytical form of the corresponding derivatives. The investigation of the lognormal function took some time but, using the results of Chapter 2 and the Gaussian fitting routines, we finally realized that it was possible to "trick" the NLS routine into fitting the lognormal functions by believing it was fitting Gaussian functions[‡]. Using this trick, we combined the scattering matrices with unimodal, dualmodal, and finally trimodal lognormal functions and fit both the parallel and perpendicular functions of the polarization ratio[‡‡]. By the time the algorithm was attempting to fit the scattering functions with a trimodal distribution, the computer was breathing heavy. We finally made it collapse in agony when we tried fitting the full polarization ratio expression. We will discuss these results in order in the following sections.

8.4.1 NLS Fit of Polynomials

In fitting polynomials, the NLS routine performed with minimal effort and seldom crashed (in later applications, the NLS routine would crash regularly). As an example of the performance of the NLS routine, we used a 9th order polynomial of the form

$$y_{original} = a_9 x^9 + a_8 x^8 + \ldots + a_1 x + a_0 \tag{8-1}$$

where the ten coefficients, $a_{0\text{-}9}$, are to be found by the NLS fitting routine. A Matlab script was written to

---

[‡] As indicated in Chapter 2, this trick was accomplished by changing the random variable from **r** to **lnr**.
[‡‡] The numerator and denominator of Eqn. 3-58.

generate the actual data for use in the NLS fitting routine. The routine also requires the user to provide initial guesses for each of the parameters to be found. To give the routine a little more of a challenge, additive white Gaussian noise was added to the original data,

$$y = y_{original} + noise \tag{8-2}$$

and it was to this combined data that the NLS routine attempted to find a fit. There are two measures of the NLS routine's success in determining the wellness of its fit. The first measure is how close the final fitting parameters match the original parameters, despite the presence of noise. Additional code was included in the NLS routine so that the user could see how the fitting parameters evolved from their initial guesses to their final values. The second measure of the NLS routines fitting success examines the overall curve with the final fitted curve. The principal parameter used in this qualification was chi-squared (χ^2). The chi-squared parameter is often found in statistics and does have a slightly different use and interpretation than it does here. In the NLS routine, the basic essence of chi-squared is (see the code for actual implementation).

$$\chi^2 = (y_{fitted} - y)^2 . \tag{8-3}$$

In our routine, we strive for as small a chi-squared value as possible.

In addition to the data to be fitted and the initial guesses of the parameters, the NLS routines also demand to know how to compute the derivatives of the entire function, y, with respect to each parameter. For polynomials, the first derivative is trivial to calculate and is given by

$$\frac{dy}{da_i} = x^i . \tag{8-4}$$

For example, the derivative of the polynomial function with respect to a_9 is x^9 while the derivative with respect to a_1 is x. Although the analytical expressions of the derivatives can and were coded into the NLS routine, simpler, easier to compute numerical derivatives can and were also used. When we get to using the NLS routine with lognormal and scattering functions, we will find the numerical approach to be somewhat easier to implement than using the full analytical expression of each derivative. We did, however, investigate both the analytical and numerical approaches to make sure they were both giving the same answers. In the case of the 9th order polynomial we are examining, the numerical derivative with respect to a_9 is given as

$$\frac{\Delta y}{\Delta a_9} = \frac{\left(y\big|_{a_9} - y\big|_{a_9+\varepsilon}\right)}{\varepsilon}, \tag{8-5}$$

where ε is some small increment (*eg.*, 0.001) added to a_9. Any choice of ε will not necessarily work as one has to be sure that their choice of ε does indeed result in a close numerical approximation to the actual derivative.

Figure 8-1 steps the reader through the process the NLS routine accomplished in obtaining the best fit to the given data while Figure 8-2 shows that the routine only need two iterations to find the solution (notice that the chi-squared value dropped by nearly 13 orders in magnitude). Table 8-1 lists the original

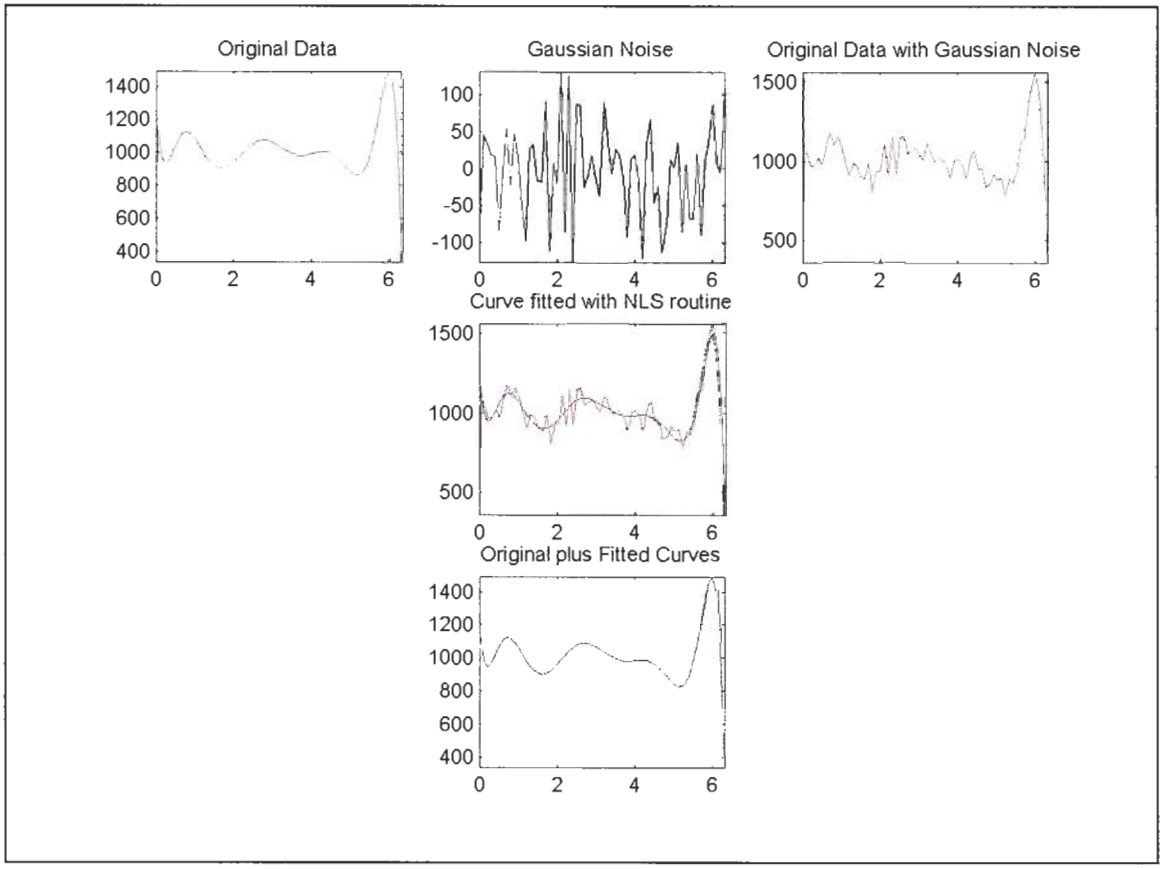

Figure 8-1: Results of the NLS routine in fitting a 9th order polynomial.

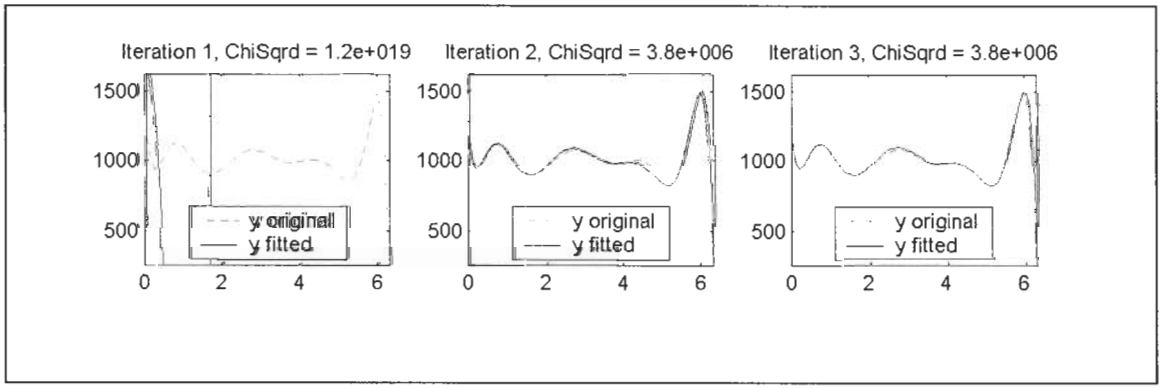

Figure 8-2: Evolution of the NLS fit for 9th order polynomial.

values of the 10 parameters, their initial guesses and their final values obtained by the NLS routine. Emboldened by the ease with which the NLS routine handled this 9th order polynomial, we next moved to fitting Gaussian functions.

Table 8-1: Coefficients of the 9th order polynomial fit

Coefficient	Actual Value	Initial Guess	Final Value
a_0	1220.87	2000	1167.71
a_1	-3290.12	-4000	-2728.15
a_2	12643.77	10000	11141.5
a_3	-19814.19	-30000	-18065.7
a_4	15907.57	17000	14811.2
a_5	-7281.20	-7000	-6872.88
a_6	1980.20	3000	1886.85
a_7	-316.69	300	-303.82
a_8	27.5	40	26.52
a_9	-1	1	-0.97

8.4.2 NLS Fit of Gaussian Functions

Using the NLS routine to fit Guassian functions was made slightly more difficult due to more complex derivatives. However, the NLS routine still performed well and was able to determine optimal fitting parameters with little difficulty. We began by trying to fit a single Gaussian of the form

$$y = \frac{N_T}{\sqrt{2\pi}\cdot\sigma}\exp\left\{-\frac{1}{2\sigma^2}(x-\mu)^2\right\}, \tag{8-6}$$

where N_T, μ and σ are the three fitting parameters to be optimized by the NLS routine. From Eqn. 8-6, we need to establish the derivatives with respect to each of the three fitting parameters. The derivative with respect to N_T is simple and is given by

$$\frac{dy}{dN_T} = \frac{1}{\sqrt{2\pi}\cdot\sigma}\exp\left\{-\frac{1}{2\sigma^2}(x-\mu)^2\right\} \tag{8-7a}$$

$$= \frac{y}{N_T}. \tag{8-7b}$$

Using Eqn. 8-7b for the derivative helps to reduce the computational demands on the program and also makes coding much easier. We could also use the numerical derivative approximation. This is accomplished by first calculating Eqn. 8-6 for some N_T and then re-calculating Eqn. 8-6 for $N_T+\varepsilon$. The

two calculations are subtracted and the result is divided by ε to arrive at the numerical derivative. In analytical form, the numerical derivative approximation for N_T is expressed as

$$\frac{\Delta y}{\Delta N_T} = \frac{\left(y\big|_{N_T} - y\big|_{N_T+\varepsilon}\right)}{\varepsilon}.$$

In the implementation, the analytical expressions for the derivatives were used, primarily due to their compactness and simplicity while the numerical derivatives were used as independent checks.

The derivative of Eqn. 8-6 with respect to μ is given by

$$\frac{dy}{d\boldsymbol{\mu}} = \frac{N_T}{\sqrt{2\pi}\cdot\boldsymbol{\sigma}}\exp\left\{-\frac{1}{2\boldsymbol{\sigma}^2}(x-\boldsymbol{\mu})^2\right\}\cdot\left[\frac{x-\boldsymbol{\mu}}{\boldsymbol{\sigma}^2}\right] \tag{8-8a}$$

$$= y\left[\frac{x-\boldsymbol{\mu}}{\boldsymbol{\sigma}^2}\right]. \tag{8-8b}$$

As with Eqn. 8-7b, Eqn. 8-8b was used in the implementation due to its compactness.

The derivative with respect to σ is rather more complicated given its position within the Gaussian expression of Eqn. 8-6. With a little work, the derivative was found to be

$$\frac{dy}{d\boldsymbol{\sigma}} = \frac{N_T}{\sqrt{2\pi}}\left(-\frac{1}{\boldsymbol{\sigma}^2}\right)\exp\left\{-\frac{1}{2\boldsymbol{\sigma}^2}(x-\boldsymbol{\mu})^2\right\} + \frac{N_T}{\sqrt{2\pi}\cdot\boldsymbol{\sigma}}\exp\left\{-\frac{1}{2\boldsymbol{\sigma}^2}(x-\boldsymbol{\mu})^2\right\}\cdot\left[-\frac{1}{2}\left(-\frac{2}{\boldsymbol{\sigma}^3}\right)(x-\boldsymbol{\mu})^2\right] \tag{8-9a}$$

$$= -\frac{1}{\boldsymbol{\sigma}}y + y\frac{(x-\boldsymbol{\mu})^2}{\boldsymbol{\sigma}^3} \tag{8-9b}$$

and Eqn. 8-9b was used in the implementation. The complexity of determining the derivative with respect to σ was a motivating factor in finding the more compact and streamlined expressions given by Eqns. 8-7b, 8-8b & 8-9b.

An example of using the NLS routine to fit a single Gaussian is shown in Figure 8-3. As with the polynomial example, the NLS had a rather easy time in finding the optimal fit. However, we began to notice that certain initial guesses at the parameters would cause the program to crash[†]. Specifically, the NLS routine did not like values that were very small (near zero). Of course, if the initial guesses were completely out of the ballpark, the program would also fail to converge. Figure 8-4 shows the NLS routine finding the optimal curve and Table 8-2 lists the evolution of the fitting parameters.

Because we knew that we would need to eventually investigate three lognormals with the NLS routine, we performed fits on two and three Guassians. For three Gaussians, the overall function is simply,

$$y = y_1 + y_2 + y_3,$$

[†] We inserted a break into the code to stop executing. Otherwise, the program would enter an infinite loop.

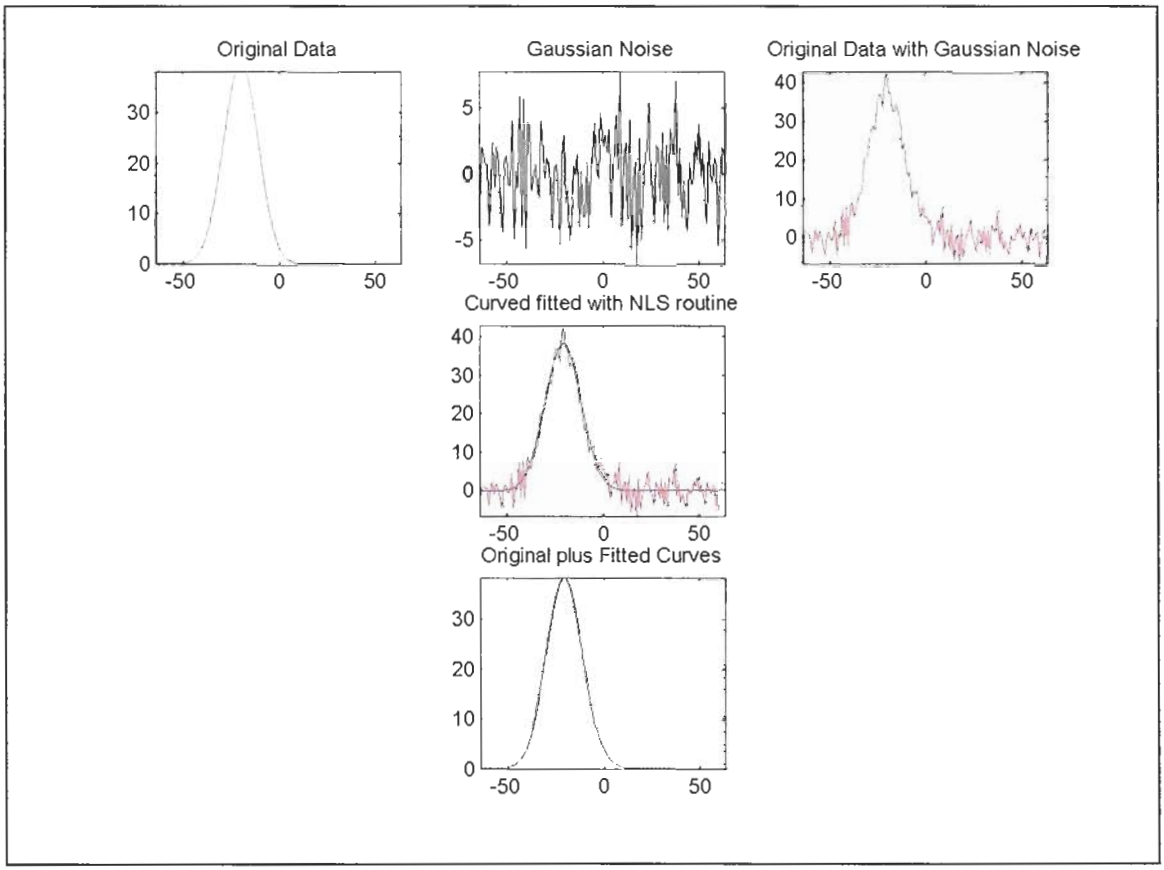

Figure 8-3: Results of the NLS routine fitting a three-parameter Gaussian.

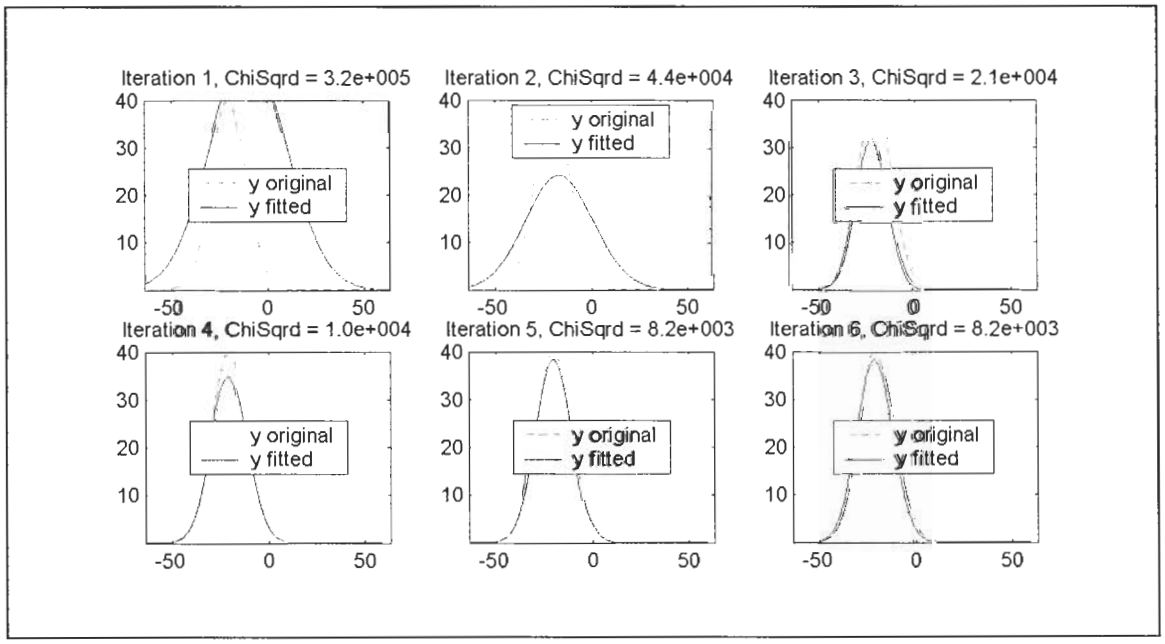

Figure 8-4: Evolution of the NLS routine for the three-parameter Gaussian.

Table 8-2: Parameters of the three parameter Gaussian NLS fit

Parameter	Actual Value	Initial Guess	Final Value
N_T	40	50	38.2979
μ	40	-10	-20.16
σ	9	20	9.4032

where each y_i is given by Eqn. 8-6. Since there are nine fitting parameters (N_{T1}, μ_1, σ_1, N_{T2}, μ_2, σ_2, N_{T3}, μ_3, σ_3), the routine needs code for nine derivatives. Eqns. 8-7b, 8-8b, & 8-9b were easily included in the code. The results of using the NLS routine to fit three Gaussians are shown in Figure 8-5, 8-6 and the parameters are summarized in Table 8-3.

Table 8-3: Parameters of the nine parameter, three Gaussian NLS fit

Parameter	Actual Value	Initial Guess	Final Value
N_{T1}	45	83	44.2805
μ_1	25	27	23.7533
σ_1	9	7	7.8891
N_{T2}	35	45	35.9061
μ_2	45	47	47.1793
σ_2	5	6	9.2738
N_{T3}	75	80	66.3013
μ_3	65	70	66.6012
σ_3	8	5	6.7416

In fitting the three Gaussians, we noticed that the NLS routine became very sensitive to the initial guesses and required such guesses to be rather close to the original values. We even found that if the guesses were indeed the actual parameters, the program would still crash. Such a stringent request by the NLS routine almost obviated its use and hampered us in getting the routine to fit the scattering expressions. Improving the routine's ability to take in more reasonable guesses and still find a fit would be a major improvement to the overall code.

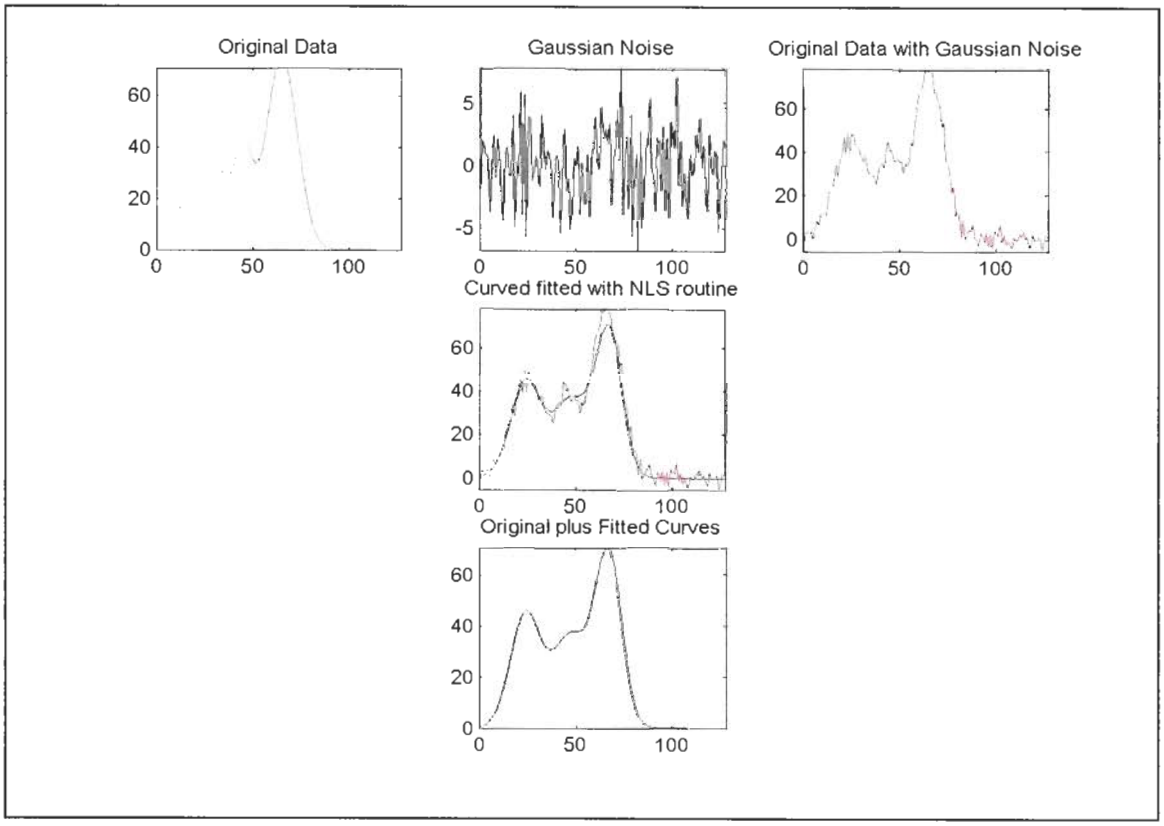

Figure 8-5: Results of the NLS routine fitting a nine parameter, three Gaussian function.

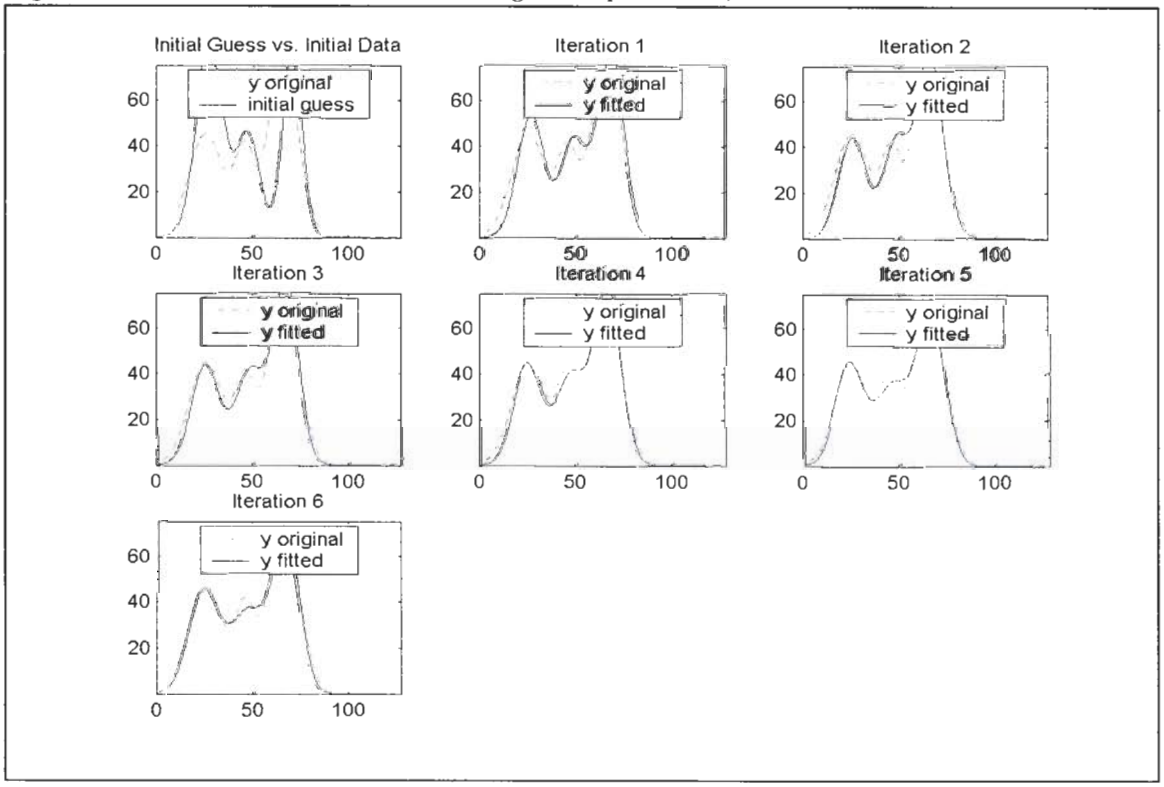

Figure 8-6: Evolution of the NLS fit to the nine parameter, three Gaussian function.

8.4.3 NLS Fit of Lognormal Functions

Inputting the code, correcting errors, and checking the results for the NLS fit of the nine parameter, three Gaussian function was not easy and took time (as most things that are new generally do). Thus, we were not looking forward to updating the code, finding the derivatives, correcting errors and checking the results all over again for the more complicated lognormal functions. Necessity and sanity motivated us to find a better way to use the NLS routine with lognormal functions. Thankfully, the work we did in Chapter 2 paid off handsomely here as we "tricked" the NLS routine into fitting Gaussian functions that were actually lognormal functions in disguise.

From Chapter 2, the basic lognormal function used in aerosol and particulate science is given as

$$\frac{dN}{dr} = \frac{N_T}{\sqrt{2\pi}\cdot \ln(\boldsymbol{\sigma}_g)\cdot r}\exp\left\{-\frac{1}{2\ln^2(\boldsymbol{\sigma}_g)}(\ln(\mathbf{r})-\ln(\mathbf{r}_{\text{median}}))^2\right\}, \tag{8-10}$$

where N_T, $\mathbf{r}_{median}$, and σ_g are the desired parameters to be found, **r** is the particle radius and N is the number density within a size range, dr. Moving **r** to the left hand side as

$$r\frac{dN}{dr} = \frac{N_T}{\sqrt{2\pi}\cdot \ln(\boldsymbol{\sigma}_g)}\exp\left\{-\frac{1}{2\ln^2(\boldsymbol{\sigma}_g)}(\ln(\mathbf{r})-\ln(\mathbf{r}_{\text{median}}))^2\right\} \tag{8-11}$$

and using

$$d\ln\mathbf{r} = \frac{d\mathbf{r}}{\mathbf{r}} \tag{8-12}$$

we have converted the random variable from **r** to **lnr** and in doing so have changed the lognormal function back to a Gaussian function. Now, using the relations of Equations 2-24 and 2-25, repeated here as,

$$\boldsymbol{\mu} = \ln(\mathbf{r}_{\text{median}})$$
$$\boldsymbol{\sigma} = \ln(\boldsymbol{\sigma}_g)$$

we have the Gaussian function,

$$\frac{dN}{dlnr} = \frac{N_T}{\sqrt{2\pi}\cdot\boldsymbol{\sigma}}\exp\left\{-\frac{1}{2\boldsymbol{\sigma}^2}(\ln(\mathbf{r})-\boldsymbol{\mu})^2\right\} \tag{8-13}$$

Equation 8-13 is identical to Eqn. 8-6, which can be seen if we let x = lnr and write

$$\frac{dN}{dx} = \frac{N_T}{\sqrt{2\pi}\cdot\boldsymbol{\sigma}}\exp\left\{-\frac{1}{2\boldsymbol{\sigma}^2}(x-\boldsymbol{\mu})^2\right\} \tag{8-14}$$

The above expressions are not quite what we need for use with the scattering functions as we need the number density distribution. Thus, we simply need to move the *dx* (or *dlnr*) to the other side of the expression. In our scattering model, the particle bins were logarithmically distributed and so *dlnr* is not a variable but rather a fixed number. So, we are left with computing the derivatives of

$$y = \frac{N_T}{\sqrt{2\pi}\cdot\sigma}\exp\left\{-\frac{1}{2\sigma^2}(x-\mu)^2\right\}\cdot d\ln r\,, \tag{8-15}$$

which we have already found (Eqns. 8-7, 8-8, 8-9). We used the NLS routine to fit one, two and three lognormal functions using Eqn. 8-15 as the translation. As one may expect, the results were identical to the fits using the Gaussian functions and so will not be shown here. We are now ready to use the NLS routine with scattering equations.

8.4.4 NLS Fit of Scattering Expressions

In truth, after we successfully used the NLS routine to fit Gaussian and lognormal functions, we felt confident that we could immediately proceed to fitting the full polarization ratio. Unfortunately our confidence was squashed by repeated failures of trying to get the routine to work past its first iteration of the parameters. We tried the program using both the analytical and numerical derivatives, only one lognormal mode and even implemented the code with the untranslated form of the lognormal functions. All trials could not get past the first iteration. We were left with breaking the polarization ratio into its numerator and denominator and trying to fit these functions separately. Because of our success with the Gaussian and lognormal functions, we felt that the program should be able to find fits using the scattering expressions and it was our hope that in breaking the problem into smaller parts that we may find the cause of our frustration.

From Chapter 3, the polarization ratio is written as

$$PR(\theta) = \frac{I_{\parallel}}{I_{\perp}} = \frac{\left[\int S_2(n,\lambda,\theta,r)\{Mode\ \#1 + Mode\ \#2 + Mode\ \#3\}\,dr\right] + Molecules_{\parallel}}{\left[\int S_1(n,\lambda,\theta,r)\{Mode\ \#1 + Mode\ \#2 + Mode\ \#3\}\,dr\right] + Molecules_{\perp}}, \tag{8-16}$$

where S_1 and S_2 are the pre-calculated scattering matrices[‡] and the modes are the number density distribution given by Eqn. 8-15. Also, the molecular component is pre-calculated and read in by the NLS routine. One can see that we would have considerable difficulty if we had started directly with Eqn. 8-16 with the NLS routine. The challenging task left to do is to find the nine derivatives of the polarization ratio with respect to each of the nine lognormal parameters. This would be a case where the numerical derivative approximation would be of benefit but we did find and implement the analytical derivative expressions using the results of the previous sections and the quotient rule from calculus. Because of the fraction, taking the derivative is a bit more complicated. However, many terms are constant with respect to

[‡] For now, we assume the index of refraction to be constant.

a particular derivative and so drop out, thus leaving greatly simplified equations. We next show the results of the NLS routine in fitting the numerator and denominator of Eqn. 8-16 separately.

8.4.4.1 NLS Fit of the Parallel Scattering Function

The parallel scattering function we will use with the NLS routine is given by the numerator of Eqn. 8-16. Using the results from sections 8.4.2 and 8.4.3, finding the derivatives is simple and will not be shown here. As we have already mentioned, the scattering function S_2 is pre-calculated and is simply read into an array by the NLS routine. Figure 8-7 shows the results of using the NLS routine to find the optimal nine lognormal parameters using the parallel scattering function. The parameters are summarized in Table 8-4 (the refractive index was fixed at 1.38).

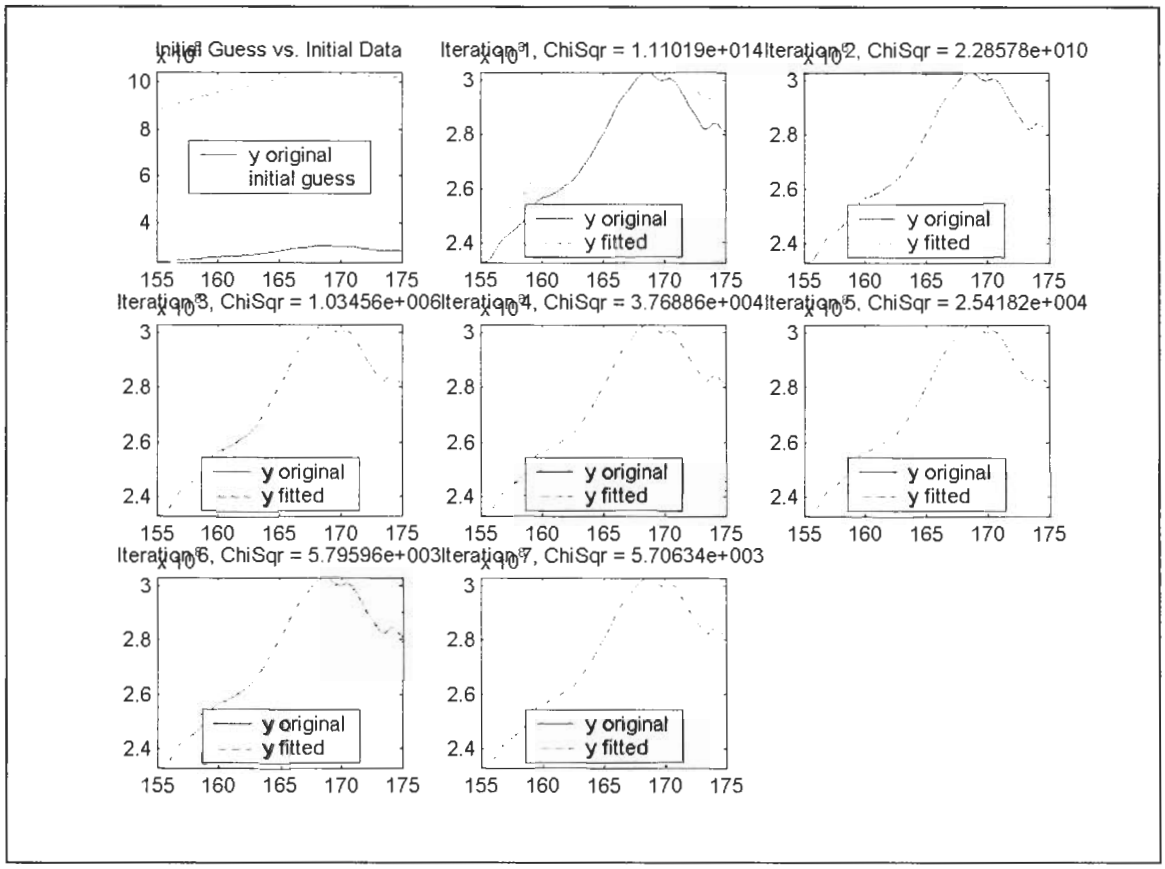

Figure 8-7: Evolution of the NLS fit to the trimodal (9 parameters) parallel scattering function.

From Figure 8-7, we note that the NLS routine performed remarkably well as the chi-squared value was reduced by nearly 11 orders of magnitude. Indeed, the routine had the basic curve after only two iterations but continued to refine the values for another 8 iterations. Such a refinement is highly desirable in obtaining the best-fit parameters and serves to illustrate the need for having an optimizing tool such as the NLS routine. We note however, that some of the parameters had to be chosen to be either very close or exactly the same as the original or else the program would fail to converge.

Table 8-4: Parameters of the trimodal, parallel scattering function NLS fit.

Parameter	Actual Value	Initial Guess	Final Value
N_{T1} (#/m^3)	4.0e10	8.0e11	1.2363e10
$\mathbf{r}_{median1}$ (μm)	0.005	0.009	0.0091037
σ_{g1}	2.7	2.5	2.4873
N_{T2} (#/m^3)	3.62e6	3.62e5	3.6321e6
$\mathbf{r}_{median2}$ (μm)	0.5	0.5	0.4995
σ_{g2}	1.75	1.75	1.7503
N_{T3} (#/m^3)	4.5e3	5.53e3	4.4998e3
$\mathbf{r}_{median3}$ (μm)	8.85	8.8	8.85
σ_{g3}	1.2	1.2	1.2

8.4.4.2 NLS Fit of the Perpendicular Scattering Function

The denominator of Eqn. 8-16 gives the perpendicular scattering function we used to accomplish the NLS fit. We should be specific and indicate that we fitted the $I_\perp$ function and not the $(I_\perp)^{-1}$ function. Building on our experience with the parallel scattering function, we also found that the NLS routine required very good initial guesses of the fitting parameters. To be a little different, Figure 8-8 shows the results of the NLS fit to the perpendicular scattering function using only the third mode (corresponding to the coarse aerosol mode) and Table 8-5 summarizes the results. However, we also ran the NLS routine using all three modes.

Table 8-5: Parameters of the NLS fit to the single large mode perpendicular scattering function.

Parameter	Actual Value	Initial Guess	Final Value
N_{T3} (#/m^3)	4.5e3	5.0e3	4.5e3
$\mathbf{r}_{median3}$ (μm)	8.85	10.1	8.85
σ_{g3}	1.2	1.05	1.2

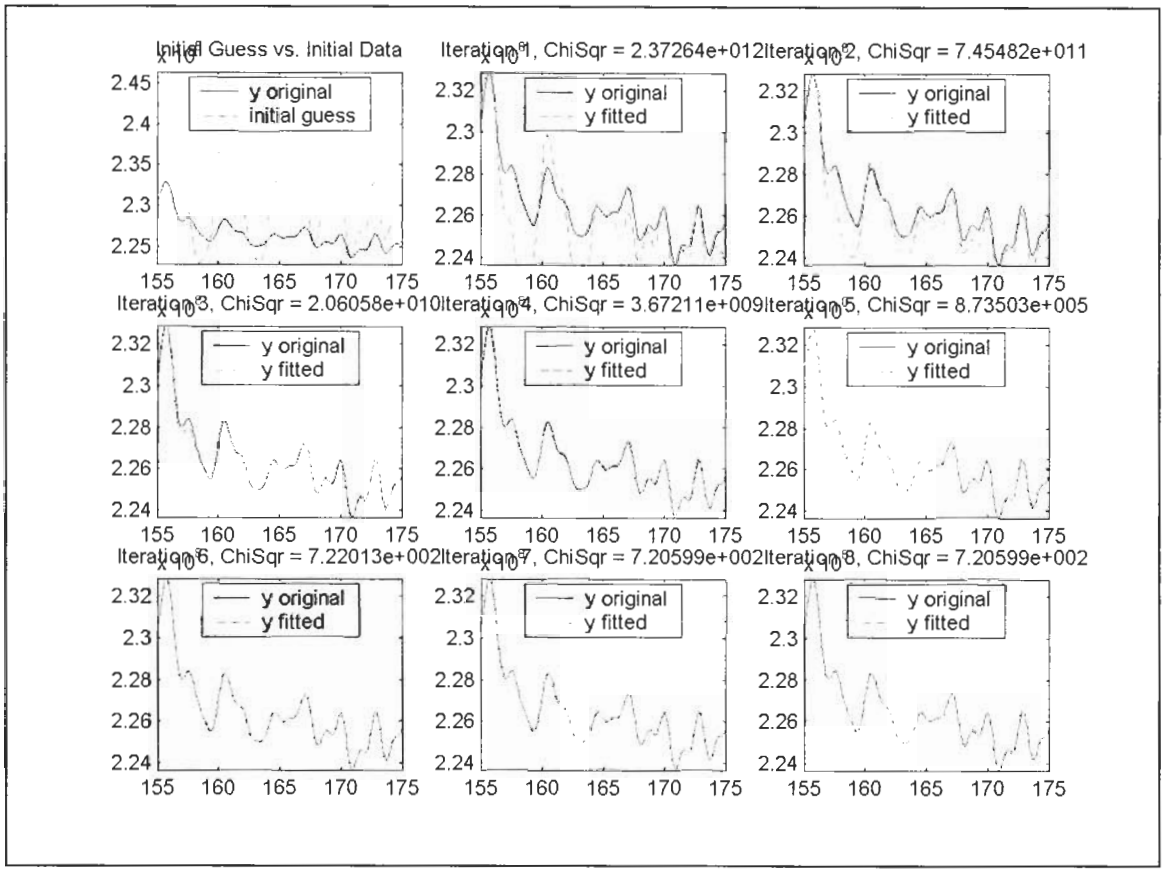

Figure 8-8: Evolution of the NLS fit of the single mode, perpendicular scattering function.

8.4.5 NLS Fit of the Polarization Ratio

After successfully fitting both the parallel and perpendicular scattering functions, we were still at a loss to explain why our fit to the entire polarization ratio failed. However, we tried to fit one other function, the $(l_{\perp})^{-1}$ function and this is where we found our problem as the NLS routine also failed to get past the first iteration. We reduced the complexity of our starting curve further by next going back to a single Gaussian function and it, too, failed to converge. Based on our intuition and later confirmed by Dr. Hans Hallen, the NLS routine has trouble fitting curves whose derivatives may result in abnormally high numbers. For example, a typical Gaussian goes to zero away from its mean. However, if one inverts this same Gaussian, the function now heads to infinity. It is this problem that has not been overcome as it requires one to understand the inner workings of the core processing routine. Such an investigation would take some time and certainly be a thesis-level project but the results would be incredibly useful and find a myriad of applications, not just in inverting polarization ratio curves. All of the NLS codes and Matlab scripts can be obtained from the author upon request.

Before leaving this section, one other major portion of the polarization ratio inversion needs to also be incorporated into the NLS processing routine and that involves the (real) index of refraction[†]. From our derivation of Mie theory in Chapter 3, the index of refraction is not easy to get at and its analytical derivative would be cumbersome to obtain. Although, we did perform a numerical approximation of the derivative of the polarization ratio with respect to the index of refraction, we cannot be absolutely certain of our results without comparing it to the exact analytical expression. No runs of the NLS routine were performed to optimize the index of refraction.

[†] Remember, Mie theory is insensitive to the imaginary part of the index and so should not be included in the NLS routine.

References

Journals:

Andronova, A.V., L. Gomes, V.V. Smirnov, A.V. Ivanov, and L.M. Shukurova, "Physico-chemical Characteristics of Dust Aerosols Deposited During the Soviet-American Experiment (Tadzhikistan, 1989)", *Atmospheric Environment*, Vol. 27A., No. 16, pp. 2487-2493, 1993.
RA576.A81 Earth & Mineral Sciences Library

Ansmann, A., D. Althausen, U. Wandinger, K. Franke, D. Müller, F. Wagner, and J. Heintzenberg, "Vertical Profiling of the Indian Aerosol Plume with Six-Wavelength Lidar During INDOEX: A First Case Study", *Geophysical Research Letters*, Vol. 27, No. 7, pp. 963-966, 2000.
QC801.G44 Earth & Mineral Sciences Library

Ansmann, A., D. Althausen, U. Wandinger, D. Müller, and F. Wagner, "Physical Properties of the Indian Aerosol Plume Derived from Six-Wavelength Lidar Observations on 25 March 1999 of the Indian Ocean Experiment", *Geophysical Research Letters*, Vol. 27, No. 9, pp. 1403-1406, 2000.
QC801.G44 Earth & Mineral Sciences Library

Barber, P. and C. Yeh, "Scattering of Electromagnetic Waves by Arbitrarily Shaped Dielectric Bodies", *AppliedOptics*, Vol. 14, No. 12, pp. 2864-2872, 1975.
QC350.O62 Physical Sciences Library

Barnett, C.E. and G.G. Simon, "Particle Size Distribution of Rutile Pigment from Spectral Turbidity", *Journal of Colloid and Interface Science*, Vol. 34, No. 4, pp. 580-584, 1970.
QD549.J67 Physical Sciences Library

Berry, E.X., "Cloud Droplet Growth by Collection", *Journal of the Atmospheric Sciences*, Vol. 24, pp. 688-701,1967.
QC851.A283 Earth & Mineral Sciences Library

Bhandari, R., "Scattering Coefficients for a Multilayered Sphere: Analytic Expressions and Algorithms", *AppliedOptics*, Vol. 24, No. 13, pp. 1960-1967, 1985.
QC350.O62 Physical Sciences Library

Binkowski, F. S. and U. Shankar, "The Regional Particulate Matter Model. 1. Model Description and Preliminary Results", *Journal of Geophysical Research*, Vol. 100, No. D12, pp. 26191-26209, 1995.
QC811.T3 Earth & Mineral Sciences Library

Blifford Jr., I.H. and L.D. Ringer, "The Size and Number Distribution of Aerosols in the Continental Troposphere", *Journal of the Atmospheric Sciences*, Vol. 26, pp. 716-726, 1969.
QC851.A283 Earth & Mineral Sciences Library

Bohren, C.F., "Applicability of Effective-Medium Theories to Problems of Scattering and Absorption by Nonhomogeneous Atmospheric Particles", *Journal of the Atmospheric Sciences*, Vol. 43, No. 5, pp.468-475, 1986.
QC851.A283 Earth & Mineral Sciences Library

Bohren, C.F., "Multiple Scattering of Light and Some of Its Observable Consequences", *American Journal Of Physics*, Vol. 55, No. 6, pp. 524-533, 1987.
QC1.A47 Physical Sciences Library

Bohren, C.F. and S.B. Singham, "Backscattering by Nonspherical Particles: A Review of Methods and Suggested New Approaches", *Journal of Geophysical Research*, Vol. 96, No. D3, pp. 5269-5277, 1991.
QC811.T3 Earth & Mineral Sciences Library

Burges, S.J. and K. Hoshi, "Approximation of a Normal Distribution by a Three-Parameter Log Normal Distribution", *Water Resources Research*, Vol. 14, No. 4, pp. 620-622, 1978.
GB651.W33 Earth & Mineral Sciences Library

Burges, S.J., D.P. Lettenmaier, and C.L. Bates, "Properties of the Three-Parameter Log Normal Probability Distribution", *Water Resources Research*, Vol. 11, pp. 229-235, 1975.
GB651.W33 Earth & Mineral Sciences Library

Cantrell, B.K. and K.T. Whitby, "Aerosol Size Distributions and Aerosol Volume Formation for a Coal-Fired Power Plant Plume", *Atmospheric Environment*, Vol. 12, pp. 323-333, 1978.
RA576.A8 Earth & Mineral Sciences Library

Chow, J.C., D.H. Lowenthal, J.G. Watson, S.D. Kohl, B.A. Hinsvark, E.I. Hackett, and J.K. McCormack, "Light Absorption by Black Sand Dust", *Applied Optics*, Vol. 39, No. 24, pp. 4232-4236, 2000.
QC350.O62 Physical Sciences Library

Clark, W.E. and K.T. Whitby, "Concentration and Size Distribution Measurements of Atmospheric Aerosols and a Test of the Theory of Self-Preserving Size Distributions", *Journal of the Atmospheric Sciences*, Vol. 24, pp. 677-687, 1967.
QC851.A283 Earth & Mineral Sciences Library

Davies, C.N. "Size Distribution of Atmospheric Particles", *Journal of Aerosol Science*, Vol. 5, pp. 293-300, 1974.
QC882.J68 Earth & Mineral Sciences Library

Doddridge, B.G., R.R. Dickerson, S. Kondragunta, G. Stenchikov, K.L. Civerolo, and B.N. Holben, "The Impact of Aerosols on Solar Ultraviolet Radiation and Photochemical Smog", *Science*, Vol. 278, pp. 827-830, 1997.
Available through Inter-Library Loan

Epstein, B., "The Mathematical Description of Certain Breakage Mechanisms Leading to the Logarithmico-normal [sic] Distribution", *Journal of the Franklin Institute*, Vol. 244, pp. 471-477, 1947.
T1.F8 Annexed Materials

Eiden, R., "Determination of the Complex Index of Refraction of Spherical Aerosol Particles", *Applied Optics*, Vol. 10, No. 4, pp. 749-754, 1971.
QC350.O6 Physical Sciences Library

Feingold, G. and Z. Levin, "The Lognormal Fit to Raindrop Spectra from Frontal Convective Clouds in Israel", *Journal of Climate and Applied Meteorology*, Vol. 25, pp. 1346-1363, 1986.
QC851.A6601 Earth & Mineral Sciences Library

Fitch, B.W. and T.S. Cress, "Spatial and Temporal Variations of Tropospheric Aerosol Volume Distributions", *Journal of Climate and Applied Meteorology*, Vol. 22, pp. 1262-1269, 1983.
QC851.A6601 Earth & Mineral Sciences Library

Fuller, K.A., W.C. Malm and S. M. Kreidenweis, "Effects of Mixing on Extinction by Carbonaceous Particles", Journal of Geophysical Research, Vol. 104, No. D13, pp. 15941-15954, 1999.
QC811.T3 Earth & Mineral Sciences Library

Gerber, H., "Probability Distribution of Aerosol Backscatter in the Lower Marine Atmosphere at CO_2 Wavelengths", *Journal of Geophysical Research*, Vol. 96, No. D3, pp. 5307-5314, 1991.
QC811.T3 Earth & Mineral Sciences

Goedecke, G.H. and S.G. O'Brien, "Scattering by Irregular Inhomogeneous Particles via the Digitized Green's Function Algorithm", *Applied Optics*, Vol. 27, No. 12, pp. 2431-2438, 1988.
QC350.O62 Physical Sciences Library

Goedecke, G.H. and S.G. O'Brien, "Scattering of Millimeter Waves by Snow Crystals and Equivalent Homogeneous Symmetric Particles", *Applied Optics*, Vol. 27, No. 12, pp. 2439-2444, 1988.
QC350.O62 Physical Sciences Library

Grams, G.W., "In-Situ Measurements of Scattering Phase Functions of Stratospheric Aerosol Particles in Alaska During July 1979", *Geophysical Research Letters*, Vol. 8, No. 1, pp. 13-14, 1981.
QC801.G44 Earth & Mineral Sciences Library

Grams, G.W., I.H. Blifford, Jr., D.A. Gillette and P.B. Russell, "Complex Index of Refraction of Airborne Soil Particles", *Journal of Applied Meteorology*, Vol. 13, pp. 459-471, 1974.
QC851.A66 Earth & Mineral Sciences Library

Granqvist, C.G. and R.A. Buhrman, "Log-Normal Size Distributions from Magnetization Measurements on Small Superconducting Al Particles", *Journal of Applied Physics*, Vol. 47, No. 5, pp. 2220-2222, 1976. QC1.J83 Physical Sciences Library

Granqvist, C.G. and R.A. Buhrman, "Ultrafine Metal Particles", *Journal of Applied Physics*, Vol. 47, No. 5, pp. 2200-2219, 1976.
QC1.J83 Physical Sciences Library

Gras, J.L., "Southern Hemisphere Tropospheric Aerosol Microphysics", *Journal of Geophysical Research*, Vol. 96, No. D3, pp. 5345-5356, 1991.
QC811.T3 Earth & Mineral Sciences Library

Gras, J.L. and J.E. Laby, "Southern Hemisphere Stratospheric Aerosol Measurements. 3. Size Distribution 1974-1979", *Journal of Geophysical Research*, Vol. 86, No. C10, pp. 9767-9775, 1981.
QC811.T3 Earth & Mineral Sciences Library

Hale, G.M. and M. R. Querry, "Optical Constants of Water in the 200-nm to 200-um Wavelength Region", *Applied Optics*, Vol. 12, No. 3, pp. 555-563, 1973.
QC350.O62 Physical Sciences Library

Hansen, J.E. and J.W. Hovenier, "Interpretation of the Polarization of Venus", *Journal of the Atmospheric Sciences*, Vol. 31, pp. 1137-1160, 1974.
QC851.A283 Earth & Mineral Sciences Library

Harasaka, T., T. Nakajima, S. Ohta, and M. Tanaka, "Optical and Chemical Properties of Urban Aerosols in Sendai and Sapporo Japan", *Atmospheric Environment*, Vol. 26A, No. 11, pp. 2053-2062, 1992.
RA576.A8 Earth & Mineral Sciences Library

Harrison, R.M., C.A. Pio, "Size-Differentiated Composition of Inorganic Atmospheric Aerosols of Both Marine and Polluted Continental Origin", *Atmospheric Environment*, Vol. 17, No. 9, pp. 1733-1738, 1983.
RA576.A8 Earth & Mineral Sciences Library

Hatch, T., "Determination of 'Average Particle Size' from the Screen-Analysis of Non-Uniform Particulate Substances", *Journal of the Franklin Institute*, Vol. 215, pp. 27-37, 1933.
T1.F8 Annexed Materials

Hatch, T. and S. Choate, "Statistical Description of the Size Properties of Non-Uniform Particulate Substances", *Journal of the Franklin Institute*, Vol. 207, pp. 369-387, 1929.
T1.F8 Annexed Materials

Heisler, S.L., S.K. Friedlander, and R.B. Husar, "The Relationship of Smog Aerosol Size and Chemical Element Distributions to Source Characteristics", *Atmospheric Environment*, Vol. 7, pp. 633-649, 1973.
RA576.A8 Earth & Mineral Sciences Library

Hering, S.V. and S.K. Friedlander, "Origins of Aerosol Sulfur Distributions in the Los Angeles Basin", *Atmospheric Environment*, Vol. 16, pp. 2647-2656, 1982.
RA576.A8 Earth & Mineral Sciences Library

Hobbs, P.V., D.A. Bowdle and L.F. Radke, "Particles in the Lower Troposphere Over the High Plains of the United States. Part I: Size Distributions, Elemental Compositions and Morphologies", *Journal of Climate and Applied Meteorology*, Vol. 24, pp. 1344-1356, 1985.
AC851.A6601 Earth & Mineral Sciences Library

Hodkinson, J.R. and I. Greenleaves, "Computations of Light-Scattering and Extinction by Spheres According to Diffraction and Geometrical Optics, and Some Comparisons with the Mie Theory", *Journal of the Optical Society of America*, Vol. 53, No. 5, pp. 577-588, 1963.

Hovenier, J.W., "Structure of a General Pure Mueller Matrix", *Applied Optics*, Vol. 33, No. 36, pp. 8318-8324, 1994.

Hovenier, J.W., H.C. van de Hulst and C.V.M. van der Mee, "Conditions for the Elements of the Scattering Matrix", *Astronomy and Astrophysics*, Vol. 157, pp. 301-310, 1986.

Hovenier, J.W. and C.V.M. van der Mee, "Fundamental Relationships Relevant to the Transfer of Polarized Light in a Scattering Atmosphere", *Astronomy and Astrophysics*, Vol. 128, pp. 1-16, 1983.

Hovenier, J.W. and C.V.M. van der Mee, "Scattering of Polarized Light: Properties of the Elements of the Phase Matrix", *Astronomy and Astrophysics*, Vol. 196, pp. 287-295, 1988.

Hovenier, J.W. and C.V.M. van der Mee, "Structure of Matrices Transforming Stokes Parameters", *Journal of Mathematical Physics*, Vol. 33, No. 10, pp. 3574-3584, 1992.

Hovenier, J.W. and C.V.M. van der Mee, "Bounds for Degree of Polarization", *Optics Letters*, Vol. 20, No. 24, pp. 2454-2456, 1995.

Hovenier, J.W. and C.V.M. van der Mee, "Testing Scattering Matrices: A Compendium of Recipes", *Journal of Quantum Spectroscopy and Radiation Transfer*, Vol. 55, No. 5, pp. 649-661, 1996.

Iskander, M.F., A. Lakhtakia and C.H. Durney, "A New Procedure for Improving the Solution Stability and Extending the Frequency Range of the EBCM", *IEEE Transactions on Antennas and Propagation*, Vol. AP-31, No. 2, pp. 317-324, 1983.
TK7872.A612 Engineering Library

Jaenicke, R. and C.N. Davies, "The Mathematical Expression of the Size Distribution of Atmospheric Aerosols", *Journal of Aerosol Science*, Vol. 7, pp. 255-259, 1976.
QC882.J68 Earth & Mineral Sciences Library

John, W., S.M. Wall, J.L. Ondo and W. Winklmayr, "Modes in the Size Distributions of Atmospheric Inorganic Aerosols", *Atmospheric Environment*, Vol. 24A, pp. 2349-2359, 1990.
RA576.A8 Earth & Mineral Sciences Library

Junge, C. and R. Jaenicke, "New Results in Background Aerosols Studies from the Atlantic Expedition of the R.V. *Meteor*, Spring 1969", *Journal of Aerosol Science*, Vol. 2, pp. 305-314, 1971.
QC882.J68 Earth & Mineral Sciences Library

Kelkar, D.N. and P.V. Joshi, "A Note on the Size Distribution of Aerosols in Urban Atmospheres", *Atmospheric Environment*, Vol. 11, pp. 531-534, 1977.
RA576.A8 Earth & Mineral Sciences Library

Kent, G.S., G.K. Yue, U.O. Farrukh and A. Deepak, "Modeling Atmospheric Aerosol Backscatter at C02 Laser Wavelengths. 1: Aerosol Properties, Modeling Techniques, and Associated Problems", *Applied Optics*,
Vol. 22, No. 11, pp. 1655-1665, 1983.
QC350.O62 Physical Sciences Library

Kerker, M., E. Daby, G.L. Cohen, J.P. Kratohvil and E. Matijevi◖, "Particle Size Distributions in La Mer Sulfur Sols", *Journal of Physical Chemistry*, Vol. 67, pp. 2105-2111, 1963.
QD1.J66 Physical Sciences Library

Kerker, M., P. Scheiner and D.D. Cooke, "The Range of Validity of the Rayleigh and Thomson Limits for Lorenz-Mie Scattering", *Journal of the Optical Society of America*, Vol. 68, No. 1, pp. 135-137, 1978.
QC350.O6 Physical Sciences Library

Kim, Y.J., H. Sievering, and J.F. Boatman, "Airborne Measurement of Atmospheric Aerosol Particles in the Lower Troposphere Over the Central United States", *Journal of Geophysical Research*, Vol. 93, No. D10, pp. 12631-12644, 1988.
QC811.T3 Earth & Mineral Sciences Library

King, M.D., and B.M. Herman, "Determination of the Ground Albedo and the Index of Absorption of Atmospheric Particulates by Remote Sensing. Part I: Theory", *Journal of the Atmospheric Sciences*, Vol. 36, pp. 163-173, 1979.
QC851.A283 Earth & Mineral Sciences Library

King, M.D.,"Determination of the Ground Albedo and the Index of Absorption of Atmospheric Particulates by Remote Sensing. Part II: Application", *Journal of the Atmospheric Sciences*, Vol. 36, pp. 1072-1083, 1979.
QC851.A283 Earth & Mineral Sciences Library

Koepke, P. and M. Hess, "Scattering Functions of Tropospheric Aerosols: The Effects of Nonspherical Particles", *Applied Optics*, Vol. 27, No. 12, pp. 2422-2430, 1988.
QC350.O62 Physical Sciences Library

Krumbein, W.C., "Application of Logarithmic Moments to Size Frequency Distributions of Sediments", *Journal of Sedimentary Petrology*, Vol. 6, No. 1, pp. 35-47, 1936.
QE420.J69 Annexed Materials

Larsen, R.I., "A New Mathematical Model of Air Pollutant Concentration Averaging Time and Frequency", *Journal of the Air Pollution Control Association*, Vol. 19, No. 1, pp. 24-30, 1969.
TD883.A48 Annexed Materials

Lary, D.J., D.E. Shallcross and R. Toumi, "Carbonaceous Aerosols and Their Potential Role in Atmospheric Chemistry", *Journal of Geophysical Research*, Vol. 104, No. D13, pp. 15929-15940, 1999.
QC811.T3 Earth & Mineral Sciences Library

Leaitch, W.R. and G.A. Isaac, "Tropospheric aerosol size distributions from 1982 to 1988 over Eastern North America", *Atmospheric Environment*, 25A, pp. 601-619, 1991.
RA576.A81 Earth & Mineral Sciences Library

Low, R.D.H., "A Theoretical Investigation of Cloud/Fog Extinction Coefficients and Their Spectral Correlations", *Contributions to Atmospheric Physics*, Vol. 52, No.1, pp. 44-57, 1979.
QC851.B4 Annexed Materials

Mage, D.T. and W.R. Ott, "Refinements of the Lognormal Probability Model for Analysis of Aerometric Data", *Journal of the Air Pollution Control Association*, Vol. 28, No. 8, pp. 796-798, 1978
TD883.A48 Engineering Library

Malm, W.C., F.F. Sisler, D. Huffman, R.A. Eldred and T.A. Cahill, "Spatial and Seasonal Trends in Particle Concentration and Optical Extinction in the United States", *Journal of Geophysical Research*, Vol. 99, No. D1, pp. 1347-1370, 1994.
QC811.T3 Earth & Mineral Sciences Library

Margari, S.R., R. Hauser, J. Schwartz, P.L. Williams, T.J. Smith, D.C. Christiani, "Association of Heart Rate Variability with Occupational and Environmental Exposure to Particulate Air Pollution", *Circulation*, Vol. 104, pp. 986-991, 2001.
RC681.A1C6 4th Floor Paterno Library

Matteson, M.J. and W. Stöber, "The Generation of Aerosols from Various Electrolyte Solutions", *Journal of Colloid and Interface Science*, Vol. 23, pp. 203-214, 1967.
QD549.J67 Physical Sciences Library

Meehan, E.J. and A.E. Gyberg, "Particle-Size Determination by Low-Angle Light Scattering: Effect of Refractive Index", *Applied Optics*, Vol. 12, No. 3, pp. 551-554, 1973.
QC350.O62 Physical Sciences Library

Meng, Z. and J.H. Seinfeld, "On the Source of the Summicrometer Droplet Mode of Urban and Regional Aerosols", *Aerosol Science and Technology*, Vol. 20, pp. 253-265, 1994.
TP244.A3A335 Earth & Mineral Sciences Library

Mishchenko, M.I., A.A. Lacis, B.E. Carlson, and L.D. Travis, "Nonsphericity of Dust-Like Tropospheric Aerosols: Implications for Aerosol Remote Sensing and Climate Modeling", *Geophysical Research Letters*, Vol. 22, No. 9, pp. 1077-1080, 1995.
QC801.G44 Earth & Mineral Sciences Library

Mishchenko, M.I. and J.W. Hovenier, " Depolarization of Light Backscattered by Randomly Oriented Nonspherical Particles", *Optics Letters*, Vol. 20, No. 12, pp. 1356-1359, 1995.

Pachenko, M.V., S.A. Terpugova, B.A. Bodhaine, A.A. Isakov, M.A. Sviridenkov, I.N. Sokolik, E.V. Romashova, B.I. Nazarov, A.K. Shukurov, E.I. Chistyakova, and T.C. Johnson, "Optical Investigations of Dust Storms During U.S.S.R.-U.S. Experiments in Tadzhikistan, 1989", *Atmoshperic Environment*, Vol. 27A., No. 16, pp. 2503-2508, 1993.
RA576.A81 Earth & Mineral Sciences Library

Patterson, E.M. and D.A. Gillette, "Commonalities in Measured Size Distributions for Aerosols Having a Soil-Derived Component", *Journal of Geophysical Research*, Vol. 82, No. 15, pp.2074-2082, 1977.
QC811.T3 Earth & Mineral Sciences Library

Penndorf, R., "Tables of the Refractive Index for Standard Air and the Rayleigh Scattering Coefficients for The Spectral Region Between 0.2 and 20.0 u and Their Application to Atmospheric Optics", *Journal of the Optical Society of America*, Vol. 47, No. 2, pp. 176-182, 1957.
QC350.O6 Physical Sciences Library

Peters, A., D.W. Dochery, J.E. Muller and M.A. Mittleman, "Increased Particulate Air Pollution and the Triggering of Myocardial Infarction", *Circulation*, Vol. 103, pp. 2810-2815, 2001.
RC681.A1C6 4th Floor Paterno Library

Philbrick, C.R., "Raman Lidar Measurements of Atmospheric Properties", *in Proc. Of Atm. Prop. And Remote Sensing III, SPIE 2222*, p. 922, 1994.

Philbrick, C.R., "Investigations of Factors Determining the Occurrence of Ozone and Fine Particles in Northeastern USA," *Meas. Of Toxic and Related Air Pollutants*, Vol. 1, pp. 248-260, 1998.

Reagan, J.A., D.M. Byrne, M.D. King, J.D. Spinhirne, and B.M. Herman, "Determination of the Complex Refractive Index and Size Distribution of Atmospheric Particulates from Bistatic-Monostatic Lidar and Solar Radiometer Measurements", *Journal of Geophysical Research*, Vol. 85, No. C3, pp. 1591-1599, 1980.
QC811.T3 Earth & Mineral Sciences Library

Rosen, J.M., R.G. Pinnick and D.M. Garvey, "Nephelometer Optical Response Model for the interpretation of Atmospheric Aerosol Measurements", *Applied Optics*, Vol. 36, No. 12, pp. 2642-2649, 1997.
QC350.O62 Physical Sciences Library

Sangal, B.P. and A.K. Biswas, "The 3-Parameter Lognormal Distribution and Its Applications in Hydrology", *WaterResources Research*, Vol. 6, No. 2, pp. 505-515, 1970.
GB651.W33 Earth & Mineral Sciences Library

Singham, S.B. and G.C. Salzman, "Evaluation of the Scattering Matrix of an Arbitrary Particle Using the Coupled Dipole Approximation", *The Journal of Chemical Physics*, Vol. 84, No. 5, pp. 2658-2667, 1986.
QD1.J94 Physical Sciences Library

Smith, J.E. and M.L. Jordan, "Mathematical and Graphical Interpretation of the Log-Normal Law for Particle Size Distribution Analysis", *Journal of Colloid Science*, Vol. 19, pp. 549-559, 1964.
QD549.J67 Physical Sciences Library

Sokolik, I., A. Andronova, and T.C. Johnson, "Complex Refractive Index of Atmospheric Dust Aerosols", *Atmospheric Environment*, Vol. 27A, No. 16, p. 2495-2502, 1993.
RA576.A81 Earth & Mineral Sciences Library

Spinhirne, J.D., J.A. Reagan and B.M. Herman, "Vertical Distribution of Aerosol Extinction Cross Section And Inference of Aerosol Imaginary Index in the Troposphere by Lidar Technique", *Journal of Applied Meteorology*, Vol. 19, No. 4, pp. 426-438, 1980.
QC851.A66 Earth & Mineral Sciences Library

Stevens, T.D. and C.R. Philbrick, "Particle Size Distributions and Extinction Determined by a Unique Bistatic Lidar Technique", in *Proceedings of IGARSS96 Conference on Remote Sensing for a Sustainable Future*, Vol II, pp. 1253-1256, 1996.

Stoffels, W.W., E. Stoffels, G.H.P.M. Swinkels, M. Boufnichel and G.M.W. Kroesen, "Etching a Single Micrometer-Size Particle in a Plasma", *Physical Review* E, Vol. 59, No. 2, pp. 2302-2304, 1999.
QC1.P4242 Physical Sciences Library

Sviridenkov, M.A., D.A. Gillette, A.A. Isakov, I.N. Sokolik, V.V. Smirnov, B.D. Belan, M.V. Pachenko, A.V. Andronova, S.M. Kolomiets, V.M. Zhukov, and D.A. Zhukovsky, "Size Distributions of Dust Aerosol Measured During the Soviet-American Experiment in Tadzhikistan, 1989", *Atmospheric Environment*, Vol. 27A, No. 16, pp. 2481-2486, 1993.
RA576.A81 Earth & Mineral Sciences Library

Swinkels, G.H.P.M., E. Stoffels, W.W. Stoffels, N. Simons, G.M.W. Kroesen and F.J. de Hoog, "Treatment of Dust Particles in an RF Plasma Monitoried by Mie Scattering Rotating Compensator Ellipsometry", *Pure and Applied Chemistry*, Vol. 70, No. 6, pp. 1151-1156, 1998.
QD1.I88152 Physical Sciences Library

Tachibana, K., Y. Hayashi, T. Okuno and T. Tatsuta, "Spectroscopic and Probe Measurements of Structures in a Parallel-Plate RF Discharge with Particles", *Plasma Sources Science and Technology*, Vol. 3, pp. 314-319, 1994.

Tanaka, M., T. Takamura and T. Nakajima, "Refractive Index and Size Distribution of Aerosols as Estimated from Light Scattering Measurements", *Journal of Climate and Applied Meteorology*, Vol. 22, pp. 1253-1261, 1983.
QC851.A6601 Earth & Mineral Sciences Library

Tang, I.N. and H.R. Munkelwitz, "Water Activities, Densities, and Refractive Indices of Aqueous Sulfates and Sodium Nitrate Droplets of Atmospheric Importance", *Journal of Geophysical Research*, Vol. 99, No. D9, pp. 18801-18808, 1994.
QC811.T3 Earth & Mineral Sciences Library

Twitty, J.T., and J.A. Weinman, "Radiative Properties of Carbonaceous Aerosols", *Journal of Applied Meteorology*, Vol. 10, pp. 725-731, 1971.
QC851.A66 Earth & Mineral Sciences Library

Varadan, V.V., A. Lakhtakia, and V.K. Varadan, "Scattering by Three-Dimensional Anisotropic Scatterers", *IEEETransactions on Antennas and Propagation*, Vol. 37, No. 6, pp. 800-802, 1989.
TK7872.A612 Engineering Library

Volz, F.E., "Infrared Refractive Index of Atmospheric Aerosol Substances", *Applied Optics*, Vol. 11, No. 4, pp. 755-759, 1972.
QC350.O62 Physical Sciences Library

Volz, F.E., "Infrared Absorption by Atmospheric Aerosol Substances", *Journal Of Geophysical Research*, Vol. 77, No. 6, pp. 1017-1031, 1972.
QC811.T3 Earth & Mineral Sciences Library

Volz, F.E., "Infrared Optical Constants of Ammonium Sulfate, Sahara Dust, Volcanic Pumic, and Flyash", *AppliedO ptics*, Vol. 12, No.3, pp. 564-568, 1973.
QC350.O62 Physical Sciences Library

Watanabe, Y., M. Shiratani and M. Yamashita, "Observation of Growing Kinetics of Particles in a Helium-Diluted Silane RF Plasma", *Applied Physics Letters*, Vol. 61, No. 13, pp. 1510-1512, 1992.

Ward, G., K.M. Cushing, R.D. McPeters, and A.E.S. Green, "Atmospheric Aerosol Index of Refraction and Size-Altitude Distribution from Bistatic Laser Scattering and Solar Aureole Measurements", *Applied Optics*, Vol. 12, No. 11, pp. 2585-2592, 1973.
QC350.O62 Physical Sciences Library

Weber, R.J., J.J. Marti, P.H. McMurry, F.L. Eisele, D.J. Tanner, and A. Jefferson, "Measurements of New Particle Formation and Ultrafine Particle Growth Rates at a Clean Continental Site", *Journal of Geophysical Research*, Vol. 102, No. D4, pp. 4375-4385, 1997.
QC811.T3 Earth & Mineral Sciences Library

Whitby, K.T., R.B. Husar and B.Y.H. Liu, "The Aerosol Distribution of Los Angeles Smog", *Journal of Colloid andInterface Science*, Vol. 39, No. 1, pp. 177-204, 1972.
QD549.J67 Physical Sciences Library

Whitby, K.T., "The Physical Characteristics of Sulfur Aerosols", *Atmospheric Environment*, Vol. 12, pp. 135-159, 1978.
RA576.A8 Earth & Mineral Sciences Library

Willeke, K. and K.T. Whitby, "Atmospheric Aerosols: Size Distribution Interpretation", *Journal of the Air Pollution Control Association*, Vol. 25, No. 5, pp. 529-534, 1975.
TD883.A48 Engineering Library

Willeke, K., K.T. Whitby, W.E. Clark and V.A. Marple, "Size Distributions of Denver Aerosols – A Comparison of Two Sites", *Atmospheric Environment*, Vol. 8, pp. 609-633, 1974.
RA576.A8 Earth & Mineral Sciences Library

Winkler, P., "Chemical Analysis of Aitken Particles (<0.2um Radius) over the Atlantic Ocean", *Geophysical Research Letters*, Vol. 2, No. 2, pp. 45-48, 1975.
QC801.G44 Earth & Mineral Sciences Library

Wiscombe, W.J. and A. Mugnai, "Scattering from Nonspherical Chebyshev Particles. 2: Means of Angular Scattering Patterns", *Applied Optics*, Vol. 27, No. 12, pp. 2405-2421, 1988.
QC350.O62 Physical Sciences Library

Xing, Z.F., "On the Deterministic and Non-Deterministic Mueller Matrix", *Journal of Modern Optics*, Vol. 39, No. 3, pp. 461-484, 1992.

Yue, G.K., G.S. Kent, U.O. Farruk and A. Deepak, "Modeling Atmospheric Aerosol Backscatter at CO_2 Laser Wavelengths. 3: Effects of Changes in Wavelength and Ambient Conditions", *Applied Optics*, Vol. 22, No. 11, pp. 1671-1678, 1983.
QC350.O62 Physical Sciences Library

Zakharova, N.T. and M.I. Mishchenko, " Scattering Properties of Needlelike and Platelike Ice Spheroids with Moderate Size Parameters", *Applied Optics*, Vol. 39, No. 27, pp. 5052-5057, 2000.

Books:

Abramowitz, M. and I.A. Stegun (eds.), ***Handbook of Mathematical Functions with Formulas, Graphs, and Mathematical Tables***, Dover Publications, Inc., New York City, 1046 p., 1972.
Personal Library

Aitchison, J. and J.A.C. Brown, ***The Lognormal Distribution***, Cambridge University Press, Cambridge, 176 p.,1957.
QA273.A38 Mathematics Library

d'Almeida, G.A, P. Koepke, and E.P. Shettle, ***Atmospheric Aerosols***, A. Deepak Publishing, Hampton, Virginia, 561 p., 1991.
QC882.42.D35 Earth & Mineral Sciences Library

Barber, P.W. and R.K. Chang, ***Optical Effects Associated with Small Particles***, World Scientific, Singapore, 336 p., 1988.
QC882.O66 Physical Sciences Library

Barber, P.W. and S.C. Hill, ***Light Scattering by Particles: Computational Methods***, World Scientific Publishing, Singapore, 261 p., 1990.
Personal Library

Bohren, C.F. and D.R. Huffman, ***Absorption and Scattering of Light by Small Particles***, John Wiley & Sons, New York City, 530 p., 1983.
QC882.B63 Engineering Library

Brown, T.L. and H.E. LeMay, ***Chemistry: The Central Science, 4^{th} edition***, Prentice Hall, Englewood Cliffs, New Jersey, 1028 p., 1988.
Personal Library

Crow, E.L. and K. Shimizu, ***Lognormal Distributions***, Marcel Dekker, New York City, 387 p., 1988.
QA273.6.L64 Mathematics Library

Deepak, A., editor, ***Atmospheric Aerosols: Their Formation, Optical Properties, and Effects***, Spectrum Press, Hampton Virginia, 480 p., 1982.
QC882.A869 Earth & Mineral Sciences Library

Deirmendjian, D., ***Electromagnetic Scattering on Spherical Polydispersions***, American Elsevier Publishing Company, New York City, 290 p., 1969.
QC173.D29 Annexed Materials

Frock, H.N., ***Analysis of Particle Size Measurements Using Laser Light Scattering***, Master's Thesis, Mechanical Engineering, The Pennsylvania State University at Great Valley, W. Edwin Sauer Advisor, 77 p., 1977.
Thesis 1977pFrock, HN Annexed Materials

Goueslet, G. and G. Grehan, editors, ***Optical Particle Sizing: Theory and Practice***, Plenum Press, New York City, 642 p. 1988.
TA418.8.076 Engineering Library

Hald, A., ***Statistical Theory with Engineering Applications***, John Wiley & Sons, New York City, 783 p., 1952.
QA276.H314 Engineering Library

Handbook of Chemistry and Physics, 67th edition 1986-1987, R.C. Weast (editor in chief), M.J. Astle, W.H. Beyer (associate editors), CRC Press, Inc., Boca Raton, FL, 1986
Personal Library

Handbook of Optics, Vol. I, Fundamentals, Techniques, and Design, 2nd edition, M. Bass (editor in chief), E.W. Van Stryland, D.R. Williams and W.L. Wolfe (associate editors), McGraw-Hill Inc., New York City, 1995.
C.R. Philbrick Personal Library

Handbook of Optics, Vol. II, Devices, Measurements and Properties, 2nd edition, M. Bass (editor in chief), E.W. Van Stryland, D.R. Williams and W.L. Wolfe (associate editors), McGraw-Hill Inc., New York City, 1995.
C.R. Philbrick Personal Library

Hecht, E. ***Optics***, 2nd ed., Addison-Wesley, Reading, Massachusetts, 676 p., 1987.
Personal Library (EE 320)

Herdan, G., ***Small Particle Statistics***, 2nd ed., Butterworths, London, 418 p., 1960.
TA406.7.H47 Earth & Mineral Sciences Library

Hobbs, P.V., editor, ***Aerosol-Cloud-Climate Interactions***, Academic Press, San Diego, 233 p., 1993.
QC882.42.A34 Earth & Mineral Sciences Library

Hobbs, P.V. and M.P. McCormick, editors, ***Aerosols and Climate***, A. Deepak Publishing, Hampton, Virginia, 486 p., 1988.
QC882.A358 Earth & Mineral Sciences Library

Irani, R.R. and C.F. Callis, ***Particle Size: Measurement, Interpretation and Application***, John Wiley & Sons, New York City, 165 p., 1963.
TA406.7.17 Earth & Mineral Sciences Library

Jaynes, E.T., ***Papers on Probability, Statistics and Statistical Physics***, Kluwer Academic Publishers, Dordrecht, The Netherlands, 434 p., 1983 (Reprinted 1989).
QC174.8.J38 Physical Sciences Library

Junge, C.E., ***Air Chemistry and Radioactivity***, Academic Press, New York City, 382 p., 1963.
QC881.J8 Earth & Mineral Sciences Library

Kerker, M., ***The Scattering of Light and Other Electromagnetic Radiation***, Academic Press, New York City, 666 p., 1969.
QC670.K4 Physical Sciences Library

Larsen, R.J. and M.L. Marx, ***An Introduction to Probability and Its Applications***, Prentice-Hall, Englewood Cliffs, New Jersey, 404 p., 1985.
Personal Library (STAT 418)

McCartney, E.J., ***Optics of the Atmosphere – Scattering by Molecules and Particles***, John Wiley & Sons, New York City, 408 p., 1976.
QC976.S3 M3 Earth & Mineral Sciences

Mischenko, M.I., J.W. Hovenier, and L.D. Travis (eds.), ***Light Scattering by Nonspherical Particles: Theory, Measurements and Applications***, Academic Press, San Diego, 690 p., 2000.
QC427.4.L545 Earth & Mineral Sciences

Monin, A.S., ***An Introduction to the Theory of Climate***, D. Reidel Publishing Company, Dordrecht, The Netherlands, 261 p., 1986.
QC981.M6613 Earth & Mineral Sciences Library

Palick, E.D. (ed.), ***Handbook of Optical Constants of Solids***, Vols. 1-5, Academic Press, San Diego, 1998.
QC176.8.O6H36 Physical Sciences Library

Papoulis, A., ***Probability, Random Variables, and Stochastic Processes***, 3rd ed., McGraw-Hill, New York City, 666 p., 1991.
Personal Library (EE459)

Pratt, J.W., editor, ***Statistical and Mathematical Aspects of Pollution Problems***, Marcel Dekker, New York City, 392 p., 1974.
TD177.S22 Annexed Materials

Ramo, S., J.R. Whinnery, and T. Van Duzer, ***Fields and Waves in Communication Electronics,*** 3rd ed., John Wiley & Sons, Inc., New York City, 844 p., 1994.
Personal Library (EE 411)

Rogers, R.R., and M. K. Yau, ***A Short Course in Cloud Physics***, 3rd edition, Pergamon Press, Oxford, 290 p., 1989.
QC921.5. R63 Earth & Mineral Sciences Library

Seinfeld, J.H. and S.N. Pandis, *Atmospheric Chemistry and Physics, From Air Pollution to Climate Change*, John Wiley & Sons, Inc., New York City, 1326 p., 1998.
QC879.6.S45 Earth & Mineral Sciences Library

Shardanand NASA Wallops Flight Center and A.D. Prasad Rao, ***Absolute Rayleigh Scattering Cross Sections of Gases and Freons of Stratospheric Interest in the Visible and Ultraviolet Regions***, *NASA TN 0-8442*, 35 p., 1977.
TL521.A3501 Annexed Materials

Stevens, T.D., ***Bistatic Lidar Measurements of Lower Tropospheric Aerosols***, PhD Thesis, The Pennsylvania State University, 247 p., 1996.
Thesis 1996dSteve,TD Engineering Library

U.S. Standard Atmosphere, 1976, U.S. Government Printing Office, Washington, D.C., 227 p., 1976.
C.R. Philbrick Personal Library

Watson, J.G., and J.C. Chow, ***Reconciling Urban Fugitive Dust Emissions Inventory and Ambient Source Contribution Estimates: Summary of Current Knowledge and Needed Research***, Desert Research Institute, Energy and Environmental Engineering Center, DRI Document No. 6110.4D2, 1999. (DRAFT)

Appendix A: The True Statistics of the Lognormal Distribution

Chapter 2 provided the mathematics of the lognormal function as used in aerosol and particle science. Here, we establish the true statistics of the lognormal function from a mathematical point of view. The principle difference between Chapter 2 and this appendix is the random variable. The random variable used here is **x** while in Chapter 2 it is **lnx**. These random variables are obviously related through a simple transformation but it is the resulting mathematics and applications that can be a source of confusion.

A.1 THE LOGNORMAL PROBABILITY DENSITY FUNCTION

For convenience, we re-iterate the beginning of section 2.3 here. The transformation relating the Gaussian random variable, Y, to the lognormal random variable, X, is

$$X = e^{Y} = g(Y), \tag{A-1}$$

which has the root, $y_1 = \ln x$. Proceeding as in Eqn. 2-8, the lognormal pdf is given by

$$f_X(x) = \frac{f_Y(Y_1)}{|g'(Y_1)|} = \frac{f_Y(Y_1)}{|e^{Y_1}|}$$

and substituting for the root, y_1, yields

$$f_X(x) = \begin{cases} \dfrac{1}{\sqrt{2\pi}\cdot\sigma x}\exp\left(-\dfrac{1}{2\sigma^2}(\ln(x)-\mu)^2\right), & x > 0 \\ 0, & x < 0 \\ \text{undefined}, & x = 0 \text{ (singularity)}. \end{cases} \tag{A-2}$$

Equation A-2 is the formal mathematical definition of the lognormal probability density function.

A.1.1 Statistics of the Lognormal Probability Density Function

Because of the transformation given by Eqn. 2-14, determination of the various moments (expected value and variance) by direct integration is difficult. Further, simple relations between the statistics of the Gaussian random and lognormal random variables, such as those that exist between the standard and Gaussian random variables are also obscured by the transformation of Eqn. 2-14. Fortunately, there exists a method of obtaining the moments of the lognormal pdf.

Characteristic functions, $\phi_x(t)$, which are very similar to Fourier Transforms (Larsen and Marx, p. 367), are complex-valued functions that produce the moments of a pdf. However, a subset of characteristic functions are the moment-generating functions, $M_x(t)$. Although the characteristic equations are more general and always exist, moment generating functions are often enough in most cases needed to obtain the desired moments of a pdf (Larsen and Marx, p. 286, p.371; Papoulis, p.115).

The moment-generating function is defined as

$$\mathbf{M}_X(t) = \mathbf{E}\left\{e^{tx}\right\}, \quad \forall t \ni \mathbf{E}\left\{e^{tx}\right\} \text{ exists} \tag{A-3}$$

and the moments can be "generated" by

$$\mathbf{E}\left\{x^k\right\} = \mathbf{M}_X^{(k)}(0), \tag{A-4}$$

i.e., the moments of the random variable X are found by differentiating the moment-generating function k times and evaluating at $t = 0$ (t is simply a placeholder and does not represent time). So, evaluating Eqn. A-3 yields the moment-generating function for a lognormal pdf

$$\mathbf{M}_X(t) = \mathbf{E}\left\{e^{tx}\right\} = \frac{1}{\sqrt{2\pi}\cdot\boldsymbol{\sigma}}\int_{-\infty}^{\infty}\frac{\exp(tx)}{x}\exp\left(-\frac{1}{2\boldsymbol{\sigma}^2}(\ln(x)-\boldsymbol{\mu})^2\right)dx, \tag{A-5}$$

which is not any easier to evaluate than simply examining $\mathbf{E}\{x\}$. However, there is still one more card to play: The transformation between X and Y. This relationship will be exploited but first, the moment-generating function of the Gaussian pdf needs to be established.

A.1.1.1 Moment Generating Function of Gaussian Probability Density Function

The moment-generating function of a standard pdf is (Larsen and Marx, p. 378)

$$\mathbf{M}_Z(t) = e^{t^2/2} \tag{A-6}$$

and by using the transformations, the moment-generating functions of other random variables can also be obtained (Papoulis, p.119, *Determination of the Density of g(x)*; Larsen and Marx, Theorem 5.5.4, p.297

and Theorem 7.5.5, p. 377). Using the transformation of Eqn. 2-9 in the definition of the moment-generating function, yields,

$$\begin{aligned}\mathbf{M}_Y(t) &= \mathbf{E}\left\{e^{Yt}\right\} = \mathbf{E}\left\{e^{(\sigma z+\mu)t}\right\} \\ &= \int_{-\infty}^{\infty} e^{(\sigma z+\mu)t} f_Y(y)dy.\end{aligned}$$

Since $Y = \sigma Z + \mu$, then $dy = \sigma\, dz$ and

$$\begin{aligned}f_Y(\sigma z+\mu) &= \frac{1}{\sqrt{2\pi}\cdot\sigma}\exp\left(-\frac{1}{2\sigma^2}(\sigma z+\mu-\mu)^2\right) \\ &= \frac{1}{\sqrt{2\pi}\cdot\sigma}\exp\left(-\frac{z^2}{2}\right),\end{aligned}$$

so, substituting, we have

$$\begin{aligned}\mathbf{M}_Y(t) &= \frac{1}{\sqrt{2\pi}}\int_{-\infty}^{\infty}\exp((\sigma z+\mu)t)\exp\left(-\frac{z^2}{2}\right)dz \\ &= \frac{\exp(\mu t)}{\sqrt{2\pi}}\int_{-\infty}^{\infty}\exp\left(-\frac{1}{2}\left(z^2-2\sigma zt\right)\right)dz.\end{aligned}$$

Next, completing the square yields

$$\begin{aligned}\mathbf{M}_Y(t) &= \frac{e^{\mu t}}{\sqrt{2\pi}}\int_{-\infty}^{\infty}\exp\left(-\frac{1}{2}\left(z^2-2\sigma zt+\sigma^2t^2\right)\right)\exp\left(\frac{\sigma^2t^2}{2}\right)dz \\ &= \frac{e^{\mu t}\exp\left(\sigma^2t^2/2\right)}{\sqrt{2\pi}}\int_{-\infty}^{\infty}\exp\left(-\frac{(z-\sigma t)^2}{2}\right)dz.\end{aligned}$$

Now, making a change of variables by letting $\mathbf{q} = \mathbf{z} - \sigma t$, $\therefore$ $d\mathbf{q} = d\mathbf{z}$ and substituting,

$$\mathbf{M}_Y(t) = e^{\mu t}\exp\left(\sigma^2t^2/2\right)\left\{\frac{1}{\sqrt{2\pi}}\int_{-\infty}^{\infty}e^{-q^2/2}\,dq\right\}.$$

Since the expression in the braces evaluates to unity, the moment-generating function for a Gaussian random variable Y is

$$\begin{aligned}\mathbf{M}_Y(t) &= e^{\mu t+\sigma^2t^2/2} \\ &= e^{\mu t}\mathbf{M}_Z(\sigma t).\end{aligned} \tag{A-7}$$

We are now ready to determine the moment-generating function for a lognormal pdf.

A.1.1.2 Pseudo Moment Generating Function for the Lognormal Probability Density Function

By definition, central moments are found by (Papoulis, eqn. 5-38, p. 109)

$$\mathbf{E}\left\{x^k\right\} = \int_{-\infty}^{\infty} x^k f_X(x)\,dx\ . \tag{A-8}$$

Using the transformation of Eqn. A-1 and substituting into Eqn. A-8, yields

$$\mathbf{E}\left\{x^k\right\} = \int_{-\infty}^{\infty} e^{ky} f_X\left(e^y\right) dx.$$

Since, $dx = e^y\,dy$,

$$\begin{aligned}\mathbf{E}\left\{x^k\right\} &= \int_{-\infty}^{\infty} e^{ky} \cdot \frac{1}{\sqrt{2\pi}\cdot\sigma\, e^y} \exp\left(-\frac{1}{2\sigma^2}\left(\ln\left(e^y\right)-\mu\right)^2\right) e^y\,dy \\ &= \int_{-\infty}^{\infty} e^{ky} \cdot \frac{1}{\sqrt{2\pi}\cdot\sigma} \exp\left(-\frac{1}{2\sigma^2}(y-\mu)^2\right) dy \\ &= \int_{-\infty}^{\infty} e^{ky} f_Y(y)\,dy.\end{aligned}$$

The final integral is the definition of the moment-generating function of the Gaussian random variable, Y (with a simple interchange of t with k). Hence, the moments of the lognormal random variable, X, in terms of the moment generating function of Y, are given by

$$\begin{aligned}\mathbf{E}\left\{x^k\right\} &= \mathbf{M}_Y(k) \\ &= e^{\mu k + \sigma^2 k^2/2}.\end{aligned} \tag{A-9}$$

Notice that we did not actually determine the moment-generating function for the lognormal random variable, X. This is the reason for the label "pseudo" moment-generating function. Later, when we re-examine characteristic equations and moment generating functions in the determination of surface area and volume distributions, we will find that neither are expressly unique for lognormal functions. In other words, the lognormal function, unlike the normal function, is not uniquely identified by its moments. This point will be re-iterated in the next several sections.

A.1.1.3 Mean (Expected Value) of the Lognormal Probability Density Function

The term, geometric, is applied to random variables that result from a multiplication process, while the term, arithmetic, is applied to random variables that result from an additive process. As shown in Section

2.1, the standard pdf was derived from random variables that were added. The result is more succinctly stated in the Central Limit Theorem (CLT) (Papoulis, p. 214). However, the CLT is also applicable to the product of random variables with it resulting in lognormal distributions (Papoulis, p. 220).

Using Eqn. A-9, the mean of a lognormal random variable is (Shimizu and Crow, eqn. 4.2, p. 9; Aitchison and Brown, eqn. 2-7, p.8)

$$\begin{aligned} \mathbf{E}\{x\} &= \mathbf{M}_Y(1) \\ &= e^{\mu+\sigma^2/2} \\ &\equiv \mu_{\mathrm{LN}} \,. \end{aligned} \tag{A-10}$$

This is the true mean of a lognormally distributed random variable. However, this is not the geometric mean reported in the scientific literature. (See Section 2.4). The geometric mean and the mean of a lognormal random variable are different.

A.1.1.4 Variance of the Lognormal Probability Density Function

Using Eqn. A-9, the variance of a lognormal random variable is (Shimizu and Crow, eqn. 4.3, p. 9; Aitchison and Brown, eqn. 2.8, p.8)

$$\begin{aligned} \mathbf{Var}\{x\} &= \mathbf{E}\{x^2\} - \mathbf{E}^2\{x\} \\ &= \left(e^{2\mu+2\sigma^2}\right) - \left(e^{2\mu+\sigma^2}\right) \\ &= \left(e^{2\mu+\sigma^2}\right)\left(e^{\sigma^2}-1\right) \\ &\equiv \sigma^2_{\mathrm{LN}} \end{aligned} \tag{A-11}$$

and the standard deviation is $\sqrt{\sigma^2_{\mathrm{LN}}}$. As with the mean of the previous section, this standard deviation is not what is used and reported in the scientific literature since the standard deviation and geometric standard deviation of a lognormal random variable are different. Once we have established the true mathematical properties of the lognormal distribution, we will then show what is used in the literature, how it is derived and why it came about. (See section 2.4). Finally, the appropriate notation for a lognormal pdf which would match a normal pdf's description of $N(\mu,\sigma^2)$, is $\Lambda(\mu_{LN}, \sigma^2_{LN})$, which also indicates mean and variance.

A.1.1.5 Percentiles, Quantiles and Quartiles

The q^{th} percentile of a random variable X is represented by the smallest number x_q such that (Papoulis, p. 68)

$$q = P\{X \le x_q\} = F_X(x_q)$$

where F_X is the cumulative distribution function (cdf). To compute the probability of an event or range of events for a normal (or lognormal) function, the pdf would have to be integrated. Before examining the percentiles of the lognormal function, first consider the standard normal pdf given by Eqn. 2-1. For the continuous random variable Z, the cdf is

$$\begin{aligned} F_Z(z) &= P\{Z \le z\} \\ &= \int_{-\infty}^{z} f_Z(z)\,dz \\ &= \frac{1}{\sqrt{2\pi}} \int_{-\infty}^{z} e^{-z^2/2}\,dz. \end{aligned} \tag{A-12}$$

Although there is no closed form expression for the above integral, various tables related to this integral, such as the error function (erf), complementary error function (erfc) or the quality function (Q), can be found in texts. For the following, we reference the table listed in Larsen and Marx (p. 388), which is the actual numerical integration of Eqn. A-12.

Since most tables are given for the standard normal pdf, *i.e.*, N(0,(1)^2), to find the correct values for a Gaussian pdf, N(μ, σ^2), a simple scaling and shifting transformation is used. For example, suppose a random variable Y, is normally distributed as N(1000, (50)^2). The probability that a value of Y is less than 1050 is

$$P\{Y \le 1050\} = F_Y(1050) = \int_{-\infty}^{1050} \exp\left(-\frac{1}{2}\left(\frac{y-1000}{50} \right)^2 \right) dy,$$

which can be easily determined with a computer. However, since we have tabular values for N(0,(1)^2), given by F_Z, and, using the transformation of Eqn. 2-7, we have

$$\begin{aligned} F_Y(y) &= F_Z\left(\frac{y-\boldsymbol{\mu}}{\boldsymbol{\sigma}} \right) \\ F_Y(1050) &= F_Z\left(\frac{1050-1000}{50} \right) \\ &= F_Z(1) \\ &= 0.8413. \end{aligned}$$

The result indicates that 84.13% of the random variable Y lies below 1050. Special terminology is given to particular probability points. For example, the point where the probability is 25% is termed the lower quartile while the 75% point is termed the upper quartile. For a general percentile/quantile,

$$F_Z\left(\frac{y_q - \boldsymbol{\mu}}{\boldsymbol{\sigma}}\right) = q\,,$$

which occurs when

$$\frac{y_q - \boldsymbol{\mu}}{\boldsymbol{\sigma}} = t_q$$
$$y_q = \boldsymbol{\mu} + \boldsymbol{\sigma}\, t_q \qquad \text{(A-13)}$$

where t_q is the appropriate value from the tables for a standard pdf (There is no closed form expression which relates q with t_q). So, from the tables, the lower and upper quartiles are

$$y_{25\%} = \boldsymbol{\mu} - 0.67\boldsymbol{\sigma}$$
$$y_{75\%} = \boldsymbol{\mu} + 0.67\boldsymbol{\sigma}\,.$$

However, of more importance is the 50% point, termed the median. The median of a Gaussian random variable, $\mathbf{y}_{\text{median}}$, occurs when

$$F_Z\left(\frac{\mathbf{y}_{\text{median}} - \boldsymbol{\mu}}{\boldsymbol{\sigma}}\right) = 0.5\,,$$

which, from the tables, requires,

$$\frac{\mathbf{y}_{\text{median}} - \boldsymbol{\mu}}{\boldsymbol{\sigma}} = 0\,.$$

So, the median for a Gaussian random variable is

$$\mathbf{y}_{\text{median}} = \boldsymbol{\mu}\,. \qquad \text{(A-14)}$$

We have not yet told the reader quite where we are heading with this information but it will become relevant when we describe modes of the lognormal function. We will see this in the next section.

A.1.1.5.1 Median of the Lognormal Probability Density Function

The transformation between lognormal, X, Gaussian, Y, and standard normal, Z, random variables is

$$X = e^{Y} = e^{\boldsymbol{\sigma} Z + \boldsymbol{\mu}}\,.$$

Since percentiles represent points of the random variables, the transformation holds, i.e., percentiles are found through the transformation of the random variables and since the percentiles of Y are given by Eqn. A-13, then the percentiles of X are given by (Shimizu and Crow, eqn. 4.6, p.11; Aitchison and Brown, eqn. 2-14, p.9)

$$x_q = e^{\mu + \sigma t_q} .$$

Thus, the 50% percentile (geometric median) of a lognormal random variable, **x**, is (Shimizu and Crow, eqn. 4.4)

$$\mathbf{x}_{\text{median}} = e^{\boldsymbol{\mu}} . \tag{A-15}$$

A.1.1.6 Mode of a Random Variable

The mode of a random variable is the most likely value of the random variable (Papoulis, p. 73), i.e., $\mathbf{x}_{\text{mode}}$ is the point where $f_X(x)$ is a maximum. To determine the mode point, take the derivative of the pdf and set equal to zero. The result is shown next.

A.1.1.6.1 Mode of a Gaussian Probability Density Function

The derivative of Eqn. 2-10 is

$$\frac{df_Y(y)}{dy} = \frac{1}{\sqrt{2\pi}\cdot\boldsymbol{\sigma}}\left[-\frac{1}{2\boldsymbol{\sigma}^2}(2y - 2\boldsymbol{\mu})\right]\exp\left(-\frac{1}{2\boldsymbol{\sigma}^2}(y-\boldsymbol{\mu})^2\right)$$

From the definition of pdfs, $f_Y(y)$ goes to zero as $y \to \pm\infty$ and this is indicated in the derivative above. For finite values of the random variable, the derivative is zero only at

$$\begin{aligned} y &= \boldsymbol{\mu} \\ &\equiv \mathbf{y}_{\text{mode}} . \end{aligned} \tag{A-16}$$

Notice that the mean, median and mode of a Gaussian random variable all occur at the same point. This is not true for the lognormal distribution.

A.1.1.6.2 Mode of a Lognormal Probability Density Function

The derivative of Eqn. 2-15 is

$$\frac{df_X(x)}{dx} = \left[\frac{1}{\sqrt{2\pi}\cdot\sigma\, x^2} + \frac{1}{\sqrt{2\pi}\cdot\sigma\, x}\left(\frac{1}{2\sigma^2}\right)\left[\frac{2\ln(x)}{x} - \frac{2\mu}{x}\right]\right]\exp\left(-\frac{1}{2\sigma^2}(\ln(x)-\mu)^2\right).$$

As with the Gaussian function, the lognormal function is unimodal and so the peak value of X occurs between 0 and ∞. So, for finite values of μ and σ, the exponential term and common terms can be removed and the derivative simplifies to

$$1 + \frac{1}{\sigma^2}[\ln(x) - \mu] = 0\,.$$

Solving, yields (Shimizu and Crow, eqn. 4-5, p. 9; Aitchison and Brown, p.9).

$$x = e^{\mu - \sigma^2} \equiv x_{mode}\,. \tag{A-17}$$

Finally, we note that for a lognormal random variable, the mode, median and mean occur at different points with

$$x_{mode} \le x_{median} \le x_{mean}\,.$$

A.1.1.7 Summary of Statistical Parameters for Gaussian and Lognormal Probability Density Functions

TableA.1 summarizes the (true) mathematical statistics for both the Gaussian and lognormal pdfs. However, the lognormal parameters are not the parameters used in atmospheric science and small particle physics.

A.1.2 The Lognormal Probability Density Function for a Generic base

The lognormal pdf derived in section 2.3 used the exponential transformation of Eqn. 2-14. However, in the literature, the lognormal pdf is often written using log10 rather than log$e$ (i.e., natural log, ln). In this section we generalize the lognormal pdf to a base a from which the statistics for base 10 will be set forth.

A.1.2.1 Derivation of the Lognormal Probability Density Function for an Arbitrary Base

The transformation which relates the Gaussian random variable, Y, with a random variable, X, to the base a is

$$X = a^Y\,. \tag{A-18a}$$

Using the definition,

$$a = e^{\ln(a)}, \tag{A-18b}$$

Table A.1 – Statistical parameters of the Gaussian and lognormal (Base *e*) probability density functions

Statistics	Probability Density Function	
	Gaussian; $N(\mu, \sigma^2)$	Lognormal; $\Lambda(\mu, \sigma^2)$[††]
Functional Form	$f_Y(y) = \frac{1}{\sqrt{2\pi}\cdot\boldsymbol{\sigma}} \exp\left(-\frac{1}{2\boldsymbol{\sigma}^2}(y-\boldsymbol{\mu})^2\right)$	$f_X(x) = \frac{1}{\sqrt{2\pi}\cdot\boldsymbol{\sigma}\, x} \exp\left(-\frac{1}{2\boldsymbol{\sigma}^2}(\ln(x)-\boldsymbol{\mu})^2\right.$
Expected Value (Mean)	μ	$\exp\left(\boldsymbol{\mu}+\frac{1}{2}\boldsymbol{\sigma}^2\right)$
Variance	σ^2	$\exp(2\boldsymbol{\mu}+\boldsymbol{\sigma}^2)\{\exp(\boldsymbol{\sigma}^2)-1\}$
Median	μ	$\exp(\boldsymbol{\mu})$
Mode	μ	$\exp(\boldsymbol{\mu}-\boldsymbol{\sigma}^2)$

the transformation becomes

$$X = \left(e^{\ln(a)}\right)^Y = g(Y)$$

which has the root

$$Y_1 = \frac{\ln(X)}{\ln(a)}.$$

Using the Gaussian pdf of Eqn. 2-10 and the expression of Eqn. 2-8, yields

[††] The parameters, μ and σ should be strictly looked at as shape parameters that, for the Gaussian pdf only, take on the dual definitions of mean and standard deviation.

$$f_X(x) = \frac{f_Y(Y_1)}{|g'(Y_1)|}$$
$$= \frac{f_Y(Y_1)}{|x \ln(a)|}$$
$$= \frac{1}{\sqrt{2\pi}\cdot\sigma\, x \ln(a)} \exp\left(-\frac{1}{2\sigma^2}\left(\frac{\ln(x)}{\ln(a)} - \mu \right)^2 \right).$$

Now, using the conversion of a logarithm of a general base to the natural log (Abromowitz and Stegun, p. 67, eqn. 4.1.18)

$$\log_a(x) = \frac{\ln(x)}{\ln(a)}, \tag{A-19}$$

the lognormal pdf for an arbitrary base a is[†]

$$f_X(x) = \frac{1}{\sqrt{2\pi}\cdot\sigma\, x \ln(a)} \exp\left(-\frac{1}{2\sigma^2}(\log_a(x) - \mu)^2 \right) \tag{A-20}$$

or,

$$f_X(x) = \frac{1}{\sqrt{2\pi}\cdot\sigma\, x \ln(a)} \exp\left(-\frac{1}{2\sigma^2 \ln^2(a)}(\ln(x) - \mu \ln(a))^2 \right). \tag{A-21}$$

A.1.2.2 (Pseudo) Moment Generating Function of a Lognormal Function of Arbitrary Base

To determine the expected value, variance, and other moments of a lognormal function of a generic base a, we will follow the same procedure as shown in section 2.3.1.2. As before, we are not actually finding the moment-generating function but rather some function that will provide us with the desired moments.

Rewriting Eqn. A-8 here and substituting the transformation of Eqn. A-18a and the definition of Eqn. A-18b, yields,

$$\mathbf{E}\{x^k\} = \left. \frac{d^k \mathbf{M}_X(t)}{dt^k} \right|_{t=0} = \int_{-\infty}^{\infty} x^k f_X(x)\, dx$$
$$= \int_{-\infty}^{\infty} \left(e^{Y \ln(a)}\right)^k f_X\left(e^{Y \ln(a)}\right) dx.$$

Substituting Eqn. A-20 and using

[†] From here on, unsubscripted μ and σ are from the original natural logarithm form of the lognormal function (Eqn. 2-13).

$$dx = d\left(e^{Y\ln(a)}\right)dy$$
$$= \ln(a)e^{Y\ln(a)}dy$$
$$= \ln(a)a^{Y}dy$$

yields,

$$\mathbf{E}\left\{x^{k}\right\} = \int_{-\infty}^{\infty}\left(e^{ky\ln(a)}\right)\left[\frac{1}{\sqrt{2\pi}\cdot\boldsymbol{\sigma}\left(e^{y\ln(a)}\ln(a)\right)}\exp\left(-\frac{1}{2\boldsymbol{\sigma}^{2}\ln^{2}(a)}\left(\ln\left(e^{y\ln(a)}\right)-\boldsymbol{\mu}\ln(a)\right)^{2}\right)\right]\ln(a)e^{y\ln(a)}\,dy\,.$$

Noting that

$$\frac{\ln\left(e^{y\ln(a)}\right)}{\ln(a)} = \frac{\ln\left(a^{y}\right)}{\ln(a)} = \frac{\log_{a}\left(a^{y}\right)\ln(a)}{\ln(a)} = \log_{a}\left(a^{y}\right) = y$$

we have

$$\mathbf{E}\left\{x^{k}\right\} = \int_{-\infty}^{\infty}\left(e^{ky\ln(a)}\right)\left[\frac{1}{\sqrt{2\pi}\cdot\boldsymbol{\sigma}}\exp\left(-\frac{1}{2\boldsymbol{\sigma}^{2}}(y-\boldsymbol{\mu})^{2}\right)\right]dy$$
$$= \int_{-\infty}^{\infty}\left(e^{ky\ln(a)}\right)f_{Y}(y)\,dy\ .$$

which is equivalent to $\mathbf{M}_{Y}(t)$ of Eqn. A-7 but with $t = k\ln(a)$. Therefore, the (pseudo) moment-generating function of a lognormal probability density function of arbitrary base a is

$$\mathbf{E}\left\{x^{k}\right\} = e^{\left(\boldsymbol{\mu}k\ln(a)+\boldsymbol{\sigma}^{2}k^{2}\ln^{2}(a)/2\right)}. \qquad \text{(A-22)}$$

By substituting for the exponent base ($a = e$) shows that Eqn. A-22 yields Eqn. A-9.

A.1.2.3 Expected Value of a Lognormal Probability Density Function of an Arbitrary Base

Using Eqn. A-22, the expected value for a lognormal pdf of base a is

$$\mathbf{E}\{x\} = e^{\boldsymbol{\mu}\ln(a)+\boldsymbol{\sigma}^{2}\ln^{2}(a)/2} \qquad \text{(A-23)}$$
$$\equiv \boldsymbol{\mu}_{a}\,.$$

A.1.2.4 Variance of a Lognormal Probability Density Function of an Arbitrary Base

Using Eqn. A-22, the variance for a lognormal pdf of base a is

$$\begin{aligned} \mathbf{E}\left\{(x-\boldsymbol{\mu}_a)^2\right\} &= \mathbf{E}\left\{x^2\right\} - \boldsymbol{\mu}_a^2 \\ &= e^{2\boldsymbol{\mu}\ln(a)+2\boldsymbol{\sigma}^2\ln^2(a)} - e^{2\boldsymbol{\mu}\ln(a)+\boldsymbol{\sigma}^2\ln^2(a)} \\ &= \left(e^{2\boldsymbol{\mu}\ln(a)+\boldsymbol{\sigma}^2\ln^2(a)}\right)\left(e^{\boldsymbol{\sigma}^2\ln^2(a)}-1\right) \\ &\equiv \boldsymbol{\sigma}_a^2 . \end{aligned} \tag{A-24}$$

A.1.2.5 Percentiles of a Lognormal Probability Density Function of an Arbitrary Base

The q^{th} percentile is defined as the point, $\mathbf{x}_q$, for which the area up to $\mathbf{x}_q$ contains q% of the total area of the pdf. The explicit expression is

$$P\left\{X \le \mathbf{x}_q\right\} = q = \int_{-\infty}^{\mathbf{x}_q} f_X(x)dx . \tag{A-25}$$

Previously, we showed $\mathbf{y}_q$, given by

$$\mathbf{y}_q = \boldsymbol{\mu} + \boldsymbol{\sigma}\, t_q , \tag{A-26}$$

is the q^{th} percentile point for a Gaussian pdf and t_q is the corresponding tabular value from the standard normal distribution, N(0, $(1)^2$). Combining Eqns. A-18a and b, we have the transformation

$$x = e^{y\ln(a)} \tag{A-27}$$

and therefore

$$\begin{aligned} \mathbf{x}_q &= e^{\mathbf{y}_q \ln(a)} \\ &= e^{\boldsymbol{\mu}\ln(a)+\boldsymbol{\sigma}\ln(a)t_q} . \end{aligned} \tag{A-28}$$

A.1.2.5.1 Median of a Lognormal Probability Density Function of an Arbitrary Base

The median, $\mathbf{x}_{\text{median}}$, of a pdf is the point up to which contains 50% of the total area of the pdf. For a lognormal pdf of base a, the median is given by

$$P\left\{X \le \mathbf{x}_{\text{median}_a}\right\} = 0.5 = \int_{-\infty}^{\mathbf{x}_{\text{median}_a}} f_X(x)dx .$$

From the Gaussian pdf, the median point, $\mathbf{y}_{\text{median}}$, was found when $t_q = t_{0.5} = 0$. Using the transformation of Eqn. A-28, the median of a lognormal pdf of base a is given by

$$\mathbf{x}_{\text{median}_a} = e^{\boldsymbol{\mu}\ln(a)}. \tag{A-29}$$

A.1.2.6 Mode of a Lognormal Probability Density Function of an Arbitrary Base

The mode, $\mathbf{x}_{\text{mode}}$, of a pdf is the point where $f_X(x)$ is a maximum. The modal point(s) can be found by taking the first derivative of the pdf, setting it equal to zero and solving. Taking the derivative of Eqn. A-21,

$$\frac{df_X(x)}{dx} = 0 = \frac{-1}{\sqrt{2\pi}\cdot\boldsymbol{\sigma}x^2\ln(a)}\exp\left(-\frac{1}{2\boldsymbol{\sigma}^2\ln^2(a)}\left(\ln(x)-\boldsymbol{\mu}\ln(a)\right)^2\right)+$$
$$\frac{1}{\sqrt{2\pi}\cdot\boldsymbol{\sigma}x\ln(a)}\left[-\frac{1}{2\boldsymbol{\sigma}^2\ln^2(a)}\left(\frac{2\ln(x)}{x}-\frac{2\boldsymbol{\mu}\ln(a)}{x}\right)\right]\exp\left(-\frac{1}{2\boldsymbol{\sigma}^2\ln^2(a)}\left(\ln(x)-\boldsymbol{\mu}\ln(a)\right)^2\right).$$

From Figures 2-2 and 2-3, the lognormal pdf goes to zero as $x \to 0$ and $x \to \infty$. Since by the definition of pdfs, these values cannot occur (probability of occurring is zero), we can divide out the exponential terms as well as similar like terms and so we have

$$0 = -1 - \frac{1}{\boldsymbol{\sigma}^2\ln^2(a)}\left(\ln(x)-\boldsymbol{\mu}\ln(a)\right).$$

Rearranging and solving for x, the modal point of a lognormal pdf of arbitrary base a is

$$\begin{aligned} -\boldsymbol{\sigma}^2\ln^2(a) &= \ln(x)-\boldsymbol{\mu}\ln(a) \\ \ln(x) &= \boldsymbol{\mu}\ln(a)-\boldsymbol{\sigma}^2\ln^2(a) \\ x &= e^{\boldsymbol{\mu}\ln(a)-\boldsymbol{\sigma}^2\ln^2(a)} \\ &\equiv \mathbf{x}_{\text{mode}_a}. \end{aligned} \tag{A-30}$$

A.1.2.7 Transformation Between Lognormal Functions of Different Bases

Since any appropriate base can be used as a lognormal function, it will helpful to determine how to relate the parameters, μ and σ, between two arbitrary bases, a and b. This will prove to be useful especially when comparing lognormal functions of the base e and base 10.

By equating two lognormal functions of base a and b,

$$f_{X_a}(x) = f_{X_b}(x)$$

$$\frac{1}{\sqrt{2\pi}\cdot\boldsymbol{\sigma}_a x}\exp\left(-\frac{1}{2\boldsymbol{\sigma}_a^2}\left(\log_a(x)-\boldsymbol{\mu}_a\right)^2\right) = \frac{1}{\sqrt{2\pi}\cdot\boldsymbol{\sigma}_b x}\exp\left(-\frac{1}{2\boldsymbol{\sigma}_b^2}\left(\log_b(x)-\boldsymbol{\mu}_b\right)^2\right), \tag{A-31}$$

we wish to determine the relationship between μ_a and μ_b and σ_a and σ_b for which A-31 is valid. Canceling like terms and taking the natural log of both sides yields

$$-\frac{1}{2\boldsymbol{\sigma}_a^2}\left(\log_a(x)-\boldsymbol{\mu}_a\right)^2-\ln\left(\boldsymbol{\sigma}_a\ln(a)\right)=\frac{1}{2\boldsymbol{\sigma}_b^2}\left(\log_b(x)-\boldsymbol{\mu}_b\right)^2-\ln\left(\boldsymbol{\sigma}_b\ln(b)\right).$$

Equating similar terms yields two equations and two unknowns:

$$-\ln\left(\boldsymbol{\sigma}_a\ln(a)\right)=-\ln\left(\boldsymbol{\sigma}_b\ln(b)\right) \tag{A-32}$$

$$-\frac{1}{2\boldsymbol{\sigma}_a^2}\left(\log_a(x)-\boldsymbol{\mu}_a\right)^2=-\frac{1}{2\boldsymbol{\sigma}_b^2}\left(\log_b(x)-\boldsymbol{\mu}_b\right)^2. \tag{A-33}$$

We will use these two expressions in the next sections.

A.1.2.7.1 Relation Between the σ of Two Bases

Raising both sides of Eqn. A-32 to the power e yields

$$\begin{aligned}&\boldsymbol{\sigma}_a\ln(a)=\boldsymbol{\sigma}_b\ln(b)\\&\therefore\quad\boldsymbol{\sigma}_b=\boldsymbol{\sigma}_a\frac{\ln(a)}{\ln(b)}.\end{aligned} \tag{A-34}$$

A.1.2.7.2 Relation Between the μ of Two Bases

Taking the square root of both sides of Eqn. A-33 yields

$$\frac{1}{\boldsymbol{\sigma}_a}\left(\log_a(x)-\boldsymbol{\mu}_a\right)=\frac{1}{\boldsymbol{\sigma}_b}\left(\log_b(x)-\boldsymbol{\mu}_b\right).$$

Now, using the relation of Eqn. A-34 and the conversion of Eqn. A-19, the above expression simplifies to

$$\frac{\ln(a)}{\ln(b)}\left(\frac{\ln(x)}{\ln(a)}-\boldsymbol{\mu}_a\right)=\frac{\ln(x)}{\ln(b)}-\boldsymbol{\mu}_b$$

and therefore,

$$\boldsymbol{\mu}_b=\frac{\ln(a)}{\ln(b)}\boldsymbol{\mu}_a. \tag{A-35}$$

A.1.2.8 Summary of Statistical Parameters for a Lognormal Probability Density Function of Arbitrary Base

Using the expressions which relate an arbitrary base a to the exponential base (Abramowitz and Stegun, eqns. 4.1.18 and 4.2.7, pp. 67-69),

$$\log_a(x) = \ln(x) \Big/ \ln(a) \tag{A-36}$$

$$a^k = e^{k \ln(a)}, \tag{A-37}$$

we can convert Eqns. A-23, A-24, A-29, and A-30 to powers of a. Table A-2 summarizes the statistical parameters for a lognormal pdf of arbitrary base a and also gives the specific parameters for the base 10 function.

Table A-2: Statistical parameters of a lognormal pdf of base *a* and base 10.

Statistics	Probability Density Function	
	Base a, $\Lambda_a(\mu, \sigma^2)$	Base 10, $\Lambda_{10}(\mu, \sigma^2)$
Functional Form $f_{X_a}(x)$	$\frac{1}{\sqrt{2\pi}\cdot\sigma\, x \ln(a)} \exp\left(-\frac{1}{2\sigma^2}(\log_a(x)-\mu)^2\right)$	$\frac{1}{\sqrt{2\pi}\cdot\sigma\, x \ln(10)} \exp\left(-\frac{1}{2\sigma^2}(\log_{10}(x)-\mu)^2\right)^{\dagger}$
Expected Value (Mean)	$a^{\mu + \sigma^2 \ln(a)/2}$	$\mu_{10} \equiv 10^{\mu + \sigma^2 \ln(10)/2}$
Variance	$\left(a^{2\mu+\sigma^2\ln(a)}\right)\left(a^{\sigma^2\ln(a)}-1\right)$	$\sigma_{10}^2 \equiv \left(10^{2\mu+\sigma^2\ln(10)}\right)\left(10^{\sigma^2\ln(10)}-1\right)$
Median	a^{μ}	10^{μ}
Mode	$a^{\mu-\sigma^2\ln(a)}$	$10^{\mu-\sigma^2\ln(10)}$

* $\ln(10) = 2.303$

Comparing Tables A-1 and A-2, we see that base 10 and base e lognormal functions give different statistics for the same parameters μ and σ.

---

† Here, $\log_{10}$ is used to differentiate between base 10 and base a functions. Later, when the base 10 logarithm is used, the subscript will be dropped and it should be understood that base 10 is implied (ln will be used for the exponential base). However, examining Eqn. A-21 shows that a natural logarithm can be

A.2 HIGHER MOMENTS OF THE LOGNORMAL FUNCTION

In this section we show the true area and volume distributions of the lognormal function. This section differs from section 2.5 in that the random variables used are area, **A**, and volume, **V**, and not powers of the random variable **r**.

A.2.1 The Statistics of the Lognormal Surface Area Distribution

Assuming the particles are spherical, the transformation of the random variable **r** (particle radius) to the random variable, A (surface area), is given by

$$\begin{aligned} A &= 4\pi r^2 \\ &= g(r). \end{aligned} \tag{A-38}$$

Following the steps in Section 2.3, the area probability density function, $f_A(A)$, is (using Eqn. 2-8) (See Aitchison and Brown, Theorem 2.1, p. 11)

$$f_A(A) = \frac{f_R(r_1)}{|g'(r_1)|} + \frac{f_R(r_2)}{|g'(r_2)|}$$

where r_1 and r_2 are the roots of $g(r)$ given by

$$r_{1,2} = \pm\sqrt{\frac{A}{4\pi}}\,. \tag{A-39}$$

Since a negative particle radius is meaningless, there is only one root, r_1. Thus,

$$f_A(A) = \frac{f_R(r_1)}{|g'(r_1)|} = \frac{f_R(r_1)}{\left|8\pi\sqrt{A/4\pi}\right|}$$

$$= \frac{1}{8\pi\sqrt{A/4\pi}} \frac{1}{\sqrt{2\pi}\cdot\boldsymbol{\sigma}\sqrt{A/4\pi}} \exp\left(-\frac{1}{2\boldsymbol{\sigma}^2}\left(\ln\left(\sqrt{A/4\pi}\right) - \boldsymbol{\mu}\right)^2\right),$$

which simplifies to

---

present in the pdf for an arbitrary base. The key to understanding what base is used is to look for the 1/ln(a) term before the exponent.

$$f_A(A) = \frac{1}{\sqrt{2\pi}\cdot(2\sigma)A}\exp\left(-\frac{1}{2\sigma^2}\left[\frac{1}{2}(\ln(A)-\ln(4\pi))-\mu\right]^2\right)$$
$$= \frac{1}{\sqrt{2\pi}\cdot(2\sigma)A}\exp\left(-\frac{1}{2(2\sigma)^2}(\ln(A)-(\ln(4\pi)+2\mu))^2\right). \quad \text{(A-40)}$$

Comparing Eqn. A-40 with the lognormal probability density function for radius of Eqn. A-2, we define the characteristic parameters of the lognormal probability density function for area as

$$\mu_A = \ln(4\pi)+2\mu$$
$$\sigma_A = 2\sigma \quad \text{(A-41)}$$

and so

$$f_A(A) = \frac{1}{\sqrt{2\pi}\cdot\sigma_A A}\exp\left(-\frac{1}{2\sigma_A^2}(\ln(A)-\mu_A)^2\right) \quad \text{(A-42)}$$
$$\equiv \Lambda\left(\mu_A,(\sigma_A)^2\right).$$

It is interesting to note that the transformation of the lognormal random variable **r** by Eqn. A-38 resulted in another lognormal function. The lognormal's relative insensitivity to transformation may be one of the reasons why so many different functions are used to fit particle size data. Because Eqn. A-42 is identical in form to Eqn. A-2, the statistics of $f_A(A)$ follow directly from Section 2.3.1 and so the moments of the surface area pdf are given by

$$\mathbf{E}\{A^k\} = e^{\mu_A k+\sigma_A^2 k^2/2}. \quad \text{(A-43)}$$

A.2.1.1 Mean of the Surface Area Lognormal Probability Density Function

The mean of $f_A(A)$ is given by

$$\mathbf{A}_{\text{mean}} \equiv \mathbf{E}\{A\} = e^{\mu_A+\frac{1}{2}\sigma_A^2} \quad \text{(A-44)}$$
$$= (4\pi)e^{2\mu+2\sigma^2}.$$

Therefore, the corresponding surface mean radius is (Shimizu and Crow, eqn. 2-7, p.334)

$$\sqrt{\mathbf{A}_{\text{mean}}/4\pi} = e^{\mu+\sigma^2}. \quad \text{(A-45)}$$

A.2.1.2 Variance of the Surface Area Lognormal Probability Density Function

The variance of $f_A(A)$ is given by

$$\mathbf{A}_{\text{variance}} \equiv \mathbf{E}\left\{\left(A - \mathbf{A}_{\text{mean}}\right)^2\right\} = \left(e^{2\boldsymbol{\mu}_A + \boldsymbol{\sigma}_A^2}\right)\left(e^{\boldsymbol{\sigma}_A^2} - 1\right). \tag{A-46}$$

A.2.1.3 Median of the Surface Area Lognormal Probability Density Function

The median of $f_A(A)$ is given by

$$\begin{aligned} \mathbf{A}_{\text{median}} &= e^{\boldsymbol{\mu}_A} \\ &= 4\pi e^{2\boldsymbol{\mu}}. \end{aligned} \tag{A-47}$$

A.2.1.4 Mode of the Surface Area Lognormal Probability Density Function

The mode of $f_A(A)$ is

$$\begin{aligned} \mathbf{A}_{\text{mode}} &= e^{\boldsymbol{\mu}_A - \boldsymbol{\sigma}_A^2} \\ &= 4\pi\, e^{2\boldsymbol{\mu} - 4\boldsymbol{\sigma}^2}\ . \end{aligned} \tag{A-48}$$

A.2.1.5 (Particle) Geometric Mean and (Particle) Geometric Standard Deviation of Surface Area Probability Density Function

Using the definitions of Eqns. 2-24 and 2-25 for the (particle) geometric mean (i.e., median) and the (particle) geometric standard deviation, expressions for the (particle) area geometric mean and the (particle) area geometric standard deviation are easily expressed in terms of Eqns. 2-24 and 2-25 as

$$\begin{aligned} \mathbf{A}_{\text{mean}} = \mathbf{A}_g &= e^{\boldsymbol{\mu}_A} \\ &= 4\pi e^{2\boldsymbol{\mu}} = 4\pi\left(e^{\boldsymbol{\mu}}\right)^2 \\ &= 4\pi\ \mathbf{r}_g^2 \\ &= 4\pi\ \mathbf{r}_{\text{median}}^2 \end{aligned} \tag{A-49}$$

and,

$$\begin{aligned} \boldsymbol{\sigma}_{g_A} &= e^{\boldsymbol{\sigma}_A} = e^{2\boldsymbol{\sigma}} = \left(e^{\boldsymbol{\sigma}}\right)^2 \\ &= \boldsymbol{\sigma}_g^{\,2}\ . \end{aligned} \tag{A-50}$$

Although we could certainly re-write Eqn. A-40 using Eqns. A-49 and A-50, this will not be shown here for the simple reason that this section is setting forth the (true) mathematical statistics of surface area

distribution for eventual comparison with the surface area statistics used by small particle physicists. None of the above expressions are used in the aerosol/particle literature. It was necessary to establish the above mathematical statistics both for the reader's reference but also to illustrate the confusion that arises when one speaks of an area distribution from a mathematical perspective and an area distribution (i.e., distribution of areas) from a particle perspective.

A.2.2 The Statistics of the (True) Lognormal Volume Distribution

Assuming the particles are spherical, the transformation of the random variable **r** (particle radius) to the random variable, V (volume), is given by

$$\begin{aligned} V &= \frac{4}{3}\pi r^3 \\ &= g(r). \end{aligned} \tag{A-51}$$

Following the steps for the surface area pdf, the volume probability density function, $f_V(V)$, is

$$f_V(V) = \frac{f_R(r_1)}{|g'(r_1)|} + \frac{f_R(r_2)}{|g'(r_2)|} + \frac{f_R(r_3)}{|g'(r_3)|}$$

where r_1, r_2, and r_3 are the roots of g(r). Since two of the three roots are complex, only the root

$$r_1 = \sqrt[3]{V/\tfrac{4}{3}\pi}\ . \tag{A-52}$$

is allowed. Thus,

$$f_V(V) = \frac{f_R(r_1)}{|g'(r_1)|} = \frac{f_R(r_1)}{\left|4\pi\left(V/\tfrac{4}{3}\pi\right)^{\frac{2}{3}}\right|}$$

$$= \frac{1}{4\pi\left(V/\tfrac{4}{3}\pi\right)^{\frac{2}{3}}} \frac{1}{\sqrt{2\pi}\cdot\sigma\left(V/\tfrac{4}{3}\pi\right)^{\frac{1}{3}}} \exp\left(-\frac{1}{2\sigma^2}\left(\ln\left(\left(V/\tfrac{4}{3}\pi\right)^{\frac{1}{3}}\right)-\mu\right)^2\right),$$

which simplifies to

$$f_V(V) = \frac{1}{\sqrt{2\pi}\cdot(3\sigma)V}\exp\left(-\frac{1}{2(3\sigma)^2}\left(\ln(V)-\left(\ln\left(\tfrac{4}{3}\pi\right)+3\mu\right)\right)^2\right). \tag{A-53}$$

Comparing Eqn. A-53 with the lognormal probability density function for radius of Eqn. A-2, we define the characteristic parameters of the lognormal probability density function for volume as

$$\begin{aligned} \boldsymbol{\mu}_V &= \ln\left(\tfrac{4}{3}\pi\right) + 3\boldsymbol{\mu} \\ \boldsymbol{\sigma}_V &= 3\boldsymbol{\sigma} \end{aligned} \tag{A-54}$$

and so

$$\begin{aligned} f_V(V) &= \frac{1}{\sqrt{2\pi}\cdot\boldsymbol{\sigma}_V V}\exp\left(-\frac{1}{2\boldsymbol{\sigma}_V^2}\left(\ln(V)-\boldsymbol{\mu}_V\right)^2\right) \\ &\equiv \Lambda\left(\boldsymbol{\mu}_V, (\boldsymbol{\sigma}_V)^2\right). \end{aligned} \tag{A-55}$$

Because Eqn. A-55 is identical in form to Eqn. A-2, the statistics of $f_V(V)$ follow directly from Section 2.3.1 and so the moments of the volume pdf are given by

$$\mathbf{E}\left\{V^k\right\} = e^{\boldsymbol{\mu}_V k + \boldsymbol{\sigma}_V^2 k^2/2}. \tag{A-56}$$

A.2.2.1 Mean of the Volume Lognormal Probability Density Function

The mean of $f_V(V)$ is given by

$$\begin{aligned} \mathbf{V}_{\text{mean}} \equiv \mathbf{E}\{V\} &= e^{\boldsymbol{\mu}_V + \frac{1}{2}\boldsymbol{\sigma}_V^2} \\ &= \left(\frac{4}{3}\pi\right)e^{3\boldsymbol{\mu}+\frac{9}{2}\boldsymbol{\sigma}^2}. \end{aligned} \tag{A-57}$$

Therefore, the corresponding volume mean radius is (Shimizu and Crow, eqn. 2-7, p.334)

$$\sqrt[3]{\mathbf{V}_{\text{mean}}\Big/\tfrac{4}{3}\pi} = e^{\boldsymbol{\mu}+\frac{3}{2}\boldsymbol{\sigma}^2}. \tag{A-58}$$

A.2.2.2 Variance of the Volume Lognormal Probability Density Function

The variance of $f_V(V)$ is given by

$$\mathbf{V}_{\text{variance}} \equiv \mathbf{E}\left\{\left(V-\mathbf{V}_{\text{mean}}\right)^2\right\} = \left(e^{2\boldsymbol{\mu}_V+\boldsymbol{\sigma}_V^2}\right)\left(e^{\boldsymbol{\sigma}_V^2}-1\right). \tag{A-59}$$

A.2.2.3 Median of the Volume Lognormal Probability Density Function

The median of $f_V(V)$ is given by

$$\begin{aligned} \mathbf{V}_{\text{median}} &= e^{\boldsymbol{\mu}_V} \\ &= \tfrac{4}{3}\pi e^{3\boldsymbol{\mu}}. \end{aligned} \tag{A-60}$$

A.2.2.4 Mode of the Volume Lognormal Probability Density Function

The mode of $f_V(V)$ is

$$\begin{aligned} \mathbf{V}_{\text{mode}} &= e^{\boldsymbol{\mu}_V - \boldsymbol{\sigma}_V^2} \\ &= \frac{4}{3}\pi\, e^{3\boldsymbol{\mu} - 9\boldsymbol{\sigma}^2}. \end{aligned} \tag{A-61}$$

A.2.2.5 (Particle) Geometric Mean and (Particle) Geometric Standard Deviation of Volume Probability Density Function

Using the definitions of Eqns. 2-24 and 2-25 for the (particle) geometric mean (i.e., median) and the (particle) geometric standard deviation, expressions for the (particle) volume geometric mean and the (particle) volume geometric standard deviation are easily expressed in terms of Eqns. 2-24 and 2-25 as

$$\begin{aligned} \mathbf{V}_{\text{mean}} = \mathbf{V}_g &= e^{\boldsymbol{\mu}_V} \\ &= \tfrac{4}{3}\pi\, e^{3\boldsymbol{\mu}} = \tfrac{4}{3}\pi \left(e^{\boldsymbol{\mu}}\right)^3 \\ &= \tfrac{4}{3}\pi\, \mathbf{r}_g^3 \\ &= \tfrac{4}{3}\pi\, \mathbf{r}_{\text{median}}^3 \end{aligned} \tag{A-62}$$

and,

$$\begin{aligned} \boldsymbol{\sigma}_{g_V} &= e^{\boldsymbol{\sigma}_V} = e^{3\boldsymbol{\sigma}} = \left(e^{\boldsymbol{\sigma}}\right)^3 \\ &= \boldsymbol{\sigma}_g^3. \end{aligned} \tag{A-63}$$

B

Appendix B:
Matlab Data Processing Script

The two main scripts are get_data.m and process_data.m. All of the other scripts simply take the data from resulting from these two scripts and processes it further into ratios, profiles and composites. Since get_data.m simply finds the file numbers, only process_data.m is shown.

B.1 PROCESS_DATA.M

```
% process_data.m
% E.J. Novitsky
% 16 May 2001

% NOTE: BE SURE TO CHANGE THE FILE DESTINATION FOR EACH DATA RUN

% This file does as its name states. It takes each image file, subtracts the background, subtracts the
% darkcounts, finds the beam end point, and finally, sums the beam's transverse pixels. This file also
% contains a de-activated histogram routine which, due to the length of time it takes to run (1+ hrs for
EACH
% .fts file), should be part of standalone program. (There is probably a better way to do an image
histogram
% (probably work directly in C/C++.)

% The output of this program are files which contain the beam summation, the corresponding row and
column pixels
% and as a check, the number of elements that were summed across the beam (the same number of
elements should
% be summed for each camera and for each beam location all the way to the beam's end point).


function [Processed_Data, beam_end_column_pixel] = process_data(Parallel_file, Perpendicular_file,
CCD_Index, dark_file, back_file)
% The camera is unimportant to this routine so we do not need to specify it in the file name.


switch CCD_Index
        case 1   % CCD A's beam width for pixel summation
                 beam_width = 8;  % Number of pixels the beam covers in its transverse direction.
                                  % Obtained by examining the data.
        case 2   % CCD B's beam width for pixel summation
                 beam_width = 8;
        case 3   % CCD C's beam width for pixel summation
                 beam_width = 8;
end
```

```
% Load in image file.
sprintf('Loading data in file %s',Parallel_file)
[header_par,data_par] = fitsload(Parallel_file);
sprintf('Loading data in file %s',Perpendicular_file)
[header_per,data_per] = fitsload(Perpendicular_file);


% 16-bit fts file formats yield data from -32768 to +32768.  Here, bias data by +32768.
data_par = data_par + 32768;  % Data is 512 rows by 768 columns
data_per = data_per + 32768;

% Subtract dark counts and background
%sprintf('Loading dark counts...')
%[header_dark, data_dark] = fitsload(dark_file);
%data_dark = data_dark + 32768;

sprintf('Loading background...')
[header_back, data_back] = fitsload(back_file);
data_back = data_back + 32768;

%sprintf('Subtracting dark counts and background...')
sprintf('Subtracting background...')
%data_par = data_par - data_back - data_dark;
%data_per = data_per - data_back - data_dark;
data_par = data_par - data_back;
data_per = data_per - data_back;



%clear data_back data_dark
clear data_back;

sprintf(' ')

%%%%%%%%%%%%%%%%%%%%%%%%%%%%%%%%%%%%%%%%%%%%%%%%%%%
%%%%%%%%%%%%%%%%%%%%%%%%%%%%%%%%%%%%%%%%%%%%%%%%%%%
%
% Create a histogram in order to locate the beam.
%binwidth = 8;
%number_of_bins = ceil((max(max(data)) - min(min(data)))./binwidth) + 1;

% Initialize and create bin array and counting array
%bin_array = min(min(data)) + (0:number_of_bins-1)*binwidth;
%counts = zeros(size(bin_array));

% Create histogram
% Begin counting each pixel in the image
rows = 512;
columns = 768; % Note that these definitions of rows and columns are reversed with respect to image
                                        % processing conventions.

%for i = 1:rows
%    i
%    for j = 1:columns
%         for k = 1:length(bin_array)
%                   if data(i,j) >= bin_array(k) & data(i,j) < bin_array(k+1)
```

```
%                       counts(k) = counts(k) + 1;
%                       k = length(bin_array) + 1; % Exits loop
%               end
%       end
%   end
%end

%temp = log10(counts + 1); % The 1 is added so that when the log is taken, negative infinity will not result
%bar(bin_array,temp)
%%%%%%%%%%%%%%%%%%%%%%%%%%%%%%%%%%%%%%%%%%%%%%%%%%%%%%%%%%%%%%%%%%%%%%%%%%%%%%%%%%%%%%%%%%%%%%%%%%%%%%



% Next, determine where the beam is.  The procedure is to locate the maximum of every column, which
% should locate the beam.  However, checks of the pixels around the maximum point should also confirm
the
% location of the beam.  A FIXED number of pixels will be summed to give the collective value of the
% beam at the pixel's assigned altitude.  Corrections for volume and range will be applied after
% the beam is located.

disp('Acquiring maximum of each of the 768 columns...')
for j = 1:columns
    tempmax_par(j,:) = [min(data_par(:,j))' 0 0];       % Initialize matrices
    tempmax_per(j,:) = [min(data_par(:,j))' 0 0];
    for i = 1:rows
        if data_par(i,j) > tempmax_par(j)
                tempmax_par(j,:) = [data_par(i,j) i j]; % Each ROW of tempmax holds a CCD column
        end
        if data_per(i,j) > tempmax_per(j)
                tempmax_per(j,:) = [data_per(i,j) i j];
        end
    end
end

disp('Column maximums found')
disp(' ');
disp(' ');
disp(' ');
% Examine pixels surrounding each column's maximum.  The first check is to acquire the rows where
% the beam most likely lies.  This information is then used to decide if each column's maximum is indeed
% part of the beam.  There are two cases where the column maximum will not yield the beam location:
% 1) The last columns will not have the beam as the beam's infinity point will be somewhere in a previous
% column (albeit near the edge, i.e., in columns around pixel 760), 2) A source of bright light not due
% to scattering by the beam.  This may be due to bright stars(?), insects flying near the beam and
% providing a decent reflection, aircraft running lights, or the moon.  The moon is a particular
% problem because it may be massive.  Hopefully, data runs will not image the moon at all.

% To identify the most likely rows of where the beam is, a number of procedures can be applied.  For
% example, a least squares fit to obtain the equation of the laser line may be used.  Here, we simply
% take the average row number and indicate that the beam should be located within 5 pixels on either side
% of the row average.

% To promote a good average, we will not consider every column, but only those columns which are in
```

```
% the middle of the CCD array.  This should remove the beam end point which could have a large impact
on
% the beam row average.

% As a last point, the underlying assumption is that the beam has been aligned as close to horizontal
% on the CCD array as possible.  Simple corrections can be applied to correct for beam misalignment

% Get an initial row average
row_average_par = round(sum(tempmax_par(50:600,2))/length(tempmax_par(50:600)));
                                % Takes the 2nd column of tempmax,
                                % which correspond to the rows
                                %where the maximum was found.
row_average_per = round(sum(tempmax_per(50:600,2))/length(tempmax_per(50:600)));



% Find beam end point

% We know the beam should be above pixel 725 (on clear nights).  However, at the same time that we're
looking for the beam
% end point, we'll also correct for misinterpreted data which indicates incorrect beam location.
% The beam's end pixel will be verified during the experiment during clear nights and recorded.
% The procedure works by examining successive row maximums.  If two rows are different by more
% that the equation of the row maximum pixel line, then we have found the beam.  If not, then we correct
the
% erroneous row maximum.
disp('Correcting data file...')
j = 1;
if abs (tempmax_par(j,2) - row_average_par) > 5 % Bad start, as this has a bad maximum.  Correct.
      corrected_max_par = data_par(row_average_par-10,j);
      for k = row_average_par-9:row_average_par+10
            if data_par(k,j) > corrected_max_par
                        corrected_max_par = data_par(k,j);
                        corrected_row_par = k;
            end
      end
tempmax_par(j,1) = corrected_max_par;      % Corrects maximum point
tempmax_par(j,2) = corrected_row_par;      % Corrects corresponding row
clear corrected_max_par corrected_row_par
end

if abs (tempmax_per(j,2) - row_average_per) > 5 % Bad start, as this has a bad maximum.  Correct.
      corrected_max_per = data_per(row_average_per-10,j);
      for k = row_average_per-9:row_average_per+10
            if data_per(k,j) > corrected_max_per
                        corrected_max_per = data_per(k,j);
                        corrected_row_per = k;
            end
      end
tempmax_per(j,1) = corrected_max_per;      % Corrects maximum point
tempmax_per(j,2) = corrected_row_per;      % Corrects corresponding row
clear corrected_max_per corrected_row_per
end

disp('Data file corrected.  Next, finding beam end point...')
```

```
% Next, examine all of the remaining columns, correcting as we go, and finding the end of the beam.

j = 2;
beam_end_column_pixel_par = 500; % We expect the beam to be above this pixel under most conditions.
See fov.m.
while j <= 767    % During the experiment, we desire NOT to have the end of the beam on the last pixel as
                  % it's too difficult to get anyway and also because we want to be sure exactly where the
                  % beam does end, i.e., it doesn't end at some virtual pixel such as 769 or 770, etc.


% Check Parallel Image File
check_row_1_par = abs(tempmax_par(j,2) - tempmax_par(j-1,2));        % Examining the neighboring rows
check_row_2_par = abs(tempmax_par(j-1,2) - tempmax_par(j+1,2));

if j <= 766
    check_row_3_par = abs(tempmax_par(j-1,2) - tempmax_par(j+2,2));
else
 check_row_3_par = 10; %Avoids entering a conditional statement below
end

    if check_row_1_par > 5
        if (check_row_2_par > 5 & j < beam_end_column_pixel_par)
                disp('Check data file because two successive rows differ greatly in parallel file (Bug?)')
       bad_row_par = tempmax_par(j,2);
       tempmax_par(j,2) = row_average_par; % Correct using the row_average
       tempmax_par(j,1) = data_par(row_average_par,j);
       disp('Corrected data maximum at [row column] for parallel polarization image')
       [bad_row_par j]
         elseif (check_row_2_par <= 5 & j < beam_end_column_pixel_par)       % Erroneous max
detected.  Correct.
                bad_row_par = tempmax_par(j,2);
                corrected_max_par = data_par(row_average_par-10,j);
                for k = row_average_par-9:row_average_par+10
                        if data_par(k,j) > corrected_max_par
                                corrected_max_par = data_par(k,j);
                                corrected_row_par = k;
                        end
                end
                tempmax_par(j,1) = corrected_max_par;      % Corrects maximum point
                tempmax_par(j,2) = corrected_row_par; % Corrects corresponding row
                disp('Corrected data maximum at [row column] for parallel polarization image')
                [bad_row_par j]
        elseif (check_row_2_par <=5 & j >= beam_end_column_pixel_par)
                        bad_row_par = tempmax_par(j,2);
                        corrected_max_par = data_par(row_average_par-10,j);
                for k = row_average_par-9:row_average_par+10
                        if data_par(k,j) > corrected_max_par
                                corrected_max_par = data_par(k,j);
                                corrected_row_par = k;
                        end
                end
                tempmax_par(j,1) = corrected_max_par;      % Corrects maximum point
                tempmax_par(j,2) = corrected_row_par; % Corrects corresponding row
                beam_end_column_pixel_par = j;
                disp('Updated beam_end_pixel and corrected data Maximum at [row column] for parallel
polarization image')
```

```
                [bad_row_par j]
        elseif (check_row_2_par > 5 & check_row_3_par <= 5 & j >= beam_end_column_pixel_par)
                bad_row_par = tempmax_par(j,2);
                corrected_max_par = data_par(row_average_par-10,j);
                for k = row_average_par-9:row_average_par+10
                        if data_par(k,j) > corrected_max_par
                                corrected_max_par = data_par(k,j);
                                corrected_row_par = k;
                        end
                end
                tempmax_par(j,1) = corrected_max_par;      % Corrects maximum point
                tempmax_par(j,2) = corrected_row_par; % Corrects corresponding row
                beam_end_column_pixel_par = j;
                disp('Updated beam_end_pixel and corrected data maximum at [row column] for parallel
polarization image')
                [bad_row_par j]
        else
                beam_end_column_pixel_par = j-1;% Three successive row maximums above the
expected beam end point are

    % different.  This is a sufficient condition for the beam end point.
                j = 9000; % Exit while loop
        end

    elseif (check_row_1_par <= 5 & j >= beam_end_column_pixel_par) % Start moving beam end point
    % LAPS is a very strong beam, especially in comparison to the Ar-Ion.  Thus, it is likley that the entire
    % length of the beam will also be very strong and little if any, corrections will need to be made.
However, as the algorithm
    % stands, it checks the neighboring row pixel numbers and not the pixel values.  This is corrected here.

        if beam_end_column_pixel_par >= 760       % Begin checking neighboring rows' values 'cause I
think I'm getting close to the beam endpoint
                %value = abs(tempmax_par(j,1) - tempmax_par(j-1,1));  This way didn't seem to work,
so the next line was implemented.
                if tempmax_par(j,1) <= 1000         %1000 is arbitrary but reasonable
                        %beam_end_column_pixel_par = j-1;
                        j = 9000;             % Exit while loop
                else
                        beam_end_column_pixel_par = j;
                end
        else
                beam_end_column_pixel_par = j;
        end
    end
j = j+1;
end

clear corrected_max_par corrected_row_par j bad_row_par

j = 2;
beam_end_column_pixel_per = 500;
while j <= 767
% Check Perpendicular Image File
check_row_1_per = abs(tempmax_per(j,2) - tempmax_per(j-1,2));       % Examining the neighboring rows
check_row_2_per = abs(tempmax_per(j-1,2) - tempmax_per(j+1,2));
```

```
if j <= 766
    check_row_3_per = abs(tempmax_per(j-1,2) - tempmax_per(j+2,2));
else
    check_row_3_per = 10; %Avoids entering a conditional statement below
end

    if check_row_1_per > 5
        if (check_row_2_per > 5 & j < beam_end_column_pixel_per)
                disp('Check data file because two successive rows differ greatly in polarization file
(Bug?)')
        bad_row_per = tempmax_per(j,2);
        tempmax_per(j,2) = row_average_per; % Correct using the row_average
        tempmax_per(j,1) = data_per(row_average_per,j);
        disp('Corrected data maximum at [row column] for perpendicular polarization image')
        [bad_row_per j]
         elseif (check_row_2_per <= 5 & j < beam_end_column_pixel_per)      % Erroneous max
detected.  Correct.
                bad_row_per = tempmax_per(j,2);
                corrected_max_per = data_per(row_average_per-10,j);
                for k = row_average_per-9:row_average_per+10
                        if data_per(k,j) > corrected_max_per
                                corrected_max_per = data_per(k,j);
                                corrected_row_per = k;
                        end
                end
                tempmax_per(j,1) = corrected_max_per;      % Corrects maximum point
                tempmax_per(j,2) = corrected_row_per; % Corrects corresponding row
                disp('Corrected data maximum at [row column] for perpendicular polarization image')
                [bad_row_per j]
        elseif (check_row_2_per <=5 & j >= beam_end_column_pixel_per)
                        bad_row_per = tempmax_per(j,2);
                        corrected_max_per = data_per(row_average_per-10,j);
                for k = row_average_per-9:row_average_per+10
                        if data_per(k,j) > corrected_max_per
                                corrected_max_per = data_per(k,j);
                                corrected_row_per = k;
                        end
                end
                tempmax_per(j,1) = corrected_max_per;      % Corrects maximum point
                tempmax_per(j,2) = corrected_row_per; % Corrects corresponding row
                beam_end_column_pixel_per = j;
                disp('Updated beam_end_pixel and corrected data Maximum at [row column] for
perpendicular polarization image')
                [bad_row_per j]
        elseif (check_row_2_per > 5 & check_row_3_per <= 5 & j >= beam_end_column_pixel_per)
                bad_row_per = tempmax_per(j,2);
                corrected_max_per = data_per(row_average_per-10,j);
                for k = row_average_per-9:row_average_per+10
                        if data_per(k,j) > corrected_max_per
                                corrected_max_per = data_per(k,j);
                                corrected_row_per = k;
                        end
                end
                tempmax_per(j,1) = corrected_max_per;      % Corrects maximum point
                tempmax_per(j,2) = corrected_row_per; % Corrects corresponding row
                beam_end_column_pixel_per = j;
```

```
                disp('Updated beam_end_pixel and corrected data maximum at [row column] for
perpendicular polarization image')
                [bad_row_per j]
        else
                beam_end_column_pixel_per = j-1;% Two successive row maximums above the
expected beam end point are

    % different.  This is the condition for the beam end point.
                j = 9000; % Exit while loop
        end

    elseif (check_row_1_per <= 5 & j >= beam_end_column_pixel_per) % Start moving beam end point
    % LAPS is a very strong beam, especially in comparison to the Ar-Ion.  Thus, it is likley that the entire
    % length of the beam will also be very strong and little if any, corrections will need to be made.
However, as the algorithm
    % stands, it checks the neighboring row pixel numbers and not the pixel values.  This is corrected here.

        if beam_end_column_pixel_per >= 760      % Begin checking neighboring rows' values 'cause I
think I'm getting close to the beam endpoint
                %value = abs(tempmax_per(j,1) - tempmax_per(j-1,1));
                if tempmax_per(j,1) <= 1000
                        %beam_end_column_pixel_per = j-1;
                        j = 9000;           % Exit while loop
                else
                        beam_end_column_pixel_per = j;
                end
        else
                beam_end_column_pixel_per = j;
        end
    end
j = j+1;
end

clear corrected_max_per corrected_row_per j bad_row_per

disp(' ')
disp(' ')
disp(' ')
disp(' ')
disp('Finished finding beam end point and correcting data files')



% Check to make sure each polarization image has the same beam endpoint.
if abs(beam_end_column_pixel_par - beam_end_column_pixel_per) <= 3          % Small difference in end
points.  Adjust
% A small difference actually has a large impact on the the high altitudes but since these points will not be
% examined, we make a simply adjustment by taking the larger of the two.
    beam_end_column_pixel = max([beam_end_column_pixel_par beam_end_column_pixel_per]);
else
    Parallel_file
    Perpendicular_file
    error('Beam end points do not match for above files.  Check images')
end

clear beam_end_column_pixel_par beam_end_column_pixel_per
```

```
% Note:  There are a lot of errors in the algorithm with respect to the end point of the beam.  Since this
% part of the beam is not under consideration, it really isn't critical at this point that we get it absolutely
correct.


% For every image, under every operating condition, the beam cross section in terms of number of
% pixels should be fixed and should correspond to clear-night operation and calm conditions.  This
% is because if the environment is hazy, multiple scattering will be evident as a bloom around the
% beam and this should NOT be counted as part of the scattering volume.  Tests will have to be made
% to determine the number of pixels to sum.  Additionally, each camera, being a different distance
% from the laser, may also have beam widths different than other cameras.



% Sum each column's cross-section of the beam.  MAY WANT TO COMBINE THIS WITHIN THE
BEAM'S END POINT
% FINDING ROUTINE IN ORDER TO NOT HAVE TOO MANY LOOPS.  WE LEAVE IT HERE AS
IS SO WE CAN TEST THE ALGORITHM.
% NOTE:  The maximum is NOT necessarily in the middle of the beam!
disp(' ')
disp(' ')
disp('Summing pixels across beam...')

% Start with parallel polarization file
for j = 1:beam_end_column_pixel

        sum_column = tempmax_par(j,1);              % The maximum element begins the summation
        first_plus_value = tempmax_par(j,1);
        first_minus_value = first_plus_value;
        upper_row = tempmax_par(j,2);
        lower_row = tempmax_par(j,2);
        elements = 1;      % The maximum number of elements, i.e. pixels, to be summed is =
beam_width
        n = 1;
        while n <= beam_width
                second_plus_value = data_par(tempmax_par(j,2)+n,j);% Examines rows above
maximum row point
                difference = first_plus_value - second_plus_value;     % ASSUMPTION:  The values are
~monotonically

                                                        % decreasing from maximum point.
                if elements < fix(2*beam_width/3)  % We only want to add, at most, approx. 2/3 of the
beam width on either

        % side of the max should be added.  This is for haze, fog, or pollution events.
                        if (difference > 11 | n <= 3)           % We allow neighbors within three row
pixels of the max to be close in

    % value, i.e., there does not need to be a large change in value between

    % the maximum point and its adjoining neighbors.
                                sum_column = sum_column + second_plus_value;
                                first_plus_value = second_plus_value;
                                upper_row = tempmax_par(j,2)+n;
                                elements = elements + 1;
                                n = n+1;
```

```
                        else
                                n = beam_width + 1;        % Terminate the while loop
                        end
                else
                        n = beam_width + 1;        % Terminate the while loop
                end
        end

        junk = beam_width - elements;
        n = 1;
        while n <= junk
                second_minus_value = data_par(tempmax_par(j,2)-n,j);                    % Examines
rows below maximum row point
                difference = first_minus_value - second_minus_value;;
                if (difference > 11 | n <= 3)
                        sum_column = sum_column + second_minus_value;
                        first_minus_value = second_minus_value;
                        lower_row = tempmax_par(j,2)-n;
                        elements = elements + 1;
                        n=n+1;
                else
                        n = junk + 1;
                end
        end

        if (beam_width - elements) > 2 & j < (beam_end_column_pixel - 3)      % Missing too many
pixels in the summation
                j
                error('Not enough pixels in summation.  Check beam at above column')
        end

    Processed_Data(j,1) = sum_column;                    % Sum of the pixels in the beam
    Processed_Data(j,2) = tempmax_par(j,2);          % Row Value
    Processed_Data(j,3) = tempmax_par(j,3);          % Column Value - To determine altitude
    Processed_Data(j,4) = elements;                                % Must make sure that every sum
is the same number of pixels in an image

        % and BETWEEN images BEFORE taking the ratio OR applying corrections.

    clear sum_column elements junk upper_row lower_row first_plus_value first_minus_value
    clear second_plus_value second_minus_value difference n junk j

end

% Perpendicular polarization file
for j = 1:beam_end_column_pixel

        sum_column = tempmax_per(j,1);
        first_plus_value = tempmax_per(j,1);
        first_minus_value = first_plus_value;
        upper_row = tempmax_per(j,2);
        lower_row = tempmax_per(j,2);
        elements = 1;      % The maximum number of elements, i.e. pixels, to be summed is =
beam_width
        n = 1;
        while n <= beam_width
```

```
                second_plus_value = data_per(tempmax_per(j,2)+n,j);                    %
Examines rows above maximum row point
                difference = first_plus_value - second_plus_value;     % ASSUMPTION:  The values are
~monotonically

                                                        % decreasing from maximum point.
                if elements < fix(2*beam_width/3)  % We only want to add, at most, approx. 2/3 of the
beam width on either

        % side of the max should be added.  This is for haze, fog, or pollution events.

                        if (difference > 11 | n <= 3)           % We allow neighbors within three row
pixels of the max to be close in

    % value, i.e., there does not need to be a large change in value between

    % the maximum point and its adjoining neighbors.
                                sum_column = sum_column + second_plus_value;
                                first_plus_value = second_plus_value;
                                upper_row = tempmax_per(j,2)+n;
                                elements = elements + 1;
                                n = n+1;
                        else
                                n = beam_width + 1;         % Terminate the while loop
                        end
                else
                        n = beam_width + 1;         % Terminate the while loop
                end
        end



        junk = beam_width - elements;
        n = 1;
        while n <= junk
                second_minus_value = data_per(tempmax_per(j,2)-n,j);                   % Examines
rows below maximum row point
                difference = first_minus_value - second_minus_value;;
                if (difference > 11 | n <= 3)
                        sum_column = sum_column + second_minus_value;
                        first_minus_value = second_minus_value;
                        lower_row = tempmax_per(j,2)-n;
                        elements = elements + 1;
                        n=n+1;
                else
                        n = junk + 1;
                end
        end

        if (beam_width - elements) > 2 & j < (beam_end_column_pixel - 3)      % Missing too many
pixels in the summation for the altitudes

                                                                                % of interest
(upper altitudes are not to be processed at this time).
                j
                error('Not enough pixels in summation.  Check beam at above column')
```

```
        end

    Processed_Data(j,5) = sum_column;                    % Sum of the pixels in the beam
    Processed_Data(j,6) = tempmax_per(j,2);          % Row Value
    Processed_Data(j,7) = tempmax_per(j,3);          % Column Value - To determine altitude
    Processed_Data(j,8) = elements;                                % Must make sure that every sum
is the same number of pixels in an image

        % and BETWEEN images BEFORE taking the ratio OR applying corrections.

    clear sum_column elements junk upper_row lower_row first_plus_value first_minus_value
    clear second_plus_value second_minus_value difference n junk

end




disp('...Finished summing pixels')



clear data_par data_per tempmax_per tempmax_par row_average_par row_avarage_per
beam_end_column_pixel_par
clear beam_end_column_pixel_per beam_width

return
```

C

Appendix C: Polarization Ratio Data

Selected times are plotted on the following pages.

Table C.1: Summary of observation times during July NE-OPS campaign, 2001 (all times EST).

6th (pm) / 7th (am)	7th (pm) / 8th (am)	11th (pm) / 12th (am)	12th (pm) / 13th (am)	22nd (pm) / 23rd (am)	23rd (pm) / 24th (am)	24th (am) / 25th (pm)
1:45a	11:05p	12:00a	11:30p	11:20p	11:01p	11:00p
2:30a	11:35p	12:15a	11:45p	11:45p	11:31p	11:30p
2:37a	11:50p	12:30a	12:00a	12:15a	12:00a	12:10a
2:57a	12:10a	12:45a	12:15a	12:45a	12:30a	12:30a
3:15a	2:25a	1:00a	12:30a	1:15a	1:00a	1:00a
3:35a	2:35a	1:15a	12:45a	1:50a	1:31a	1:30a
4:00a	2:45a	1:30a	1:20a	2:15a	2:00a	2:00a
4:20a	2:55a	1:45a	1:30a	2:45a	2:35a	2:31a
4:30a	3:05a	2:00a	1:45a	3:15a	3:01a	3:00a
4:45a	3:15a	2:15a	2:00a	3:20a	3:30a	3:31a
		2:30a	2:10a	3:27a	4:03a	4:00a
		2:45a	2:20a	3:30a		4:30a
		3:00a	2:30a	3:37a		5:00a
		3:15a	2:40a	3:45a		
		3:30a	2:50a	3:50a		
		3:45a	3:00a	3:56a		
		4:00a	3:10a	4:02a		
		4:40a	3:20a	4:07a		
		4:50a	3:30a	4:12a		
			3:40a	4:16a		
			3:50a	4:46a		
			4:00a			
			4:10a			

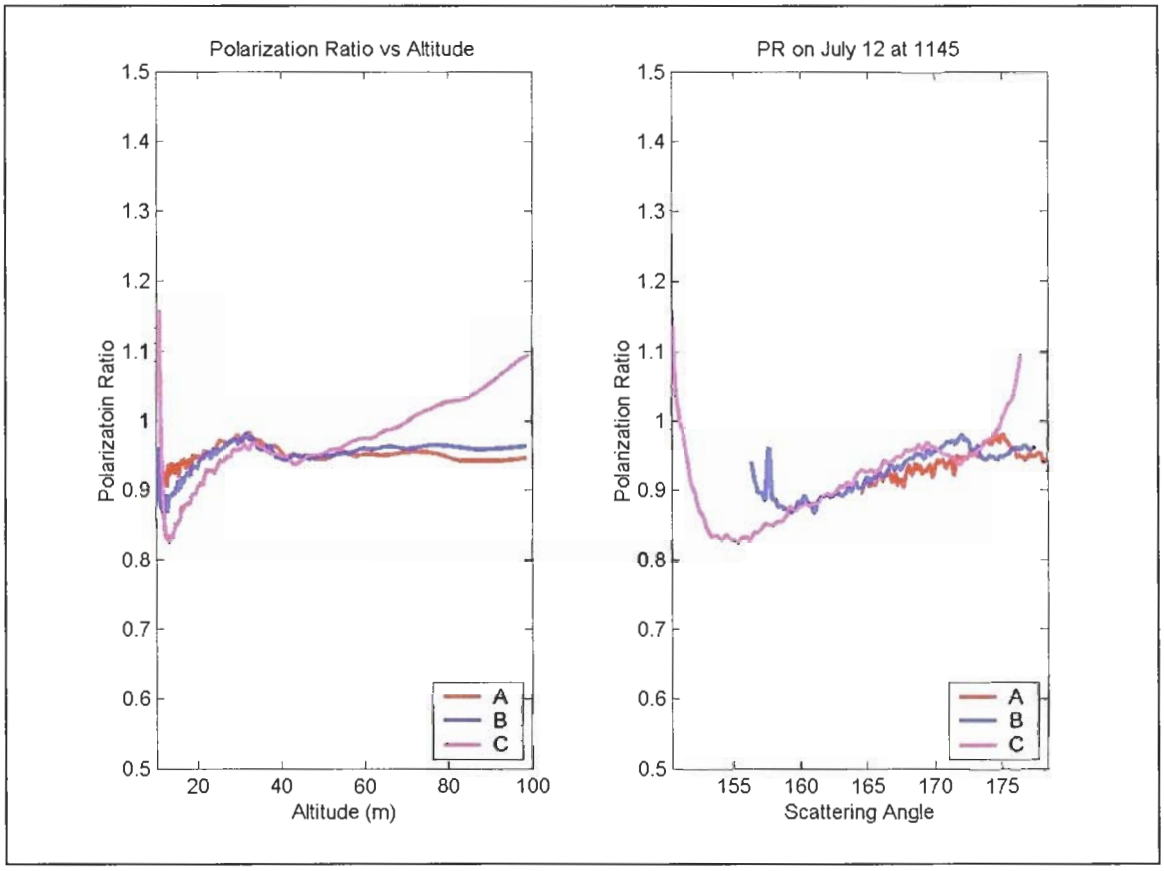
Polarization Ratio vs Altitude
Polarizatoin Ratio
Altitude (m)
A
B
C
PR on July 12 at 1145
Polarization Ratio
Scattering Angle
A
B
C

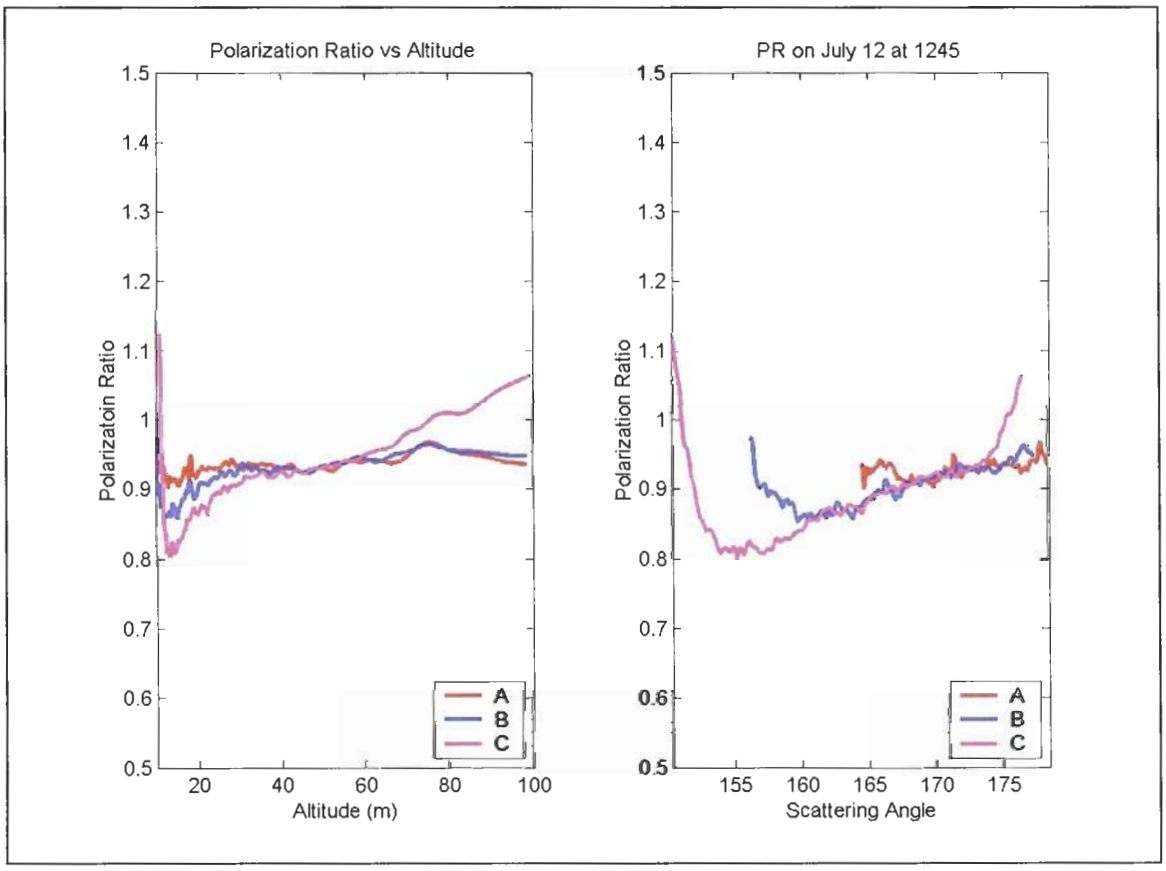
Polarization Ratio vs Altitude
Polarizatoin Ratio
Altitude (m)
A
B
C
PR on July 12 at 1245
Polarization Ratio
Scattering Angle
A
B
C

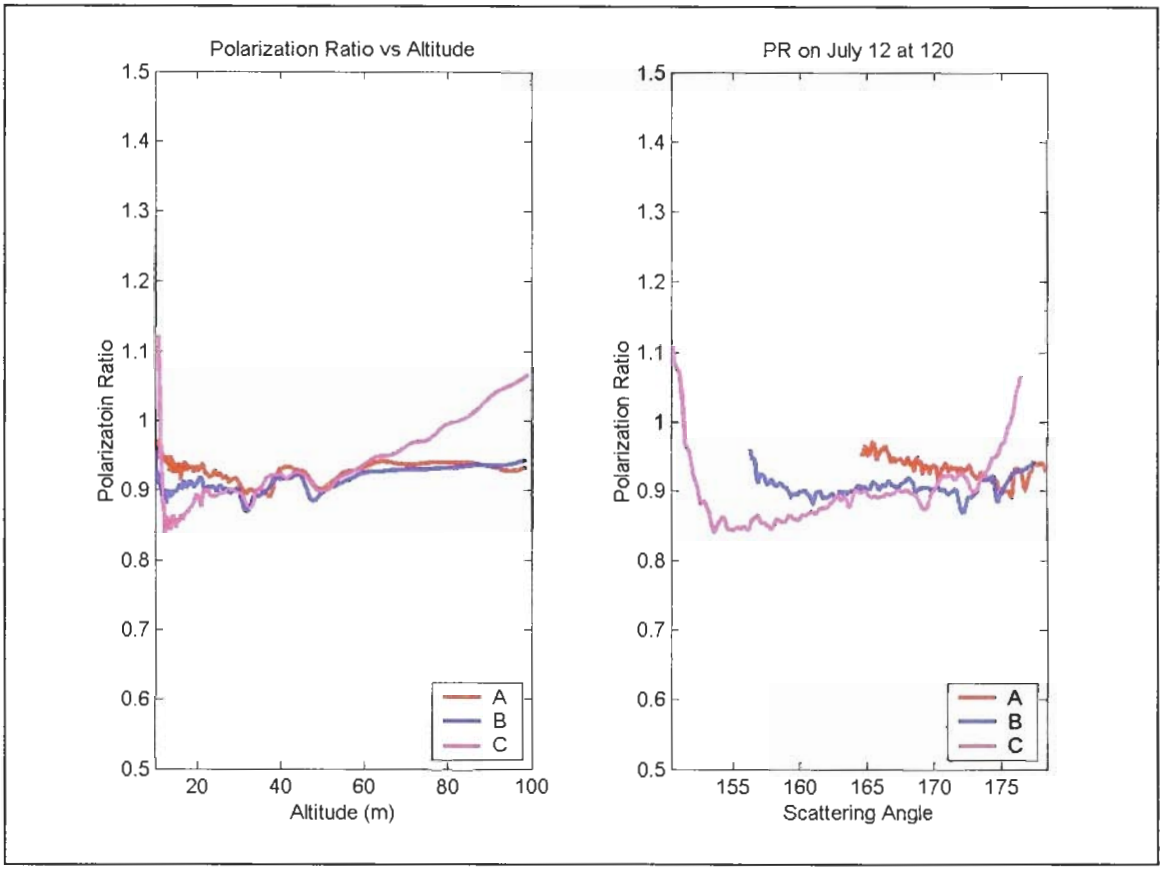
Polarization Ratio vs Altitude
Polarizatoin Ratio
Altitude (m)
A
B
C
PR on July 12 at 120
Polarization Ratio
Scattering Angle
A
B
C

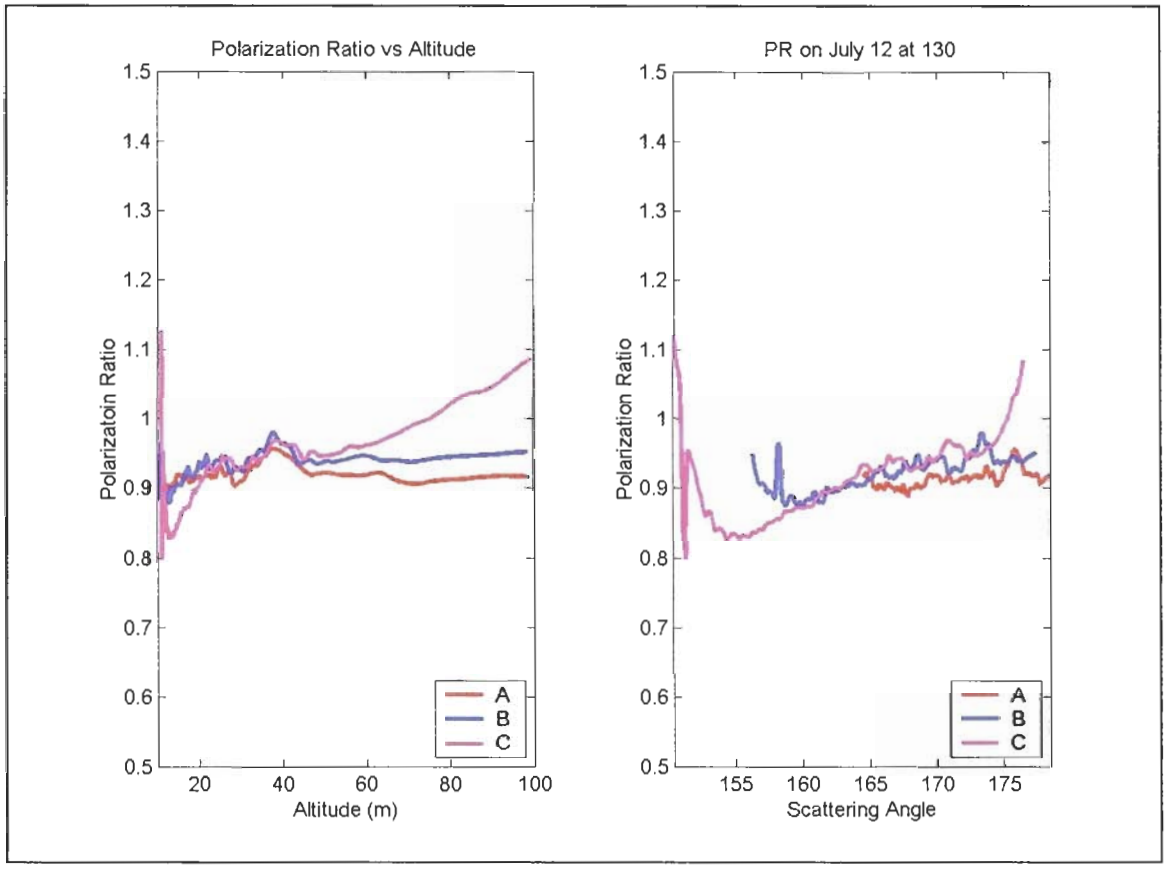
Polarization Ratio vs Altitude
Polarizatoin Ratio
Altitude (m)
A
B
C
PR on July 12 at 130
Polarization Ratio
Scattering Angle
A
B
C

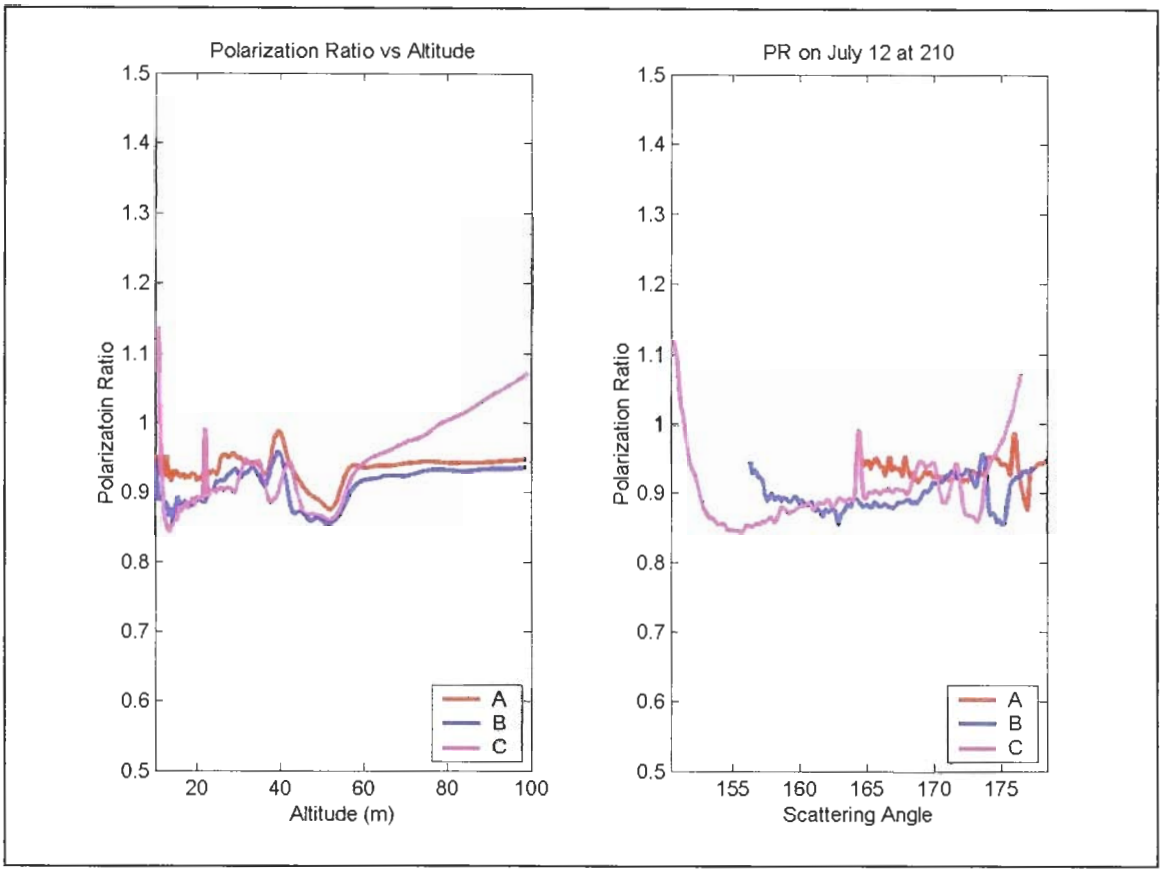
Polarization Ratio vs Altitude
Polarizatoin Ratio
Altitude (m)
A
B
C
PR on July 12 at 210
Polarization Ratio
Scattering Angle
A
B
C

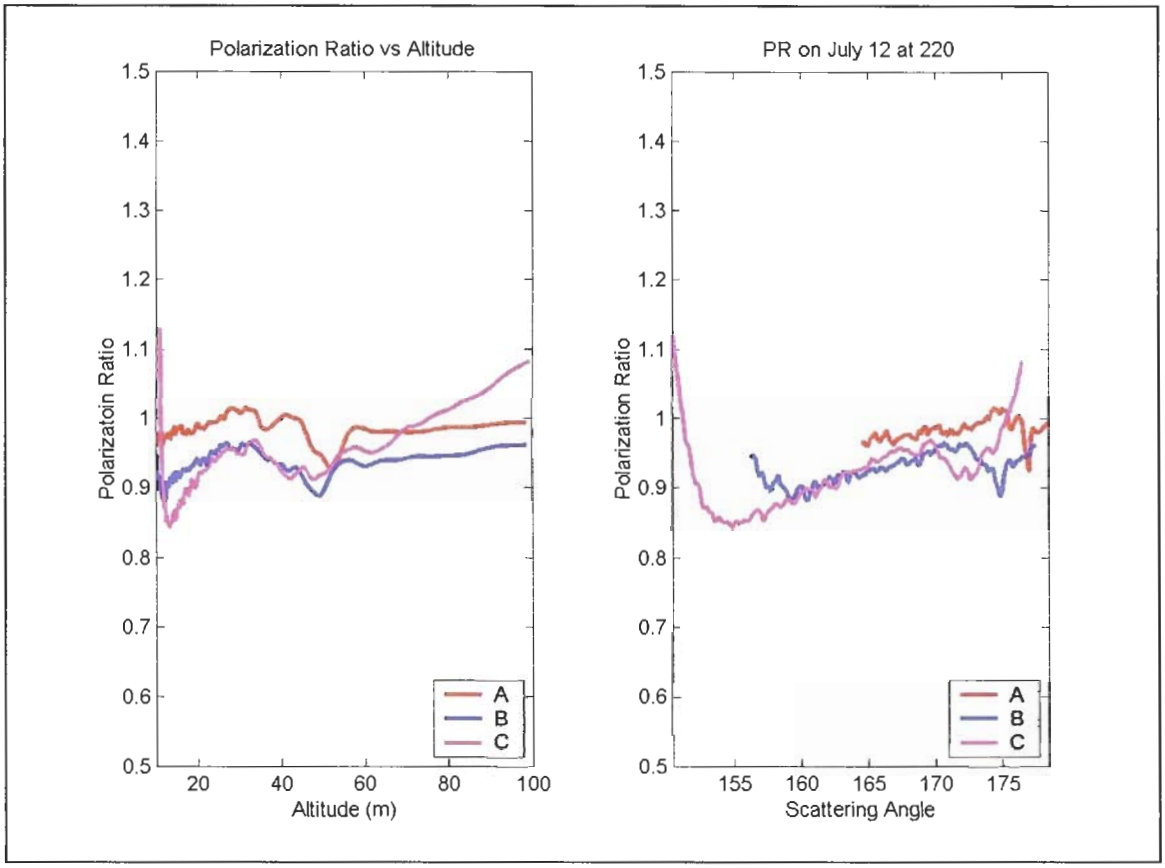
Polarization Ratio vs Altitude
Polarizatoin Ratio
Altitude (m)
A
B
C
PR on July 12 at 220
Polarization Ratio
Scattering Angle
A
B
C

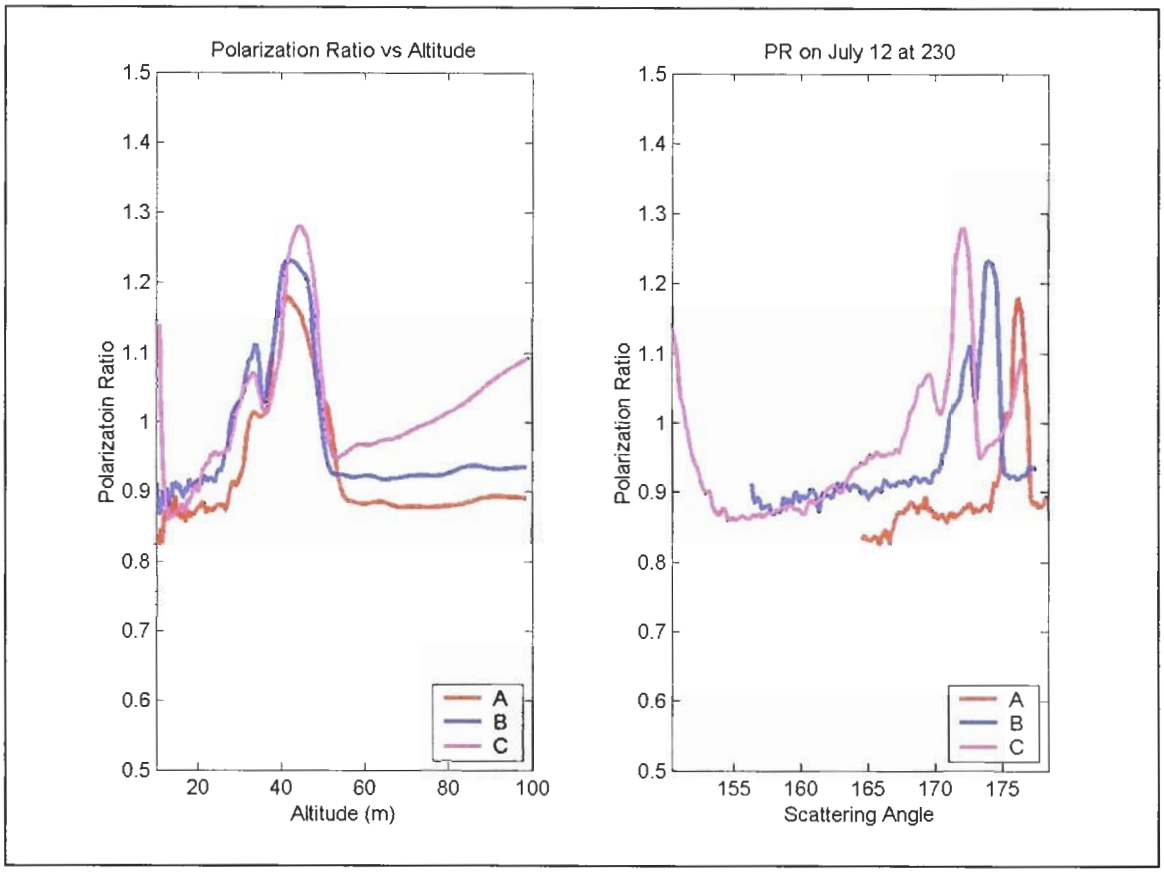
Polarization Ratio vs Altitude
Polarizatoin Ratio
Altitude (m)
A
B
C
PR on July 12 at 230
Polarization Ratio
Scattering Angle
A
B
C

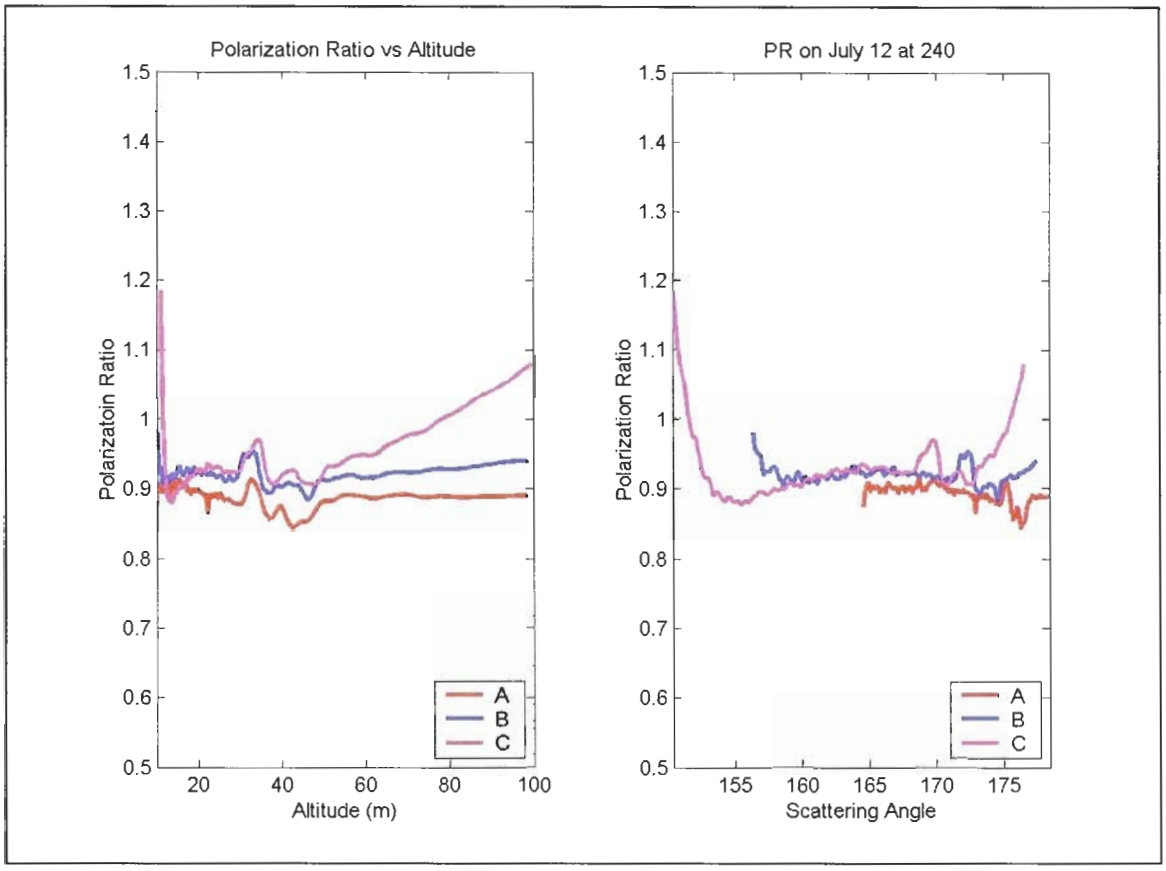
Polarization Ratio vs Altitude
Polarizatoin Ratio
Altitude (m)
A
B
C
PR on July 12 at 240
Polarization Ratio
Scattering Angle
A
B
C

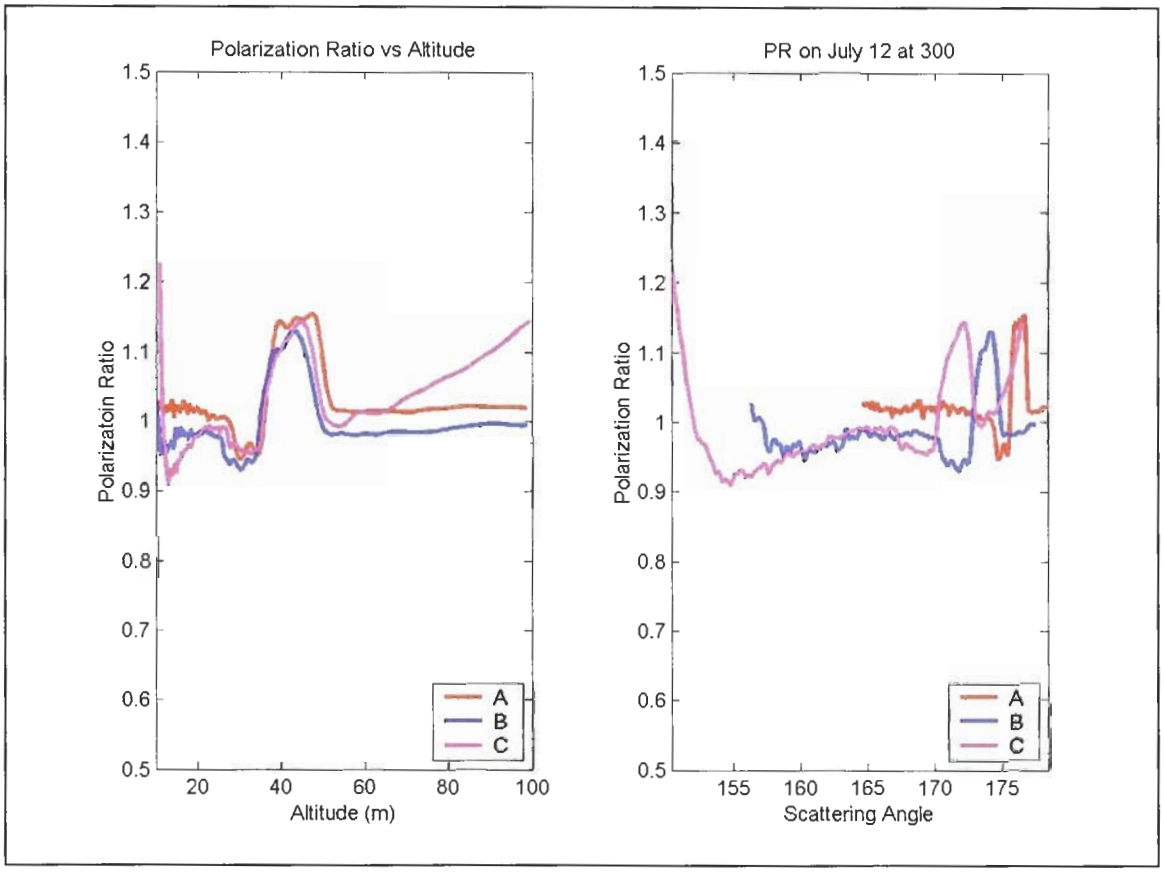
Polarization Ratio vs Altitude
Polarizatoin Ratio
Altitude (m)
A
B
C
PR on July 12 at 300
Polarization Ratio
Scattering Angle
A
B
C

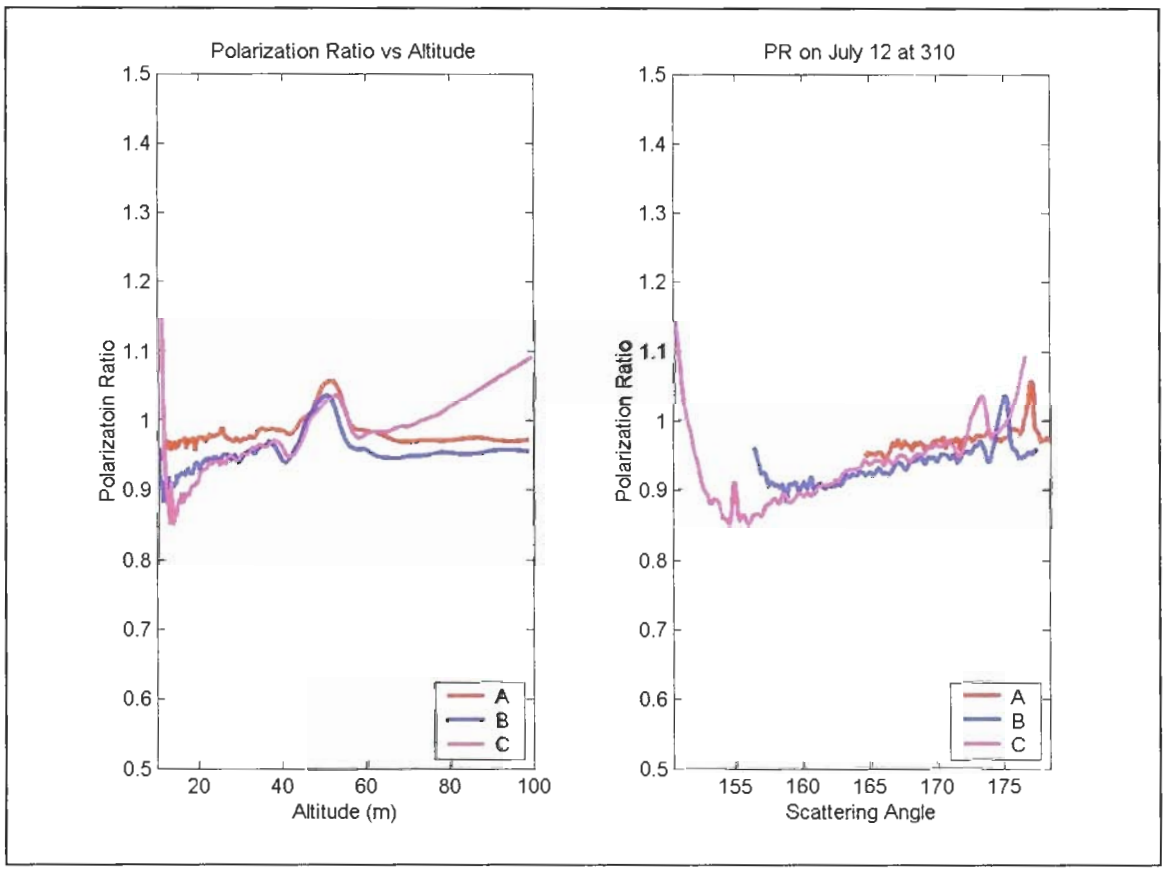
Polarization Ratio vs Altitude
Polarizatoin Ratio
Altitude (m)
A
B
C
PR on July 12 at 310
Polarization Ratio
Scattering Angle
A
B
C

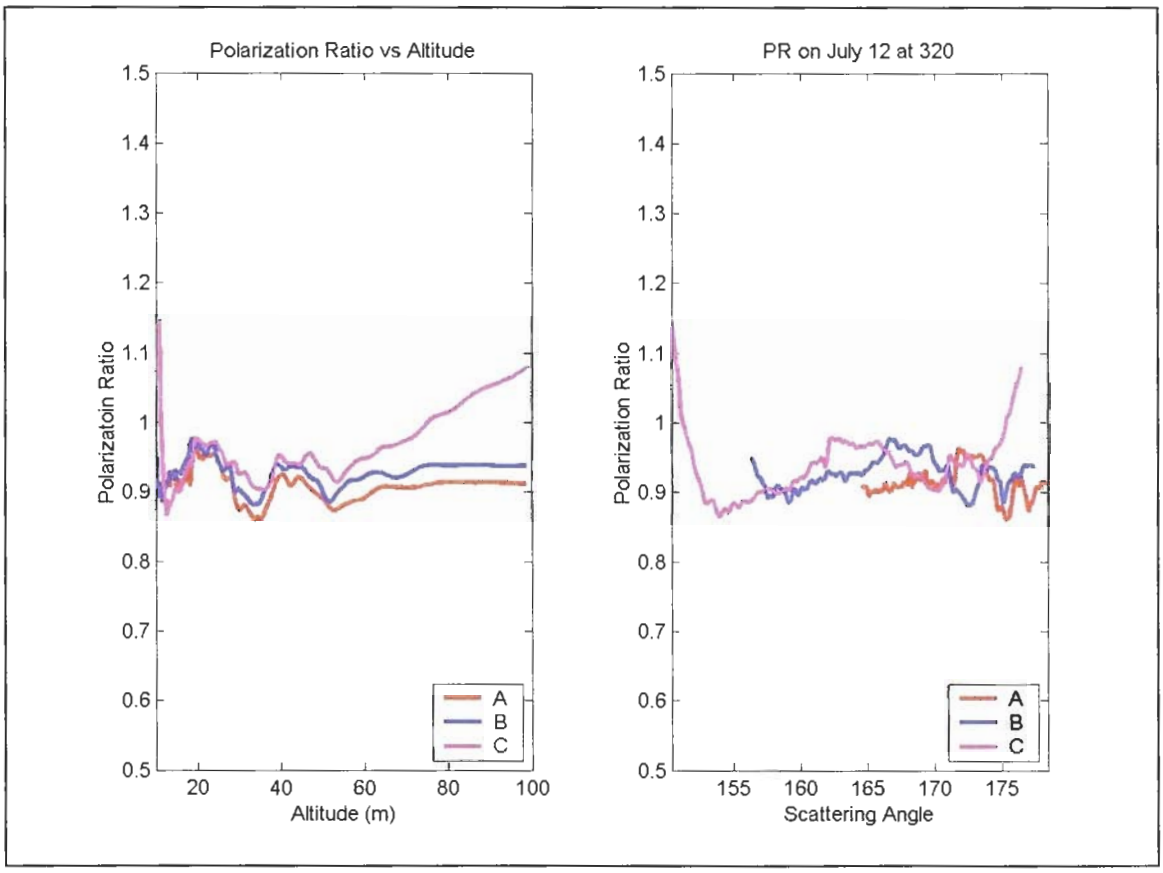
Polarization Ratio vs Altitude
Polarizatoin Ratio
Altitude (m)
A
B
C
PR on July 12 at 320
Polarization Ratio
Scattering Angle
A
B
C

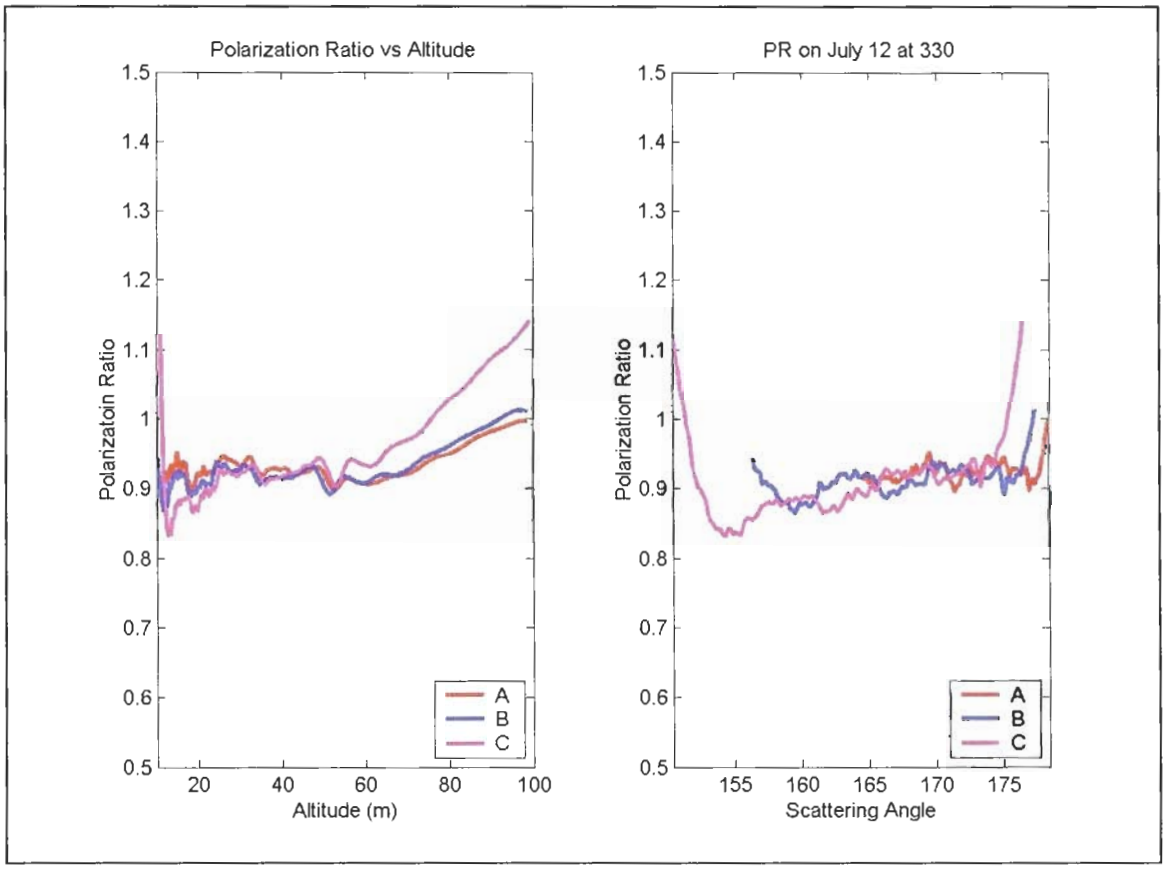
Polarization Ratio vs Altitude
Polarizatoin Ratio
Altitude (m)
A
B
C
PR on July 12 at 330
Polarization Ratio
Scattering Angle
A
B
C

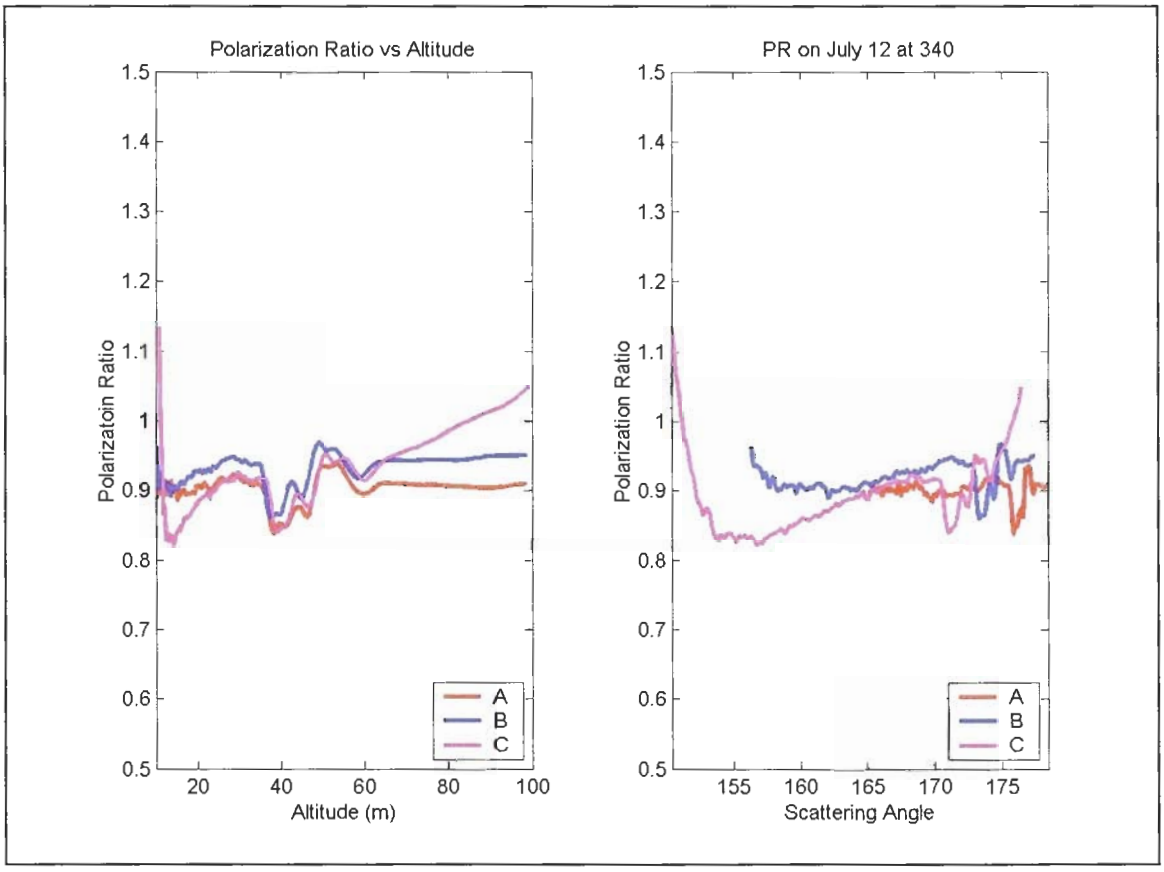
Polarization Ratio vs Altitude
Polarizatoin Ratio
Altitude (m)
A
B
C
PR on July 12 at 340
Polarization Ratio
Scattering Angle
A
B
C

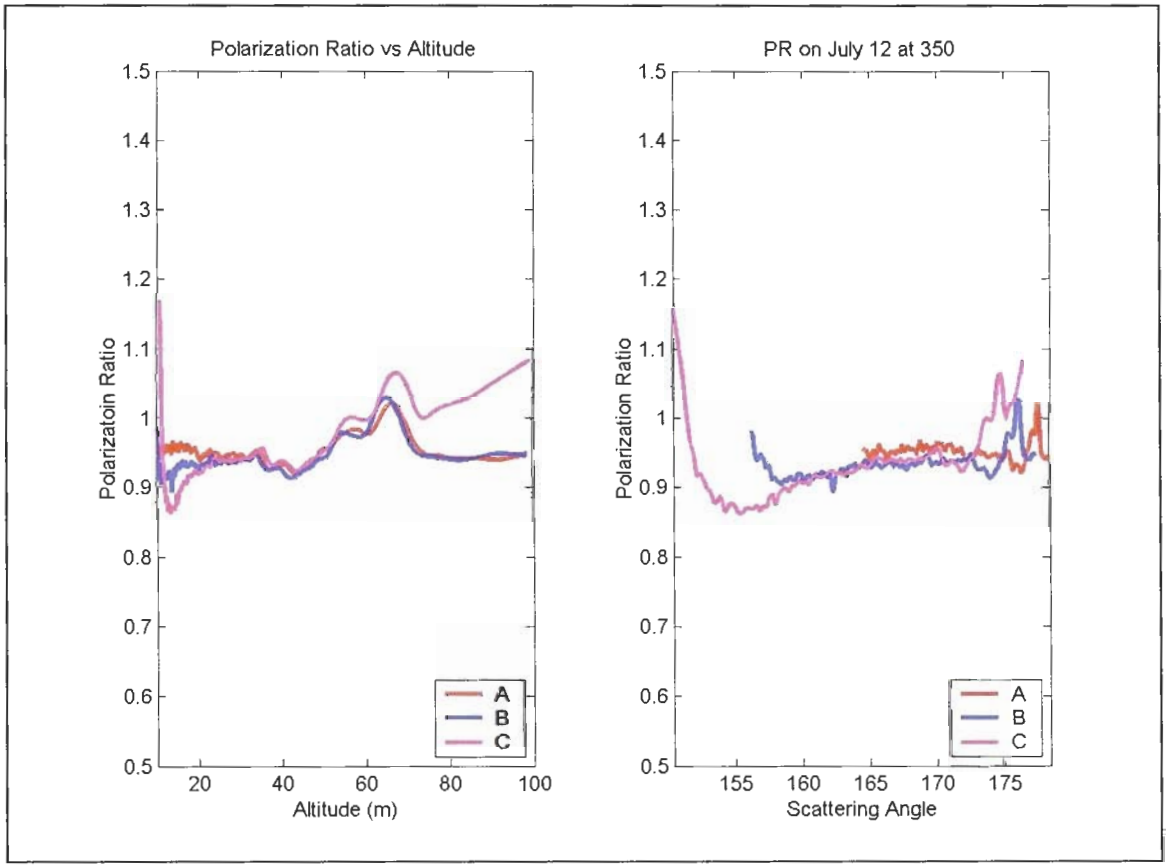
Polarization Ratio vs Altitude
Polarizatoin Ratio
Altitude (m)
A
B
C
PR on July 12 at 350
Polarization Ratio
Scattering Angle
A
B
C

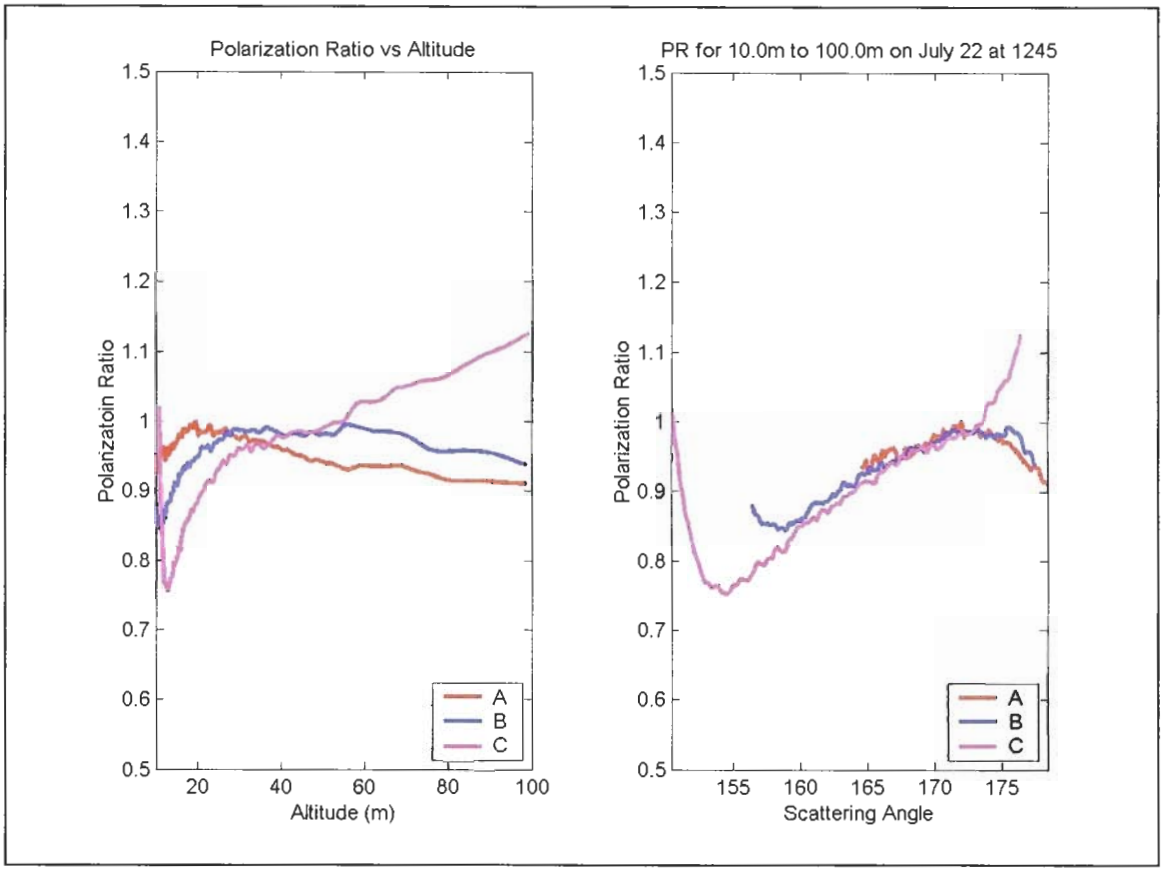
Polarization Ratio vs Altitude
Polarizatoin Ratio
Altitude (m)
A
B
C
PR for 10.0m to 100.0m on July 22 at 1245
Polarization Ratio
Scattering Angle

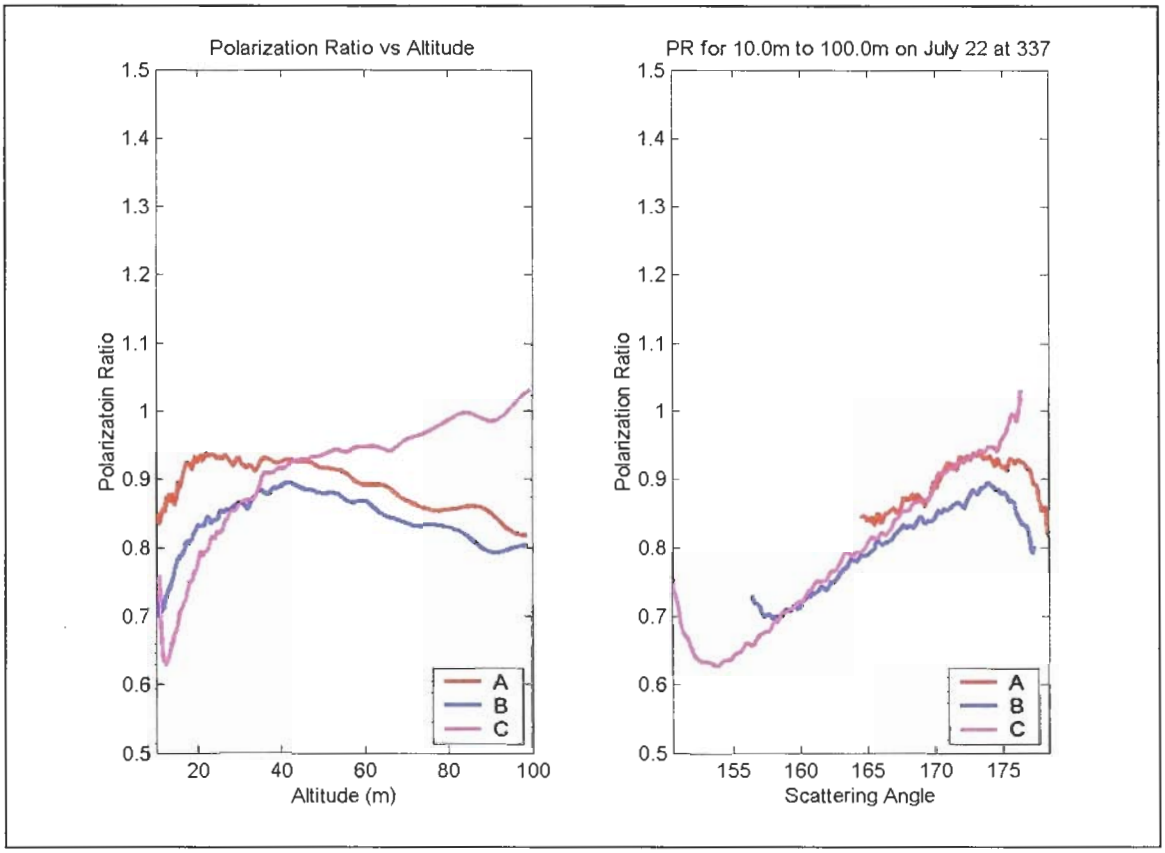
Polarization Ratio vs Altitude
Polarizatoin Ratio
Altitude (m)
A
B
C
PR for 10.0m to 100.0m on July 22 at 337
Polarization Ratio
Scattering Angle

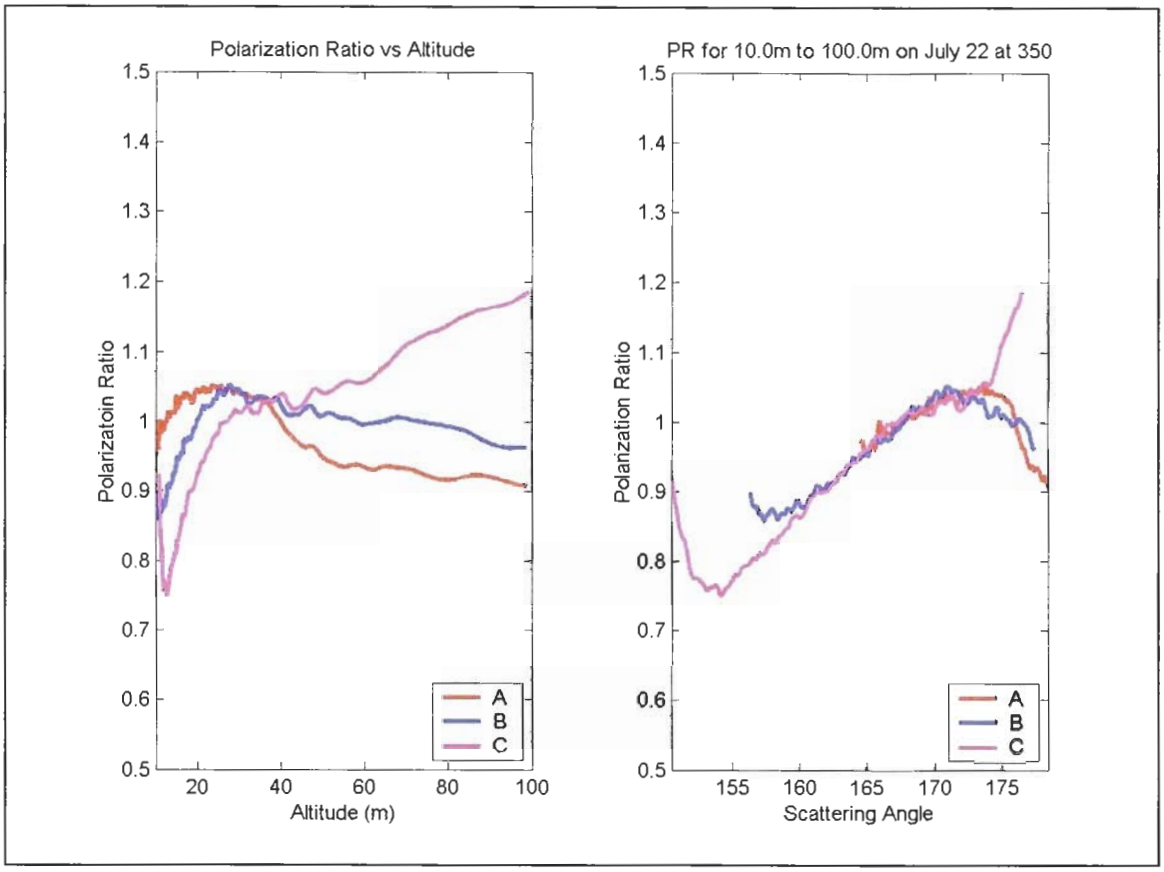
Polarization Ratio vs Altitude
Polarizatoin Ratio
Altitude (m)
A
B
C
PR for 10.0m to 100.0m on July 22 at 350
Polarization Ratio
Scattering Angle
A
B
C

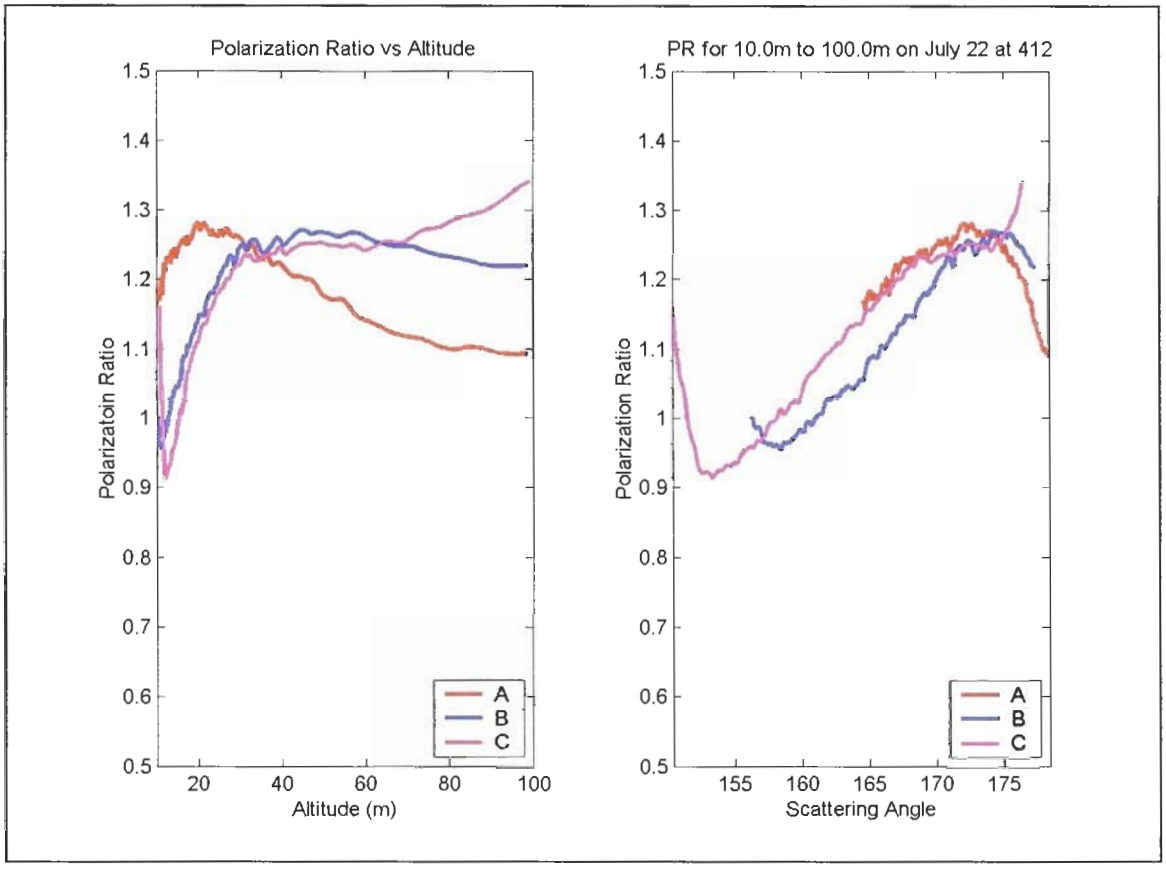
Polarization Ratio vs Altitude
Polarizatoin Ratio
Altitude (m)
A
B
C
PR for 10.0m to 100.0m on July 22 at 412
Polarization Ratio
Scattering Angle
A
B
C

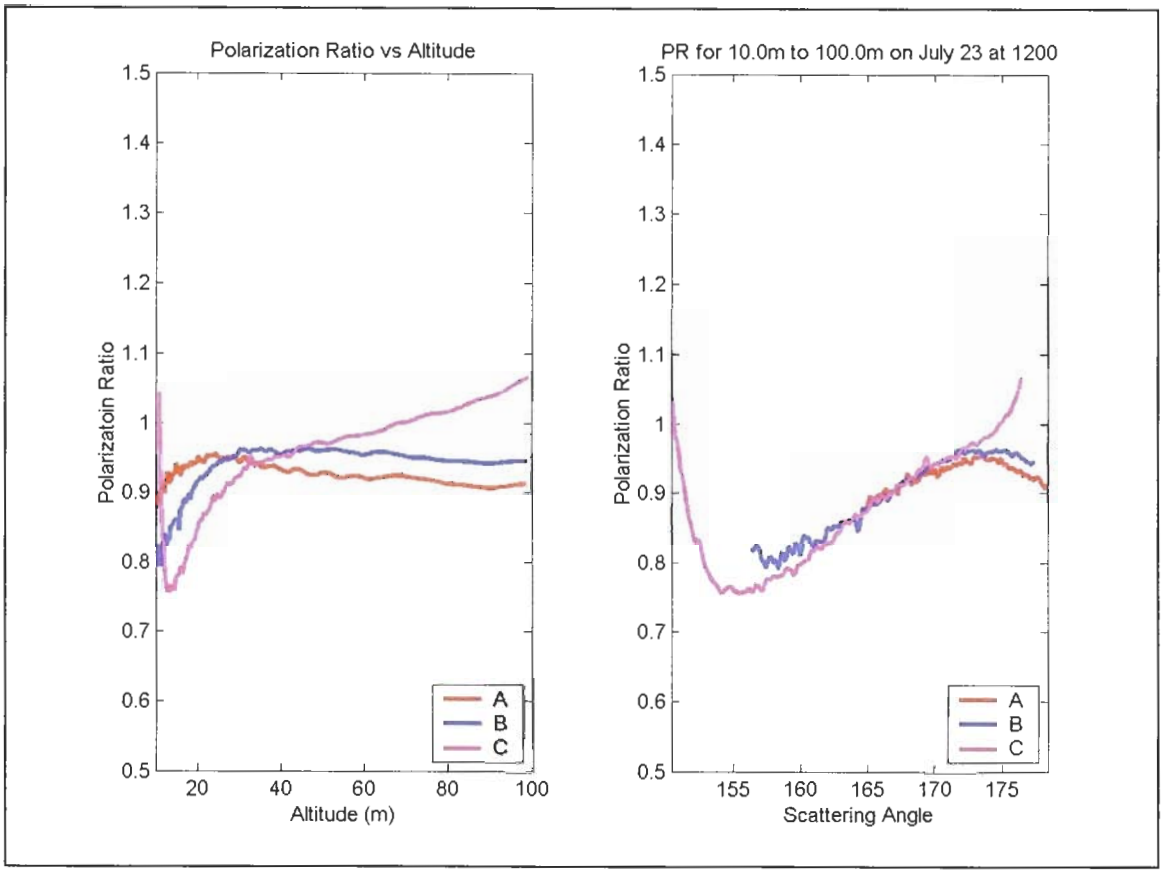
Polarization Ratio vs Altitude
Polarizatoin Ratio
Altitude (m)
A
B
C
PR for 10.0m to 100.0m on July 23 at 1200
Polarization Ratio
Scattering Angle
A
B
C

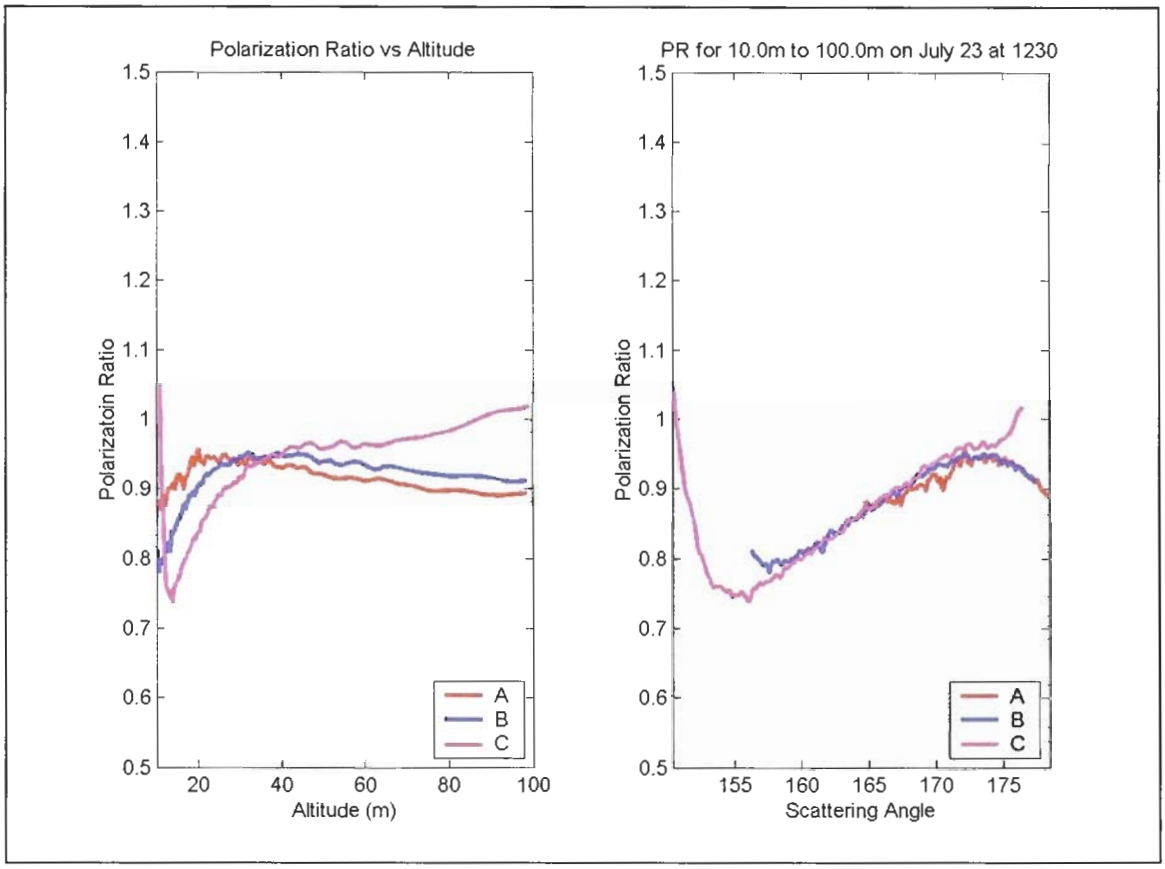
Polarization Ratio vs Altitude
Polarizatoin Ratio
Altitude (m)
A
B
C
PR for 10.0m to 100.0m on July 23 at 1230
Polarization Ratio
Scattering Angle
A
B
C

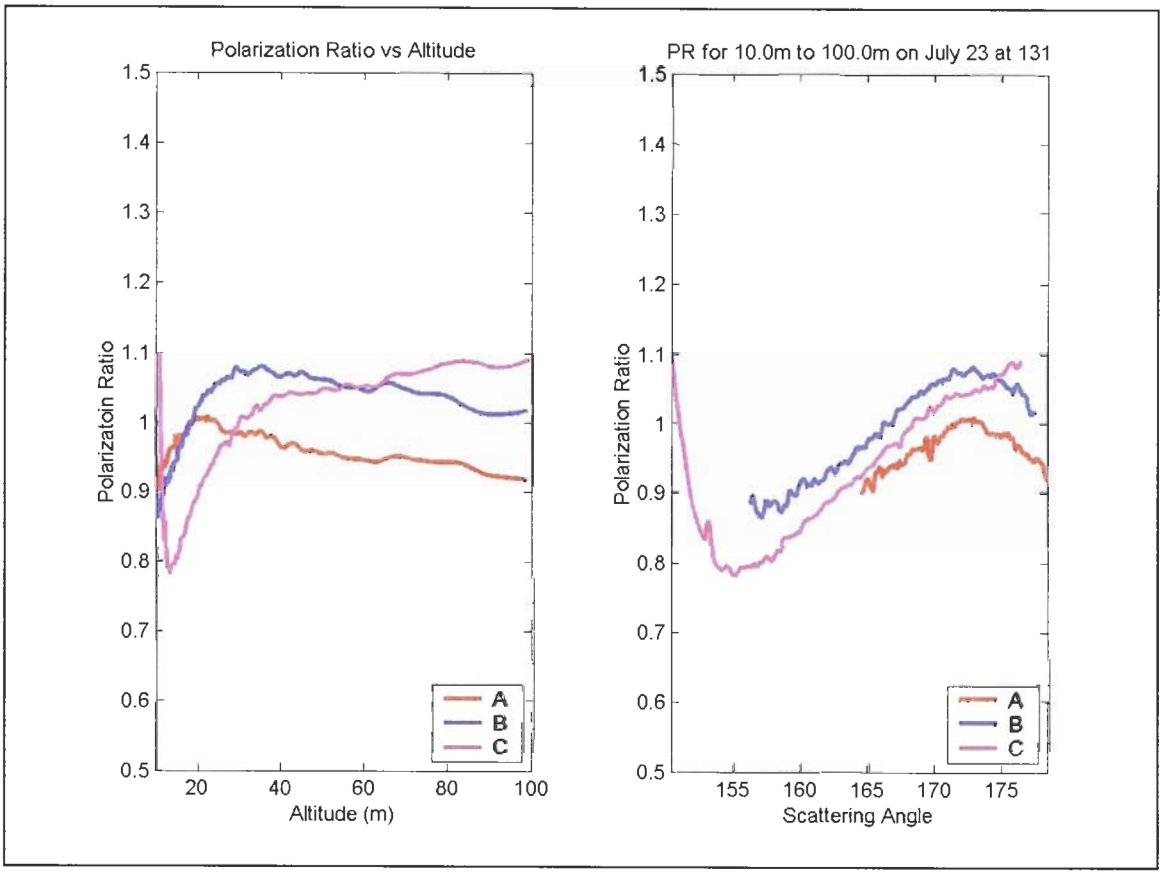
Polarization Ratio vs Altitude
Polarizatoin Ratio
Altitude (m)
A
B
C
PR for 10.0m to 100.0m on July 23 at 131
Polarization Ratio
Scattering Angle
A
B
C

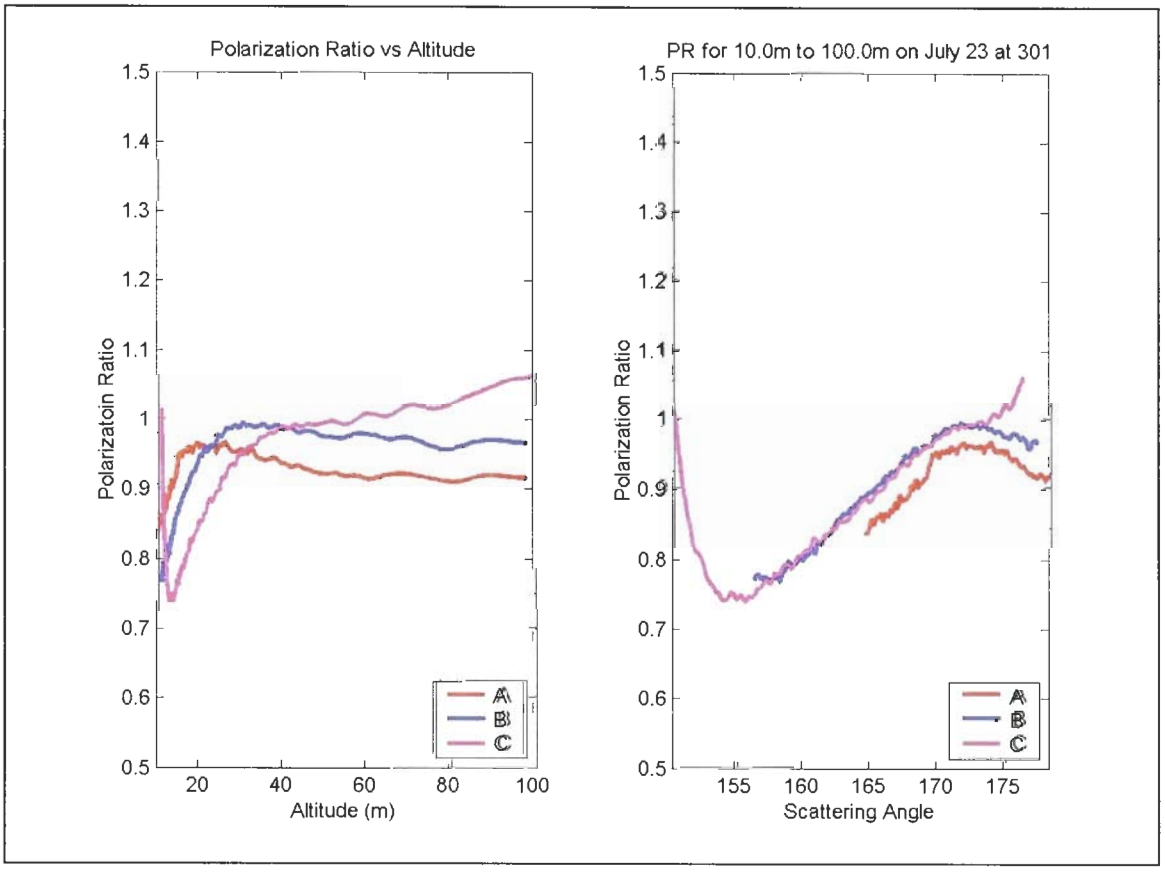
Polarization Ratio vs Altitude
Polarizatoin Ratio
Altitude (m)
A
B
C
PR for 10.0m to 100.0m on July 23 at 301
Polarization Ratio
Scattering Angle
A
B
C

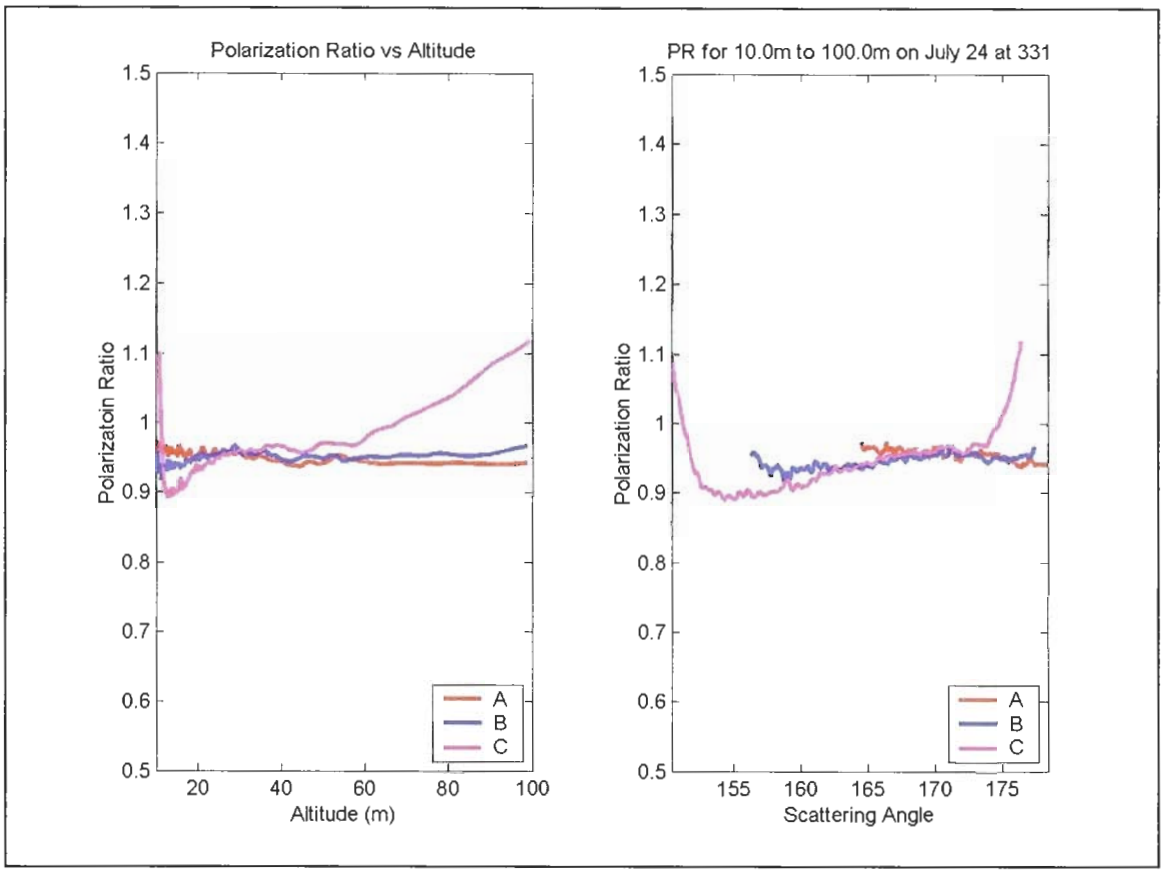
Polarization Ratio vs Altitude
Polarizatoin Ratio
Altitude (m)
A
B
C
PR for 10.0m to 100.0m on July 24 at 331
Polarization Ratio
Scattering Angle
A
B
C

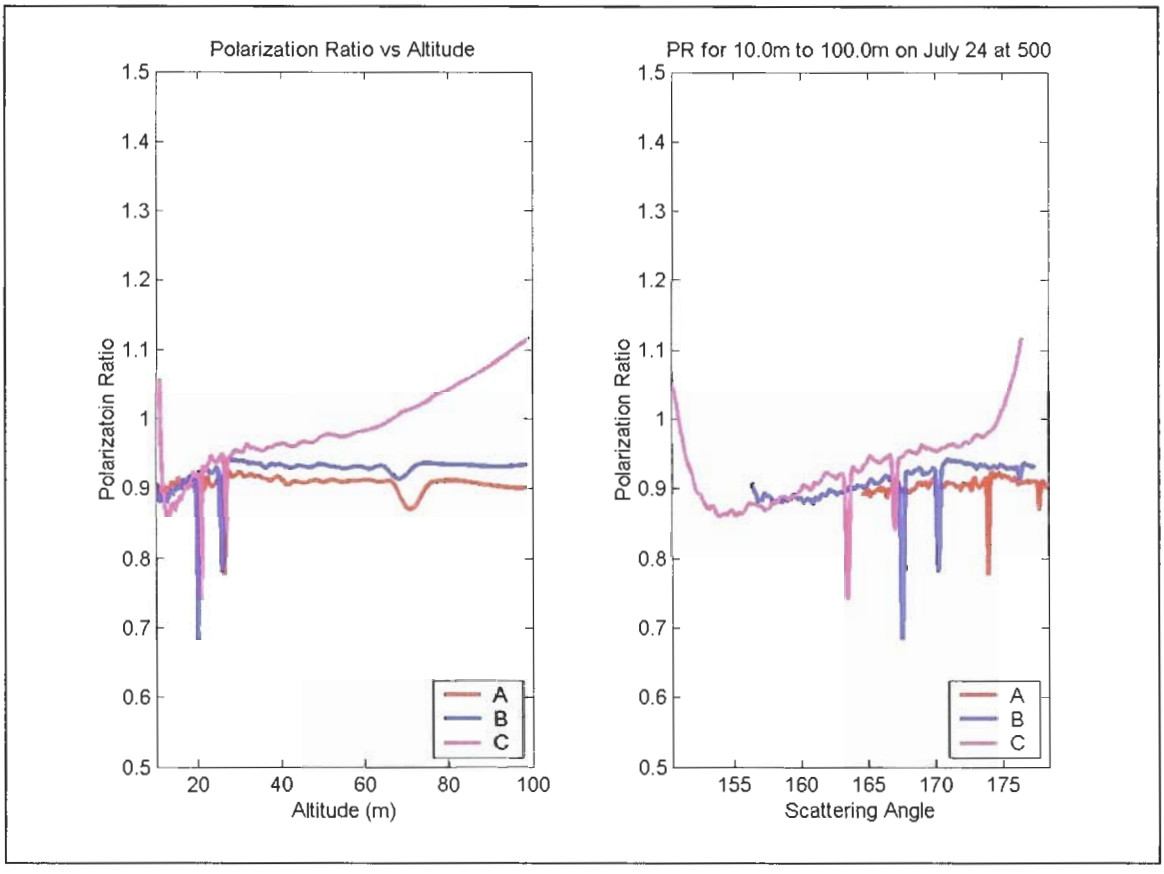
Polarization Ratio vs Altitude
Polarizatoin Ratio
Altitude (m)
A
B
C
PR for 10.0m to 100.0m on July 24 at 500
Polarization Ratio
Scattering Angle
A
B
C

D

Appendix D: Explanation of Subtitles

After each chapter's heading, there is a small subtitle. The point of the subtitles was to not only capture the essence of each chapter but also to add a bit of levity to the work as a whole. The author has noticed that scientific journals offer some of the most boring reading material on the planet mainly in an attempt to appear to be objective and dispassionate. While this author certainly does not advocate slapstick humor to begin appearing in the literature, a few poignant comments judiciously dispersed throughout a work can have more of a memorable impact than the work itself. Here, we wish to explain the origins of the subtitles. They may not mean anything to the reader, but they have significance to the author.

Chapter 1's subtitle is attributed to Emerson. This particular quote rather astonishingly captures the essence of the entire thesis and was considered for a time to be the title of this manuscript. In effect, the quote is a reminder to the reader to stay in balance and never let logic completely supplant emotion. After all, a sunset should be as much appreciated for its beauty as analyzed for its composition.

Chapter 2's subtitle comes from a television show, X-Files. This particular program dealt with conspiracies and the supernatural. In our investigation of the lognormal distribution, we were confronted with conflicting information not only from mathematicians but also from atmospheric physicists. The length and detailed description presented in Chapter 2 resulted from an exhaustive search of the literature and independent analysis in order to put forth a complete and truthful picture of the mathematics of the lognormal distribution. Several times during our investigative research, we mused that there was actually some dark and secret agency that did not want us to understand the lognormal distribution.

Chapter 3's subtitle is paraphrased from Confucius. It is a very simple yet direct quote that says one must do things on their own rather than simply reading about them. This has particular significance in the scientific community as experiments and equations must be tested and used in order to gain a better appreciation for their significance. Never assume that just because it is written that it is universally true. Although many of the expressions in Chapter 3 are well documented, actually going through the gory details and derivations proved to be beneficial in establishing a strong foundation for the work as a whole.

Occam's principle states that the simplest explanation is generally the correct one. While we have taken the simplified approach in this thesis, it appears that, in the case of light scattering from atmospheric particles, a more complicated approach may be needed. Chapter 4, while not exhaustive, does serve to show just how vast and complex the atmosphere is.

Chapter 5 is a well-known quote from Arthur C. Clarke. It seemed a rather appropriate quote to use in describing the instruments used in this thesis. However, we do not want to mislead our reader by suggesting our instrumentation exhibited magical properties.

The author of Chapter 6's quote is unknown so giving credit is somewhat difficult. Because of the inordinate amount of time spent on analyzing the data and the myriad of possible solutions to pursue, this quote is extraordinarily appropriate to Chapter 6.

Chapter 7's quote is not attributed to anyone but is a general comment on research in general. Anyone who spends time researching journal articles knows how convoluted research can be.

The final quote given in Chapter 8 is attributed to a friend of the author.

VITA

Edward J. Novitsky earned a B.S. from The Pennsylvania State University, an M.S. from Drexel University and a Ph.D. from The Pennsylvania State University. His primary research interests are in optics and he continues to pursue topics within this area that are interesting to him and have widespread practical applications.